
Imperial College London
Department of Chemistry

Design and evaluation of organic semiconductors for spintronic, singlet fission and bioelectronic device applications



Adam Marks

Submitted: 4th May 2020

Submitted in partial fulfilment of the requirements for the degree of
Doctor of Philosophy in Chemistry

DECLARATION OF ORIGINALITY AND COPYRIGHT

The work contained within this thesis is original work carried out by the author or in collaboration with acknowledged co-workers. The work of others' is mentioned throughout to support the original data and is referenced to the best knowledge of the author when deemed appropriate.

The copyright of this thesis rests with the author. Unless otherwise indicated, its contents are licensed under a Creative Commons Attribution-Non-Commercial 4.0 International Licence (CC BY-NC). Under this licence, you may copy and redistribute the material in any medium or format. You may also create and distribute modified versions of the work. This is on the condition that: you credit the author and do not use it, or any derivative works, for a commercial purpose. When reusing or sharing this work, ensure you make the licence terms clear to others by naming the licence and linking to the licence text. Where a work has been adapted, you should indicate that the work has been changed and describe those changes. Please seek permission from the copyright holder for uses of this work that are not included in this licence or permitted under UK Copyright Law.

ACKNOWLEDGEMENTS

Firstly, I must thank Professor Iain McCulloch for supporting me throughout my eight years at Imperial. From personal tutor to academic supervisor Iain has been assisting me from day one, all the way back in September of 2012. I am eternally grateful for all his continued supervision, knowledge and advice. Secondly, I would like to thank my entire family, especially my Mum, Dad, brother Dan and his girlfriend Serina, not only for their unyielding belief in me but for their constant love and support. I certainly would not have made it this far without them and I will be forever in their debt. Jess I don't know how or why you put up with me throughout the final stages of my PhD, but I can assure you I would not have been able to finish this without you. I will never be able to thank you for all you have done; you continue to inspire me every single day.

I must thank all my peers to whom I am forever indebted for their continued support, especially Max Moser for the constant encouragement, advice and importantly laughs. Sophie Griggs and Flo Moruzzi for lighting up the room with your radiant smiles and positivity. Mark Little and Cameron Jellett for teaching me all that I know and always being a voice of reason, I will never forget that '*you can do it!*'. James Ponder and Karl Thorley thank you for all the invaluable advice and intellectual discussions. Iuliana Maria for holding the group together and putting up with me since the first day of undergrad. Also thank you to Nadia Hoyas Perez, Ben Wilner, Andrew Wandsworth, Matt Bidwell, Maxime Babics, Helen Bristow, Ada Onwubiko, Alex Giovannitti and Sam Cryer for your friendship and support. Thank you to all the Heeney group, from Martin to the dynamic duos of Martina & Simon, Qiao & Tao or Notina & Charlotte, Tom, Simeng and Florian, your encouragement is greatly appreciated. Thank you to all members of the department who kept Harwood and now MSRH ticking over, especially

Oswald for your welcome distractions in the lab, Steve for the countless laughs, without your hard work my research would simply not be possible and finally Pete for all your insight and knowledge. Jenny Nelson, Hang Yu and Sachetan Tuladhar thank you for your patience and enthusiasm, **Chapter 5** is dedicated to you. To those from KAUST; Sahika Inal, Rawad Hallani, Weiyuan Du, Xingxing Chen, Rajendar Sheelamanthula and Tania Hidalgo thank you for offering your expertise and working on my materials, without you this thesis would be incomplete. Thank you to all members of the ERC Synergy project especially Henning Sirringhaus, Deepak Venkateshvaran, Sam Schott, Remmington Carey and Angela Wittmann without your knowledge, measurements and understanding **Chapter 3** would not exist. To my Australian friend Murad Tayebjee and Chanakarn Phansa (Rao group) your assistance, measurements and advice has been priceless, I sincerely thank you both. To those from Northwestern; Jonathan Rivnay, Bryan Paulsen, Ruiheng Wu and Xudong Ji, thank you for fabricating devices and analysing my polymers. A special thank you to Suhao Wang (Fabiano group) for your heartfelt messages and meticulous thermoelectric measurements. To those that I have not named you are not forgotten, and my journey would not have been possible without your understanding and support throughout the years.

Yesterday was history, tomorrow is a mystery, today is a gift, that is why it's called the present

- Grand Master Oogway, Kung Fu Panda.

Grands, this one is for you...

ABSTRACT

Organic semiconductors combine the attractive properties of common plastics with electrical conductivities typical of metals, enabling their use across a wide range of emerging technologies. The synthetic utility of these materials allows the optoelectronics to be manipulated towards a diverse set of applications, ranging from photovoltaics to biological sensors. As such this thesis spans across four unique disciplines with organic semiconductors acting as the underlying motif throughout.

Chapter 2 focuses on singlet fission, a third-generation photovoltaic technology, aiming to surpass the Shockley-Queisser limit of solar cell efficiency. The synthesis of an original series of indenofluorene dimers, separated by a phenyl bridging unit, is presented herein. The complex optoelectronics of this system were then investigated using transient absorption spectroscopy to elucidate the feasibility for singlet fission. The indenofluorene backbone is further investigated in **Chapter 3** as a spin sink material, demonstrating the versatility of this backbone. The quinoidal nature of this unit, alongside the corresponding thiophene-containing analogue of indacenodithiophene and a series of higher biradical character materials are synthesised and probed within a unique spintronic device, specifically the ferromagnetic linewidth broadening experiment.

Chapter 4 moves towards the area of organic semiconducting polymers, presenting the effects of sidechain manipulation on the mode of operation for a series of novel *n*-type polymers containing a fused aromatic backbone and ethylene glycol solubilising chains. These fused systems, synthesised using a metal catalyst free Aldol polycondensation, show excellent ambient stability and promise as semiconductor materials in both thermoelectric devices and organic electrochemical transistors (OECTs). Complementary to the *n*-type OECT channel materials in **Chapter 4**, a series of *p*-type materials is showcased in **Chapter 5**, investigating

ABSTRACT

the effect of hybrid polarity (alkyl and ethylene glycol based) sidechains on OECT device performance. The four disciplines detailed herein are just a sampling of the versatility of organic semiconducting materials.

TABLE OF CONTENTS

DECLARATION OF ORIGINALITY AND COPYRIGHT.....	i
ACKNOWLEDGEMENTS	ii
ABSTRACT	iv
TABLE OF CONTENTS	vi
LIST OF ABBREVIATIONS	xi
CHAPTER ONE: INTRODUCTION.....	1
1.1 SEMICONDUCTIVITY & BAND STRUCTURE.....	2
1.2 CHARGE TRANSPORT & ENERGY LEVELS.....	3
1.3 ORGANIC SEMICONDUCTOR DEVICES.....	5
1.3.1 ORGANIC SOLAR CELL DEVICES.....	6
1.3.2 ORGANIC FIELD EFFECT TRANSISTOR (OFET).....	8
1.3.3 ORGANIC ELECTROCHEMICAL TRANSISTOR (OECT).....	11
1.4 ORGANIC SEMICONDUCTING POLYMERS	14
1.4.1 DONOR-ACCEPTOR COPOLYMERS	17
1.4.2 SYNTHESIS OF CONJUGATED POLYMERS	18
1.4.3 BANDGAP ENGINEERING	20
1.4.4 SOLUBILISING SIDECHAINS	22
1.4.5 ETHYLENE GLYCOL BASED SIDECHAINS.....	24
1.5 ORGANIC BIOELECTRONICS	26
1.6 DOPING, CONDUCTIVITY & THERMOELECTRICS.....	27

TABLE OF CONTENTS

1.6.1	<i>p</i> -TYPE DOPING	29
1.6.2	<i>n</i> -TYPE DOPING	31
1.6.3	CONDUCTIVITY.....	32
1.6.4	THERMOELECTRICS.....	33
1.7	OPTOELECTRONICS.....	35
1.7.1	SINGLET FISSION	36
1.7.2	DESIGNING SINGLET FISSION CHROMOPHORES	39
1.8	OUTLINE.....	40
	CHAPTER TWO: SINGLET FISSION MATERIALS.....	43
2.1	ABSTRACT	44
2.2	INDENOFUORENE (IDF) BACKBONE	44
2.3	DESIGN RATIONALE FOR SINGLET FISSION	48
2.4	Sn^{II}-MEDIATED REDUCTIVE DEAROMATISATION.....	53
2.5	DX-IDF SYNTHESIS & CHARACTERISATION.....	54
2.6	INDENOFUORENE MONOMER SYNTHESIS	59
2.7	INDENOFUORENE DIMER SYNTHESIS.....	61
2.8	INDENOFUORENE DIMER RESULTS.....	63
2.9	CONCLUSIONS.....	71
	CHAPTER THREE: SPINTRONIC MATERIALS	72
3.1	ABSTRACT	73
3.2	SPIN CURRENTS.....	73
3.3	FERROMAGNETIC RESONANCE LINEWIDTH BROADENING	75
3.4	BIRADICAL CHARACTER	78

3.5	DX-IDF DERIVATIVES	79
3.6	DX-IDT	82
3.7	INCREASING BIRADICAL CHARACTER.....	86
3.7.1	ATTEMPTED SYNTHESIS OF DIINDENO-CHRYSENE TARGET.....	87
3.7.2	ATTEMPTED SYNTHESIS OF DIINDENO-PYRENE TARGET	93
3.7.3	DIINDACENODITHIOPHENE[<i>b,i</i>]ANTHRACENE TARGET	95
3.8	DIAnDX SYNTHESIS & CHARACTERISATION	99
3.9	QUINOIDAL NON-FULLERENE ACCEPTOR	108
3.10	QUINOIDAL POLYMER SERIES.....	115
3.11	CONCLUSIONS.....	122
CHAPTER FOUR: <i>n</i>-TYPE POLYMER SERIES		123
4.1	INFORMATION AND CREDITS	124
4.2	ABSTRACT	124
4.3	BACKGROUND & MOTIVATION	125
4.4	ACID-CATALYSED ALDOL POLYCONDENSATION.....	127
4.5	BISISATIN SYNTHESIS	129
4.6	BISOXINDOLE SYNTHESIS	131
4.7	N-GLYCOLATION	133
4.8	BISOXINDOLE MONOMERS	139
4.9	POLYMER SYNTHESIS	143
4.9.1	AM413: BRANCHED GLYCOL-LINEAR C ₁₂ ALKYL	144
4.9.2	AM424: BRANCHED GYCOL N _p -LINEAR ALKYL An.....	145
4.9.3	AM431: BRANCHED GLYCOL-LINEAR C ₁₆ ALKYL	146
4.9.4	AM463: LINEAR GLYCOL-LINEAR C ₁₂ ALKYL.....	147

TABLE OF CONTENTS

4.9.5	AM464: BRANCHED GLYCOL-LINEAR GLYCOL.....	149
4.9.6	AM467: LINEAR GLYCOL-BRANCHED ALKYL.....	150
4.9.7	AM520: BRANCHED GLYCOL-LINEAR C ₁₀ ALKYL	151
4.9.8	PgNaN & PgNgN.....	153
4.10	RESULTS & DISCUSSION	155
4.10.1	OPTOELECTRONIC PROPERTIES	156
4.10.2	GIWAXS MORPHOLOGICAL STUDY	157
4.10.3	OECT RESULTS	160
4.10.4	THERMOELECTRIC PERFORMANCE.....	164
4.10.5	ELECTRICAL CONDUCTIVITY.....	165
4.10.6	SEEBECK COEFFICIENT & POWER FACTOR.....	167
4.10.7	DISCUSSION.....	168
4.11	CONCLUSION.....	170
	CHAPTER FIVE: <i>p</i>-TYPE POLYMER SERIES	172
5.1	INFORMATION AND CREDITS.....	173
5.2	BACKGROUND & MOTIVATION	173
5.3	SYNTHESIS.....	175
5.3.1	MONOMER SYNTHESIS	175
5.3.2	p(gC _n T ₂ -T) POLYMER SYNTHESIS	181
5.3.3	p(gC _n T ₂ -TT) POLYMER SYNTHESIS.....	182
5.4	RESULTS & DISCUSSION.....	184
5.4.1	p(gC _n T ₂ -T) OPTOELECTRONICS	184

5.4.2	p(gC _n T2-TT) OPTOELECTRONICS	188
5.4.3	GIWAXS MORPHOLOGICAL STUDY	192
5.5	OECT DEVICE PERFORMANCE.....	195
5.5.1	SPECIFIC CAPACITY	196
5.5.2	ELECTRICAL IMPEDANCE SPECTROSCOPY (EIS).....	197
5.5.3	p(gC _n T2-T) TRANSISTOR RESULTS	198
5.5.4	p(gC _n T2-TT) TRANSISTOR RESULTS.....	202
5.5.5	STABILITY MEASUREMENTS	204
5.6	CONCLUSION.....	206
	CHAPTER SIX – EXPERIMENTAL.....	208
6.1	METHODS & MATERIALS	209
6.1.1	GENERAL	209
6.1.2	ELECTROCHEMICAL CHARACTERISATION.....	209
6.1.3	THERMOELECTRIC: CONDUCTIVITY & SEEBECK MEASUREMENTS	210
6.1.4	TRANSISTOR FABRICATION & ANALYSIS	211
6.2	CHAPTERS TWO & THREE SYNTHESIS & CHARACTERISATION.....	212
6.3	CHAPTER FOUR SYNTHESIS & CHARACTERISATION.....	271
6.4	CHAPTER FIVE SYNTHESIS & CHARACTERISATION.....	327
	BIBLIOGRAPHY	413

**LIST OF
ABBREVIATIONS**

Abbreviation	Full Term
An	Anthracene
DCM	Dichloromethane
DFT	Density Functional Theory
DMF	Dimethylformamide
DPP	Diketopyrrolopyrrole
DSC	Differential Scanning Calorimetry
EA	Electron Affinity
EIS	Electrical Impedance Spectroscopy
FMR	Ferromagnetic Resonance
GIWAXS	Grazing Incidence Wide-Angle X-Ray Scattering
GPC	Gel-Permeation Chromatography
HOMO	Highest Occupied Molecular Orbital
I	Current
IDF	Indenofluorene
IDT	Indacenodithiophene
IDTBT	Poly(indacenodithiophene-benzothiadiazole)
IP	Ionisation Potential

LIST OF ABBREVIATIONS

LDA	Lithium Diisopropylamide
LUMO	Lowest Unoccupied Molecular Orbital
MALDI	Matrix-Assisted Laser Desorption/Ionization
M_n	Number Average Molecular Weight
M_w	Weight Average Molecular Weight
NBS	N-bromosuccinimide
NDI	Naphthalenediimide
NFA	Non-fullerene Acceptor
NMR	Nuclear Magnetic Resonance
Np	Naphthalene
OECT	Organic Electrochemical Transistor
OEG	Oligo(ethylene glycol)
OFET	Organic Field-Effect Transistor
OLED	Organic Light-Emitting Diode
OPV	Organic Photovoltaic
P3HT	Poly(3-hexylthiophene-2,5-diyl)
PCE	Power Conversion Efficiency
$\text{Pd}(\text{PPh}_3)_4$	Tetrakis(triphenylphosphine)palladium(0)
PDI	Polydispersity Index
PESA	Photoelectron Spectroscopy

LIST OF ABBREVIATIONS

SF	Singlet Fission
TAS	Transient Absorption Spectroscopy
THF	Tetrahydrofuran
TLC	Thin-Layer Chromatography
TT	Thieno[3,2-b]thiophene
T2	2,2'-bithiophene
UV-Vis	Ultraviolet–Visible Spectroscopy
V	Voltage
XRD	X-ray diffraction
XRR	X-ray reflectivity
λ	Wavelength
γ_0	Biradical Character
μ	Mobility

CHAPTER ONE: INTRODUCTION

1.1 SEMICONDUCTIVITY & BAND STRUCTURE

In order to describe the nature of a semiconductor the electronic energy band concept must be described first.¹ Chemical bonding requires a degree of electron delocalisation which is propagated by molecular orbitals (MOs). Low lying (dominantly bonding) MOs come together to form the *valence band*, which will be thought of as analogous to the highest occupied molecular orbital (HOMO). Whereas the high energy (dominantly anti-bonding) unoccupied MOs group to form the *conduction band*, referred to as the lowest unoccupied molecular orbital (LUMO). Furthermore, the HOMO can be roughly estimated as the ionisation potential (IP); the energy required to remove a valence electron from this MO. Similarly, the LUMO can be approximated as the electron affinity (EA); the energy released when an electron is added to form a negative ion.²

The separation between these two states (HOMO \rightarrow LUMO) is known as the *bandgap*.³ For an organic material the optical bandgap is equal to the energy associated with exciton (bound electron-hole pair) formation. The electrical bandgap also includes the energy needed to separate excitons into free charges (exciton binding energy $\sim 0.1 \rightarrow 0.3$ eV). The average level to which these MOs are occupied, by electrons, is called the *Fermi level*, for a pristine undoped semiconductor the Fermi level resides equidistant between the conduction and valence bands. In turn the energy difference between the Fermi level and vacuum is known as the work function *i.e.* the energy needed to remove an electron.⁴

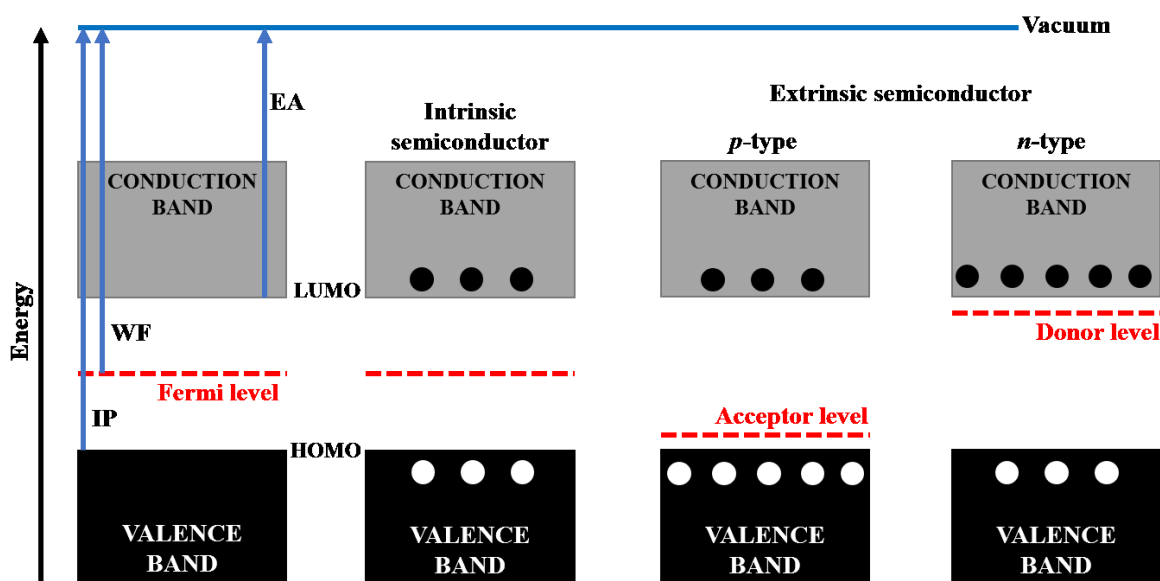


Figure 1. Semiconductor band structure and energy band diagrams for pristine, *p*- and *n*-doped semiconductors, respectively. Black dots represent electrons, white dots are electron holes.

Extrinsic semiconductors, generally referred to as *doped* depend on external dopants adding or removing valence electrons which can be achieved by chemical or electrochemical means. *p*-Type dopants are electron acceptors, withdrawing electrons from the valence band (HOMO), resulting in a net excess of hole charge carriers. The opposite is true for *n*-type dopants which are electron donors and supply electrons into the conduction band (LUMO) resulting in a net excess of negative charge carriers. Conceptually this can be thought of as shifting the Fermi level towards the valence band (*p*-type) or conduction band (*n*-type) respectively.⁵

1.2 CHARGE TRANSPORT & ENERGY LEVELS

A key quantity that characterises electronic charge transport is the carrier mobility (μ) and is used as the principle measure of an organic semiconductors (OSCs) performance.⁶ Efficient transport requires electron delocalisation and intermolecular MO overlap, whereby conjugated polymers are a class of materials which satisfy both of these conditions.⁷ For a non-polymeric organic material to operate as a semiconductor there must be sufficient intermolecular π -bonding interactions, as without extensive MO overlap the material will not exhibit band-like

transport. Fortunately, many organic materials are made up of a conjugated backbone, which facilitates charge transport. This can loosely be defined as a chain of sp^2 hybridised atoms, with electron density above and below the plane of a σ -bonded carbon framework. On a chemical level, this manifests itself as alternating single and double bonds, present in a myriad of carbon-based systems.⁵

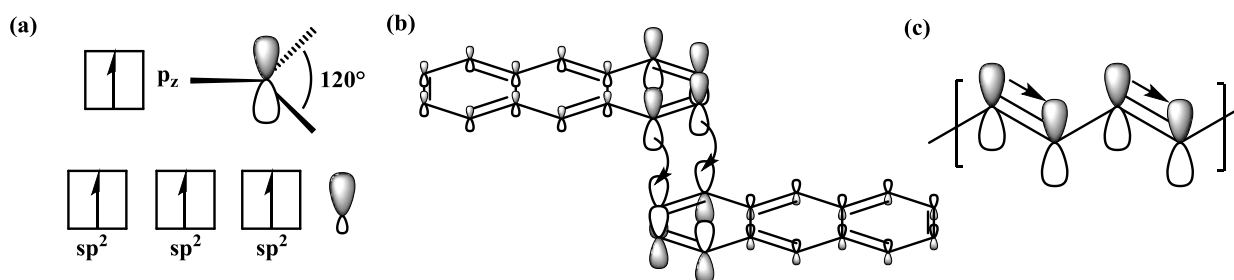


Figure 2. (a) sp^2 hybridisation leading to conjugation (b) charge transport (π -overlap) in small molecule anthracene and (c) charge transport along a conjugated polymer backbone.

The extent of the π -electron delocalisation (conjugation) affects both the electrical conductivity and optical properties. The conjugated segment of an OSC is known as the *chromophore*, as such a polymer can be described as a sequence of chromophores bound together by strong intramolecular interactions. However, most organic semiconductors (including conjugated polymers) have some level of disorder due to the inherently weak intermolecular interactions. This can occur due to either kinks in the polymer backbone or other impurities acting as defects resulting in localised states in the bandgap that can trap charge carriers.⁸ This can be overcome through polymer purification or compensation via doping to fill trap sites.⁹

Organic semiconductors are separated into three main categories depending on how they transport charges. Firstly, *p*-type semiconductors transport charge by positive electron holes conversely, *n*-type materials transport charge via negative electrons.^{1,10} Ambipolar semiconductors marry these concepts together and can transport both electrons and holes.¹¹ A material displays *p*- or *n*-type behaviour dependant on how the energy levels relate to the work

function (defined as the energy required to remove an electron from the Fermi level)¹² of the device electrodes. *p*-Type materials have a valence band close to the Fermi level of the electrode, whereas *n*-type materials have a low-lying conduction band. Practically, to optimise performance the HOMO energy level (*p*-type) or LUMO energy (*n*-type) must closely match the work function of the electrode to reduce the charge injection barrier which could limit device performance.

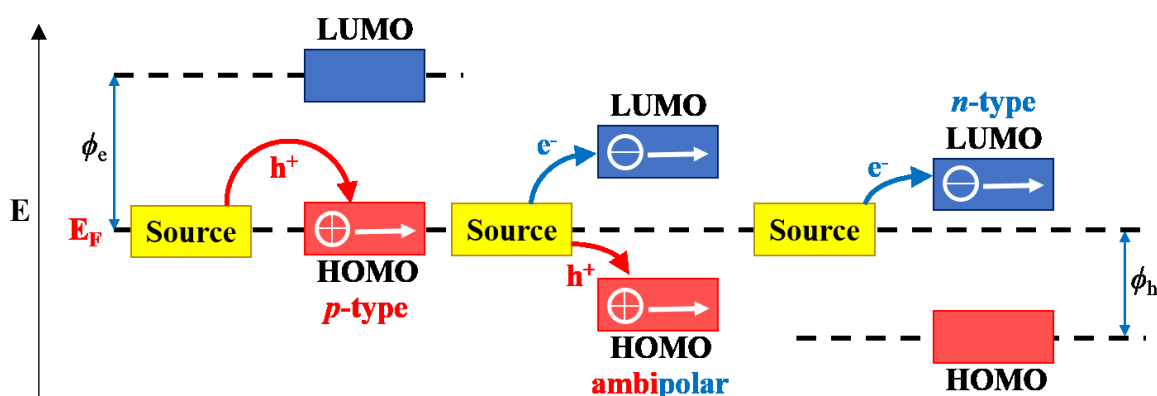


Figure 3. Energy level schematic showing the relationship between the source electrode Fermi energy (E_F) and frontier orbitals of the organic semiconductor. Illustrating the three major categories of charge transport, namely *p*-type, *n*-type and ambipolar. ϕ_e and ϕ_h denote the electron and hole injection barrier heights, respectively.¹³

1.3 ORGANIC SEMICONDUCTOR DEVICES

The versatility of materials with a plethora of electronic energy levels is essential for modern day organic photovoltaic (OPV) devices. In its most simplified form, an OPV device converts incident light ($h\nu$) into electrical energy. A typical device contains a multitude of surface treated photoactive layers (comprised of both a donor and an acceptor) sandwiched between two electrodes. Upon light absorption these photoactive materials convert photons into excitons, leading to electrons being excited from the valence band to the conduction band. The excitons can then diffuse to the donor-acceptor interface, driven by the concentration gradient

differential. Here they separate into holes (positive charge carriers) and electrons (negative charge carriers); these can then be extracted at the corresponding electrodes. The donor material (D) transports holes and donates electrons to the acceptor material (A) which in turn withdraws and transports these electrons.

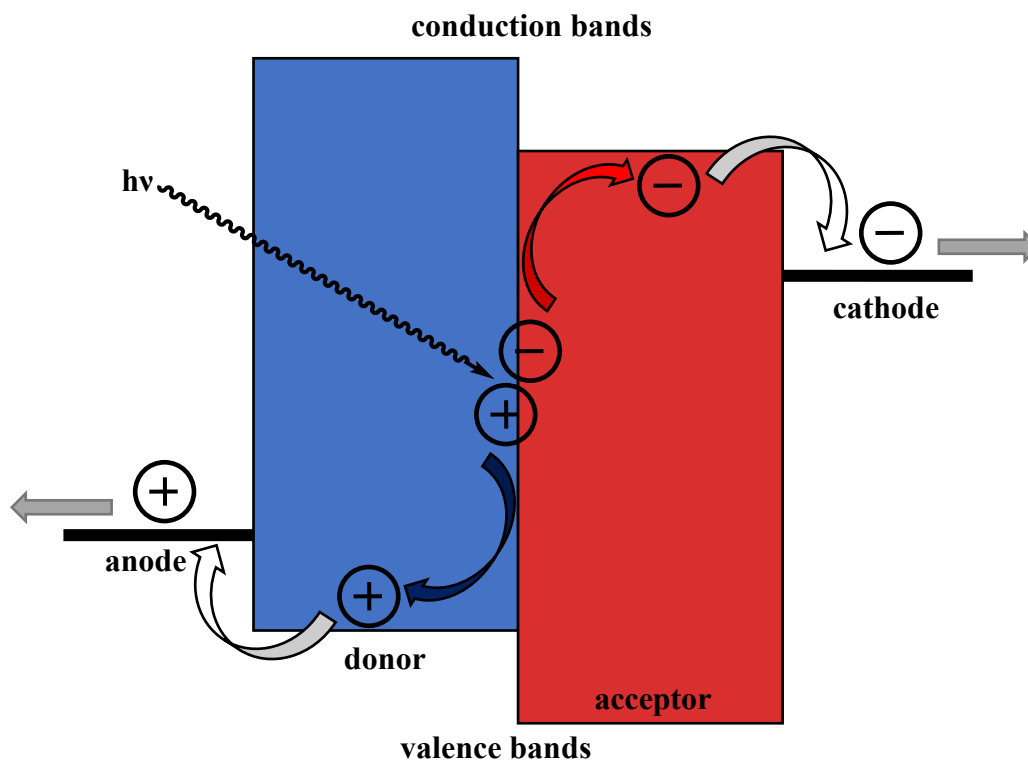


Figure 4. Simplified diagram of a bilayer OPV cell, showing light absorption, exciton generation, charge separation and extraction. In practice, photovoltaic cells are fabricated with multiple layers to act as barriers for current leakage or to increase charge transport or improve light absorption.^{14,15}

1.3.1 ORGANIC SOLAR CELL DEVICES

Bulk heterojunction organic solar cells are another specific example of organic photovoltaic devices which have garnered much interest as an alternative to their inorganic counterparts. These devices consist of a multi-layered structure, much akin to the simple OFET (**Figure 7**) here the active (absorbing) layer is comprised of a donor material (usually a conjugated

polymer) and an acceptor material (often a fullerene derivative *vide infra*). This photoactive layer is sandwiched between the anode electrode and low work functioning cathode.¹⁶ In order to improve both performance and stability an electron transport and hole transport layer are inserted between the cathode and anode interfaces respectively.¹⁶ Again, similarly to OFETs an inverted architecture exists in which the bottom layer acts as the cathode and the top layer as the anode electrode, both architectures are depicted below:

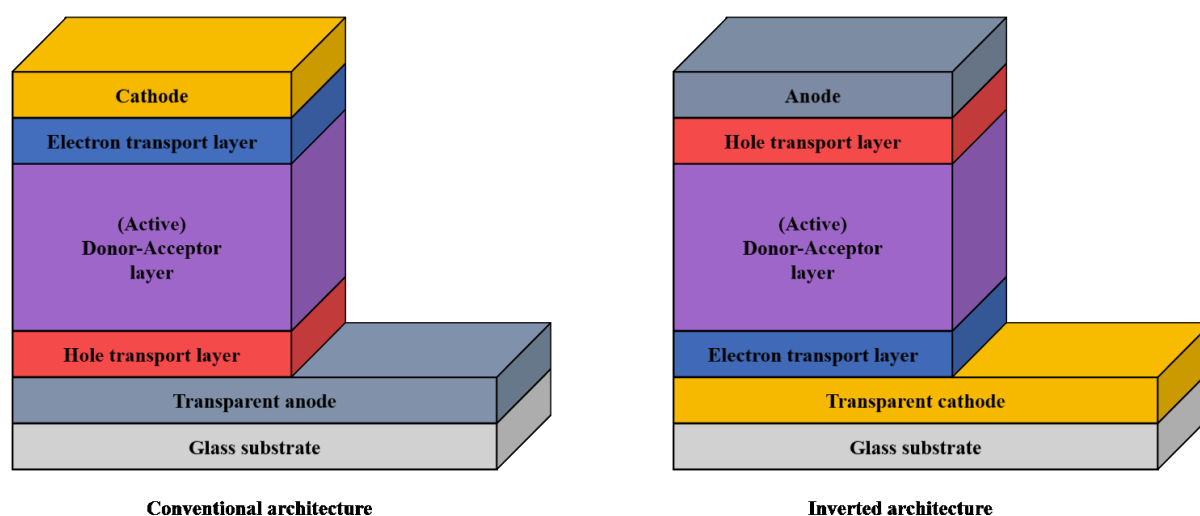


Figure 5. Bulk heterojunction organic solar cells, conventional and inverted architecture where the purple (active) region is a blend of electron donating and acceptor materials.

The vast majority of reported organic solar cells are fabricated with a low-bandgap electron donating polymer in conjunction with a fullerene-based acceptor, namely phenyl- C_{60} -butyric acid methyl ester ($PC_{60}BM$) or indene- C_{60} bisadduct (ICBA). These three-dimensional fullerene cages have multiple advantages and disadvantages; their extremely delocalised LUMO allows for efficient electron transport across the entire surface¹⁶ however the same motif renders some optical transitions forbidden due to the highly symmetric wavefunction. As such fullerenes absorb a very limited number of photons in the UV-visible region, confining most fullerene based solar cells to *p*-type photon excitation (**Figure 6**), where the majority of photons are absorbed by the donor material.

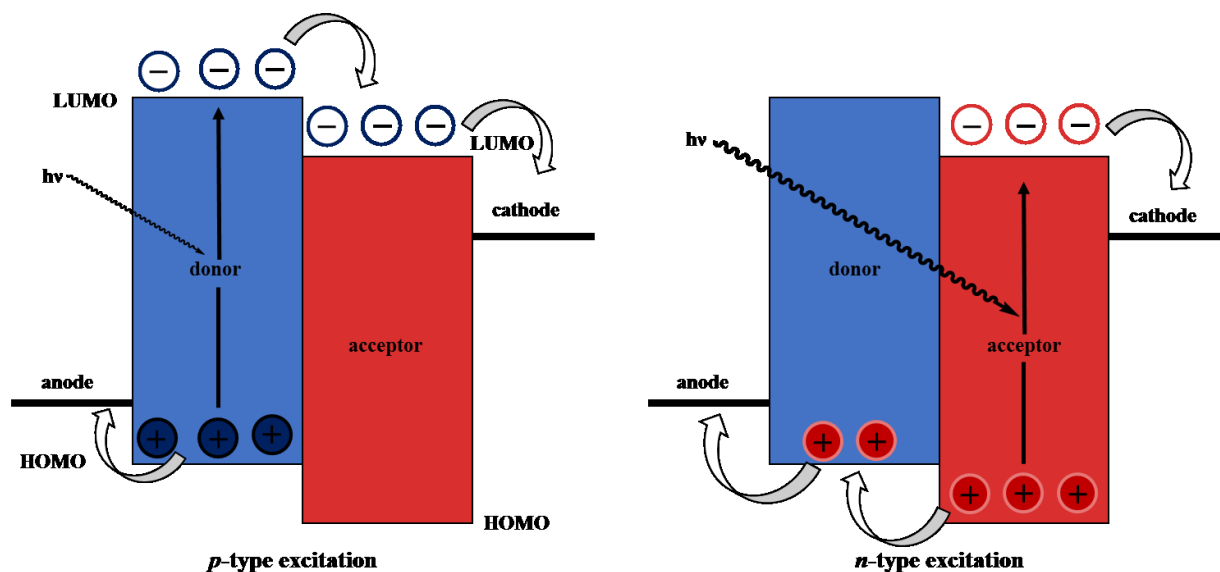


Figure 6. *p*- and *n*-type excitation pathways for organic solar cells.

Whilst fullerene devices have continued to be optimised, they are seen as an ageing class of materials and in recent years have begun to be replaced by bespoke electron accepting materials; non-fullerene acceptors (NFAs). These materials are specifically designed to optimise their transport properties, stability and optical behaviour.¹⁷ The vast majority of NFAs mimic common donor polymers and absorb strongly within the visible region of the solar spectrum. In contrast to fullerenes, upon excitation, the NFA absorbs most of the photons, forming excitons in an *n*-type excitation process (**Figure 6**). Furthermore, if both the NFA and donor polymer absorb in different regions across the UV-visible spectrum the number of photons absorbed increases, maximising the resultant photocurrent.

1.3.2 ORGANIC FIELD EFFECT TRANSISTOR (OFET)

The nature of organic semiconductor materials renders them ideal candidates for *field-effect* transistor operation, where the conductivity of a semiconductor changes due to the application of an external electric field. Thin-film transistors (TFTs) are the most common device architecture for OSC materials. Organic field effect transistors (OFETs) are composed of a thin film of the OSC deposited on top of an insulating dielectric layer with an underlying gate

(needed to apply the electric field) termed bottom-gate geometry or the reverse architecture namely top-gate geometry. Charge injecting source and drain electrodes are defined either on top of the OSC layer (top-contact configuration) or the reverse (bottom-contact configuration).¹⁶ When no voltage is applied between the gate and source electrodes minimal current is measured between the source and drain electrodes, with the device being in its “off” state. The device can then be switched ‘on’ by applying a voltage of the same sign to both the gate and drain electrodes. Application of a voltage at the gate electrode leads to the formation of an electrical double layer at the interface between the dielectric and the OSC, while application of a potential at the drain electrode then sweeps the generated charges across the device. The voltage required to turn the device on is referred to as the threshold voltage (V_{th}) needed to turn the device on for linear and saturation regions of operation.¹¹

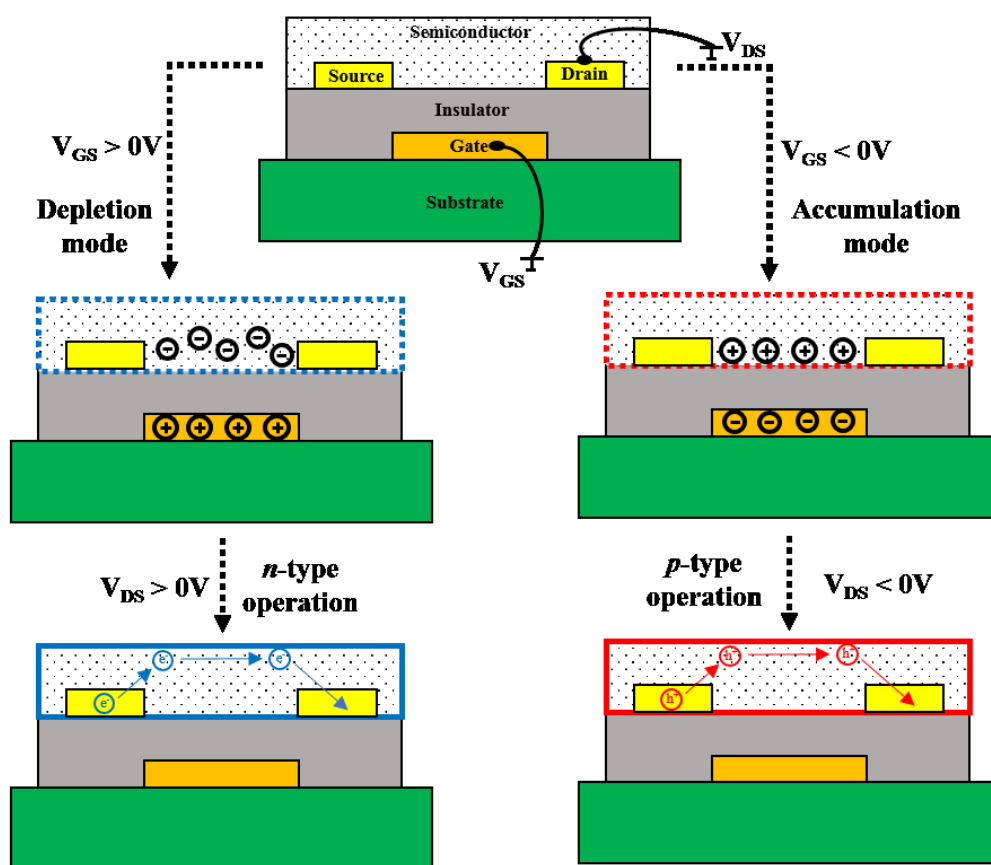


Figure 7. Schematic of bottom-contact, bottom-gate OFET device architecture showing *p*- and *n*-type transistor operation modes, redrawn from Facchetti.¹⁶

The majority of OFETs research has been conducted on *p*-type operation OSCs, where holes are the majority charge carriers in the conductive channel between the source and drain electrodes which occurs in *accumulation* mode by applying a negative gate bias V_{GS} and V_{DS} . The opposite is true when a positive V_{GS} and V_{DS} is applied, electrons become mobile and the device is in *depletion* mode, *n*-type operation. In order to achieve optimal charge transport OSC materials, specifically for OFETs, materials are required to have a high carrier mobility and hence an exceptional purity to avoid detrimental charge trapping effects.¹¹

Once the threshold voltage (V_{th}) has been overcome, as the gate voltage increases the source-drain current also increases proportionally, here the device is acting in the linear regime. After a certain gate voltage, the “*pinch-off*” will occur where additional charge accumulation stops, observed as a plateauing in the output curve (I_D vs V_D). This is known as the saturation regime where the source-drain current is independent of the gate voltage, represented as:

$$I_{D,sat} = \frac{W}{2L} \mu_{sat} C_d (V_G - V_{th})^2 \quad (1)$$

where $I_{D,sat}$ is the source-drain current, W is the channel width, L is the channel length, μ_{sat} the charge carrier mobility, C_d the capacitance per unit area of the dielectric, V_G is the gate voltage and V_{th} the threshold voltage, respectively. As such, plotting the square root of the saturation current against gate voltage results in a straight line (**Figure 8**). The mobility can then be extracted from the slope of the line, while the threshold voltage corresponds to the extrapolation of the line at zero current. In the saturation regime the device transconductance (g_m) is defined as the derivative of the drain current with respect to the gate voltage and is written as:

$$g_m = \frac{\partial I_D}{\partial V_G} = \frac{W}{L} \mu_{sat} C_d (V_G - V_{th}) \quad (2)$$

Charge carrier mobility of the OSC layer is the main figure of merit used for OFET devices, formally described as a measure of how fast charge carriers can transport through the OSC

when an electric field is applied across the channel.¹¹ Owing to the device architecture, described above, the mobility extracted from an OFET is related to charge movement at the dielectric interface and may not be representative of the OSC mobility in the bulk.

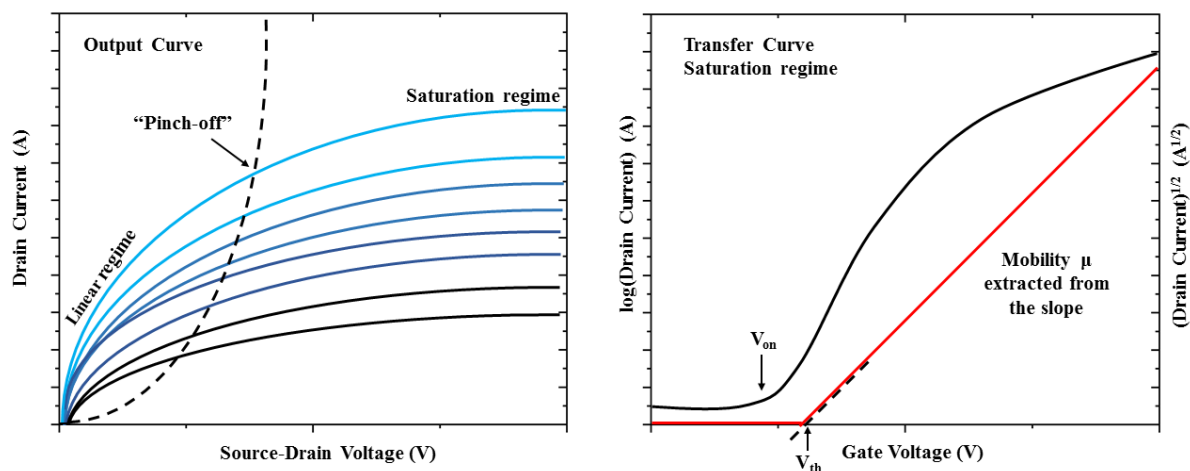


Figure 8. Representative illustration of characteristic OFET output curve (left) showing the drain current as a function of source-drain voltage at varied gate voltages. Transfer curve (right) of the saturated regime showing the drain current (on a semi-log scale) as a function of gate voltage, showing the linear dependence of the square root of the drain current. Turn on voltage (V_{on}), threshold voltage (V_{th}) and mobility can be extracted from these curves.¹¹

1.3.3 ORGANIC ELECTROCHEMICAL TRANSISTOR (OECT)

A typical OFET contains a solid insulating dielectric layer (**Figure 7**). Replacing the dielectric with an electrolyte facilitates mobile ion transport and under the influence of an electric field charges can accumulate at the electrolyte-semiconductor interface. This modified device architecture is known as an electrolyte-gated organic field effect transistor (EGOFET).¹⁸ If the channel material is permeable to ions, charges no longer accumulate at the interface and instead can permeate into the semiconducting layer. This concept was first presented as a basic organic electrochemical transistor (OECT) in 1984 by White, Kittlesen and Wrighton.¹⁹ Since then multiple iterations, optimisations and modifications have been employed to fabricate OECT devices.²⁰ However, the distinguishing feature remains unchanged, an OECT is not limited by

interface accumulation and ions can permeate throughout the entire volume. This permeation process couples together both ionic and electronic transport, an essential combination for bioelectronic applications.²¹

Similarly to OFET devices, OECTs can operate in accumulation (where the active material is semiconductor e.g. a conjugated polymer and the device turns “on” when a gate voltage is applied)²² or in depletion mode (where the active material is a conductive polymer and the device is “on” at no external bias).²³ Again for both devices an important figure of merit is the transconductance (g_m), which within the saturation regime ($V_D > V_G - V_{th}$) can be represented as²⁴:

$$g_m = \left(\frac{Wd}{L}\right) \mu C^* (V_{th} - V_G) \quad (3)$$

defined by the width (W), channel length (L), charge carrier mobility (μ), volumetric capacitance (C^*), threshold voltage (V_{th}) and gate voltage (V_G). Indeed, the charge carrier mobility, threshold voltage and volumetric capacitance are all important device performance parameters, the ability to extract this data is detailed in the literature.²³ This can be collapsed to **Equation (2)** in a monolayer FET device as the product of d and C^* is C_d the capacitance per unit area.

It should be noted that owing to the motion of both electronic and ionic charges the mobility cannot be extracted in the same manner as for OFET devices. For this reason, transconductance is often reported as the OECT device performance figure of merit. However, reporting standards were not well established until a paper titled “*benchmarking organic mixed conductors for transistors*” was published by Inal, Malliaras and Rivnay in 2017.²⁵ Here, they state that whilst the g_m value is a useful measure for OECT steady-state device performance it is not an accurate representation of the mixed conductor performance. They propose that the

$[\mu C^*]$ product is the more appropriate figure of merit for OECT devices, including the only geometry- and bias-independent terms.

$[\mu C^*]$ encapsulates the mixed conduction ionic and electronic transport properties, the mobility term (μ) represents the electronic charge carrier mobility within the channel. C^* is a measure of the capacitance of the bulk material, a volumetric term, which combines the ionic penetration/transport properties with the material's ability to store electronic charges. This value can be recorded independently by performing electrochemical impedance spectroscopy (EIS) measurements, which can then be fit to a simplified equivalent $R_S(R_P||C)$ circuit (see **Methods Section 6.1**) where R_S is the electrolyte resistance, R_P and C describe the resistance and capacitance of the polymer, respectively. Taking **Equation (3)** and plotting g_m as a function of $Wd/L \times (V_{th} - V_G)$ the product $[\mu C^*]$ can be extracted from the slope. It should be emphasised that many materials do not show a direct match between product $[\mu C^*]$ and the independent summation of $[\mu][C^*]$, with the latter generally underestimated.²⁵ As such, the $[\mu C^*]$ term will be used to compare materials within **Chapters 4 & 5** to other benchmarked literature OECT devices.

The operation of an *n*-type accumulation mode OECT is illustrated below (**Figure 9**). The OSC is reduced when a positive gate voltage is applied as electrons are injected into the OSC and cations from the electrolyte migrate into the bulk OSC to compensate for the negative charges accumulating along the polymer backbone. This is equivalent to a volumetric *n*-doping of the OSC which facilitates electron transport towards the drain electrode. Finally, the *n*-type doped OSC is oxidised back to its neutral form when the gate voltage is reversed, and cations migrate back into the electrolyte out of the bulk.

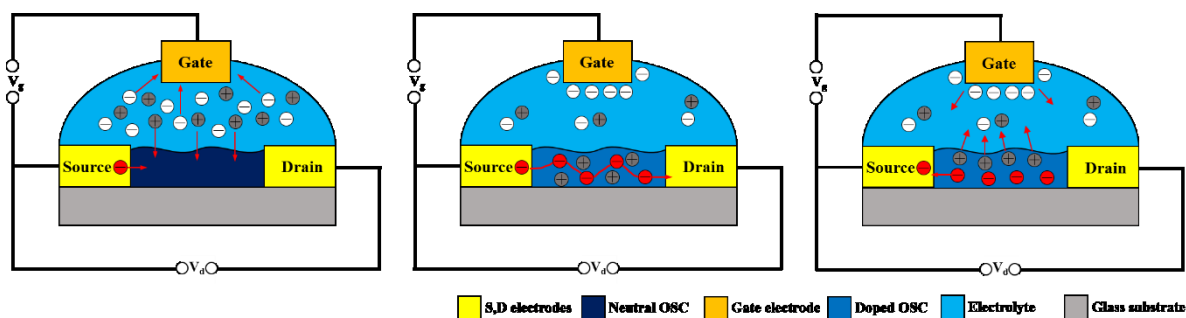


Figure 9. Operation of a *n*-type accumulation mode OECT (a) electron injection from the source upon applying a positive gate bias with cations migrating into the film, (b) transport through the *n*-type doped OSC from source to drain, (c) reversal of the gate bias leading to oxidation of the *n*-type doped OSC, electron collection at the source and migration of the cations out of the active layer (i.e. switching).

1.4 ORGANIC SEMICONDUCTING POLYMERS

OSCs are usually comprised of conjugated polymers, the first of which, polyacetylene, was reported by Shirakawa in 1967.²⁶ These materials have become common place in OFET, OECT, solar cell and thermoelectric devices, all of which will be discussed in the context of this thesis. Following the sp^2 -hybridised bonding regime (**Figure 2**) the resultant alternating single bond–double bond structure in the conjugated backbone results in 1-dimensional delocalisation of the π -electrons, forming a filled valence band (π -band) and empty conduction bands (π^* -band).⁵ The energy difference between these two bands is defined as the bandgap, which generally ranges from 1 \rightarrow 4 eV for a semiconductor.²⁷ For conjugated polymers the magnitude of the bandgap and the energy levels of the HOMO and LUMO are the most important characteristics for determining the optoelectronic properties, heavily influencing their respective device performance.

As discussed in **Section 1.2**, conjugated polymers are bonded together through strong intramolecular interactions but exhibit weaker intermolecular electronic interactions due to poorer electronic wavefunction overlap between adjacent chains. This manifests in the ground

state as a localisation of the wavefunction to a single chromophore. These effects combine to facilitate conjugated polymers holding an excess of charge, arising from oxidation, reduction, charge injection (doping) or photoinduced charge transfer. This additional charge, formally a quasi-particle, is defined as a polaron which can either be positive (**Figure 10**) or negative (**Figure 11**) depending on the charge carrier, a hole or electron respectively.²⁸

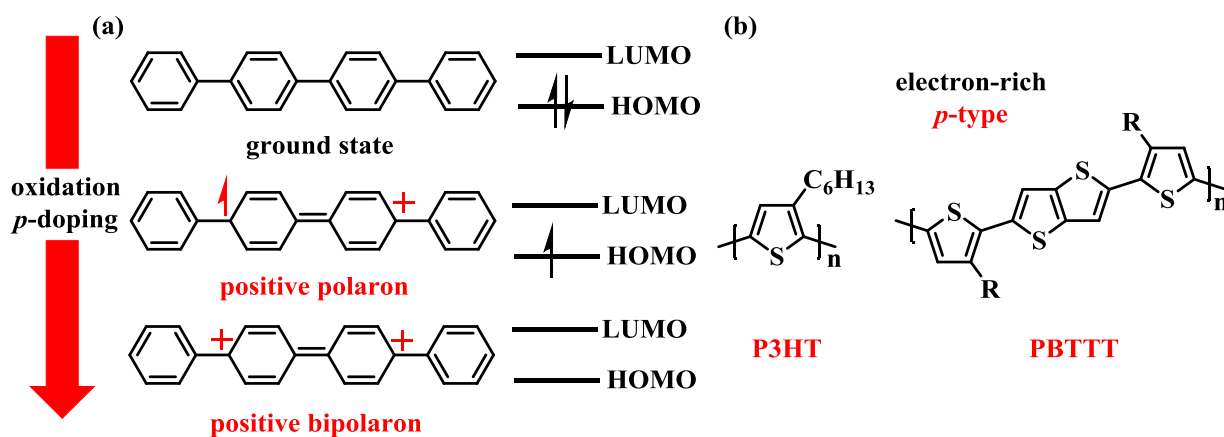


Figure 10. (a) Structural changes of poly(*p*-phenylene vinylene) and the resultant HOMO and LUMO level occupancies for the neutral (ground state) and positively charged ((bi)polaron) excited states.⁴ (b) Electron-rich thiophene based *p*-type polymers **P3HT**²⁹ and **PBTTT**³⁰.

Most π -conjugated polyaromatic materials contain electron-rich aromatic cores, with relatively high HOMO levels thus operating as *p*-type semiconductors.⁶ Over the last 40 years the thiophene ring has become one of the most popular building blocks for polymer OFET devices, with the most famous thiophene based material to date being poly(3-hexylthiophene) (**P3HT**), an alkylated polythiophene which has been synthetically manufactured to adopt a regioregular structure.²⁹ The field of OSCs has been dominated by *p*-type materials, with multiple approaches to improve their stability and performance being extensively investigated. These strategies range from side chain engineering to studying the torsion of the backbone and introducing conjugated units into the polymer backbone.³¹ Employing these rules, work within our group raised the HOMO energy (~ 0.3 eV cf. **P3HT**), by delocalising electrons along the

extended aromatic polymer chain, creating a series of copolymers based on thieno[3,2-*b*]thiophene (TT) and thiophene rings namely **PBTTT**, enhancing the charge carrier mobility through the highly organised morphology imparted by interdigitation of the sidechains.³⁰

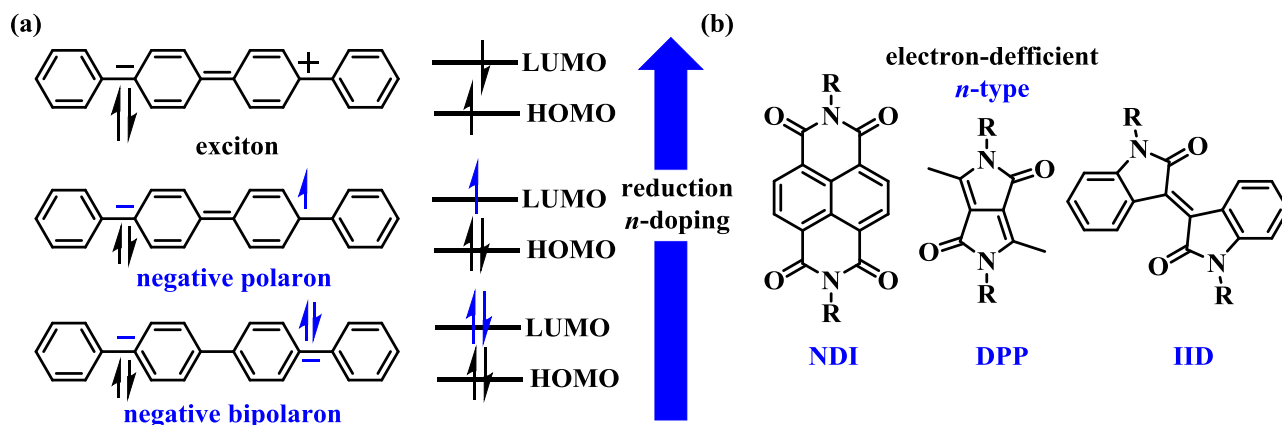


Figure 11. (a). Structural changes of poly(*p*-phenylene vinylene) and the resultant HOMO and LUMO level occupancies for the neutral (exciton) and negatively charged ((bi)polaron) excited states.⁴ (b) Electron-deficient building blocks; naphthalenediimides (**NDI**)³², diketopyrrolopyrrole (**DPP**)³³ and isoindigo (**IID**)³⁴.

The development of *n*-type OSCs has historically lagged behind their *p*-type counterparts. Theory and experiment has shown this is due to the inherent ambient instability of electron transporting materials, during device operation and not due to alternate transport mechanisms compared to hole carriers.³⁵ This instability arises if a material has a high LUMO energy (or low electron affinity) as materials with populated LUMOs (π -radical anions) can be readily oxidised, trapping or annihilating the injected electrons through ambient reactions with O₂ and H₂O.¹³ It was reasoned that in order for ambient atmospheric stability *n*-type organic semiconductors should exhibit a LUMO energy deeper than ~ -4.0 eV, to avoid unwanted H₂O reduction and O₂ oxidation, respectively.³⁶ These requirements have been met, for numerous examples,³⁷ generally by utilising electron deficient units or through the inclusion of electron-withdrawing functionality. Common electron-deficient building blocks include

naphthalenediimides (NDI)³², diketopyrrolopyrrole (DPP)³³ and isoindigo (IID)³⁴. Alternatively the electron-density on aromatic building blocks can be further modulated by the introduction of heteroatoms or cyano groups to withdraw additional electron density.

1.4.1 DONOR-ACCEPTOR COPOLYMERS

Donor-acceptor copolymers are comprised of an electron rich (donor) and electron deficient (acceptor) unit. The overall optoelectronic properties of a D-A polymer are determined by the hybridisation of the parent monomer HOMO-LUMO energy levels which form an intramolecular charge transfer complex (ICT). As such copolymers can be synthetically designed to optimise the optoelectronic properties by manipulating the parent monomers. The HOMO level resides primarily on the donor unit whilst the LUMO level is more localised on the acceptor moiety allowing the energy levels to be tuned relatively independently, a major advantage in terms of molecular design.

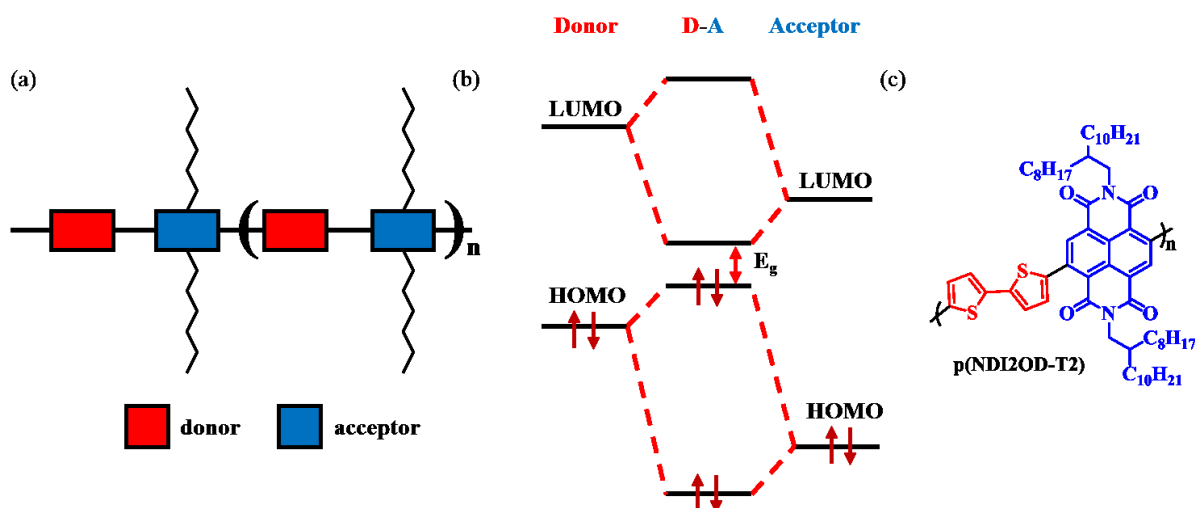


Figure 12. (a) Donor-acceptor alternating copolymer schematic, (b) molecular orbital hybridisation of parent donor and acceptor monomers reducing the bandgap (E_g) of the D-A copolymer, (c) *N,N'*-dialkyl naphthalenedicarboximide-dithiophene an example of a D-A copolymer (NDI2OD-T2).³⁸

Following the rules of perturbation theory, the HOMO of the donor unit interacts with the HOMO of the acceptor, splitting to yield two new bonding orbitals for the D-A copolymer. The LUMO levels also interact with each other, splitting to form two new hybridised anti-bonding orbitals. Electrons redistribute into these hybridised orbitals leading to an overall increase in HOMO energy and a decrease in LUMO level narrowing the optical bandgap. As such, the HOMO wave function is mainly localised on the donor unit whilst the LUMO wave function is more localised across the acceptor unit.²⁷

An example of this is *N,N'*-dialkylnaphthalenedicarboximide-dithiophene (**NDI2OD-T2**)³⁸ a D-A copolymer composed of an electron-rich bithiophene (**T2**) unit that is coupled with the strong acceptor naphthalenedicarboximide (**NDI**) moiety. The copolymer displays a narrow bandgap (1.45 eV) and a relatively deep LUMO (high electron affinity) of -3.9 eV, which allows for electrons to be injected into the copolymer thus operating as an *n*-type material. The experimental LUMO energy is close enough to the suggested ~ -4 eV that **NDI2OD-T2** has high stability and owing to the regioregular polymeric backbone shows good electron mobilities in the order of $\sim 0.1 \text{ cm}^2 \text{ V}^{-1} \text{ s}^{-1}$.³⁸

1.4.2 SYNTHESIS OF CONJUGATED POLYMERS

The construction of conjugated polymers heavily relies on the myriad of available C-C bond forming reactions.³⁹ Historically, transition-metal-catalysed cross-coupling reactions have proven to be the most prevalent methods with Stille⁴⁰ and Suzuki-Miyura⁴¹ being the most notable examples. Both cross-coupling methods excel in the formation of donor-acceptor (D-A) alternating copolymers. Generally, the reaction cycle involves a metal-catalysed oxidative addition inserting into the C-X bond of an electrophile, followed by transmetalation with the organometallic nucleophile. Finally, reductive elimination affords the desired carbon-carbon bond and regenerates the active catalyst, ready to initiate the next reaction cycle. Nickel or

palladium-based complexes are the most common transition-metal catalysts, often requiring activation via reduction from the (II) to the (0) state, to initiate the catalytic cycle. Stille cross-couplings require the use of highly toxic stannyl organometallic nucleophiles whereas Suzuki-Miyaura requires boronic acids or esters which are generally non-toxic.

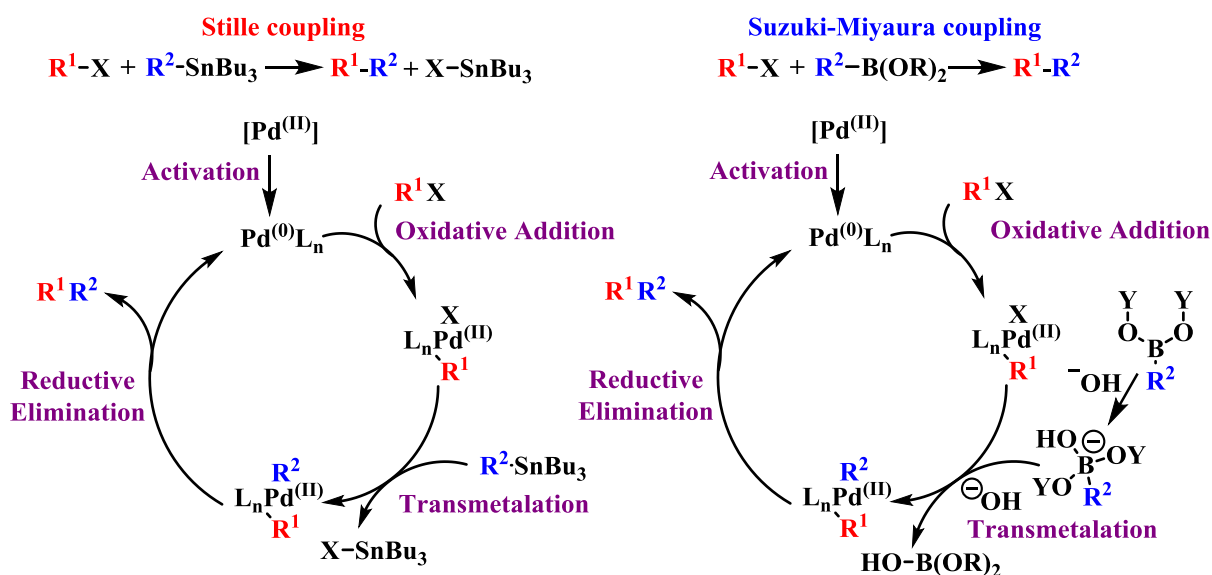


Figure 13. (a) Simplified Stille⁴⁰ cross coupling cycle compared to (b) a generic mechanism for Suzuki –Miyaura (SM) coupling.^{41,42}

It is of note that under Stille coupling conditions stannyl-substituted benzene rings have very poor reactivity with aryl-halide coupling partners. Conveniently Suzuki-Miyaura coupling is favoured and as such cross-coupling reactions with benzene are generally performed from the parent boronic group functionalised monomers. Indeed, Suzuki-Miyaura coupling is limited to mainly electron deficient copolymers, the boronic moiety is known to be unstable in the presence of electron rich monomers such as thiophene. This is because the bond between an electron rich compound and a boronic acid (or ester) is weak and can easily undergo protodeboronation decomposition under the cross-coupling conditions.²⁷

1.4.3 BANDGAP ENGINEERING

The search for true “*organic metals*” requires the bandgap (E_g) to be reduced to zero as close as possible, thereby increasing the thermal population of the conduction band and in turn increasing the intrinsic number of charge carriers. Subsequently, this will increase the intrinsic electrical conductivity, reducing the need for oxidative or reductive doping, whilst also stabilising the corresponding doped states.⁴³ However, owing to the considerable development of OSC devices, π -conjugated polymers with tailored electronic properties are now essential and the search for the lowest possible bandgap is no longer the primary focus. Fortunately the bandgap engineering toolbox has expanded alongside the popularity of OSC devices (**Figure 14**).^{27,44}

Conjugated polymers exist in the ground state as a resonance between aromatic (confined π -electrons) and quinoid (delocalised π -electrons) forms. As aromaticity is lost during this conversion the overall resonance energy of the quinoid form is lower. Therefore, stabilising the quinoid form will lead to a reduction in bandgap energy of related conjugated polymers.⁴⁵ This resonance conversion can be described by the bond length alternation term (BLA) defined as the average of the difference in bond length between adjacent C-C bonds and describes the ratio of aromatic to quinoid population. The BLA can be manipulated by tuning the aromatic stabilisation resonance energy of the conjugated backbone, decreasing aromaticity will facilitate π -electron delocalisation favouring the quinoid form, decreasing BLA and HOMO-LUMO bandgap concurrently. Examples of this are detailed in **Chapter 3** where increasing the antiaromatic core of indenofluorene derivatives leads to a more favourable quinoidal resonance form in the ground state.

The introduction of chemical rigidity is also known to alter the bandgap energy with increased planarity in the conjugated polymer backbone significantly lowering E_g . This is due to a

combination of reduced rotational disorder and an overall decrease in BLA. Whilst this strategy is an attractive one it often requires complex synthetic pathways which could limit large-scale production. Indeed, this strategy will be demonstrated in **Chapter 4** detailing the synthesis of a series of fused rigid rod *n*-type polymers based on an extended isoindigo backbone.

Another bandgap manipulation strategy is to tune the HOMO and LUMO energy levels through the incorporation of electron-donating or electron-withdrawing substituents. Electron-donating units (alkyl, alkoxy or alkylsulfonyl groups) raise the HOMO level whereas electron-withdrawing groups (nitro, carboxyl or cyano units) lower the LUMO. These effects can be combined to minimise the bandgap where the aromatic core and functional groups can be seen as an alternating donor-acceptor system.⁴⁴ These inductive and mesomeric effects must be carefully considered during the design of any conjugated polymer requiring a judicious selection of sidechain functionality (**Section 1.4.4**).

Finally, the intermolecular properties in the solid state can also alter the bandgap due to induced interchain delocalisation leading to a stereoregular structure. This highly ordered closely packed arrangement can also increase charge carrier mobility. One drawback of this phenomena is the loss of solubility with increased π -stacking interactions.²⁷ These strategies for bandgap manipulation are summarised illustratively (**Figure 14**), it is clear that whilst backbone manipulations and donor-acceptor combinations can contribute heavily to the bandgap the choice of functional sidechains must also be carefully considered.

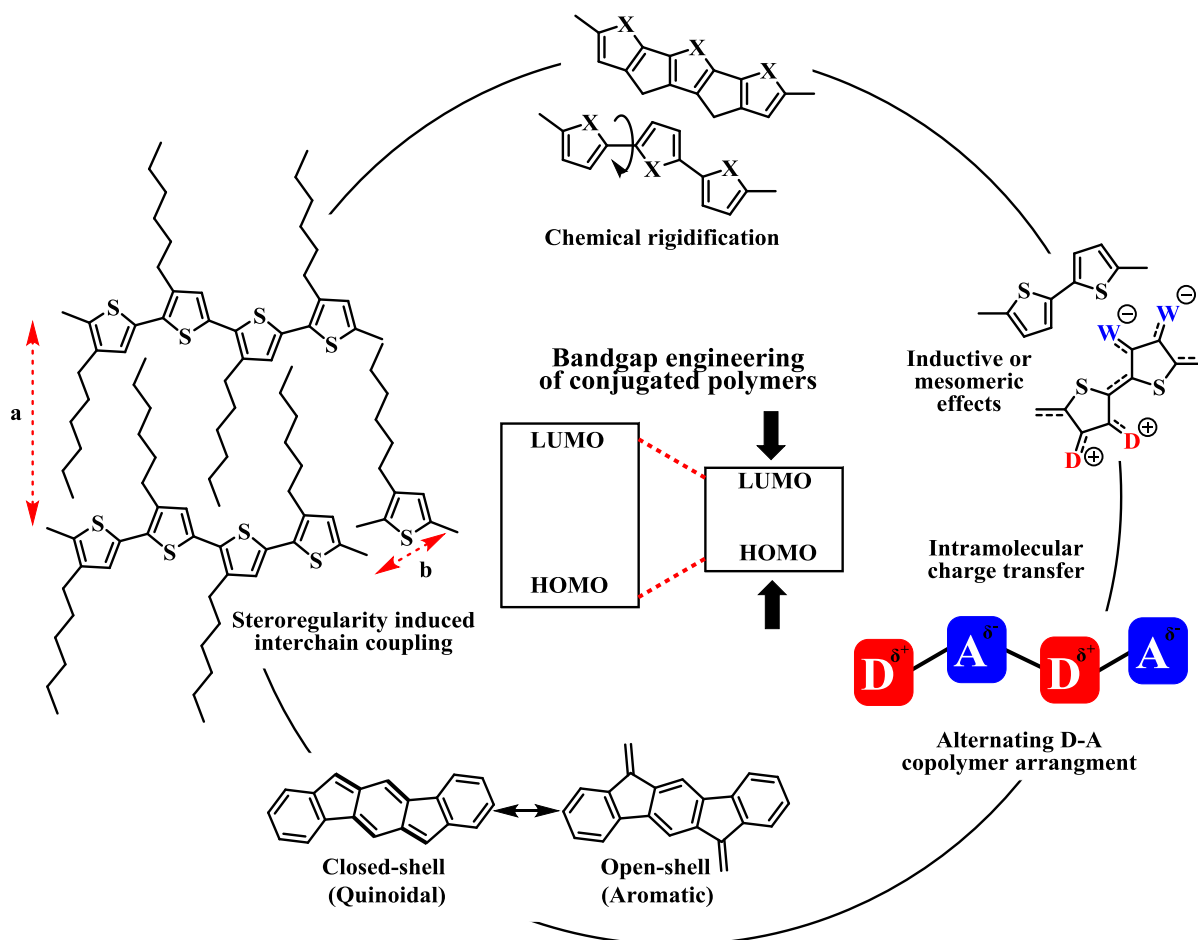


Figure 14. Summative illustration of common bandgap engineering strategies, adapted from Cheng *et al.*²⁷

1.4.4 SOLUBILISING SIDECHAINS

Whilst strong π -bonding interactions are essential for good charge transport this renders many conjugated polymer and small molecule systems to inherently more difficult to dissolve at appreciable concentrations. Good solution-processability is however an essential property for successful device fabrication and is governed by multiple structural factors. These include the degree of polymerisation, nature and length of solubilising sidechains, the polarity of attached functionalities, backbone rigidity and intermolecular interactions.²⁷ The simplest and most utilised design strategy for increasing polymer solubility is through the introduction of aliphatic side chains, covalently attached to the polymer backbone. The addition of linear alkyl chains

is an undoubtable method for increasing solubility in common organic solvents such as chloroform or chlorobenzene, while branched alkyl chains induce solubility even further.

However, one cannot simply add aliphatic chains to a polymer without caution, as the inclusion of alkyl sidechains is typically accompanied by the introduction of significant disorder within the polymer packing structure, which in turn can negatively impact device performance. An optimal material must strike a balance to render the material solution processable without hindering the charge transport properties. One such example is **PBTTT (Figure 10)** which forms a highly ordered semi-crystalline interdigitated phase, in the solid state, when functionalised with linear alkyl chains, facilitating high charge carrier mobility.³⁰

The strategy of introducing aliphatic solubilising chains has also been used for **DPP** and **NDI (Figure 11)** copolymers which aggregate so strongly that it is generally necessary to include branched alkyl chains to induce solubility in common organic solvents.^{33,38,46} The strength of aggregation in these units is facilitated by the presence of polar carbonyl and imide moieties, respectively, which form a hydrogen bond network. Inducing solubility is not the only role that sidechains play when designing a conjugated polymer, in fact the importance of sidechain engineering cannot be understated.

Sidechains can be used to tune multiple photophysical properties including bandgap, absorption, emission, molecular packing and charge transport.⁴⁷ As such a diverse toolbox of sidechains has been reported over the last few decades as the field of conjugated polymers has continued to expand,^{47,48} including sidechains bearing ionic,⁴⁹ electron donating, electron accepting, hydrosilanes⁵⁰ and hydrophilic oligo ethylene glycol (OEG) functionalities,^{22,39,51} which will be discussed separately herein as these OEG sidechains are of key importance to this thesis.

1.4.5 ETHYLENE GLYCOL BASED SIDECHAINS

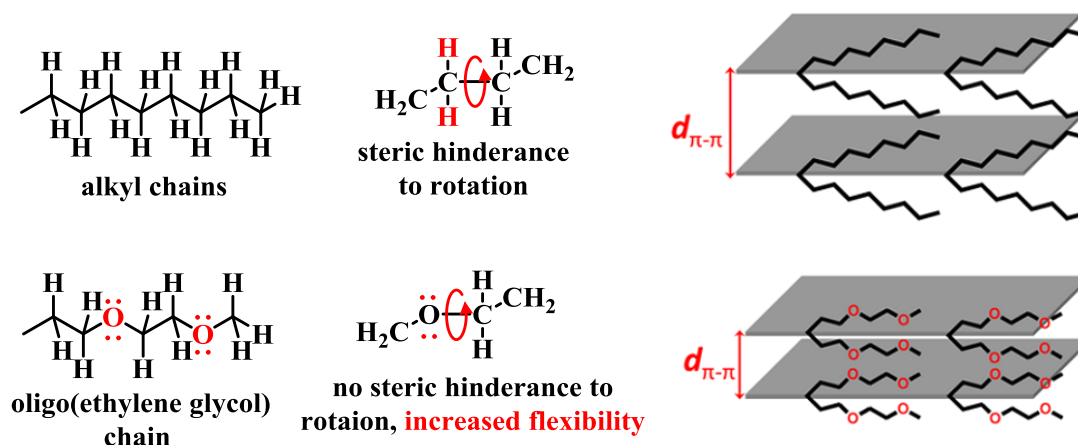


Figure 15. Schematic illustration of the increased flexibility and reduced π - π stacking distance for OEG chains compared to their alkyl counterparts.⁵²

In recent years the field of organic electronics has seen an uptake in the number of so called “*mixed conduction*” (mixed ionic/electronic transport) polymers, with the majority of these containing polar oligo(ethylene glycol) (OEG) chains. These OEG, which from here onwards will also be referred to simply as *glycol* chains, have been demonstrated to facilitate ion transport in aqueous electrolytes, thus allowing ions to penetrate into the bulk volume of the polymer during electrochemical doping.⁵³ This is facilitated by the lone pairs on the oxygen atoms which can hydrogen bond with polar protic solvents and also chelate to cations.⁵⁴ Conjugated polymers with glycol chains can transport electronic charge carriers (electrons and holes) along the backbone and ions (cations and anions) between the chains, the inclusion of these polar sidechains has been reported to improve OPV⁵⁵, OFET⁵⁵ and OECT^{22,39,53} device performance.

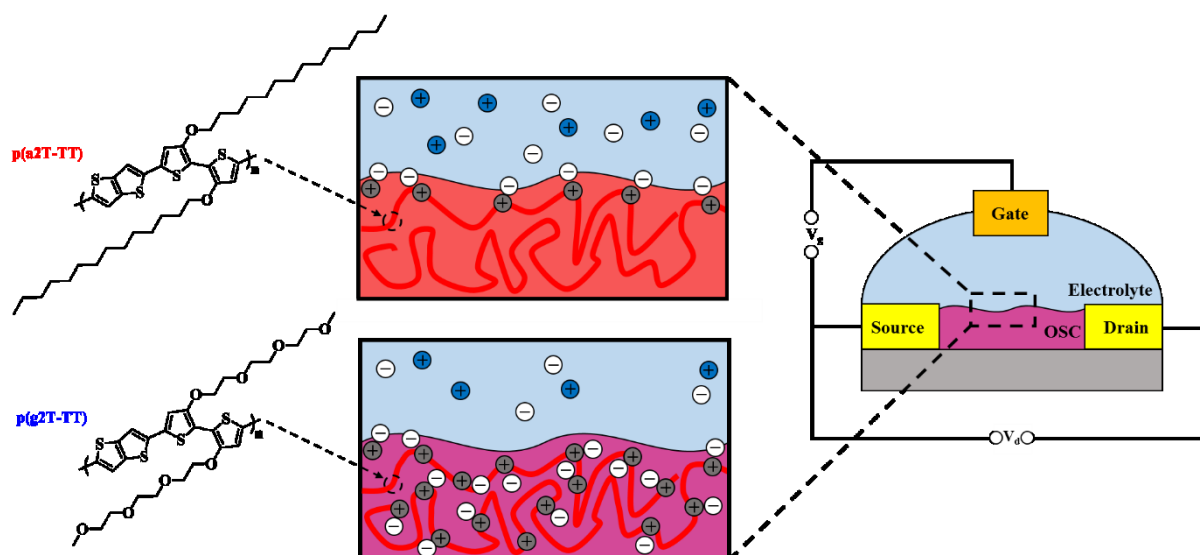


Figure 16. Molecular structures and OECT cross-section schematic of ionic interactions of alkylated $p(a2T-TT)$ and glycolated $p(g2T-TT)$. Cations (Na^+) depicted in blue, anions (Cl^-) in white and holes distributed along the polymer backbone in grey, adapted with permission from Giovannitti *et al.*⁵¹

Compared with their typical alkyl counterparts OEG sidechains endow a smaller π - π stacking distance, narrower optical band gap, higher dielectric constant, and an increased surface energy (**Figure 15**). The shorter π - π distance is a result of amplified flexibility, compared to hindered alkyl chains, allowing for more efficient packing of polymer backbones.⁵²

A good example of incorporating OEG sidechains was presented by Giovannitti *et al.*⁵¹ where replacing alkyl chains with glycols afforded the high performing OECT material $p(g2T-TT)$ exhibiting high volumetric capacitance, transconductance and currents compared to the alkylated analogue $p(a2T-TT)$. The inclusion of glycol chains shifted the mode of OECT operation into the bulk doping and transport regime, facilitated by ion penetration and hydration (**Figure 16**). This design strategy has been exploited numerous times by our group and others to improve device performance, improve biocompatibility and produce mixed conduction systems.^{21,22,39,49,51,53,56}

1.5 ORGANIC BIOELECTRONICS

Bioelectronics encapsulates the area of science which involves the transduction of electronic signals into biological ones and vice versa.^{57,58} The field can be dated back to the 18th century where Luigi Galvani's twitching frog experiment has earned him the title of the father of bioelectronics. Today the field is dominated by novel strategies aiming to achieve a seamless interface between electronic devices and biological environments. Over the past 20 years interest and research within the field has grown rapidly, as illustrated in **Figure 17** comparing the number of publications including the term "bioelectronics" from 1999 to 2019. As such, there is a plethora of in depth literature reviews covering the current challenges and cataloguing the achievements within the field^{21,57,58}, and only a brief introduction and overview is presented here.

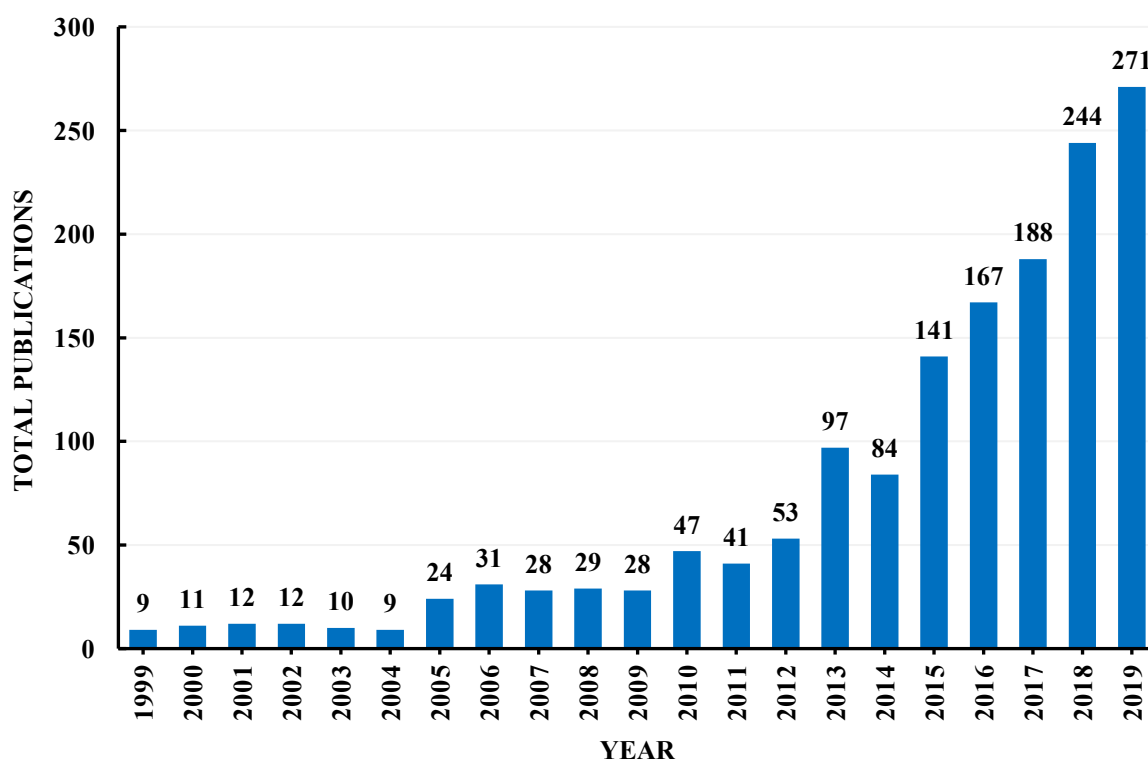


Figure 17. Total number of publications including the term "bioelectronics" from 1999 to 2019, statistics obtain from Web of Science.

Modern day bioelectronics is dominated by the use of organic semiconductors, owing in part to their unique and highly tuneable optical and electrical properties. However, possibly the most important feature is the weak van der Waals' intermolecular forces rendering OSCs as "soft" materials.⁵⁸ Indeed, this can be further enhanced through judicious choice of polymer sidechains, enhancing the uptake of ions via swelling which in turn increases efficiency of the ion-to-electron signal conversion.²¹ A prime example of this is the inclusion of OEG chains (**Section 1.4.5**) which has been shown to facilitate ion transport and used to produce multiple highly efficient OECT materials.^{25,39}

The biotransduction conversion of ionic biological signals into an electronic signal renders OECT devices as ideal biosensor materials.⁵⁹ Owing to their ability to undergo reversible electrochemical reactions and support both electronic charge transport and ionic transport organic mixed conductors, which make up these OECT devices, have also shown potential as electron relays.⁵⁶ Recent studies have reported *p*-type OECT devices comprised of **PEDOT:PSS** which are able to detect numerous disease related metabolites⁶⁰ and a lactate detector *n*-type OECT device using an **NDI-T2** polymer.⁵⁶ These are just a small sampling of recent successes within the field and the general area of biosensors spans across a multitude of device applications from medical diagnostics to quality control and drug discovery.⁶¹ As the number of publications (**Figure 17**) rises so does the number of potential bioelectronic devices which utilise the unique and tuneable properties of organic mixed conductor materials.

1.6 DOPING, CONDUCTIVITY & THERMOELECTRICS

A common method to improve semiconductor performance in inorganic materials is to dope them via the addition of external atoms, often boron (*p*-type) or phosphorus (*n*-type), to modify the intrinsic conductivity.⁶² Rather than simple atom substitutions in the crystalline lattice, organic materials are doped by either oxidation or reduction reactions (chemically or

electrochemically). This phenomenon can be applied to organic semiconductors however the level of doping varies wildly, from ppm (around 1%) for inorganics and up to ~35% for organics.⁵

Similar to inorganics, OSCs can be doped in the solid state but owing to their inherent processability can also be doped in solution, which is often a much simpler method and is a major advantage for organic materials. Generally, this involves a form of redox chemistry, either oxidation (*p*-type) or reduction (*n*-type). This is a facile process and can be achieved simply by treating a solution of the OSC with a complimentary dopant solution, the doped OSC can subsequently be deposited using conventional solution processing techniques. This method is not without its flaws, in this case the dopant will also be deposited along with the OSC which could lead to disorder, lowering device performance and OSC conductivity once the critical dopant concentration is surpassed.⁵ The Siringhaus group⁶³ has shown that this can be avoided through solid-state doping, using vacuum deposition to treat pre-fabricated OSC films observing diffusion in the bulk similar to solution doping.

p-Type doping involves removing electrons from the HOMO, conversely *n*-type doping adds electrons to the LUMO, both scenarios increase the charge carrier density, altering the conductivity and optoelectronic properties.^{5,64} A simplified version of the doping process is presented in the band structure of organic semiconductors discussion (**Figure 1**) however the nature of the doped state is more complex and will be expanded upon herein.

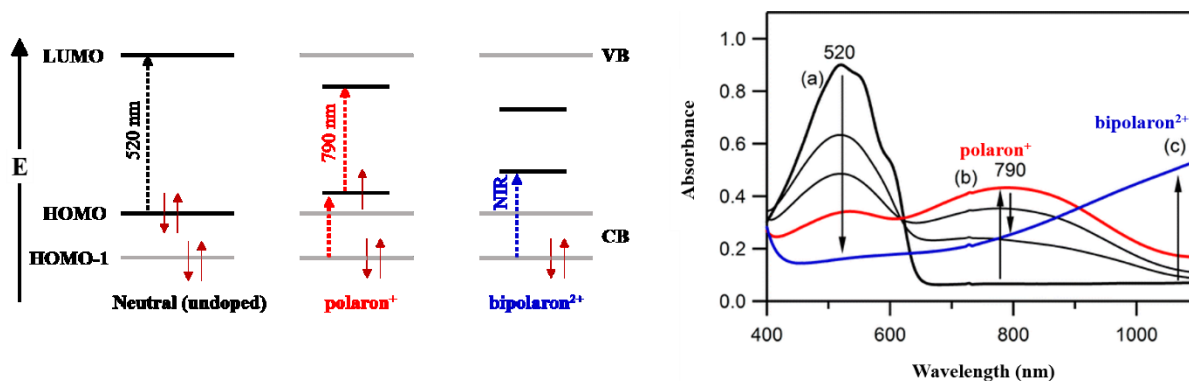


Figure 18. Schematic of the HOMO-1, HOMO and LUMO levels of undoped, polaron⁺ and bipolaron²⁺ respectively. Allowed optical transitions are represented by dashed arrows and correlate to the absorption spectrum for P3HT doped with FeCl₃, adapted from Furukawa and Giovannitti.^{65,66}

Taking the *p*-type doping of **P3HT** with FeCl₃ as an example of chemical doping, oxidation of the OSC forms a positive radical, referred to as a polaron, which is stabilised by the reduced dopant counterion. Formation of the positive polaron shifts the relative HOMO level and shrinks the optical bandgap facilitating an observable change in the absorption spectrum, the absorption at 520 nm is suppressed as the new 790 nm polaron absorption forms. Upon increased levels of doping further oxidation forms a dication, namely a bipolaron. Here the optical bandgap is reduced even more and a low energy NIR absorption dominates the resultant UV-Vis spectrum (**Figure 18**).⁶⁵ The same effect can be achieved via electrochemical doping which involves placing the OSC between a metal electrode and an electrolyte. Extra charge carriers are injected into the OSC from the metal electrode, assuming the electron energy levels are appropriately aligned to facilitate charge transfer.

1.6.1 *p*-TYPE DOPING

The *p*-type doping of **P3HT** can give an important insight into the nature of the doped state for the thiophene ring which will be essential for the discussion in **Chapter 5**. Previous reports have shown that the positive cation (polaron) can be delocalised across multiple aromatic rings,

inducing planarity, quinoidal character and reducing the overall BLA of the alternating single and double bonds.^{5,65}

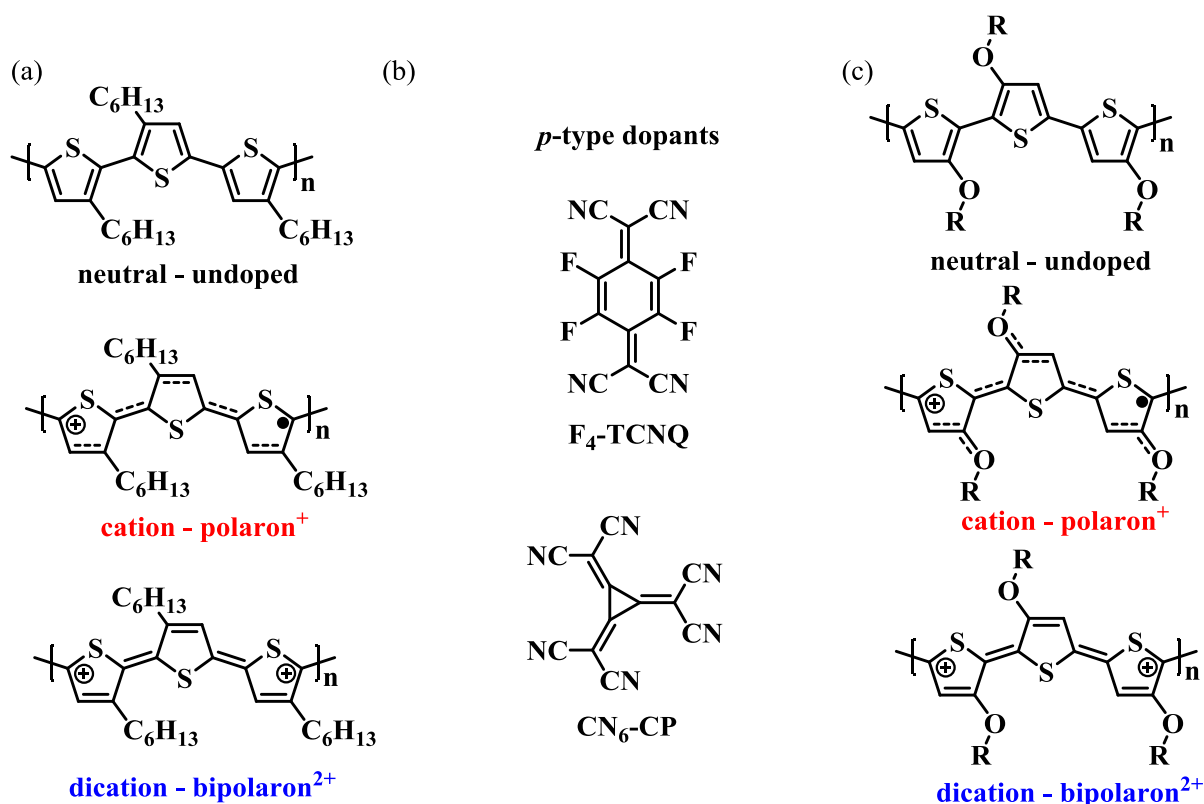


Figure 19. (a) P3HT in its neutral, polaron and bipolaronic forms (b) common *p*-type dopants F₄-TCNQ and CN₆-CP, (c) alkoxythiophene polymer, polarons stabilised further due to resonance with donating oxygen units.

In general, polarons and bipolarons are stabilised by electron donating groups attached to the backbone.⁶⁷ Indeed, this is the case (**Figure 19**) for alkoxythiophene based polymers where delocalisation of the radical cation is extended to include the oxygen atoms. Here, the lone pair of the oxygen atoms can donate into the aromatic core and stabilise the polaron through increased delocalisation, stabilising the quinoid form. This design motif has been shown to increase *p*-type performance in OFETs, OECTs and thermoelectric devices, generally through the use of glycolated thiophenes bonded through the alkoxy functionality.^{21,39,49}

Current state of the art *p*-type dopants are based on electron-deficient quinones; these quinoidal molecules can be reduced to their aromatic form by removing electrons from the OSC HOMO level. Quinones decorated with electron-withdrawing functional groups will increase the electron accepting capability thus acting as better *p*-type dopants. The most notable example and industry standard *p*-type dopant is tetrafluorotetracyanoquinodimethane (**F₄-TCNQ**), a quinone decorated with both cyano- and fluorine- groups and a deep lying LUMO of -5.2 eV.^{68,69} Reduction of the 6- membered aromatic core to a cyclopropane unit affords hexacyano-trimethylene-cyclopropane (**CN₆-CP**) with an increased electron affinity of 5.87 eV, improving the electron accepting capability.⁷⁰

1.6.2 *n*-TYPE DOPING

The chemical opposite of *p*-type oxidative doping is reductive *n*-type doping, where a negative electron polaron can be formed for materials with large electron affinities. However, as discussed above (**Section 1.4**) the nature of the radical anion is inherently more reactive and unstable compared to the cationic counterpart. Despite this, several *n*-type backbones (**Figure 11**) can sufficiently stabilise a radical anion, again through delocalisation and the use of electron-withdrawing functionalities.

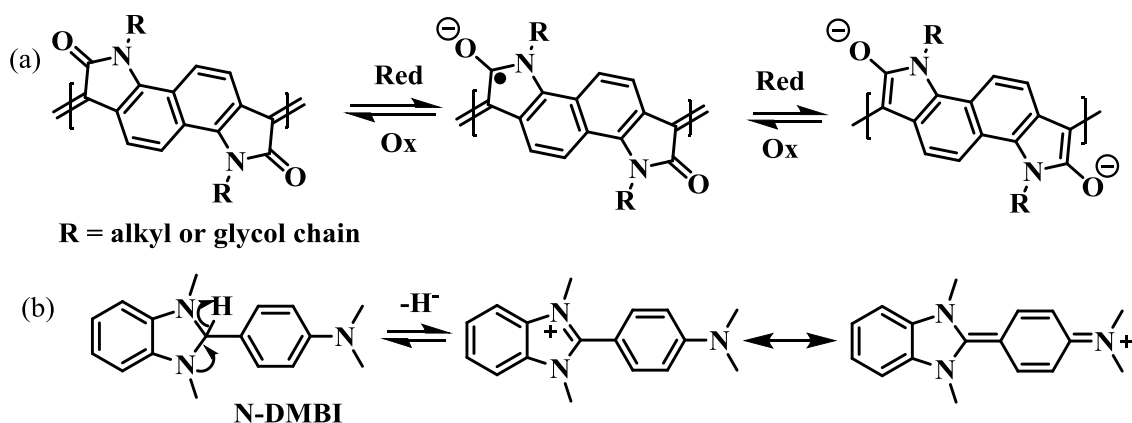


Figure 20. (a) Extended isoindigo fused rigid rod anion and dianion, stabilised through resonance delocalisation, (b) N-DMBI doping mechanism and stabilising resonance forms.

Examples of this are the isoindigo (**IID**) and naphthalenediimide (**NDI**) backbones which can form an enolate structure to delocalise the anion and dianion resonance forms. Following a similar motif to *p*-type doping the radical anion is stabilised via resonance and delocalisation across the **IID** or **NDI** core, respectively. Electron-rich amines have recently become the go to class for *n*-type dopants with electron-donors such as 1,3-dimethyl-2-phenyl-2,3-dihydro-1H-benzoimidazole (**N-DMBI**) being of the most common. During doping hydride loss, to an acceptor, aromatises the five-membered imidazole ring, the positive charge can be delocalised along the molecule via the resonance forms shown (**Figure 20**), the electron donating methyl substituents further stabilise the cation, reducing the HOMO and increasing *n*-type donor ability.

1.6.3 CONDUCTIVITY

The electrical conductivity of a material is an intrinsic property which is defined as the inverse of resistivity, in other words the amount of electrical current a material can carry (conduct). For conjugated polymers and organic semiconductors electrical conductivity can be defined as:

$$\sigma = ne\mu \quad (4)$$

where σ is the conductivity in S cm^{-1} , n is the concentration term (charge carrier density), e is the elementary charge and μ is the mobility in $\text{cm}^2 \text{ V}^{-1} \text{ s}^{-1}$, sometimes referred to as the drift mobility (to distinguish from standard OFET mobility).⁵ Undoped conjugated polymers are known to exhibit low charge carrier density ($n \approx 10^{22} \text{ cm}^{-3}$ in organic systems)⁷¹ which following **Equation (4)** accounts for their low electrical conductivity. Fortunately, using the doping process described above the number of charge carriers can be increased dramatically and at the time of writing electrical conductivities on the order of 10^3 S cm^{-1} have been reported for **PEDOT:PSS** doped systems.⁷² The introduction of additional charge carriers and the attractive Coulomb potentials between counterions causes traps to appear along the chain, as

such at low doping concentration mobility is often suppressed by these traps and the loss of ordered structure.⁵ Upon increased doping these Coulomb traps overlap forming a more ordered cascade and facilitate polaron hopping, leading to a significant increase in charge carrier mobility. A reported example for doped **P3HT** increased mobility by four orders of magnitude from $10^{-5} \text{ cm}^2 \text{ V}^{-1} \text{ s}^{-1}$ to $10^{-1} \text{ cm}^2 \text{ V}^{-1} \text{ s}^{-1}$ as the dopant level was increased.⁷³

1.6.4 THERMOELECTRICS

Spurred by the increasing demand for distributed energy generation, the ability to harvest electricity from renewable heat sources has steadily gained in popularity over the past few decades. Thermoelectric (TE) materials meet this requirement and are governed by the Seebeck effect, which describes a generated potential difference for a temperature difference across a material, the physics of which are beyond the scope of this thesis. The thermoelectric efficiency is determined by the figure of merit:

$$ZT = \frac{S^2 \sigma T}{\kappa} \quad (5)$$

where S , σ , T , and κ are the Seebeck coefficient (V K^{-1}), electrical conductivity (S cm^{-1}), absolute temperature (K), and thermal conductivity ($\text{W m}^{-1} \text{ K}^{-1}$), respectively.^{62,71}

Organic materials are promising TE candidates owing to their intrinsically low thermal conductivity, diverse molecular design and solution processability. Conducting polymers and high mobility organic semiconductors which can be doped to maximise their mobility and thus maximise ZT are two classes of potential organic thermoelectric (OTE) materials. Practically measuring the thermal conductivity of OSC films is limited and challenging, instead the more commonly reported figure of merit is the power factor:

$$PF = S^2 \sigma \quad (6)$$

The Seebeck effect is a direct energy conversion of heat into a voltage potential and occurs due to the movement of charge carriers within the semiconductors. The majority charge carrier determines the sign of the Seebeck coefficient, positive for p -type hole charge carriers and negative for n -type electron carrier materials, justification of the S^2 term to determine the overall power factor, always yielding a positive comparable figure regardless of p - or n -type operation.⁵

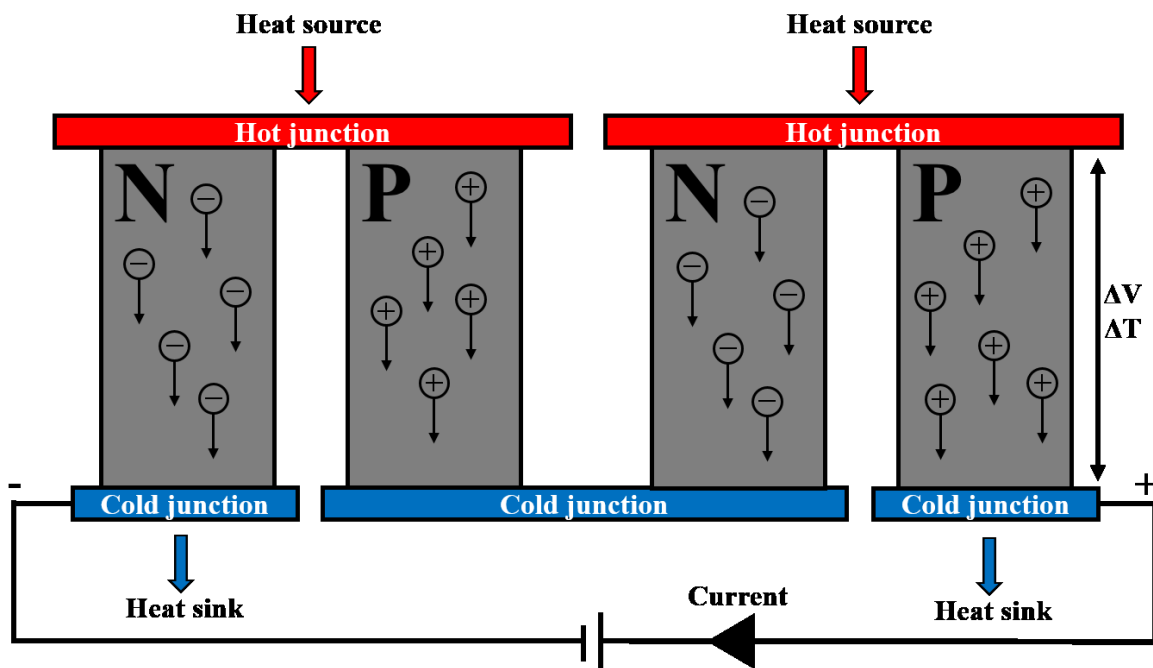


Figure 21. Schematic diagram of a simple thermoelectric generator, n - and p -type semiconductors coupled electrically in series and thermally in parallel.

In a simple thermoelectric generator p - and n -type semiconductors are connected electrically in series and thermally parallel. The thermal gradient applied orthogonally causes charge carriers to diffuse away from the hot side of the semiconductor (**Figure 21**). These mobile charges create a potential across the device which is directly proportional to the temperature difference across the semiconductor. The most efficient thermoelectric generators will be comprised of p - and n -type materials with similar ZT values.⁷⁴

1.7 OPTOELECTRONICS

Organic semiconductors and conjugated polymers are not only used for electronic (charge carrier) applications. Indeed owing to their tuneable optical properties, these materials have also been utilised in the successful fabrication of many light-emitting (e.g. OLED) and light-detecting (e.g. organic solar cell) devices.⁷⁵ The field has continually evolved over the past few decades and continues to be at the forefront of organic chemistry, as such many novel design paradigms such as singlet fission (SF) have emerged as potential processes to surpass the Shockley- Queisser (SQ) limit (*vide infra*).

Organic semiconductors generally exhibit a low dielectric constant ($\epsilon_r < 4$),⁷⁶ thus the coulombic attraction between oppositely charged holes and electrons is weakly screened. This facilitates the formation of electron-hole pairs, referred to as *Frenkel* excitons, with a relatively large exciton binding energy (work needed to separate electron and hole) on the order of 0.3 – 0.5 eV.^{77,78} Excitons (**Figure 11**) are formed via *photoexcitation* (process of electron excitation by photon absorption) formally referred to as a neutral quasi-particle. Electrons exist in either the spin-up ($S = +\frac{1}{2}$) or spin-down ($S = -\frac{1}{2}$) state, as such excitons are defined by the total spin, specifically the spin quantum number (S) and can be singlets ($S=0$) or triplets ($S=1$). Triplet states have an increased binding energy cf. singlet excitons due to the attractive exchange interaction between an electron and hole with the same spin orientation.⁷⁹

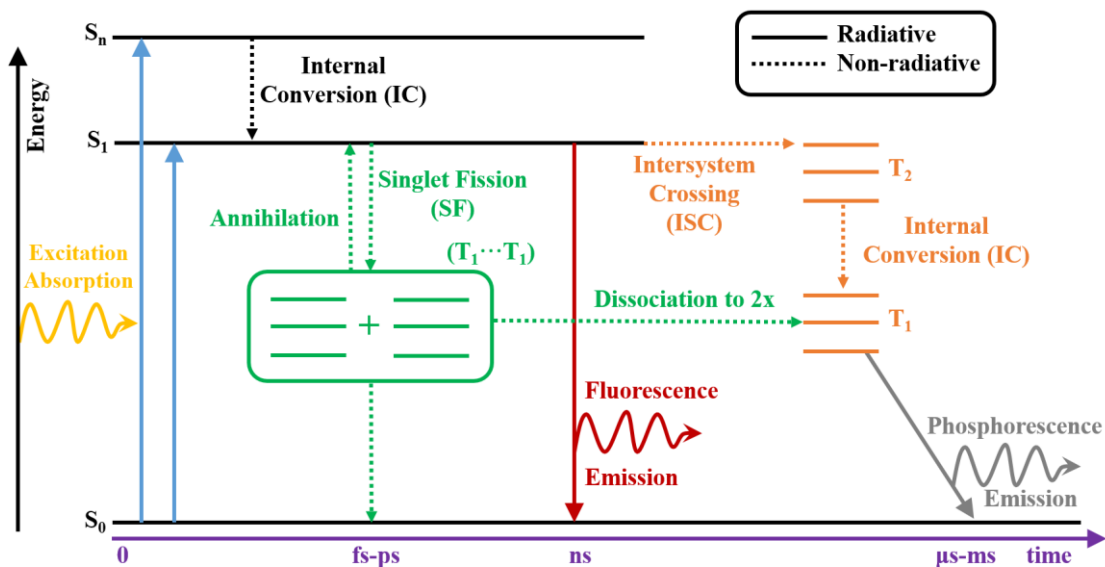


Figure 22. Modified Jablonski diagram depicting the various radiative and non-radiative decay transitions, where S_0 , S_1 and S_n are the ground state, first excited and n^{th} excited state respectively. T_1 indicates a triplet state and $(T_1 \cdots T_1)$ is the coupled triplet intermediate necessary for singlet fission which is detailed within the text.⁸⁰

After a molecule has absorbed an incident photon, it can relax back to the ground (S_0) state via radiative or non-radiative decay pathways (**Figure 22**). Non-radiative processes include internal conversion (IC); the radiationless transition between energy states of the same spin state, intersystem crossing (ISC); radiationless transition between different spin states and vibrational relaxations. Radiative decay transitions include fluorescence; emission between states of the same spin (e.g. $S_1 \rightarrow S_0$), phosphorescence; emission between states of differing spin (e.g. $T_1 \rightarrow S_0$) and singlet fission (*vide infra*).^{75,81}

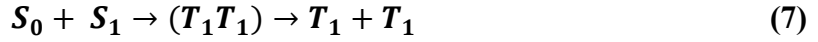
1.7.1 SINGLET FISSION

Singlet fission (SF) was first presented in the literature in the early 1960s, where SF was proposed to rationalise delayed fluorescence in anthracene.⁸² Much later in 2010 Smith and Michl published a comprehensive review⁸¹ of the available SF materials/systems which has fuelled the rejuvenation of the field. They followed this in 2013⁸³ with a report on the

fundamentals of SF which was recently updated last year by Miyata *et al.*⁸⁴, providing a wealth of insight into the nature of the extremely complex triplet state, an essential part of SF. Each of these reviews suggest that SF materials could be used in conjunction with a lower bandgap absorber to potentially raise power conversion efficiency (PCE) and surpass the Shockley-Queisser (SQ) limit which has reignited current interest and research within the field.

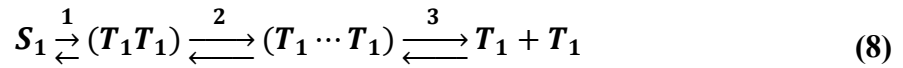
SF is an example of multiple exciton generation (MEG), specifically the conversion of a high-energy singlet exciton into a correlated triplet pair ($T_1 \cdots T_1$) which dissociates into two low-energy triplet excitons.⁸³ This process has gathered considerable attention with the potential to obtain solar cells with up to 200% internal quantum efficiency (IQE).⁷⁵ The two generated triplet excitons initially interact, making SF an overall spin allowed process. The triplet excitons produced can be used to generate two electron-hole pairs, a promising route to overcome the SQ limit⁸⁵, which constrains the power conversion efficiency of single-junction solar cells to ~33%.⁸⁶ Specifically, a recent suggestion by Nozik *et al.*⁸⁶ that when a SF chromophore (absorbing $\geq 2E_g$) is combined with a conventional semiconductor (absorbing $\geq E_g$) part of the excess excitation energy can be harvested, increasing the theoretical PCE to ~44%, invigorating the solar energy conversion community. Moreover, the triplet excitons generated are also stable, having no radiative dipole-allowed optical transitions to the singlet ground state, facilitating a range of energy transport and extraction methods. Please note that the detailed physics of singlet fission are far beyond the scope of this thesis but are excellently reviewed in the literature,^{81,83} instead a brief history and a summary of the basic principles will be presented herein from the view of a synthetic chemist.

Despite these recent advances, the fundamental mechanism of SF remains unclear. In 1969, Merrifield and co-workers⁸⁷ proposed a kinetic model for the singlet fission process, represented as:



where $S_0 + S_1$ is the lowest (allowed) singlet excited state coupled with the S_0 ground state, T_1T_1 corresponds to a doubly excited pair of spin-correlated triplets with overall singlet spin character and $T_1 + T_1$ is a pair of independent (separated) triplet states.

Equation (7) is an oversimplification of the overall SF mechanism but holds true for relatively slow SF cases, such as solution SF. However, the formation of the correlated triplet pair state (T_1T_1) can occur on a subpicosecond timescale^{88,89} and is a dynamic evolving process thus requiring an expansion of this simplistic depiction. Initially, the correlated triplet pair state (T_1T_1) is a multi-electron singlet state where the two constituent triplets are coupled preserving electron coherence. Over time this electronic coherence is lost and the properties of the two individual triplets produced depend heavily on this process. Adapting the work of Smith *et al.*⁸¹ current nomenclature for SF is now represented as a three step process, as proposed by Miyata *et al.*⁸⁴:



where $(T_1 \cdots T_1)$ represents the triplet pair without electronic coupling but retaining spin consistency. In this vein the rate of singlet fission should be attributed to the formation of $(T_1 \cdots T_1)$ and not of (T_1T_1) which has shown marked differences in spectroscopic features compared to the individual T_1 states, in pentacene dimers.⁸¹

Following Kasha's rule (that photon emission, fluorescence or phosphorescence, occurs only from the lowest excited state thus emission and excitation wavelength are independent)⁹⁰ and recent reviews^{83,84}, it is clear that the most important state in the singlet fission process is the low lying correlated triplet pair state, $(T_1 \cdots T_1)$. Whilst the precise singlet fission mechanism is still disputed, a recent algorithm based computational study presents an analogous mechanism to that presented in **Equation (8)**, further supported by Krylov *et al.* reporting

intramolecular singlet fission (iSF) in both polymeric and dimer systems respectively.^{91,92} These studies also agree with the work of Zimmerman *et al.*⁹³ where photoexcitation, from the S_0 ground state, to the lowest allowed excited state is followed by a rapid conversion, via conical intersection, to a dark multi-exciton singlet state. From this state fission can occur and split into two uncoupled triplets ($T_1 + T_1$) (**Figure 22**). Whilst this process has been demonstrated for multiple molecular solids the problem of efficient separation (avoiding annihilation) followed by transport of triplets, required for most applications, remains, again this is beyond the scope of this thesis and is well summarised in the literature.^{75,83,94}

1.7.2 DESIGNING SINGLET FISSION CHROMOPHORES

For a SF chromophore to be useful it must meet several conditions. In no particular order, exhibit up to a 200% triplet yield, have extended triplet lifetimes, be capable of efficient charge separation and have sustained photostability.⁸³ For this process to occur efficiently a material suitable for SF requires $E(S_1) \geq 2E(T_1)$. Furthermore, the rate of decay to the correlated triplet pair must outcompete other decay mechanisms such as triplet recombination or triplet annihilation. Once these parameters have been overcome experimental detection of this state is also hindered by the multi-exciton character and the triplet nature of the constituents.⁹⁵

Paci *et al.*⁹⁶, justified by an extensive computational investigation, propose two general classes of molecules as viable singlet fission candidates. Firstly, alternant hydrocarbons (conjugated materials comprised of only even-membered rings) such as pentacene and tetracene, which have been studied extensively.⁸¹ Secondly, biradical, open-shell molecules (*vide infra*) indeed these two classes have been combined, alternant hydrocarbons with high biradical character, as particularly promising SF materials.⁹⁷

SF is known to occur rapidly on the subpicosecond timescale and can outcompete fluorescence, however a fluorescence yield close to unity will help to ensure that this potential relaxation

pathway does not hinder the SF process. Additional competing channels may exist within dimers and aggregates originating from intermolecular interactions which also need to be pondered. Triplets are also known to annihilate each other, quenching potential SF, thus the correlated triplet state must be long-lived in order to diminish this possibility. To limit this concern Smith and Michl⁸³ recommend $E(T_2) \geq 2E(T_1)$ where T_2 is the next available molecular triplet state. Fulfilling this condition will make the formation of the T_2 state endogernic (absorption of energy) rendering this annihilation pathway slow and unfavourable.

An effective SF sensitizer also requires the chromophores to be physically coupled, strong enough to outcompete fluorescence but not too strong as to hinder dissociation of the coupled triplet state (T_1T_1). However, recent studies of polyacenes suggest that excimer formation may act as an intermediate, mediated by charge transfer, in the formation the separated T_1 triplet states. Reports have argued for the importance of this excimer intermediate in the singlet fission of both tetracene and pentacene.⁹⁸

The multitude of requirements and design factors make SF extremely difficult to predict, occur and finally to be observed/measured and is one of many reasons for the lack of current SF devices. Despite these difficulties the field has certainly progressed rapidly over the past ten years and continues to be of major interest as a feasible means of surpassing the SQ limit. Herein (**Section 2.8**) a selection of indenofluorene dimers, linked by a phenyl spacer, will be discussed as highly photostable materials with good predicted energy levels for singlet fission.

1.8 OUTLINE

This thesis is split into four distinct chapters, with common synthetic undertones running throughout. The first two chapters focus on an exploration of the indenofluorene (IDF) and indacenodithiophene (IDT) frameworks. Specifically, **Chapter 2** reports the development of a series of phenyl- bridged xylene substituted IDF dimers (**DX-IDF_[0-2]**) for potential singlet

fission applications. The materials were studied using transient absorption spectroscopy (TAS) in search of the coupled triplet state ($T_1 \cdots T_1$). Whilst evidence for this was not concrete the series displayed a unique set of optoelectronic properties which through further synthetic tuning could lead to novel singlet fission materials.

In **Chapter 3** the same IDF monomers were used to investigate their potential as spin-sink materials in a ferromagnetic resonance (FMR) linewidth broadening experiment. The sulphur analogue, indacenodithiophene, was also synthesised and tested in a similar manner. These open-shell polycyclic hydrocarbon systems were synthetically expanded in order to increase their intrinsic spin density by manipulating the biradical character. As such, after a series of synthetic challenges (*vide infra*), higher biradical character materials were isolated and tested in the FMR linewidth experiment. Initially the aim of this study was simply to observe spin injection from a ferromagnetic metal into an organic semiconductor, previous unheard of before 2018. After successful observation the study shifted aiming to elucidate a potential link between biradical character and organic spin-injection. It was found that whilst undoubtedly spin-density plays a large role so does the structure and packing of the OSC at the ferromagnet interface. This chapter is concluded with additional work carried out on these diverse IDF and IDT monomers, including the development of a potential quinoidal non-fullerene acceptor and a series of quinoidal copolymers.

Following the work on small molecules, focused around indenofluorene and indacenodithiophene frameworks, **Chapter 4** reports a shift into the realm of bioelectronics. Here, the synthetic N-glycolation and polymerisation of bisisatin (an extended isoindigo derivative) is detailed, leading to a series of mixed conduction rigid rod polymers. These polymers showed deep LUMOs (with consequently high electron affinities) and operated under *n*-type regime in OECTs with moderate performance. The *n*-type thermoelectric device performance is also reported, specifically the electrical conductivity, Seebeck coefficient and

the power factor. These novel N-glycolated bisisatin-bisoxindole fused polymers are the first reported mixed conduction copolymers for this specific backbone motif and offer valuable insight into the effect of mixing non-polar (alkyl) and polar (glycol) sidechains on device performance.

Chapter 5 marries together this motif and details the synthesis of a series of modified **p(g2T-TT)** and **p(g2T-T)** polymers (**Figure 16**). Here the inclusion of a non-polar alkyl *spacer* unit acts as a sheath to shield the electron rich core from the polar OEG sidechains. This differs from the previous work within the group from Giovannitti *et al.*⁵¹ who replaced the entire alkyl sidechain with an OEG chain. Herein, the synthesis, characterisation and OECT device performance will be reported for six *spacer* polymers, increasing the alkyl spacer from C₂- to C₄-, C₆- and C₈-, respectively. This non-polar shielding effect has a profound impact on ion transport and volumetric capacitance of the resultant mixed conduction polymers.

CHAPTER TWO: SINGLET FISSION MATERIALS

2.1 ABSTRACT

Third generation photovoltaic technology aims to improve the power conversion efficiency (PCE) of solar cells. Intermolecular singlet fission (xSF), is a multi-exciton generation (MEG) process which has been shown to raise the external quantum efficiency above 100% in photovoltaic devices.⁷⁵ Intramolecular singlet fission (iSF) materials aim to build upon this success, potentially allowing for more facile device fabrication, owing to their modular nature. Pentacene is currently one of the most studied SF scaffolds however the antiaromatic analogue indenofluorene (IDF) backbone is also a promising skeleton for synthetic manipulation, with predicted energy levels ideally suited towards singlet fission. Herein, we explore the potential for IDF derivatives towards intramolecular singlet fission, specifically through dimerisation of IDF units. The synthesis of a series of phenyl-bridged IDF dimers is presented, with computed energetics supporting intramolecular singlet fission. The materials possess high photostability and demonstrate the formation of a long-lived excimer state upon thin film photoexcitation, which is subsequently investigated for singlet fission.

2.2 INDENOFUORENE (IDF) BACKBONE

Conjugated polycyclic hydrocarbons have been extensively researched during the last twenty years owing to their potential materials applications which vary from organic light-emitting diodes to solar cells and transistor devices. In particular the indeno[1,2-*b*]fluorene (IDF) backbone has been investigated at length as a fully conjugated skeleton with multiple sites available for post functionalisation.⁹⁹ In contrast to pentacene which is commonly regarded as the go to SF material,¹⁰⁰ the indeno[1,2-*b*]fluorene skeleton (**Figure 23**) contains two fewer carbon atoms and subsequently possesses two fewer π -electrons, formally rendering the core antiaromatic.

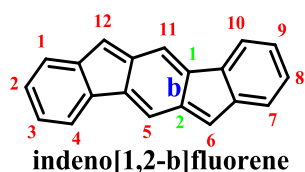


Figure 23. Conjugated indeno[1,2-*b*]fluorene core including numbering. Red numbers denote carbon atom; green numbers denote apical carbon orientation number; blue letter denotes the face of indene fusion.⁹⁹

Polycyclic systems can be evaluated by the number of Clar sextets which are defined as six π -electrons localised in a single benzene-like ring.¹⁰¹ For IDF the open-shell resonance structure exhibits a greater number of Clar's sextets, all three benzene rings, compared to only two benzene rings for the closed-shell structure. This is a direct result of the existence of the proaromatic quinodimethane structure (**Figure 24**) present within the indenofluorene backbone.¹⁰² This unique biradicaloid character has been suggested to play a role in singlet fission, by lowering the triplet state energy level (*vide infra*).⁹⁷ The reasons for studying the IDF backbone as opposed to pentacene, include (i) high stability, (ii) tuneability; late-stage functionalisation (EDG, EWG, ligand groups) (iii) and good predicted energetics for singlet fission in silicon PV (**Table 1**). Owing to these inherent advantages posed by IDF over pentacene, we chose to further evaluate the suitability of IDF for SF applications'.

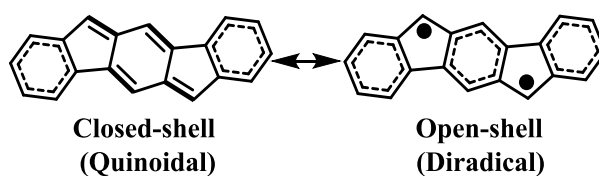


Figure 24. Resonance structure of indeno[1,2-*b*]fluorene ground states, emboldened; proaromatic quinodimethane structure. The delocalised benzene-rings depict the Clar's sextets.

To further expand upon the utility of the IDF scaffold, I intended to explore functionalisation at both the 6- and 12- positions (necessary to stabilise the biradical backbone),⁹⁹ in addition to studying the effects of additional substituents at the termini of the IDF core.

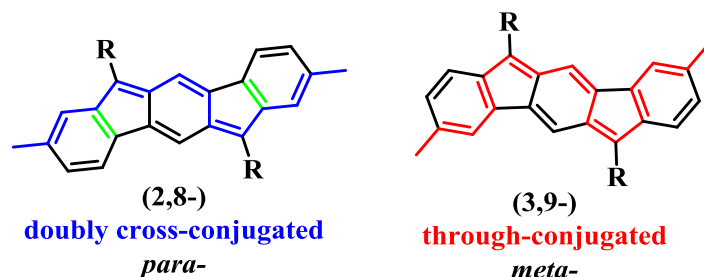


Figure 25. Synthetic expansion of 6,12- aryl substituted IDF scaffold at both the 2,8- (left) and 3,9- (right) terminal positions. Cross- and through- conjugation arrangements with cross-conjugated double bonds highlighted in green.

Arylation at the 6- and 12- positions has been shown to alter the optoelectronic properties of the resultant material.¹⁰³ Using either donor, acceptor or sterically hindering substituents the highest occupied molecular orbital (HOMO) and lowest unoccupied molecular orbital (LUMO) can be manipulated.

Whilst substitution at the 6- and 12- positions has been explored extensively by the Haley group⁹⁹ very little work has been conducted in post functionalisation of these IDF derivatives, specifically at the 2,8- and 3,9- positions respectively (**Figure 25**). Previous studies have shown that substitution of electron-rich or electron-poor groups at the 2- and 8- position had a moderate, but not significant, effect on the electronic properties of the resultant material.¹⁰⁴ This is in agreement with the calculated HOMO level, for **DX-IDF (6.2.1)**, which showed minimal orbital density at the 2- and 8- positions (**Figure 26**).

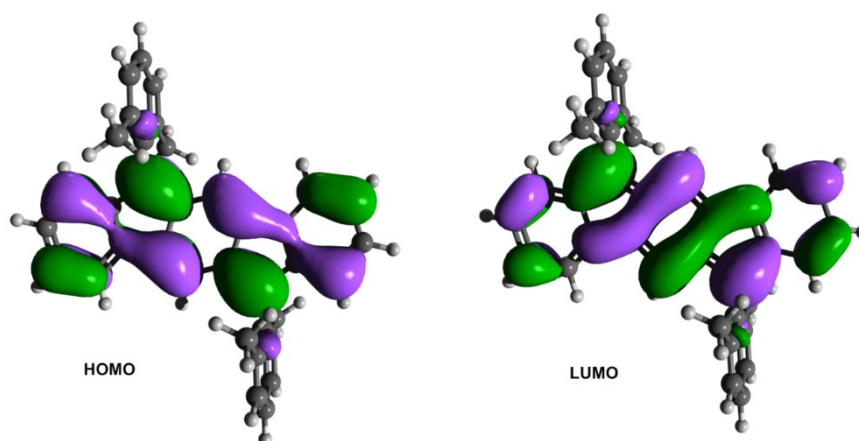


Figure 26. HOMO (left) and LUMO (right) plots for **DX-IDF (6.2.1)**.

In contrast HOMO/LUMO plots showed considerable orbital density at the 6- and 12-positions, supporting the concept that aromatic functionalisation at these positions will significantly alter the optoelectronic properties. Indeed, most literature examples of functionalised IDFs focus on synthetic functionalisation at the 6- and 12-positions, with very little work on synthetic expansion of the terminal 3- and 9- carbon positions. The Haley lab are well known pioneers of IDF chemistry; however, the bulk of their work has been on modifying the skeletal backbone studying the expanded quinoidal analogues rather than simple extension (through functionalisation at 3- and 9-positions) of the IDF core itself.⁹⁹

Interestingly, a paper published towards the end of 2016 demonstrated triplet formation (a key SF intermediate) for a series of pentacene dimers¹⁰⁵, the aromatic analogue of IDF. The reported triplets existed on the order of hundreds of femtoseconds, fulfilling one of the requirements for efficient SF (**Section 1.7.1**). This motivated the design rationale to form IDF-linked dimer materials, which would not only be more stable but also offer facile functionalisation strategies compared to the aromatic pentacene analogues. Therefore, the focus of the following two chapters will be the synthesis and exploration of the myriad of applications that substituted IDF materials offer, firstly towards the areas of intramolecular

singlet fission and secondly towards spintronics (**Chapter 3**), through the synthesis of dimeric and polymeric compounds, beginning initially with the synthesis of the parent IDF chromophore.

2.3 DESIGN RATIONALE FOR SINGLET FISSION

Singlet fission (described at length in **Section 1.7**), is the process in which a singlet-excited molecule and a molecule in the ground state ($S_1 + S_0$) share energy to produce a correlated pair of triplet excited molecules (T_1T_1), which dissociate into two individual triplets ($2xT_1$).¹⁰⁶ In order for SF to occur the thermodynamic and kinetic condition that the singlet energy must be approximately twice that of the triplet $E(S_1) \geq 2E(T_1)$ must be met. The material must also be able to avoid deactivation channels which quench fission such as triplet recombination or conical intersection decay pathways (*vide infra*).

Following preliminary experimental results, computational simulations supported the viability of the IDF core towards singlet fission and spintronic applications. It should be noted that the thiophene analogue (detailed in **Section 3.6**) 4,9-bis(2,6-dimethylphenyl)-s-indaceno[1,2-*b*:5,6-*b'*]dithiophene (**DX-IDT**) was predicted to not have favourable energetics for SF and hence was not included in this initial investigation (**Table 1**).

Table 1. Computational energy levels calculated using tuned wB97XD/6-311G**.

	DX-IDF	DX-IDT
S₀ – S₁ (eV)	2.58	2.45
S₀ – T₁ (eV)	1.24	1.28
S₁/T₁ (eV)	2.1	1.91

These computational results suggest that **DX-IDF** satisfies the staple rule for singlet fission with $E(S_1) \geq 2E(T_1)$ making it a feasible candidate for SF. Furthermore, the findings of Minami

and Nakano⁹⁷ suggest that the diradical character (**Figure 24**) of the IDF core could also promote efficient singlet fission, as this quinoid-diradical resonance lowers the triplet energy level. These computational results (**Table 1**) agree with recent literature¹⁰⁷ which suggests that the reduced aromatic character and electron-rich nature of thiophene inhibits the reduced singlet-triplet energy gap cf. the all carbon IDF analogue.

A recent publication by Sanders *et al.*¹⁰⁸ demonstrated singlet fission, through intramolecular triplet isolation, for a series of pentacene dimers and this was used as inspiration for novel expansion of the IDF skeleton. However, care has to be taken during the design of dimeric systems for SF as Basel *et al.*¹⁰⁹ suggest that intramolecular singlet fission requires the electronic coupling between the two monomer units to be limited, to allow spin decoherence leading to the formation of two independent triplet states, to successfully outcompete the triplet–triplet annihilation process. Although, Sanders *et al.*¹⁰⁸ have shown that the rate of triplet pair annihilation can be reduced by using a ‘bridge’ between each monomer unit to spatially reduce the coupling between triplet states.

Synthetically this can be achieved by introducing a chemical spacer (conjugated or non-conjugated) between the two monomer units. This prompted the design rationale behind creating a series of **DX-IDF** based dimers, centred around the hypothesis of stimulating the separation of triplet states by introducing phenyl bridges, spatially separating the **DX-IDF** monomer units and effectively decoupling the IDF chromophores. In theory, this design strategy should promote the dissociation of the triplet pair state, via conformational rotation of the aryl bridge, to form two isolated triplet excitons, allowing for sufficient and measurable intramolecular singlet fission (**Figure 27**).¹⁰⁸

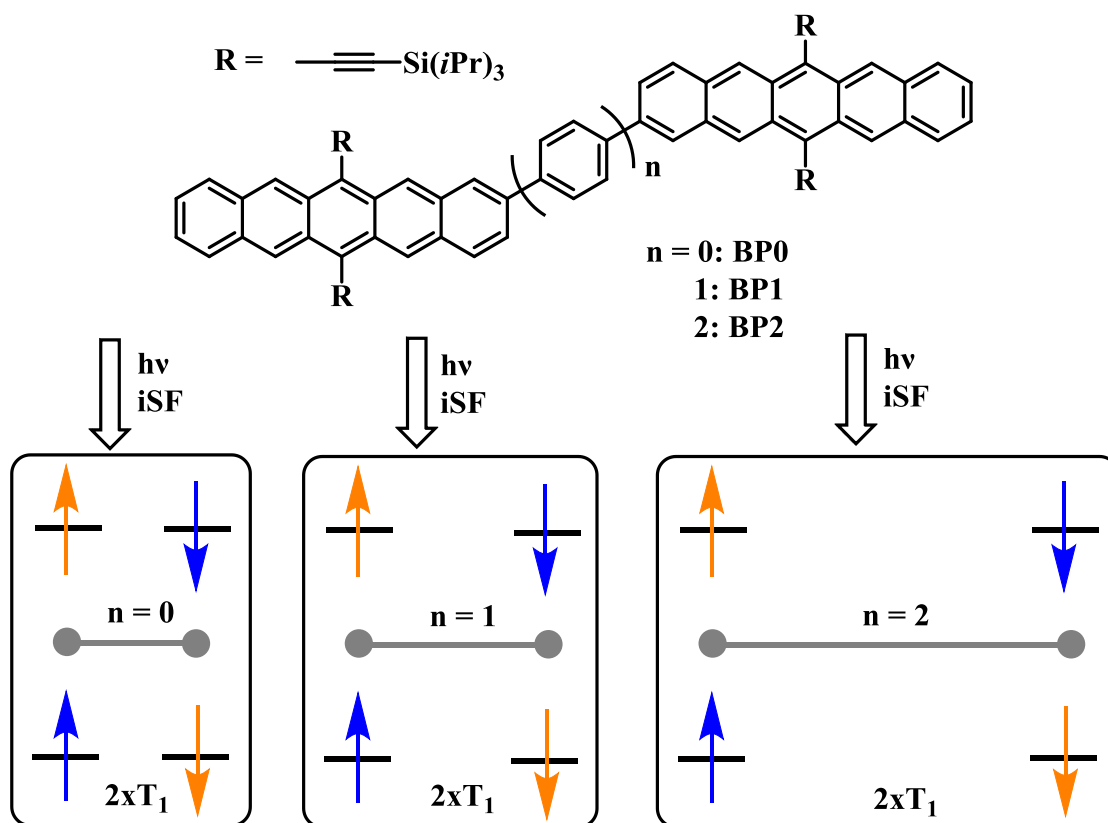


Figure 27. Pentacene chromophores separated by 0, 1 or 2 phenyl groups, reproduced from Sanders *et al.*¹⁰⁸

A major challenge in modern multiexcitonic devices is the incredibly short-lived existence of the triplet pair ($2xT_1$), hindering efficient charge extraction and limiting overall performance. It was hoped that by incorporating a phenyl spacer, between two flanking **DX-IDF** units, that the rate of singlet fission could be controlled through mediation of the overall conjugation and chromophore proximity relative to each other. Recreating the beneficial effects observed in Sanders' work¹⁰⁸ and combining this strategy with the inherent advantages of using the IDF core.

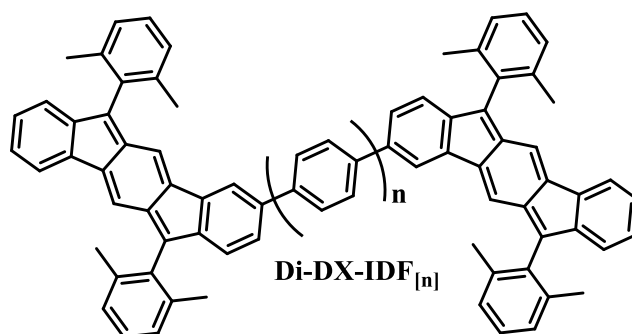


Figure 28. Molecular structure of **Di-DX-IDF_[n]** dimers where n=number of phenyl rings between IDF units.

Computational simulations were used to estimate the singlet excitation energy along with the expected triplet energy level for each dimer (**Figure 28**) (**Table 2**). The calculated $S_0 - T_1$ bandgap, for both **Di-DX-IDF_[1]** and **Di-DX-IDF_[2]** are close to the theoretical optimum energy value for maximum efficiency SF-based solar cells, proposed to be ~ 1.0 eV.⁸⁶ DFT calculations coupled with recent publications inspired the investigation into a series of **DX-IDF** dimer materials for intramolecular singlet fission (iSF) which will be described below.^{105,108}

Table 2. Computational energy levels for **DX-IDF** dimer series, calculated using tuned wB97XD/6-311G**.

	Di-DX-IDF_[0]	Di-DX-IDF_[1]	Di-DX-IDF_[2]
S₀ – S₁ (eV)	2.40	2.46	2.49
S₀ – T₁ (eV)	1.92	1.20	1.21
S₁/T₁ (eV)	1.25	2.04	2.06

Interestingly, the calculated $S_0 - T_1$ transition for the directly coupled dimer (**Di-DX-IDF_[0]**) is much higher than expected. However, spin density calculations can be used to explain this anomaly, which suggest that the triplet state is not isolated to one monomer of **DX-IDF** but is shared between both (**Figure 29**). Conversely, the triplet state of both **Di-DX-IDF_[1]** and **Di-DX-IDF_[2]** is computed to be isolated to one monomer, a phenomenon which should promote

singlet fission.^{105,110} The multiradical molecular orbital (MO) occupation is at the same level and the degeneracy of the occupations in dimers **Di-DX-IDF_[1]** and **Di-DX-IDF_[2]** shows the two isolated triplets, versus the higher radical character in the directly linked dimer **Di-DX-IDF_[0]**.

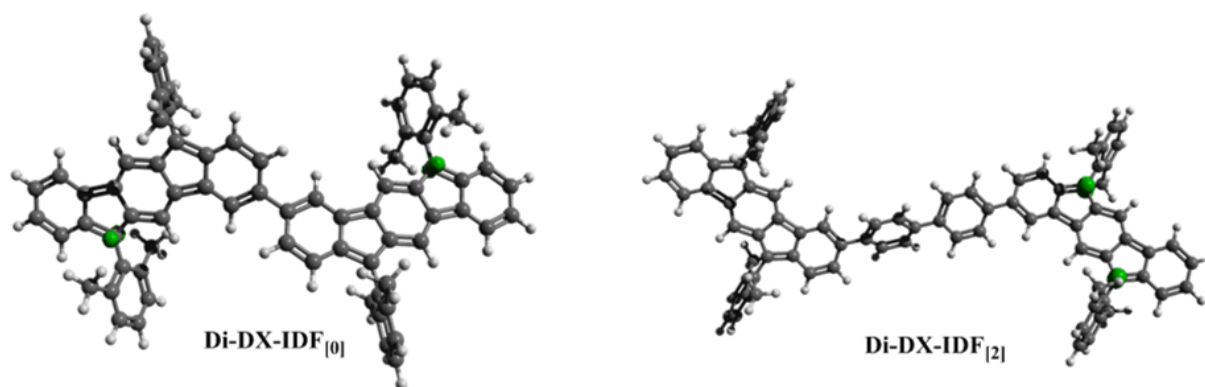


Figure 29. Spin density DFT calculations of the triplet state for **Di-DX-IDF_[0]** (left) and **Di-DX-IDF_[2]** (right). Calculated at the UHF/6-311G* level.

These calculations demonstrate that iSF is energetically feasible in both **Di-DX-IDF_[1]** and **Di-DX-IDF_[2]** dimeric compounds and not **Di-DX-IDF_[0]** due to a localisation of triplets on each IDF unit, resulting from favourable exchange energy interactions. Unlike monomeric xSF molecules, which depend on intermolecular interactions for singlet fission, these IDF dimers yield two triplets independent of intermolecular coupling. The use of progressively longer spacers hopes to extend the triplet pair lifetimes in order to facilitate harvesting of two electron-hole pairs for photovoltaic devices.¹⁰⁸ Conceptually this can be depicted as:

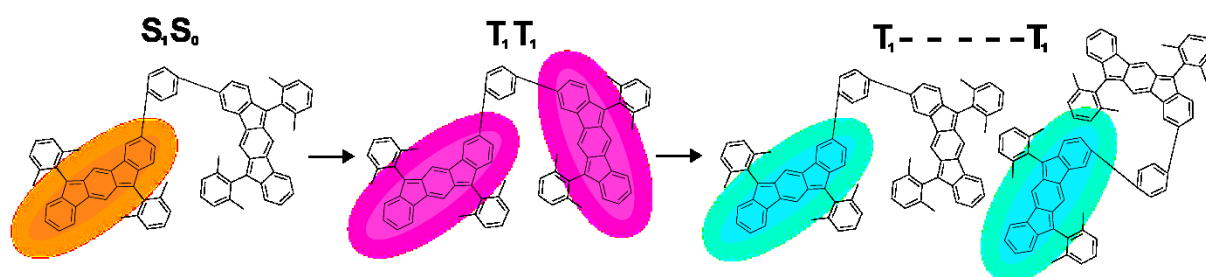


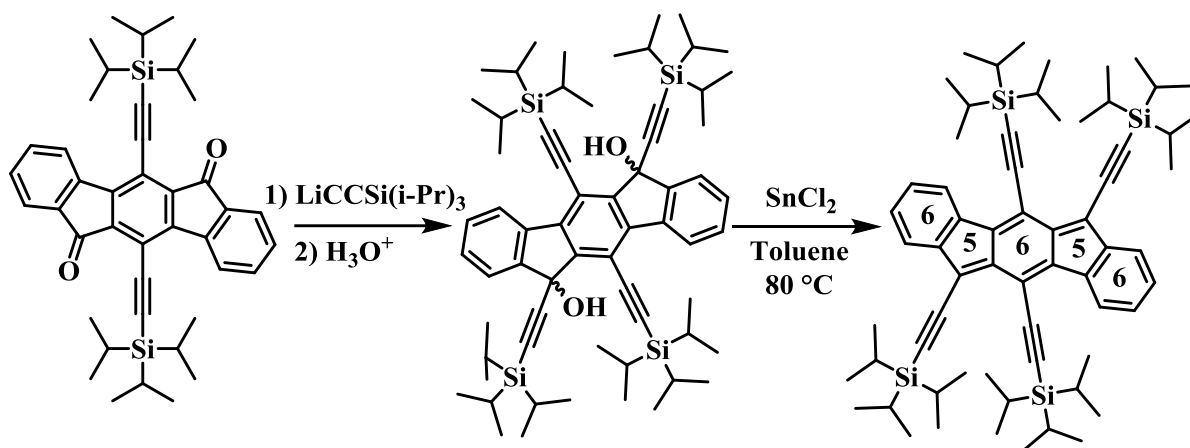
Figure 30. Simple graphical representation of the desired mechanism of singlet fission within an indenofluorene dimer.

were the initial excited state splits into the correlated (T_1T_1) triplet pair state, in this instance localised on a single phenyl linked dimer. This state then loses its electronic coherence and splits into the ($T_1 \cdots T_1$) spin coherent state spread over two individual chromophores.

Following both the experimental and synthetic success of the reported 2,2'-bipentacene dimers it was decided that Suzuki coupling¹¹¹ (known to work well for phenyl rings (1.4.2)) would be used to afford the desired **DX-IDF** dimers, this required the synthesis of both **mono-Br-DX-IDF** (6.2.5) & its boronic ester (6.2.8) coupling partner, both of which will be discussed in **Section 2.6**. The synthesis and characterisation of the parent chromophore **DX-IDF** is detailed first as this monomer unit will also feature in **Chapter 3**.

2.4 Sn^{II} -MEDIATED REDUCTIVE DEAROMATISATION

The atypical quinoidal motif has become increasingly common for multiple conjugated polycyclic systems in order to decrease the overall aromaticity or to increase the diradical character.¹¹² In 2009 the Haley lab reported an effective “addition-reduction” protocol to form a triisopropylsilyl acetylene substituted indenofluorene, the first known report of a SnCl_2 mediated reductive dearomatization (**Scheme 1**).¹¹³

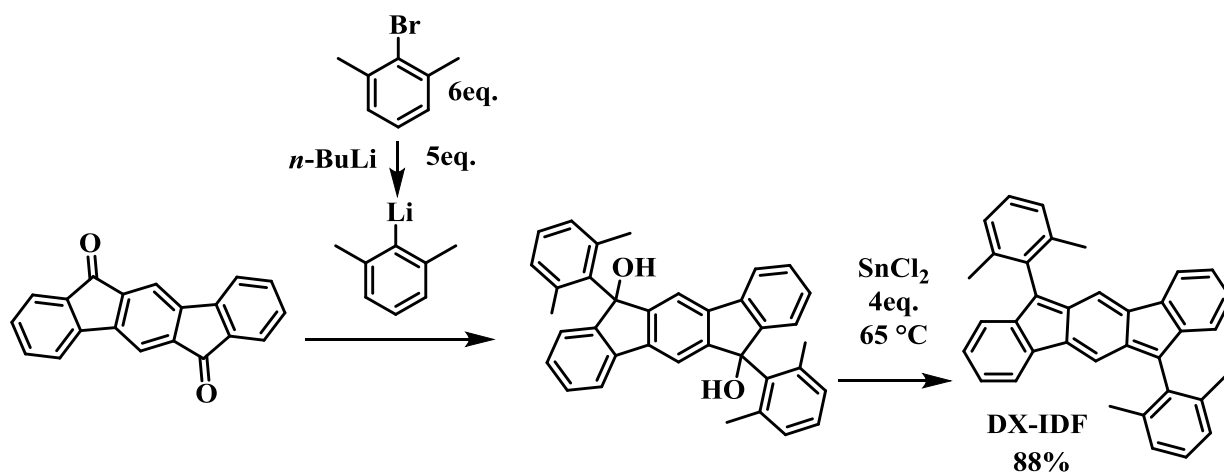


Scheme 1. SnCl_2 -mediated reductive dearomatization to form fully conjugated indenofluorene.¹¹³

Since then a wide variety of substituted and heteroatom-containing fluorene derivatives have been realised, giving merit to the utility of the SnCl_2 -mediated reductive dearomatization. Surprisingly, despite its excessive use throughout polycyclic antiaromatic chemistry the precise mechanism of the Sn^{II} -mediated reduction is still inconclusive. Multiple in-depth studies have been conducted claiming that the presence of acid is key to the reaction, however as shown above (**Scheme 1**) and *vide infra* there are multiple successful reactions without the presence of a Brønsted acid.¹¹⁴

2.5 DX-IDF SYNTHESIS & CHARACTERISATION

Following the proposed project plan, 6,12-bis(2,6-dimethylphenyl)indeno[1,2-*b*]fluorene (**DX-IDF**) was synthesised from the IDF diketone precursor following the standard procedure of Chase *et al.*¹⁰³ Addition of lithiated 2-bromo-*m*-xylene afforded crude diol, and subsequent reduction using SnCl_2 afforded **DX-IDF (6.2.1)** over two simple steps (**Scheme 2**).



Scheme 2. Synthesis of 6,12-bis(2,6-dimethylphenyl)indeno[1,2-*b*]fluorene **DX-IDF** (6.2.1).

DX-IDF was analysed by solution and thin film UV-vis spectroscopy (**Figure 31**) yielding comparable λ_{max} (wavelength corresponding to strongest photon absorption) (solution: 516 nm, film; 526 nm), absorption onsets (solution: 547 nm, film: 553 nm) and optical bandgaps (solution: 2.26 eV, film: 2.24 eV), which were consistent with published computational and experimental data.^{103,115} HOMO and LUMO energy levels were estimated, by cyclic voltammetry, at -5.49 and -3.18 eV, respectively, giving a bandgap of 2.31 eV, aligning with computational calculations, literature and UV-vis results.

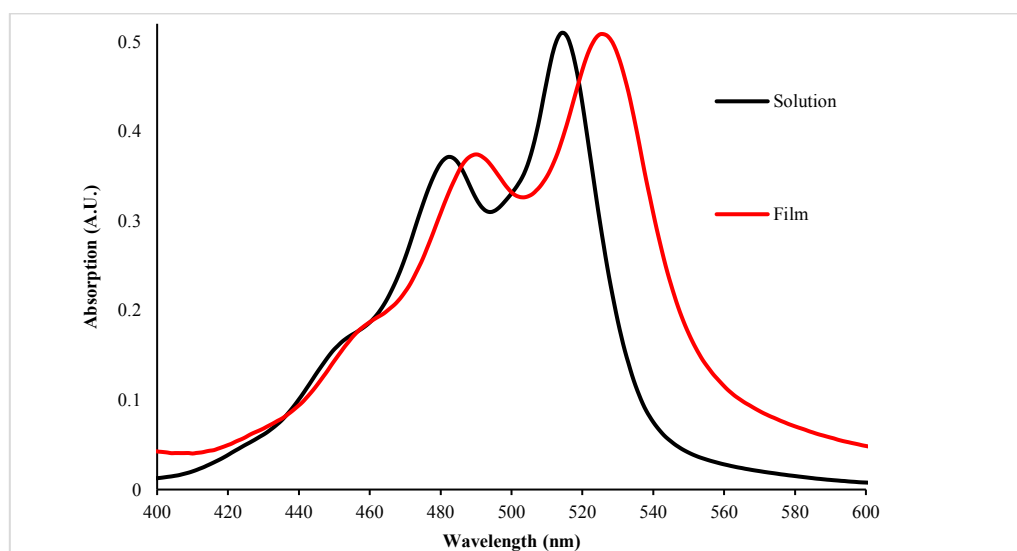


Figure 31. UV-vis absorption spectra for **DX-IDF** (6.2.1), recorded in CHCl₃ and from a thin film, spun at 1000 rpm from a 5 mg mL⁻¹ solution in chloroform.

A sample of **DX-IDF** was supplied to Dr Murad Tayebjee (Cavendish Laboratory, Cambridge) to be studied using transient absorption spectroscopy (TAS). The resultant spectrum shows rapid non-radiative decay of the excited state as the transient absorption bleach recovers within 12 picoseconds and no triplet formation was observed (**Figure 32**). The different subpicosecond dynamics observed in the blue portion (photoinduced absorption) portion of the plot is due to cooling to the bottom of the S_1 state after excitation with a broadband pump. This rapid relaxation inhibits photoluminescence and explains why this class of quinoidal molecules are non-emissive.

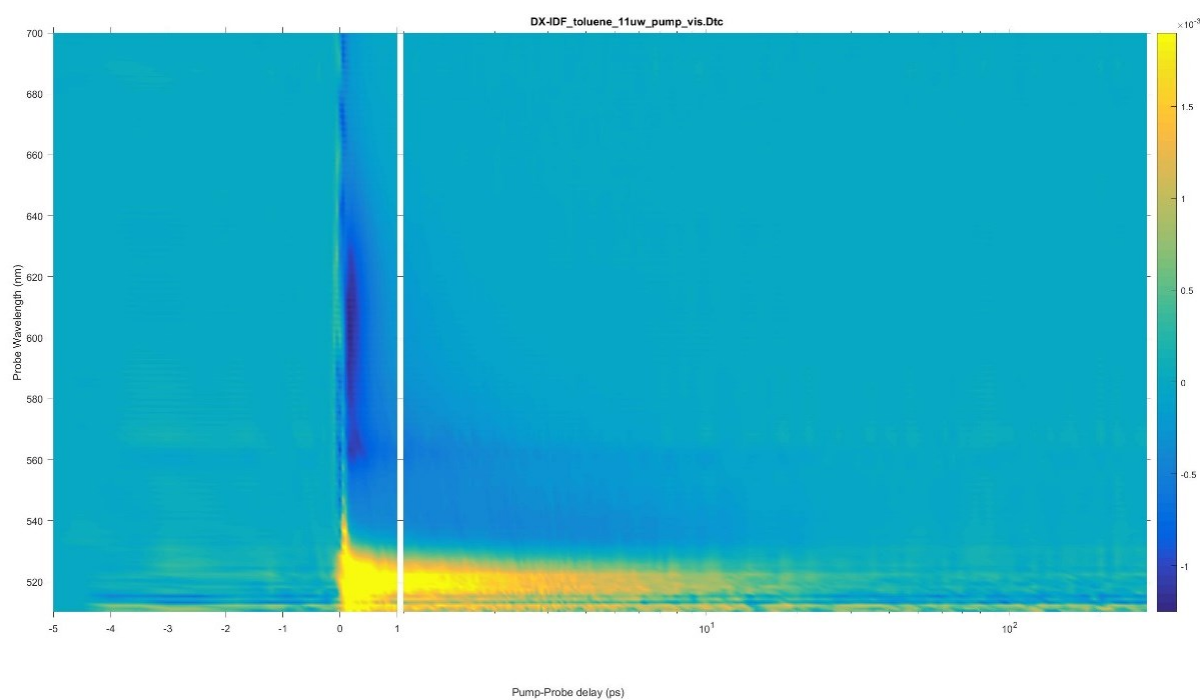


Figure 32. Solution (toluene) transient absorption data for **DX-IDF**, pumping at ~ 520 nm.

Whilst this was a disappointing measurement, the observation of triplet formation in solution, as not expected for the **DX-IDF** monomer. This short excited-state lifetime agrees with previous literature, which prescribes this phenomenon to the *p*-quinodimethane motif in IDF (**Figure 24**). Calculations also show that the lack of emission is due to internal conversion between the S_0 (ground) and S_1 (singlet excited state) via a conical intersection.¹¹⁶ However,

previous studies have shown that intramolecular SF should outcompete the non-radiative decay, occurring on a sub-picosecond timescale.¹⁰⁸

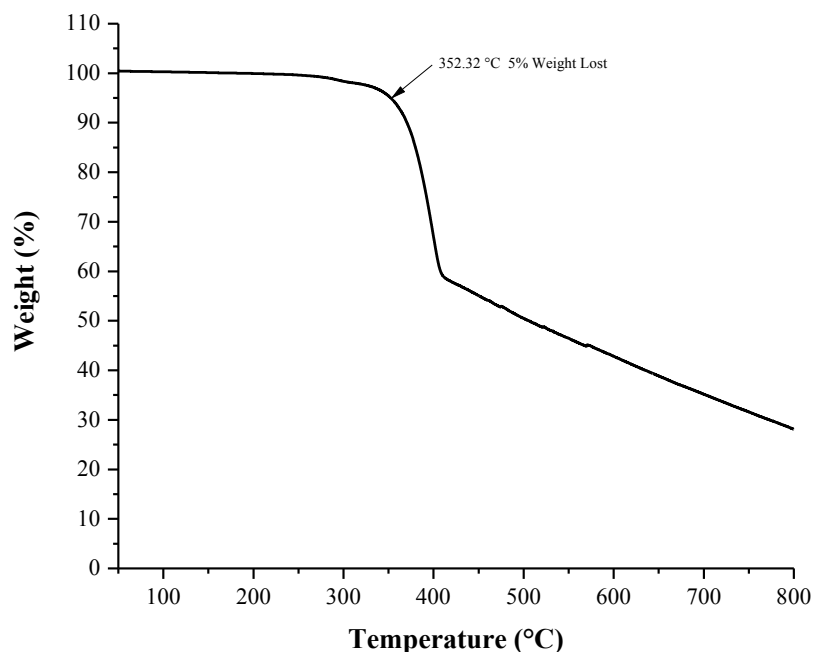


Figure 33. TGA trace for DX-IDF (6.2.1) recorded from 30 to 800 °C.

Thermostability investigation found the decomposition temperature (T_d) for **DX-IDF** occurs at 352 °C, assessed by the onset temperature of 5% weight loss by thermogravimetric analysis (TGA) (**Figure 33**). Furthermore, differential scanning calorimetry (DSC) which measures the energy released or absorbed by a sample as a function of time or temperature was used to determine the crystallisation/melting process. DSC provides a direct calorimetric measurement of the transition energy, at the specific temperature, when a thermal transition occurs in the sample. Both the melting point and crystallisation temperature can be determined during endothermic and exothermic phase transitions respectively. The DSC trace for **DX-IDF** was featureless, sweeping from 30 to 320 °C, suggesting no crystallisation or melting within the time period and temperature range of the scan. Despite this, a single crystal of **DX-IDF** was grown from slow evaporation from a concentrated CDCl_3 solution and was analysed by X-ray crystallography.

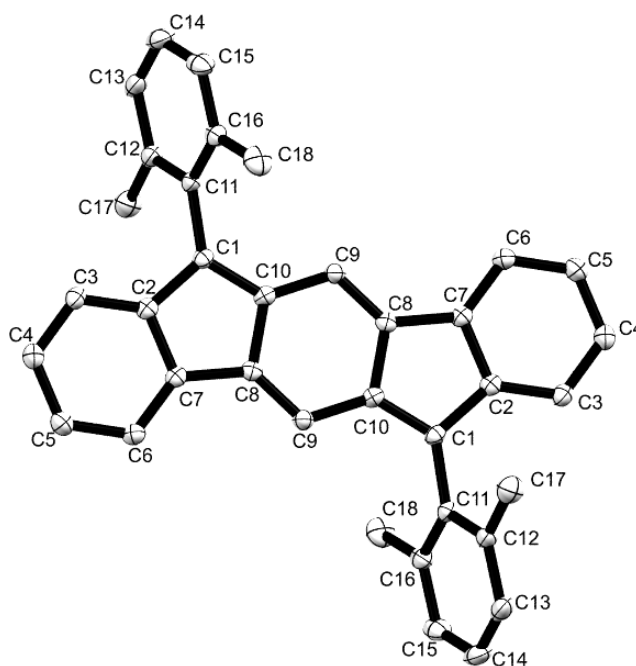
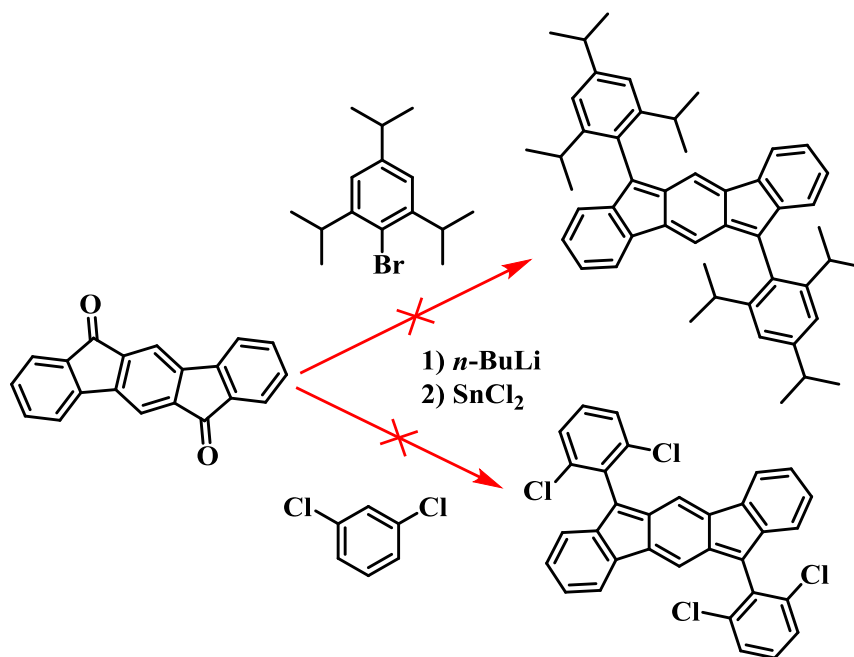


Figure 34. X-ray crystal structure of **DX-IDF (6.2.1)**; H atoms have been omitted for clarity, and ellipsoids are drawn at the 30% probability level.

The X-ray crystal structure of **DX-IDF (Figure 34)** has a dihedral angle between the *m*-xylene and indenofluorene rings of 72° and demonstrates herringbone type packing, in agreement with a similar structure published by the Haley group.¹⁰³ The packing shows little electronic communication between the π systems, which reduces the intermolecular conjugation path length. Similar reactions were attempted, substituting 2-bromo-*m*-xylene with 2,4,6-triisopropylbenzene and 1,3-dichlorobenzene (**Scheme 3**) however these nucleophilic additions proved to be unsuccessful. In both cases, tetramethylethylenediamine TMEDA was added to assist with deaggregation (chelating to lithium cations in *n*-BuLi)¹¹⁷ and LiCl was added to increase the electrophilicity of the IDF core, again however these reactions were unsuccessful.⁹⁹ These substituents may simply be too large and sterically bulky or electronically unfavourable to successfully add to the 6- and 12- positions, which has also been suggested in the Haley lab.⁹⁹ This consolidated the use of *m*-xylene as the functional group of choice which will be demonstrated throughout this thesis. The xylene motif strikes a steric

balance between stabilising the biradical 6- and 12- positions of the IDF core whilst still being able to be successfully reduced, using SnCl_2 to form the antiaromatic **DX-IDF**. Furthermore, the vacant 5- position can be functionalised, with additional solubilising units (**Section 3.9**), supporting the use of the *m*-xylene motif.



Scheme 3. Unsuccessful synthesis of 6,12-bis(2,4,6-triisopropylphenyl)indeno[1,2-*b*]fluorene (top) and 6,12-bis(2,6-dichlorophenyl)indeno[1,2-*b*]fluorene (bottom).

2.6 INDENOFUORENE MONOMER SYNTHESIS

Initially, the synthetic plan was to extend the IDF core, via selective bromination at the 2- and 8- positions (**Figure 23**). However, after bromination of **DX-IDF** with *N*-bromosuccinimide it was found, through ^1H - ^1H nuclear Overhauser effect spectroscopy (NOESY NMR), that bromination favoured the 3- and 9- positions (**Figure 35**). This was confirmed by the through-space coupling between the methyl group singlet (2.19 ppm) and the two doublets (7.19 and 6.56 ppm). If the bromination had occurred at the 2- and 8- positions the methyl group singlet would only couple to a singlet, from the hydrogen at the 1- and 7- position. This is in line with

the calculated HOMO density of states diagram (**Figure 26**) which showed considerable delocalisation of the HOMO at both the 3- and 9- position (further detailed in **Section 2.2**).

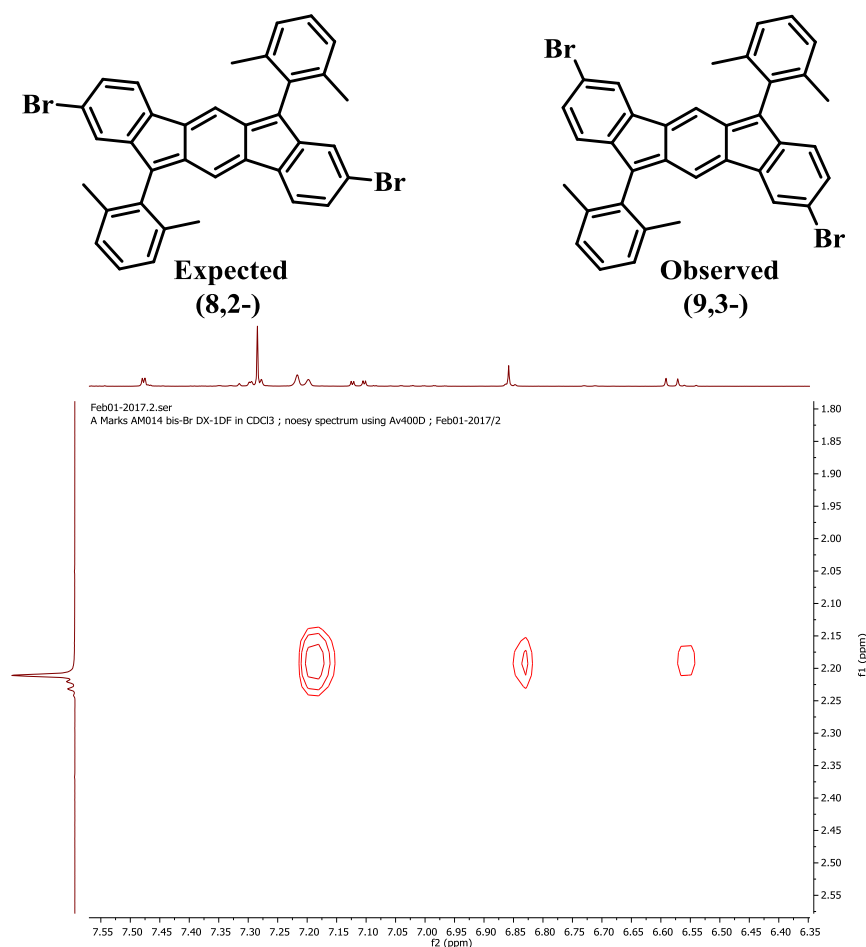


Figure 35. Expected (left) and observed (right) product of **DX-IDF** bromination and NOSEY NMR confirming this result.

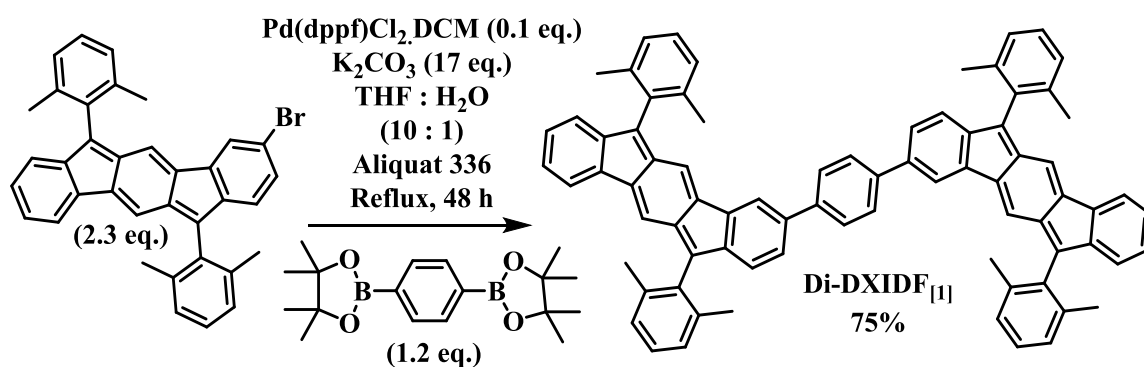
Mono-brominated DX-IDF was synthesised in high yield (97%) but required the addition of glacial acetic acid to protonate NBS, decreasing the photodissociation energy and promoting heterolysis of NBS to Br^+ aiding electrophilic bromination. The **DX-IDF mono-BPin (6.2.7)** coupling partner was also successfully synthesised, in slightly decreased yield (74%), using a standard Miyaura borylation reaction.¹¹⁸ KOAc was used as the base with $\text{Pd}(\text{dppf})_2\text{Cl}_2$.DCM as the catalyst, to afford the stable boronate species. Whilst this coupling partner was needed for the directly coupled **Di-DX-IDF_[0]** dimer (**Scheme 5**) the further extended dimers **Di-DX-**

IDF_[1] and **Di-DX-IDF**_[2] required the respective diboronic acid bis(pinacol) ester of the phenyl bridge coupled with two equivalents of the **mono-brominated DX-IDF** unit (**Scheme 4**).

2.7 INDENOFLOURENE DIMER SYNTHESIS

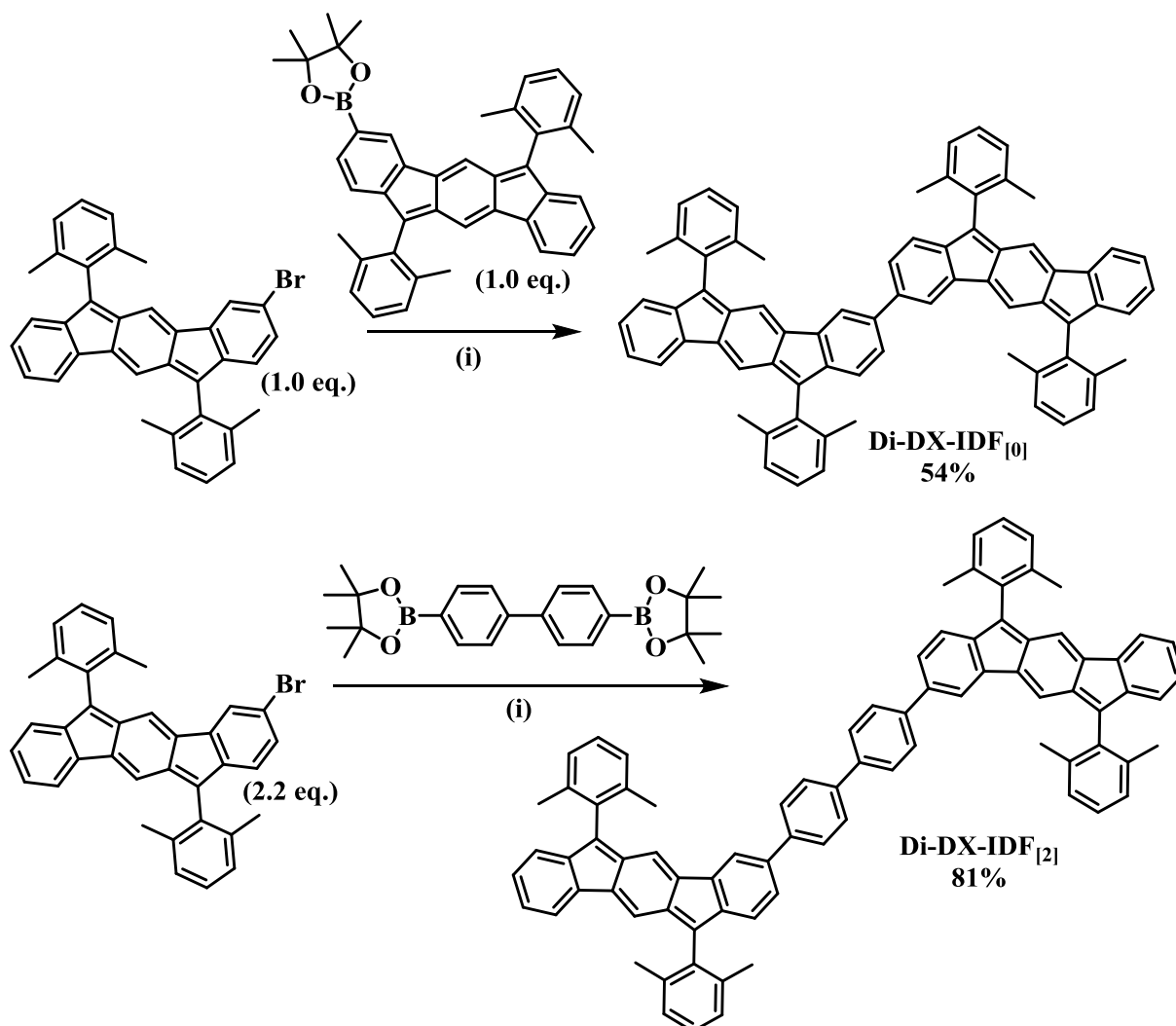
The Suzuki–Miyaura coupling reaction was first published in 1979 and multiple advancements have led to this coupling mechanism (**Figure 13**) becoming one of the “gold standards” for biaryl construction.^{41,42,119} Whilst this chemistry is extremely well known, the synthesis of the single phenyl spaced dimer (**Di-DX-IDF**_[1]) proved to be troublesome with multiple test scale reactions yielding little to no product.

Initially Pd(PPh₃)₄ was used as the catalyst, a common reagent for many standard Suzuki cross-coupling reactions, however these conditions (**6.2.10**) only afforded a yield of 22%. Multiple reactions were conducted, each altering one unique element of the reaction, firstly several catalyst systems were investigated including Pd(PPh₃)₄, Pd(OAc)₂, PEPPSI-IPr, PdCl₂(PPh₃)₂ and Pd(dppf)₂Cl₂.DCM. Secondly the base was changed between K₂CO₃ and K₃PO₄, finally the temperature was changed between the range of 60-90 °C. The most successful combination was found to include Pd(dppf)₂Cl₂.DCM as the catalyst, a reduced amount of base and a temperature of 85 °C. The combination of which successfully improved the yield of the coupling reaction three-fold, affording the **Di-DX-IDF**_[1] dimer (**Scheme 4**) in a 75% yield.



Scheme 4. Suzuki cross coupling reaction to afford **Di-DX-IDF**_[1] 1,4-bis(6,12-bis(2,6-dimethylphenyl)indeno[1,2-*b*]fluoren-3-yl)benzene (**6.2.10**).

Once Pd(dppf)₂Cl₂.DCM was identified a viable catalyst for the Suzuki coupling the directly coupled dimer **Di-DX-IDF_[0]** (**6.2.9**) and the bisphenyl bridged derivative **Di-DX-IDF_[2]** (**6.2.11**) were synthesised using similar conditions, affording 54% and 81% yield respectively. The identity of the coupling products was confirmed by NMR and matrix-assisted laser desorption/ionization (MALDI) mass spectrometry.



Scheme 5. Suzuki coupling to yield **Di-DX-IDF_[0]** (**6.2.9**) and **Di-DX-IDF_[2]** (**6.2.11**). Reaction conditions: (i) Pd(dppf)₂Cl₂.DCM (0.1 eq.), K₂CO₃ (17 eq.), Aliquat 336, THF:H₂O (10:1 v/v), 85 °C, overnight.

2.8 INDENOFUORENE DIMER RESULTS

The optical absorption of each material was studied in both solution and solid state (thin film) (**Figure 36**), showing a slight redshift in λ_{\max} upon increasing the separation between the **DX-IDF** monomer units.

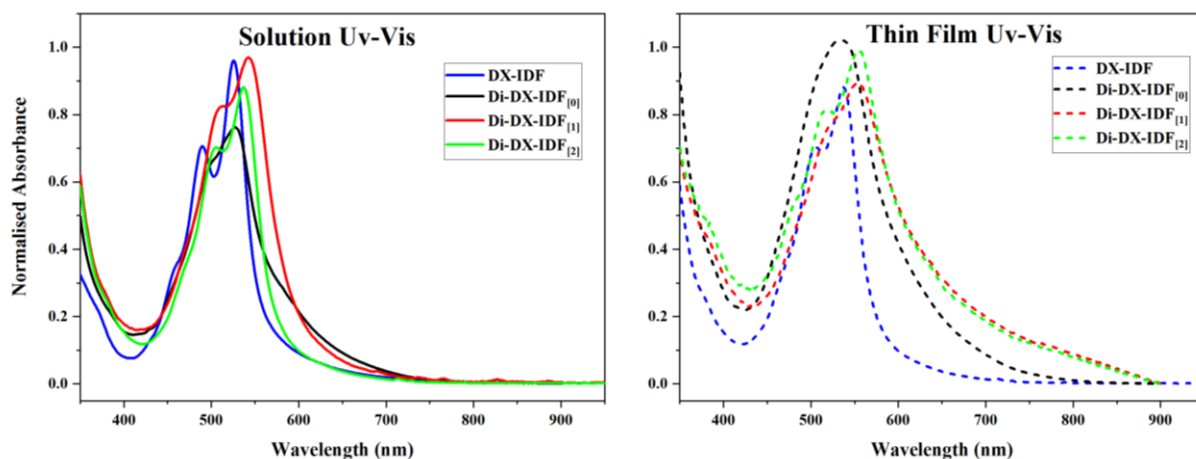


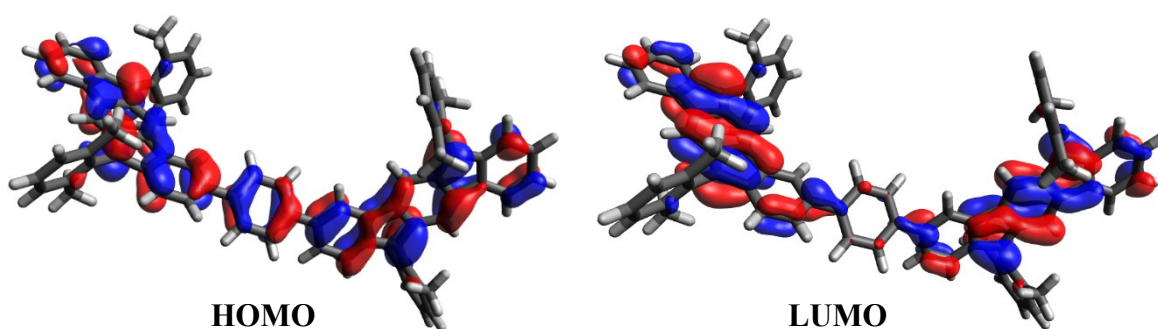
Figure 36. Solution (solid line - left) and thin film (dashed line - right) UV-Vis for **DX-IDF** and series of DX-IDF dimers.

Unsurprisingly the optoelectronics of all three phenyl bridged dimers are very similar, showing a decrease in overall bandgap compared to the **DX-IDF** monomer unit. The minimal differences in λ_{\max} across the series suggests that the through conjugation (**Figure 25**) 3- and 9- carbon bonded phenyl linker has minimal effects on the optoelectronic properties, which are dominated by the **DX-IDF** chromophores. A slight redshift (to longer wavelengths) was observed for λ_{\max} when moving from solution to film for each of the tested materials, suggesting some degree of aggregation in the solid state. Optoelectronic gaps (HOMO-LUMO gap) were in general agreement between solution, film and computational predictions.

Table 3. UV-Vis absorption table for **DX-IDF** and dimeric derivatives.

	DX-IDF	Di-DX-IDF_[0]	Di-DX-IDF_[1]	Di-DX-IDF_[2]
Bandgap [Uv-Vis Onset] [CH ₂ Cl ₂]	2.26 eV (547 nm)	1.99 eV (623 nm)	2.12 eV (586 nm)	2.16 eV (574 nm)
λ_{\max} [CH ₂ Cl ₂]	516 nm	528 nm	542 nm	537 nm
Bandgap [Uv-Vis Onset] [Film]	2.24 eV (553 nm)	2.03 eV (611 nm)	1.93 eV (642 nm)	1.95 eV (636 nm)
λ_{\max} [Film]	526 nm	535 nm	552 nm	554 nm

Density Functional Theory (DFT) was used to model each indenofluorene dimer, tuned at the ω B97XD/6-31G* level. Mapping the electron density isosurfaces for the frontier molecular orbitals was conducted to investigate the nature of the HOMO and LUMO. Similar to the monomer, the HOMO for **Di-DX-IDF_[1]** has a longitudinal configuration, with lobes spanning over five carbon centres and across all three ring systems (**Figure 37**). This spreads across the phenyl bridge to form a fully delocalised HOMO across the entire molecule. This is conducive to the abundance of electron density found at the *meta*- (3- and 9-) positions within the monomer (**Figure 25**), facilitating through-coupling of the quinoidal core.

**Figure 37.** DFT calculated HOMO (left) and LUMO (right), for **Di-DX-IDF_[1]** tuned at the ω B97XD/6-31G* level.

The lack of planarity shown for each of the dimers is likely due to the nature of the *meta*-coupling, forcing the bulky xylene groups to repel apart freely twisting about the aryl linker.

This could negatively affect the possibility for singlet fission as geometric relaxation could accelerate the crossing of excited state and conical intersection potential energy surfaces leading to rapid decay and quenching fission.

Following this initial chemistry focused investigation, a sample of each dimer and the **DX-IDF** monomer were studied by Dr. Murad Tayebjee and his student Chanakarn Phansa, conducting multiple transient absorption measurements in the hopes to observe singlet fission within these materials. The results were interesting and somewhat inconclusive due to the extremely short timescale upon which this phenomenon occurs and is detectable.

It should be noted that for each measurement the excitation is to the S_2 (B_u) state since the S_0 (A_g) to S_1 (A_g) transition is symmetry forbidden (these symmetry labels are calculated for the indenofluorene core without the xylene groups (C_{2h} point group)). Computational calculations predict a symmetry forbidden S_0 to S_1 transition for symmetric indenofluorenes as these compounds contain an inversion centre, which is attributed to a HOMO-1 to LUMO transition.⁹⁹ Relaxation from S_2 (B_u) to S_1 (A_g) is symmetry allowed and is observed as the favoured relaxation pathway for both the monomer and each DX-IDF dimer. Haley *et al.*¹¹⁶ demonstrated the subsequent rapid relaxation from S_1 to S_0 occurs via a conical intersection, a crossing of potential energy surfaces between each state. This is mainly due to the small difference in energy and geometry of the S_1 and conical intersection promoting efficient non-radiative decay to the ground state, which was indeed observed for **DX-IDF** in solution (**Figure 32 & Figure 38**).

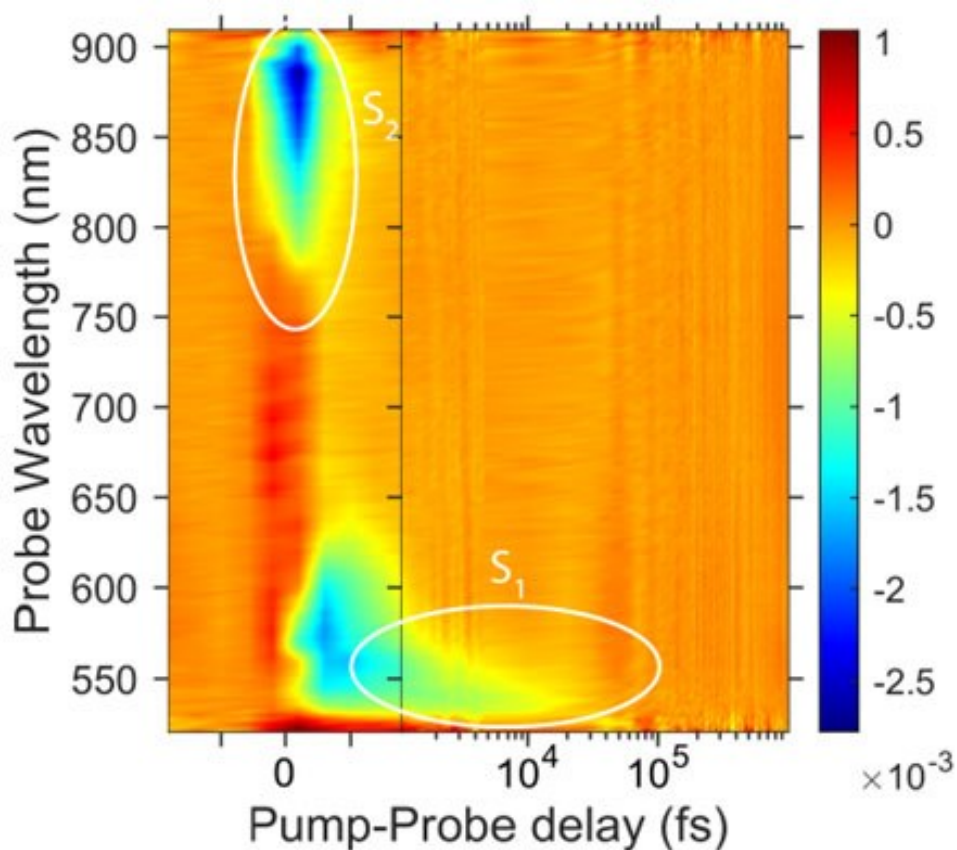


Figure 38. Solution transient absorption spectrum for **DX-IDF** (5 mg mL^{-1} in chloroform), showing the rapid decay from S_2 to S_1 .

The negative differential transmission signals observed within the picosecond range correspond to excited state absorptions¹⁰⁶, specifically the expected S_0 to S_2 excitation (**Figure 39**). No long-lived state (related to triplet states) was observed for either the toluene or chloroform solution measurement with the **DX-IDF** dimer. The rapid decay from S_1 to S_0 , via conical intersection, was measured at ~ 9 picoseconds meaning fission will need to outcompete this rapid relaxation.

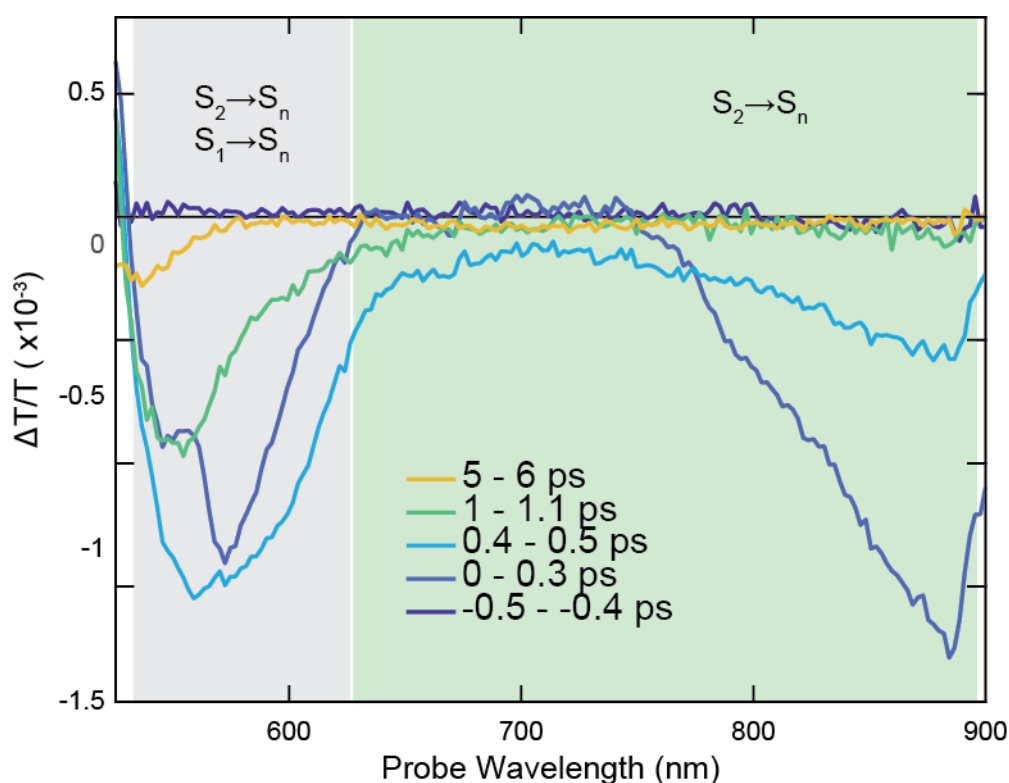


Figure 39. DX-IDF monomer 5 mg mL⁻¹ chloroform solution transient absorption map.

The rapid decay, via conical intersection, for the **DX-IDF** monomer follows the report from Haley *et al.*¹¹⁶, however the recent work with bipentacenes¹⁰⁸ has shown that fission can occur on a sub-picosecond timescale. In terms of chemical approaches there are two issues: first the S₀-S₁ transition is symmetry forbidden (previously reported DFT calculations)¹¹⁶. Therefore, excitation occurs to the S₂ state which rapidly decays to the S₁. In principle this will not stop fission because the S₁ has a similar energy to the S₂, similar observations have been reported in carotenoids.¹⁰⁶ The second issue is the conical intersection from the S₁ state to the ground state. This means that fission must compete with a ~9 ps process. This arises in part, from a large difference in the equilibrium S₀ and S₁ molecular geometries. In IDF this is mainly due to an enlargement and distortion (away from a regular hexagon, but still planar) of the 6-membered rings at the two ends of the molecule. It was hoped that incorporating a phenyl bridge spacer, akin to previous reports^{105,120}, would limit geometric vibration and reduce crossing points for the potential energy surface of the S₁ state and conical intersection.

Encouragingly, the transient absorption spectra for the **DX-IDF** dimers differed from the monomer and did indeed suggest the presence of a long-lived excited state between the S_2 and S_0 ground state (**Figure 22**). Various measurements were conducted to confirm the legitimacy of this state, concluding a repeat experiment using films on sapphire (vs quartz) which yielded the same outcome, confirming that this state is not associated with a thermal artefact. The film dynamics (**Figure 40**) suggest that the long-lived emissive state can be equated to an excimer, formerly known as an excited dimer. For both phenyl-bridged dimers (**Di-DX-IDF_[1]** & **[2]**) this excimer is the preferred relaxation pathway from the originally excited S_2 state. The excimer exists on a nanosecond timescale, a factor of one thousand times longer than the rapid picosecond relaxation times observed for both the monomer and S_2 to S_1 relaxation. This is shown in (**Figure 40**) as a long-lived bleaching of the transient absorption spectrum, specifically for the **Di-DX-IDF_[1]** single phenyl-bridged dimer.

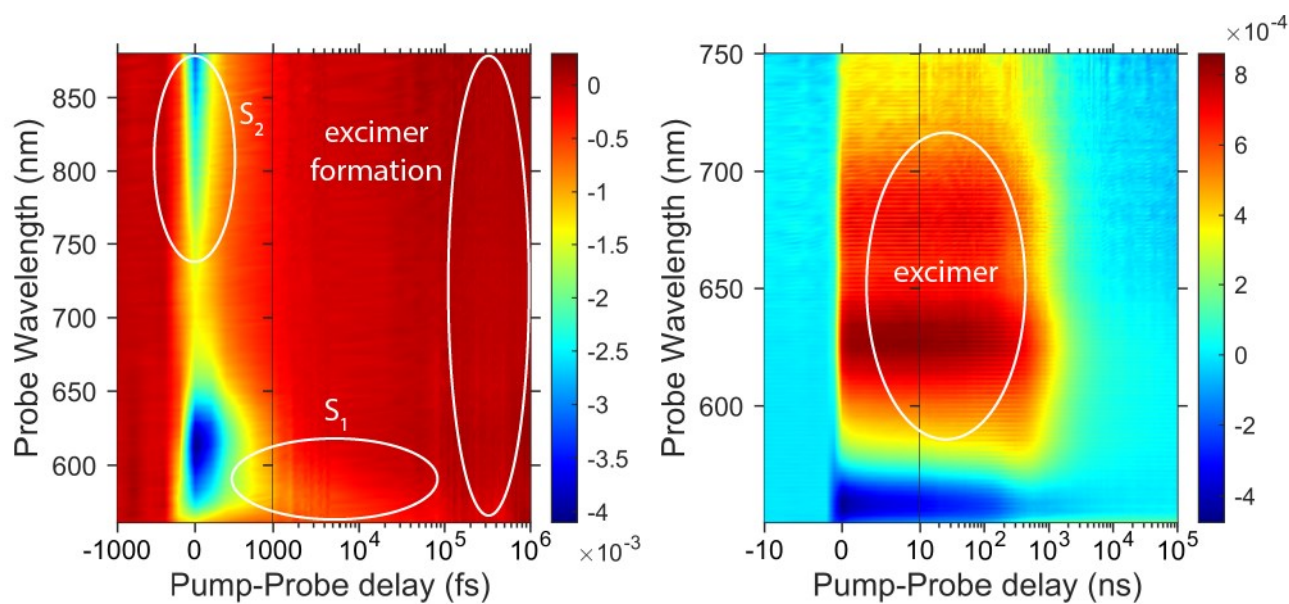


Figure 40. Solid state transient absorption spectrum for **Di-DX-IDF_[1]** film, excited at 532 nm. A simple description of the order events follows excitation from S_0 to S_2 , subsequent rapid relaxation to S_1 followed by relaxation to a long-lived emissive state which then decays biexponentially to the ground state. This can be depicted, albeit simplistically, as a Jablonski

diagram which is a reasonable visual representation of the film dynamics observed for **Di-DX-IDF_[1]**.

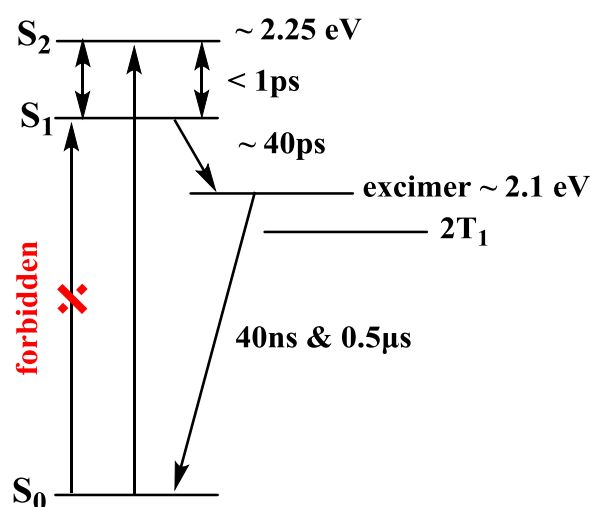


Figure 41. Proposed Jablonski diagram for the excited states of **Di-DX-IDF_[1]** dimer films.

The next question that arises is whether this excimer can be related to singlet fission, i.e. is this excimer a coupled triplet state? This was relatively tedious to measure, the rapid decay of the S₁ state (to the excimer) poses a problem for defining the exact energy of the underlying triplet as phosphorescence will be negligible and non-measurable. Previous reports for both pentacene and tetracene have shown that an excimer state is a key intermediate prior to triplet dissociation to form two T₁ states.^{98,108,120} For both of these systems initial excitation is followed by geometric relaxation to an excimer state, pentacene then undergoes a rapid nonadiabatic transition to a multi-exciton dark state. This dark state is directly linked to two T₁ states. It was hoped that the same process was being observed for the indenofluorene dimer.

Sadly, ESR measurements and magnetic field dependent photoluminescence could not find any evidence for fission occurring in any of the dimers. It was found that the excimer would simply relax back to the S₀ ground state, albeit biexponentially, with no dark state intermediate being detected. This agrees with the DFT calculations above (**Table 2**) which suggest that the triplet energy level is slightly below that detected for the excimer. It seems that the excimer originates

from a dimming of the singlet state that can't quite access the conical intersection. This finding along with the T_1 and T_2 relaxation times is summarised in the time dependant population diagram below (**Figure 42**).

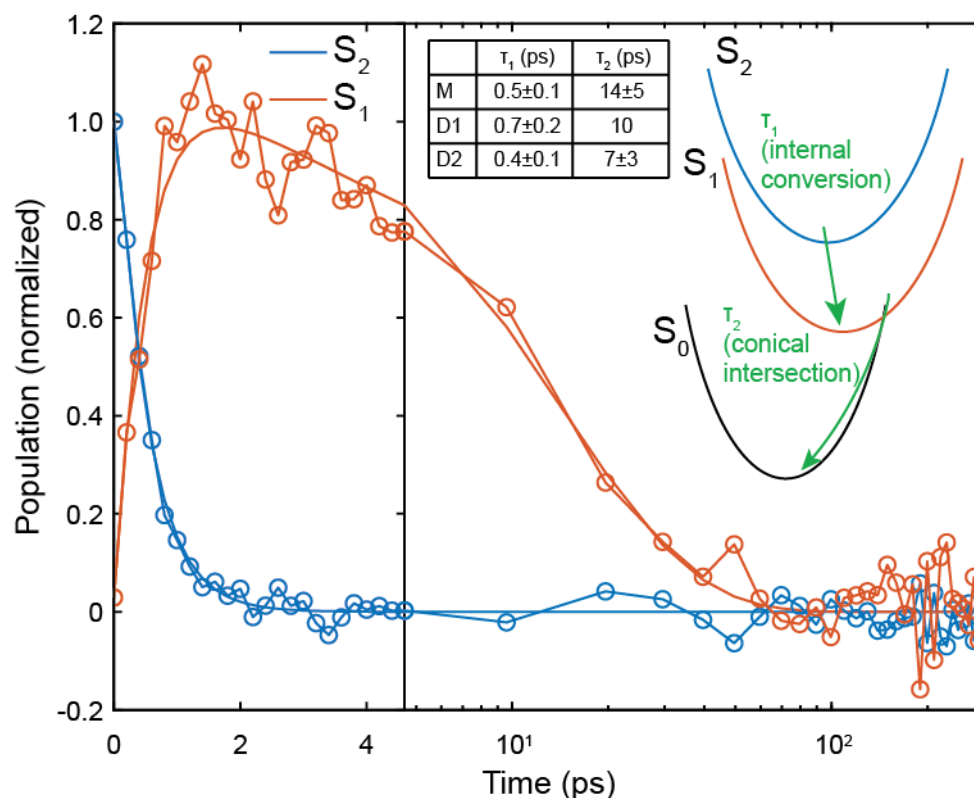


Figure 42. Time dependence of the excited state population kinetics, linear combinations of the principal components were used to recreate the S_1 and S_2 transient absorption spectra and the reconstructed dataset is shown as open circles.

Whilst, these results were disappointing, as fission was not observed, the inclusion of a phenyl bridge between the two **DX-IDF** chromophores did partially succeed in retarding access to the conical intersection. This was promising as the excimer had a relatively long lifetime, fitting one of the criteria for efficient SF. This is also a promising route to surpass the conical intersection which has plagued the field of optoelectronics with indenofluorene based systems.¹¹⁶ Further chemical manipulation of the spacer linker may indeed sufficiently limit geometric relaxation leading to crossing the potential energy surface of the conical intersection. More recently this has been demonstrated by Wang *et al.*¹²¹ who prepared a series of

indeno[1,2-*b*]fluorene-based [2,2]cyclophanes, fused across the central 5- and 11- positions (**Figure 23**) covalently binding the IDF chromophores in a sandwich motif compared to the extended dimers presented above. This was also shown to be an effective way to retard access to the conical intersection with the resultant excimer showing a long decay time of ~ 3.6 ps. Both methods could be employed in the future to probe the unusual electrochemical and photophysical properties of the IDF backbone.

2.9 CONCLUSIONS

In summary these measurements show that fission does not occur or is very inefficient despite the favourable energetics in terms of the rapid decay of the singlet. Perhaps this is why these materials are so photochemically stable, as all absorbed energy is rapidly dumped through the conical intersection decay pathway. This has shown to be true even under intense UV irradiation and thus these extended phenyl-bridged indenofluorene dimers may be suited for dye/paint applications. Positively, these measurements confirm that access to the conical intersection, which has plagued indenofluorene optoelectronic applications, is indeed retarded by including phenyl-bridges between two chromophores.¹¹⁶ This could be employed as a design strategy moving forward to utilise the stability and functionality of the quinoidal core. However, it appears from the ESR results that this is merely delaying access and not utterly blocking this decay pathway as no fission could be observed for any of the dimers. Further studies could be conducted with altering the bridging unit to planarize the dimeric system or perhaps locking rotation about the spacer unit which could be methods to further retard decay via the conical intersection. Recent work, published after this investigation, also suggests that the SF within these dimeric systems is linker dependent.⁹⁷ Following these promising results along with recent advancements in the field perhaps a more well-tuned IDF dimer system could be pursued in the future.

CHAPTER THREE: SPINTRONIC MATERIALS

3.1 ABSTRACT

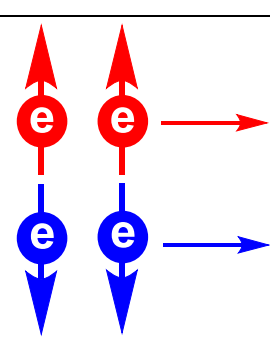
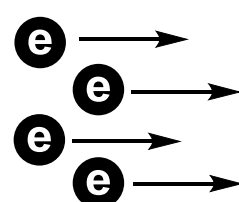
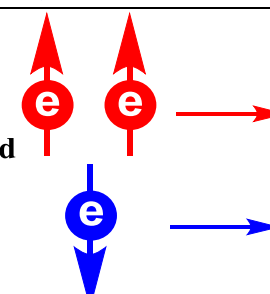
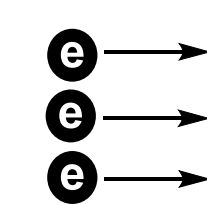
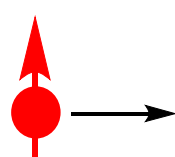
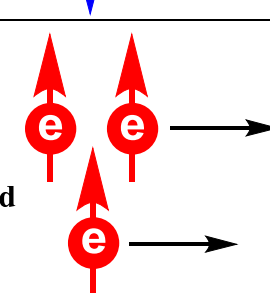
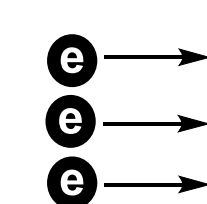
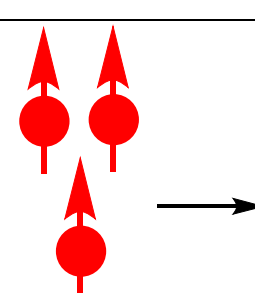
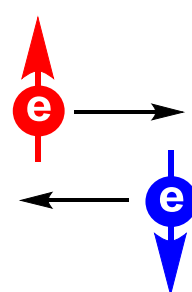
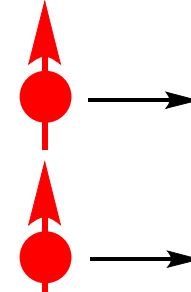
Chapter 2 discussed the synthesis of di-xylene substituted indenofluorene (**DX-IDF**) and detailed the subsequent singlet fission investigation for a set of phenyl bridge dimers. This chapter will further expand on the versatility of **DX-IDF** and its halogenated derivatives. In addition, the synthesis of the sulphur-containing analogue indacenodithiophene (**DX-IDT**) will also be detailed. As part of the ERC Spintronics Synergy project, headed by Prof. Henning Sirringhaus (University of Cambridge), the series of materials herein was designed to probe the effect of biradical polycyclic aromatics in spintronic devices. The effect of biradical character on the ability to transport a spin current is investigated using the bespoke ferromagnetic linewidth broadening experiment (*vide infra*). This required the synthesis of higher biradical character materials, the troublesome synthesis of which is also detailed herein. Encouragingly, **DX-IDF** recorded a ferromagnetic linewidth broadening of $\delta\Delta H = 0.60 \pm 0.03$ G and a spin mixing conductance of $g_{eff}^{\uparrow\downarrow} = 3.74 \times 10^{18}$. These results surpass those recently published for dinaphtho[2,3-*b*:2',3'-*f*]thiopheno[3,2-*b*]thiophene (**DNTT**) which was previously the record holder within this experiment. Finally, the utility of the IDF and IDT cores were expanded upon once more through the synthesis of a potential quinoidal non-fullerene acceptor and a series of conjugated polymers with various co-monomers, the details of both are also reported below.

3.2 SPIN CURRENTS

Spintronics is a relatively new field, evolving rapidly over the past decade as an important communication technology. The principle of spintronics involves studying the spin angular momentum inherent to an electron opposed to standard information processing involving manipulation of charge. The field has been well reviewed in recent years^{122,123} and the underlying physics is far beyond the reach of this thesis, instead a general introduction and

understanding from the view of a synthetic chemist is presented. The challenge of a chemist in this domain is to identify and design materials that can generate, detect and manipulate spin.

Table 4. Illustration of the four classes of current, adapted from Feng *et al.*¹²⁴

	Charge Current	Spin Current
<p>Unpolarised current</p> 		<p>0</p>
<p>Spin-polarised current</p> 		
<p>Fully spin-polarised current</p> 		
<p>Pure spin current</p> 	<p>0</p>	

There are four distinct types of current, within this context, each depicted in (Table 4). Firstly, a normal (unpolarised) electric current is the motion of electrons with random spins (spin-up or spin-down) cancelling out to have zero overall spin current. Secondly, a spin polarised

current which consists of the motion of electrons with ordered spins, carrying an overall spin, this category can be further divided into partial and fully spin-polarised current. Finally, and most important to the field is the pure spin current, a motion of ordered spin without any net motion of charge.

Spin currents offer a potential way to circumvent problems inherent to the motion of charge, such as heat accumulation and resistivity power losses.¹²⁴ However, pure spin-currents are extremely difficult to generate¹²² and thus have been the focus of many recent studies in the field. Once reliable generation of pure spin-currents is developed we can expect the future of computing and communication technologies to shift towards this architecture.

3.3 FERROMAGNETIC RESONANCE LINEWIDTH BROADENING

Previous research has shown that spin-currents can be injected from ferromagnets (materials with a net magnetic moment) into nonmagnetic materials through spin pumping. Spin pumping can be thought of as spintronics analogy for a conventional electronic battery, as a method for generating spin current. This can be achieved through the precession of magnetization, via excitation, within a ferromagnet under ferromagnetic resonance (FMR) conditions leading to harvestable spin accumulation.^{125,126}

When this research began back in 2018, there was yet to be any published reports of direct measurement of spin injection from a ferromagnetic metal into an organic semiconductor, through spin pumping, with all previous studies focusing on inorganic mediums. The initial proposal was to try and identify potential organic materials which could facilitate spin injection from a ferromagnet, via the spin pumping technique mentioned above. This would then be detected by measuring the ferromagnetic resonance linewidth broadening associated with spin injection through the OSC layer, using the following device architecture:

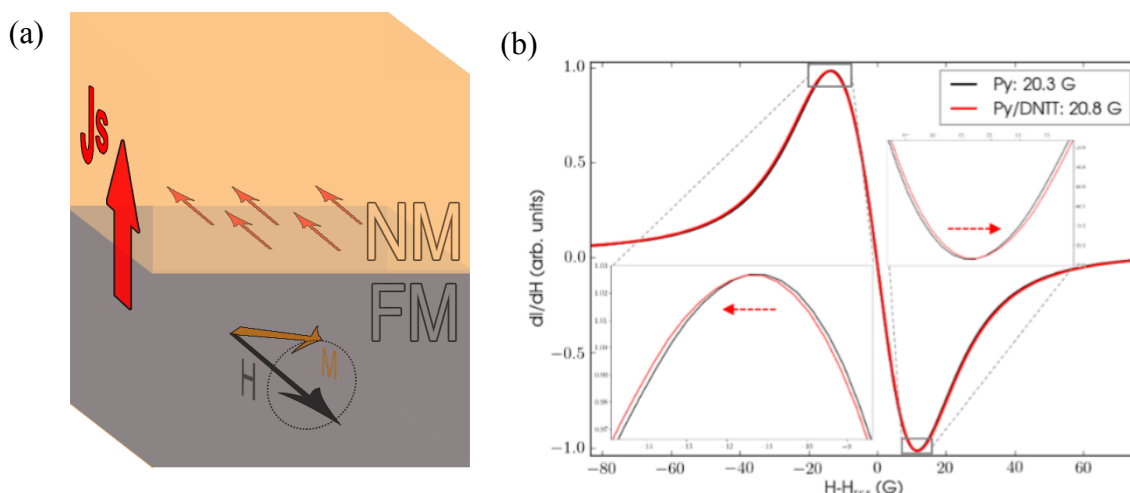


Figure 43. (a) Schematic representation of pure spin current injection at FMR via spin pumping through the FM. (b) Absorption spectra of uncoated permalloy layer (black) and after **DNTT** deposition (red), insets show the measurable linewidth increase, reproduced from Wittmann *et al.*¹²⁷

Where J_s is the spin current, M is the precession of magnetization about the external magnetic field H and NM is the nonmagnetic layer. The dynamics of this process (rate of change of the precession of magnetization) are well defined by the Landau-Lifshitz-Gilbert equation^{128,129}:

$$\frac{dM}{dt} = -\gamma M H_{eff} + \frac{\alpha}{M_s} M \frac{dM}{dt} \quad (9)$$

where γ is the gyromagnetic ratio, M_s the saturation magnetization and H_{eff} the effective magnetic field. The Gilbert dampening term α is directly proportional to the width ΔH_{FM} of the ferromagnetic absorption when sweeping the magnetic field across the FMR. As the FM pumps spins into the adjacent NM layer the effective dampening increases due to the loss of spin angular moment, within the FM, thus leading to an increased linewidth $\Delta H_{FM/NM}$. This is explained in much greater detail by Wittmann *et al.*¹²⁷ in her recent paper which summarises the early results of these experiments with the first reports of spin injection through OSC materials.

A simplified view of this complicated device architecture is presented in **Figure 43**. Conceptually if spin injection occurs through the FM into the OSC layer then this will lead to an overall ferromagnetic linewidth broadening for the microwave absorption of the FM. Which can then be measured quantitatively. Furthermore, the efficiency of spin injection can be quantified by the spin mixing conductance term $g_{eff}^{\uparrow\downarrow}$:

$$g_{eff}^{\uparrow\downarrow} = \frac{4\pi\gamma M_s t_{NM}}{g\mu_B\omega} (\Delta H_{FM/NM} - \Delta H_{FM}) \quad (10)$$

here t_{NM} is the thickness of the NM layer, ω is the driving frequency, the electron g -factor and Bohr magneton μ_B .¹³⁰ The underlying physics and explanation of both **Equations (9) & (10)** will not be discussed here but are presented as context for the results which will feature later.

Practically there have been widespread theoretical and experimental reports studying spin injection into inorganic materials.^{125,131,132} Many of these studies suggest that the nature of the interface, between the FM and NM is key for facilitating efficient spin injection. This is a very intuitive observation, the atomic interface (i.e. packing of the NM) will hinder or facilitate spin injection depending on the interface interactions with the FM. Owing to this there has been a rise in the study of organic semiconductors (OSC) as spintronic materials.^{133,134} Unlike their inorganic counterparts, most OSCs possess long spin diffusion lengths, extended spin relaxation times and much broader interface tunability. The long spin relaxation times originate from the inherently weak hyperfine coupling¹³⁵ (spin-spin interaction between electrons and the nucleus) within OSCs whereas the long spin diffusion length derives from the 2-dimensional stacking properties and spin-orbit coupling of the material. For the purpose of spintronics these properties make OSCs potential nonmagnetic spin conductors, commonly referred to as spin-sink materials.

3.4 BIRADICAL CHARACTER

Open-shell polycyclic hydrocarbons, molecules with multiple unpaired electrons, have surged in recent publications due to potential in photovoltaic devices, nonlinear optics and spintronic devices, *vide infra*.⁹⁷ The measure of contribution from a biradical resonance form to the complete structure of the ground state is classified by the biradical character:

$$0 \leq \gamma_0 \leq 1 \quad (11)$$

where the index ranges from $\gamma_0 = 0$ (pure closed shell) to $\gamma_0 = 1$ (pure open shell). In general most biradical polycyclic hydrocarbons have a singlet ($S = 0$) spin-paired ground state along with a low-lying triplet ($S = 1$) spin-parallel excited state.⁹⁹

Computationally this was calculated following the methods of Nakano *et al*¹³⁶ relating the highest occupied natural orbital (HONO- i) and lowest unoccupied natural orbital (LUNO+ i). They define the diradical character as:

$$\gamma_0 = 1 - \frac{2T_i}{1 + T_i^2} \quad (12)$$

where T_i is the orbital overlap between the HONO and LUNO and can be expressed as:

$$T_i = \frac{n_{\text{HONO}-i} - n_{\text{LUNO}+i}}{2} \quad (13)$$

Moving forward throughout this text, the combination of these equations will be used to determine the biradical character of each material.

Clar's aromatic sextet rule has been used extensively to predict both the stability and reactivity of closed-shell polycyclic hydrocarbons for a number of decades.¹⁰¹ The rule states that *for polycyclic aromatic hydrocarbons, specifically benzenoids, with an identical chemical composition, the molecule with a greater number of aromatic sextet rings will be more stable with lower reactivity*.¹³⁷ The increased stability originates from a large resonance energy

inherent to a six π electron containing benzene ring. More recently, Clar's rule has been adapted to predict the biradical character of open-shell polycyclic aromatic hydrocarbons. Sun *et al.*¹³⁷ report that an increase in aromatic sextets will help to stabilise the biradical resonance form, manifesting a larger biradical character measurement. These results expand Clar's aromatic sextet rule to include open-shell biradicaloids and offer a method of predicting and synthetically manipulating this useful and versatile property.

Open shell polycyclic hydrocarbons have been extensively reviewed and importantly the biradical character index has shown to be a good measure for property predictions. These range from singlet fission to spintronics and various studies into the link between biradical character and multiple electronic processes has led to a recent spike in the field.^{138,139} One proposal for devolving OSCs capable of spin injection from a FM was to synthesise a series of molecules with heightened spin-sink character by utilising the intrinsically high spin density of biradical materials. The following materials were synthesised as part of the ERC Synergy collaboration and were supplied to A.Wittmann for prospective ferromagnetic linewidth broadening experiments. The synthesis, characterisation and finally LWB results will be discussed in the following sections.

3.5 DX-IDF DERIVATIVES

The general synthesis of **DX-IDF** (Section 2.5) has been reported above, this section will focus on the biradical character and functionalisation with various halogens to form promising spin-sink materials. DFT calculations predict the biradical character of **DX-IDF** to be $\gamma_0 = 0.24$ in agreement with previous literature.^{99,140} In an attempt to increase the viability as a spin sink material **DX-IDF** was subsequently halogenated, with bromine and iodide respectively, aiming to increase the spin orbit coupling via the heavy atom effect. It was hoped that the inclusion of

heavier atoms at the meta- positions would increase both biradical character and lead to more favourable spin injection from the FM.^{127,141}

As shown in **Section 2.6** halogenation of **DX-IDF** lead to substitution at the 3- and 9-positions, with through conjugation across the quinoidal core. This reaction proved to be kinetically slow and required the addition of acetic acid to promote heterolysis of NBS to Br⁺, stimulating the electrophilic bromination. The same was required for the synthesis of **di-iodo-DX-IDF**, despite the need for acidic promotion both reactions were successful in high yields, 94%+. Computational predictions indeed suggested that the inclusion of heavier atoms lead to an increased biradical character, $\gamma_0 = 0.27$ for **di-Br-DX-IDF** and $\gamma_0 = 0.29$ for **di-iodo-DX-IDF**, respectively.

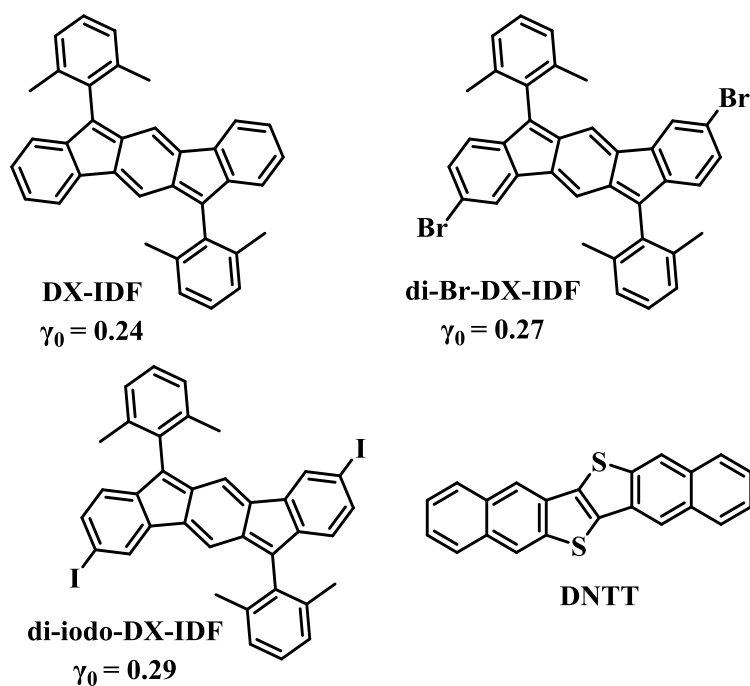


Figure 44. Molecular structures of **DX-IDF** and the di-halogenated derivatives, along with their predicted biradical character, in addition to the previously reported naphtho[2,3-*b*]naphtho[2',3':4,5]thieno[2,3-*d*]thiophene (**DNTT**).¹²⁷

These materials were sent to A. Wittmann for testing within the FMR linewidth measurement outlined above (**Figure 43**). Both halogenated derivatives of **DX-IDF** produced no measurable linewidth broadening, most likely due to the amorphous nature of their solid-state films. This is likely due to the size of the halogenated atoms at the meta- positions leading to reduced packing efficiency of the molecule compared to the **DX-IDF** monomer.

For **DX-IDF** the spin diffusion length (λ_s) can be estimated to be in the range of 45 to 50 nm. The average increase in linewidth was extrapolated to be $\delta\Delta H = 0.60 \pm 0.03 G$ and the spin mixing conductance, estimated using **Equation (10)**, was found to be $g_{eff}^{\uparrow\downarrow} = 3.74 \times 10^{18}$. These results surpass those recently published for dinaphtho[2,3-*b*:2',3'-*f*]thiopheno[3,2-*b*]thiophene (**DNTT**), the current record holding organic material, which has a reported linewidth broadening of $\Delta H = 0.54 \pm 0.05 G$, spin mixing conductance $g_{eff}^{\uparrow\downarrow} = 3.35 \times 10^{18}$ and spin diffusion length $\lambda_s = 40nm$.¹²⁷ This overall improvement could be attributed to the increase in biradical character as both **DX-IDF** and **DNTT** share an in-plane 2D herringbone packing structure.

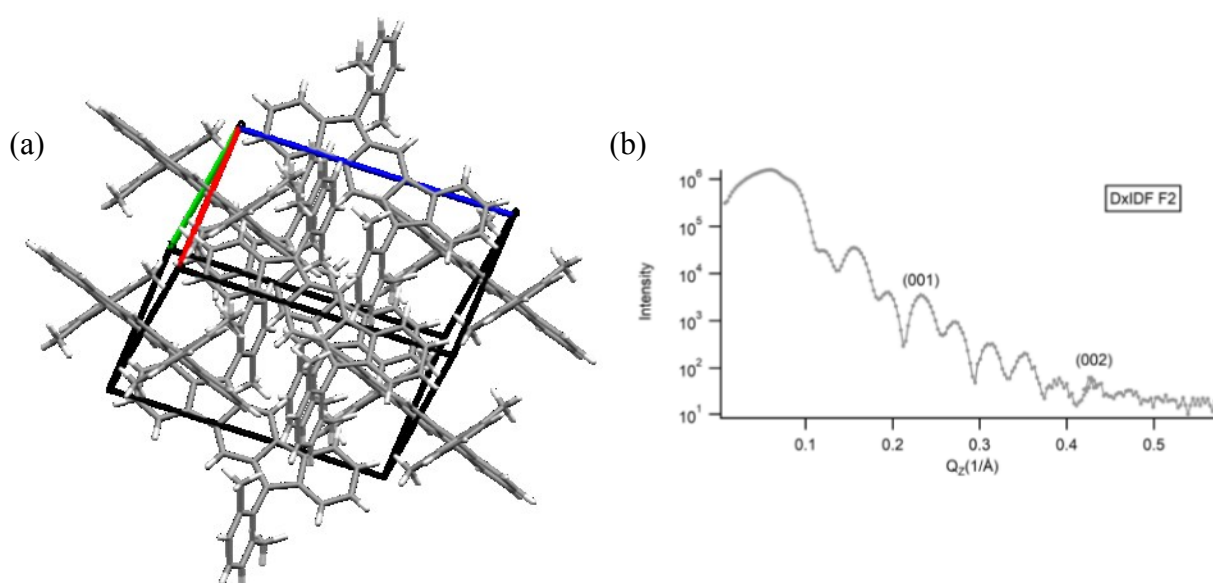


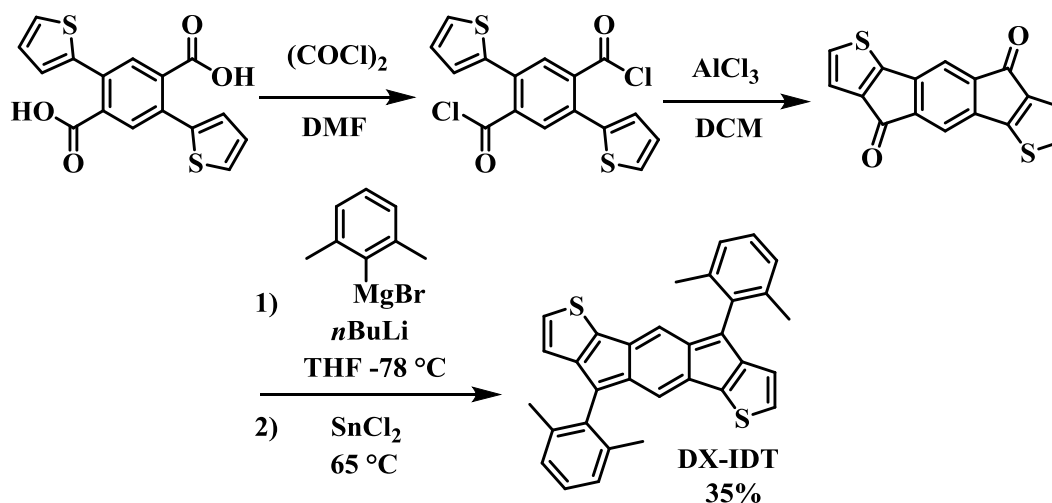
Figure 45. (a) Packing diagram for **DX-IDF**. (b) XRR spectra for a **DX-IDF** film deposited on a Permalloy substrate.

The structural properties of **DX-IDF** were studied by crystallography (single crystal) and by X-ray reflectivity (XRR) by depositing a film on a Permalloy substrate. XRR shows two Bragg peaks at $Q_z = 0.21 \text{ \AA}^{-1}$ and $Q_z = 0.42 \text{ \AA}^{-1}$ respectively, which agrees with the monoclinic crystal structure obtained from X-ray diffraction (XRD). To confirm the theory that an increased biradical character did indeed lead to the increase in spin injection the sulphur containing analogue of **DX-IDF** was studied and is discussed in the following section.

3.6 DX-IDT

In order to test the effect of altering the biradical character and introducing heteroatoms into the carbon backbone the thiophene containing analogue of the IDF skeleton, indacenodithiophene (IDT), was subsequently investigated. This backbone has also been reported to have good performance in both OFETs and organic photovoltaic devices.¹⁴² In addition to providing the first example of a SnCl_2 -mediated reductive dearomatization (**Section 2.4**) the Haley group has also shown that replacing the outer ring of the [1,2-*b*]indeno[fluorene with a thiophene drastically increases the antiaromaticity of the *s*-indacene core.¹⁰⁴

Unlike **DX-IDF**, which was synthesised from the commercially available indeno[1,2-*b*]fluorene-6,12-dione, the 6,12-indacenodithiophenediketone core had to be synthesised from an earlier precursor. Following the procedure,¹³⁵ developed in-house, the diacid was converted to the acid chloride, with oxalyl chloride (**Scheme 6**). Subsequent intramolecular Friedel-Crafts acylation afforded the *anti*-IDT-diketone in good yield and isolated as a bright blue powder. Due to its general lack of solubility the material was subsequently used without purification.



Scheme 6. Synthesis of 4,9-bis(2,6-dimethylphenyl)-4,9-dihydro-*s*-indaceno[1,2-*b*:5,6-*b'*]dithiophene (**DX-IDT**).

Once the diketone was obtained an analogous procedure to the formation of substituted indenofluorenes was employed with the addition of a nucleophile followed by the reductive dearomatization using SnCl_2 . Again, following from the work with **DX-IDF** (Scheme 2), the chosen nucleophile was a (2,6-dimethylphenyl)magnesium bromide, the nucleophilic Grignard reaction yielded 4,9-bis(2,6-dimethylphenyl)-*s*-indaceno[1,2-*b*:5,6-*b'*]dithiophene (**DX-IDT**) as a deep purple crystalline solid. Using the same design motif as **DX-IDF**, employing the sterically demanding xylene groups to kinetically stabilise the quinoidal IDT core.

UV-vis absorption data was acquired with the optoelectronic gap onset at 601 nm, 2.06 eV which suggests that this skeletal backbone is not suitable for singlet fission which requires a much wider bandgap, hence the previous (Chapter 2) section focused on IDF based dimeric materials. The peak absorption ($\lambda_{max} = 555$ nm) is significantly red shifted compared to **DX-IDF**. Density functional theory (DFT) calculations suggest that **DX-IDT** has a narrower bandgap compared to its IDF analogue, which can be explained by its increased antiaromatic character.¹⁴³ This was further supported by the ^1H NMR spectrum, the two protons located on

the central 6-membered ring were significantly shielded appearing at 6.04 ppm compared to 6.83 ppm for the all carbon IDF analogue.

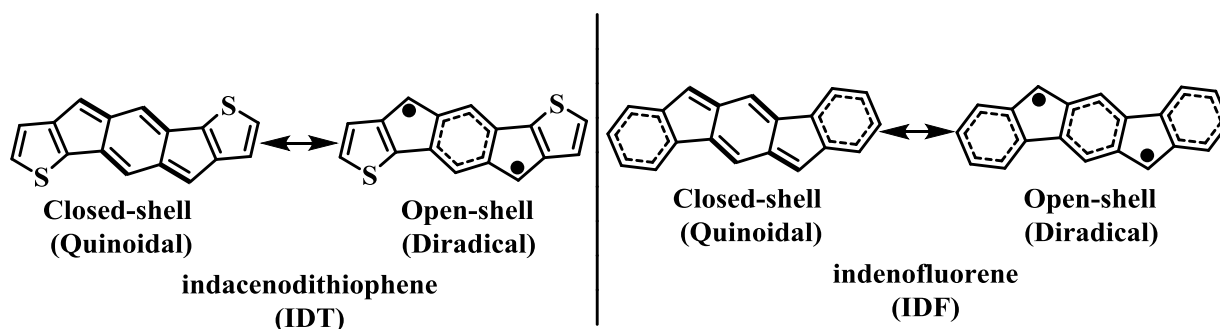


Figure 46. Closed-shell and open-shell resonance forms for IDT (left) and IDF (right) cores.

Along with the decreased aromaticity of the indacenodithiophene the biradical character of **DX-IDT** ($\gamma_0 = 0.19$) is lower than its IDF partner. Whilst the increase in the number of Clar sextets is one for both **DX-IDT** and **DX-IDF** (between the open- and closed- shell resonance forms) the overall total of one versus three means that the IDF derivative exhibits a larger overall biradical character ($\gamma_0 = 0.24$), both are in good agreement with previous literature.^{99,140} These results are summarised in **Table 5** showing the ~ 0.2 eV decrease in bandgap between the di-xylene substituted IDT and IDF derivatives.

Table 5. Computational and experimental results comparing the properties of both **DX-IDT** and **DX-IDF**.

	DX-IDT	DX-IDF
$S_0 \rightarrow S_1$ (eV)	2.45	2.58
$S_0 \rightarrow T_1$ (eV)	1.28	1.24
λ_{max} (nm)	555	516
E_{OPT} (eV)	2.06	2.24
γ_0	0.19	0.25

The decomposition temperature (T_d) for **DX-IDT** occurs at 304 °C, which is almost 50 °C below that of **DX-IDF** (**Figure 33**), however similarly the DSC trace is featureless, showing no significant thermal transitions when sweeping across the temperature range of -30 to 800 °C. Crystals suitable for X-ray diffraction were grown by slow evaporation of CD_2Cl_2 over multiple days. The structure and crystal packing of the C_2 symmetric **DX-IDT** is shown (**Figure 47**) displaying herringbone-like packing along with both sulphur atoms making short contacts with the adjacent molecules five membered ring, flanking the central six membered ring. The dihedral angle between the plane of the xylene group and the IDT core is 68.0°, twisting out of plane due to the steric bulk which is necessary to provide kinetic stability to the core.

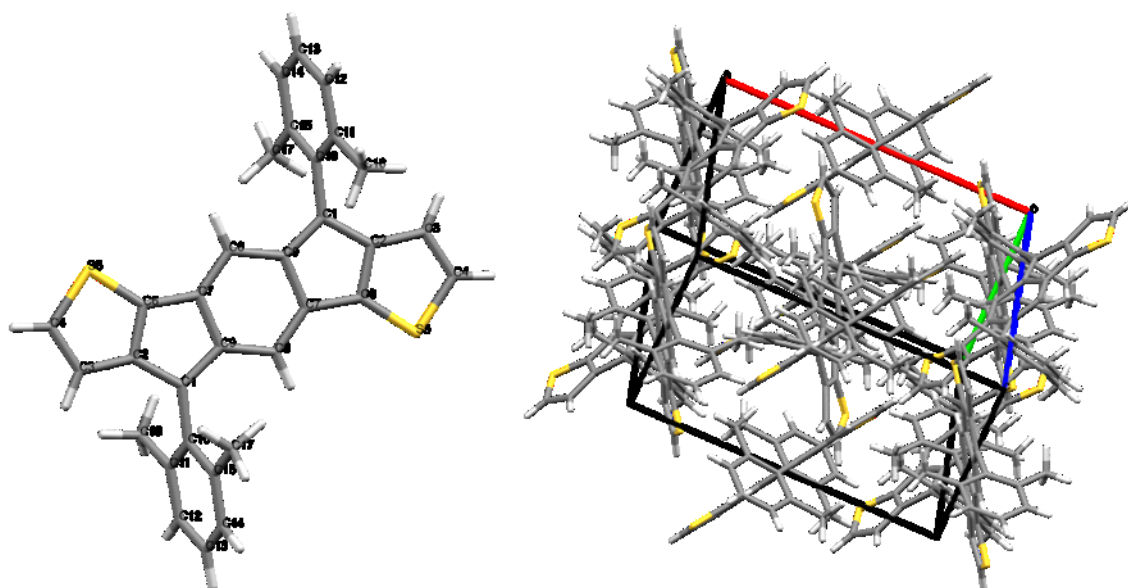


Figure 47. Molecular structure of **DX-IDT** alongside the herringbone-like packing pattern.

Following this initial characterisation a sample of **DX-IDT** was supplied to A. Wittmann for testing within the ferromagnetic resonance linewidth broadening experiment, outlined in **Section 3.3**. The average increase in linewidth was extrapolated to be $\delta\Delta H = 0.23 \pm 0.14 G$ and the spin mixing conductance, estimated using **Equation (10)**, was found to be $g_{eff}^{\uparrow\downarrow} =$

1.43×10^{18} . From these measurements the spin diffusion length (λ_s) can be estimated to be approximately 20 nm.

These results support the theory that an increase in the biradical character would lead to an increase in the measured FMR linewidth broadening, keeping as many other factors as unchanged as possible. **DX-IDT** showed a decrease of $0.37 \pm 0.14 G$ for the measured linewidth broadening compared to more biradicaloid **DX-IDF**. As both structures have the same molecular packing motif it could be argued that these results indeed support the proposed theory of linking an increase in biradical character to an improved spin injection from the FM within the FMR device.

3.7 INCREASING BIRADICAL CHARACTER

Whilst the comparison between **DX-IDF** and **DX-IDT** in the context of the FMR linewidth broadening experiment seemed to support the promised hypothesis, two results is not enough to make any conclusive claims especially within an extremely complex experimental framework. This section will focus on three target molecules (**Figure 48**), each with a predicted biradical character far exceeding that of the indenofluorene (**DX-IDF** $\gamma_0 = 0.25$) and indacenodithiophene (**DX-IDT** $\gamma_0 = 0.19$) derivatives discussed previously.

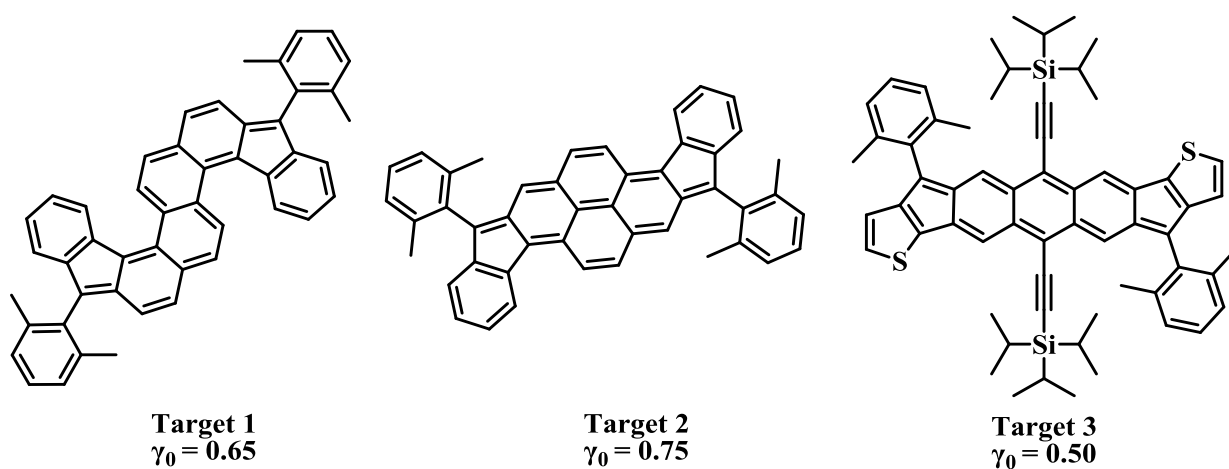


Figure 48. Synthetic targets with their respective predicted biradical character from DFT calculations.

3.7.1 ATTEMPTED SYNTHESIS OF DIINDENO-CHRYSENE TARGET

The first molecule (**Figure 48:Target 1**) marries together the indenofluorene work above with the previous work of my postdoctoral supervisor Dr M. Little who studied chrysene, a phenacene fluorophore, extensively during his PhD and early research career.¹⁴⁴ DFT calculations estimate the biradical character to be $\gamma_0 = 0.65$, a marked increase compared to both **DX-IDF** and IDT molecules discussed in the previous sections. Due to the presence of four Clar sextets, in the open-shell state, compared to only two Clar sextets residing in the peripheral six membered rings of the indenofluorene moiety (**Figure 49**). The predicted structure is expected to be incredibly twisted and strained; it was hoped that the presence of the bulky xylene groups would help to stabilise the conjugated core, in a similar manner to that shown previously for the indenofluorene and indacenodithiophene derivatives.

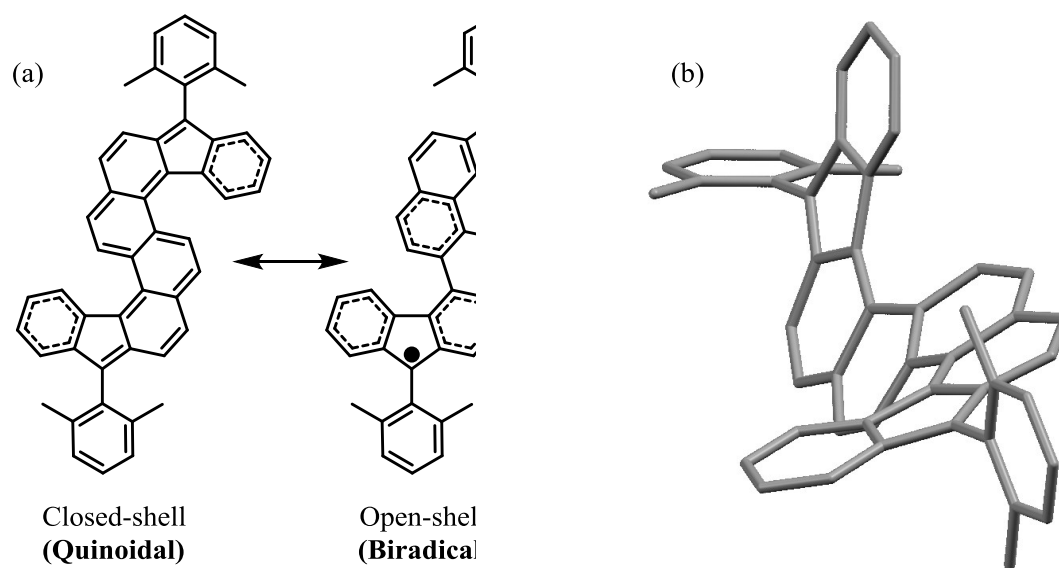
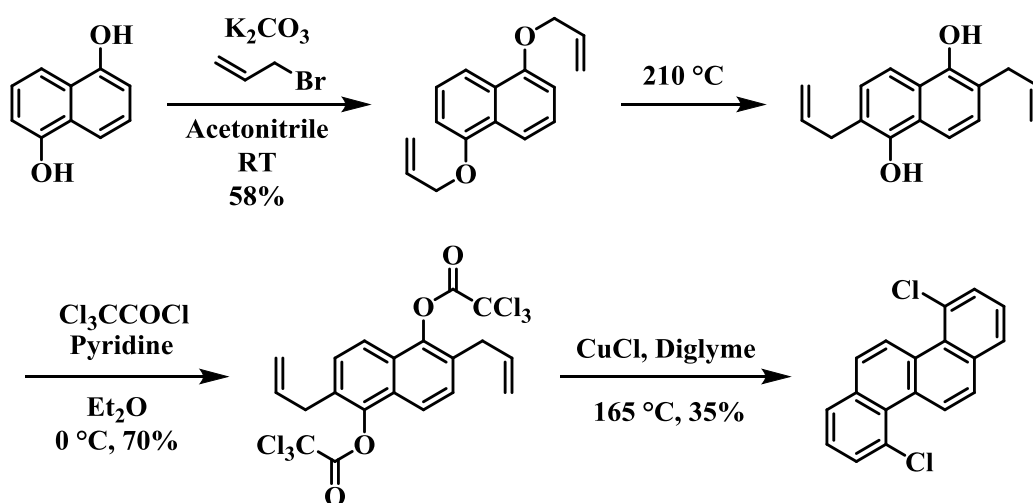


Figure 49. (a) Quinoidal and biradical resonance forms, depicting the increase from two to four Clar sextets. (b) DFT calculated molecular structure showing the twisted nature of **target 1**.

This novel melding of the chrysene core and the indenofluorene flanking motif would require a lengthy synthetic pathway. This began with 1,5-dihydroxynaphthalene, a commercially available reagent, common to the dyestuff industry, to furnish 4,10-dichlorochrysene¹⁴⁴ after four steps. Typical Williamson etherification conditions were used for the allylation of 1,5-dihydroxynaphthalene to yield 1,5-bis(allyloxy)naphthalene.¹³⁷ The moderate yield of this reaction has been attributed to the formation of monoallylated product.¹⁴⁴ Furthermore, the prolonged periods of heating (**Scheme 7**) promotes the aromatic alkylation, in order to limit this the literature procedure was followed meticulously.

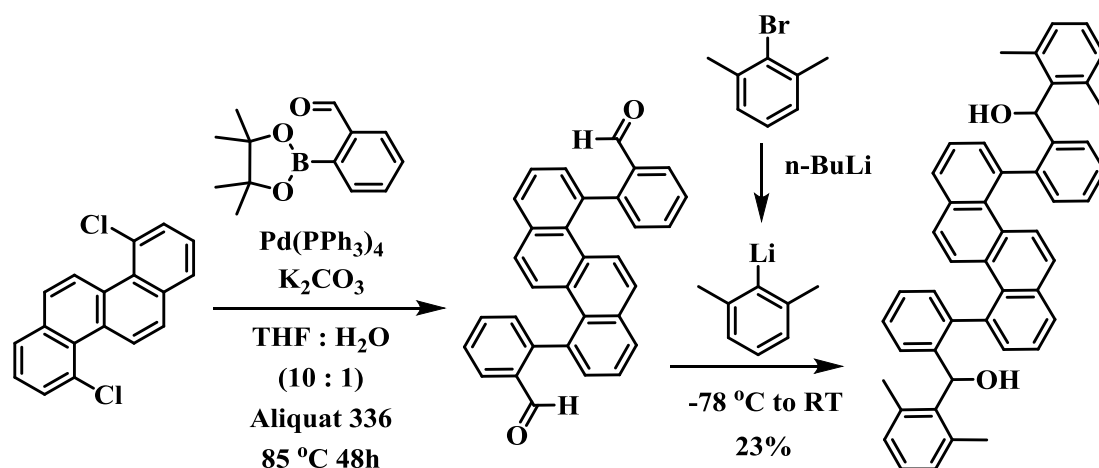


Scheme 7. Synthetic route to 4,10-dichlorochrysene, beginning from 1,5-dihydroxynaphthalene, commercially available diol.¹⁴⁴

Excessive heating, without solvent, (210°C) was employed to promote the Claisen rearrangement of to afford the diol intermediate, which was used immediately in order to limit rapid atmospheric oxidation from stifling the overall yield. Subsequent treatment with trichloroacetyl chloride, following a common esterification process, afforded the substituted naphthalene. The final benzannulation (BHQ) reaction, which was first discovered by Bull *et al.*¹⁴⁵ in 2007, has been extensively studied and optimised by Dr M. Little in order to find a set of reliable and practical conditions.¹⁴⁴ He found the best reproducibility when using a CuCl at

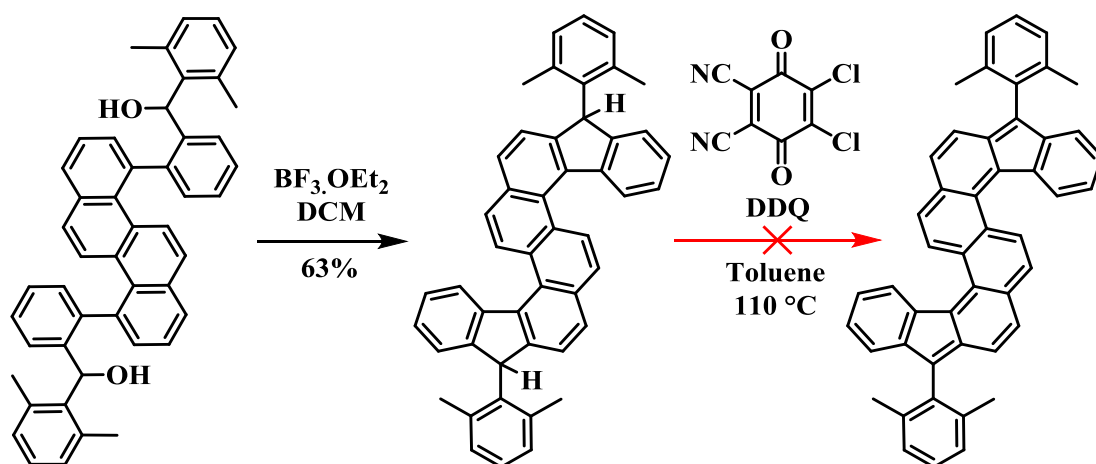
5 mol% catalyst loading, refluxing in diglyme for two hours. The insoluble by-products were easily removed during purification to afford **4,10-dichlorochrysene** as fine golden crystals, in comparable yield to the published procedure.

The aryl chloride functionality, injected by the BHQ reaction, allows for a multitude of synthetic pathways to expand the central core. Despite aryl chlorides not being the most optimal coupling partners, palladium-catalysed cross-coupling was employed to build the outer IDF motif. Previous reports have shown that the strength of the C-Cl bond deters oxidative addition of the catalytic palladium, this can be mitigated to a certain extent via the inclusion of electron-deficient aryl chlorides.¹⁴⁴ Conversely, a plethora of boronic acids are commercially available or facile to synthesise, whilst also being non-toxic and relatively stable, rendering them an ideal coupling partner. As such, Suzuki cross coupling (**Figure 13**) was employed as the first method to the expand the chrysene core. Conditions were adapted from literature¹⁴⁶ utilising Aliquat 336 (also known as Stark's catalyst) a quaternary ammonium salt phase transfer catalyst, known to accelerate Suzuki cross couplings for sterically bulky systems.¹⁴⁷ The biphasic medium is known to limit unwanted boronate side reactions (protodeboronation, oxidation and palladium catalysed homocoupling) in addition to promoting phase transfer of hydroxide ions between the mixed aqueous-organic media.¹¹⁹

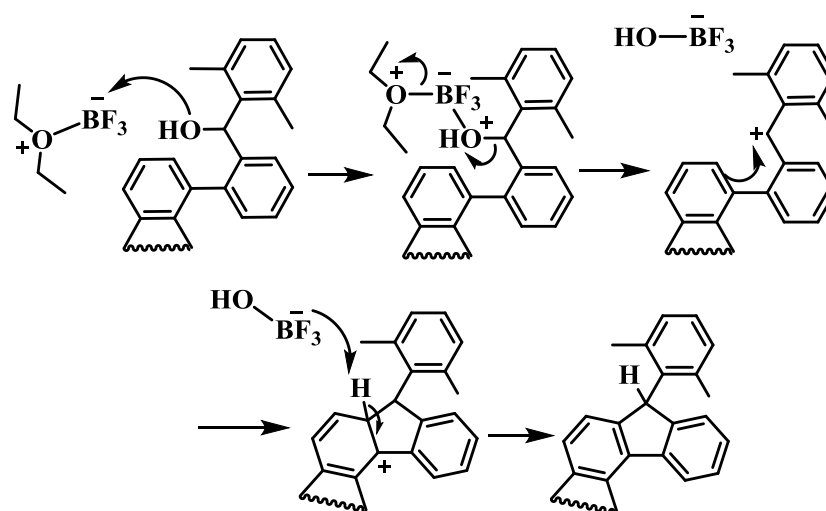


Scheme 8. Synthetic pathway for the Suzuki cross coupling expansion of **4,10-dichlorochrysenes**, followed by nucleophilic addition to yield the diol.

Owing to the inherent instability and unknown reactivity the crude dialdehyde was used immediately in the subsequent nucleophilic addition, hoping that the bulky xylene groups would help to hinder further reactivity and kinetically stabilise the strained core. Following a similar procedure used to synthesise both **DX-IDF** and **DX-IDT**, 2-bromo-1,3-dimethylbenzene was subjected to a lithium halogen exchange to afford the aryllithium nucleophile. The sterically hindered diol was afforded in limited yield across the two synthetic steps. Frustratingly, the reaction was highly non-reproducible, this is likely due to the unnatural steric and electronic limitations of the highly strained chrysenes core. Furthermore, an appreciable amount of dehalogenation occurred during the attempted couplings, however this was able to be limited by using the polar aprotic solvent THF.¹⁴⁴ It is of note that the methyl peaks, belonging to the bulky xylene motif, are in two different chemical environments, with two singlets (1.76 ppm (s, 6H), 1.70 ppm (s, 6H)) appearing in the ^1H NMR spectrum, further evidence for the strained and twisted nature of this molecule. The twisting is significant enough that each methyl group (per xylene unit) experiences a different degree chemical shielding, presumably due to the above and below plane interactions with the distorted chrysenes core.



Scheme 9. Intramolecular Friedel Crafts ring closure initiated with $\text{BF}_3 \cdot \text{OEt}_2$ followed by the oxidative dearomatization DDQ-promoted reaction attempting to afford the **target 1** molecule. The penultimate synthetic step involved reacting the diol intermediate with $\text{BF}_3 \cdot \text{OEt}_2$ promoting the intramolecular Friedel Crafts ring closure. Boron trifluoride diethyl etherate, a common Lewis acid, is known to rapidly promote dehydration of tertiary alcohols.¹⁴⁸ Mechanistically (**Scheme 10**) the tertiary alcohol attacks the boron trifluoride, as the formation of the negative charge can be inductively stabilised by the fluorine atoms. The tertiary carbocation formed is subsequently attacked by the aromatic six membered ring to cyclise and form the 5 membered cyclopentadiene ring. The final aromatisation, promoted by the BF_3OH^- anion, affords the product in an overall intramolecular Friedel Crafts aromatic ring cyclisation.



Scheme 10. Mechanism for the intramolecular Friedel Crafts cyclisation of (**target 1**), note that only half of the molecule is shown for demonstrative purposes.

This reaction proceeded quickly with modest efficiency at room temperature to yield the aromatic chrysene core flanked with indenofluorene units. The most distinctive and evidential peaks of the ^1H NMR spectrum belong to the two hydrogens (5.90 ppm) which protrude from the 5 membered indenofluorene ring at the carbon connecting the terminus of each xylene group.

The final step proved to be the most aggravating (**Scheme 9**), previous studies¹⁴⁹ have shown the versatility of quinone oxidisers in the role of oxidative dehydrogenation and thus multiple attempts were made using 2,3-dichloro-5,6-dicyano-1,4-benzoquinone (DDQ) in order to try and form the antiaromatic target molecule. These attempts proved to be fruitless as all efforts to form the dearomatized product by oxidative dehydrogenation, caused either total decomposition or the retrieval of unreacted starting material. The Haley group have reported identical difficulties with similar systems¹⁵⁰, suggesting that the protons at the apical carbon of the five-membered rings are simply too sterically hindered to undergo oxidative dehydrogenation. Replacing DDQ with *p*-chloranil, another member of the quinone family, also proved to be unsuccessful. Frustratingly, no method was found to effectively dearomatize

the penultimate compound and the desired target molecule has yet to be successfully synthesised.

3.7.2 ATTEMPTED SYNTHESIS OF DIINDENO-PYRENE TARGET

Similarly, to chrysene, pyrene is another example of a non-linear polycyclic aromatic hydrocarbon. However unlike chrysene, which is incredibly twisted, pyrene is a flat aromatic system, both are formed of four fused benzene rings.¹⁴⁴ Simultaneously with the synthesis reported above (Section 3.7.1) a diindeno-pyrene system was targeted as an increased biradical character molecule. DFT calculations predict this value to be $\gamma_0 = 0.75$ slightly higher than the chrysene analogue, potentially due to the planar nature of the molecule, allowing for more orbital interaction across the entire system despite the number of Clar sextets, between closed and open-shell resonance forms, being identical for both **target 1 & 2**.

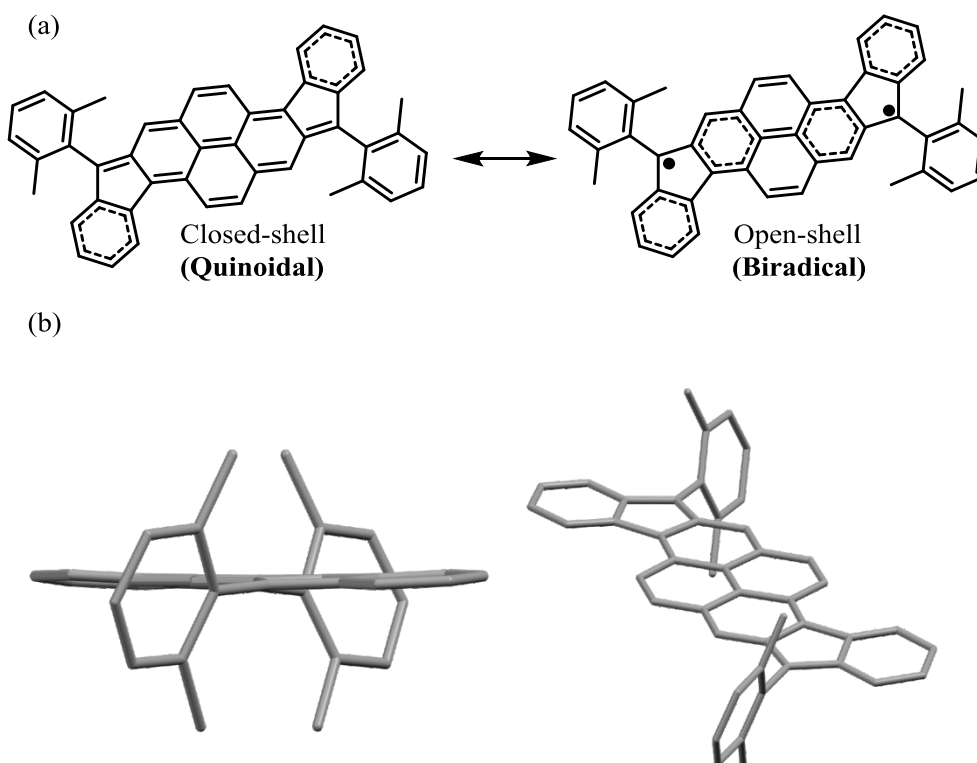
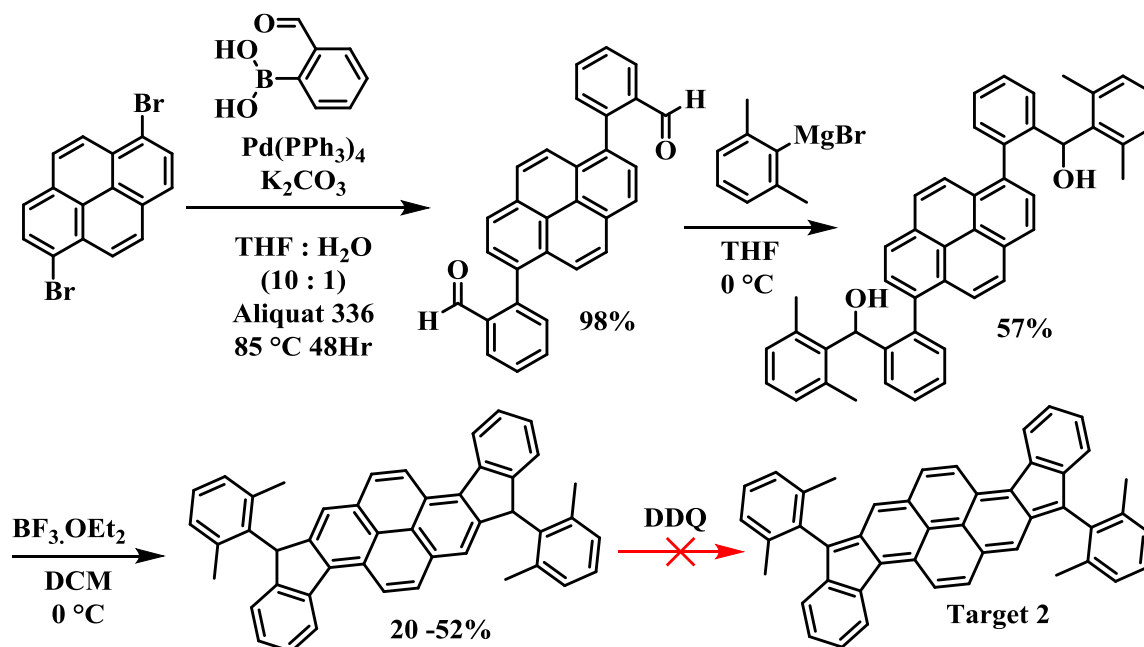


Figure 50. (a) Quinoidal and biradical resonance forms of **target 2**, Clar's sextets depicted by dashed bonds. (b) DFT calculated molecular structure showing the flat aromatic pyrene core.

Synthesis began from the commercially available 1,6-dibromopyrene, expansion followed a similar route as the chrysene partner beginning with a Suzuki cross-coupling with (2-formylphenyl)boronic acid as the coupling partner.



Scheme 11. Synthetic pathway towards the diindeno-pyrene (aromatic) precursor to **target 2**.

Two different sets of conditions were employed, both yielding the desired dialdehyde in high yield, the first employed conditions identical to the chrysene analogue and the second using $\text{Pd}(\text{OAc})_2$ as the catalyst with the electron-rich SPhos ligand, known to be an effective coupling reagent for bulky biaryl systems.¹⁵¹ The diol was synthesised in a comparable manner to **target 1** however, instead of generating the aryl lithium nucleophile, from 2-bromo-*m*-xylene, the Grignard reagent (2,6-dimethylphenyl)magnesium bromide was added directly. The diol was used without further purification and following the same mechanism as (**Scheme 10**) was subject to an intramolecular Friedel Crafts cyclisation prompted by the addition of boron trifluoride diethyl etherate ($\text{BF}_3 \cdot \text{OEt}_2$). Unlike the aforementioned chrysene analogue, the cyclisation proceeded with an extremely diminished yield, upon the first attempt however this was increased markedly when the number of equivalents was calculated based on the expected

yield of the diol opposed to the actual yield. In practice upon re-running the Friedel Crafts cyclisation the number of equivalents of $\text{BF}_3 \cdot \text{OEt}_2$ was increased from 2.28 eq. to 4.0 eq. with all other conditions remaining unchanged the yield was increased to 52%. Despite the successful isolation of hundreds of milligrams of the ring closed product as was the case for the diindeno-chrysene target oxidative dehydrogenation to afford the antiaromatic target was unsuccessful. While it was hoped that the planar pyrene core would not suffer the same steric hinderance as the chrysene any attempts to oxidise the molecule proved fruitless. Again, both DDQ and *p*-chloranil¹⁴⁹ were employed as the oxidising agents, yet as before each effort only afforded starting material or more commonly total degradation and loss of material. This is likely due to the formation of unstable charge complex intermediates which are well known decomposition mechanisms for the electron accepting quinones.¹⁴⁴ This was undoubtedly another setback in the pursuit of a higher biradical character material.

3.7.3 DIINDACENODITHIOPHENE[*b,i*]ANTHRACENE TARGET

Despite the previous failures of the chrysene and pyrene derivatives, hope was not lost and inspiration was again taken from the Haley lab who in the summer of 2016 published a stable organic diindeno[*b,i*]anthracene biradical.¹⁵² In the pursuit of novelty, a similar framework was applied to marry the previous indacenodithiophene (**DX-IDT**) motif with an anthracene core, namely diindacenodithiophene[*b,i*]anthracene (**DIDTAn**). DFT calculations were used to predict both the biradical character index ($\gamma_0 = 0.50$) and molecular structure (**Figure 51**).

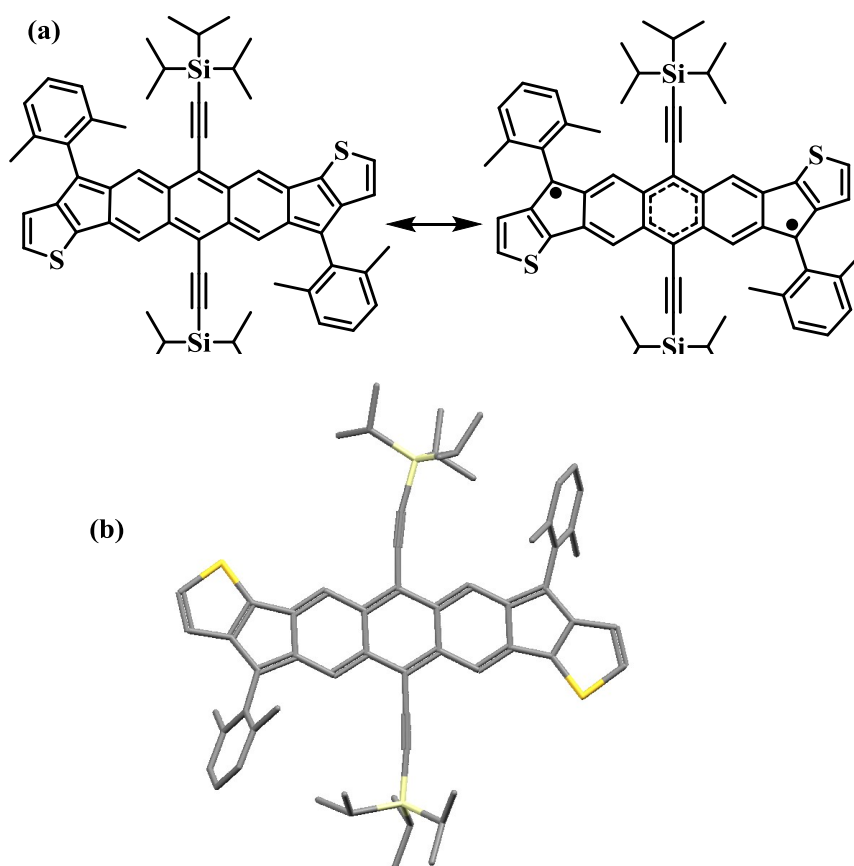
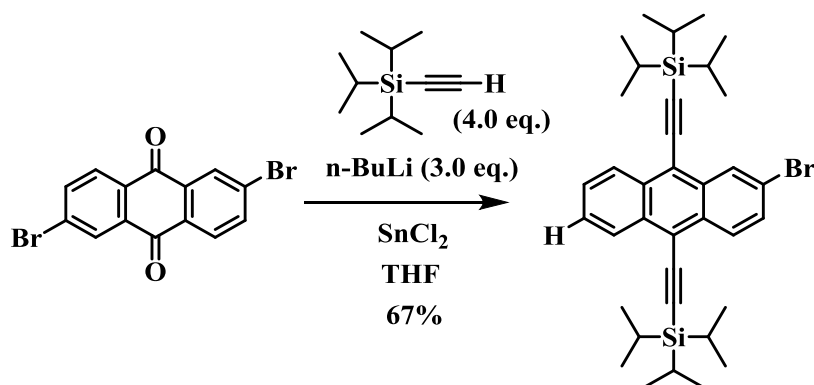


Figure 51. (a) Quinoidal and biradical resonance forms, Clar's sextets depicted by dashed bonds. (b) DFT calculated molecular structure for **DIDTAn (target 3)**.

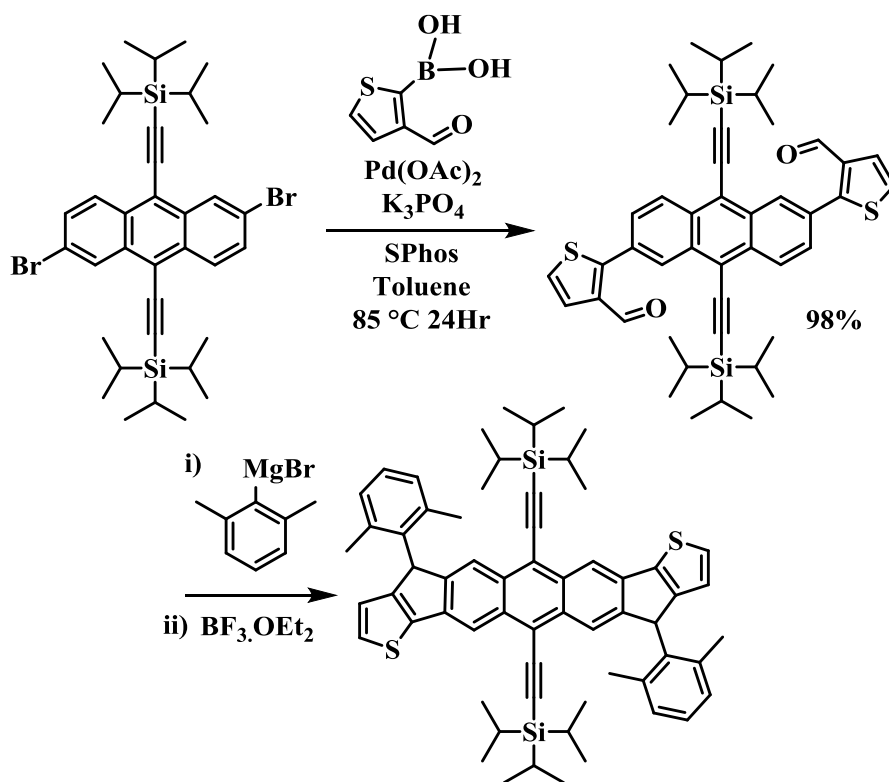
Following the failures of both the chrysene and pyrene target molecules it was decided that the sites of high spin should be sufficiently stabilised by bulky substitutes, clearly the xylene motif was not enough and (triisopropylsilyl)ethynyl groups were introduced at the central 6-membered ring of the anthracene core. These groups are also known to markedly improve solubility, transport properties and limit oxidation, a common decomposition pathway for acenes.^{153,154}



Scheme 12. ((2,6-dibromoanthracene-9,10-diyl)bis(ethyne-2,1-diyl))bis(triisopropylsilane) synthetic pathway, from commercially available 2,6-dibromoanthracene-9,10-dione.¹⁵⁵

Indeed, synthesis began with installing the (triisopropylsilyl)ethynyl groups to the commercially available 2,6-dibromo-9,10-anthraquinone.¹⁵⁵ Lithium-hydrogen exchange (metalation) of triisopropylsilyl acetylene afforded the necessary nucleophile to attack the carbonyl at the central anthracene ring. The resultant diol was reduced with SnCl_2 (following **Section 2.4**) to afford the (triisopropylsilyl)ethynyl decorated 2,6-dibromoanthracene as bright orange crystals in modest yield.¹⁵⁵

The building blocks of the indacenodithiophene flanking units began with palladium-catalysed Suzuki cross-coupling with 3-formyl-2-thienyl boronic acid. As with the previous pyrene section two different sets of conditions were ran simultaneously in order to optimise the coupling. Again, the first set of conditions followed the success of the chrysene coupling, utilising $\text{Pd}(\text{PPh}_3)_4$ as the catalyst, K_2CO_3 as the base and Aliquat 336 as the phase transfer agent, affording the dialdehyde in 77% yield. The second set of conditions proved even more fruitful with an almost quantitative yield, at 98%, employing $\text{Pd}(\text{OAc})_2$ as the catalyst, K_3PO_4 as the base and the electron rich SPhos ligand to form the dialdehyde. Repeat experiments were conducted using the later conditions, which could be successfully scaled to several grams.



Scheme 13. Synthetic pathway towards the diindacenodithiophene[*b,i*]anthracene (DIDTAn) target molecule.

The addition of 2,6-dimethylphenylmagnesium bromide afforded the secondary alcohol in near quantitative yield and was used without purification. Boron trifluoride was again added (**Scheme 10**) to promote the intramolecular Friedel-Crafts alkylation to form the heptacyclic core. This step proved to be problematic and despite multiple attempts a pure product could not be isolated. Indeed difficulties with this exact procedure have been reported before, the Haley group emphasise that the proximity of the ethynyltriisopropylsilane and the steric blocker, in this case the xylene group, is essential for producing an oxidisable material.¹⁵⁰ Perhaps also the electron-rich thiophene unit does not facilitate the cyclic ring closure from the diol. Frustratingly, this was the third higher biradical target which could not be successfully synthesised, demonstrating the difficulty in isolating this extended quinoidal systems which are inherently unstable until the final anti-aromatisation step.⁹⁹

3.8 DIAnDX SYNTHESIS & CHARACTERISATION

In a final attempt to provide A. Wittmann with a material possessing increased biradical character inspiration was sought from previous work on indenofluorene (**Chapter 2**). This prior experience coupled with the recent success from the Haley lab¹⁵² conceptualised diindeno[*b,i*]anthracene dixylene (**DIAnDX**) as the fourth molecular target in this so far unsuccessful series. As with the previous molecules DFT calculations were used to predict the biradical character $\gamma_0 = 0.55$, slightly lower than both the chrysene and pyrene molecules but an increase from its indacenodithiophene analogue, matching the trend between **DX-IDF** and **DX-IDT** (Section 3.6).

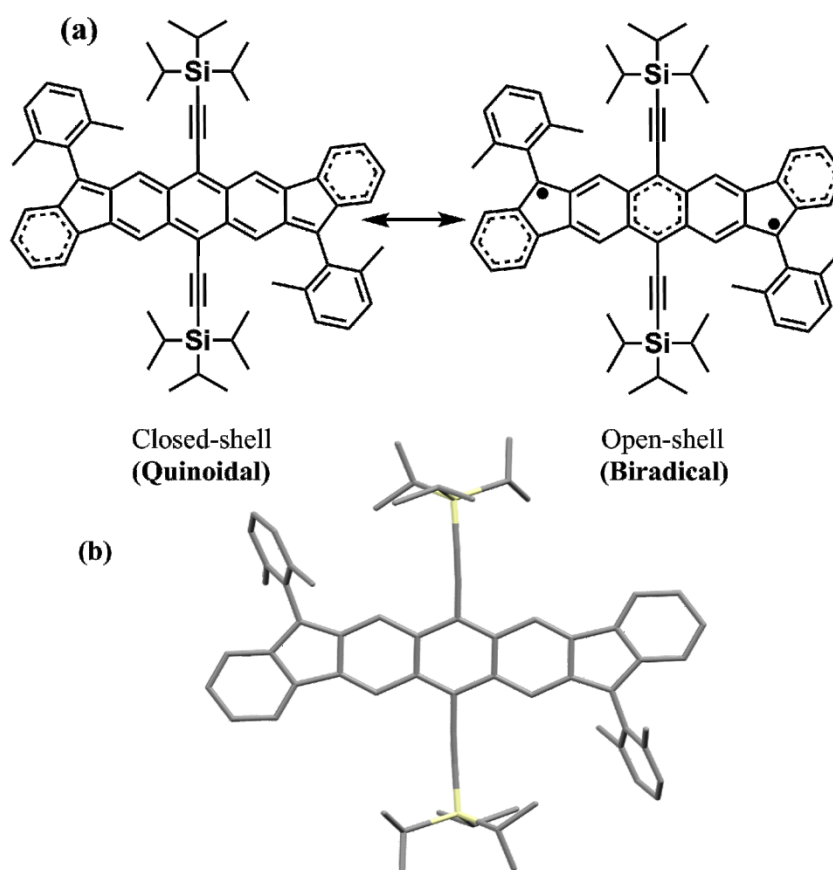
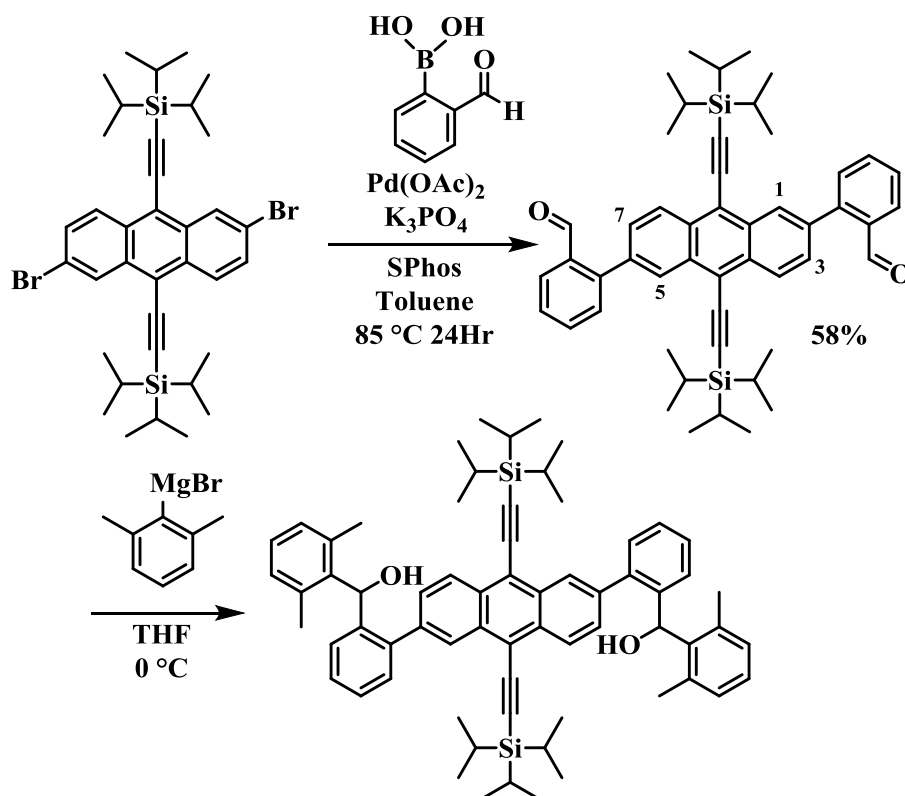


Figure 52. (a) Quinoidal and biradical resonance forms, Clar's sextets depicted by dashed bonds. (b) Molecular structure of **DIAnDX** by XRD, hydrogens omitted for clarity.

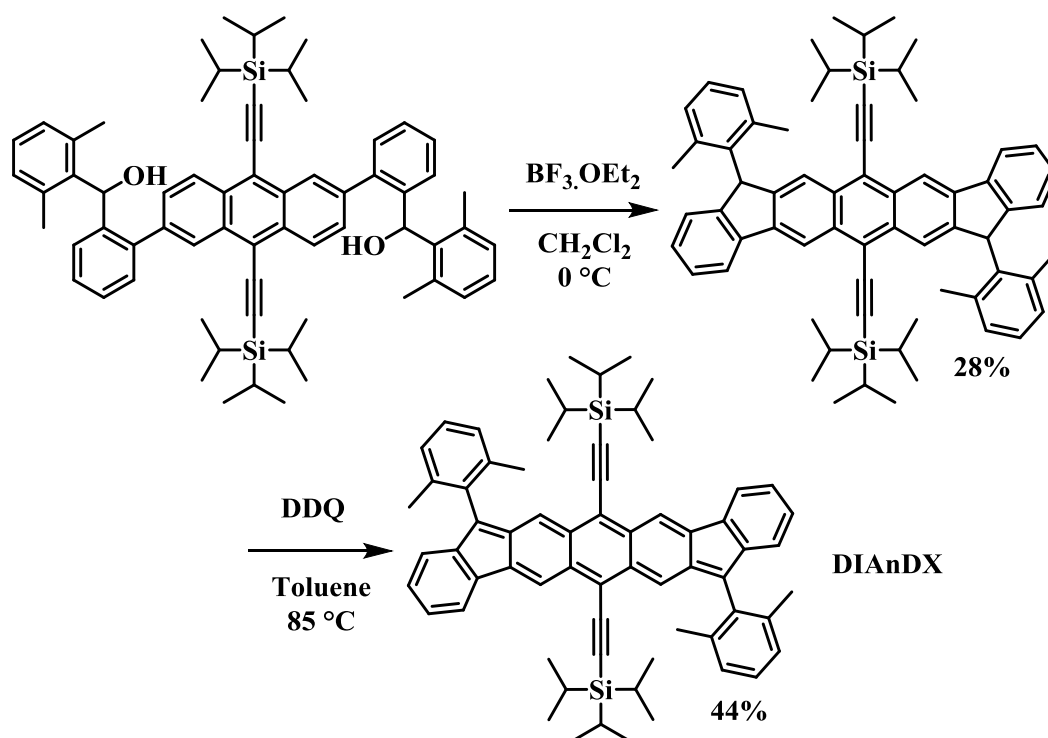
Whilst the previous reports in this chapter were unsuccessful in obtaining a material with higher biradical character, the practical techniques acquired were neatly combined in the synthesis of **DIAnDX**. Beginning with the previously synthesised ((2,6-dibromoanthracene-9,10-diyl)bis(ethyne-2,1-diyl))bis(triisopropylsilane), Suzuki-Miyaura cross-coupling, using the optimised Pd(OAc)₂ and SPhos conditions, afforded the dialdehyde in modest yield.



Scheme 14. Synthetic pathway for both the dialdehyde and diol ring opened precursors to **DIAnDX**.

Treatment with Grignard solution 2,6-dimethylphenylmagnesiumbromide, at 0 °C, facilitated nucleophilic attack at the aldehyde to install the bulky xylene group, flanking the extremity of the anthracene core. The unstable diol was used immediately without further purification. As previously shown, the addition of BF₃.OEt₂ promoted the selective intramolecular Friedel-Crafts alkylation (**Scheme 10**) directed by the steric hinderance between the bulky xylene

group and the (triisopropylsilyl)ethynyl units. Preferentially closing at the C(3) and C(7) carbons, as opposed to the more activated C(1) and C(5) sites.¹⁵²



Scheme 15. Selective Friedel-Crafts alkylation at the C(3) and C(7) positions followed by oxidative dehydrogenation to afford **DIAnDX**.

Difficulties were once again encountered throughout the synthesis, notably traces of aliquat 336 proved to be difficult to remove potentially harming both the yield and conversion of each subsequent reaction. As was the case for previous attempts, oxidative dehydrogenation, using DDQ returned starting material or caused rapid decomposition. However, using the ring-closed product, initially coupled under the $\text{Pd}(\text{OAc})_2$, SPhos Suzuki conditions, afforded the dearomatized diindeno[*b,i*]anthracene dixylene (**DIAnDX**) in modest yield. Once isolated the deep blue crystalline solid can be stored under ambient conditions with no sign of decomposition, which is common for most anthracene based materials.¹⁵⁶ The steric hinderance between the (triisopropylsilyl)ethynyl units and the xylene groups not only lead to a selective ring closure but also provide an inherent kinetic stability to the entire molecule. ^1H NMR was

collected upon initially obtaining the material and later, after benchtop storage for over 28 months (**Figure 53**), showing near identical spectra, confirming the long lasting stability and lack of degradation of **DIAnDX**.

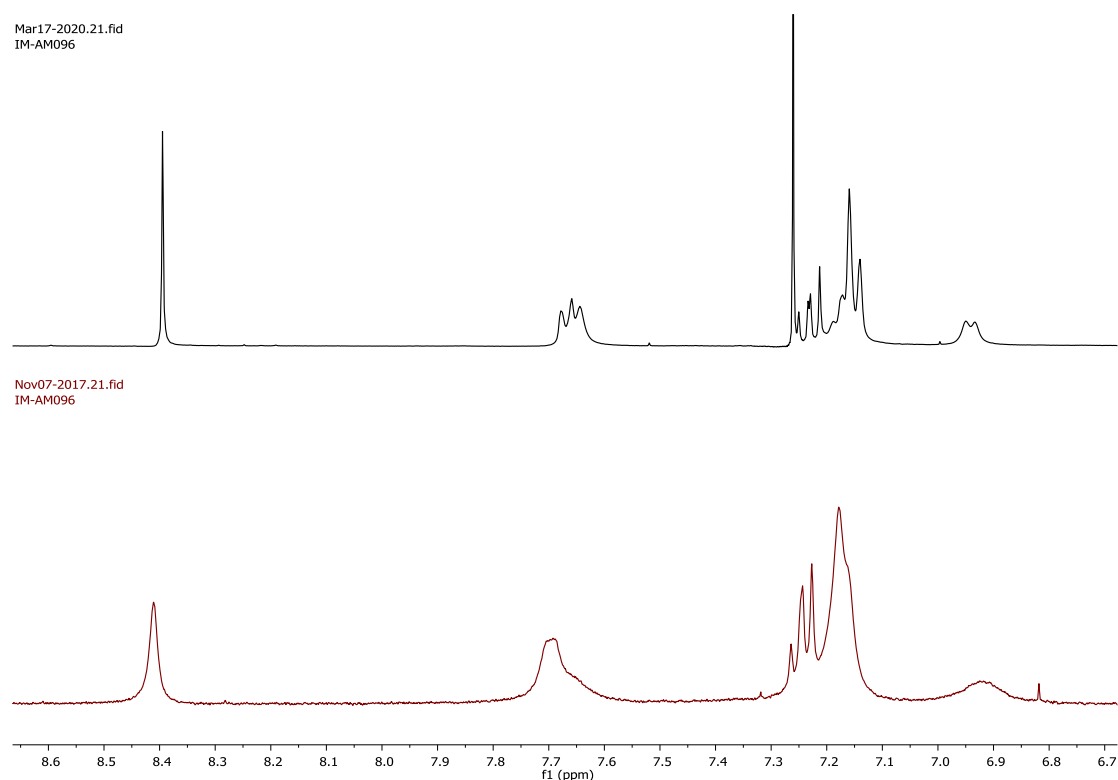


Figure 53. ^1H NMR spectrum, recorded at room temperature for **DIAnDX**. The top spectrum was recorded in CDCl_3 and obtained 28 months after the bottom spectrum, which was ran in CD_2Cl_2 .

The UV-Vis absorption spectrum for **DIAnDX** shows a λ_{max} of 725 nm, red shifted by almost 200 nm compared to the simple **DX-IDF** parent molecule (**Figure 31**). This strong absorption lead to the intense blue colour observed in solution. This can be ascribed to a symmetry allowed $S_0 \rightarrow S_2$ transition while the feeble shoulder extending out past 800 nm, is evidence for the symmetry forbidden $S_0 \rightarrow S_1$ transition.¹⁵² A similar optoelectronic characteristic was observed for the **DX-IDF** dimer series which also exhibited a symmetry forbidden $S_0 \rightarrow S_1$ transition (**Section 2.8**). The estimated optical band gap, taken from the onset of $\lambda_{max} \sim 860$ nm, of 1.44 eV agrees with literature and is notably narrower than most PCHs, despite the lack of any

dominant electron withdrawing functionality. These unusual optoelectronic properties and seemingly broad ^1H NMR peaks, observed at room temperature, prompted a deeper investigation into the nature of the ground state of **DIAnDX**.

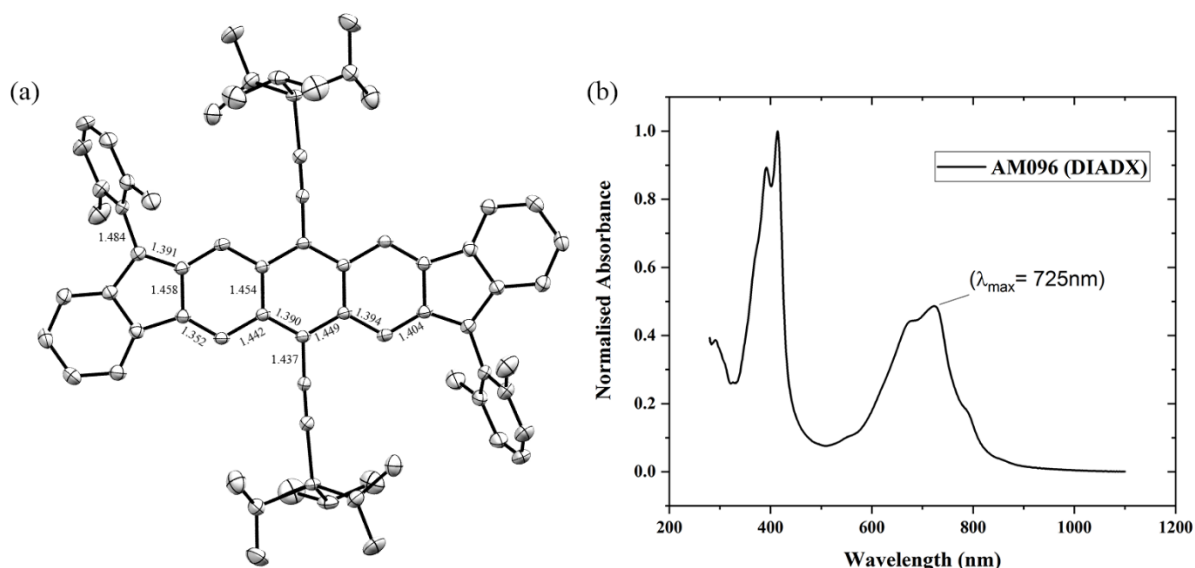


Figure 54. (a) XRD crystal structure of **DIAnDX**; ORTEP image with notable bond distances (Å), shown with 35% thermal ellipsoids and hydrogens omitted for clarity. (b) Thin film UV-Vis absorption spectrum.

X-ray diffraction (XRD) was used to study a single triclinic crystal of **DIAnDX**, which was grown by the prolonged evaporation of CDCl_3 . The bond lengths across the quinoidal core vary from 1.352 – 1.458 Å, suggesting a dynamic mix of single, double and benzenoid carbon-carbon bonds. This disparity implies that the quinoidal core has delocalised partial double bond character, supporting the existence of the ground state as a resonance hybrid between closed-shell and open-shell motifs (**Figure 52**). The Haley lab have also reported that the bond distance from the apical sp^2 carbon to the acene core can give an insight into predicting the biradical character.¹⁵⁷ They have established an indicative spectrum ranging from 1.377 Å (closed-shell) to 1.437 Å (open-shell) based on similar substituted indenofluorene isomers. **DIAnDX** sits

roughly 23% along this scale, suggesting closed-shell dominance, but the varied bond lengths and ^1H NMR (see below) suggest otherwise.

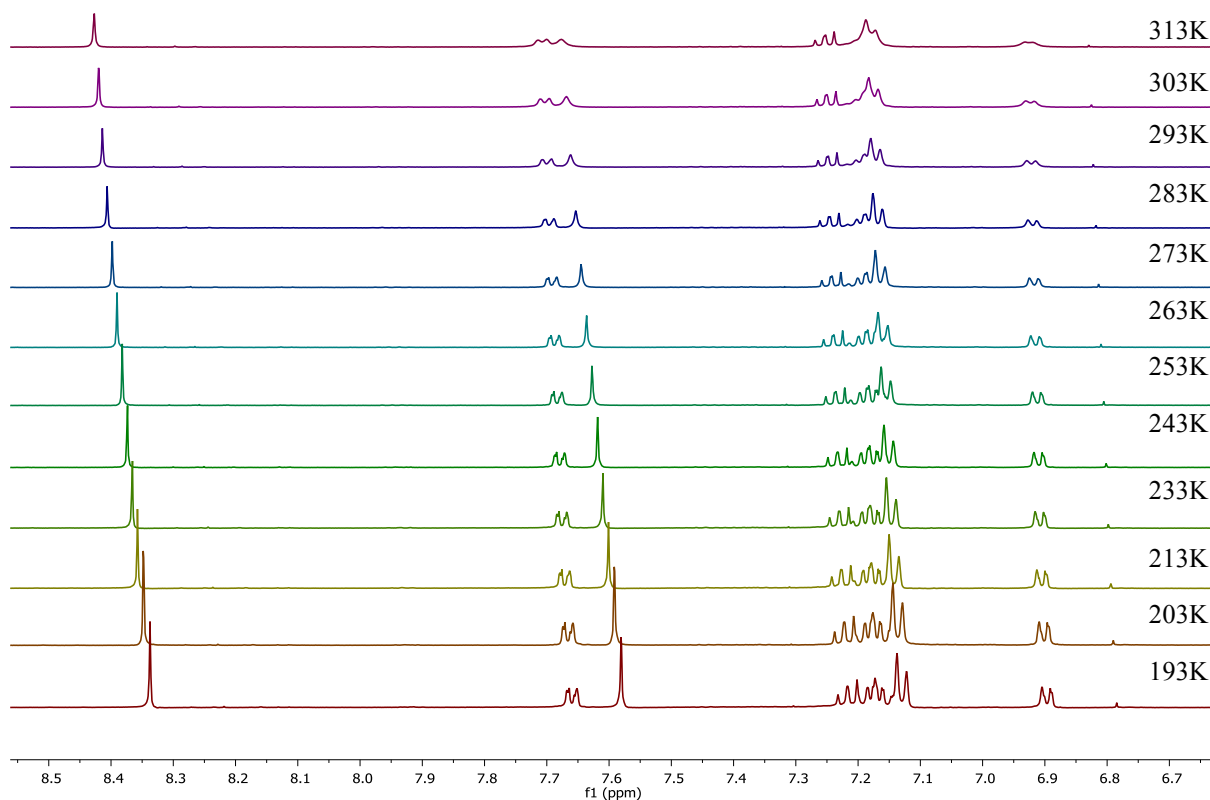


Figure 55. Variable temperature ^1H NMR, decreasing in 10 K increments from 313K to 193K, showing the aromatic region for **DIAnDX**, recorded in CD_2Cl_2 .

Variable temperature ^1H NMR shows a distinctive signal sharpening as the temperature is decreased, in 10K increments, from 313K to 193K. This stark increase in the linewidth broadening, upon heating, is indicative of a thermally accessible triplet state which has been previously reported.¹⁵⁸ Furthermore, DFT calculations conducted by Dr. K. Thorley suggest that the $S_0 \rightarrow T_1$ transition occurs at approximately 0.26 eV, which is also in agreement with similar biradical hydrocarbon systems.¹⁵⁹

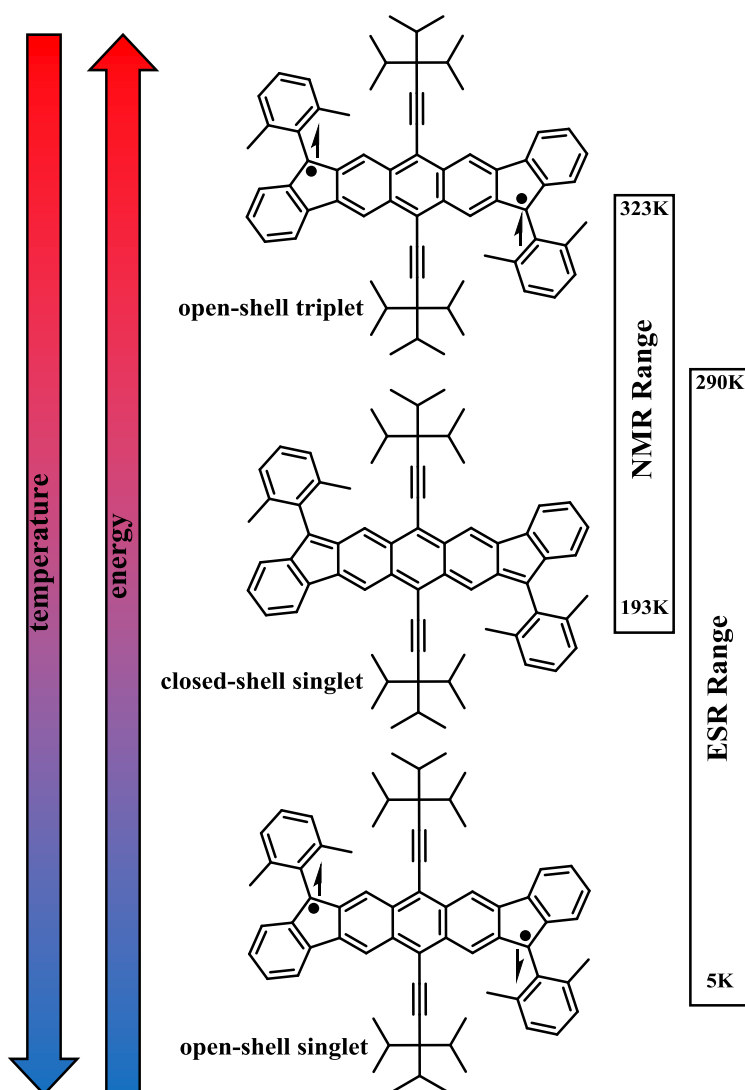


Figure 56. Proposed temperature/energy dependant resonance ground state structures for **DIAnDX**.

The magnetic properties of **DIAnDX** were kindly investigated by Dr S. Schott, who obtained both magnetic susceptibility and electron spin resonance (ESR) data. The magnetic susceptibility is shown to decrease as the temperature is increased from 0 K to 298 K this can be attributed to thermal isolation of the open-shell singlet radical at lower temperatures which leads to an uptake in magnetic susceptibility (χ) due to the inherent biradical nature. As the temperature is increased the resonance between open-shell and closed shell structures swings back in favour of the closed shell, quinoidal structure, which exhibits near zero magnetic susceptibility as this state begins to dominate. The temperature dependence almost follows

Curie susceptibility indicating a very small exchange coupling constant.¹⁴¹ If the temperature was increased past 300 K a large increase in χ would be expected as the thermally accessible triplet state begins to be populated. Previous experiments have demonstrated this above 300K, suggesting the $S_0 \rightarrow T_1$ energy gap is an order of magnitude above this at ~ 2000 K,¹⁵⁸ in agreement with the DFT calculations of **DIAnDX** (0.26 eV = 3017.2 K).

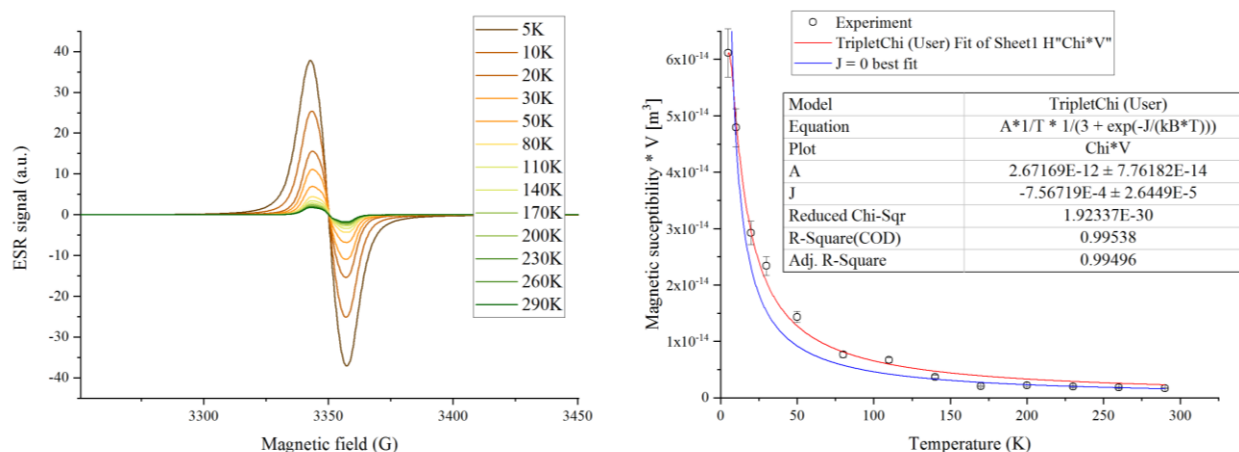


Figure 57. Electron spin resonance (ESR) spectroscopy as a function of magnetic field (left) and the magnetic susceptibility as a function of temperature for **DIAnDX**.

The ESR spectrum also agrees with the proposed structural hierarchy (**Figure 56**), transitioning from an open-shell singlet to close shell quinoidal structure upon increasing temperature, supported by the decrease in ESR signal upon increasing temperature up to 290 K.

Finally, this molecule was supplied to Dr A. Wittmann. For the principle measurement within the bespoke ferromagnetic resonance linewidth broadening experiment. **DIAnDX** was layered on top of a permalloy substrate the average increase in linewidth was extracted as $\delta\Delta H = 0.20 \pm 0.03$ G (**Figure 58**) and the spin mixing conductance, estimated using **Equation (10)**, to be $g_{eff}^{\uparrow\downarrow} = 1.26 \times 10^{18}$. Sadly, this result did not follow the hypothesis that an increase in biradical character would lead to an increase of spin injection from the FM. However, as

previously stated the molecular packing motif must also be considered as the structure at the interface is also key for efficient spin injection.

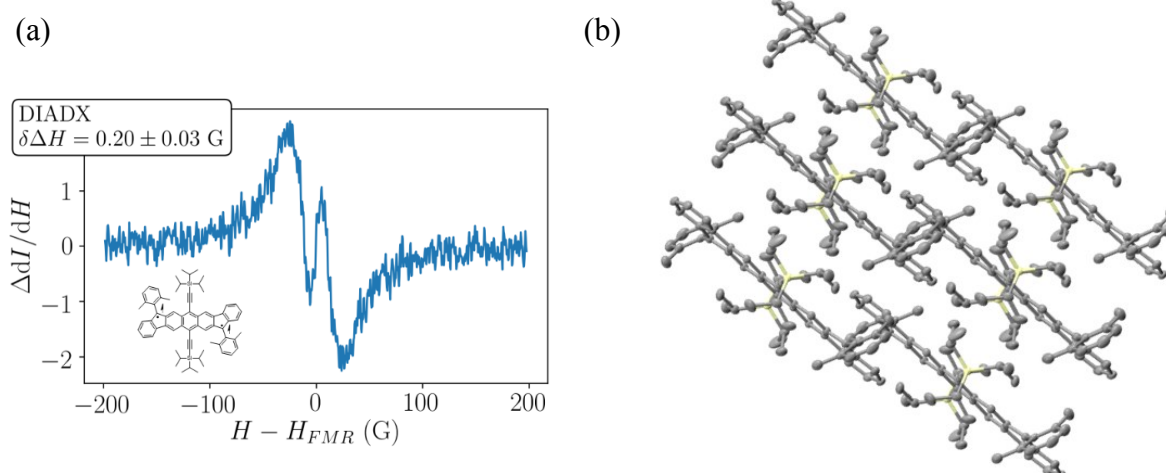


Figure 58. (a) Illustrated change in linewidth for **DIAnDX**. The difference of symmetric component of the normalised FMR spectra before and after deposition of the biradical NM. Amplitude of the peaks is proportional to the difference in FMR linewidth.¹⁶⁰ (b) Single crystal packing diagram for **DIAnDX**, exhibiting 1D structure.

Indeed, the single crystal, studied by XRD (**Figure 54**), shows **DIAnDX** packs into parallel 1D columns, notably different from the in-plane 2D herringbone pattern exhibited in **DX-IDF** and **DX-IDT** (**Figure 45** & **Figure 47**). The presence of the bulky linear solubilising (triisopropylsilyl)ethynyl units dominates the molecular packing structure, in a similar way to TIPS-anthracene, affording an intermediate between herringbone and brickwork packing motifs.¹⁶¹ This makes conclusions relating the biradical character to spin injection challenging, a compromise must be made between the structure at the interface and the biradical character of a material to optimise spin injection from the FM. A balance could be achieved by replacing the anthracene (An) core with naphthalene (Np), in order to bring the system more in line with that of indenofluorene and indacenodithiophene. DFT calculations of a xylene functionalised diindenonaphthalene (**DINDX**) suggest a similar molecular structure to **DX-IDF**, notably the xylene moieties are significantly less twisted due to the relief of steric hinderance caused by expanding the central core to feature two six membered rings.

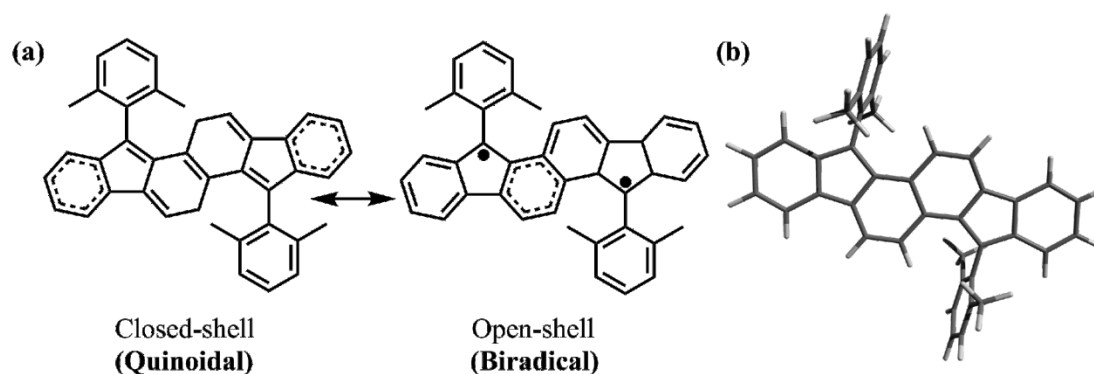


Figure 59. (a) Quinoidal and biradical resonance forms, Clar's sextets depicted by dashed bonds. (b) DFT calculated molecular structure for **DINDX**.

The biradical character index ($\gamma_0 = 0.45$) for **DINDX** predicted to be almost twice the value of **DX-IDF** ($\gamma_0 = 0.24$). It would also be expected to conform to a herringbone type packing motif based upon DFT optimised geometry. This could be a potential candidate to further investigate the link between increased biradical character and uptake of spin injection for these PAH spin sink materials. For now, a definitive conclusion cannot be made between biradical character and spin injection despite **DX-IDF** showing the highest recorded increase in linewidth $\delta\Delta H = 0.60 \pm 0.23 G$ and spin mixing conductance $g_{eff}^{\uparrow\downarrow} = 1.43 \times 10^{18}$ for this bespoke FMR measurement.

3.9 QUINOIDAL NON-FULLERENE ACCEPTOR

Despite di-xylene-indacenodithiophene (**DX-IDT**) not having suitable energetics for singlet fission and showing a reduced FMR linewidth broadening (**Section 3.6**) compared to its increased biradicaloid all carbon analogue **DX-IDF**, the functionalised indacenodithiophene is an interesting synthetic building block for quinoidal systems. One potential area of application for quinoidal systems is the field of non-fullerene acceptors (NFA). The role of this acceptor materials along with the basic function and structure of a bulk heterojunction organic solar cell is described in (**Section 1.3.1**). Over the last 20 years fullerenes have dominated high performing organic solar cells as the electron accepting material of choice. Recently, however,

this somewhat archaic class of materials is being replaced with the emergence of an abundance of non-fullerene acceptors, displaying increased synthetic flexibility, performance and stability.¹⁶² Last year we published an extensive review of the current state of the art non-fullerene acceptors which range from perylene diimide (PDI) and indacenodithiophene small molecules to polymeric naphthalene diimide (PNDI) acceptors.¹⁷ It is clear that the field of organic photovoltaics has been rejuvenated by the emergence of these exciting new acceptor materials.

One of the most promising non-fullerene acceptors is a linear n-octyl substituted indacenodithiophene-benzothiadiazole-rhodanine named **O-IDTBR (Figure 60)**, which at the time of publishing in 2016, held the record performance for fullerene-free P3HT devices at 6.4% power conversion efficiency.¹⁶³ This work from our group along with more recent studies specifically targeting the performance of organic solar cells suggested that an increase in quinoidal character, of the acceptor unit, can lead to an increased fill factor and PCE.¹⁶⁴ This led to the inspiration to extend the dixylene substituted indacenodithiophene, detailed in (**Section 3.6**), to afford a new quinoidal non-fullerene acceptor (**C₁₂-O-DX-IDTBR**), documented herein.

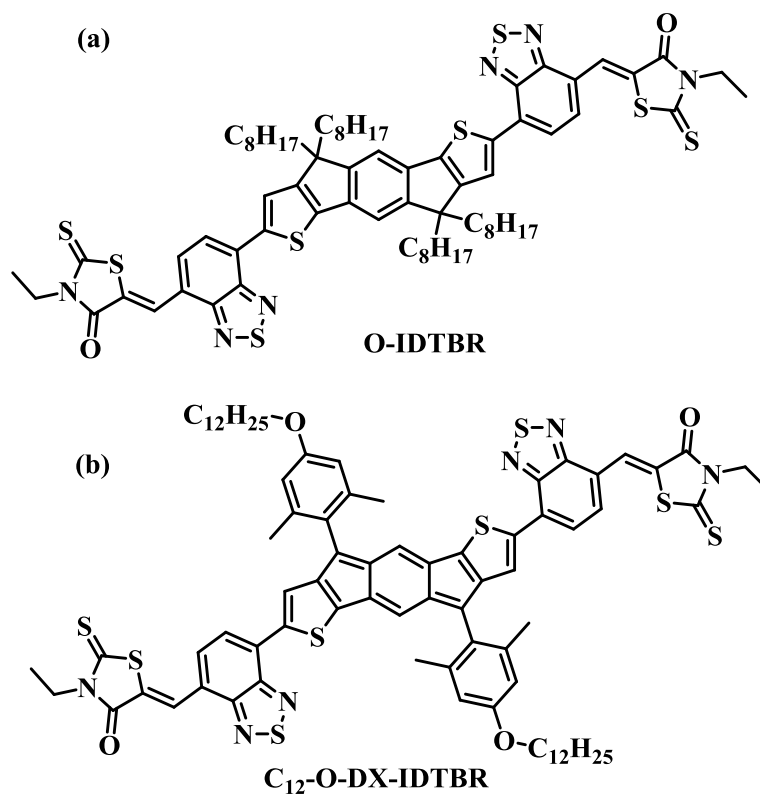
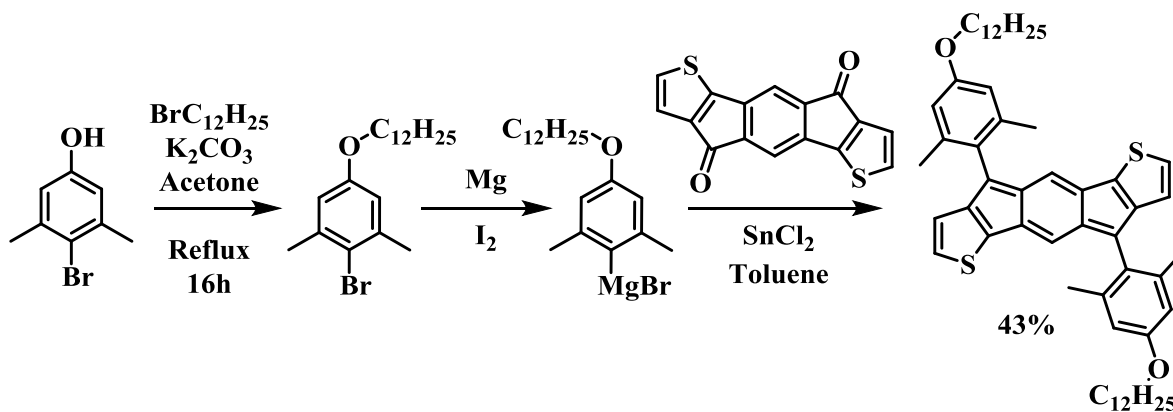


Figure 60. (a) Chemical structure of **O-IDTBR**¹⁶³ and (b) of **C₁₂-O-DX-IDTBR**.

Whilst, **DX-IDT** (Section 3.6) offered a good building block for creating a quinoidal core non-fullerene acceptor it was decided that the xylene group alone would likely render the resultant extended system with very limited solubility. The effects of adding a linear dodecyl-alkyl chain are not only expected to increase the solubility but should also promote intermolecular packing, known to lead to increased performance.¹⁶³

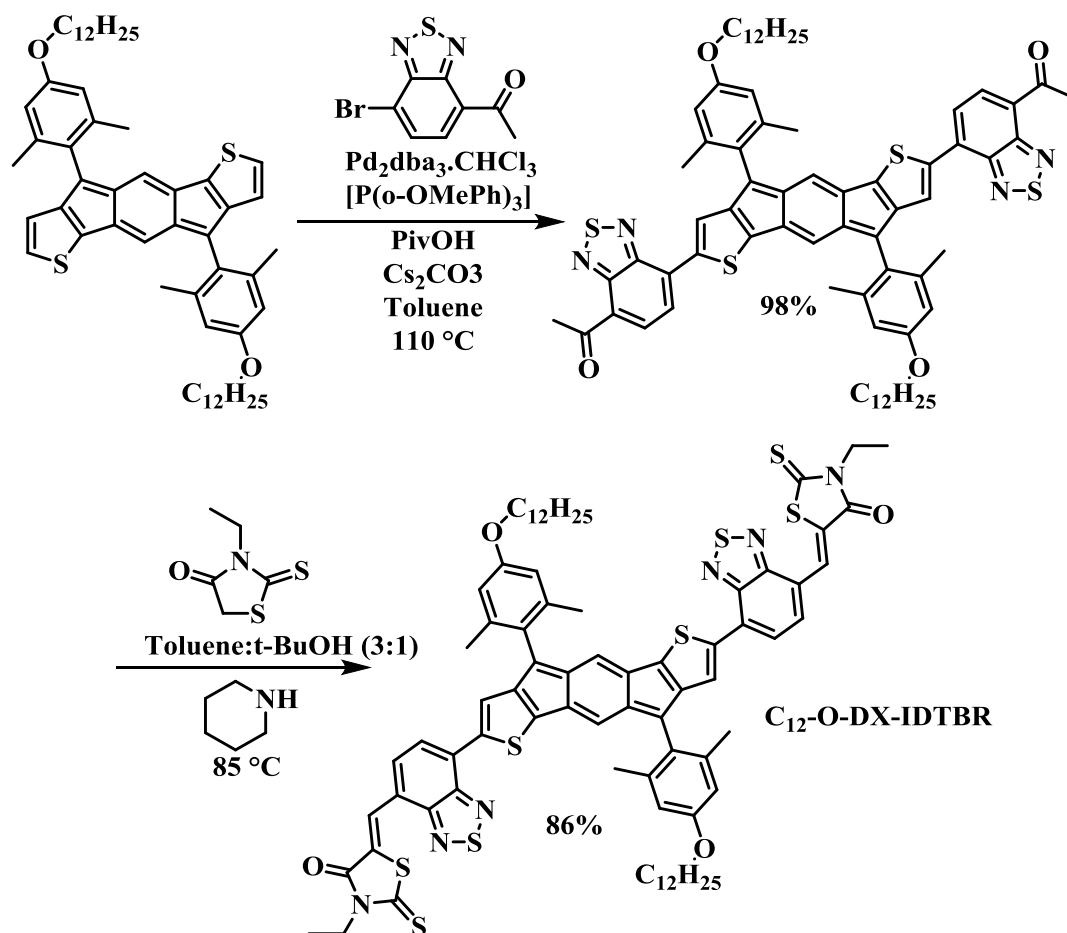


Scheme 16. Synthetic pathway to **C₁₂-O-DX-IDT** via Grignard formation and addition to IDT-diketone.

As such the synthetic pathway begins with synthesis of the bulky, solubilising 2-bromo-5-(dodecyloxy)-1,3-dimethylbenzene group, necessary to stabilise the quinoidal IDT core. A standard Williamson ether synthesis was employed to install the dodecyl alkyl chain as an alkoxy group at the 5- position of the xylene core. Unlike the all-carbon indenofluorene attempts to add the lithiated xylene motif to the IDT-diketone core resulted in the utter decomposition or no reaction at all. In order to overcome this the Grignard reagent was created *in situ* and subsequently added to the IDT-diketone to afford the crude diol which underwent reductive dearomatization upon treatment with SnCl₂ (**Section 2.4**).

The reactivity of the 2- position of the outer thiophene rings was exploited through direct C-H activation¹⁶⁵ to attach the benzothiadiazole-carboxaldehyde moiety. Pd₂dba₃.CHCl₃ was used as the catalyst alongside tris(o-anisyl) phosphine [P(o-OMePh)₃] which has been reported as an efficient supporting ligand for direct arylation reactions in nonpolar media.¹⁶⁶ The pivalic acid additive improves the rate of direct arylation, forming the carboxylate anion under the basic (Cs₂CO₃) reaction conditions by co-ordinating to the palladium stabilising the transition state.¹⁶⁷ Indeed, the reaction progressed almost quantitatively with a 98% yield, to afford the pre-cursor to the final NFA as a purple crystalline solid. Satisfyingly, this route bypasses the need for toxic tin chemistry, avoiding the Stille cross coupling reaction demonstrated in the

synthesis of O-IDTBR.¹⁶³ Finally, Knoevenagel condensation with 3-ethylrhodanine afforded the desired quinoidal acceptor unit, **C₁₂-O-DX-IDTBR** in considerable yield (86%).



Scheme 17. Direct C-H activation arylation followed by Knoevenagel condensation to afford the **C₁₂-O-DX-IDTBR** NFA.

Much akin to **O-IDTBR**, DFT calculations predict a near planar configuration of the quinoidal core, attributed to the quinoidal nature of the thienyl-phenyl bond and reduced steric hinderance from adjacent α -C-H bonds between the coupled thienyl-phenyl rings.^{142,163}

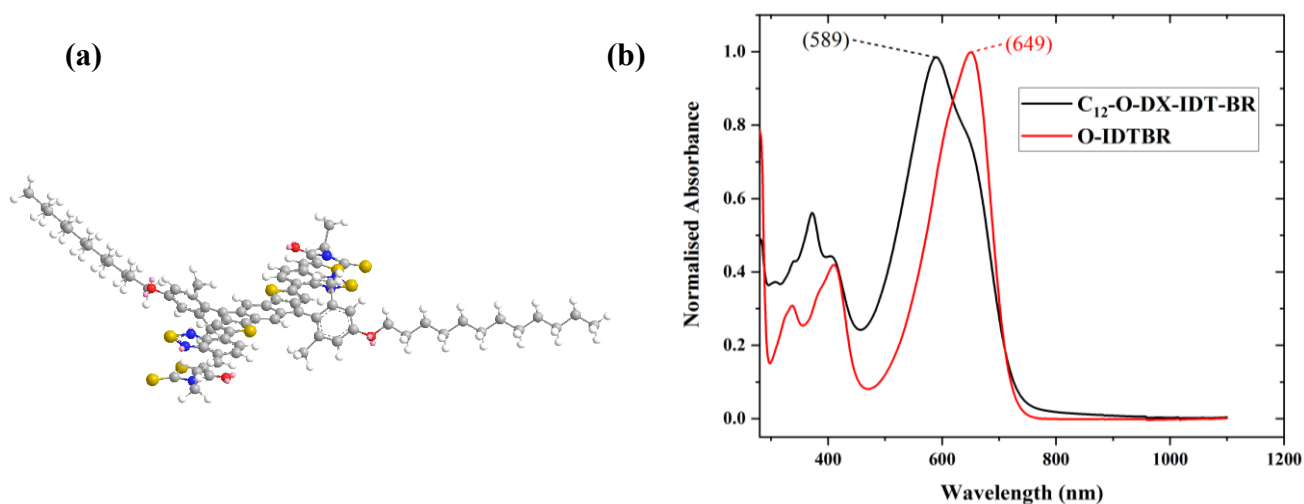


Figure 61. (a) DFT calculated geometry of **C₁₂-O-DX-IDTBR**. (b) Thin-film UV-Vis spectrum comparing to **O-IDTBR**.

The quinoidal nature of the core leads to a slight reduction in the optical bandgap (1.60 eV) compared to O-IDTBR (1.63 eV), despite the 60 nm redshift of λ_{max} the broad shoulder extends past 750 nm narrowing the optical bandgap.

A sample of the quinoidal NFA was given to H. Bristow and M. Bidwell who kindly agreed to test the material within an inverted architecture bulk heterojunction. Solar cells were fabricated using PBDB-T (PCE12), one the highest performing donor polymers, known to give efficiencies over 12% for similar small-molecule acceptor organic solar cells.¹⁶⁸ Multiple C₁₂-O-DX-IDTBR films were spun varying both the revolutions per minute and the thermal annealing time, these were then studied and compared to blends of **O-IDTBR**, summarised below:

Table 6. Comparison between PCE12:NFA (1:1) blend devices, cast from 20 mg mL⁻¹ in chlorobenzene.

No	NFA	Spin Conditions	Anneal	J _{sc} (mAcm ⁻²)	V _{oc} (V)	FF	PCE (%)	Thickness (nm)
9	C ₁₂ -O-DX-IDTBR	2500rpm/60s	None	0.17	0.30	0.27	0.013	106
10	C ₁₂ -O-DX-IDTBR	2500rpm/60s	120°C/10mins	0.16	0.33	0.27	0.014	-
11	C ₁₂ -O-DX-IDTBR	2500rpm/60s	65°C/10mins	0.15	0.29	0.27	0.012	-
12	C ₁₂ -O-DX-IDTBR	3500rpm/60s	None	0.18	0.20	0.26	0.0094	90
13	C ₁₂ -O-DX-IDTBR	2500rpm/60s	120°C/10mins	0.18	0.27	0.26	0.013	-
14	O-IDTBR	2500rpm/60s	None	12.3	1.00	0.49	6.0	84
15	O-IDTBR	2500rpm/60s	120°C/10mins	14.2	0.92	0.48	6.3	-
16	O-IDTBR	2500rpm/60s	65°C/10mins	13.3	0.99	0.52	6.8	-

These results were extremely disappointing, with a maximum power conversion efficiency of only 0.014%, with the testing standard **O-IDTBR** exhibiting an increased PCE of 6.8% an increase of almost three-orders of magnitude compared to the quinoidal acceptor. This ruled out device fabrication as the reason for the lack of performance with **C₁₂-O-DX-IDTBR** as all devices were created equally in the same session. This prompted an investigation into the quality of the films themselves. Firstly, the thickness was tested (**Table 6**). The thickness of each **C₁₂-O-DX-IDTBR** film ranged between 6-22 nm thicker than the test **O-IDTBR** film. Upon inspection under a profilometer microscope it was found that, unlike **O-IDTBR**, the films were amorphous and inhomogeneous, far from the crystalline structure necessary for efficient charge transport.¹⁷ This could potentially arise from an impurity within the material, further

purification was attempted utilising recycling GPC and recrystallisation techniques however once again the material underperformed in devices. ^1H proton NMR would suggest that the material was isolated in high purity, thus the quality of the films is likely the dominant factor for the observed poor device performance. Future work will look to scale up the synthesis of this material in order to expose it to multiple methods/runs of purification. **C₁₂-O-DX-IDTBR** is undoubtedly an interesting molecule and a pure sample would provide great insight into a potential new class of quinoidal NFAs.

3.10 QUINOIDAL POLYMER SERIES



Figure 62. Photograph of **DX-IDF** copolymers [2-4] and **DX-IDT** copolymers [6-8] dissolved in DCM at equal concentrations, demonstrating the spectrum of absorption wavelengths, resulting in the varying coloured solutions.

The final body of work on quinoidal, biradical materials was a collaborative effort with my post-doctoral researcher M. Little. Whilst the previous sections within this chapter focused on small molecule derivatives of **IDF** and **IDT** an exploration into the polymeric forms of these quinoidal molecules is described herein. Indeed, quinoidal polymers have been widely sought after due to their notable charge-transport properties, reduced bandgaps and high polarisability.¹⁶⁹ As a result of the resonant π -bonds quinoidal molecules tend to exhibit extended delocalisation compared to their aromatic counterparts. An exploratory set of reactions was conducted to afford a series of quinoidal polymers based on the **DX-IDF** and **DX-IDT** precursor monomers. These will be reported below for synthetic interest and to

complete the work on both the indenofluorene and indacenodithiophene motifs, the work is documented with full permission from M. Little.

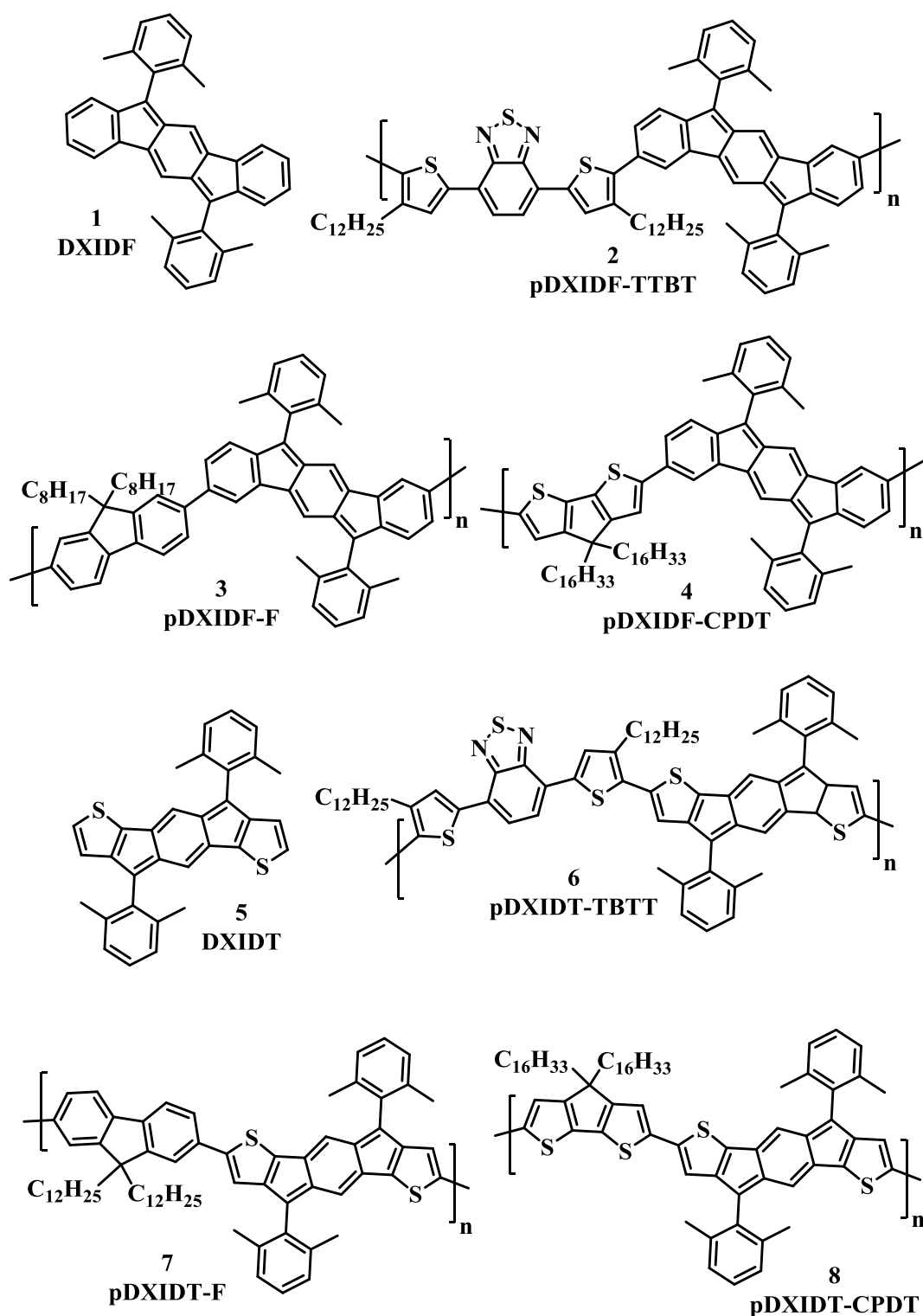
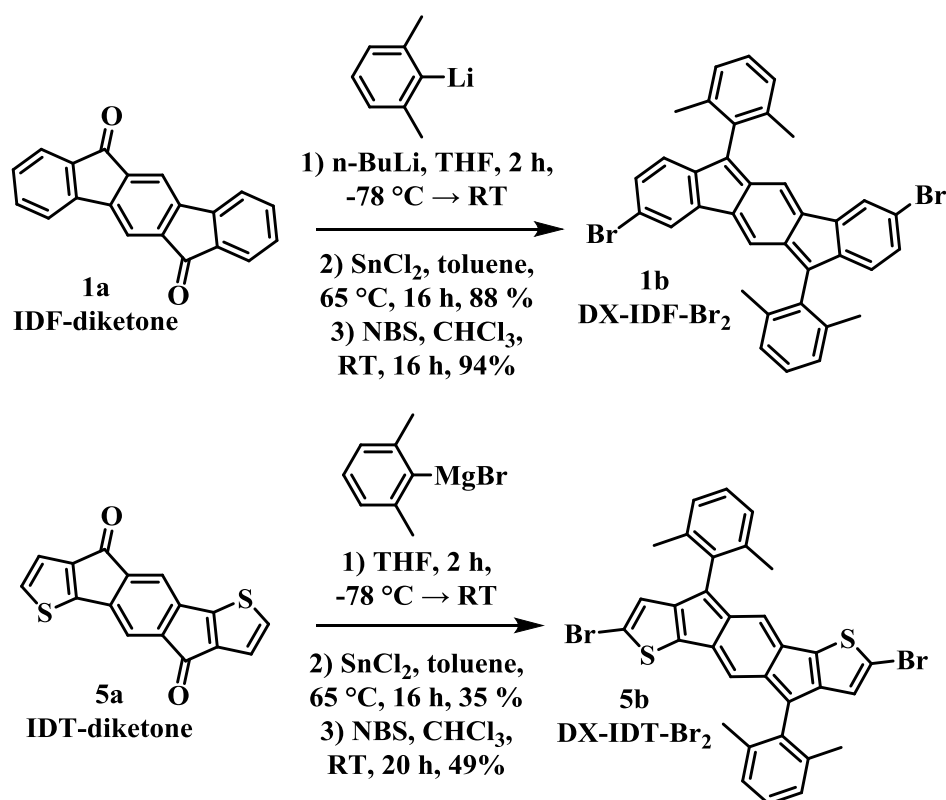


Figure 63. Series of DX-IDF copolymers [2-4] and DX-IDT copolymers [6-8] synthesised in combination with M. Little.

Conveniently the **di-brominated DX-IDF** had already been synthesised for use in the FMR linewidth broadening experiment (**Section 3.5**). As previously mentioned, upon treatment with N-bromosuccinimide **DX-IDF** is selectively brominated at the 3- and 9- position, opening multiple synthetic pathways for expansion of the quinoidal core through standard aryl-bromide manipulations. This regioselectivity renders the addition of conjugated units, at these positions, to adopt a *meta*- arrangement, this contrasts with **DX-IDT** which selectively brominates at the carbon adjacent to the thiophene moiety, leading to a *para*-conjugation arrangement (**Figure 64**).



Scheme 18. Synthetic pathway for the selectively brominated **DX-IDF** and **DX-IDT** monomer units.

The six polymers described herein are just a sampling of the chemistry undertaken with these quinoidal monomers, both monomers are amenable to a variety of coupling conditions from Suzuki to Stille and direct heteroarylation polymerisation (DHAP).^{111,165,170} It should be noted that the halogenated **DX-IDT** monomer seems somewhat resistant to DHAP chemistry

affording black insoluble conglomerates, suggesting that C-H adjacent to the bromide position is not chemically inert leading to a cross-linking and unwanted reaction pathways. For clarity, the monomer units were synthesised by me whilst the polymerisations (reported herein) were conducted by Dr M. Little. However, due to the synthetic ease of obtaining large quantities of indacene monomers multiple copolymers were synthesised (by me) with bi-thiophene (T2), thieno[3,2-*b*]thiophene (TT), EDOT₂ and vinyl co-monomers to name a few, these will not be compared here but were synthesised and are currently awaiting further data analysis. This section will focus on six unique quinoidal polymers using three different co-monomers, namely electron-poor dithienobenzothiadiazole (TBTT), electron-neutral 9,9-dioctylfluorene and electron-rich cyclopentadithiophene (CPDT):

Table 7. Optoelectronic, electrochemical and molecular weight data for **DX-IDF** and **DX-IDT** copolymers.

No.	Polymer	λ_{max} (nm)	E_{GAP} (eV) ^a	E_{HOMO} (eV) ^b	E_{LUMO} (eV) ^c	M_n^d	PDI	Coupling
1	DX-IDF	526	2.22	-5.61	-3.39	-	-	-
2	p(DX-IDF-TBTT)	649	1.67	-5.58	-3.91	13900	1.28	DHAP
3	p(DX-IDF-Fluorene)	573	1.93	-5.51	-3.58	12300	1.55	Suzuki
4	p(DX-IDF-CPDT)	722	1.45	-5.20	-3.75	51500	1.62	Stille
5	DX-IDT	555	2.11	-5.40	-3.28	-	-	-
6	p(DX-IDT-TBTT)	580	1.75	-5.22	-3.47	5000	1.38	Stille
7	p(DX-IDF-Fluorene)	474	2.02	-5.25	-3.23	21400	1.91	Suzuki
8	p(DX-IDF-CPDT)	564	2.02	-5.17	-3.16	44400	2.09	Stille

a) estimated optical gap from axis intercept of absorption spectra onset $E_{GAP} = 1240 / \lambda_{ONSET}$

b) extracted from CV, thin film on a glassy carbon electrode with propylene carbonate / Bu₄NPF₆ electrolyte solution c) Sum of E_{HOMO} and E_{GAP} d) gel permeation chromatography (GPC) in chlorobenzene.

DX-IDF copolymers with both fluorene and TBTT are moderately redshifted and broadened compared to the parent indenofluorene monomer. The situation changes drastically when **DX-IDF** is copolymerised with the electron-rich cyclopentadithiophene (CPDT), a large redshift of almost 200 nm is observed (**Figure 64**). This stark shift suggests the polymer's conjugated backbone to have a donor-acceptor character, whereby the **DX-IDF** moiety acts as the electron acceptor unit. This finding is rather remarkable for a pure hydrocarbon polycycle that does not contain any electron withdrawing motifs or electronegative atoms and is one of the few materials in literature displaying this similar feature to fullerenes. This is likely due to a combination of the antiaromatic [4n] electron count and the observed quinodimethane (QDM) motif (**Figure 24**) within the central tricyclic core. The push-pull donor-acceptor interaction is also mediated by the delocalised molecular orbitals which are facilitated by the *meta*-bonding arrangement allowing through conjugation at the 3- and 9- positions.

For **DX-IDT** there is much less shift in λ_{max} across all three copolymers, surprisingly however **pDX-IDT-Fluorene** is blue-shifted with respect to its indacenodithiophene parent monomer, the peak is still extremely broad and gives a comparable E_{GAP} to that of the **pDX-IDT-CPDT** polymer. The bandgaps for the **pDX-IDT** series are only slightly reduced from that of the parent monomer, again likely due to the *cross*-conjugation arrangement owing to the *para*-coupling motif. The differences in coupling arrangements and hence conjugation is illustrated below:

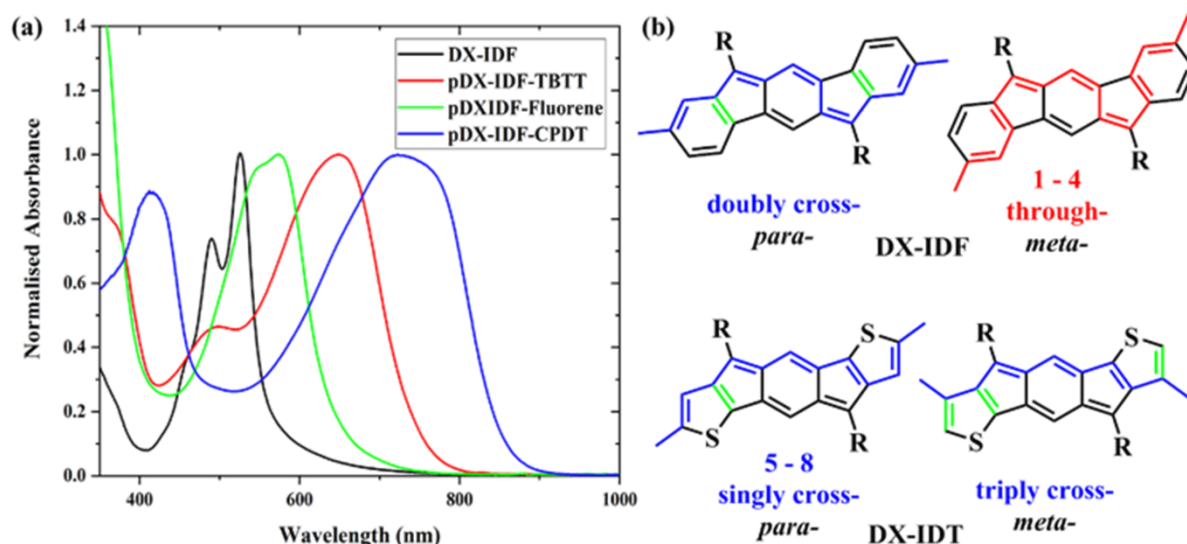


Figure 64. (a) UV-Vis absorption spectrum for thin films of **DX-IDF** and polymers [1-4]. (b) Cross- and through- conjugation arrangements for **DX-IDF** and **DX-IDT**, cross-conjugated double bonds highlighted in green.

The electronic properties of these polymers are also varied opening up a range of potential applications for these quinoidal materials. Each material [1-8] displays HOMO levels appropriate for most *p*-type device architectures ranging from -5.17 eV to -5.61 eV (**Figure 65**).³¹ The through- conjugation observed within the **pDX-IDF** series enables sufficient delocalisation of the HOMO extending out from the central indenofluorene core. This reduces the transfer integral; splitting of the highest occupied molecular orbital (HOMO) and the lowest unoccupied molecular orbital (LUMO). The electronics of **pDX-IDF-CPDT** are complimentary to that of **O-IDTBR** (**Section 3.9**), however the IP is reduced by ~0.2 eV and the bandgap is also reduced which could render **pDX-IDF-CPDT** as a good candidate for NFAs. Both **pDX-IDT-Fluorene** and **pDX-IDT-CPDT** have very similar electronic profiles and almost mimic that of **P3HT** (**Figure 10**), one of the benchmark electron donating, hole transporting, polymers of recent memory.¹⁷¹

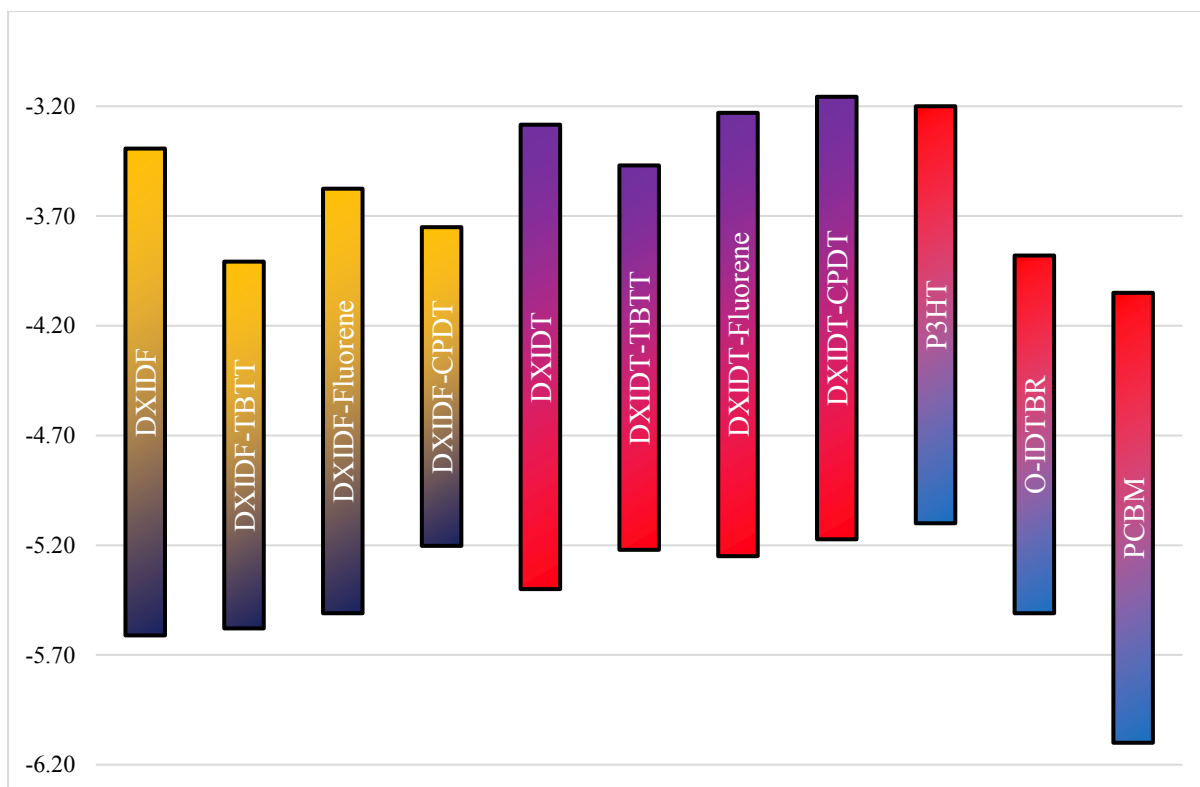


Figure 65. Energy level (HOMO, LUMO, bandgap) comparison of **pDX-IDF**, **pDX-IDT** series and select benchmark polymers.

The entire series of materials also show excellent photostability, the image (**Figure 62**) was taken after 18 months of benchtop storage in a bright chemistry laboratory. The measured λ_{max} values deteriorated by as little as 5% over this time period. Preliminary investigations into the polymers' OFET performance afforded a single functioning device, **pDX-IDT-CPDT**, which showed modest hole mobilities of up to $0.009 \text{ cm}^2 \text{ V}^{-1} \text{ s}^{-1}$, current on/off ratios in the order of 0.5×10^2 and threshold voltages of between -1.1 to -3.7 V. Initial electrochromic measurements also show that the indenofluorene analogue, **pDX-IDF-CDPT**, performs relatively well achieving a ($\Delta T(\lambda_{max}) = 30 \%$) contrast with a colour-neutral oxidised film. Further evidence for the **DX-IDF** motif acting as a pure hydrocarbon acceptor unit.

3.11 CONCLUSIONS

This section demonstrates the broad array of applications applicable to quinoidal/biradical systems. The underlying motif throughout this chapter is the indenofluorene (**IDF**) and indacenodithiophene (**IDT**) backbone which runs throughout each section. Indeed, it is the marked stability and synthetic freedom inherent to these systems that has allowed them to cross multiple disciplines from singlet fission, to spin-pump experiments to organic solar cells and finally as quinoidal polymer building blocks. These backbones have been extensively studied by the Haley group^{103,104,113} but it is hoped that the investigations herein expand the understanding and potential of these fascinating indacenes. Novel investigation of **DX-IDF** recorded ferromagnetic linewidth broadening $\delta\Delta H = 0.60 \pm 0.03 G$ and a spin mixing conductance of $g_{eff}^{\uparrow\downarrow} = 3.74 \times 10^{18}$ the highest value for any reported organic material. The indacenodithiophene analogue was investigated in both the FMR experiment and synthetically extended to produce a potential non-fullerene acceptor. The successful synthesis of diindeno[b,i]anthracene dixylene (**DIAnDX**) is reported, showing an increased biradical character with a low lying thermally populated triplet state. Some interesting results were gathered and whilst undoubtedly there were many frustrations along the way; the eternal battle to avoid the conical intersection, stubborn antiaromatic oxidative dehydrogenation with **DDQ** and amorphous solar cell films, the knowledge gained will steer future advances towards fully understanding these quinoidal systems.

CHAPTER FOUR: *n*-TYPE POLYMER SERIES

4.1 INFORMATION AND CREDITS

The hybrid alkyl-glycol monomer and polymer synthesis, optimisation and characterisation were conducted in my own work. Dr. Rajendar Sheelamanthula carried out GPC measurements (McCulloch group, KAUST). OECT devices were fabricated by Dr Bryan Paulsen (Rivnay group, Northwestern) who also conducted OECT performance measurements and obtained GIWAXS data. Thermoelectric measurements were collected by Dr Suhao Wang (Fabiano group, Linköping University).

4.2 ABSTRACT

Typical semiconducting polymer synthesis utilises transition metal-catalysed coupling reactions, forming single C-C bond linkages along the polymer backbone. These single bonds can easily rotate leading to conformational and energetic disorder, known to limit charge delocalisation and reduce device performance. The use of transition metal coupling catalyst limits the biocompatibility and long-term polymer sustainability. This chapter reports on the use of a simple Aldol condensation to form polymer backbones linked by C=C double bonds, conformationally locking the backbone to form a fused polymeric system. Novel N-glycolated bisatin and bisoxindole monomers are coupled together to form a series of electron-deficient fused rigid polymers for *n*-type OECT and thermoelectric device applications. The avoidance of both transition metal catalysts and toxic organometallic monomers during polymer synthesis imparts intrinsic biocompatibility, which is only enhanced upon inclusion of glycol sidechains. These polar sidechains facilitate ion transport and render the resultant polymers as mixed conductors. The electron deficient extended isoindigo core drives down the energy of the LUMO allowing the reported polymers to function in *n*-type operation mode. The effect of tuning the sidechain will be investigated with linear alkyl, branched alkyl, linear glycol and branched glycol chains used in various combinations to afford a range of mixed alkyl-glycol

or all glycol functionalised polymers. These mixed conduction polymers show potential as both thermoelectric materials and channel materials in organic electrochemical transistors.

4.3 BACKGROUND & MOTIVATION

The field of organic semiconductors has long been dominated by polymeric materials which have shown excellent performances in various applications including solar cells, OLEDs and OFETs to name but a few.^{10,14,16} Despite this, as technology advances, the desire for additional device optimisation is further sought after. As such, there is still a recurring effort to improve the parameters which affect device performance. Herein we will focus on OECT and thermoelectric device applications. It is well known that the electrical properties of such devices are heavily dependent on the molecular conformation of the polymer and its subsequent solid-state morphology.¹⁷² Both structural properties are related to the charge carrier mobility, one of the fundamental properties which must be optimised for high efficiency devices. The electronics of a polymer must also be carefully considered and controlled to improve charge injection and avoid unfavourable charge trapping, this is crucial for *n*-type (electron transport) materials which require a high electron affinity.³⁷ One common design approach to accommodate these requirements is to utilise dipole-dipole interactions affording closer intermolecular packing, stronger π - π interactions and an overall improvement of charge carrier transport via morphological manipulations.

The versatile electron-deficient isomer of the well-known dye indigo, named isoindigo is a prime example of a material which exhibits many of these desirable properties. Comprised of a bis-lactam motif, known to promote strong intermolecular interactions via the dipolar carbonyl groups, isoindigo copolymers have been reported with relatively high ambipolar charge carrier mobilities ($\sim 0.1 \text{ cm}^2 \text{ V}^{-1} \text{ s}^{-1}$).³⁴ Furthermore, substantial electron affinities (between 3.7 and 3.8 eV) and a LUMO delocalised along the polymer backbone render electron

injection and transport as a favourable process. A high electron affinity also imparts redox stability, limiting potential side-reactions with oxygen and water, which are known to be detrimental towards performance. Typically, this electron acceptor would be paired with an electron rich monomer in a standard donor-acceptor type polymer, most likely utilising some form of metal catalysed cross-coupling chemistry. A different approach has been to develop unipolar electron transport polymers in order to try to optimise *n*-type performance. Lee *et al.*¹⁷³ published an *n*-type conjugated polymer comprised of all electron deficient moieties, i.e. an acceptor-acceptor, A-A, backbone structure. Recent studies have also suggested that energetic disorder within a polymer network can strongly limit electron transport.¹⁷⁴ These findings motivated previous work within the group, conducted by Dr A. Onwubiko and Dr C. Jellett, to develop a series of fused electron-deficient semiconducting polymers capable of air stable electron transport.¹⁷⁵

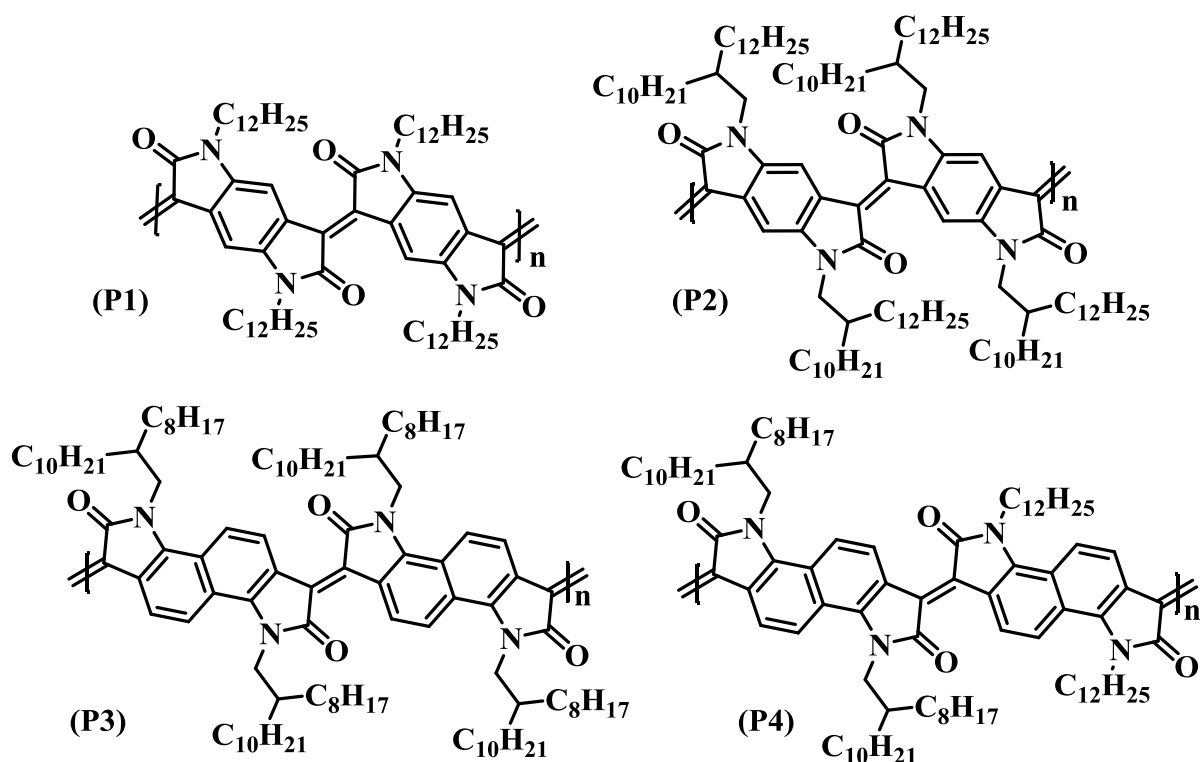


Figure 66. All alkyl chain Aldol condensation polymers **P1-4** synthesised by Dr A. Onwubiko.¹⁷⁵

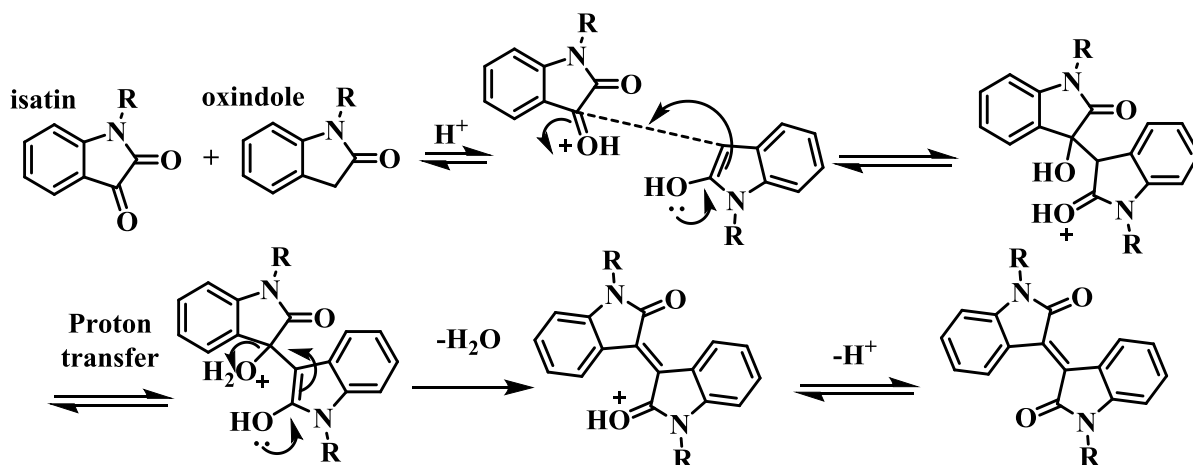
The effect of the number of aromatic rings, dihedral angle of the backbone and alkyl chain density on the electron transport properties was explored within this range of polymers [P1-4]. For P4 air stable electron mobilities of up to $0.03 \text{ cm}^2 \text{ V}^{-1} \text{ s}^{-1}$ were achieved.

This work will document an attempt to improve the biocompatibility, for OECT device application, and increase performance of these rigid rod polymers by side chain engineering. Specifically, the synthesis of a series of mixed alkyl-glycol and glycol-glycol rigid rod polymers will be discussed. This combines the previous work of Dr A. Giovannitti⁵³, again from within the group, with that described above to further investigate the effect of *glycolation* (replacing alkyl sidechains with linear/branched ethylene glycol units) on transport properties. Some of the benefits of *glycolation* are described in (Section 1.4.5), this chapter will focus on what turned out to be a very difficult synthetic process to afford a series of glycolated polymers. Herein, seven unique polymers will be documented, across the series both the aromatic core (naphthalene vs anthracene) and sidechains (alkyl, linear or branched glycol) were altered, with multiple combinations of monomers affording a diverse set of rigid rod materials.

4.4 ACID-CATALYSED ALDOL POLYCONDENSATION

Throughout the field of organic electronics, the vast majority of C-C bond forming reactions have made use of transition metals.³⁹ Whilst these reactions are undoubtedly essential to modern day chemistry, the use of precious metals, highly toxic reagents and coupling partner compatibility limit the field, especially in the formation of electron-deficient polymers. One attractive alternative to this is the acid-catalysed Aldol condensation reaction, requiring no precious transition metals. This method has been employed to develop some of the most important and high performing semiconductors, ranging from diketopyrrolopyrrole (DPP) to isoindigo.^{34,176}

The synthesis of isoindigo mimics that of the polymer series (**Figure 66**), whereby the initial step is to form the oxindole coupling partner. The oxindole is synthesised by subjecting isatin to a Wolff-Kishner reduction, using harsh hydrazine conditions. The carbonyl group at the 3-position of the isatin ring is more electron-deficient than the amide carbonyl functionality at the 2-position, thus leading to a selective reduction of the carbonyl at the 3-position. Isatin and 2-oxindole are subsequently subjected in equimolar equivalents to acid-catalysed Aldol condensation, to afford isoindigo and one equivalent of H₂O. The mechanism for this condensation (**Scheme 19**) begins with proton exchange to form the protonated isatin which is attacked by the enol form of the oxindole forming the new carbon-carbon bond. Finally, via a proton transfer, loss of water and regeneration of the acid catalyst isoindigo (or any isatin-oxindole coupled material) is formed.



Scheme 19. Mechanism for the acid-catalysed aldol condensation of isoindigo.

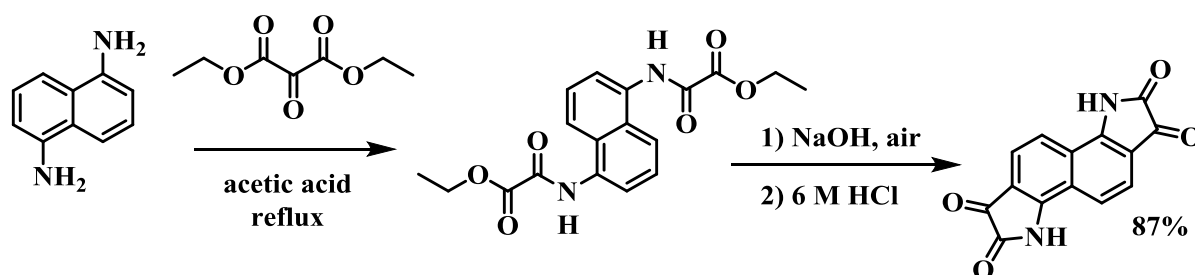
This general condensation reaction can be extended to form polymer backbones, without the necessity of a transition metal catalyst. Indeed, this method was used with moderate success to produce polymers **P1-4** (**Figure 66**), condensing together a functionalised bisisatin with a similarly functionalised bisoxindole. This polymerisation technique allows the bisisatin and bisoxindole monomers to be synthetically manipulated prior to polymerisation and allows for

a single functionalised bisisatin to be synthesised and reduced, forming the necessary bisoxindole to couple together to form a homo-polymer.

4.5 BISISATIN SYNTHESIS

In order to fit the design criteria for a high mobility and high conductivity *n*-type material, fused bisisatin and bisoxindole monomers were selected as targets for *glycolation*. Here the bisisatin acts as the electrophile, absent of an active methylene group and the bisoxindole (semi-reduced isatin) acts as the nucleophile. The acidic protons vicinal to the carbonyl group, an active methylene group, can be converted to the enol form under acidic conditions allowing for the polycondensation reaction to occur.

The first step in the bisisatin/bisoxindole monomer synthesis is to form the bisisatin core. Whilst multiple routes exist they are beyond the scope of this thesis and here we employ a Martinet isatin synthesis, which was first reported in 1913.¹⁷⁷ This was later expanded and the synthesis of electron-deficient bisisatin (bisisoindigo) follows this motif:

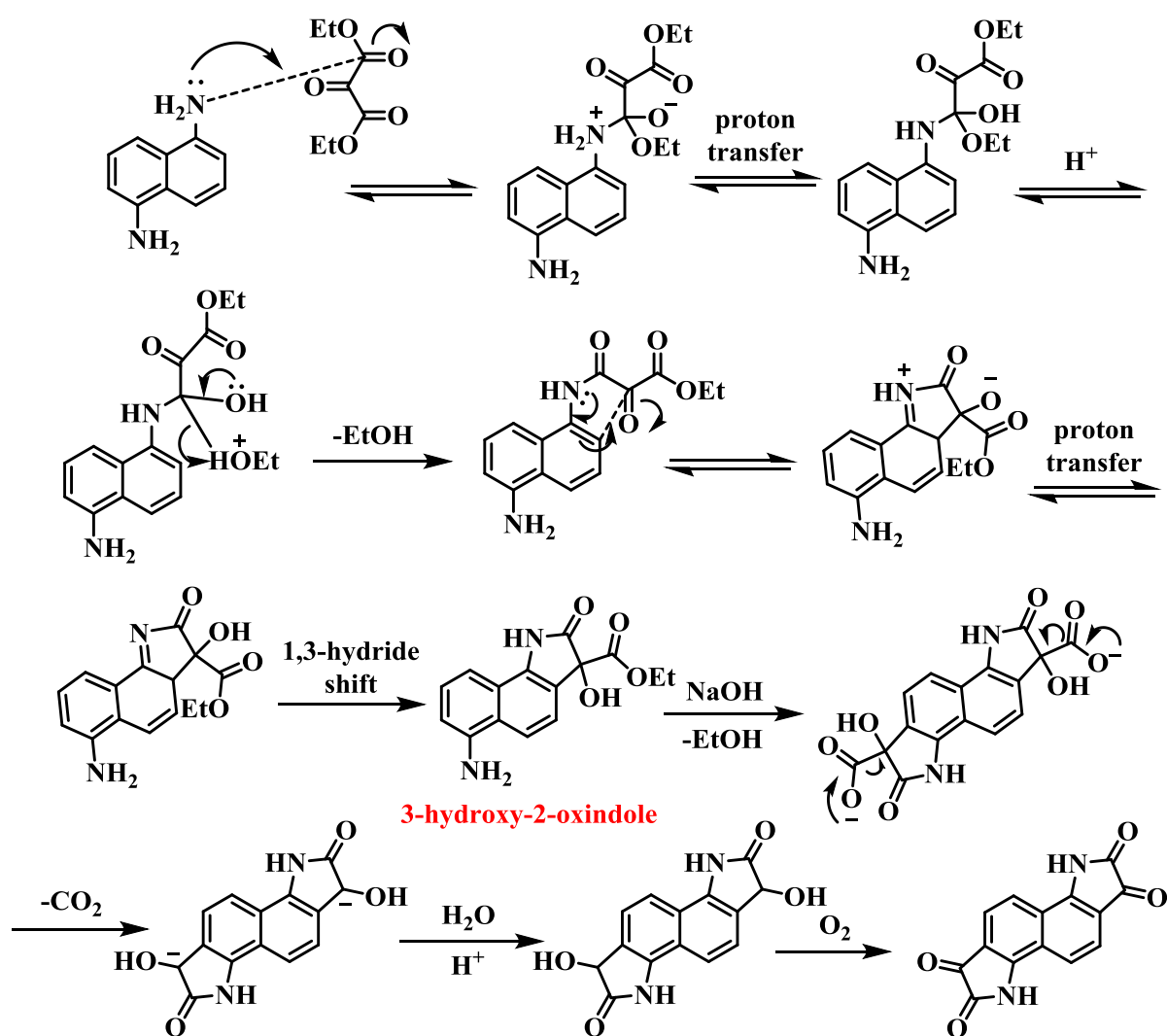


Scheme 20. Martinet synthesis of bisisatin, 1,5-diaminonaphthalene is refluxed in acetic acid with diethyl ketomalonate, oxidative ring closure is mediated by passing air through the reaction mixture under basic conditions.¹⁷⁸

The initial literature synthesis of bisisatin proved to be problematic with common isatin forming mechanisms, such as the Sandmeyer reaction, affording bisisatin as a minor product.¹⁷⁹

This was due to the electron withdrawing nature of the formation of the initial isatin ring, the subsequent electrophilic aromatic substitution, to form the second isatin ring, could not proceed

due to a lack of electron density.¹⁷⁸ The Martinet route overcomes this issue as the initial ring closure produces a 3-hydroxy-2-oxindole intermediate which is far less electron withdrawing than an isatin, allowing the second ring closure to proceed affording the desired bisisatin in good yield.¹⁷⁸ The mechanism for this transformation is detailed below, please note that only one isatin ring is depicted, however the key 3-hydroxy-2-oxindole intermediate is highlighted, it is at this point that the cycle would restart and form the second isatin ring prior to the addition of NaOH.

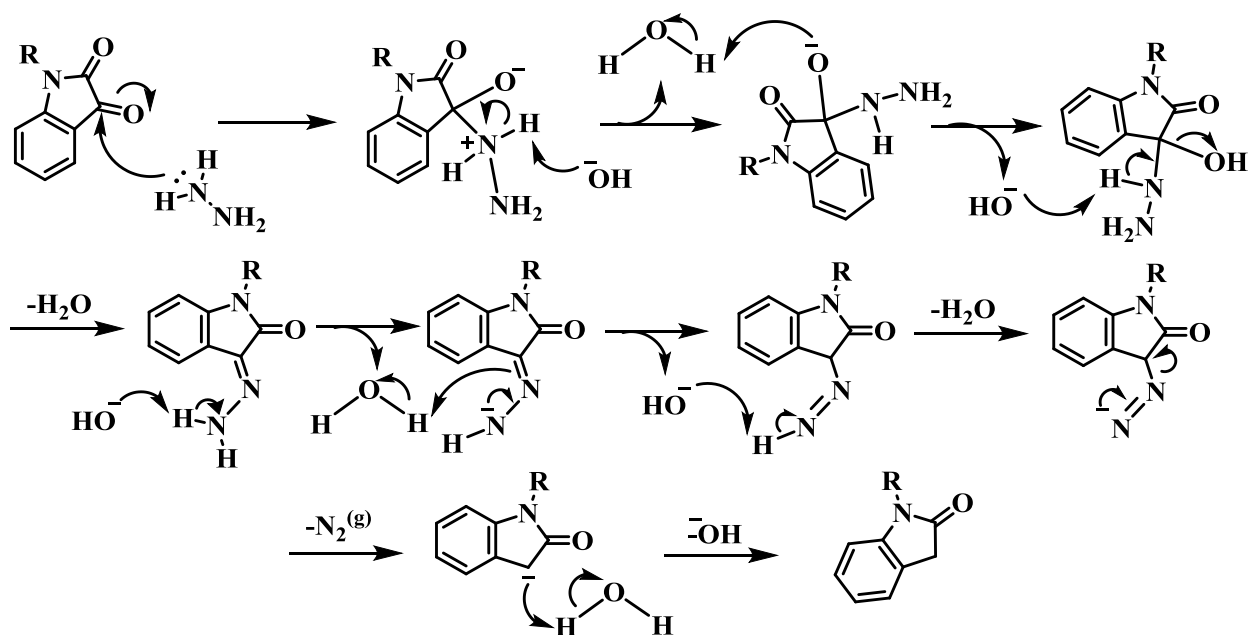


Scheme 21. Detailed mechanism for the Martinet synthesis formation of bisisatin. Note that only one isatin ring is illustrated, the key 3-hydroxy-2-oxindole intermediate is highlighted.

The 3-step process reported by Randell *et al.*¹⁷⁸ is the most reliable route to form bisisatin (formally 3,8-dihydroindolo[7,6-g]indole-1,2,6,7-tetraone) however the resultant purple solid is undoubtedly impure, with formation of the minor single ring closed product being inevitable. The lack of solubility in most common solvents renders further purification extremely limited and as such the material is used in the subsequent reactions after being washed with copious amounts of water and methanol. Even though the purity of this compound varied from batch to batch, this only became apparent after alkylation/*glycolation* when the crude TLC plate would return a brick red spot on the baseline with no evidence of the purple/blue product spots. This was incredibly frustrating and a more optimal route to forming the bisisatin is much needed if this area of *n*-type rigid rod chemistry is to be further explored in the future.

4.6 BISOXINDOLE SYNTHESIS

Akin to the Sandmeyer synthesis of isatin¹⁷⁹ the formation of bisoxindole monomers, from diamionaphthalene parent molecules, are also deactivated towards the second ring formation reaction. One method to overcome this is to simply reduce a functionalised bisisatin, via a standard Wolff-Kishner reduction to afford the functionalised bisoxindole. The simplified mechanism for the isatin reduction reaction is depicted below (**Scheme 22**), note that an identical mechanism would also be expected for the bisisatin to bisoxindole reduction. Whilst this is undoubtedly an effective and simple single step route, the harsh conditions typically involve refluxing hydrazine and tend to lead to extremely modest yields.

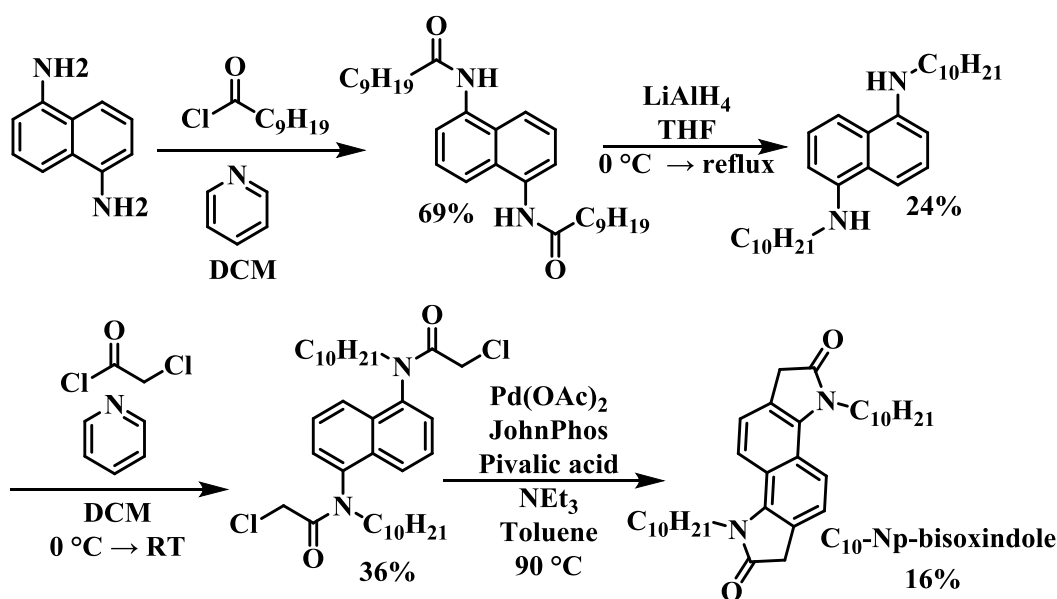


Scheme 22. Mechanism for the Wolff-Kishner reduction of isatin to form oxindole.

Diminished yields of the reduction alone are not too problematic but when combined with the reported yields of alkylated bisisatins only ranging from as little as 5-15%¹⁷⁵ this becomes an extremely unattractive route unless a large quantity of the aforementioned functionalised bisisatin can be synthesised, which is known to be problematic. Despite this, the Wolff-Kishner reduction was performed successfully, to afford a glycolated bisoxindole (*vide infra*), but an alternate method was also utilised to synthesise linear and branched alkyl chain functionalised bisoxindole monomers.

Previous work within the group by Dr C. Jellett has shown that the Stolle synthesis, known to form oxindoles in good yield, was not amenable to forming bisoxindole, again likely due to the deactivated intermediate mentioned above.¹⁸⁰ In light of this in 2016 Jiang *et al.*¹⁸¹ reported a C₁₂-alkylated bisoxindole derivative, following the bisisatin synthesis. Specifically, this involved reacting 1,5-diaminonaphthalene with dodecanoyl chloride to form an insoluble intermediate. Reduction with LiAlH₄ was followed by treatment with chloroacetyl chloride and subsequent ring closure via a direct C-H functionalisation procedure, first published by Buchwald & Hennessy,¹⁸² afforded the C₁₂-alkylated bisoxindole in moderate yield (**Scheme**

23). The reaction was mediated by JohnPhos, the sterically bulky biaryl phosphine ligand. The protic additive (pivalic acid) binds to the Pd and facilitates proton transfer relay during the C-H activation mechanism.¹⁶⁷ This route was later modified by Jellett¹⁸⁰ and subsequently used to yield both linear and branched alkyl chain functionalised bisoxindoles in appreciable yields, especially compared to the Wolff-Kishner reduction. This method was used herein to afford linear C₁₀-, C₁₂-, C₁₆- naphthalene bisoxindoles, respectively (*vide infra*).



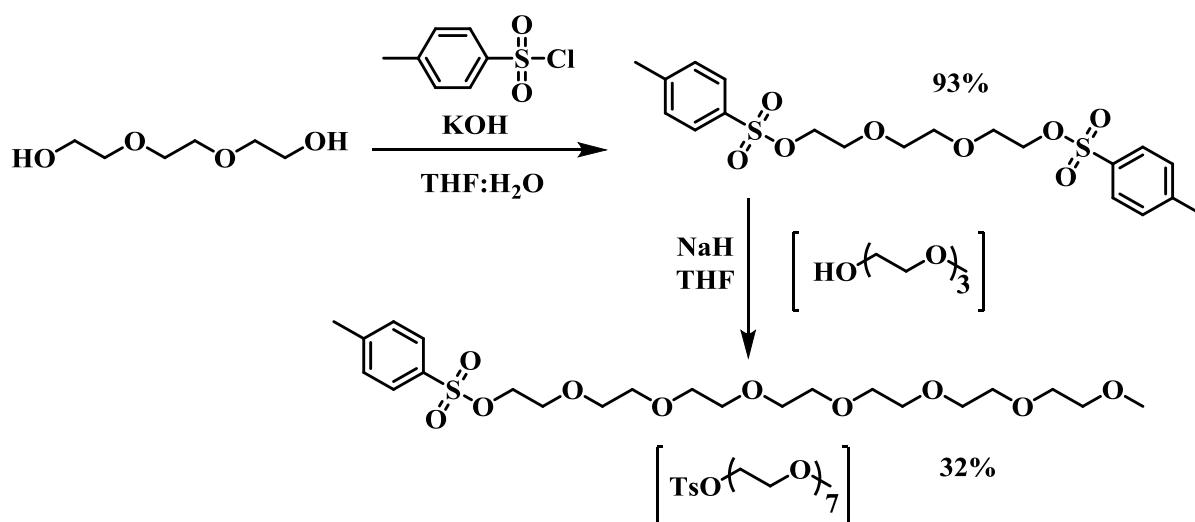
Scheme 23. Synthetic pathway to afford alkylated bisoxindole monomers, specifically C₁₀-N_p-bisoxindole.

4.7 N-GLYCOLATION

The stage was set to create a novel series of glycolated *n*-type rigid rod polymers. The first synthetic hurdle was finding the best route to install the desired glycol chain to the nitrogen moiety of bisisatin. This proved to be incredibly challenging, but was somewhat to be expected as the reported yields for alkylation were already very poor¹⁸⁰, *glycolation* is known to be even less efficient for many systems.^{52,53,183} It was also hoped that the N-glycolated product would

dominate since nitrogen is a softer nucleophile compared with the oxygen atom, however this also depends on the associated leaving group of the chain additive.¹⁶⁷

Initial attempts to afford a glycolated bisisatin began with synthesising a tosylated seven-unit oligo(ethylene glycol) (OEG) chain, reminiscent of the polar sidechain used previously within the group by Dr A. Giovannitti for a series of glycolated NDI and T2 polymers.⁵⁶ It was hoped that previous successful reports¹⁸⁴ of isatin *glycolation* with a similar tosyl functionalised OEG chain could be mimicked for bisisatin.



Scheme 24. Synthetic scheme for the ditosylation of triethylene glycol followed by the nucleophilic addition of tetraethylene glycol monomethyl ether to afford 2,5,8,11,14,17,20-heptaoadocosan-22-yl 4-methylbenzenesulfonate.

The initial double tosylation of commercially available triethylene glycol (TEG) could be performed on a large scale with almost quantitative yield. Subsequent nucleophilic addition of deprotonated tetraethylene glycol affords the extended seven-unit ethylene glycol chain with the tosyl leaving group moiety at one terminus.

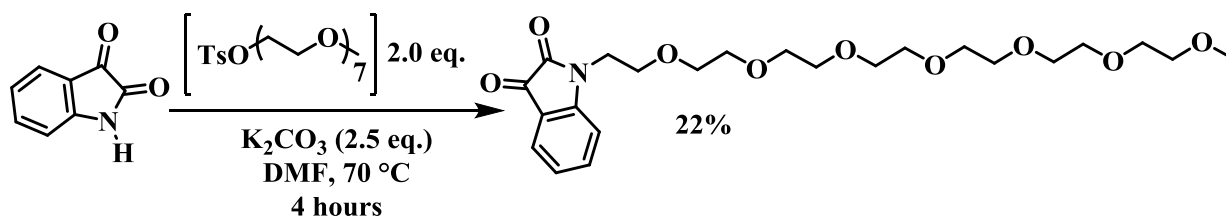
Preliminary attempts to *glycolate* bisisatin followed conditions presented by Jellett,¹⁸⁰ involving potassium carbonate (K₂CO₃) as the base to deprotonate both amides and allowing

the reaction to take place over a period of 30 minutes, stirring at 80 °C. The tosylated glycol chain was then added in a single portion and the reaction was heated overnight at 100 °C. This resulted in an insoluble black sludge which stuck to the baseline of a TLC plate no matter how polar the eluent system. The second attempt used identical equivalents of reagents (1.0 eq. bisisatin, 3.0 eq. glycol chain and 3.5 eq. of base), but potassium iodide (KI) was also added, as it is known to be an effective catalyst for N-alkylation.¹⁸⁵ The reaction conditions were also kept unchanged compared to those of the previous attempt, but again sadly to no avail, returning an opaque green sludge.

One of the most frustrating elements of this synthesis was the unknown purity of the unalkylated bisisatin core, which appeared to vary significantly across batches. This was further complicated by the extremely limited solubility of the core rendering further purification by standard column chromatography or recrystallisation impossible. With a minimum reaction time of two days needed to isolate what could turn out to be a dud-batch of bisisatin core, the consistent failure to produce anything other than an insoluble mess was becoming very tedious. Despite this, the reaction conditions were altered once again, firstly increasing the equivalents of base to 6.0 eq. whilst keeping the reaction time and temperature constant. This modification was however unsuccessful to afford any product. The next alteration was to lower the reaction temperature and time, as heating the reaction mixture at 100 °C overnight may have been responsible for product decomposition. Reducing the temperature to 80 °C and running the reaction for 5 hours resulted in the emergence of a very weak purple spot ($R_f \sim 0.6$) on the crude TLC plate (in agreement with previous N-alkylation literature).^{175,180} Sadly, after trying to run a column the purple residue obtained was not even enough to run a ¹H NMR.

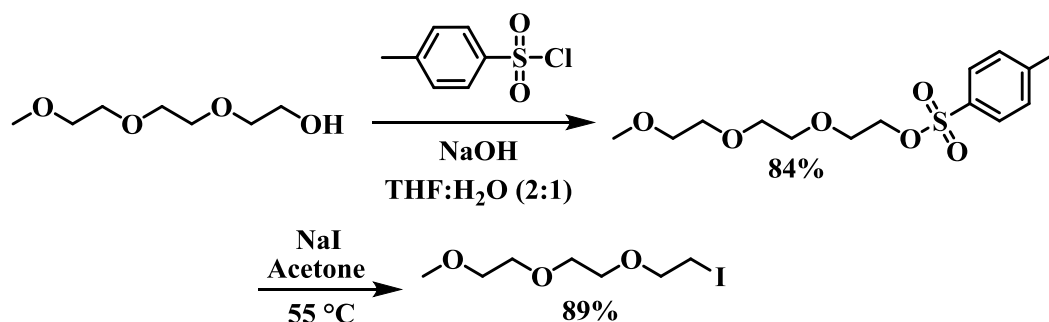
Given the synthetic challenges associated with the formation of the bisisatin core, it was decided to conduct additional reaction optimisations of the N-glycolation on isatin (one half of

bisisatin), as the latter is commercially available in large quantities. It should be noted that all previous attempts detailed above for bisisatin were also tested with isatin, unsurprisingly no N-glycolation was observed. Finally a set of conditions were found to successfully isolate 1-(2,5,8,11,14,17,20-heptaoxidocosan-22-yl)indoline-2,3-dione as an orange oil, in modest yield (22%).



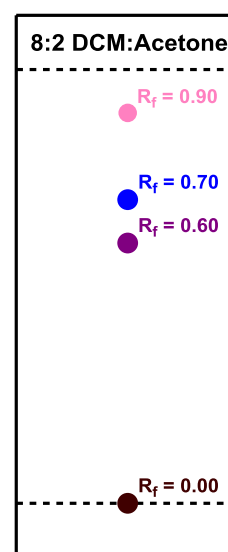
Scheme 25. Successful synthesis of N-glycolated isatin: 1-(2,5,8,11,14,17,20-heptaoxidocosan-22-yl)indoline-2,3-dione.

The temperature was reduced to a milder 70 °C, and the reaction time was reduced to four hours following the initial N-H deprotonation period, which lasted approximately 40 minutes. This success rejuvenated the efforts to apply the same chemistry to the bisisatin core. The most natural progression was to simply double the equivalents of all reagents, owing to the double isatin motif, and again attempt N-glycolation of bisisatin. Alas, as before this proved to be unsuccessful. Most likely the product could not be isolated in any reasonable quantities, given the low yields of a single glycolation reaction, which would bring the theoretical maximum yield for a double glycolation to under 5%, while not even considering any impurities in the bisoxindole core. As such, it was decided to shorten the length of the glycol chain to a much more standard triethylene glycol motif and to install an iodide terminal unit as the leaving group of choice, known to be effective for N-alkylation and a better leaving group cf. tosylate.^{175,180}

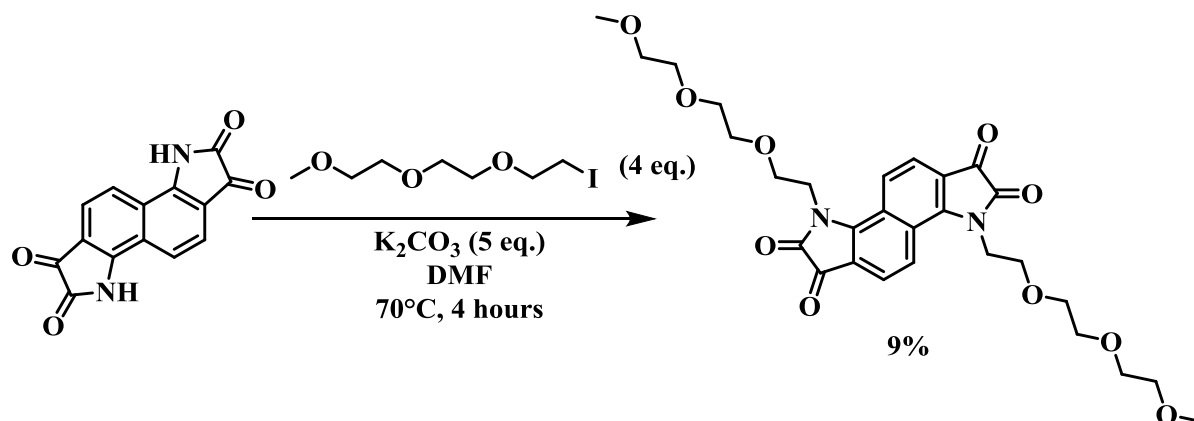


Scheme 26. Tosylation of triethylene glycol monomethyl ether followed by Finkelstein reaction with NaI to afford 1-iodo-2-(2-(2-methoxyethoxy)ethoxy)ethane.

Indeed, after extensive failures, N-glycolation of the bisisatin core was successfully achieved using 5.0 eq. of potassium carbonate as the base and 4.0 eq. of iodinated glycol chain yielding 3,8-bis(2-(2-(2-methoxyethoxy)ethoxy)ethyl)-3,8-dihydroindolo[7,6-g]indole-1,2,6,7-tetraone as a blue solid following recrystallisation from hot ethanol. The purification turned out to be almost as tedious as finding the appropriate reaction conditions, the initial TLC plate of the crude deep purple oil consisted of three major spots and a distinct black baseline spot. An

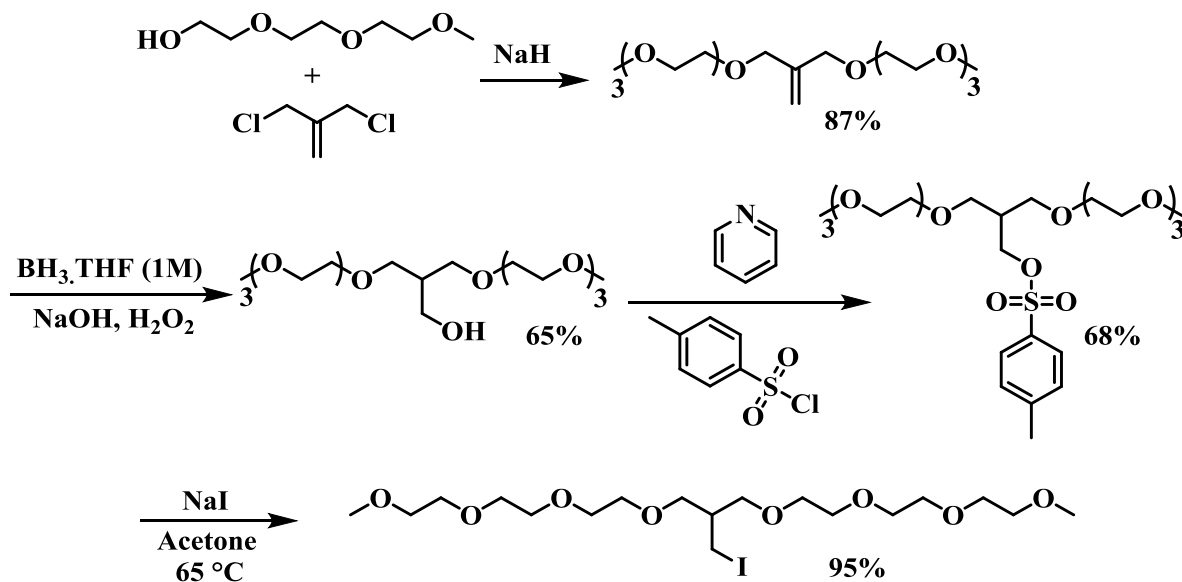


extremely polar eluent system was necessary to cause any form of separation, it was found that DCM:Acetone (8:2) provided moderate separation, at least on a TLC plate. The same could not be said once the crude material was loaded onto a silica gel column as the bands streaked together instantly and the column turned seemingly black in colour. Closer inspection, under torchlight, revealed that there was indeed a distinct blue and purple band, however the material still had to be columned a minimum of three times. Finally, upon recrystallisation from hot ethanol the desired product was isolated in an extremely modest yield (9%).



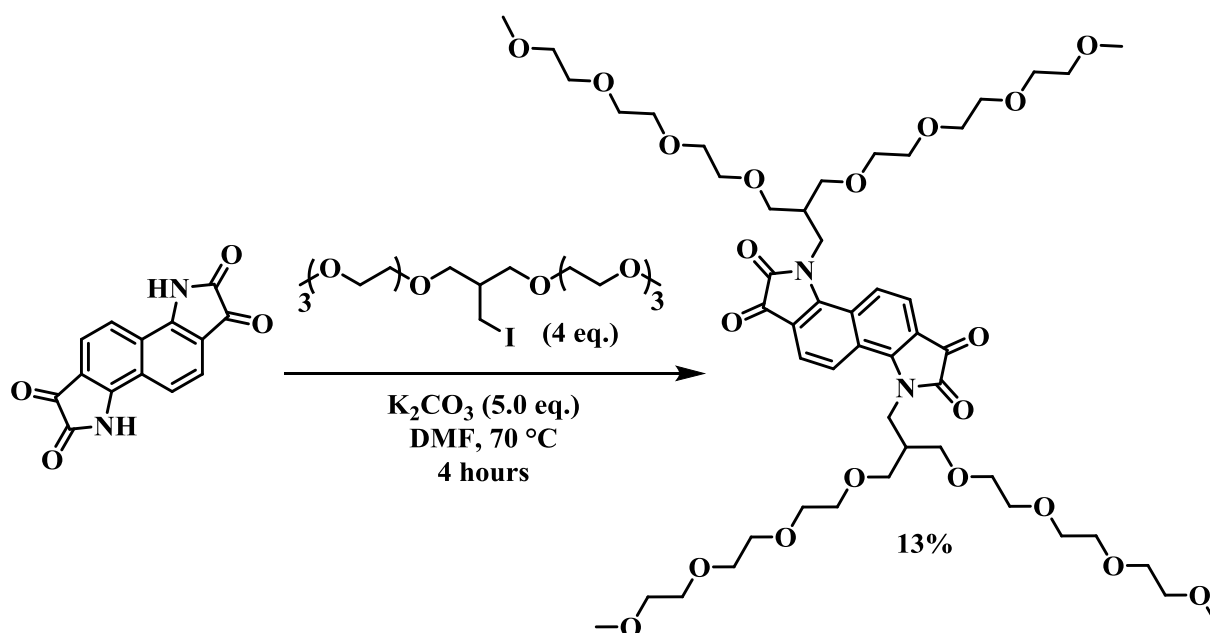
Scheme 27. Successful reaction conditions for N-glycolation of bisisatin to furnish 3,8-bis(2-(2-(2-methoxyethoxy)ethoxy)ethyl)-3,8-dihydroindolo[7,6-g]indole-1,2,6,7-tetraone.

Branched OEG chains have also been shown to provide multiple benefits towards efficient device application such as increased surface area, smaller π - π stacking distances and overall improved PCE (**Section 1.4.5**).¹⁸⁶ In order to compare the effects of branched vs. linear glycol, within these rigid rod systems, an iodine functionalised 2-branched OEG was synthesised.



Scheme 28. 4-step synthetic route to afford 13-(iodomethyl)-2,5,8,11,15,18,21,24-octaaxapentacosane, 2-branched OEG chain.

This four step synthesis began with the S_N2 nucleophilic substitution of 3-chloro-2-(chloromethyl)prop-1-ene with triethylene glycol monomethyl ether, followed by a two-step hydroboration-oxidation reaction. The resulting alcohol was easily tosylated by using the standard pyridine catalysed route, demonstrated throughout this thesis, before finally conducting a Finkelstein reaction to isolate the desired iodinated 2-branched OEG chain. This route proved to be reliable and scalable to form multiple grams of sidechain at a time, routinely affording consistent yields and purities. Following the successful conditions (**Scheme 28**) detailed above, this 2-branched OEG chain was used to N-glycolate bisisatin, forming the second fully glycolated indole derivative.



Scheme 29. Synthesis of N-glycolated 2-branched OEG bisisatin (**6.3.13**).

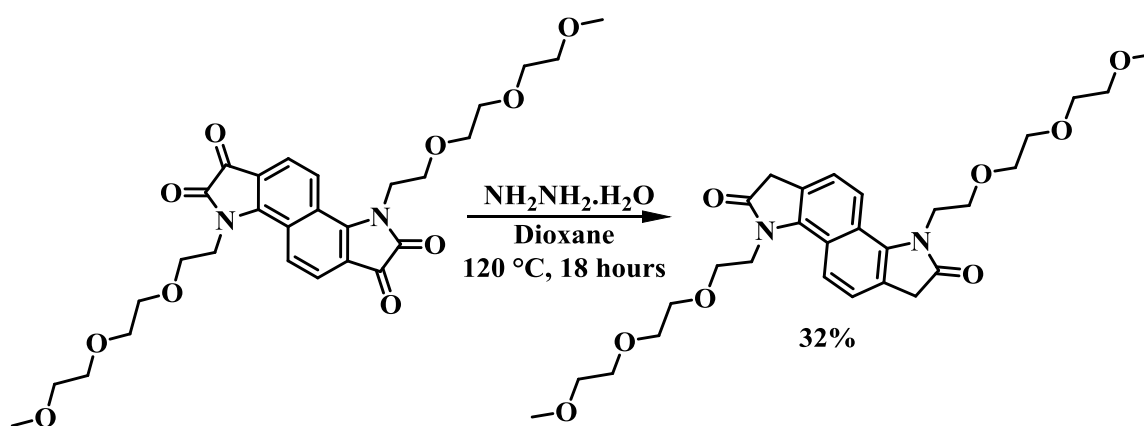
These two monomers will be staple reactants, coupling to multiple functionalised oxindole monomers respectively to form the series of polymers detailed herein.

4.8 BISOXINDOLE MONOMERS

Once the N-glycolated bisisatin derivatives were isolated, their bisoxindole coupling partners were the next synthetic targets. Luckily, due to the extensive work by Jellett and Onwubiko a

library of N-alkylated bisoxindole pre-cursors were available to use with their respective permissions. Some of these intermediates were used herein, in addition to the total synthesis of some novel N-alkylated bisoxindole derivatives.

As mentioned above (**Section 4.6**) the simplest method to obtain bisoxindole monomers comes from reducing the parent bisisatin. Indeed, the linear OEG variant was subjected to the harsh Wolff-Kishner reduction to afford the bisoxindole derivative opening the potential number of coupling partners even further.

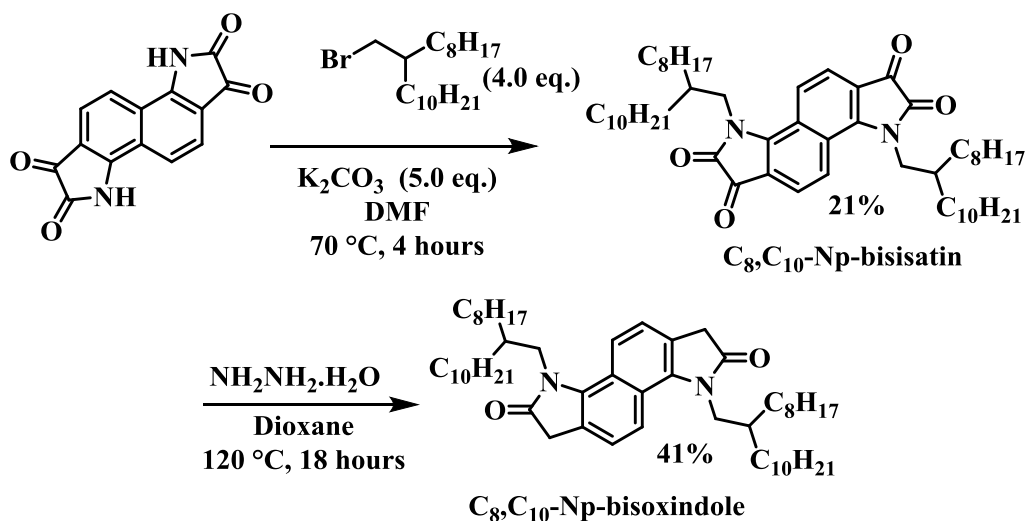


Scheme 30. Wolff-Kishner reduction using hydrazine monohydrate to afford the linear OEG functionalised bisoxindole.

With a limiting yield of only 32% this reaction is fairly destructive however this was a reliable route to afford small quantities of N-glycolated bisoxindole monomer suitable for Aldol condensation polymerisations.

The full, from scratch, synthesis of C_{10} - N-alkylated naphthalene (Np) cored bisoxindole was detailed above (**Section 4.6:Scheme 23**) the accompanying C_{12} - and C_{16} - N-alkylated Np-bisoxindole monomers were furnished in an identical fashion but beginning from intermediates present in the laboratory. The branched C_8 -, C_{10} - N-alkylated Np-bisoxindole was again isolated using the Wolff-Kishner reduction. Initial N-alkylation of bisisatin afforded the blue product

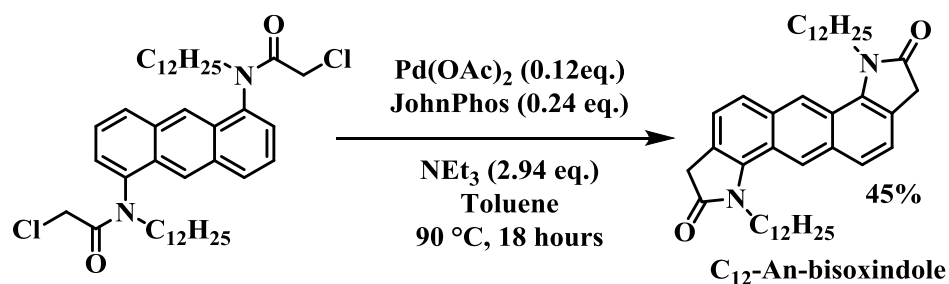
in a 21% yield, almost doubling the efficiency of N-glycolation and on par with previous literature reports.¹⁷⁵



Scheme 31. N-alkylation of bisisatin followed by Wolff-Kishner reduction to afford C_8,C_{10} -Np-bisoxindole in 41% yield.

The extremely poor yields of both N-alkylation and N-glycolation are in accord with multiple literature reports on different aromatic units, often affording yields below 30%.^{175,180,186} Perhaps the purity of the bisisatin core is not the only problem with this process and indeed the competing O-alkylation / O-glycolation reactions, along with many other side reactions, hinder the overall efficacy of these functionalisation reactions.

Following the results presented within the group's initial publication,¹⁷⁵ where it was clear that extending the aromatic core from phenyl to naphthalene led to a marked improvement in *n*-type transport, Jellett also presented an initial study on the effect of increasing the aromatic core further to study anthracene (An) core containing bisoxindoles.¹⁸⁰ The penultimate intermediate was readily available in the laboratory and using the $Pd(OAc)_2$ catalysed, JohnPhos ligand method outlined above (**Section 4.6**) the C_{12} -An-bisoxindole was isolated in sufficient yield (45%).



Scheme 32. C-H activation ring closure to afford C₁₂-An-bisoxindole, catalysed by Pd(OAc)₂ and mediated by the JohnPhos ligand.

Once the anthracene derivative had been collected the total number of functionalised bisoxindole motifs available for polymerisation had reached six, the structures of which are illustrated below:

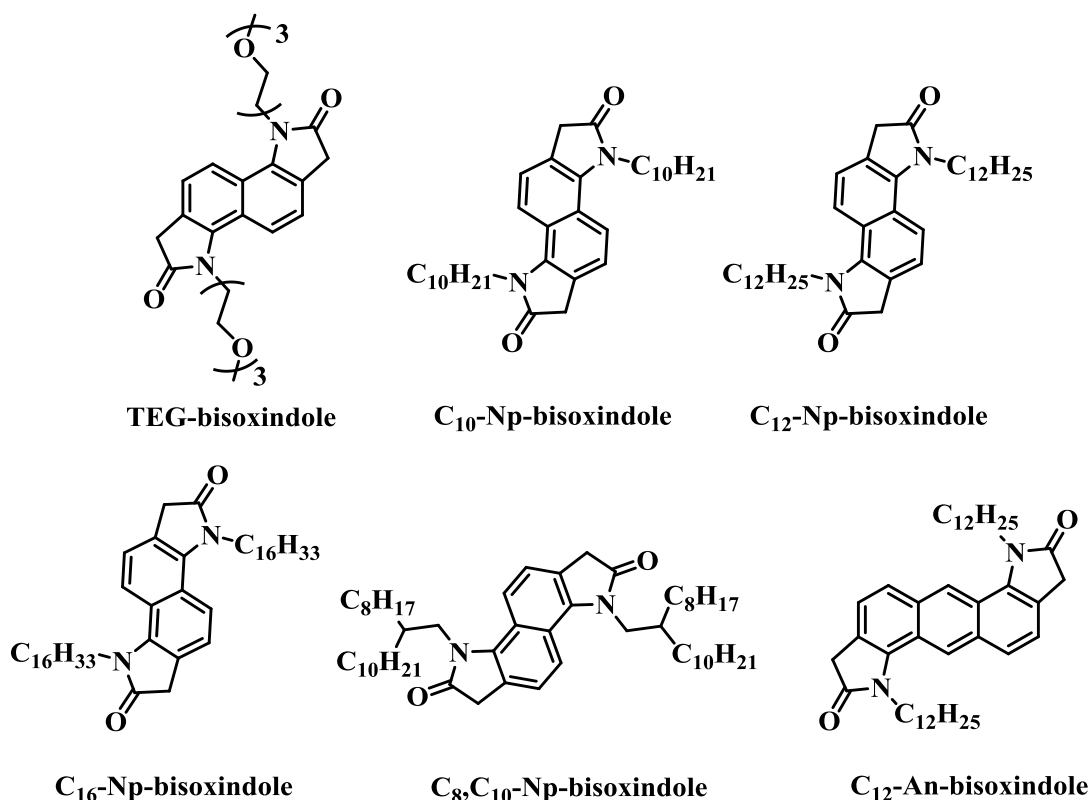
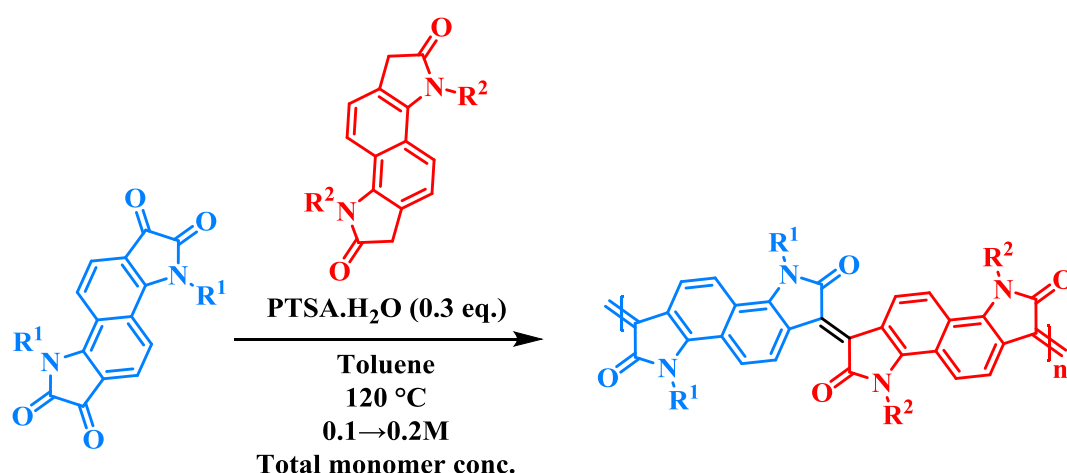


Figure 67. Six bisoxindole derivatives synthesised via the Wolff-Kishner reduction or Pd(OAc)₂ C-H activation ring closure, to be coupled with N-glycolated bisatin co-monomers.

4.9 POLYMER SYNTHESIS

After the lengthy process necessary to obtain the N-glycolated bisatin monomers and their bisoxindole co-monomers, the acid-catalysed Aldol condensation polymerisation (**Section 4.4**) was employed to afford a series of mixed N-alkyl / N-glycol rigid rod polymers, with all but one polymer featuring an all naphthalene core motif. The notable exception to this was **AM424** a naphthalene co-anthracene polymer.

The general polymerisation conditions (**Scheme 33**) featured *p*-toluenesulfonic acid monohydrate (PTSA) as the acid catalyst (loading 0.3 eq.) with toluene as the solvent of choice. Each polymerisation was left to react overnight, generally for ~18 hours, stirring rapidly at 120 °C. Upon cooling to room temperature, most polymers had gelled and exhibited an intense deep purple sheen. Crude polymers were subsequently precipitated and purified via Soxhlet extraction, generally starting with hexane and moving through, heptane, toluene, methanol and chloroform (in that order). In each case the chloroform fraction was collected, solvent removed under reduced pressure, re-precipitated and finally filtered to furnish a series of dark purple films, with a golden/green metallic lustre.



Scheme 33. Generic reaction conditions for the acid-catalysed polycondensation reaction of functionalised bisatin and bisoxindole derivatives.

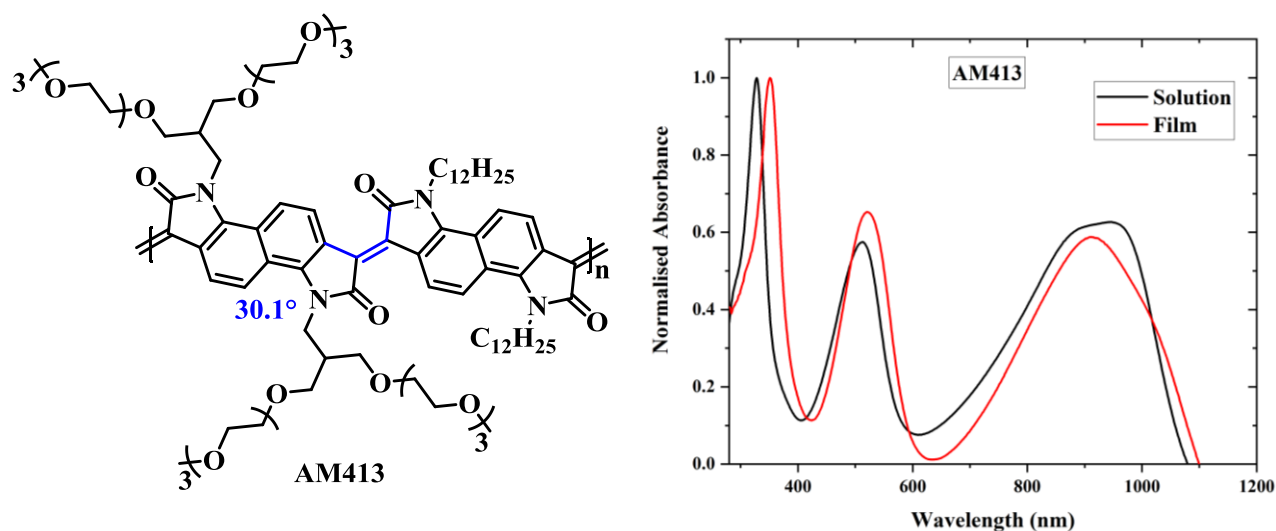
4.9.1 AM413: BRANCHED GLYCOL-LINEAR C₁₂ ALKYL

Figure 68. (a) Molecular structure of polymer **AM413** including the optimal dihedral angle between adjacent aromatic units (highlighted in blue) and the inter-unit double bond length is 1.35 Å (obtained from DFT optimised ground state structures) (b) Solution and thin-film UV-Vis absorption spectrum.

The first mixed alkyl-glycol rigid rod polymer synthesised, coupled together the branched N-glycolated bisatin with C₁₂-Np-bisoxindole. In both solution and solid state (**Figure 68**) the polymer exhibited two absorption peaks with a broad near infra-red (NIR) peak giving a λ_{max} of 902 nm, alongside a higher energy band in the visible (~510 nm). The low energy absorption onset affords an optical band gap of 1.13 eV, comparable to the all naphthalene core N-alkylated polymers previously reported.¹⁷⁵ The slightly wider optical bandgap is likely due to a combination of the increased dihedral angle, owing to the steric hinderance introduced by the bulky branched OEG chain leading to a more twisted polymer backbone and limiting aromatic delocalisation.

Table 8. AM413 polymer optical properties, electron affinities, ionisation potential and molecular weight values.

λ_{MAX} (nm) ^a	λ_{ONSET} (nm)	$E_{\text{opt}}^{\text{b}}$ (eV)	EA^{c} [UV]	IP [PESA]	EA [CV]	E_{GAP} (eV)	M_{n} (kDa)	M_{w} (kDa)	PDI
902	1102	1.13	4.09	5.22	3.70	1.52	10.2	15.1	1.48

^a λ is the peak of the first low energy absorption band of the polymers

^b E_{opt} estimated optical gap using the onset of absorption in thin-film absorption spectra $E_{\text{GAP}} = 1240 / \lambda_{\text{ONSET}}$

^cEA crudely estimated by subtraction of the UV-Vis absorption onset from IP ($EA = IP - E_{\text{opt}}$), a procedure that neglects the exciton binding energy

4.9.2 AM424: BRANCHED GYCOL N_p-LINEAR ALKYL A_n

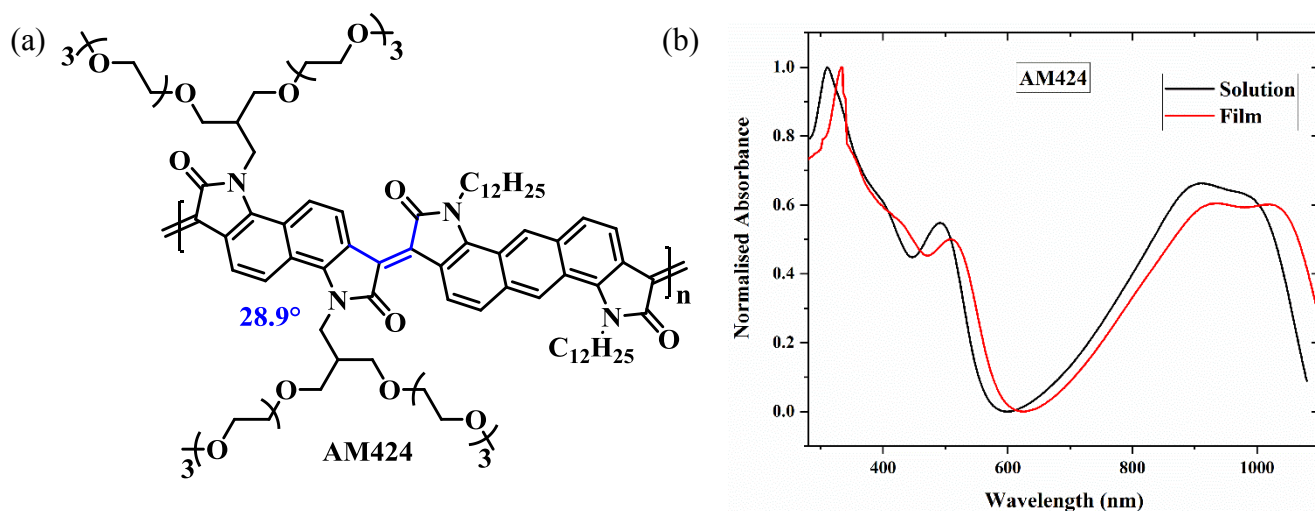


Figure 69. (a) Molecular structure of polymer AM424 including the optimal dihedral angle between adjacent aromatic units (highlighted in blue) and the inter-unit double bond length is 1.39 Å (obtained from DFT optimised ground state structures). (b) Solution and thin-film UV-Vis absorption spectrum.

AM424 is a synthetic outlier in the series in that it is the only polymer to include an anthracene core, all other polymers herein are based on all naphthalene cores. The UV-Vis spectrum is very different in comparison to AM413, the high energy visible absorption is just a shoulder from the intense short wavelength band. Notably, λ_{max} (930 nm) was slightly red shifted with the low energy NIR absorption being extremely broad and displaying somewhat bimodal

functionality, suggesting strong degrees of disorder which could limit device performance.⁴⁸ The broad nature of this absorption extends the offset and the extracted optical bandgap is reduced to 1.07 eV. Introducing an additional aromatic ring reduces the strain about the binding double bond and thus lowers the observed dihedral angle to 28.9°. This supports the reduction in bandgap, allowing for increased aromatic delocalisation along the polymer backbone.

Table 9. AM424 polymer optical properties, electron affinities, ionisation potential and molecular weight values.

λ_{MAX} (nm) ^a	λ_{ONSET} (nm)	$E_{\text{opt}}^{\text{b}}$ (eV)	EA^{c} [UV]	IP [PESA]	EA [CV]	E_{GAP} (eV)	M_{n} (kDa)	M_{w} (kDa)	PDI
930	1162	1.07	4.00	5.07	3.66	1.41	9.20	17.7	1.92

^a λ is the peak of the first low energy absorption band of the polymers

^b E_{opt} estimated optical gap using onset of the thin-film absorption spectra $E_{\text{GAP}} = 1240 / \lambda_{\text{ONSET}}$

^cEA crudely estimated by subtraction of the UV-Vis absorption onset from IP ($EA = IP - E_{\text{opt}}$), a procedure that neglects the exciton binding energy

4.9.3 AM431: BRANCHED GLYCOL-LINEAR C₁₆ ALKYL

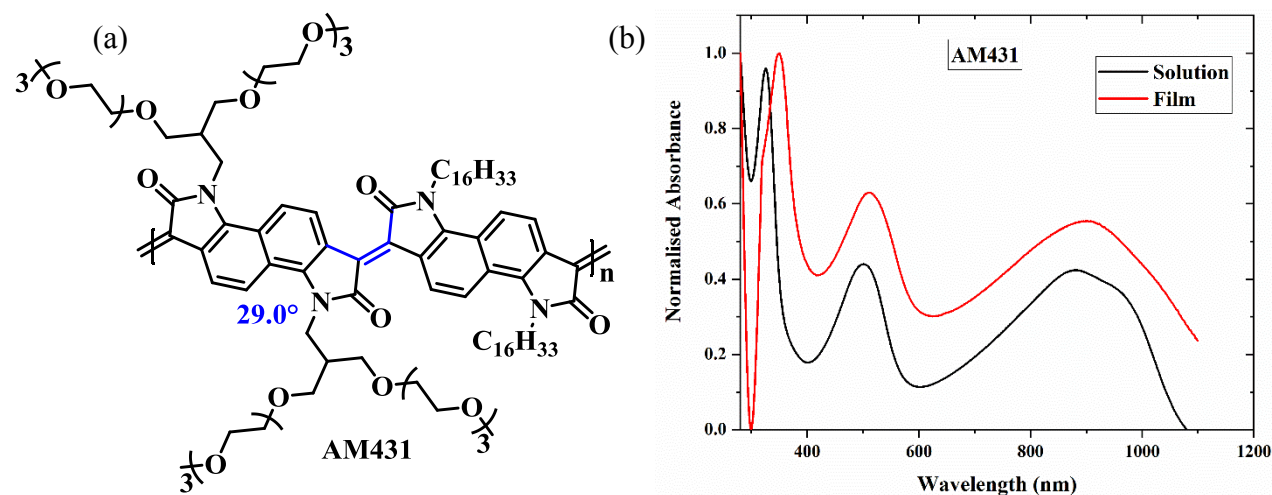


Figure 70. (a) Molecular structure of polymer AM431 including the optimal dihedral angle between adjacent aromatic units (highlighted in blue) and the inter-unit double bond length is 1.34 Å (obtained from DFT optimised ground state structures). (b) Solution and thin-film UV-Vis absorption spectrum.

Extending the length of the alkyl chain by an additional four carbon atoms, compared to **AM413**, had little effect on the optoelectronic properties. This is to be expected as the alkyl chains have little effect on the electron density of the backbone, which determines the majority of the polymers' optical and physical aspects. The solubility was slightly increased from the C₁₂- variant, increased alkyl content also slightly reduced the dihedral angle about the central, binding, double bond to 29.0°. Despite this the molecular weights obtained were consistently poor, much lower than the all alkyl derivatives presented previously in the group.^{175,180}

Table 10. **AM431** polymer optical properties, electron affinities, ionisation potential and molecular weight values.

λ_{MAX} (nm) ^a	λ_{ONSET} (nm)	$E_{\text{opt}}^{\text{b}}$ (eV)	EA^{c} [UV]	IP [PESA]	EA [CV]	E_{GAP} (eV)	M_{n} (kDa)	M_{w} (kDa)	PDI
901	1149	1.08	4.11	5.19	3.69	1.50	13.5	20.8	1.54

^a λ is the peak of the first low energy absorption band of the polymers

^b E_{opt} estimated optical gap using onset of the thin-film absorption spectra $E_{\text{GAP}} = 1240 / \lambda_{\text{ONSET}}$

^c EA crudely estimated by subtraction of the UV-Vis absorption onset from IP ($EA = IP - E_{\text{opt}}$), a procedure that neglects the exciton binding energy

4.9.4 AM463: LINEAR GLYCOL-LINEAR C₁₂ ALKYL

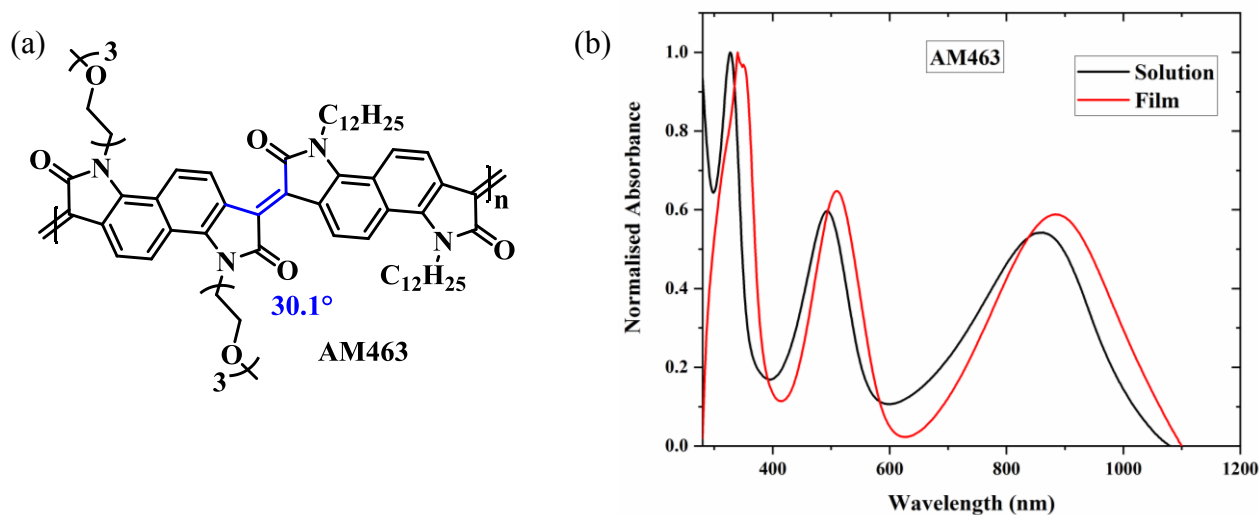


Figure 71. (a) Molecular structure of polymer **AM463** including the optimal dihedral angle between adjacent aromatic units (highlighted in blue) and the inter-unit double bond length is 1.35 Å. (b) Solution and thin-film UV-Vis absorption spectrum.

Utilising the linear N-glycolated bisisatin derivative, **AM463** was afforded upon polycondensation with C₁₂-Np-bisoxindole. λ_{MAX} (887 nm) is slightly blue shifted compared to the branched glycol analogue but the onset and therefore extracted optical bandgap are identical. Indeed, the dihedral angle, about the central double bond, is also unchanged, the effects of introducing a 2-branched OEG chain are not apparent within the optoelectronic properties of both polymers. This will be investigated further later in the text (**Section 4.10**) to determine if there is a noticeable difference upon device performance or charge carrier mobility upon altering the polar OEG sidechain.

Table 11. **AM463** polymer optical properties, electron affinities, ionisation potential and molecular weight values.

λ_{MAX} (nm) ^a	λ_{ONSET} (nm)	$E_{\text{opt}}^{\text{b}}$ (eV)	EA^{c} [UV]	IP [PESA]	EA [CV]	E_{GAP} (eV)	M_{n} (kDa)	M_{w} (kDa)	PDI
887	1102	1.13	4.03	5.16	3.72	1.44	24.1	67.5	2.80

^a λ is the peak of the first low energy absorption band of the polymers

^b E_{opt} estimated optical gap using onset of the thin-film absorption spectra $E_{\text{GAP}} = 1240 / \lambda_{\text{ONSET}}$

^c EA crudely estimated by subtraction of the UV-Vis absorption onset from IP ($EA = IP - E_{\text{opt}}$), a procedure that neglects the exciton binding energy

4.9.5 AM464: BRANCHED GLYCOL-LINEAR GLYCOL

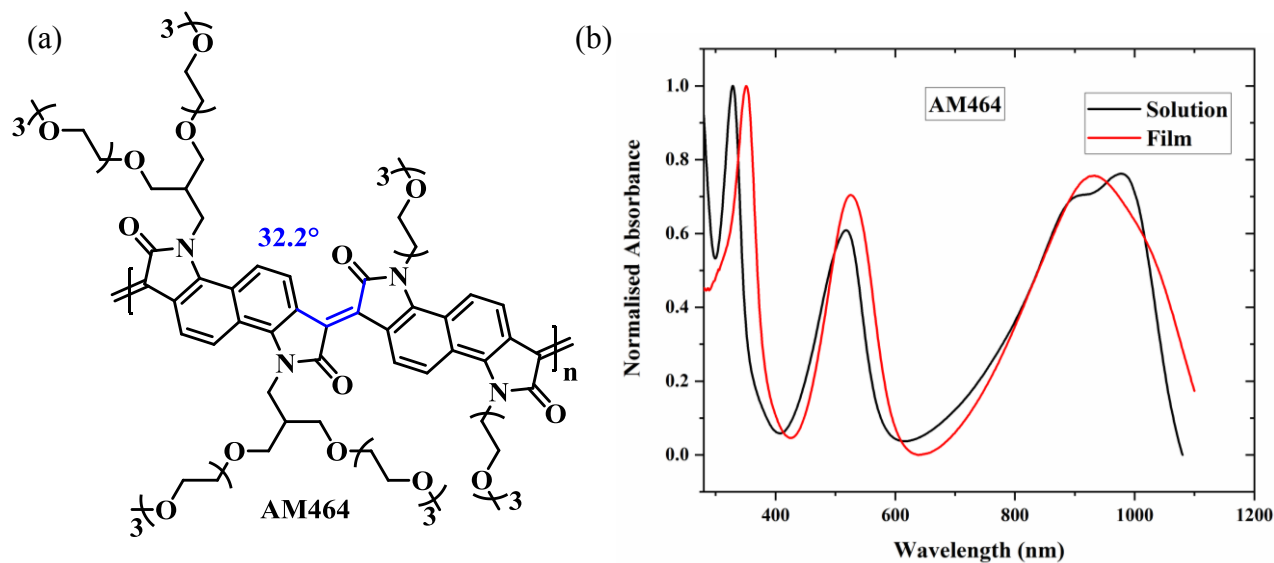


Figure 72. (a) Molecular structure of polymer **AM464** including the optimal dihedral angle between adjacent aromatic units (highlighted in blue) and the inter-unit double bond length is 1.35 Å. (b) Solution and thin-film UV-Vis absorption spectrum.

The successful Wolff Kishner reduction, previously detailed (**Section 4.6**) allowed for the polycondensation of two N-glycolated monomers to furnish a fully N-glycolated all naphthalene cored rigid rod polymer. This unique material marries together both the branched and linear OEG chain variants to yield a polymer fully decorated with polar sidechains. The all glycol polymer leads to the highest degree of torsion about the central double bond compared to each of the six mixed alkyl-glycol polymers. Once again, the optoelectronics of the material are dominated by the delocalisation along the rigid core and altering the sidechains, even as drastically as total glycolation, has a minimal effect on the measured electron affinities and ionisation potentials. **AM464** also exhibits the broadest molecular weight distribution with a polydispersity index of 3.70.

Table 12. AM464 polymer optical properties, electron affinities, ionisation potential and molecular weight values.

λ_{MAX} (nm) ^a	λ_{ONSET} (nm)	E_{opt}^b (eV)	EA^c [UV]	IP [PESA]	EA [CV]	E_{GAP} (eV)	M_n (kDa)	M_w (kDa)	PDI
929	1100	1.13	4.02	5.15	3.66	1.49	17.2	64.5	3.70

^a λ is the peak of the first low energy absorption band of the polymers

^b E_{opt} estimated optical gap using onset of the thin-film absorption spectra $E_{GAP} = 1240/\lambda_{ONSET}$

^c EA crudely estimated by subtraction of the UV-Vis absorption onset from IP ($EA = IP - E_{opt}$), a procedure that neglects the exciton binding energy

4.9.6 AM467: LINEAR GLYCOL-BRANCHED ALKYL

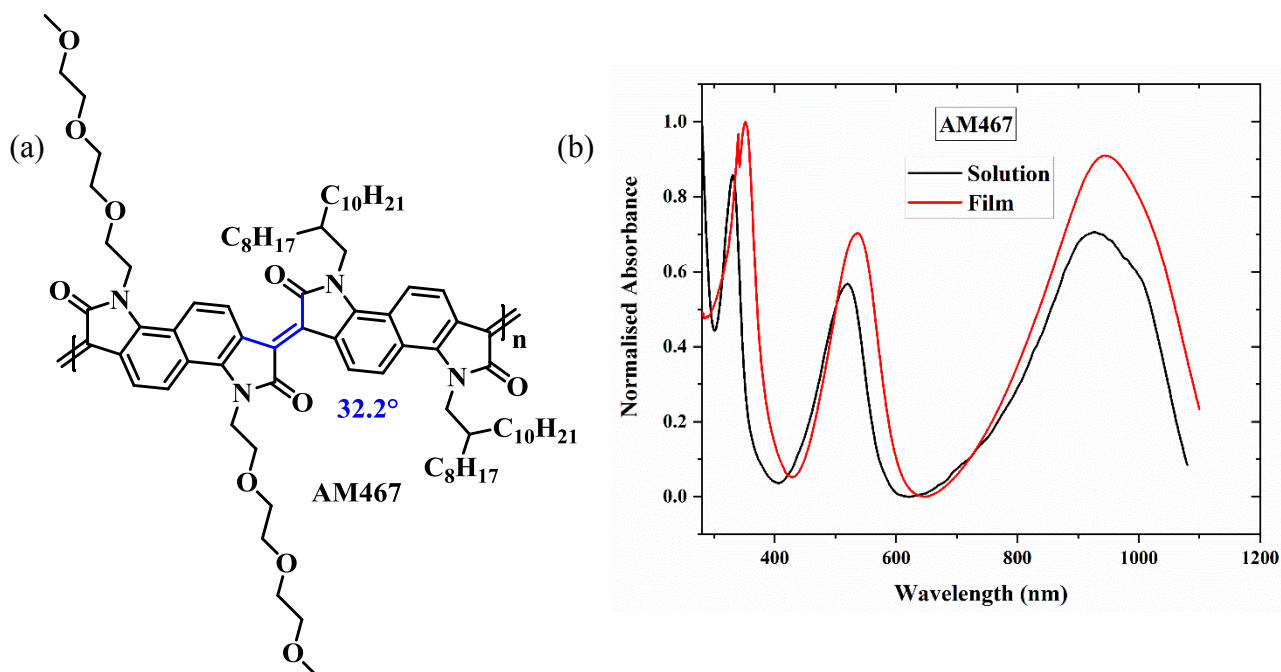


Figure 73. (a) Molecular structure of polymer **AM467** including the optimal dihedral angle between adjacent aromatic units (highlighted in blue) and the inter-unit double bond length is 1.34 Å. (b) Solution and thin-film UV-Vis absorption spectrum.

The branched C_8, C_{10} - alkyl chain renders **AM467** as the polymer with the highest alkyl density. The polymer exhibited two absorption peaks with a broad near infra-red (NIR) peak giving a λ_{max} of 944 nm, alongside a weaker high energy band in the visible (~530 nm). The low energy absorption onset affords an optical band gap of 1.11 eV, comparable to the combined EA and

IP, from PESA and CV respectively, giving a bandgap of 1.20 eV. **AM467** has the narrowest bandgap (determined by CV) of the entire series and was also collected with the highest M_n , considerably higher than the poor molecular weights observed for all other derivatives.

Table 13. **AM467** polymer optical properties, electron affinities, ionisation potential and molecular weight values.

λ_{MAX} (nm) ^a	λ_{ONSET} (nm)	E_{opt}^b (eV)	EA ^c [UV]	IP [PESA]	EA [CV]	E_{GAP} (eV)	M_n (kDa)	M_w (kDa)	PDI
944	1117	1.11	4.10	5.21	4.01	1.20	89.3	864.6	9.70

^a λ is the peak of the first low energy absorption band of the polymers

^b E_{opt} estimated optical gap using onset of the thin-film absorption spectra $E_{GAP} = 1240 / \lambda_{ONSET}$

^cEA crudely estimated by subtraction of the UV-Vis absorption onset from IP ($EA = IP - E_{opt}$), a procedure that neglects the exciton binding energy

4.9.7 AM520: BRANCHED GLYCOL-LINEAR C₁₀ ALKYL

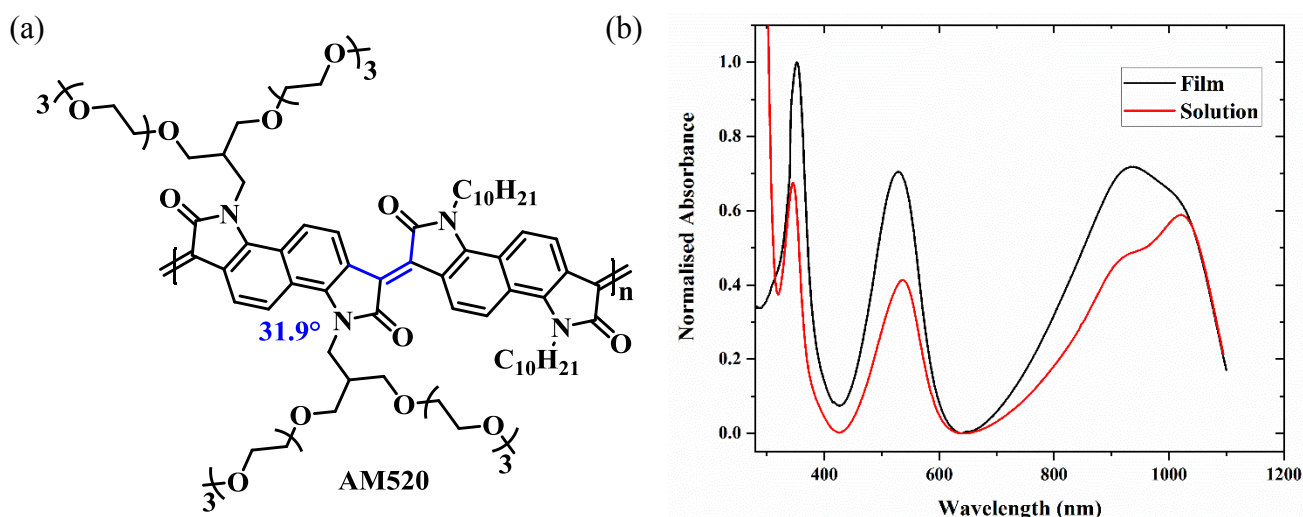


Figure 74. (a) Molecular structure of polymer **AM520** including the optimal dihedral angle between adjacent aromatic units (highlighted in blue) and the inter-unit double bond length is 1.35 Å (obtained from DFT optimised ground state structures). (b) Solution and thin-film UV-Vis absorption spectrum.

The final polymer of the series **AM520** is comprised of the shortest linear alkyl chain, reducing the carbon length to C₁₀-. The NIR low energy absorption band is extremely broad, spanning over ~500 nm, in equal intensity to the high energy absorption band within the visible region.

An appreciable number average molecular weight of >27k was an improvement over most of the rest of the series, although all of the polymers displayed molecular weights 2-3 fold less than that of the all alkyl derivatives of Jellett and Onwubiko.^{175,180} This is likely due to the nature of both N-glycolated bisisatin monomers which could only be isolated as a sticky liquid and were unable to be purified by recrystallisation, a shared property and notable disadvantage of including a high glycol content.⁵⁵ **AM520** showed good thermal stability with a thermal degradation temperature (T_d) higher than 300 °C. Whilst, also exhibiting good solubility in common organic solvents, such as chloroform and chlorobenzene at room temperature.

Table 14. **AM520** polymer optical properties, electron affinities, ionisation potential and molecular weight values.

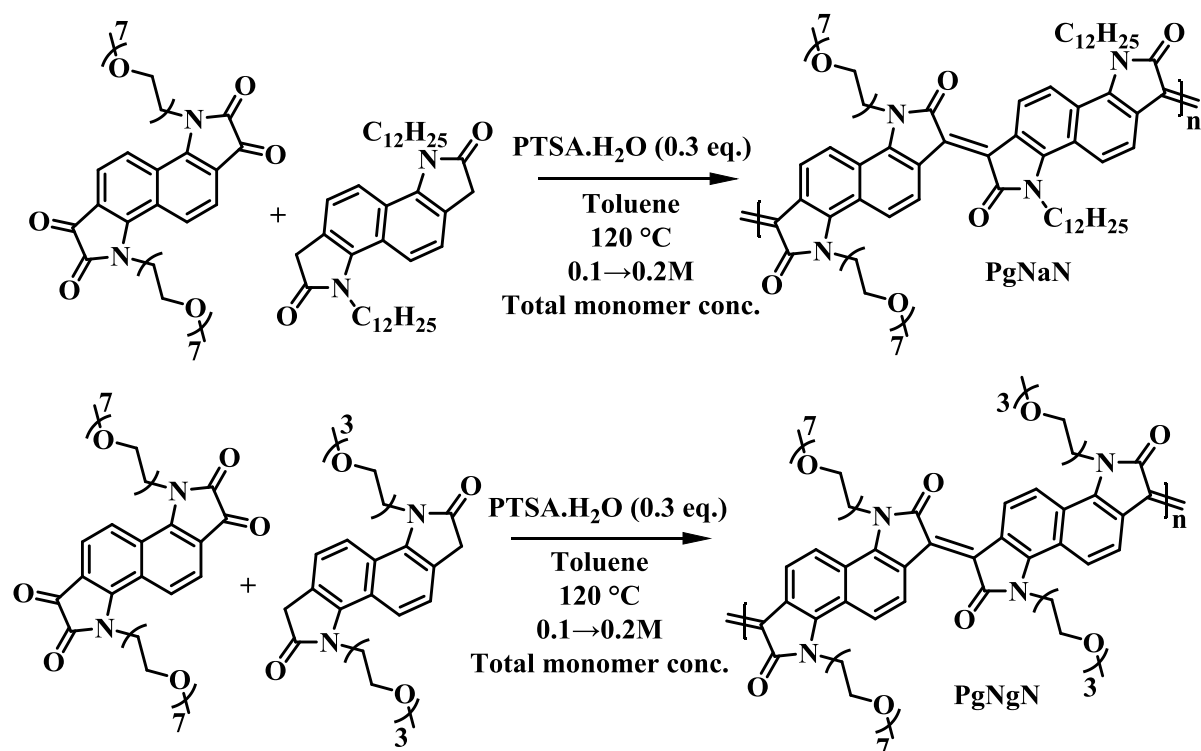
λ_{MAX} (nm) ^a	λ_{ONSET} (nm)	E_{opt}^b (eV)	EA ^c [UV]	IP [PESA]	EA [CV]	E_{GAP} (eV)	M_n (kDa)	M_w (kDa)	PDI
933	1132	1.10	4.15	5.25	3.63	1.62	27.4	75.5	2.76

^a λ is the peak of the first low energy absorption band of the polymers

^b E_{opt} estimated optical gap using onset of the thin-film absorption spectra $E_{GAP} = 1240 / \lambda_{ONSET}$

^cEA crudely estimated by subtraction of the UV-Vis absorption onset from IP ($EA = IP - E_{opt}$), a procedure that neglects the exciton binding energy

4.9.8 PgNaN & PgNgN



Scheme 34. Synthetic pathway, conducted by Dr. Chen, to afford **PgNaN** and **PgNgN** using the generic acid-catalysed polycondensation conditions and a mix of monomers synthesised by myself and Dr Chen.

As detailed above (**Section 4.7**) the struggle to successfully achieve N-glycolation of bisatin was extensive and spanned a number of weeks, this led to seeking the assistance of postdoctoral researcher Dr X. Chen, of the McCulloch group based in KAUST. His past experience with similar N-glycolation reactions^{55,186} coupled with the multitude of conditions tested above allowed us to finally settle on a set of successful conditions. Using these Dr Chen was able to isolate the seven-unit OEG bisatin, the initial target for this study. Following the generic acid-catalysed aldol polycondensation conditions (**Scheme 33**) using the C₁₂-Np-bisoxindole monomer I synthesised above (**Section 4.8**) he isolated **PgNaN**. Similarly, using the 3-unit OEG bisoxindole that I supplied he was able to synthesise the all linear OEG functionalised **PgNgN** polymer.

Table 15. Polymer optical properties, electron affinities, ionisation potential and molecular weight values.

Polymer	λ_{MAX} (nm) ^a	λ_{ONSET} (nm)	$E_{\text{opt}}^{\text{b}}$ (eV)	EA ^c [UV]	IP [PESA]	M_{n} (kDa)	M_{w} (kDa)	PDI
PgNaN	880	1148	1.08	4.06	5.14	20.7	162.1	7.80
PgNgN	912	1216	1.02	4.20	5.22	8.7	19.3	2.20

^a λ is the peak of the first low energy absorption band of the polymers

^b E_{opt} estimated optical gap using onset of the thin-film absorption spectra $E_{\text{GAP}} = 1240 / \lambda_{\text{ONSET}}$

^cEA crudely estimated by subtraction of the UV-Vis absorption onset from IP ($\text{EA} = \text{IP} - E_{\text{opt}}$), a procedure that neglects the exciton binding energy

4.10 RESULTS & DISCUSSION

The following section will discuss the initial results from this set of mixed alkyl-glycol rigid rod polymers. An all-encompassing table of data for the polymers of interest is presented below:

Table 16. Optical properties, electron affinities, ionisation potential and molecular weight values for the entire polymer series (detailed above), P1 and P4 polymers¹⁷⁵ are also included.

Polymer	λ_{MAX}^a (nm)	λ_{ONSET} (nm)	E_{opt}^b (eV)	EA^c [UV]	IP [PESA]	EA [CV]	E_{GAP} (eV)	M_n^d (kDa)	M_w (kDa)	PDI
AM413	902	1102	1.13	4.09	5.22	3.70	1.52	10.2	15.1	1.48
AM424	930	1162	1.07	4.00	5.07	3.66	1.41	9.20	17.7	1.92
AM431	901	1149	1.08	4.11	5.19	3.69	1.50	13.5	20.8	1.54
AM463	887	1102	1.13	4.03	5.16	3.72	1.44	24.1	67.5	2.80
AM464	929	1100	1.13	4.02	5.15	3.66	1.49	17.2	64.5	3.70
AM467	944	1117	1.11	4.10	5.21	4.01	1.20	89.3	864.6	9.70
AM520	933	1132	1.10	4.15	5.25	3.63	1.62	27.4	75.5	2.76
PgNaN	880	1148	1.08	4.06	5.14	-	-	20.7	162	7.80
PgNgN	912	1216	1.02	4.20	5.22	-	-	8.7	19.3	2.20
P1	850	1228	1.01	4.40	5.41	-	-	14.0	19.0	1.36
P4	927	1228	1.01	4.20	5.21	-	-	134	538	4.01

^a λ is the peak of the first low energy absorption band of the polymers

^b E_{opt} estimated optical gap using onset of the thin-film absorption spectra $E_{GAP} = 1240 / \lambda_{ONSET}$

^cEA crudely estimated by subtraction of the UV-Vis absorption onset from IP ($EA = IP - E_{opt}$), a procedure that neglects the exciton binding energy

^d M_n GPC data obtained vs. polystyrene standards at 40 °C in chloroform

4.10.1 OPTOELECTRONIC PROPERTIES

The optoelectronic properties are illustrated (**Figure 75**) comparing the ionisation potentials, electron affinities and optical bandgaps for each polymer respectively, whilst also being compared to the all alkyl naphthalene polymers **P1** & **P4** (**Figure 66**) previously reported.¹⁷⁵ All polymers show a broad absorption profile spanning across the visible spectrum towards the near-infrared region, with the absorption onset ranging between 1.01→1.13 eV. Lower ionisation potentials were recorded for the mixed N-alkyl, N-glycol functionalised series compared to the all alkyl derivatives **P1** & **P4**. The ionisation potential can roughly be prescribed to the HOMO energy and the complimentary electron affinity approximated to the LUMO value.² As such, shallower LUMO values are observed for each polymer comprised of an N-glycolated monomer. Similarly, to the IPs, only a small variation in the EAs of the polymers was found, with the EAs of the polymers spanning between 4.0→4.2 eV. The LUMO energy levels are still appreciably deep and more than sufficient for *n*-type charge transport.^{53,175} For all of the N-glycolated polymers the observed shallower LUMO values are likely due to the increase in dihedral angle, about the central binding double bond, compared to the N-alkylated literature polymers.¹⁷⁵ Whilst replacing the all carbon alkyl chains with OEG moieties is expected to lead to more favourable π - π stacking of polymer backbones⁵² the increased steric hinderance causes the backbone to have to twist about the central unit to alleviate this stress. These results suggest that for this specific fused rigid rod system replacing alkyl chains with linear or branched OEG chains leads to a shallower HOMO energy but does not contribute enough to the conjugated chromophore core to deepen the LUMO level.

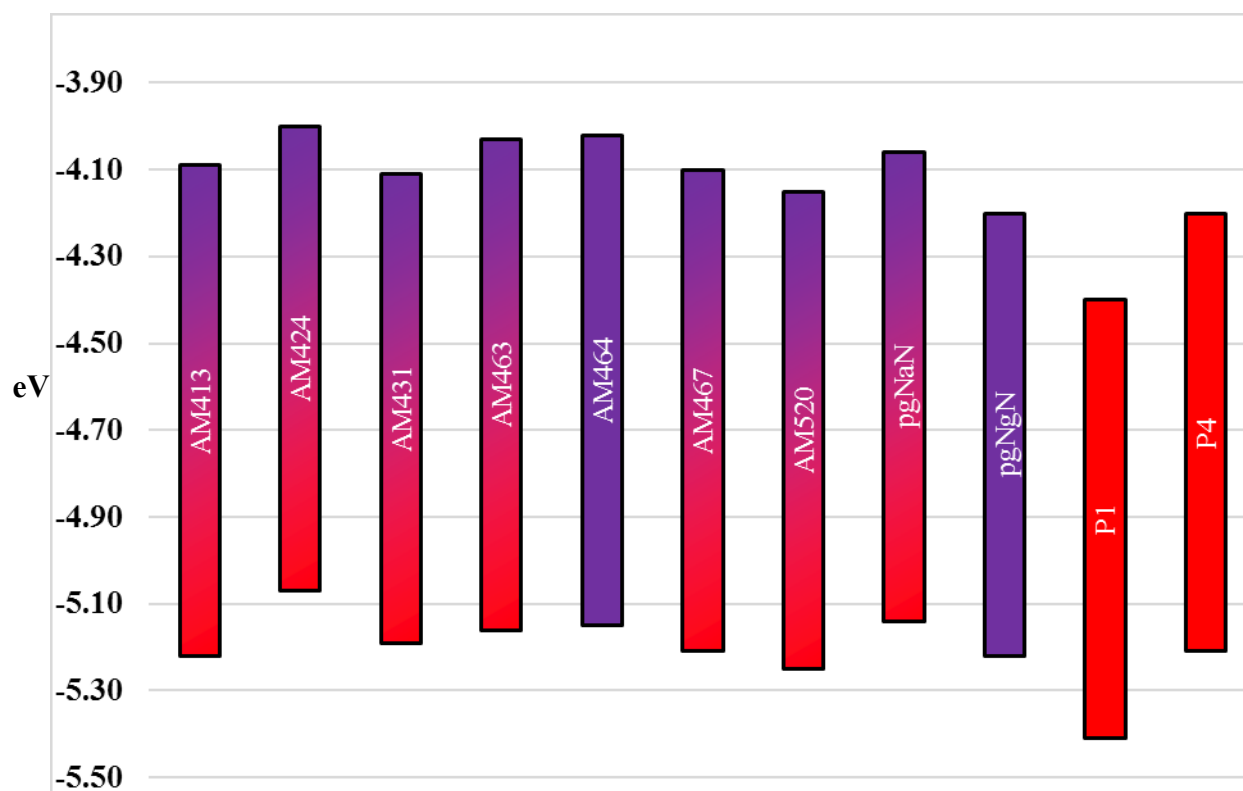


Figure 75. Optical bandgaps extracted from the absorption onset used to crudely estimate LUMO values by addition to HOMO values obtained from PESA measurements ($\text{LUMO} = \text{HOMO} + E_{\text{opt}}$), a procedure that neglects the exciton binding energy. All glycol polymers are coloured purple, all alkyl polymers red and mixed polymers coloured as a gradient.

4.10.2 GIWAXS MORPHOLOGICAL STUDY

Grazing-incidence wide angle X-ray scattering (GIWAXS) was obtained to investigate the different morphological consequences of altering the sidechain and backbone composition, respectively, of the fused electron-deficient polymers. Furthermore, the resultant morphology of the polymer relative to the substrate is known to effect charge carrier transport within OECT devices.^{25,187} As such, it is important to know whether a polymer π - π stacks perpendicular or horizontal to the substrate, especially for bottom contact top gate devices (**Figure 9**).

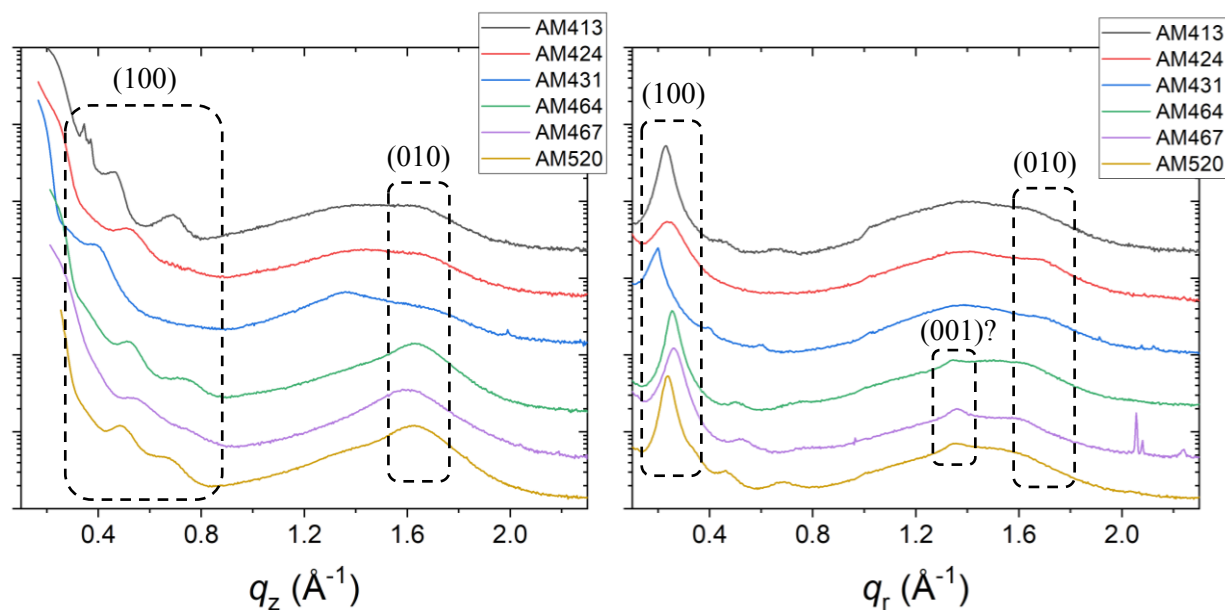


Figure 76. Out-of plane (q_z) and in-plane (q_r) line cuts of the GIWAXS measurements for n -type fused polymer series.

In both out-of-plane (q_z) and in-plane (q_r) **AM413**, **AM424** and **AM431** all showed weak isotropic π -stacking (010) that is conflated with isotropic amorphous scattering. Conversely, (010) is much stronger out-of-plane for **AM464**, **AM467** and **AM520**, each packing in a face-on orientation. Furthermore, all polymers showed lamellar scattering in- and out-of-plane. Out-of-plane the (100) peak is conflated with the background scattering with higher order, (200) and (300), peaks/shoulders also visible. In plane (q_r), the (100) peak is well resolved with polymers **AM464**, **AM467**, and **AM520** also showing a peak around 1.35 \AA^{-1} that may be indicative of a (001) backbone peak. The results of the GIWAX measurements are summarised below:

Table 17. Summary of the GIWAXS measurements for the fused electron-deficient polymer series.

Polymer	Lamellar stacking In-plane (100)		π -stacking In-plane (010)		π -stacking Out-of-plane (010)		Dominant texture
	q_r (\AA^{-1})	d (\AA)	q_r (\AA^{-1})	d (\AA)	q_z (\AA^{-1})	d (\AA)	
AM413	0.229	27.4	1.66	3.8	1.65	3.8	Isotropic
AM424	0.240	26.1	1.68	3.7	1.68	3.7	Isotropic
AM431	0.194	32.3	1.70	3.7	1.64	3.8	Isotropic
AM464	0.256	24.5	1.58	4.0	1.639	3.83	Face-on
AM467	0.261	24.1	1.60	3.9	1.600	3.93	Face-on
AM520	0.238	26.4	1.51	4.2	1.637	3.84	Face-on
PgNaN	0.222	28.3	1.67	3.76	1.67	3.77	Isotropic
PgNgN	0.207	30.3	1.72	3.65	1.71	3.67	Face-on

It should be noted that the in- and out-of-plane (010) d spacings for non-face-on minority crystallite sub populations in **AM413**, **AM424**, and **AM431** are not especially accurate due to weak π -scattering, reflected in the number of significant figures given in **Table 17**. Between face-on stacking polymers **AM464**, **AM467**, and **AM520** the (010) π -stack is slightly expanded for **AM467** and the longer alkyl sidechain on **AM431** seems to produce the largest lamellar spacing. These results demonstrate the effect sidechain engineering can have on the resultant polymer morphology with in-plane lamellar stacking ranging from 24.1 \AA to 32.3 \AA . Interestingly, the inclusion of all glycol chains (**AM464**) versus mixed alkyl-glycol sidechains (**AM467** & **AM520**) has a very limited effect on the lamellar and π -stacking distances.

The difference in polymer morphology and stacking behaviour can be used to support charge carrier transport trends in transistor devices. This GIWAX study will facilitate a comparison between polymer structure and device performance, potentially elucidating information towards a set of synthetic design rules for improved performance although a more complete investigation will need to be carried out to form concrete conclusions.

4.10.3 OECT RESULTS

The four polymers tested during this initial transistor investigation and the later thermoelectric study (Section 4.10.5 & 4.10.6) are detailed within their respective sections above and shown below for convenience:

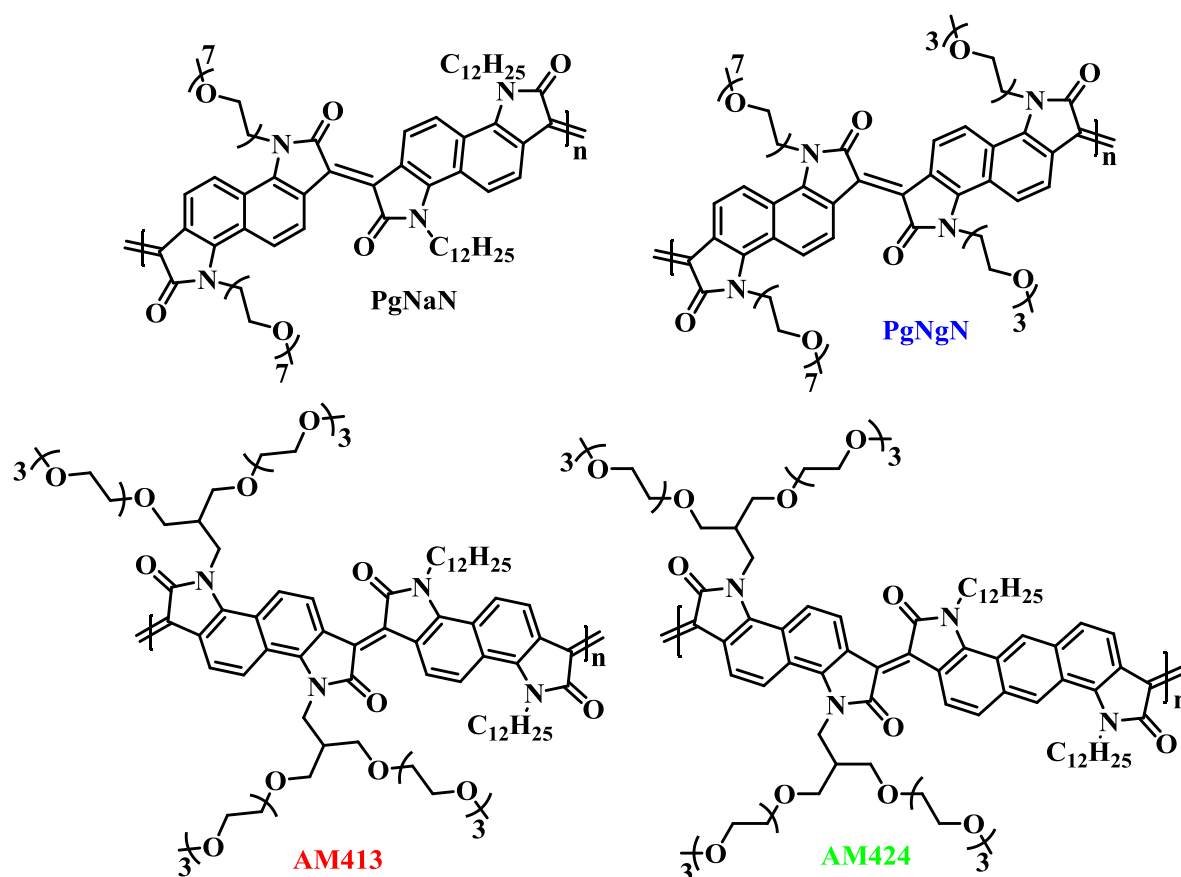


Figure 77. Chemical structure of the four polymers used within the initial OECT and thermoelectric device investigation, their properties are detailed within their respective sections above.

OECT measurements were kindly performed by Dr B. Paulsen and R. Wu of the Rivnay group at Northwestern University, Illinois. It should be noted that only a limited selection of polymers were fabricated into devices before the global outbreak of the COVID-19 pandemic. This severely limits the available data for this set of polymers, the following results and discussion focuses on the four materials presented in **Figure 77**. A selection of curves is presented herein

for clarity and conciseness, owing to three of the polymers containing an identical all naphthalene backbone the output and transfer curves have very similar characteristics. Previous mobility studies on the polymers of Jellett and Onwubiko suggest that molecular weight (M_n) is a major factor within these rigid rod systems. As such with M_n values between 8.7→20.7 kDa the electron mobilities were not expected to outperform that of the N-alkylated series with M_n values ranging from 14→214 kDa. With the initial study suggesting that perhaps, within these fused systems, electron transport is predominately one-dimensional and hence directly linked to molecular weight.^{175,188}

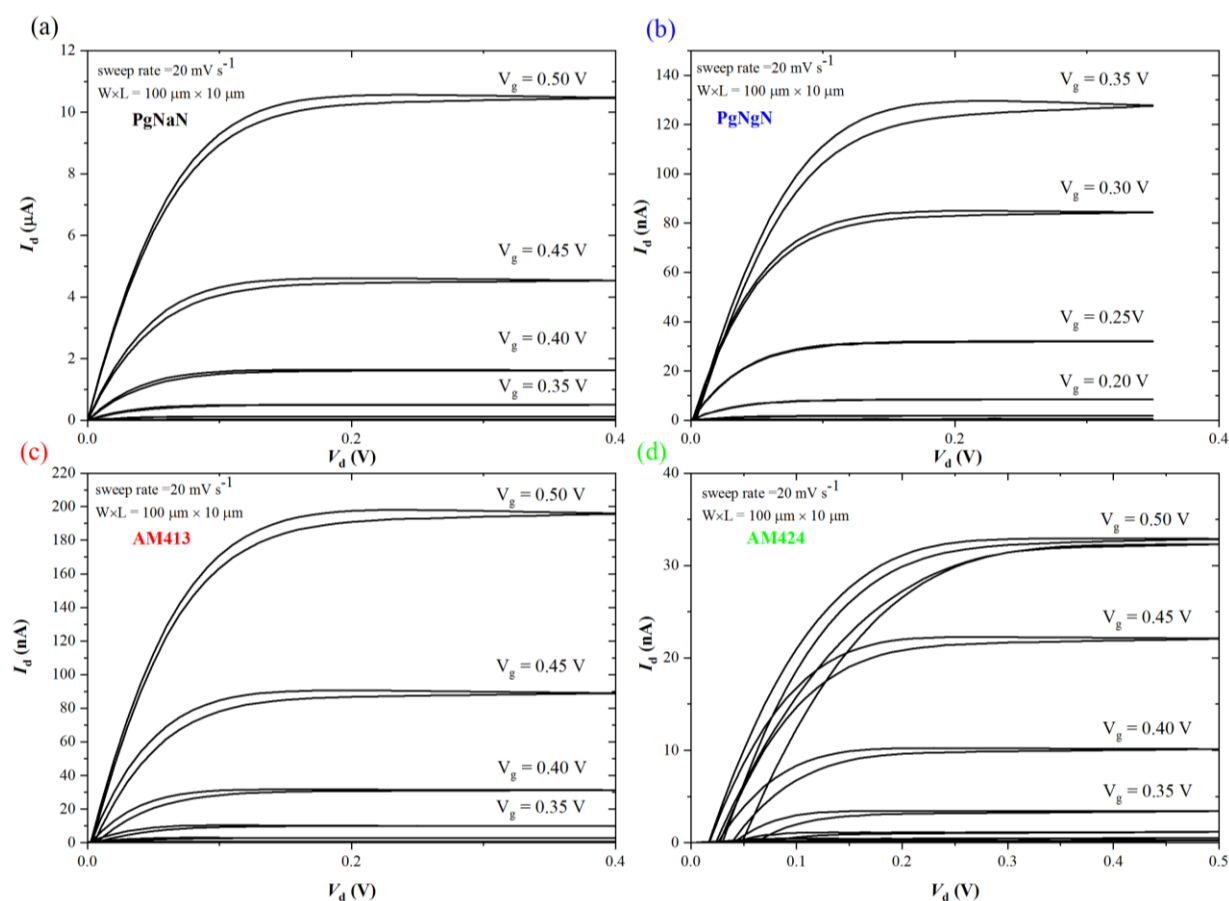


Figure 78. Output curves for OECT devices of each polymer, note all I_d axis are in nA apart from **PgNaN** which is reported in μA .

Polymer films were dropcast to ensure good film thickness, but moderate hysteresis was observed for each material hindering facile mobility determination. Both **PgNgN** and **AM413**

are reasonably stable with moderate currents, comparable to similar *n*-types,^{22,49,175} **AM424** is also stable but exhibits very low currents despite possessing a large threshold voltage. **PgNaN** was the best performer, with good stability and high current outputs on the order of μA compared to nA for the three other materials.

The stable materials showed a break in over the first half dozen cycles. I_d increased while I_g decreased, and the hysteresis was slightly reduced. However, the hysteresis remained large, significantly impeding charging at sweep rates above 100 mV s^{-1} . While the general potential stability limit of $V_g = 0.5 \text{ V}$ was similar to glycolated NDIs,^{22,53} these materials do not show the characteristic conductivity peaks of NDIs but instead continue to show increased conductivity with increasing V_g although significant sweep-to-sweep degradation is observed. For example, pushing **PgNaN** out beyond its stability limits gave I_d currents of $>50 \text{ uA}$ above $V_g = 0.6 \text{ V}$. Comparatively, **PgNgN** showed no polymer charging beyond moderate gate potentials ($V_g = 0.4 \text{ V}$), just electrochemical breakdown reactions, all the other more stable polymers showed continued pseudo-capacitive charging even when pushed beyond V_g limits of I_d stability.

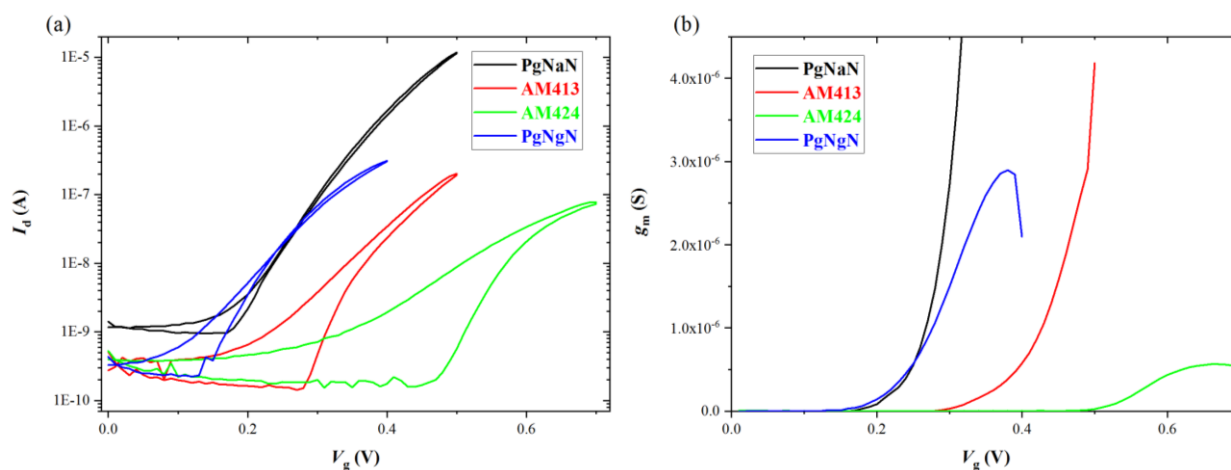


Figure 79. (a) Representative semi-logarithmic transfer curves comparing drop cast polymers.

(b) Transconductance plots showing much higher g_m of **PgNaN**.

Compared to other *n*-type OECT materials **PgNgN** and **AM413** show comparable mobilities ($\sim 10^{-4} \text{ cm}^2 \text{ V}^{-1} \text{ s}^{-1}$) and a C^* ($\sim 200 \text{ F cm}^{-3}$) on par with published glycolated materials.^{22,189} **PgNaN** shows a much higher mobility but a rather low C^* , with the μC^* product on par with **BBL**.¹⁸⁹ The reduced volumetric capacitance was to be expected upon decreasing the overall glycol content between the two otherwise identical polymers, reducing both solvation and ion injection capability.¹⁹⁰ These initial results were encouraging, even with low molecular weights the electron mobilities obtained are appreciable with an order of magnitude increase observed for **PgNaN** ($6.50 \times 10^{-3} \text{ cm}^2 \text{ V}^{-1} \text{ s}^{-1}$) compared to benchmark **BBL** ($7.0 \times 10^{-4} \text{ cm}^2 \text{ V}^{-1} \text{ s}^{-1}$).¹⁸⁹ Again, this study suggests that an optimal material would be comprised of a mixed N-alkylated, N-glycolated material, with the branched OEG sidechain seemingly reducing device performance future materials should focus on modifying the length of the linear OEG sidechain to optimize the ratio of glycol to alkyl content.

Table 18. Summary of transistor performance; electron mobilities (μ_e), threshold voltages (V_{th}), transconductance (g_m) volumetric capacitance (C^*) figures of merit (μC^*) and thickness normalised transconductance (g_m').

	μ_e ($\text{cm}^2 \text{ V}^{-1} \text{ s}^{-1}$)	V_{th} (mV)	$g_m / (W/L)$ (μS)	C^* (F cm^{-3})	μC^* ($\text{F cm}^{-1} \text{ V}^{-1} \text{ s}^{-1}$)	g_m' (S cm^{-1})
PgNaN	6.50×10^{-3} ($\pm 1.01 \times 10^{-4}$)	327.7 ± 5.3	13.0 ± 3.4	103 ± 6	0.673 ± 0.134	0.087 (0.24) ^b
PgNgN	1.89×10^{-4} (2.3 ± 10^{-5})	209.5 ± 17.3	0.30 ± 0.04	239 ± 97	0.046 ± 0.023	0.006 ± 0.002
AM413	5.73×10^{-4} (1.9 ± 10^{-5})	391.4 ± 6.4	0.25 ± 0.06	-	-	-
AM424	6.45×10^{-5} (3.3 ± 10^{-6})	479.2 ± 8.8	0.047 ± 0.09	-	-	-
BBL	7.0×10^{-4}	-	$\sim 5^a$	930	0.65	0.3

^aEstimated from the thickest reported transistor.¹⁸⁹

^bWhen $V_g = 0.6\text{V}$

4.10.4 THERMOELECTRIC PERFORMANCE

Following the preliminary OECT investigation a sampling of polymers were sent to Dr S. Wang at Linköping University, Sweden to attempt *n*-doped thermoelectric analysis following the success of the N-alkylated counterparts.¹⁸⁰ Compared to *p*-type doping, the *n*-type doping process is inherently unstable (detailed in **Section 1.6.2**). As such, the field is relatively young and unexplored, however two motifs currently dominate the field: namely solution and solid-state doped materials respectively. At the time of writing one the best-performing organic *n*-type materials is a fluorinated benzodifurandione poly(*p*-phenylene vinylene) based polymer, abbreviated as FBDPPV.⁵² This extended isoindigo is doped with N-DMBI (((4-(1,3-dimethyl-2,3-dihydro-1Hbenzoimidazol-2-yl)phenyl)dimethylamine)) in solution to give a power factor of $28 \mu\text{W m}^{-1} \text{K}^{-2}$ and an electrical conductivity of 14 S cm^{-1} . A more recent publication from late 2019 presents a donor-acceptor pyrazine-flanked DPP co-3,3'-dicyano-2,2'-bithiophene polymer (P(PzDPP-CT2)) with a power factors up to $57 \mu\text{W m}^{-1} \text{K}^{-2}$ and an electrical conductivity of 8.4 S cm^{-1} .¹⁹¹

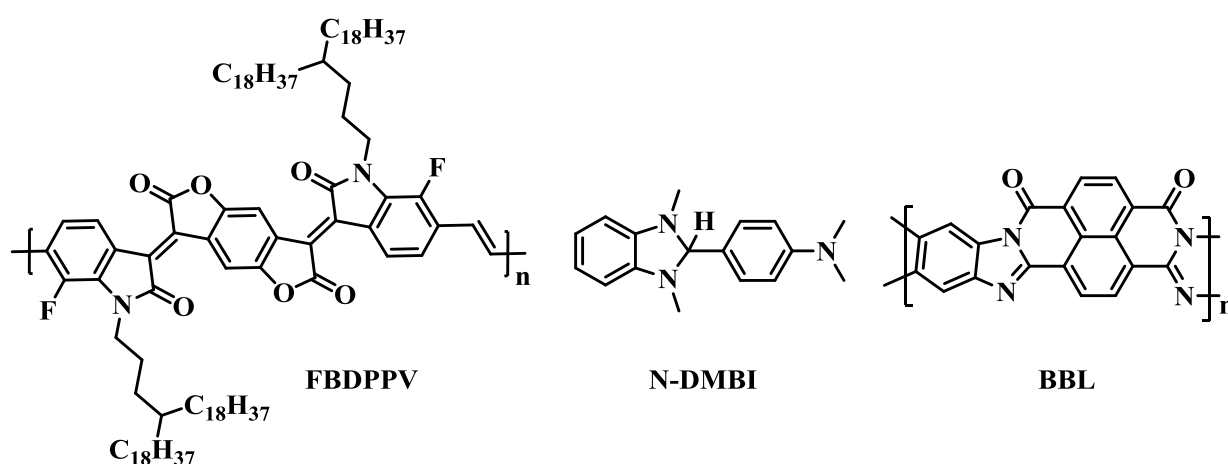


Figure 80. Chemical structure of extended isoindigo fluorinated benzodifurandione poly(*p*-phenylene vinylene), abbreviated as **FBDPPV**, *n*-type dopant **N-DMBI** and polybenzimidazobenzophenanthroline (**BBL**).

For this initial study the same four polymers (**Figure 77**) investigated for OECTs (**Section 4.10.3**) were kindly tested by Dr. S. Wang. Each polymer was *n*-doped with varying volumetric ratios of N-DMBI (**Figure 80**). More specifically, a 5 mg mL⁻¹ solution of polymer was prepared alongside a 1.35 mg mL⁻¹ solution of N-DMBI before subsequently being mixed at 3, 9, 15, 25 and 50 mol% volume ratios, respectively. Prior to film deposition, the solutions were stirred and thermally annealed at 70 °C for a minimum of 90 minutes. The solutions were then spin-coated onto cleaned glass substrates, thermally annealed at 110 °C under a nitrogen atmosphere before being allowed to cool over time to room temperature.

4.10.5 ELECTRICAL CONDUCTIVITY

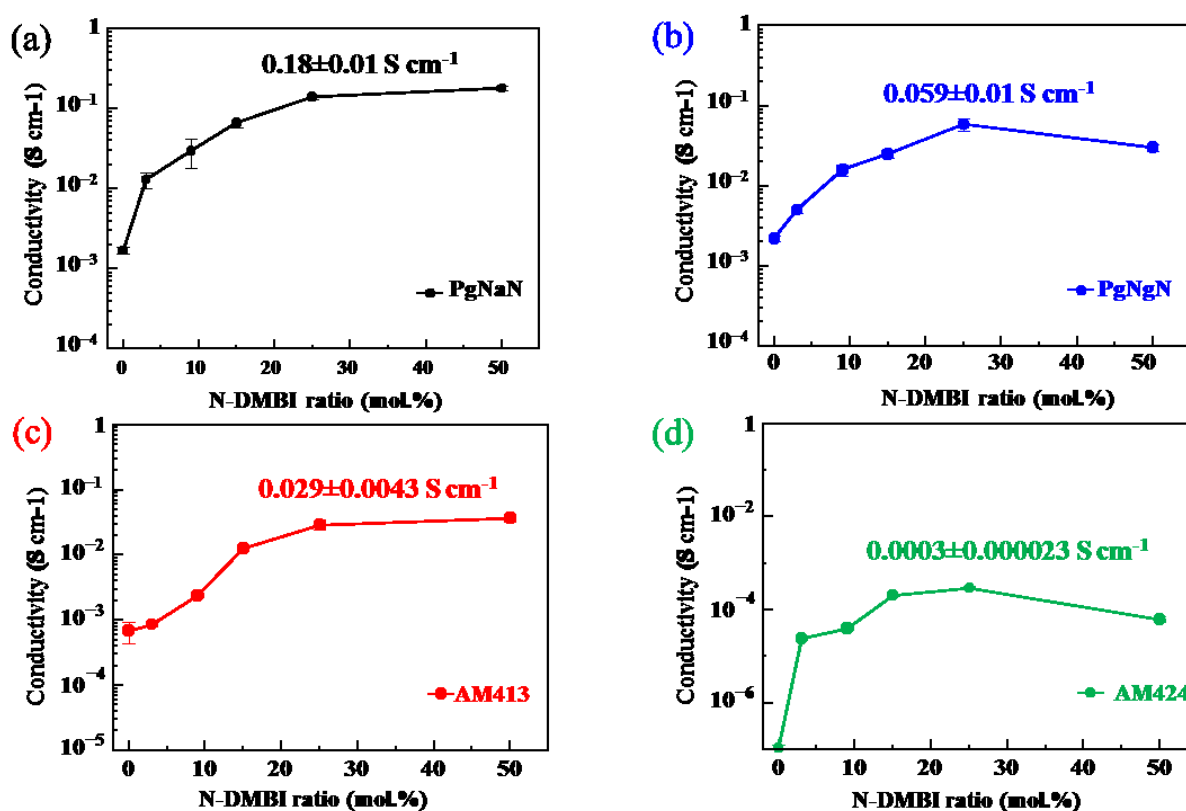


Figure 81. Electrical conductivities (S cm⁻¹) recorded as a function of N-DMBI dopant ratio. Each polymer showed a modest electrical conductivity with the linear N-glycolated polymer **PgNaN** exhibiting the highest conductivity of 0.18 S cm⁻¹ a factor of ten increase from the branched N-glycolated analogue **AM413**. These two polymers are directly comparable sharing

the same all naphthalene core motif, the same level of alkylation both possessing C₁₂- chains and only differing in the nature of the OEG sidechain. The total glycol content for both polymers is also comparable, per repeat unit **pgNaN** is comprised of 14 total OEG units with **AM413** possessing 16 total OEG units. Despite this the electrical conductivity of the branched OEG derivative **AM413** drops drastically to 0.029 S cm⁻¹. The reverse is observed when comparing **AM413** to the all N-glycolated polymer **pgNgN**, comprised of 20 total OEG per repeat unit, the electrical conductivity increases to 0.059 S cm⁻¹ this is still over 3-times smaller than the mixed N-glycol, N-alkyl polymer **pgNaN**.

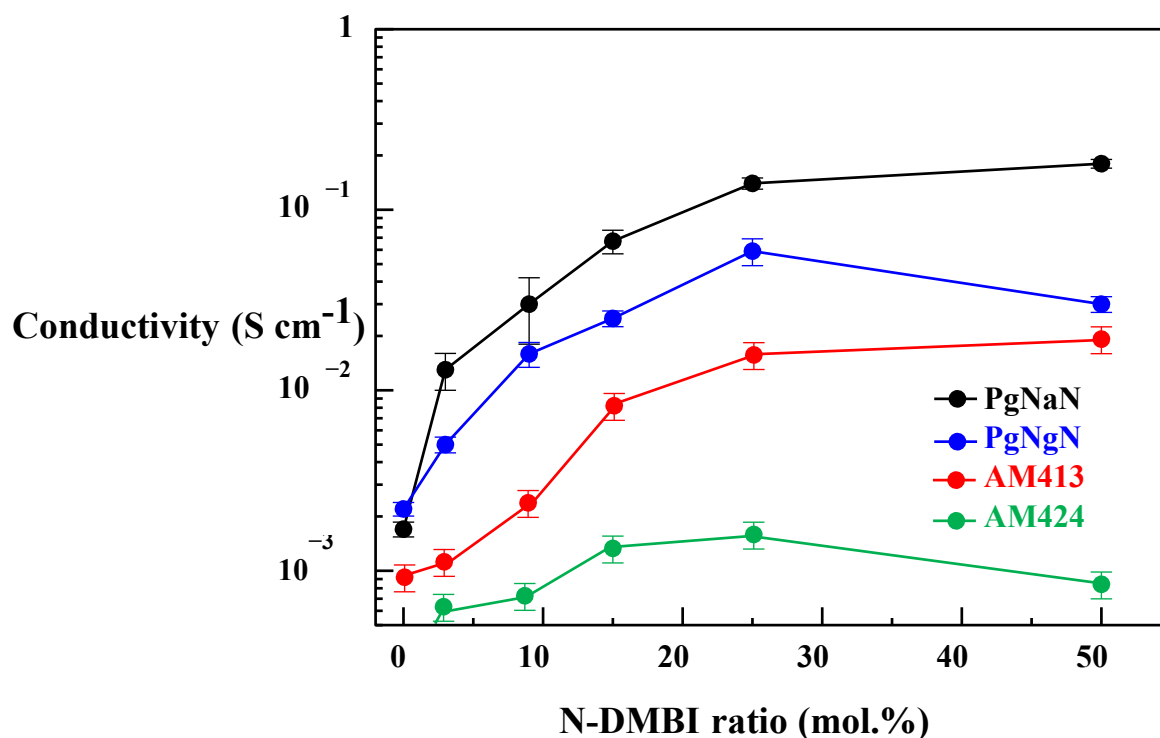


Figure 82. Electrical conductivity comparison of all four polymers tested as a function of molar ratio of *n*-type N-DMBI dopant.

The trend in electrical conductivity followed that of electron mobility (**Table 18**) which is extracted from the formal definition **Equation (4)**, as such the order of performance is AM424 < AM413 < PgNgN < PgNaN. Once again suggesting that a balance must be struck between non-polar alkyl content and polar glycol content for optimal device performance in both OECT and thermoelectric devices.

4.10.6 SEEBECK COEFFICIENT & POWER FACTOR

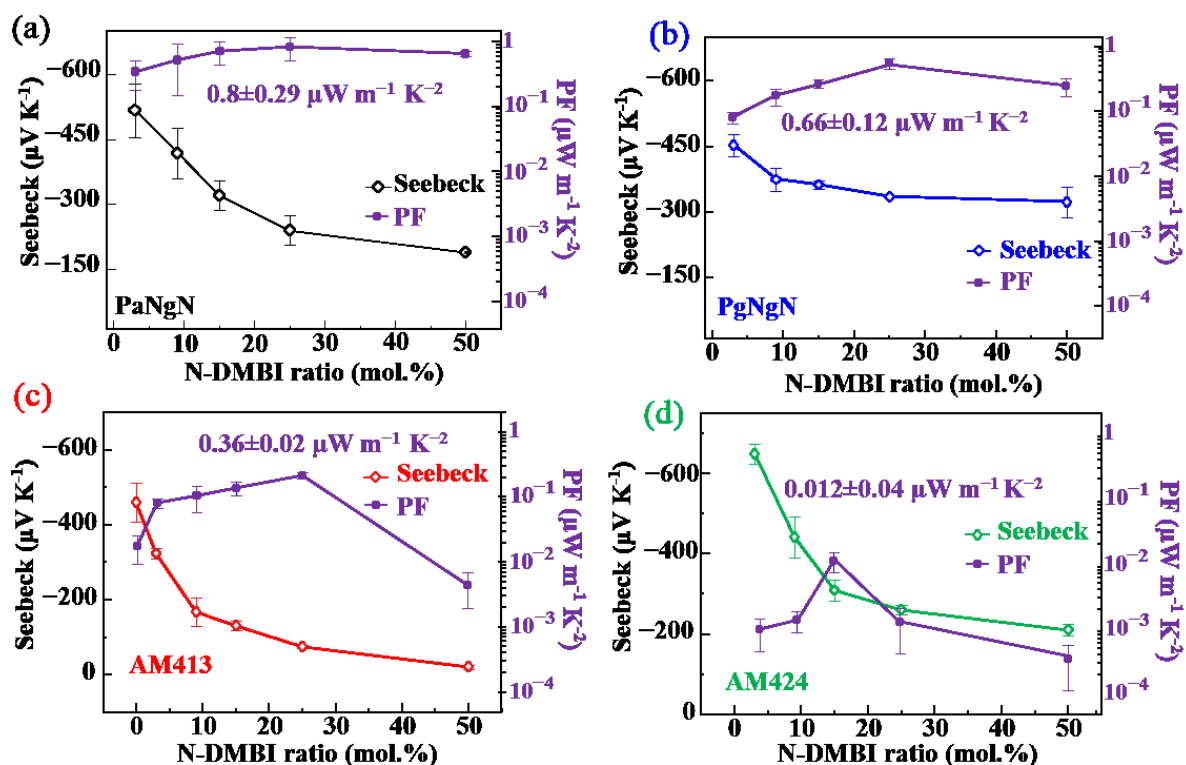


Figure 83. Thermoelectric performance of **PgNaN**, **PgNgN**, **AM413** and **AM424**, both Seebeck coefficients and power factor (PF) are plotted as a function of N-DMBI molar dopant concentration.

The thermoelectric performance of the doped films was evaluated by imposing a temperature difference across the sample and measuring the output thermovoltages. From this the Seebeck coefficients were determined and plotted as a function of molar dopant concentration (**Figure 83**). All four polymers exhibit a negative Seebeck coefficient confirming that *n*-type charge carrier (electrons) transport dominates.

The power factor of each doped polymer reaches a maximum at an optimal dopant concentration and subsequently declines either side of this ratio. Following the trend in electrical conductivity (**Figure 82**) the mixed N-glycol, N-alkyl polymer **pgNaN** exhibits the highest PF of $0.80 \pm 0.29 \mu\text{W m}^{-1} \text{K}^{-2}$ reaching a maximum at 25 mol% dopant concentration.

This concentration was also found to be the optimal amount for both **pgNgN** (PF = $0.66 \pm 0.12 \mu\text{W m}^{-1} \text{K}^{-2}$) and **AM413** (PF = $0.36 \pm 0.02 \mu\text{W m}^{-1} \text{K}^{-2}$). Conversely, **AM424** reaches a maximum PF of $0.012 \pm 0.04 \mu\text{W m}^{-1} \text{K}^{-2}$ at 15 mol% dopant ratio. Notably both **pgNaN** and **pgNgN** display power factors greater than the ladder-type **BBL** (PF $\sim 0.43 \mu\text{W m}^{-1} \text{K}^{-2}$), a benchmark *n*-type material (**Figure 80**).¹⁹²

4.10.7 DISCUSSION

As a prelude to this discussion it should be noted that prior to the global COVID-19 pandemic OECT and thermoelectric devices for the remaining polymers were due to be fabricated however this work is currently on hold and the analysis herein will only focus on four materials (**Figure 77**). In addition, spectroelectrochemistry, electrochemical impedance spectroscopy and long-term stability tests are planned for these materials. Once this data has been collected and analysed, it is hoped that more definite conclusions can be made to assist future design guidelines for these systems to improve overall device performance.

The design strategy employed condensing together a bisatin and bisoxindole affords a series of novel rigid rod polymers. The effect of replacing the alkyl solubilising group with a polar OEG sidechain, linear or branched, leads to shallower HOMO levels, appreciable electron mobilities and above average electrical conductivity and power factors. Although conformationally locked these polymers are slightly twisted due to the increased steric hinderance of the OEG sidechains and a reorganisation energy consistent with polaron formation. The electrical conductivity values would suggest that, like **BBL**, the electron polaron, formed upon doping, is delocalised along the polymer backbone.¹⁹²

Preliminary results suggest this series of materials is stable to doping, inferred from the plateau in conductivity, under inert and ambient conditions, this was previously shown for the all N-alkylated series^{175,180} and the trend seems to also apply to *glycolation*. These initial tests only

focused on a small subset of the polymers synthesised. It is hoped that once data can be collected for the entire series, testing multiple dopants and optimising device fabrication, that design trends will become more apparent. It is difficult without a complete investigation to suggest the overall effect of replacing alkyl sidechains with OEG chains, or the difference between linear and branched N-glycolation.

However, a preliminary discussion can be had based on the four polymers fabricated for both thermoelectric and OECT devices. The initial publication¹⁷⁵ suggests that extending the aromatic core from phenyl to naphthalene leads to increased *n*-type transport. This does not seem to be the case upon further increasing the core to anthracene, as seen for **AM424**, which has a mobility value an order of magnitude lower than the naphthalene cored analogues, in agreement with a previous study.¹⁸⁰ The highest mobility is observed for **PgNaN**, featuring a mix of alkyl chains (to increase mobility) and glycol chains (to increase volumetric capacitance). Switching the glycol chain to an extended branched version (**AM413**) reduces the mobility by an order of magnitude whilst also reducing both the electrical conductivity and Seebeck coefficient. Whilst the branched glycol chain imparts greater solubility the increased steric hinderance leads to a more twisted polymer backbone, limiting the delocalisation and thus reducing charge carrier mobility. This is further supported by the results for **PgNgN** which despite being fully glycolated shows increased device performance due to the presence of shorter linear chains, carrier mobility is seemingly dominated by the degree of twisting about the fused polymer backbone.^{175,180}

Even from this small subset of measurements it is clear that altering the polarity of the sidechain has a marked impact on the mobility and volumetric capacitance, figures of merit for OECT devices and must be carefully considered in order to design the optimal mixed conduction *n*-type material. Future work could study the effect of sidechains even further by synthesising a fused system without any solubilising chains, akin to **BBL (Figure 80)**, although the solubility

of such a material would be expected to heavily limit the synthesis, this would in theory provide even more insight into the role of sidechain engineering for these rigid rod systems. A comprehensive study investigating the electrochemical stability of these materials would also benefit future work in this area, whilst initial anecdotal evidence suggest that these polymers are relatively stable, operating under ambient conditions at high levels of chemical doping.^{175,180}

4.11 CONCLUSION

This chapter details the synthesis of a series of mixed conduction N-alkylated and N-glycolated polymers, arising from the Aldol condensation between different combinations of bisisatin and bisoxindole monomers. One particularly promising aspect of this synthetic route is the ability to forego any toxic organometallic monomers or transition metal catalysts, which should in turn benefit both the costs and biocompatibility of the resulting materials. Preliminary testing shows good thermoelectric performance with both **PgNaN** ($0.80 \pm 0.29 \mu\text{W m}^{-1} \text{K}^{-2}$) and **PgNgN** ($0.66 \pm 0.12 \mu\text{W m}^{-1} \text{K}^{-2}$) displaying power factors greater than the benchmark *n*-type ladder material **BBL** ($0.43 \mu\text{W m}^{-1} \text{K}^{-2}$). Organic electrochemical transistor results demonstrate *n*-type mobilities of up to $6.50 \times 10^{-3} \text{ cm}^2 \text{ V}^{-1} \text{ s}^{-1}$, with **PgNaN** recording high transconductances ($13.0 \pm 3.4 \mu\text{S}$) and product [μC^*] ($0.673 \pm 0.134 \text{ F cm}^{-1} \text{ V}^{-1} \text{ s}^{-1}$) values, again greater than the **BBL** benchmark.¹⁸⁹ The preliminary results suggest a goldilocks principle is in play when designing the optimal mixed conduction material, more alkyl density increases the mobility, but more glycol content increases ion transport and raises volumetric capacitance. Once a full set of OECT and thermoelectric devices have been fabricated and subsequently analysed a clearer picture should emerge linking the overall effect of altering the polarity of the sidechain and the structure (linear vs. branched) on the optoelectronic, thermoelectric and transistor properties of these fused *n*-type mixed conduction polymers. The steric hinderance, imparted by the choice of sidechain, must also be considered, despite these

fused systems having severely limited rotation about the sp^2 C=C linkage the slightest deviation from planarity can reduce the mobility by orders of magnitude. In conclusion nine novel mixed conduction polymers are presented within this study, demonstrating the versatility of being able to mix and match bisisatin monomers with bisoxindole coupling partners to rapidly expand the library of fused *n*-type materials. This series presents a unique selection of N-glycolated extended isoindigo cored polymers with good ambient stability, consistent operation and moderate to above average OECT and thermoelectric device performance.

CHAPTER FIVE: *p*-TYPE POLYMER SERIES

5.1 INFORMATION AND CREDITS

The hybrid alkyl-glycol monomer synthesis, optimisation and characterisation were conducted in my own work. The stannylated monomers; 2,5-bis(trimethylstannyl)thiophene and 2,5-bis(trimethylstannyl)thieno[3,2-*b*]thiophene were synthesised by previous group member Bob Schroeder. Dr. Rajendar Sheelamantula carried out GPC measurements (McCulloch group, KAUST). OECT devices were fabricated by Maximilian Moser (McCulloch group, Imperial College) & Tania Hidalgo (Inal group, KAUST) who also conducted electrical characterisation (EIS) and OECT performance measurements. Spectroelectrochemical and specific capacity measurements were recorded by Hang Yu (Nelson group, Imperial College).

5.2 BACKGROUND & MOTIVATION

Over the past decade, the field of organic electronics has been populated by conjugated polymers decorated with ethylene glycol sidechains, specifically designed for OPV,⁵⁵ OFET^{55,193} and OECT^{22,25,39,51} device application. A prime example of this is **p(g2T-T)**, a triethylene glycol substituted 2,2'-bithiophene (abbreviated as 2T or T2) copolymerised with electron rich thiophene (T), first reported by Nielsen *et al.*³⁹ in 2016. To this day, this polymer remains as one of the benchmark *p*-type OECT materials with a volumetric capacitance $C^* = 220 \pm 30 \text{ F cm}^{-3}$ and charge carrier mobility $\mu_{OECT} = 0.28 \pm 0.1 \text{ cm}^2 \text{ V}^{-1} \text{ s}^{-1}$. Combining the previous work, again from within our research group, the thienothiophene (TT) unit shown to have high rigidity and hole mobilities in **PBTtT**,³⁰ was combined with the g2T unit to afford **p(g2T-TT)**.⁵¹ Indeed, this design further enhanced OECT device performance and currently **p(g2T-TT)** is commonly regarded as one of the top performing *p*-type OECT materials with volumetric capacitance $C^* = 241 \pm 94 \text{ F cm}^{-3}$ and charge carrier mobility $\mu_{OECT} = 0.94 \pm 0.25 \text{ cm}^2 \text{ V}^{-1} \text{ s}^{-1}$.⁵¹ In this initial publication the glycolated polymer was compared to the alkylated analogue **p(a2T-TT)**, demonstrating the shift in mode of operation from interfacial to bulk

transport/doping, improved transconductance, higher OECT currents and enhanced volumetric capacitance (**Figure 16**).⁵¹

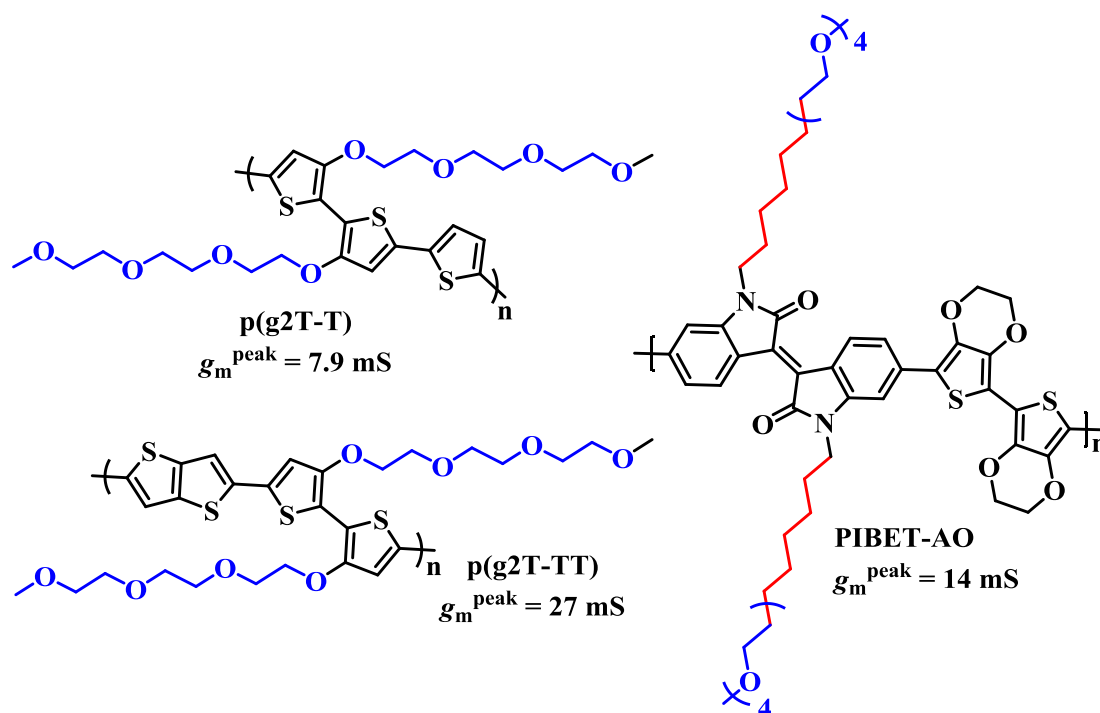


Figure 84. Molecular structures of **p(g2T-T)**³⁹, **p(g2T-TT)**⁵¹ and **PIBET-AO**¹⁹⁴ with reported peak transconductance values, hydrophilic chains highlighted in blue and hydrophobic chains in red.

Following these pronounced improvements, Wang *et al.*¹⁹⁴ presented an approach to merge the benefits of non-polar (alkyl) and polar (glycol) chains by grafting a hybrid alkyl–ethylene glycol sidechain to an isoindigo core and copolymerising the latter with an EDOT monomer, to afford the polymer **PIBET-AO**. They report an increase in substrate adhesion, owing to the hydrophobic alkyl chains and a slight increase in OECT device performance and stability, owing to the hydrophilic glycol chains.

Combining these results, it was hypothesised that using the high performing thiophene and thieno[3,2-*b*]thiophene backbones in combination with varied length alkyl spacers between the core and polar glycol sidechain would lead to increased performances. These synthetic

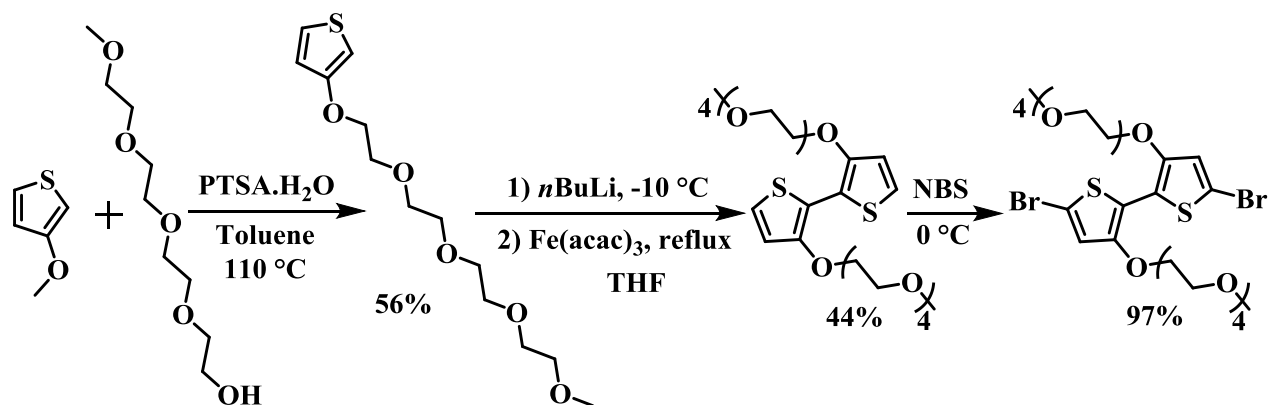
modifications should balance the polarity needed for electrolyte ion doping with the hydrophobic protection against film dissolution in aqueous electrolytes.¹⁹⁴ This chapter details the synthetic difficulty of producing a series of **p(gC_nT2-T)** and **p(gC_nT2-TT)** polymers where the C_n alkyl spacer is increased in increments of two carbons from C₂ to C₈, with the C₂ polymers acting as the reference polymers namely **p(g₄T2-T)** and **p(g₄T2-TT)**. The optoelectronic properties as well as the OECT device performance is reported herein.

5.3 SYNTHESIS

With the plethora of available procedures for synthesising **p(g₂T-TT)**, from previous group members,^{39,51,66,195} the synthesis of the desired hybrid alkyl-glycol substituted bithiophene monomers was expected to be a straightforward process. In reality, this was far from the case as the head to head coupling of the functionalised 3-alkoxythiophenes proved to be extremely problematic, the specifics will be detailed below.

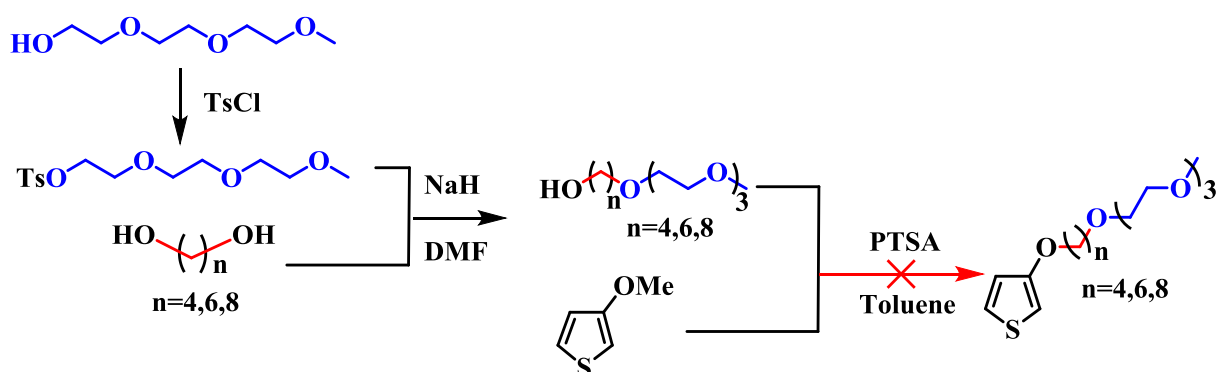
5.3.1 MONOMER SYNTHESIS

The reference, fully glycolated, bithiophene monomer was synthesised following a modified procedure from Nielsen *et al.*³⁹ Transesterification of 3-methoxythiophene with tetraethyleneglycol monomethyl ether, catalysed by *p*-toluenesulfonic acid monohydrate, afforded the glycolated thiophene in moderate yield. Oxidative C-C bond formation was mediated by selective lithiation at the 2-position, using *n*-BuLi, followed by the addition of tris(acetylacetonato)iron(III) (Fe(acac)₃) selectively isolating the head-head glycolated bithiophene. Near quantitative dibromination, using NBS, afforded the fully glycolated **g₄T2-Br₂** monomer.



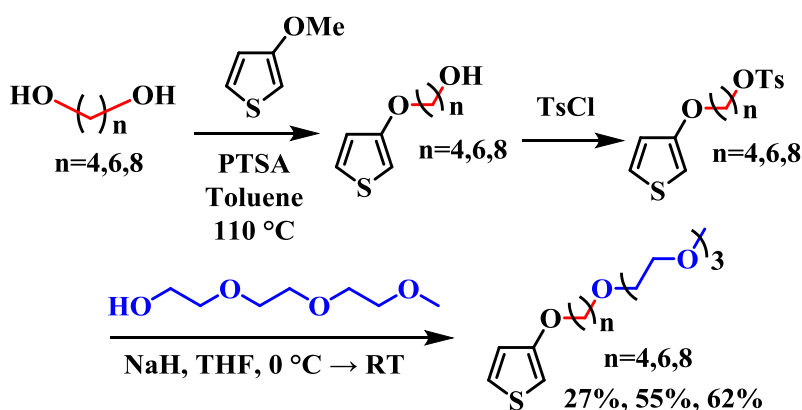
Scheme 35. Synthetic pathway starting from the transesterification of 3-methoxythiophene, oxidative coupling with Fe(acac)₃ and finally dibromination with NBS to yield the fully glycolated **g₄T₂-Br₂** monomer.

To form the alkyl-spacer glycolated bithiophene monomers, synthesis began following the pathway presented by Du,¹⁹⁵ this route involved formation of the hybrid alkyl-glycol sidechain prior to grafting to 3-methoxythiophene. The tosylation of triethylene glycol monomethyl ether was almost quantitative and the subsequent nucleophilic addition of the corresponding (alkyl spacer) diol afforded the hybrid chain in good yield. However, the transesterification with 3-methoxy thiophene proved to be extremely difficult to purify with multiple spots apparent on the crude TLC plate. It followed that this route was not suitable for the scale-up of the materials, as the correct product could only be isolated in diminished quantities.



Scheme 36. Route 1: synthesis of the hybrid alkyl-glycol sidechain prior to transesterification with the thiophene core, catalysed by *p*-toluenesulfonic acid (PTSA), proposed by Du.¹⁹⁵

It was hypothesised that the hybrid alkyl-glycol sidechains were the limiting factor in the transesterification process, thus an alternate route was devised in which the glycol portion of the hybrid alkyl-glycol chain was added in the final step as opposed to the independent sidechain synthesis above:



Scheme 37. Route 2; transesterification of the relevant alkane diol, tosylation of the resultant functionalised thiophene followed by nucleophilic attack of deprotonated triethylene glycol monomethyl ether to afford thiophenes decorated with the respective C₄, C₆ and C₈ hybrid alkyl-glycol sidechains, yields are reported for the final step.

This route proved to be much more successful and thiophene monomers decorated with C₄, C₆ and C₈ hybrid alkyl-glycol sidechains were afforded in moderate yields. After this initial hurdle was overcome, the synthesis of the bithiophene monomers could commence. Here is where the synthetic issues began. The first attempt to couple together two functionalised thiophene units followed the procedure of Giovannitti⁶⁶ using *n*-BuLi to lithiate at the 2-position followed by the addition of the oxidant Fe(acac)₃ to mediate the C-C coupling. However, once isolated the ¹H NMR spectrum (**Figure 85**) revealed that the unwanted head-tail (H-T) coupled bithiophene had been formed in a ratio of 1:5 compared to the desired head-head (H-H) product. Furthermore, these compounds could not be separated despite multiple attempts utilising all common methods of separation.

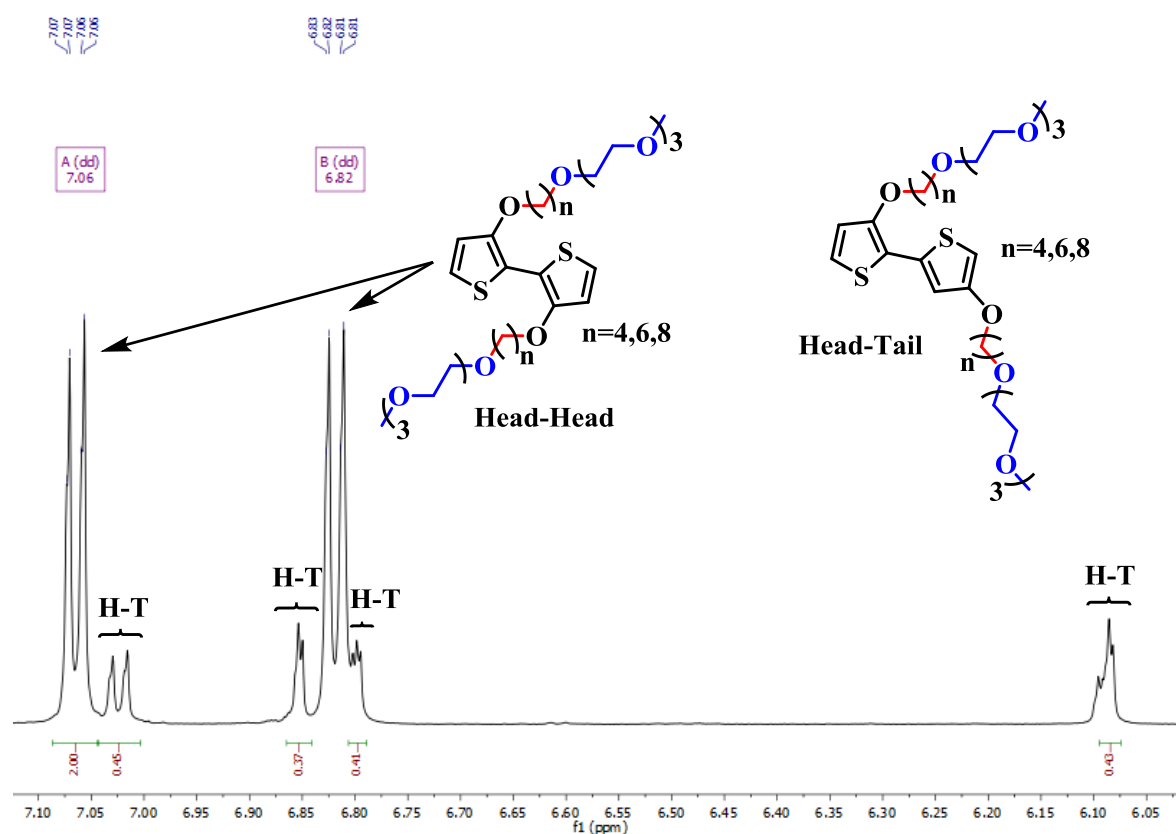


Figure 85. ¹H NMR spectrum showing the desired head to head peaks (7.06 & 6.82 ppm) in addition to the peaks corresponding to the unwanted head-tail product, including molecular structures.

This was unexpected, multiple studies have shown that lithiation of 3-substituted thiophenes occurs selectively at the 2-position when using *n*-butyllithium however some reports state that when the coordinating ability of the 3-substituent does not fully compensate for steric effects, lithiation can occur in both the 2- and 5- positions.^{51,66,195–197} This problem seems to be unique to the hybrid alkyl-glycol sidechain, as the use of an all glycol chain or all alkyl chain has been reported to selectively form the desired head-head bithiophene with no mention of any selectivity issues, as was the case for **g₄T2** (Scheme 35).^{39,51}

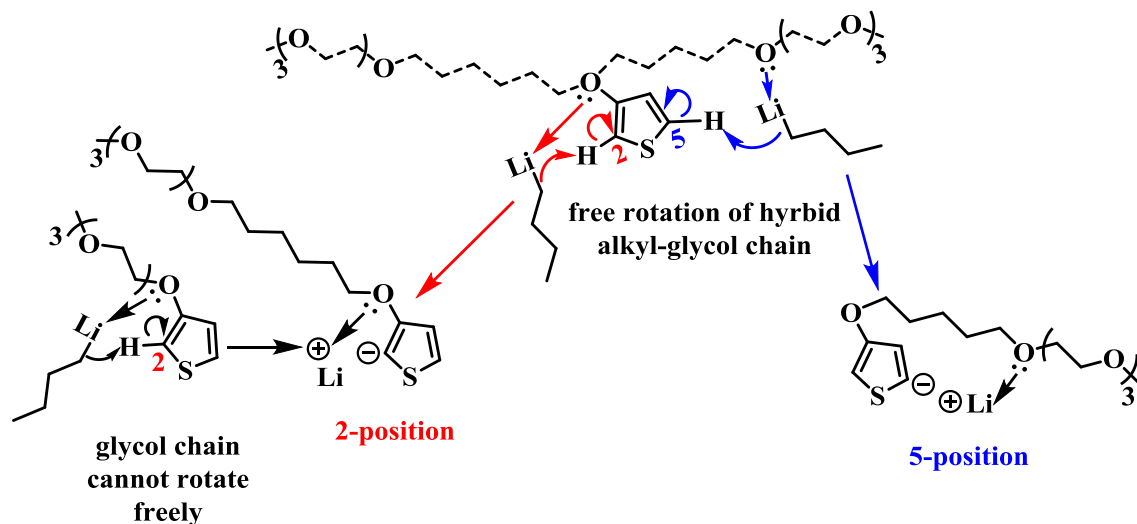
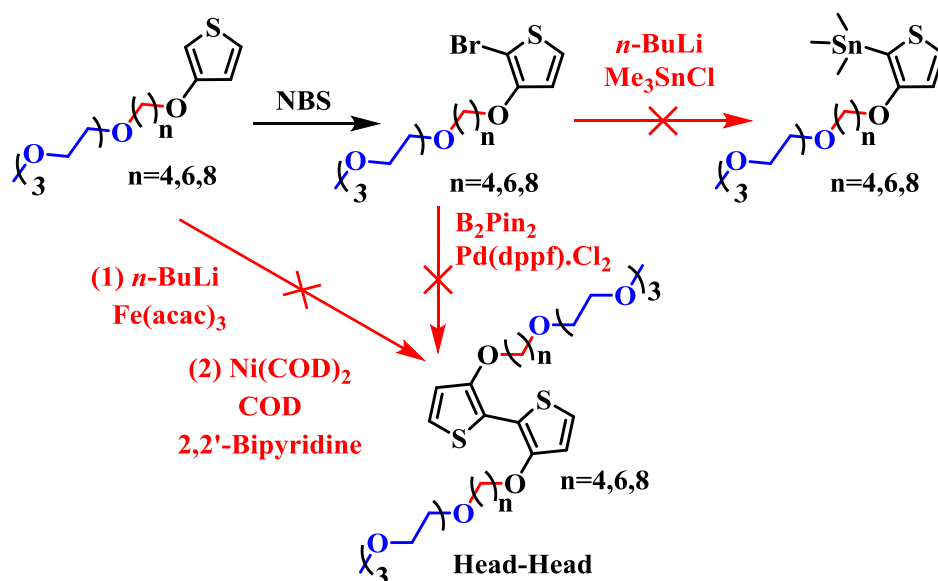


Figure 86. Proposed theory for the unexpected reactivity of the 5-position when coupling the hybrid alkyl-glycol functionalised thiophene units. Free rotation of the alkyl chain facilitates stabilisation of the 5-position α -carbon from the oxygen lone pair in the glycol portion of the sidechain, as opposed to the methoxy linker oxygen atom which can only stabilise the 2-position.

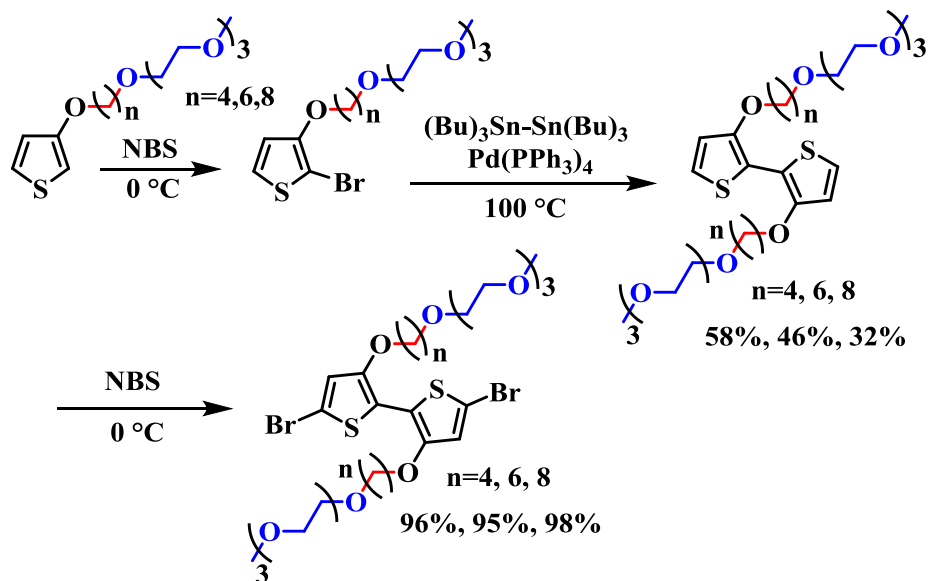
A possible explanation for the observed reactivity of the 5-position is depicted in **Figure 86**, the hybrid alkyl-glycol chain can twist and rotate freely which could explain the stabilisation of the 5-position and hence explain the unwanted head-tail coupling. The fully glycolated **g4T2** cannot twist/wrap around the thiophene core in the same manner due to the repulsive sterics of the ethylene glycol units and reduced length of the hydrophilic sidechain, hence selective lithiation is observed at the 2-position.

Similar to the $\text{Fe}(\text{acac})_3$ oxidative coupling, the Yamamoto coupling with bis(1,5-cyclooctadiene)nickel(0), COD, and 2,2'-bipyridine in DMF and the in situ Suzuki coupling lead to an inseparable mix of the head-head and head-tail regioisomers in a similar ~20% impurity ratio. Whilst incredibly frustrating, the amount of different methods and conditions available is a credit to the synthetic utility of the thiophene moiety.



Scheme 38. Summative scheme of all failed reaction conditions (highlighted in red). In each case an inseparable mix of head-head and head-tail coupled bithiophene was produced or specifically to the stannylation the product simply degraded.

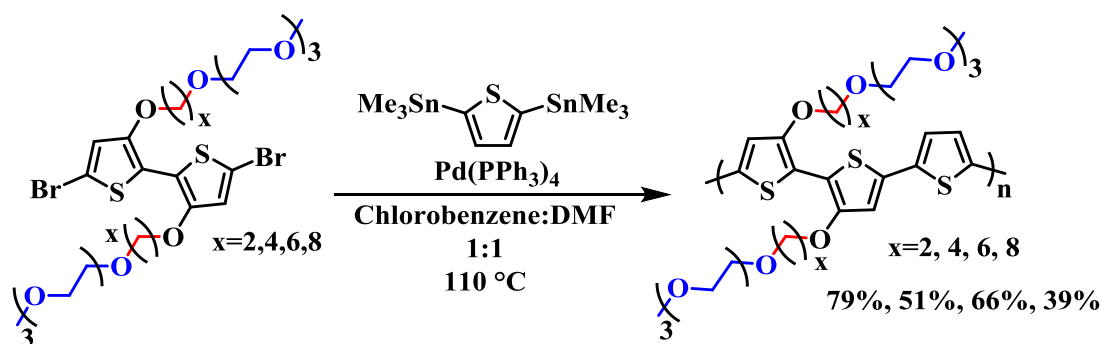
However, hope was not lost and an alternate method performing an in situ Stille coupling using the highly toxic bis(tributyltin) reagent in the presence of tetrakis(triphenylphosphine)palladium(0) catalyst, afforded selective coupling of the head-head product. Whilst admittedly not the most elegant route the desired hybrid alkyl-glycol functionalised head-head bithiophene monomers were selectively isolated in moderate yields. Bromination using NBS, afforded the di-bromo monomers required for polymerisation. Bromination of each alkoxy-2,2'-bithiophene unit was extremely fast, affording the 5,5'-substituted dibrominated monomers after 30 minutes of reaction time. This is accredited to the electron-rich nature of the bithiophene moiety. Notably the reaction time must be controlled in order to avoid any unwanted polymerisation, as such reactions were conducted in THF avoiding the common mildly acidic chloroform bromination conditions.



Scheme 39. Successful synthetic pathway to form the selective head-head coupled alkyglycol hybrid functionalised bithiophene monomers, with C_4 , C_6 and C_8 spacers, respectively.

5.3.2 $p(\text{gC}_n\text{T2-T})$ POLYMER SYNTHESIS

Stille polymerisation was used to couple the alkoxybithiophene monomers with 2,5-bis(trimethylstannyl)thiophene to afford the $p(\text{gC}_n\text{T2-T})$ series, with the alkyl spacer varying from C_2 , C_4 , C_6 and C_8 respectively:



Scheme 40. General polymerisation scheme for $p(\text{gC}_n\text{T2-T})$ polymer series.

Each polymerisation was carried out in a 1:1 (by volume) mix of chlorobenzene and DMF, keeping the overall monomer concentration between 0.1 to 0.2 M, melding literature conditions for the $p(\text{a2T-TT})$ and $p(\text{g2T-TT})$ polymers.⁵¹ Polymerisations were left overnight and gelled

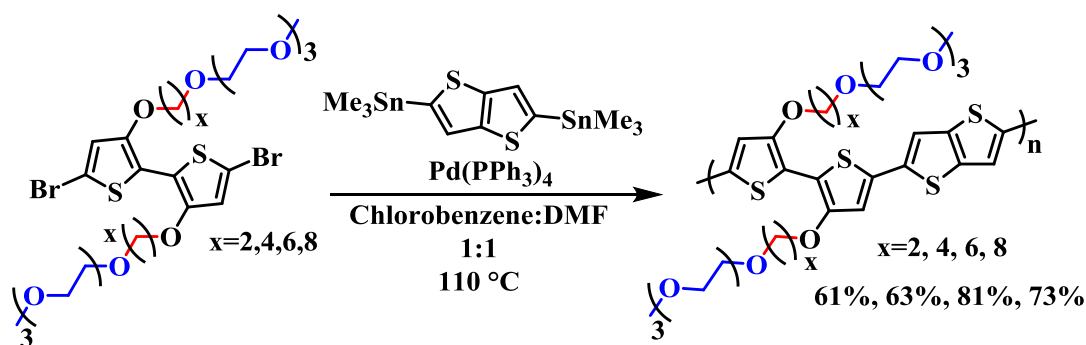
adequately upon cooling to room temperature. After precipitation purification by Soxhlet extraction with a range of solvents removed toxic tin side products. The majority fraction for each polymerisation was collected from chloroform. The yields, number average molecular weight (M_n), weight average molecular weight (M_w) and polydispersity are summarised in the following table:

Table 19. Physical properties of hybrid alkyl-glycol functionalised alkoxythiophene co-thiophene polymers, GPC data obtained vs. polystyrene standards in DMF.

Polymer	Reaction Code	M_n (kDa)	M_w (kDa)	PDI	Yield (%)
p(g ₄ T2-T)	AM575	51.1	109.6	2.15	79
p(gC ₄ T2-T)	AM572	19.9	43.7	2.20	51
p(gC ₆ T2-T)	AM568	28.0	59.2	2.11	66
p(gC ₈ T2-T)	AM583	13.3	30.0	2.26	39

5.3.3 p(gC_nT2-TT) POLYMER SYNTHESIS

Identical Stille polymerisation conditions were used to form the p(gC_nT2-TT) series, coupling the alkyl-spacer functionalised alkoxybithiophene monomers with 2,5-bis(trimethylstannyl)thieno[3,2-*b*]thiophene.



Scheme 41. General Stille polymerisation conditions for the p(gC_nT2-TT) series.

It should be noted that due to the high glycol content the 5,5'-dibromo-gC_nT2 series of monomers only solidified at reduced temperatures, hindering the weighing out process prior to

polymerisation, this could account for the lower molecular weight and diminished yield of some polymers across the series. Furthermore, the thienothiophene unit leads to additional backbone rigidification, promoting the aggregation of the polymers, thus rendering them less soluble at lower weights. This was especially the case for the thieno[3,2-*b*]thiophene polymers showing poor number average molecular weights (M_n), despite the magnitude the relative consistency allows for good comparison across the series.

Table 20. Physical properties of hybrid alkyl-glycol functionalised alkoxythiophene co-thieno[3,2-*b*]thiophene polymers, GPC data obtained vs. polystyrene standards in DMF.

Polymer	Reaction Code	M_n (kDa)	M_w (kDa)	PDI	Yield (%)
p(g₄T2-TT)	AM573	7.1	13.5	1.91	61
p(gC₄T2-TT)	AM578	10.0	21.4	2.14	63
p(gC₆T2-TT)	AM558	11.6	29.9	2.59	81
p(gC₈T2-TT)	AM585	5.9	11.4	1.92	73

5.4 RESULTS & DISCUSSION

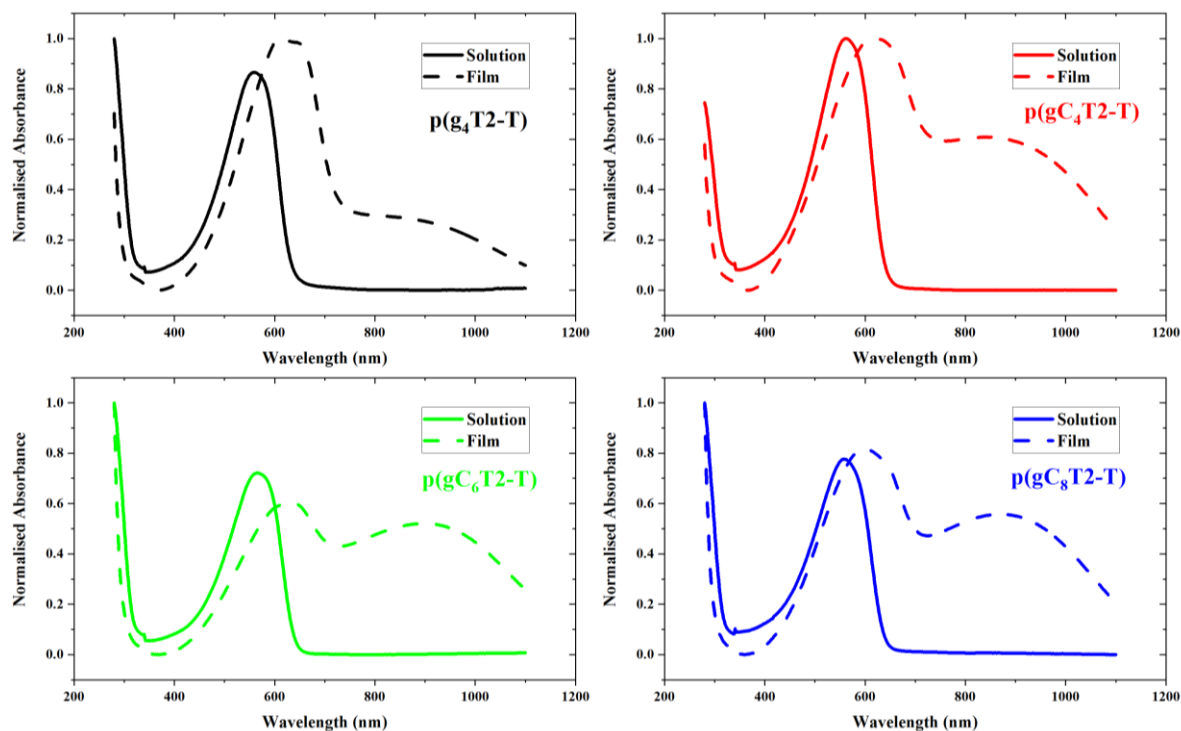
5.4.1 $p(gC_nT2-T)$ OPTOELECTRONICS

Figure 87. Normalised UV-Vis absorption spectra, solution (10 mg mL^{-1} chloroform) solid line and solid-state (thin film) dashed line, for the $p(gC_nT2-T)$ polymer series.

The absorption spectra for the fully glycolated reference polymer $p(g_4T2-T)$ is relatively similar between solution and thin film, with the slight redshift to longer wavelengths attributed to aggregation in the solid state. This becomes more pronounced for the hybrid alkyl-glycol functionalised polymers, each displaying a large redshift in absorption maxima and a bimodal distribution in the solid state. The bimodality arises from the formation of a positive polaron upon oxidation in the solid state *vide infra* (**Figure 89**). In general, the extension of the alkyl spacer had little effect on the optoelectronics of the polymer, with the conjugated backbone dominating the optical properties. These are noted in

Table 21 where little variation is seen in λ_{MAX} , λ_{ONSET} and E_{opt} values across the polymer series.

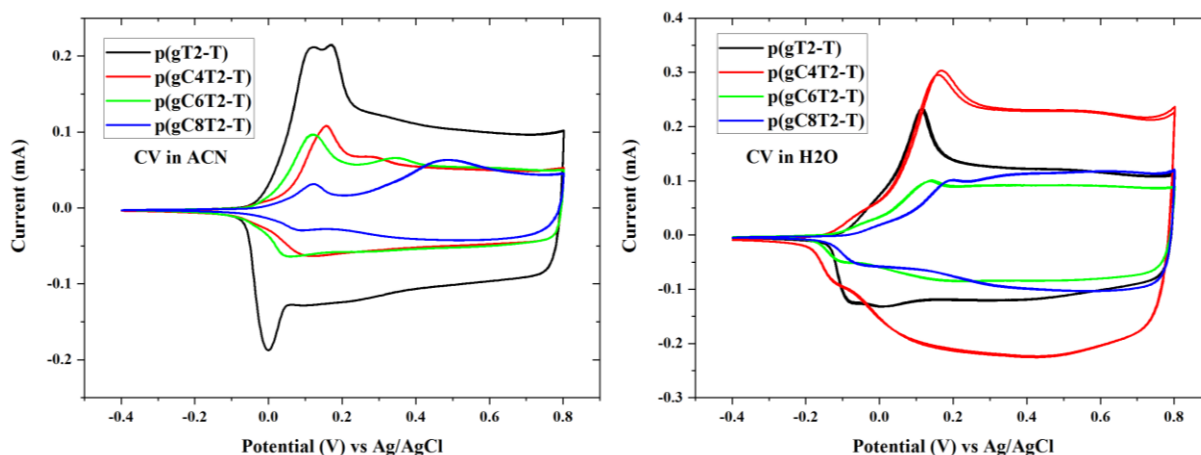


Figure 88. Cyclic voltammograms for **p(gC_nT₂-T)** series in 0.1 M NBu₄PF₆ acetonitrile solution (left) and aqueous 0.1 M NaCl solution (right) against an Ag/AgCl electrode.

Ionisation potentials were measured by CV, again with very little variation observed across the polymer series. This suggests that the addition of an alkyl spacer also has very little effect on altering the HOMO energy level, which is to be expected as each polymer still contains the alkoxy moiety facilitating intermolecular bonding interactions along the backbone thus the addition of an alkyl spacer is expected to have a minimal effect on the backbone optoelectronics.

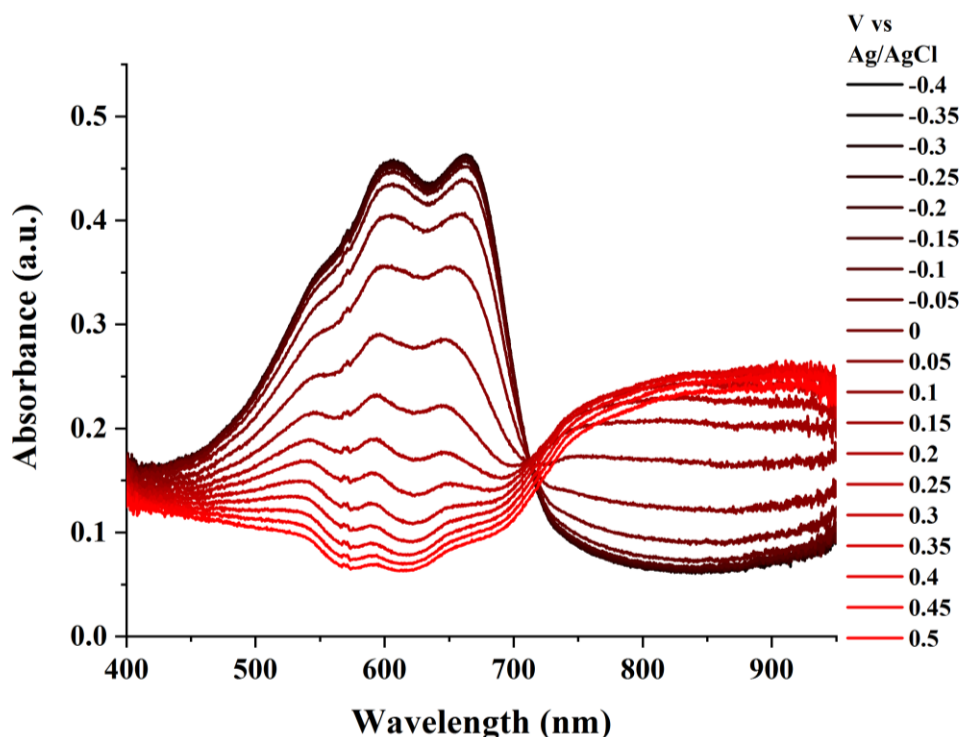


Figure 89. Spectroelectrochemical measurements from -0.4 V to 0.5 V for **p(g₄T₂-T)**, recording absorption signals at 10 second intervals throughout the whole CV scan (180 seconds in total) obtained from films blade coated with 10 mg mL⁻¹ chloroform solutions.

Spectroelectrochemistry was employed to study the change in absorption spectrum as the polymer was charged. Following the schematic (**Figure 18**) both polaron and bipolaron formation was expected upon increasing the applied voltage (**Figure 89**). For **p(g₄T₂-T)**, the neutral state absorption peak ($\lambda_{\text{MAX}} \sim 600$ nm) steadily decreases as the voltage is increased from -0.2 V where the polaron absorption peak (~ 800 nm) emerges and subsequently increases with the degree of oxidation. Further increasing the applied voltage leads to the formation of the bipolaron absorption peak (~ 950 nm), indicative of positive charges along the polymer backbone. This process could also be observed by naked eye, whereby the film absorbance changed from blue to transparent as the polymer became increasingly oxidised.

Similar trends were observed across the polymer series when comparing the onsets of oxidation in both acetonitrile (organic) and water (aqueous), notably oxidation onsets occurred at ~ 50 to

80 mV lower in water. This can be explained by the decreased size of the Cl⁻ anion (cf. PF₆⁻) in addition to the increased ion penetration due to enhanced hydration of the glycol chains in water.³⁹ The following table summarises the data obtained from both UV-Vis spectroscopy and cyclic voltammetry, including λ_{MAX} , optical bandgap, ionisation potential, electron affinity and onsets of oxidation:

Table 21. Summary of optoelectronic properties of the **p(gC_nT2-T)** series, including UV-Vis and CV extrapolated data sets.

Polymer	$\lambda_{\text{MAX}}^{\text{a}}$ (nm)	λ_{ONSET} (nm)	$E_{\text{opt}}^{\text{b}}$ (eV)	IP [CV] (eV)	EA ^c (eV)	E_{onset} [ACN](V)	E_{onset} [H ₂ O](V)
p(g ₄ T2-T)	561	638	1.94	4.30	2.36	-0.09	-0.14
p(gC ₄ T2-T)	562	645	1.92	4.28	2.36	-0.10	-0.15
p(gC ₆ T2-T)	566	644	1.93	4.31	2.38	-0.08	-0.16
p(gC ₈ T2-T)	559	645	1.92	4.34	2.42	-0.04	-0.10

^a λ is the peak of the first low energy absorption band of the polymers

^b E_{opt} estimated optical gap using onset of the thin-film absorption spectra $E_{\text{GAP}} = 1240 / \lambda_{\text{ONSET}}$

^cEA crudely estimated by subtraction of the UV-Vis absorption onset from IP ($EA = IP - E_{\text{opt}}$), a procedure that neglects the exciton binding energy

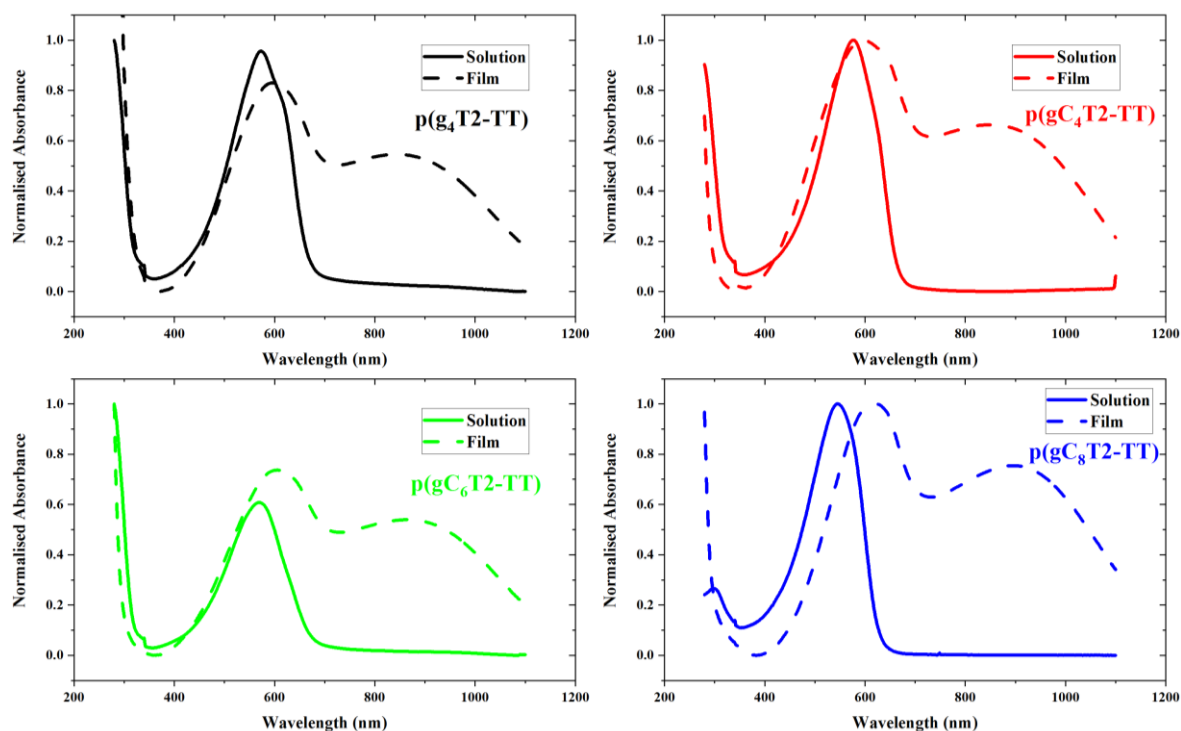
5.4.2 p(gC_nT2-TT) OPTOELECTRONICS

Figure 90. Normalised UV-Vis absorption spectra, solution (10 mg mL^{-1} chloroform) solid line and solid-state (thin film) dashed line, for the **p(gC_nT2-TT)** polymer series.

In a similar manner to the **p(gC_nT2-T)** series the co-thieno[3,2-*b*]thiophene polymers also show a distinctive bimodal distribution in the solid state, again owing to oxidation in the solid state forming the positive polaron (**Figure 92**). Again, little variation is seen between absorption profiles with **p(gC₈T2-TT)** being the notable exception, with a blue-shift in λ_{MAX} of almost 30 nm compared to the fully glycolated reference polymer. This also causes a shift in the onset, widening the optical bandgap to almost 2 eV, the broadest across both groups of materials, reducing the electron affinity by almost 0.2 eV compared to the rest of the series (**Table 22**).

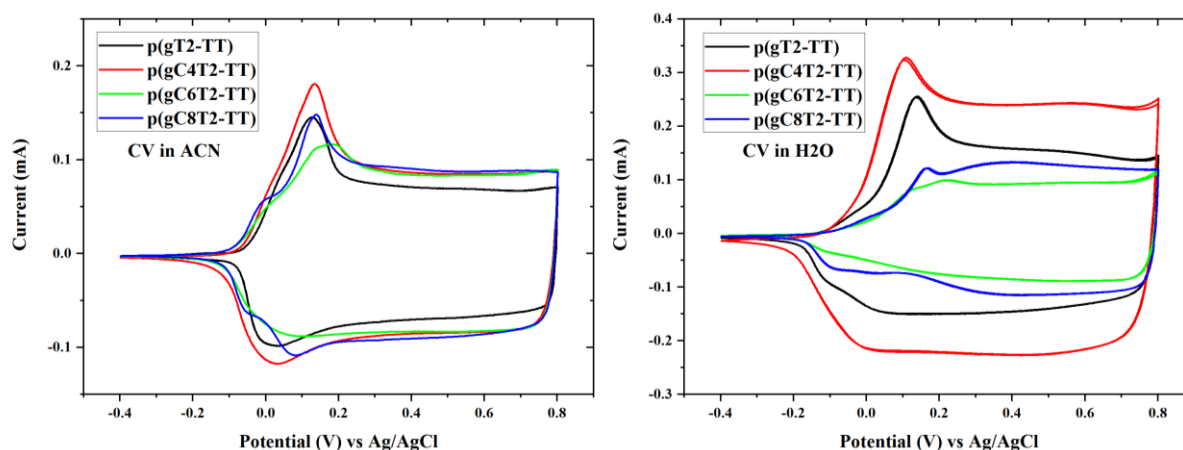


Figure 91. Cyclic voltammograms for **p(gC_nT2-TT)** series in 0.1 M NBu₄PF₆ acetonitrile solution (left) and aqueous 0.1 M NaCl solution (right) against an Ag/AgCl electrode.

As was the case above, ionisation potentials were obtained from cyclic voltammetry. Very little variation was also noted across the **p(gC_nT2-TT)** series, once again confirming the hybrid alkyl-glycol sidechains have a minimal effect on the HOMO energy level. The oxidation peaks for both the reference polymer and **p(gC₄T2-TT)** are relatively sharp, in aqueous electrolyte solution, compared to the extended alkyl spacer derivatives suggesting good reversibility. Peak sharpness follows the redshift trend (**Figure 90**) from the solid-state absorption spectrum, with CV traces become broader upon increasing the level of sidechain disorder as the alkyl spacer length is increased.

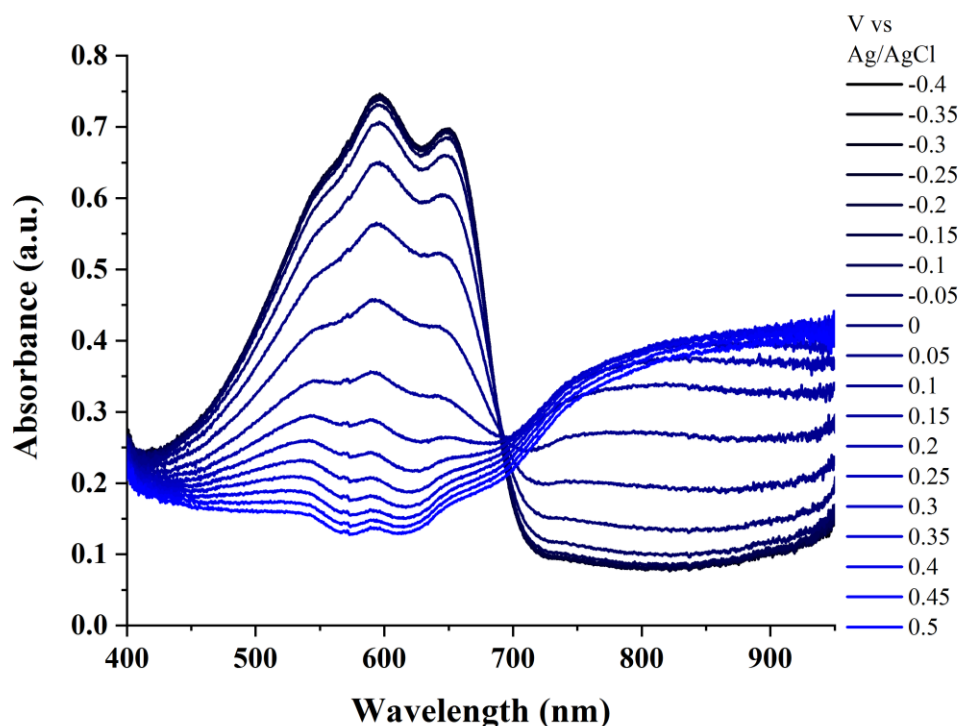


Figure 92. Spectroelectrochemical measurements from -0.4 V to 0.5 V for **p(g₄T₂-TT)**, recording absorption signals at 10 second intervals throughout the whole CV scan (180 seconds in total) obtained from films blade coated with 10 mg mL⁻¹ chloroform solutions.

The spectroelectrochemical absorption spectrum for **p(g₄T₂-TT)** follows a similar trend to **p(g₄T₂-T)** described above (**Figure 89**). The neutral absorption peak (~ 600 nm) reduces as a positive voltage is applied and the polymer oxidises, forming both the polaron and bipolaron species. Polaron absorption (~ 800 nm) reduces after charging over 0.4 V with bipolaron absorption max continuing to increase. Again, the film absorbance changed during the first charging cycle of the CV scan with an observable colour change of the film (by eye) from blue to transparent as the polymer was oxidised. Both **p(g₄T₂-TT)** & **p(g₄T₂-T)** polymers showed reversible oxidation/reduction and were stable across multiple cycles. Similar behaviour is expected for the hybrid alkyl-glycol functionalised materials however spectroelectrochemical measurements were unable to be obtained prior to the COVID-19 lockdown.

The reduction in ionisation potential (**Table 22**), albeit slight, upon increasing the length of the alkyl spacer unit could be that the anion (PF_6^-) can enter the film more readily due to an increase in disorder within the polymer chains and sidechains. The polar glycol chains could also increase anion mobility into the bulk, again in agreement with the reduced ionisation potential compared to the previously published fully alkylated **p(aT2-TT)** derivative (IP = 4.60 eV).⁵¹ This can also be explained by the reduced π - π stacking distance, imparted by glycol chains (**Section 1.4.5**), which is expected to persist despite the inclusion of an alkyl spacer unit.⁵² Indeed, the entire series follows the trend of a reduced IP compared to the alkylated derivative **p(aT2-TT)** which would suggest that the glycol units impart most of the optoelectronic differences, when the core is identical, compared to the alkyl portion. This is most likely due to the available lone pairs on the oxygen atoms which can interact with the polymer backbone, increasing the electron density. The donating capability of the alkyl chain cannot rival the contribution from the glycol units and hence the optoelectronics are more akin to the fully glycolated reference **p(g₄T2-TT)**.

Table 22. Summary of optoelectronic properties of the **p(gC_nT2-TT)** series, including UV-Vis and CV extrapolated data sets.

Polymer	$\lambda_{\text{MAX}}^{\text{a}}$ (nm)	λ_{ONSET} (nm)	$E_{\text{opt}}^{\text{b}}$ (eV)	IP [CV] (eV)	EA ^c (eV)	E_{onset} [ACN](V)	E_{onset} [H ₂ O](V)
p(g₄T2-TT)	573	674	1.84	4.30	2.46	-0.09	-0.15
p(gC₄T2-TT)	577	671	1.85	4.29	2.44	-0.10	-0.16
p(gC₆T2-TT)	570	696	1.78	4.26	2.48	-0.13	-0.16
p(gC₈T2-TT)	545	631	1.97	4.26	2.29	-0.12	-0.18

^a λ is the peak of the first low energy absorption band of the polymers

^b E_{opt} estimated optical gap using onset of the thin-film absorption spectra $E_{\text{GAP}} = 1240 / \lambda_{\text{ONSET}}$

^cEA crudely estimated by subtraction of the UV-Vis absorption onset from IP ($\text{EA} = \text{IP} - E_{\text{opt}}$), a procedure that neglects the exciton binding energy

5.4.3 GIWAXS MORPHOLOGICAL STUDY

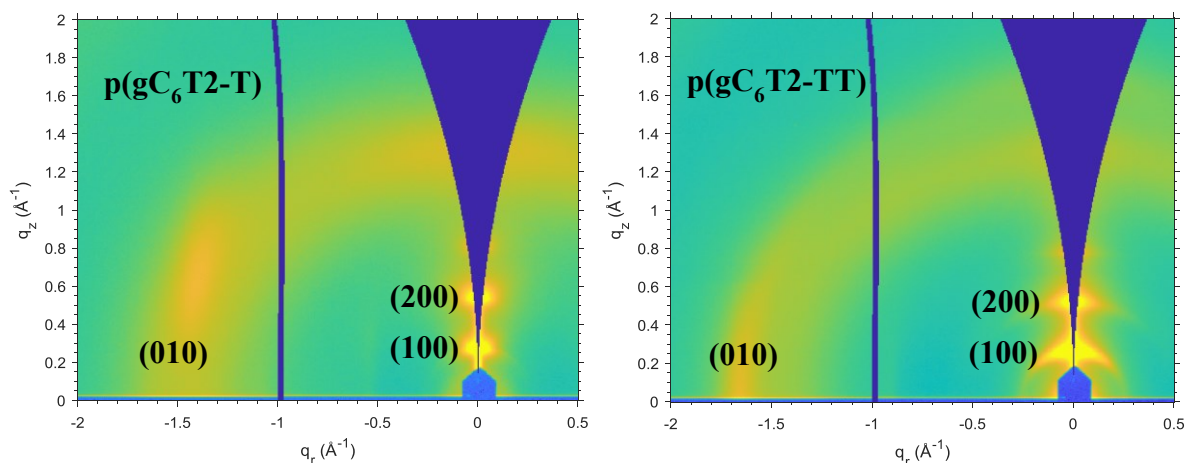


Figure 93. Grazing-incidence wide-angle X-ray scattering patterns for **p(gC₆T₂-T)** and **p(gC₆T₂-TT)** respectively, showing first order (100) lamellar peaks, second order (200) lamellar peaks and π - π stack peaks (010).

Grazing-incidence wide-angle X-ray scattering (GIWAXS) measurements were conducted for both the **p(gC_nT₂-T)** and **p(gC_nT₂-TT)** polymer series to investigate the morphological effects of altering the sidechain and backbone composition. Previous reports have shown that altering the co-monomer between thiophene and thienothiophene or exchanging alkyl for glycol sidechains respectively can have a marked impact on the overall polymer microstructure.^{52,55,66}

All polymers showed edge-on alignment of the polymer chains with strong first order out-of-plane lamellar peaks. Thiophene series **p(gC_nT₂-T)** polymers have higher lamellar spacing than the thienothiophene polymers **p(gC_nT₂-TT)** with the same hybrid alkyl-glycol chain length.

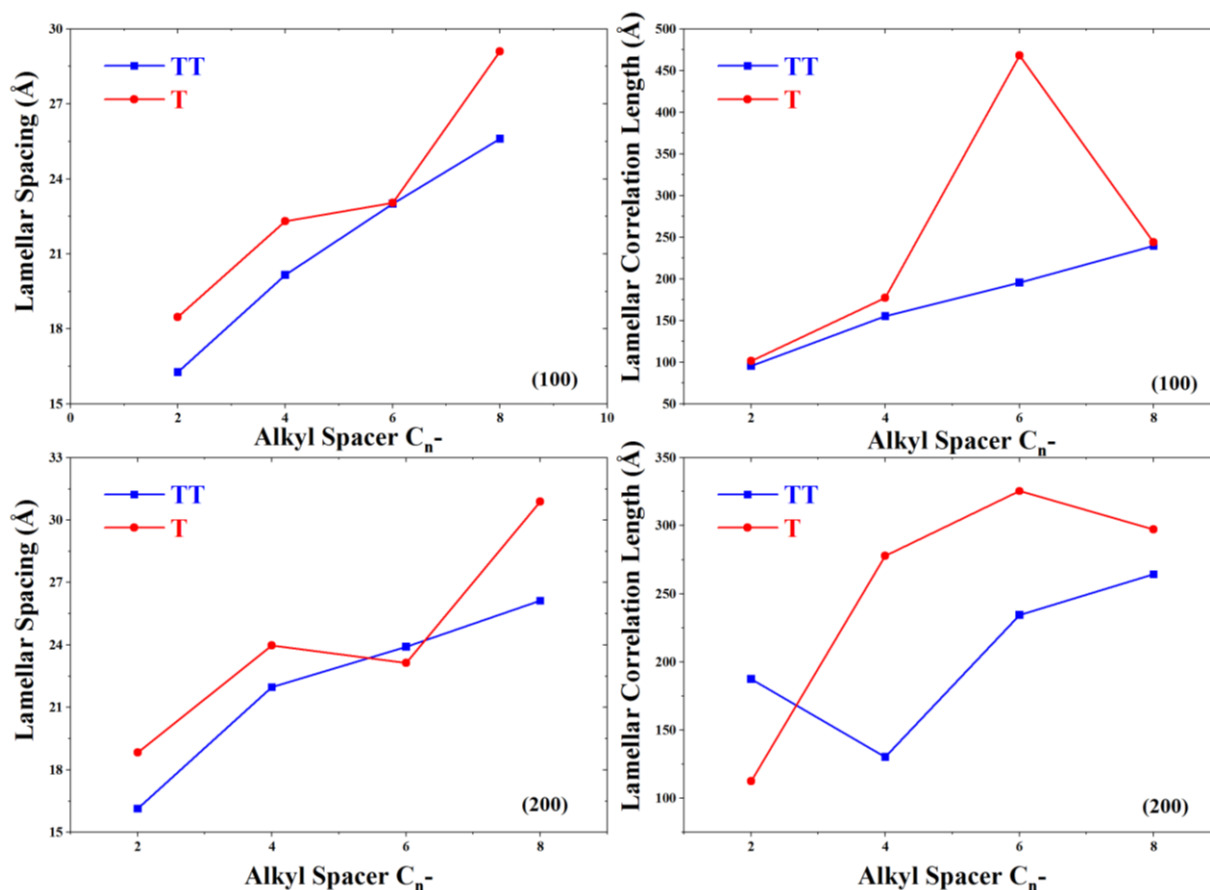


Figure 94. Lamellar spacing and lamellar correlation length trends for **p(gC_nT2-T)** (red plot) and **p(gC_nT2-TT)** (blue plot) polymer series for both first (100) and second (200) order lamellar peaks.

Upon increasing the length of the alkyl spacer (C_n-), the repulsion between glycol chains becomes weaker as the space between two adjacent polymer chains increases, across the series (n=2 to 8), the lamellar spacing rises from 16.3 Å to 25.6 Å for thienothiophene **p(gC_nT2-TT)** polymers. For thiophene **p(gC_nT2-T)** polymers, the lamellar spacing increases from 18.5 Å to 29.1 Å following the same trend of increasing alkyl spacer from C₂- to C₈- (**Figure 94**). Correlation length in the lamellar direction was calculated from peak width for all eight polymers. For the thienothiophene series, the correlation length also increases proportionally to the increase in alkyl spacer. The crystalline range changes from 5.9 repeat units to 9.4, when n is increased from 2 to 8. For the thiophene **p(gC_nT2-T)** series, the correlation length increases

as n increases from 2 to 6 and reaches a maximum. Notably the lamellar correlation length for **p(gC₆T₂-T)** is much larger than the thienothiophene analogue, which may be due to the double peak fitting of the GIWAXS pattern. The much lower result for **p(gC₈T₂-T)** would also suggest the previous to be an erroneous outlier, in general lamellar correlation lengths were consistent for both thiophene and thienothiophene backbones (**Figure 94**). Second order lamellar peaks (200) were also intense enough to be plotted and showed a similar trend to that of the first order peak. Although notable differences were observed between the $n=4$ and $n=6$ polymers, almost doubling the lamellar correlation length when altering the backbone from thienothiophene to thiophene.

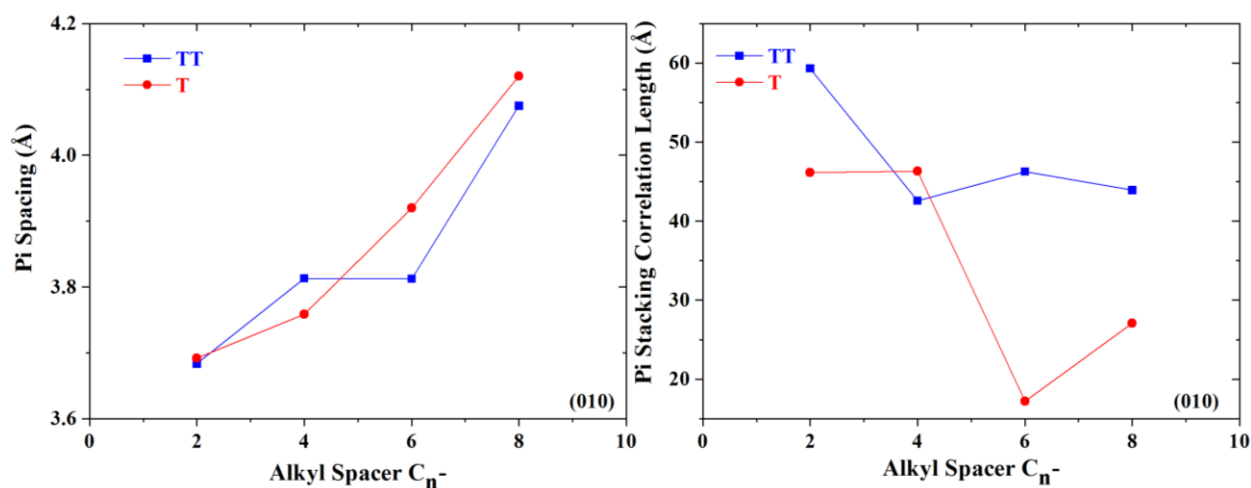


Figure 95. In-plane cut of GIWAXS patterns showing π -stacking trends for both **p(gC_nT₂-T)** (red plot) and **p(gC_nT₂-TT)** (blue plot) polymer series.

Backbone peaks (001) and π - π stack peaks (010) were clearly identified for all eight polymers. The backbone peaks were more intense for thiophene **p(gC_nT₂-T)** polymers compared to the thienothiophene **p(gC_nT₂-TT)** series showing a higher q -value. This correlates to a smaller backbone repeat length for thienothiophene series, matching the molecular structures. In addition, the trend in backbone repeat length increases slightly from 0.91 Å to 0.93 Å when the alkyl spacer is increased (from $n=2$ to 8).

Furthermore, upon increasing the length of the C_n- alkyl spacer π - π stacking spacing increases from 3.68 Å to 4.07 Å for the thiophene **p(gC_nT2-T)** polymers whilst the thienothiophene **p(gC_nT2-TT)** series increases from 3.69 Å to 4.12 Å. The π - π stacking correlation length decreases at the same time, for both thiophene and thienothiophene series, indicative of a higher degree of disorder along the π -stacking direction for longer hybrid alkyl-glycol sidechains (**Figure 95**).

5.5 OECT DEVICE PERFORMANCE

OECTs were kindly fabricated by M. Moser and T. Castillo, KAUST, Saudi Arabia, following a standard literature procedure²³ depositing **p(gC_nT2-T)** & **p(gC_nT2-TT)** polymers from chloroform solutions. A selection of graphs is shown below, specifically the best performing device from the **p(gC_nT2-T)** & **p(gC_nT2-TT)** series respectively, with the full dataset for each polymer reported in experimental section (**Section 6.4**). It should also be noted that each graph contains data from all six channels of the whole chip, denoted (C1-6), results from the best performing channel will be reported unless explicitly stated otherwise. Spectroelectrochemical (**Figure 89** & **Figure 92**) and specific capacity measurements were recorded by H. Yu (Nelson group) for the reference polymers **p(g₄T2-TT)** & **p(g₄T2-T)** respectively.

5.5.1 SPECIFIC CAPACITY

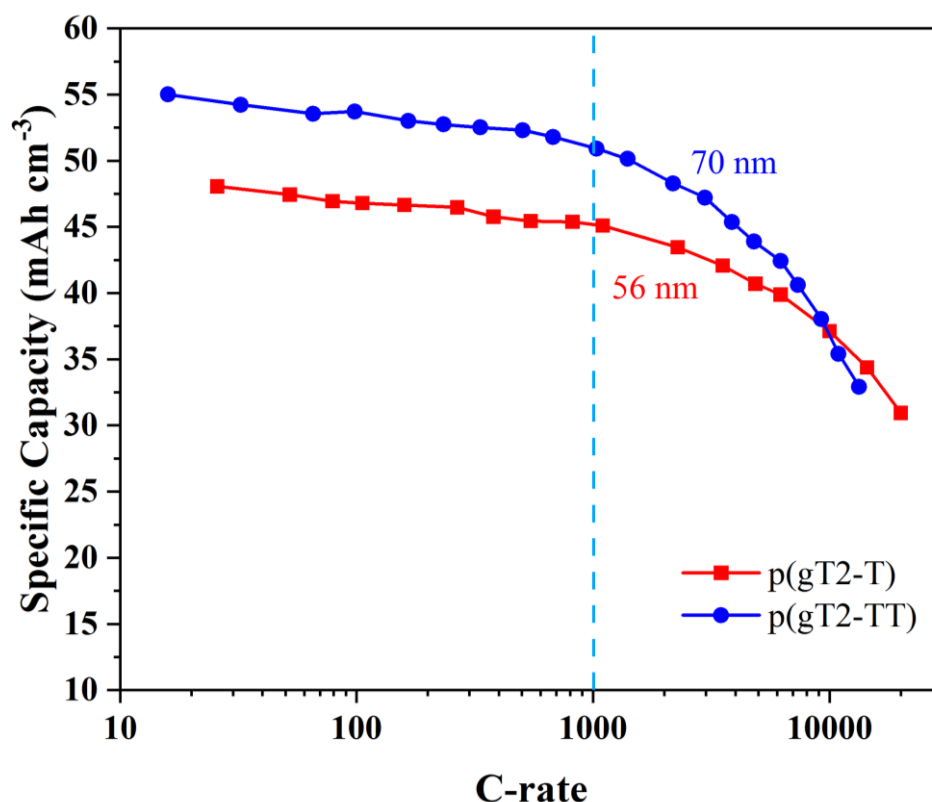


Figure 96. Specific capacity for **p(g4T2-TT)** & **p(g4T2-T)**, recorded as a function of C-rate at a constant current and voltage ranging from -0.4 V to 0.5 V.

Thin films of **p(g4T2-TT)** & **p(g4T2-T)** were blade coated from 10 mg mL⁻¹ chloroform solutions with average thicknesses of 69.63 nm and 56.00 nm, respectively. Specific capacity values were stable up to ~ 1000 C, with ~ 95% of low C-rate capacity remaining for both polymers. In addition, both films were still in visibly good conditions after the fastest charging/discharging cycles. This was further confirmed by both materials recovering the same original capacity when re-tested at a low charging/discharging rate. Interestingly **p(g4T2-TT)** with a larger relative volume occupied by backbone seems to have a larger specific capacity compared to the co-thiophene analogue. These results trump the specific capacity values for previously published *p*- and *n*-type materials.⁴⁹ This was an encouraging result but sadly only the two fully glycolated reference polymers were tested prior to the COVID-19 lockdown. Once laboratories reopen similar measurements will be recorded for the entire polymer series

in an attempt to elucidate a link between sidechain engineering and the magnitude or consistency of the specific capacity, which has been suggested to be sidechain dependant.⁴⁹

5.5.2 ELECTRICAL IMPEDANCE SPECTROSCOPY (EIS)

Electrochemical impedance spectroscopy can be used to determine the resistive ($0^\circ > \varphi > -45^\circ$) or capacitive ($-45^\circ > \varphi > -90^\circ$) nature of the conducting layer by recording the modulus of the impedance $|Z|$ and phase (φ) plotted as a function of frequency. Using the following equation:

$$Z = \sqrt{R^2 + \frac{1}{\omega C^2}} \quad (14)$$

where Z is the complex impedance, R is the resistance, $\omega = 2\pi f$ and C is the effective capacitance. The volumetric capacitance C^* can then be determined by dividing the value of capacitance at 0.1 Hz with the film volume (area x thickness).^{25,198}

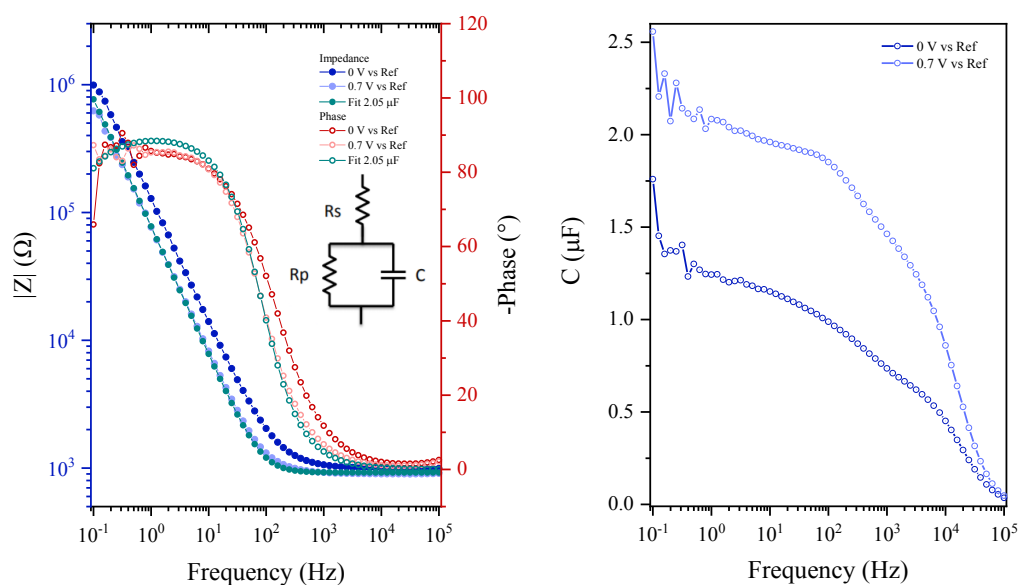


Figure 97. (left) Impedance spectra at different geometries for **p(gC₆T₂-T)**, where the OECT is used as the working electrode with source and drain contacts connected to each other. Complex impedance data is fitted to an $R_s(R_p||C)$ equivalent circuit (see inset), which

adequately described the frequency dependence for all six channels.²³ (right) Capacitance-frequency plots were constructed by using the complex impedance formula **Equation (14)**. The volumetric capacitance value for each system was extracted by determining the value of capacitance at 0.1 Hz and dividing it by the film volume (area x thickness).²⁵

For succinctness, only the electrochemical impedance spectroscopy (Bode plots) for **p(gC₆T₂-T)** are displayed in the main text, similar plots can be found within the respective experimental (**Section 6.4**). However, all polymers across both the co-thiophene and co-thieno[3,2-*b*]thiophene series exhibit similar behaviour. Application of a positive voltage offset (>0 V) leads to a saturation of the phase and effective capacitance with near ideal capacitive character ($\varphi \sim -90^\circ$) at low frequencies (**Figure 97**). This is in accordance with the literature data published for **p(g₂T-TT)** which also demonstrated the ability to accommodate a large modulation in the magnitude of effective capacitance.⁵¹

5.5.3 p(gC_nT₂-T) TRANSISTOR RESULTS

The six-carbon spacer hybrid alkyl-glycol polymer **p(gC₆T₂-T)** was the best performing device for this subseries, with a threshold voltage of ~ -0.182 V, an on/off ratio on the order of $\sim 10^6$ and a thickness normalised transconductance ($g_m \times (L/Wd)$) of 300.53 ± 15.59 S cm⁻³.

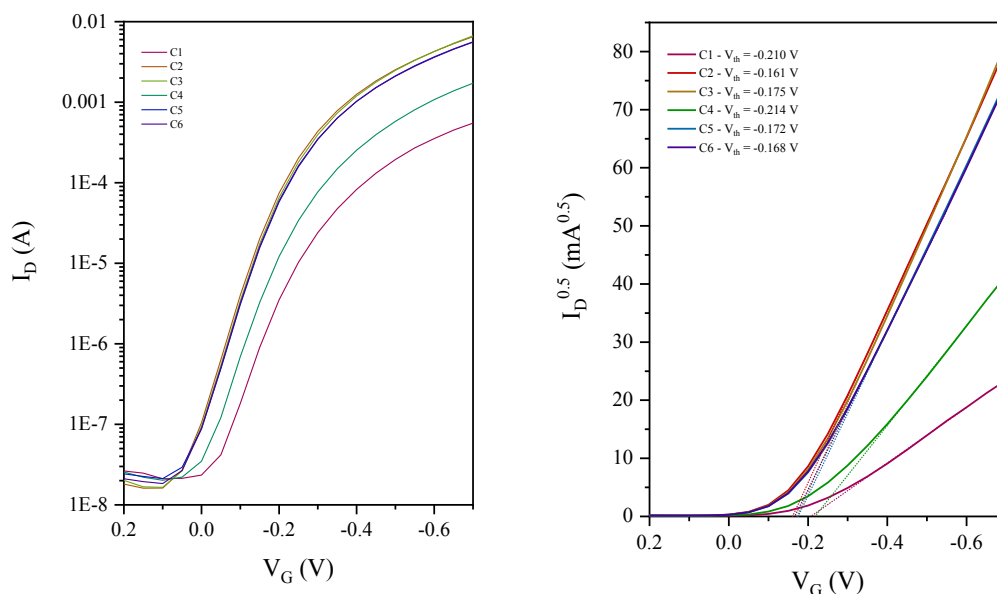


Figure 98. (left) Transfer curve for **p(gC₆T₂-T)** and (right) the square root of the drain current plotted as a function of gate voltage, following **Equation (1)** the tangent can be used to extract the threshold voltage (V_{th}).

Transconductance (g_m) is extracted from the transfer curve using **Equation (2)**, plotting this as a function of frequency response (**Figure 99**) supports the notion that OECT devices consist of two circuits.¹⁹⁹ This can be thought of as the ionic circuit, transporting ions between the electrolyte and the channel, and the electronic circuit, where holes are transported in the **p(gC_nT₂-T)** channel between the source and drain. From this the corresponding hole mobility can be extracted from bandwidth measurements to give a value of $0.240 \pm 0.020 \text{ cm}^2 \text{ V}^{-1} \text{ s}^{-1}$ for **p(gC₆T₂-T)**. These results are consistent with the literature value for the **p(g₂T-T)** backbone with an extracted hole mobility of $0.28 \pm 0.1 \text{ cm}^2 \text{ V}^{-1} \text{ s}^{-1}$.³⁹

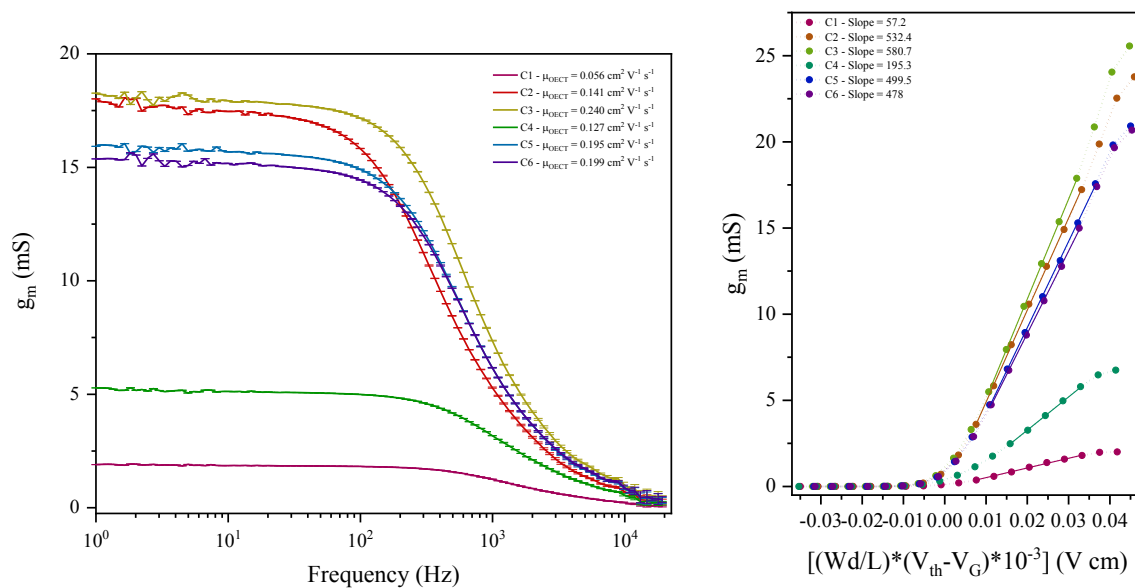


Figure 99. (left) Frequency dependence of transconductance allowing for the hole mobility to be extrapolated for each channel. (right) Transconductance (g_m) plotted as a function of $[(Wd/L) \times (V_{th} - V_G)]$ where the slope of the curve can be extracted to give μC^* .

As noted above (**Section 1.3.3**) the product μC^* in **Equation (3)** indicates the importance of balancing the electronic and ionic aspects of material performance and represents the common figure of merit for mixed conduction materials.²⁵ This value can be extracted in two ways, the first by taking the slope of transconductance (g_m) plotted as a function of $[(Wd/L) \times (V_{th} - V_G)]$ (**Figure 99**) and secondly by extrapolation from **Equation (3)** using the average thickness of the device.¹⁸⁷ For **p(gC₆T₂-T)** these values are in extremely good agreement with the slope of (**Figure 99**) giving $\mu C^* = 580.7 \text{ F cm}^{-1} \text{ V}^{-1} \text{ s}^{-1}$ and using the average thickness (measured with a profilometer) of $59.69 \pm 3.8 \text{ nm}$ with **Equation (3)** affords $\mu C^* = 572.54 \pm 29.82 \text{ F cm}^{-1} \text{ V}^{-1} \text{ s}^{-1}$. Each polymer was investigated in an identical manner and analysed following the method outline above. The following table summarises the transistor results for the entire **p(gC_nT₂-T)** series:

Table 23. Summary table for each OEET device, taking the results from the best performing channel for each polymer in the **p(gC_nT2-T)** series, respectively.

	p(g₄T2-T)	p(gC₄T2-T)	p(gC₆T2-T)	p(gC₈T2-T)
Thickness (nm)	75.93 ± 2.66	44.77 ± 5.89	59.69 ± 3.8	69.12 ± 10.5
On/Off	~10 ⁶	~10 ⁶	~10 ⁶	~10 ⁶
Threshold Voltage [V_{th}] (V)	-0.125	-0.126	-0.183	-.307
Normalised g_m [g_m×(L/Wd)] (S cm⁻¹)	210.06 ± 6.02	234.28 ± 25.38	300.53 ± 15.59	71.03 ± 8.38
μ (cm² V⁻¹ s⁻¹)	0.143 ± 0.003	0.176 ± 0.013	0.240 ± 0.020	0.078 ± 0.003
C* (F cm⁻³)	212.46 ± 6.87	196.6 ± 53.28	138.75 ± 33.81	180.16 ± 41.81
μC* [from slope] (F cm⁻¹ V⁻¹ s⁻¹)	445.8	467.7	580.7	81.67
μC* [from Eq. (3)] (F cm⁻¹ V⁻¹ s⁻¹)	319.25 ± 9.15	408.15 ± 44.22	572.54 ± 29.82	144.96 ± 17.1

Simply, looking at the main figure of merit²⁵ μC* there is a clear increase in performance upon moving from the reference fully glycolated polymer, increasing the carbon spacer and peaking product μC* for **p(gC₆T2-T)** before dipping to the lowest performer within the series **p(gC₈T2-T)**. Both mobility and thickness normalised transconductance follow this trend, however interestingly the volumetric capacitance peaks for **p(g₄T2-T)**, then upon increasing the level of alkylation dips from C₄- to C₆- before recovering for **p(gC₈T2-T)**. Despite this the limiting factor for the octyl spacer is the extremely poor hole mobility leading to a poor μC* = 144.96 ± 17.1 F cm⁻¹ V⁻¹ s⁻¹. These results would suggest that the alkyl sheath is having the desired effect on the polymer series up to a hexyl spacer before starting to hinder performance for the octyl version. The alkyl spacer is protecting the backbone facilitating efficient mobility along the conjugated thiophenes whilst the hydrophilic glycol chains facilitate ion penetration, as noted by the improved transconductance. This is further supported by the GIWAXS

measurements (Section 5.4.3) which show a primarily edge-on orientation for **p(gC₆T2-T)** which is expected to increase charge transport in the plane of the substrate.²⁹

5.5.4 p(gC_nT2-TT) TRANSISTOR RESULTS

Table 24. Summary table for each OECT device, taking the results from the best performing channel for each polymer in the **p(gC_nT2-TT)** series, respectively.

	p(g₄T2-TT)	p(gC₄T2-TT)	p(gC₆T2-TT)	p(gC₈T2-TT)
Thickness (nm)	33.163 ± 3.147	62.01 ± 3.37	34.02 ± 3.59	31.82 ± 1.01
On/Off	~10 ⁶	~10 ⁶	~10 ⁶	~10 ⁵
Threshold Voltage [V_{th}] (V)	-0.069	-0.114	-0.169	-0.311
Normalised g_m [g_m×(L/Wd)] (S cm⁻¹)	346.81 ± 26.99	77.26 ± 3.43	193.73 ± 10.24	17.28 ± 0.45
μ (cm² V⁻¹ s⁻¹)	0.256 ± 0.012	0.098 ± 0.005	0.168 ± 0.012	0.023 ± 0.003
C* (F cm⁻³)	245.45 ± 17.36	117.33 ± 14.54	239.34 ± 19.67	214.2 ± 21.22
μC* [from slope] (F cm⁻¹ V⁻¹ s⁻¹)	749.5	193.1	425.2	81.67
μC* [from Eq. (3)] (F cm⁻¹ V⁻¹ s⁻¹)	589.81 ± 45.90	143.08 ± 6.37	366.27 ± 36.35	71.41 ± 1.85

Each polymer shows a sharp turn-on, with low threshold voltages (V_{th}) in the range of ~ -0.1 → -0.3 V, which combined with the range of operation in aqueous media |V_G| < 0.6 V suggests bulk doping dominates, hence pure OECT operation.⁵¹ However, the results from the **p(gC_nT2-TT)** series are much more inconclusive, with the reference fully glycolated polymer **p(g₄T2-TT)** clearly outperforming the rest of the materials, a very different trend than the above co-thiophene polymers. Despite this, of the hybrid alkyl-glycol functionalised polymers again the C₆-spacer derivative was again the best performing polymer. This is a very interesting finding

which suggests, as expected, that a balance must be met between the degree of alkylation and total glycol content.

The volumetric capacitance for **p(gC₆T₂-TT)** was calculated to be $C^* = 239.34 \pm 19.67 \text{ F cm}^{-3}$, which is over six times the value recorded for **PEDOT:PSS** ($39.3 \pm 1.3 \text{ F cm}^{-3}$).²⁴ This dramatic increase is due to the increased density of redox active sites; for **p(gC₆T₂-TT)** each individual polymer chain is redox active whereas for **PEDOT:PSS** a large portion of the active layer is made up of redox inert polyelectrolytes (PSS⁻) which dilutes the total redox active sites hence a lower volumetric capacitance. The relatively high volumetric capacitance of the **p(gC_nT₂-TT)** series supports the notion that these polymers can stabilise both a polaron and bipolaron.⁶⁶

Extracted mobility values were moderately high across the entire series, again the **p(gC₆T₂-TT)** polymer performs generally well and a significant dip in performance is seen when extending the alkyl-spacer to the **p(gC₈T₂-TT)** polymer. This drastic ~ 7 -fold decrease in mobility is in line with the results for **p(gC₈T₂-T)** which shows an ~ 3 -fold decrease in mobility, from the C₆- analogue. This trend was seen across each channel and demonstrates that even a small difference in the overall alkyl content can significantly hamper the ability to transport charge between the polar and non-polar sidechain regime. Mobility trends are mirrored by the π -stacking correlation length (**Figure 95**) GIWAXS measurements and the impressive mobility of **p(g₄T₂-TT)** ($0.256 \text{ cm}^2 \text{ V}^{-1} \text{ s}^{-1}$) could be explained by the dominate edge-on orientation.²⁹

It is difficult to form a conclusive argument based on this initial set of results for the **p(gC_nT₂-TT)** series, the fully glycolated reference polymer **p(g₄T₂-TT)** outperforms the rest of the series by a factor of $\sim 1.7 \rightarrow 9.2$ for the respective product [μC^*] values. This would suggest that the non-polar alkyl sheath has a negative effect on the overall device performance, indeed every

important aspect, transconductance, mobility and volumetric capacitance, decreases across the board when the hybrid alkyl-glycol sidechain is used. This could be linked to several different factors, firstly the average molecular weights (M_n) of this series are relatively low, despite being comparable to literature **p(gT2-TT)**,⁵¹ and this has been shown in multiple studies to negatively affect device performance parameters, such as limiting mobility in **P3HT**.²⁰⁰

From these initial transistor results it is difficult to form a concrete argument towards a blanket optimal design strategy however, both **p(gC_nT2-TT)** and **p(gC_nT2-T)** series seem to benefit from the inclusion of a C₆-alkyl spacer between the polymer backbone and the polar ethylene glycol chain. More work will need to be done to support these preliminary tests and determine whether the benefits of an alkyl sheath outweigh the negatives, clearly even the slightest change in alkyl content has a large impact on the device performance figures of merit.

5.5.5 STABILITY MEASUREMENTS

The long-term stability of each device was analysed by applying a constant V_D of -0.6 V and V_G pulses between 0 V \rightarrow -0.6 V (5 second duration). Most devices showed a significant decrease in drain current after an hour under stress, the reference fully glycolated **p(g₄T2-TT)** demonstrated the best prolonged stability across the entire series, with the ON current only dropping to \sim 40% of the initial current after 2 hours of pulsing (**Figure 100**).

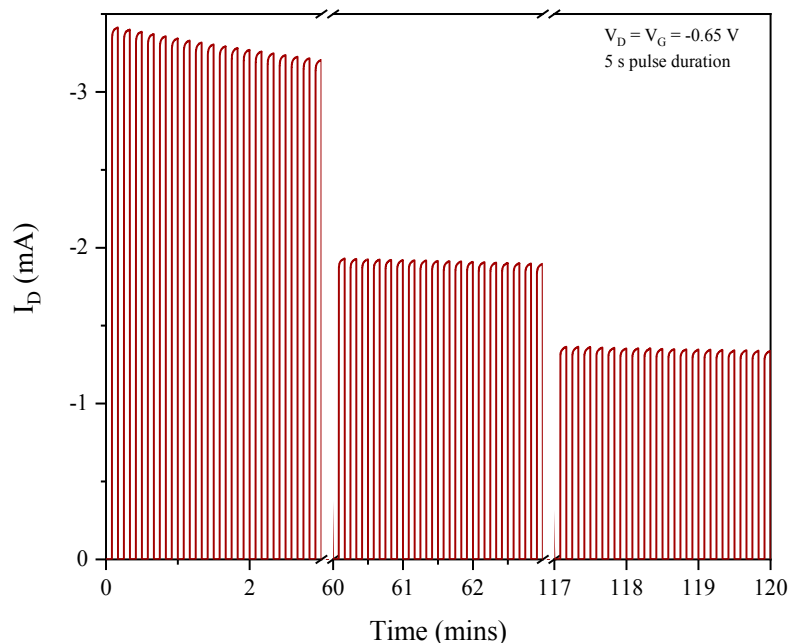


Figure 100. Change in drain current (I_D) over time for a $100 \mu\text{m} \times 10 \mu\text{m}$ **p(g4T2-TT)** OEET, with $V_D = -0.65 \text{ V}$ and V_G pulsed between $0 \text{ V} \rightarrow -0.6 \text{ V}$, measuring the long-term stability. The same long-term stability was not observed for the rest of the polymer series, except for **p(gC4T2-TT)** which showed moderate stability after 60 minutes. The remaining polymers all exhibited rapid decreases in drain current upon stressed pulsing at $V_D = -0.65 \text{ V}$, this could be attributed to polymers being in a highly oxidised state with a large proportion of bipolaron species, known to have reduced stability in aqueous mediums.⁴⁹ Previous reports have also suggested that decomposition pathways, where water molecules can interact with the positively charged oxidised polymer, can lead to an exponential decay in device performance upon pulsing at negative voltages.^{49,201} This limited stability is not uncommon for *p*-type accumulation mode materials^{39,51,66}, with the electron-rich thiophene and thieno[3,2-*b*]thiophene cores being known to oxidise easily under ambient conditions. These results would suggest that the hybrid alkyl-glycol sidechain motif does not impart any additional stability to the polymer system, a factor which must be carefully considered for potential use in circuits and sensing devices.

5.6 CONCLUSION

Two series of bithiophene copolymers were prepared with varying alkyl spacer lengths between the polymer backbone and the polar ethylene glycol sidechains, coupled with unfunctionalised thiophene and thieno[3,2-*b*]thiophene, respectively. Each series comprised of four polymers, totalling eight, starting with a fully glycolated reference then increasing the length of the alkyl-spacer in increments of two carbon units, affording C₄-, C₆- and C₈- spaced materials. Each OECT device was investigated by electrochemical impedance spectroscopy displaying near ideal capacitive character ($\varphi \sim -90^\circ$) at low frequencies. Across the six channels, transconductance, impedance and ON current measurements were collected allowing for the figures of merit; thickness normalised transconductance, hole mobility, volumetric capacitance and importantly the product [μC^*] values to be calculated.

The inclusion of the hybrid alkyl-glycol sidechain was proposed to marry together the mutual benefits of both the non-polar and polar chains. Indeed, for the **p(gC_nT2-T)** series a clear increase in OECT performance was observed upon including an alkyl-spacer between the polymer backbone and the polar glycol sidechain. All product [μC^*] figures of merit were increased from the reference polymer peaking for **p(gC₆T2-T)**, which showed high (thickness normalised) transconductance ($g_m \times (L/Wd)$) of $300.53 \pm 15.59 \text{ S cm}^{-3}$), moderate volumetric capacitance and good hole mobility ($0.240 \pm 0.020 \text{ cm}^2 \text{ V}^{-1} \text{ s}^{-1}$). Performance then dipped drastically upon further increasing the alkyl spacer to the octyl version, notably this trend was also reciprocated for the **p(gC_nT2-TT)** series.

The same overall trend in OECT device performance wasn't observed for the **p(gC_nT2-TT)** series, with the fully glycolated reference polymer outperforming the hybrid alkyl-glycol functionalised materials. This could be due to the increased level of disorder imparted upon the system due to the flexible nature of the alkyl spacer units. Average molecular weights (M_n)

were also relatively low which could lead to a decrease in both mobility and overall device output. Despite this, as was the case within the **p(gC_nT2-T)** series the C₆-alkyl spacer polymer was the highest performing material of the hybrid alkyl-glycol functional polymers. These results would suggest that a moderate degree of alkylation can be employed to positively affect the device performance, but a conclusive statement cannot be made without further investigation.

In summary the evidence presented above suggests that for certain polymer backbones (e.g. thiophene) the inclusion of a hybrid alkyl-glycol mixed polarity sidechain can lead to an increase in OECT device performance. This work also demonstrates that the benefits of non-polar alkyl chains can be coupled with the capacitive enhancements from polar glycol chains whilst maintaining the bulk doping OECT behaviour. Sidechain engineering is a plausible method to alter multiple optoelectronic and transistor properties of the resultant polymer, apparent with even the smallest changes in the overall alkyl-content or system disorder. However, this trend is highly dependent on a multitude of factors and thus cannot simply be used as an effective blanket strategy when designing new *p*-type mixed conduction materials.

CHAPTER SIX – EXPERIMENTAL

6.1 METHODS & MATERIALS

6.1.1 GENERAL

All chemicals were purchased from commercial suppliers (Sigma Aldrich or VWR Scientific) unless otherwise specified. Column chromatography was conducted with silica gel for flash chromatography supplied from VWR Scientific. ^1H - and ^{13}C -NMR spectra were obtained on a Bruker AV-400 spectrometer at 298 K and are reported in ppm relative to a TMS chemical shift reference. Deuterated solvents were purchased from Sigma Aldrich. UV-Vis absorption spectra were recorded on a UV-1601 UV-Vis spectrometer at 298 K. MALDI-ToF mass spectroscopy was performed on a Micromass MALDI μ TOF using trans-2-[3-(4-tert-butylphenyl)-2-methyl-2-propenylidene]malononitrile (DCTB) as the matrix.

Density functional theory (DFT) and electronic structure calculations were performed using Gaussian09 Revision C.01 software²⁰² by Dr. Karl Thorley and are reproduced with his permission. Density functional theory (DFT) calculations were performed with the range-separated ω B97XD functional, where the ω value was tuned to minimise the difference between ionisation potential and the highest occupied molecular orbital (HOMO) energy. Calculations based on electron spin used Hartree-Fock theory, since DFT is known to suffer from spin contamination problems.²⁰³ Energies of singlet excited states were calculated using time dependent DFT (TD-DFT) whereas higher multiplicities were calculated as differences in total energy compared to the ground state. All calculations were performed on geometries optimised for the singlet ground state.

6.1.2 ELECTROCHEMICAL CHARACTERISATION

Cyclic voltammetry was recorded using an PGSTAT101 with a standard working (ITO glass slide or polymer coated platinum disk electrode), reference (Ag/Ag⁺ calibrated against ferrocene (Fc/Fc⁺)) and counter electrode (platinum mesh) setup. Measurements were

conducted in degassed 0.1 M tetra-*n*-butylammonium hexafluorophosphate (NBu₄PF₆) anhydrous acetonitrile solution (organic) or a 0.1 M NaCl aqueous solution as the supporting electrolyte at a scan rate of 100 mV/s. Prior to organic CV measurements in acetonitrile, all glassware was oven dried at 100 °C, the cell was purged with nitrogen during the experiment to reduce oxygen contamination. Ionisation potentials (IP) were obtained using the equation $IP = (E_{ox} - E_{Fc/Fc^+} + 4.8V)$ where appropriate electron affinities (EA) were calculated from the onset of the first reduction using equation $EA = -(4.8 + E_{red} - E_{Fc/Fc^+})$.

Galvanostatic measurements were performed by applying a sequence of charging and discharging constant current levels, recording the change in voltage of the sample. The following equations were subsequently utilised: specific capacity = (current x time) / film volume and C-rate (hr⁻¹) = 1 / time where current is the applied current and time (in hours) taken for the 2nd charging process (totalling 3 charges for each applied current). Detailed methods can be found within the literature.⁴⁹

Electrochemical impedance spectroscopy (EIS) was kindly performed by Tania Hidalgo using a conventional three electrode setup using a potentiostat, platinum reference and Ag/AgCl counter electrode. A gold electrode covered with a thin layer of polymer was the working electrode using a 0.1 M NaCl aqueous solution as the electrolyte. Effective capacitance (C) was extracted by approximating $C \sim 1/(2\pi f \text{Im}(Z))$ where *f* is the frequency, and *Z* is the complex impedance taken from **Equation (14)**. The capacitance was fit to an equivalent R(R||C) circuit allowing for the volumetric capacitance (C*) to be determined by dividing the value of capacitance (at 0.1 Hz) by the film volume (area x thickness), adapted from literature.^{25,198}

6.1.3 THERMOELECTRIC: CONDUCTIVITY & SEEBECK MEASUREMENTS

Each device was fabricated using glass substrates which were sequentially cleaned in acetone, water and isopropanol and finally dried under nitrogen. Polymers were dissolved in

dichlorobenzene at a concentration of 5 mg ml⁻¹ alongside a 1.35 mg ml⁻¹ solution of N-DMBI, also in dichlorobenzene, before subsequently being mixed at 3, 9, 15, 25 and 50 mol.% volume ratios, respectively. Mixtures were then stirred at 70 °C for ~ one hour until the polymer was fully dissolved. Solutions were spin-coated onto the clean glass substrates at 1000 rpm for 30 seconds. Films were subsequently thermally annealed at 110 °C, under a nitrogen atmosphere, before being allowed to cool naturally to room temperature.

For conductivity measurements, gold (Au) electrodes with a titanium (Ti) adhesion layer (length = 30 µm, width = 1000 µm) were deposited onto the glass substrates prior to polymer deposition. Electrical conductivity measurements were obtained by operating inside a nitrogen filled glove box using a semiconductor parameter analyser (Keithley 4200-SCS). The temperature gradient (ΔT) was applied across the sample by a pair of Peltier modules, the resultant thermal voltage (ΔV) was investigated between two separate electrodes. The Seebeck coefficient was calculated from the slope of ΔV recorded as a function of various ΔT values, following the equation $S = -(\Delta V/\Delta T)$. This section and procedure was adapted from literature.²⁰⁴

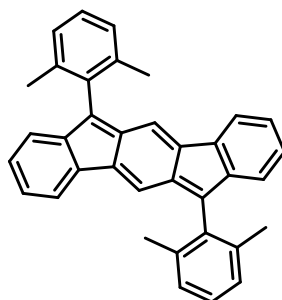
6.1.4 TRANSISTOR FABRICATION & ANALYSIS

OECTs were fabricated photolithographically using the parylene peel-off process, the detailed cleaning and modulation is described in depth within the literature.^{23,198} All polymers were spun cast at 1000 rpm from 5 mg mL⁻¹ chloroform solutions. Following film deposition, the sacrificial parylene C layer was peeled off. The resultant OECT chip contained six channels with identical geometry (W= 100 µm, L= 10 µm) and similar film thicknesses which were measured using a Dektak Profilometer, found to be between 31 nm and 76 nm. A frequency dependant approach was applied to extract the hole transit time and subsequent OECT hole mobility, this method alongside how to extract transconductance, threshold voltage, gate

current and drain current are described in depth by Rivnay *et al.*²⁰⁵ Final analysis was conducted using MATLAB and plotted with Origin.

6.2 CHAPTERS TWO & THREE SYNTHESIS & CHARACTERISATION

6.2.1 6,12-bis(2,6-dimethylphenyl)indeno[1,2-*b*]fluorene (DX-IDF)¹⁰³



Following a modified literature procedure¹⁰³ 2-bromo-*m*-xylene (1.42 mL, 10.6 mmols, 6.0 eq.) was dissolved in dry THF (30 mL), degassed with Ar and cooled to -78 °C for 15 minutes. *n*-BuLi (2.5 M in hexane, 5.52 mL, 8.85 mmols, 5.0 eq.) was added to the cold mixture and stirred for 30 minutes. In a second flask, indeno[1,2-*b*]fluorene-6,12-dione 2 (0.50 g, 1.77 mmols, 1.0 eq.) was dissolved in dry THF (30 mL) cooled to -78 °C and degassed with Ar for 30 minutes. The cold lithiate solution was transferred by cannula to the dione mixture and subsequently warmed to room temperature for 2 hours. The reaction mixture was quenched with 10% HCl solution (10 mL), extracted with Et₂O (100 mL), water (100 mL) and brine (100 mL). The organic layer was dried over anhydrous magnesium sulphate, filtered and evaporated to dryness.

The crude diol was dissolved in a solution of DCM (5 mL) and hexane (50 mL), filtered under suction, redissolved in DCM (50 mL) and evaporated to dryness to remove xylene-based impurities. Solid dissolved in toluene (50 mL) degassed with Ar before SnCl₂ (1.34 g, 7.08 mmols, 4.0 eq.) was added and stirred at 65 °C overnight. The solution was washed with

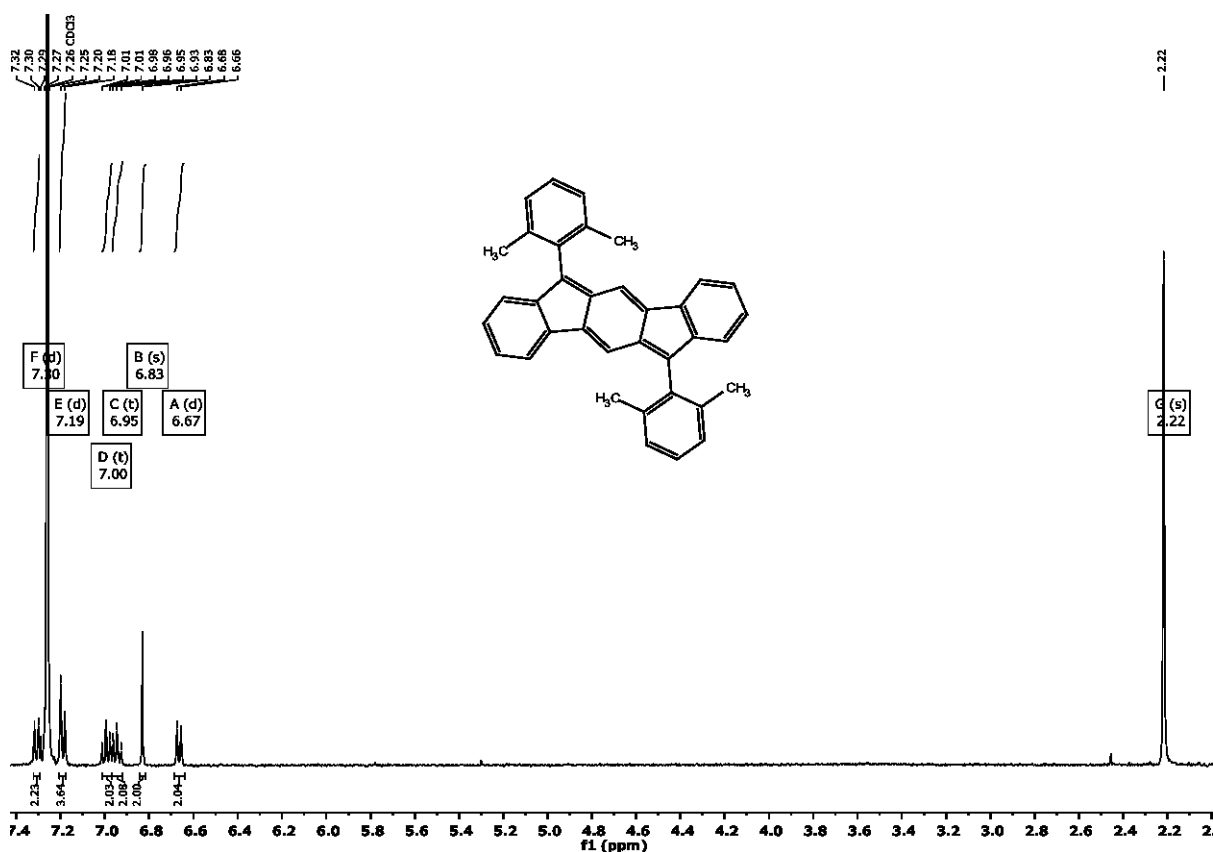
toluene, water and brine then filtered and the filtrate evaporated to dryness. The crude oil product was recrystallized from a minimal amount of 2-butanone to afford DX-IDF (0.71 g, 88%) as a brown metallic solid.

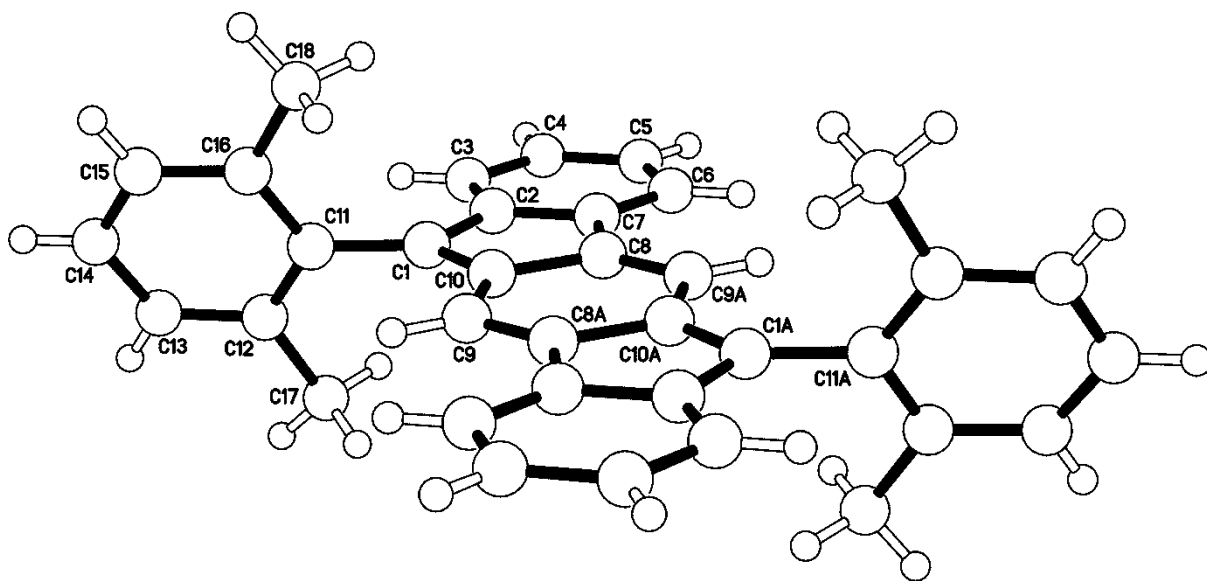
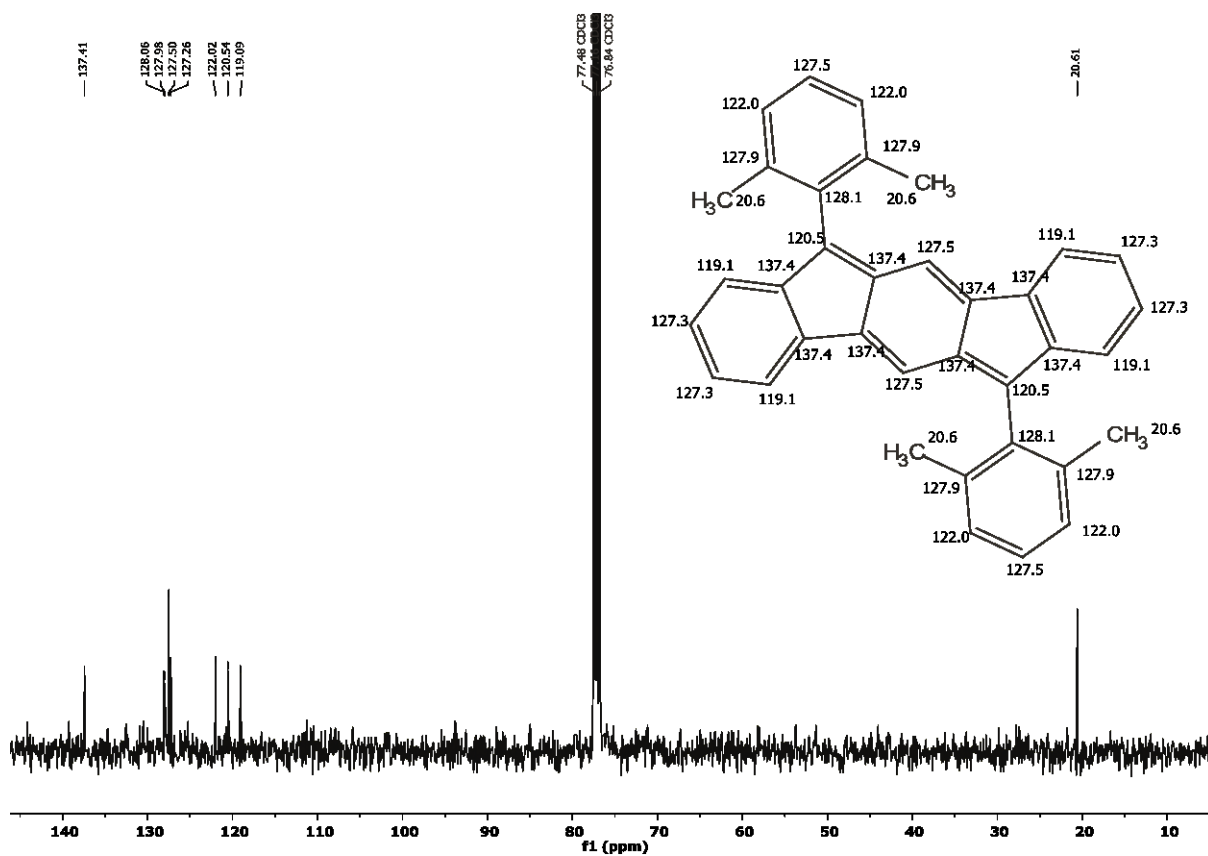
^1H NMR (400 MHz, CDCl_3): δ 7.30 (d, $J = 6.9$ Hz, 2H), 7.19 (d, $J = 7.6$ Hz, 4H), 7.00 (t, $J = 6.9$ Hz, 2H), 6.95 (t, $J = 7.6$ Hz, 2H), 6.83 (s, 2H), 6.67 (d, $J = 7.6$ Hz, 2H), 2.22 (s, 12H).

^{13}C NMR (101 MHz, CDCl_3) δ 137.41, 128.06, 127.98, 127.50, 127.26, 122.02, 120.54, 119.09, 20.61.

UV-Vis (CH_2Cl_2) λ_{max} : 516 nm.

Mass (MALDI-ToF): 460.9 $[\text{M}+\text{H}]^+$ (calc. 460.6 $\text{C}_{36}\text{H}_{28}$).





Crystal data and structure refinement for IM1709 (DX-IDF).

Identification code	IM1709
Formula	C ₃₆ H ₂₈
Formula weight	460.58
Temperature	173(2) K
Diffractometer, wavelength	Agilent Xcalibur PX Ultra A, 1.54184 Å
Crystal system, space group	Monoclinic, P2 ₁ /c

Unit cell dimensions	$a = 13.2440(5) \text{ \AA}$	$\alpha = 90^\circ$
$b = 7.3323(3) \text{ \AA}$	$\beta = 109.276(4)^\circ$	
$c = 13.7576(6) \text{ \AA}$	$\gamma = 90^\circ$	
Volume, Z	$1261.11(10) \text{ \AA}^3, 2$	
Density (calculated)	1.213 Mg/m^3	
Absorption coefficient	0.516 mm^{-1}	
$F(000)$	488	
Crystal colour / morphology	Dark red plates	
Crystal size	$0.39 \times 0.12 \times 0.09 \text{ mm}^3$	
\square range for data collection	$3.535 \text{ to } 73.803^\circ$	
Index ranges	$-16 \leq h \leq 15, -8 \leq k \leq 8, -11 \leq l \leq 16$	
Reflns collected / unique	$3976 / 2423$ [$R(\text{int}) = 0.0356$]	
Reflns observed [$F > 4 \square(F)$]	1797	
Absorption correction	Analytical	
Max. and min. transmission	0.959 and 0.902	
Refinement method	Full-matrix least-squares on F^2	
Data / restraints / parameters	$2423 / 0 / 165$	
Goodness-of-fit on F^2	1.036	
Final R indices [$F > 4 \square(F)$]	$R1 = 0.0486, wR2 = 0.1204$	
R indices (all data)	$R1 = 0.0696, wR2 = 0.1390$	
Largest diff. peak, hole	$0.397, -0.180 \text{ e\AA}^{-3}$	
Mean and maximum shift/error	0.000 and 0.000	

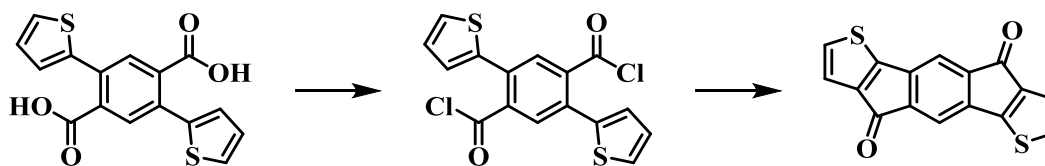
 Bond lengths [\AA] and angles [$^\circ$] for IM1709 (**DX-IDF**).

C(1)-C(10)	1.383(3)
C(1)-C(2)	1.465(3)
C(1)-C(11)	1.484(3)
C(2)-C(3)	1.394(3)
C(2)-C(7)	1.414(3)
C(3)-C(4)	1.394(3)
C(4)-C(5)	1.389(3)
C(5)-C(6)	1.398(3)
C(6)-C(7)	1.385(3)
C(7)-C(8)	1.471(2)
C(8)-C(9)#1	1.353(3)
C(8)-C(10)	1.468(3)
C(9)-C(8)#1	1.353(3)
C(9)-C(10)	1.439(3)
C(11)-C(12)	1.406(3)
C(11)-C(16)	1.410(3)
C(12)-C(13)	1.396(3)

C(12)-C(17)	1.507(3)
C(13)-C(14)	1.379(4)
C(14)-C(15)	1.381(4)
C(15)-C(16)	1.394(3)
C(16)-C(18)	1.506(3)
C(10)-C(1)-C(2)	107.83(16)
C(10)-C(1)-C(11)	129.00(17)
C(2)-C(1)-C(11)	123.17(15)
C(3)-C(2)-C(7)	120.10(17)
C(3)-C(2)-C(1)	130.83(17)
C(7)-C(2)-C(1)	109.07(15)
C(2)-C(3)-C(4)	118.81(18)
C(5)-C(4)-C(3)	120.95(18)
C(4)-C(5)-C(6)	120.69(18)
C(7)-C(6)-C(5)	118.81(18)
C(6)-C(7)-C(2)	120.64(17)
C(6)-C(7)-C(8)	132.04(17)
C(2)-C(7)-C(8)	107.31(16)
C(9)#1-C(8)-C(10)	122.31(17)
C(9)#1-C(8)-C(7)	131.48(17)
C(10)-C(8)-C(7)	106.21(15)
C(8)#1-C(9)-C(10)	118.08(17)
C(1)-C(10)-C(9)	130.83(17)
C(1)-C(10)-C(8)	109.57(16)
C(9)-C(10)-C(8)	119.61(16)
C(12)-C(11)-C(16)	120.26(18)
C(12)-C(11)-C(1)	119.52(17)
C(16)-C(11)-C(1)	120.14(18)
C(13)-C(12)-C(11)	119.0(2)
C(13)-C(12)-C(17)	119.2(2)
C(11)-C(12)-C(17)	121.69(18)
C(14)-C(13)-C(12)	121.0(2)
C(13)-C(14)-C(15)	119.7(2)
C(14)-C(15)-C(16)	121.6(2)
C(15)-C(16)-C(11)	118.4(2)
C(15)-C(16)-C(18)	119.74(19)
C(11)-C(16)-C(18)	121.83(19)

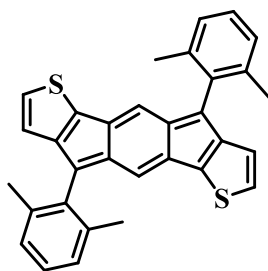
Symmetry transformations used to generate equivalent atoms:

#1 -x,-y+1,-z

6.2.2 Synthesis of 6,12-indacenodithiophenediketone (IDT-diketone)¹³⁵

2,5-di(thiophen-2-yl)terephthalic acid (5.15 g, 15.6 mmol, 1.0 eq.) added to 25 mL oven dried microwave vial, cap sealed and degassed with Argon for 10 minutes. Oxalyl chloride (5.3 mL, 62.4 mmol, 4.0 eq.) was slowly added dropwise, with the outlet needle left in the microwave seal due to excessive gas evolution. Dry DMF (2 mL) was added and the solution was left to stir at room temperature for 3 hours. The solution was poured into water and the organic phase was extracted into DCM. Once separated the organic layer was dried over MgSO_4 and the solvent was then removed under reduced pressure to yield a bright orange solid.

The solid was immediately re-dissolved in anhydrous DCM (10 mL) and was added to a suspension of AlCl_3 (9.67 g, 72.5 mmol, 4.7 eq.) dissolved in 50 mL anhydrous DCM at 0 °C. The suspension was stirred overnight before being poured into 50 mL ice cold 2M HCl solution. The precipitate was collected by suction filtration and washed with additional 2M HCl, water and finally acetone to yield the title compound as a pastel blue powder (4.54 g, 99%). Due to the lack of solubility the product was used in further experiments without additional purification.

6.2.3 4,9-bis(2,6-dimethylphenyl)-s-indaceno[1,2-b:5,6-b']dithiophene (DX-IDT)¹¹²

2-Bromo-*m*-xylene (0.85 mL, 6.38 mmol, 6.0 eq.) was dissolved in THF (20 mL), the solution purged with argon gas for 5 min and cooled to -78 °C. *n*-BuLi solution in hexanes (2.5 M, 2.13 mL, 5.32 mmol, 5.0 eq.) was added dropwise and the mixture stirred for 30 minutes. In a second flask 6,12-indacenodithiophenediketone (**6.2.2**) (310 mg, 1.06 mmol, 1.0 eq.) was suspended in THF (30 mL) and the mixture cooled to -78 °C. Upon formation of the aryl lithiate, the solution was transferred to the dione suspension by cannula and the combined reaction mixture allowed to warm to room temperature over 2 hours. The reaction was quenched by the addition of HCl solution (10 %, 10 mL), diluted with Et₂O (100 mL) and washed with water (2 x 100 mL) and brine (100 mL). The ethereal phase was dried over MgSO₄ and the solvent removed *in vacuo* to afford the crude diol product as an orange oil.

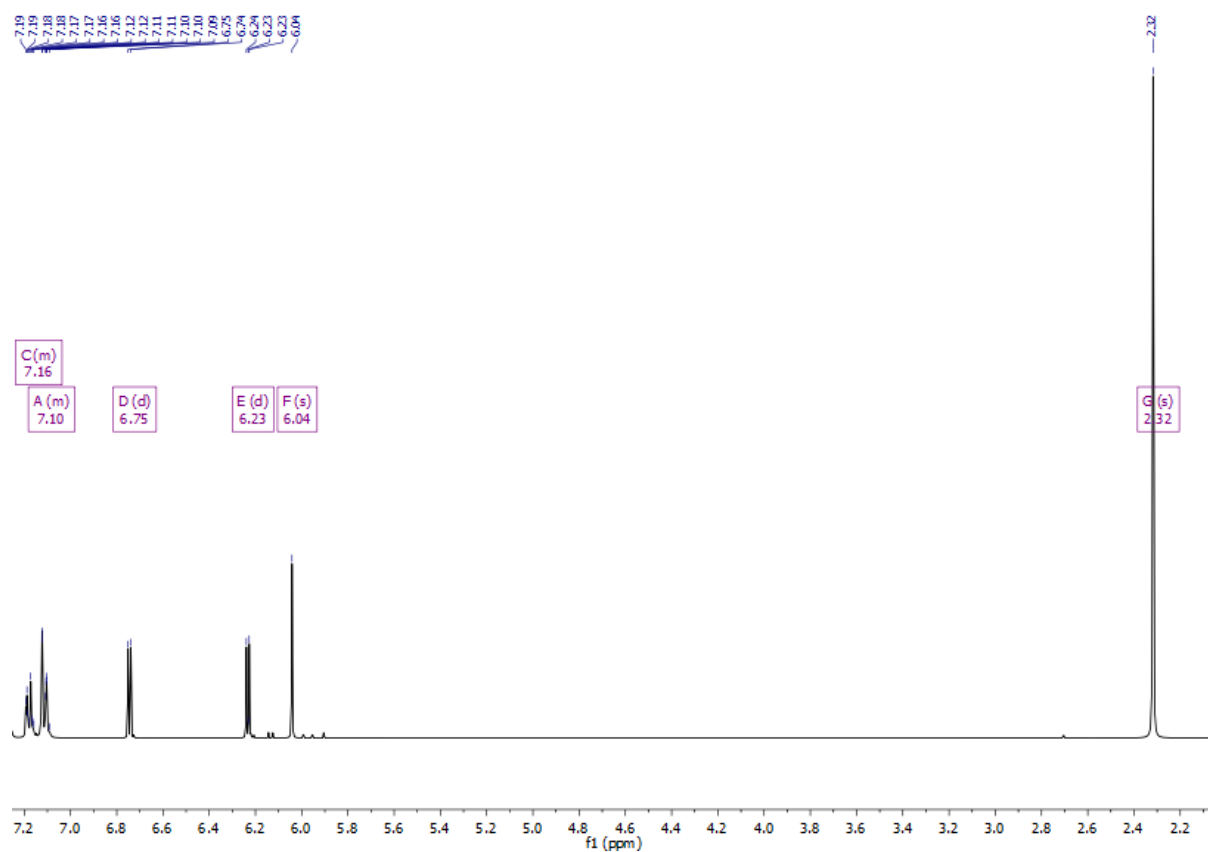
This oil was triturated with DCM:hexane to remove xylene-based impurities, affording a solid which was then dissolved in toluene (50 mL). This solution was degassed by purging with argon, SnCl₂ (810 mg, 4.25 mmol, 4.0 eq.) was then added and the mixture heated to 65 °C overnight. After cooling, the mixture was diluted with toluene (100 mL) and washed with water (3 x 100 mL) and brine (2 x 100 mL). The solvent was removed *in vacuo* and the product purified by crystallisation from hot ethyl acetate to afford the *title compound* as a deep magenta microcrystalline magenta solid (310 mg, 35%).

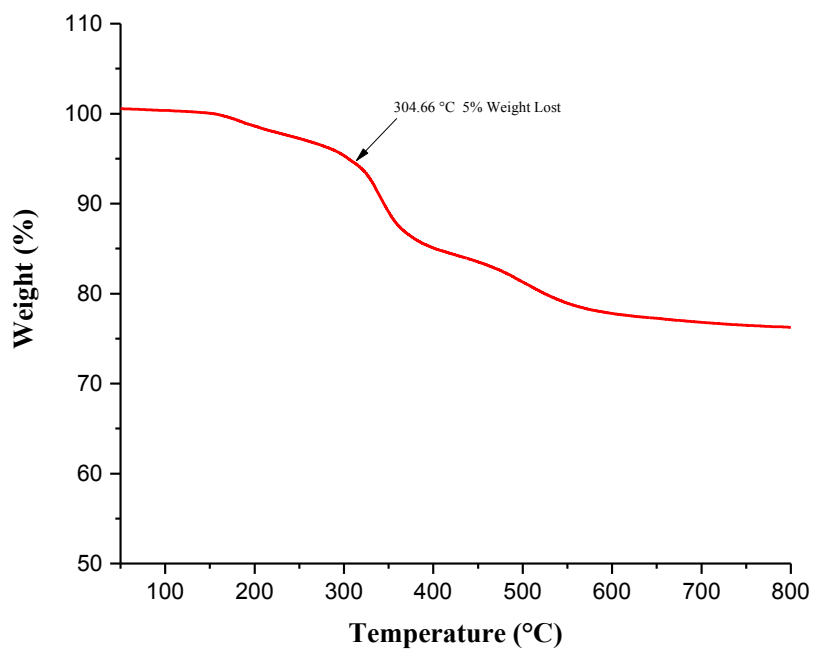
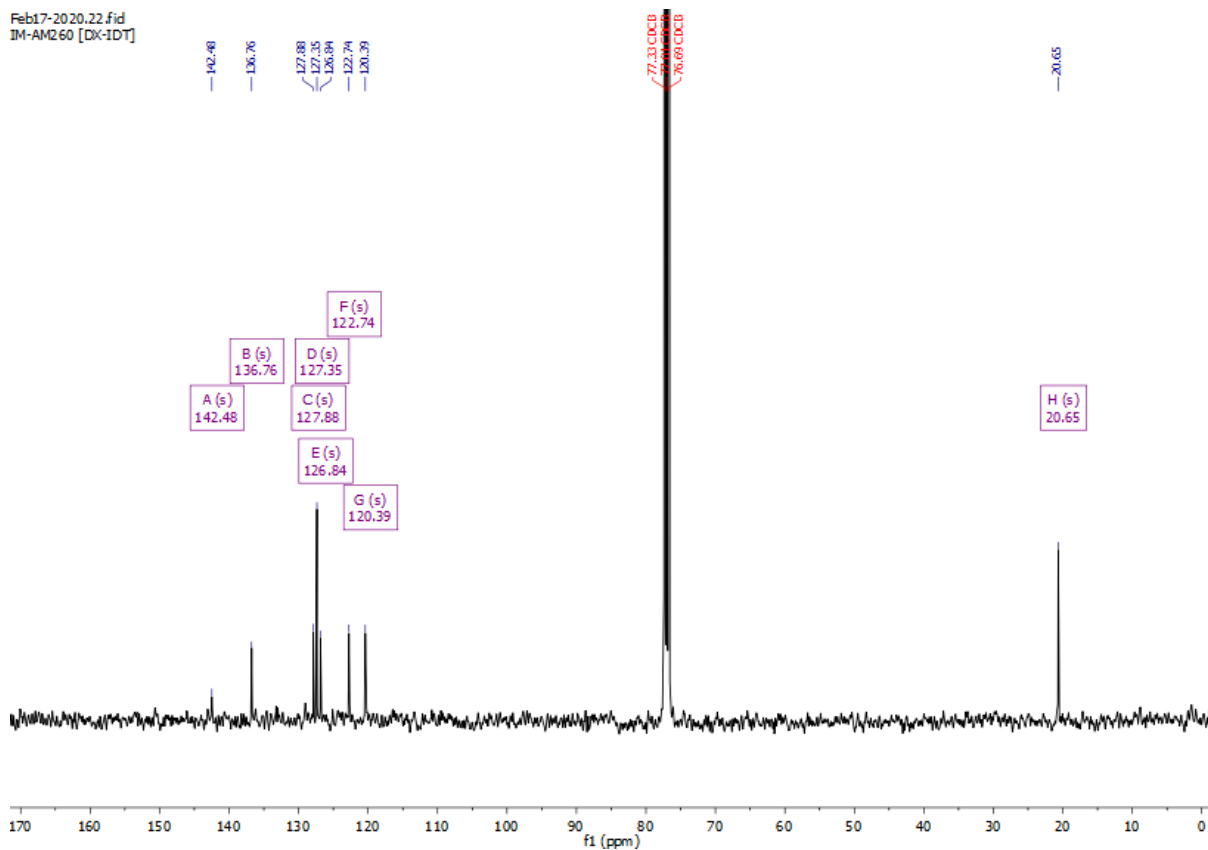
¹H NMR (400 MHz, CDCl₃): δ 7.22 – 7.16 (m, 2H), 7.11 (d, *J* = 7.5 Hz, 4H), 6.74 (d, *J* = 4.8 Hz, 2H), 6.23 (d, *J* = 4.8 Hz, 2H), 6.04 (s, 2H), 2.32 (s, 12H).

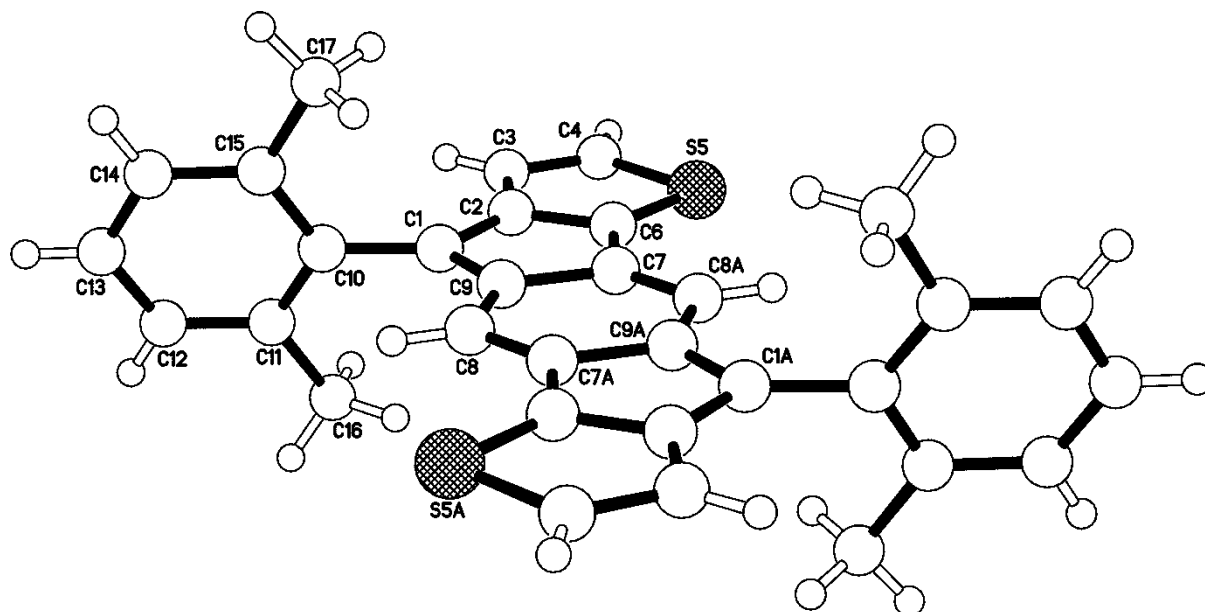
^{13}C NMR (101 MHz, Chloroform-*d*): δ 142.48, 136.76, 127.88, 127.35, 126.84, 122.74, 120.39, 20.65.

UV-Vis (CH_2Cl_2) λ_{max} : 555 nm.

Mass (MALDI-ToF): 472.8 $[\text{M}+\text{H}]^+$ (calc. 472.6 $\text{C}_{32}\text{H}_{24}\text{S}_2$).







Crystal data and structure refinement for IM1710 (**DX-IDT**).

Identification code	IM1710	
Formula	C ₃₂ H ₂₄ S ₂	
Formula weight	472.63	
Temperature	173(2) K	
Diffractionmeter, wavelength	Agilent Xcalibur 3 E, 0.71073 Å	
Crystal system, space group	Orthorhombic, P _{bca}	
Unit cell dimensions	a = 13.3736(6) Å	α = 90°
	b = 6.7136(3) Å	β = 90°
	c = 26.1050(11) Å	γ = 90°
Volume, Z	2343.83(18) Å ³ , 4	
Density (calculated)	1.339 Mg/m ³	
Absorption coefficient	0.247 mm ⁻¹	
F(000)	992	
Crystal colour / morphology	Black tablets	
Crystal size	0.47 x 0.21 x 0.03 mm ³	
θ range for data collection	3.046 to 28.190°	
Index ranges	-11 ≤ h ≤ 17, -4 ≤ k ≤ 8, -28 ≤ l ≤ 34	
Reflns collected / unique	5149 / 2411 [R(int) = 0.0235]	
Reflns observed [F > 4σ(F)]	1902	
Absorption correction	Analytical	

Max. and min. transmission	0.992 and 0.953
Refinement method	Full-matrix least-squares on F ²
Data / restraints / parameters	2411 / 0 / 156
Goodness-of-fit on F ²	1.058
Final R indices [F>4σ(F)]	R1 = 0.0434, wR2 = 0.0934
R indices (all data)	R1 = 0.0608, wR2 = 0.1018
Largest diff. peak, hole	0.361, -0.228 eÅ ⁻³
Mean and maximum shift/error	0.000 and 0.001

Bond lengths [Å] and angles [°] for IM1710 (**DX-IDT**)

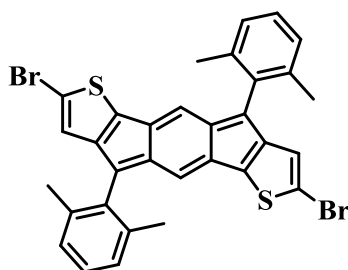
C(1)-C(9)	1.387(3)
C(1)-C(2)	1.457(3)
C(1)-C(10)	1.485(3)
C(2)-C(6)	1.386(3)
C(2)-C(3)	1.416(3)
C(3)-C(4)	1.366(3)
C(4)-S(5)	1.729(2)
S(5)-C(6)	1.708(2)
C(6)-C(7)	1.449(3)
C(7)-C(8)#1	1.360(3)
C(7)-C(9)	1.462(3)
C(8)-C(7)#1	1.360(3)
C(8)-C(9)	1.425(3)
C(10)-C(11)	1.404(3)
C(10)-C(15)	1.407(3)
C(11)-C(12)	1.386(3)
C(11)-C(16)	1.507(3)
C(12)-C(13)	1.381(3)
C(13)-C(14)	1.371(3)
C(14)-C(15)	1.394(3)
C(15)-C(17)	1.504(3)
C(9)-C(1)-C(2)	107.24(16)
C(9)-C(1)-C(10)	126.37(17)
C(2)-C(1)-C(10)	126.40(17)
C(6)-C(2)-C(3)	112.43(18)
C(6)-C(2)-C(1)	108.45(18)
C(3)-C(2)-C(1)	139.12(18)
C(4)-C(3)-C(2)	111.97(18)
C(3)-C(4)-S(5)	112.39(16)
C(6)-S(5)-C(4)	91.20(10)
C(2)-C(6)-C(7)	109.61(17)
C(2)-C(6)-S(5)	111.99(15)
C(7)-C(6)-S(5)	138.39(14)

C(8)#1-C(7)-C(6)	133.72(18)
C(8)#1-C(7)-C(9)	121.44(17)
C(6)-C(7)-C(9)	104.83(15)
C(7)#1-C(8)-C(9)	118.70(17)
C(1)-C(9)-C(8)	130.26(17)
C(1)-C(9)-C(7)	109.88(17)
C(8)-C(9)-C(7)	119.86(16)
C(11)-C(10)-C(15)	119.80(17)
C(11)-C(10)-C(1)	121.06(17)
C(15)-C(10)-C(1)	119.14(17)
C(12)-C(11)-C(10)	119.37(19)
C(12)-C(11)-C(16)	119.64(19)
C(10)-C(11)-C(16)	121.00(18)
C(13)-C(12)-C(11)	120.72(19)
C(14)-C(13)-C(12)	120.22(19)
C(13)-C(14)-C(15)	120.9(2)
C(14)-C(15)-C(10)	118.91(18)
C(14)-C(15)-C(17)	120.52(18)
C(10)-C(15)-C(17)	120.57(17)

Symmetry transformations used to generate equivalent atoms:

#1 -x+1,-y+1,-z+1

6.2.4 2,7-dibromo-4,9-bis(2,6-dimethylphenyl)-s-indaceno[1,2-b:5,6-b']dithiophene



N-bromosuccinimide (226 mg, 1.27 mmol 3.0 eq.) was added portion wise to a solution of DXIDT (**6.2.3**) (200 mg, 0.42 mmol, 1.0 eq.) in chloroform (10 mL). The mixture was stirred in the dark for 20 hours before being quenched by the addition of saturated NaHCO₃ solution (50 mL) and saturated Na₂SO₃ solution (50 mL). The mixture was diluted with chloroform (150 mL) and the organic phase washed with water (3 x 100 mL) and brine (100 mL) before the solvent was removed in vacuo to afford the crude product as a black solid. This solid was

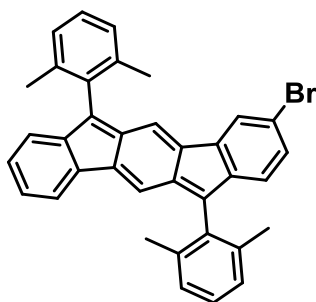
purified by repeated precipitation from DCM solution by the addition of methanol to afford the title compound as a black, crystalline solid (130 mg, 49%).

^1H NMR (400 MHz, CDCl_3): δ 7.21 – 7.16 (dd, J = 8.2, 6.8 Hz, 2H), 7.10 (d, J = 7.6 Hz, 4H), 6.26 (s, 2H), 5.94 (s, 2H), 2.31 (s, 12H) ppm.

^{13}C NMR (101 MHz, CDCl_3): δ 149.29, 145.87, 142.83, 136.77, 135.49, 133.38, 132.62, 128.34, 127.60, 123.57, 123.37, 113.20, 20.81 ppm.

MALDI-MS: 628.8 $[\text{M}^+\text{H}]^+$ (calc. 628.0 $\text{C}_{32}\text{H}_{22}\text{S}_2\text{Br}_2$).

6.2.5 3-bromo-6,12-bis(2,6-dimethylphenyl)indeno[1,2-*b*]fluorene (mono-Br DX-IDF)

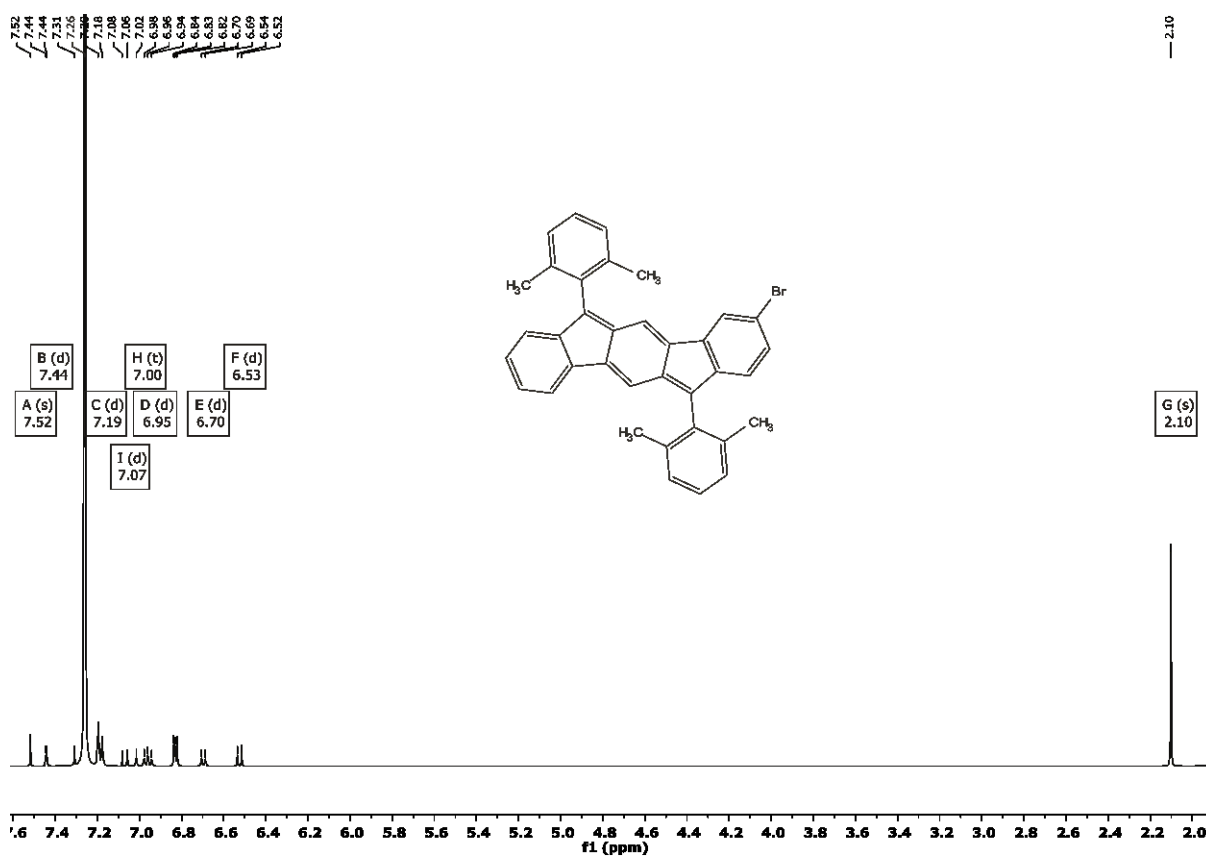


N-bromosuccinimide (0.25 g, 1.39 mmol, 0.9 eq.) was added to a solution of 6,12-bis(2,6-dimethylphenyl)indeno[1,2-*b*]fluorene (**6.2.1**) (0.71 g, 1.55 mmol, 1.0 eq.) dissolved in chloroform (50 mL) and stirred under an inert atmosphere in the dark. After two hours, glacial acetic acid (10 mL) was added to accelerate the reaction. The solution was left stirring, in the dark, for 16 hours. The crude solution was diluted with chloroform (150 mL), quenched with sodium metabisulphite, washed with water (200 mL) and ammonium chloride before separation and subsequent removal of solvent under reduced pressure to yield a brown metallic solid (0.81 g, 97%).

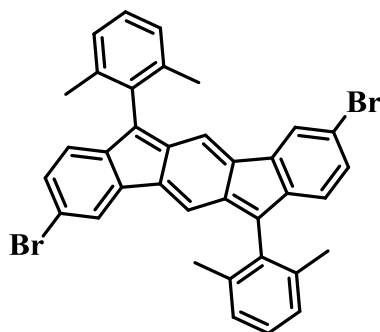
^1H NMR (400 MHz, CDCl_3): δ 7.52 (s, 1H), 7.44 (d, $J = 1.7$ Hz, 1H), 7.19 (d, $J = 7.5$ Hz, 4H), 7.07 (d, $J = 9.8$ Hz, 1H), 7.00 (t, $J = 14.9$ Hz, 2H), 6.95 (d, $J = 7.3$ Hz, 2H), 6.70 (d, $J = 6.9$ Hz, 2H), 6.53 (d, $J = 8.1$ Hz, 2H), 2.10 (s, 12H).

UV-Vis (CH_2Cl_2) λ_{max} : 520 nm.

Mass (MALDI-ToF): 538.9 $[\text{M}+\text{H}]^+$ (calc. 538.1 $\text{C}_{36}\text{H}_{27}\text{Br}$).



6.2.6 3,9-dibromo-6,12-bis(2,6-dimethylphenyl)indeno[1,2-*b*]fluorene (bis-Br DX-IDF)

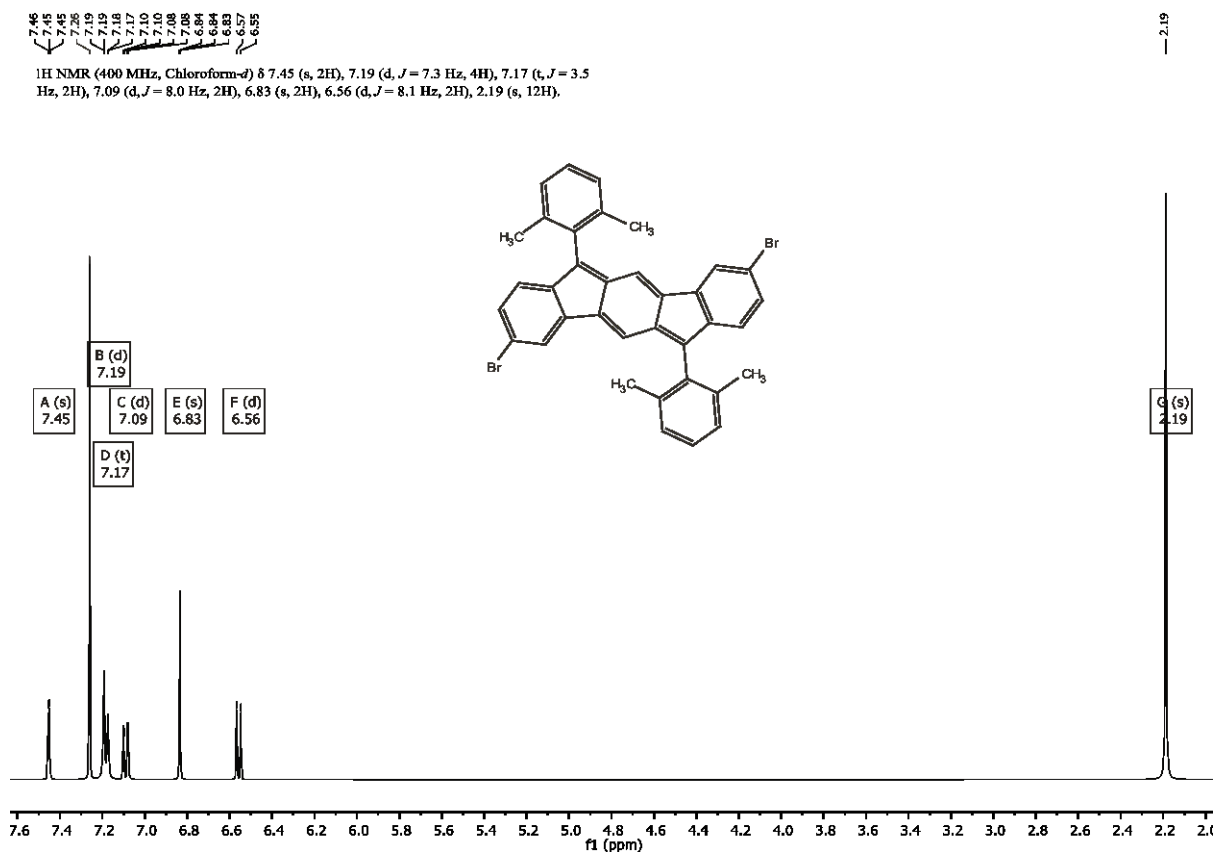


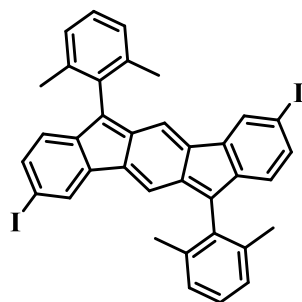
Following the same procedure as (6.2.5) N-bromosuccinimide (0.15 g, 0.81 mmol, 2.5 eq.) and 6,12-bis(2,6-dimethylphenyl)indeno[1,2-*b*]fluorene (0.15 g, 0.33 mmol, 1.0 eq.) were reacted to yield a brown solid (0.19 g, 94%).

$^1\text{H NMR}$ (400 MHz, CDCl_3): δ 7.45 (s, 2H), 7.19 (d, $J = 7.3$ Hz, 4H), 7.17 (t, $J = 3.5$ Hz, 2H), 7.09 (d, $J = 8.1$ Hz, 2H), 6.83 (s, 2H), 6.56 (d, $J = 8.1$ Hz, 2H), 2.19 (s, 12H).

UV-Vis (CH_2Cl_2) λ_{max} : 528 nm.

Mass (MALDI-ToF): 618.4 $[\text{M}+\text{H}]^+$ (calc. 618.0 $\text{C}_{36}\text{H}_{26}\text{Br}_2$).



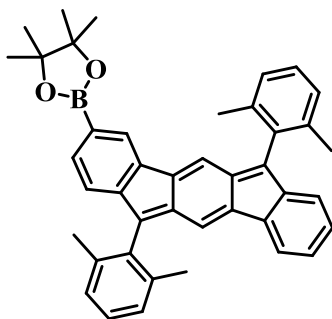
6.2.7 6,12-bis(2,6-dimethylphenyl)-3,9-diiodoindeno[1,2-*b*]fluorene (di-iodo-DX-IDF)

Following the same procedure as (6.2.5) N-iodosuccinimide (122 mg, 0.54 mmol, 2.5 eq.) and 6,12-bis(2,6-dimethylphenyl)indeno[1,2-*b*]fluorene (100 mg, 0.22 mmol, 1.0 eq.) were reacted to yield a dark purple crystalline solid (143 mg, 93%).

^1H NMR (400 MHz, Chloroform-*d*) δ 7.64 (s, 2H), 7.29 (s, 2H), 7.00 (t, $J = 7.8$ Hz, 2H), 6.82 (d, $J = 2.6$ Hz, 4H), 6.69 (d, $J = 7.3$ Hz, 2H), 6.41 (d, $J = 7.8$ Hz, 2H), 2.21 (s, 12H).

^{13}C NMR (101 MHz, Chloroform-*d*) δ 143.59, 139.88, 137.50, 137.08, 133.20, 130.08, 128.74, 127.98, 123.97, 120.24, 112.19, 93.28, 20.86.

Mass (MALDI-ToF): 712.6 $[\text{M}+\text{H}]^+$ (calc. 712.0 $\text{C}_{36}\text{H}_{26}\text{I}_2$).

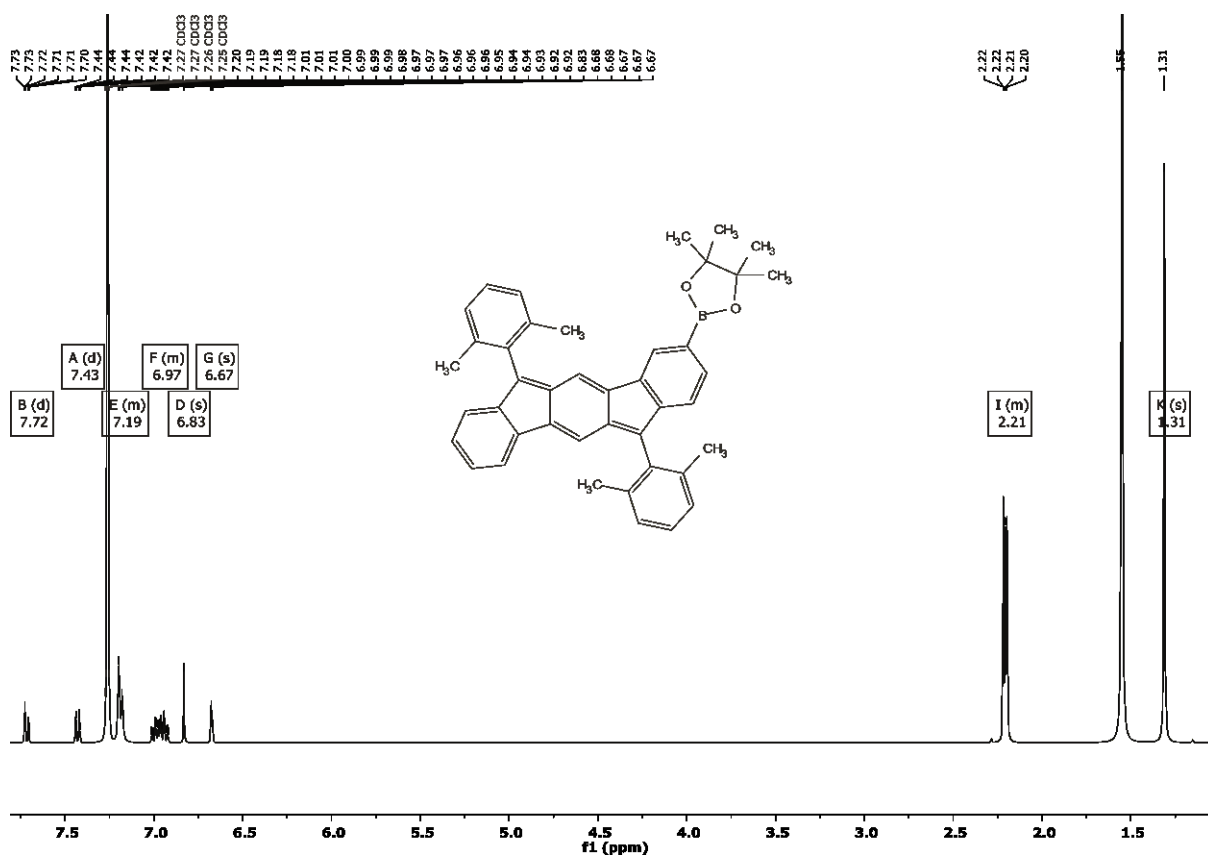
6.2.8 2-(6,12-bis(2,6-dimethylphenyl)indeno[1,2-*b*]fluoren-3-yl)-4,4,5,5-tetramethyl-1,3,2-dioxaborolane (DX-IDF mono-BPin)

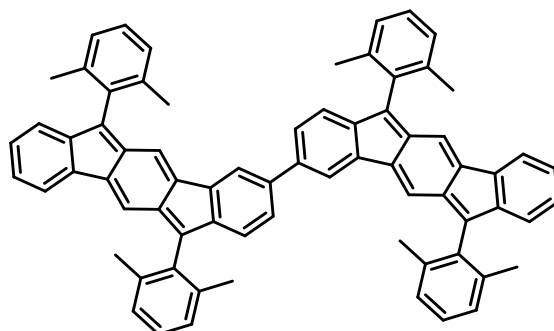
To a 10 mL microwave vial was added mono-Br DX-IDF (6.2.5) (0.10 g, 0.19 mmol, 1.0 eq.), 4,4'-biphenyldiboronic acid dipinacol ester (0.07 g, 0.28 mmol, 1.5 eq.), potassium acetate

(KOAc) (0.07 g, 0.74 mmol, 4.0 eq.) and Pd(dppf)₂Cl₂.DCM (7.60 mg, 0.05 eq.). The vial was sealed and degassed with argon followed by the addition of degassed 1,2-dimethoxyethane (6.0 mL). The mixture was heated to 80 °C and stirred vigorously for 24 hours. The reaction was then cooled to room temperature and transferred to a separating funnel containing DCM (250 mL) and water (300 mL). The organic layer was separated and dried over anhydrous MgSO₄, filtered and the solvent was removed under reduced pressure to yield the crude product. The crude was subsequently washed with cold methanol, to remove excess 4,4'-biphenyldiboronic acid dipinacol ester, yielding a brown metallic solid (0.08g, 74%).

¹H NMR (400 MHz, CDCl₃): δ 7.72 (d, *J* = 8.0 Hz, 1H), 7.43 (d, *J* = 8.0 Hz, 1H), 7.22 – 7.15 (m, 6H), 7.04 – 6.89 (m, 4H), 6.83 (s, 1H), 6.67 (s, 2H), 2.24 – 2.17 (m, 12H), 1.31 (s, 12H).

Mass (MALDI-ToF): 586.9 [M+H]⁺ (calc. 586.3 C₄₂H₃₉BO₂).



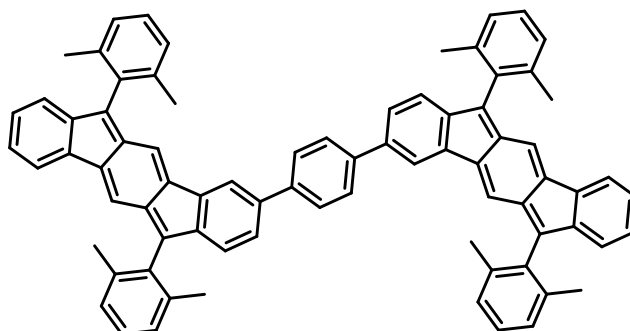
6.2.9 6,6',12,12'-tetrakis(2,6-dimethylphenyl)-3,3'-biindeno[1,2-*b*]fluorene (Di-DX-IDF_[0])

To a 10 mL microwave vial was added mono-Br DX-IDF (**6.2.4**) (47.8 mg, 0.09 mmol, 1.0 eq.), mono-BPin DX-IDF (**6.2.7**) (52.0 mg, 0.09 mmol, 1.0 eq.), K₂CO₃ (208 mg, 1.51 mmol, 17.0 eq.) and Pd(dppf)₂Cl₂.DCM (3.61 mg, 0.05 eq.). The vial was sealed and degassed with argon followed by the addition of degassed THF (6 mL), H₂O (0.6 mL) and a single drop of Aliquat 336. The mixture was heated to 70 °C and stirred vigorously for 24 hours. The reaction was then cooled to room temperature and transferred to a separating funnel containing DCM (50 mL) and water (250 mL). The organic layer was separated and dried over anhydrous MgSO₄, filtered and the solvent was removed under reduced pressure to yield the crude product. The crude was subsequently purified by silica chromatography using mixtures of hexane/DCM as an eluent to obtain Di-DX-IDF_[0] as a deep purple solid (44 mg, 54%).

¹H NMR (400 MHz, CDCl₃) δ 7.82 (s, 2H), 7.70 (d, *J* = 7.2 Hz, 2H), 7.57 (d, *J* = 7.2 Hz, 2H), 7.20 (d, *J* = 8.5 Hz, 8H), 7.03 – 6.92 (m, 4H), 6.88 (s, 2H), 6.84 – 6.80 (m, 4H), 6.69 (d, *J* = 8.2 Hz, 2H), 6.52 (d, *J* = 8.0 Hz, 2H), 6.41 (s, 2H), 2.22 (s, 24H).

UV-Vis (CH₂Cl₂) λ_{max}: 528 nm.

Mass (MALDI-ToF): 919.2 [M+H]⁺ (calc. 918.4 C₇₂H₅₄).

6.2.10 1,4-bis(6,12-bis(2,6-dimethylphenyl)indeno[1,2-*b*]fluoren-3-yl)benzene (Di-DX-IDF_[1])

(Route 1) To a 20 mL microwave vial was added mono-Br DX-IDF (**6.2.5**) (100 mg, 0.19 mmol, 2.2 eq.), 1,4-benzenediboronic acid bis(pinacol) ester (27.8 mg, 0.08 mmol, 1.0 eq.), K₂CO₃ (349 mg, 2.53 mmol, 30.0 eq) and Pd(PPh₃)₄ (9.71 mg, 0.1 eq.). The vial was sealed and degassed with argon followed by the addition of degassed THF (10 mL), H₂O (1 mL) and a single drop of Aliquat 336. The mixture was heated to 75 °C and stirred vigorously for 24 hours. The reaction was then cooled to room temperature and transferred to a separating funnel containing DCM (50 mL) and water (250 mL). The organic layer was separated and dried over anhydrous MgSO₄, filtered and the solvent was removed under reduced pressure to yield the crude product. The crude was subsequently purified by silica chromatography using mixtures of hexane/CHCl₃ as an eluent to obtain Di-DX-IDF_[1] as a deep purple metallic solid (18.7 mg, 22%).

(Optimised route 2). To a 20 mL microwave vial was added mono-Br DX-IDF (**6.2.5**) (250 mg, 0.46 mmol, 2.3 eq.), 1,4-benzenediboronic acid bis(pinacol) ester (80 mg, 0.24 mmol, 1.2 eq.), K₂CO₃ (473 mg, 3.42 mmol, 17.0 eq.) and Pd(dppf)₂Cl₂.DCM (16.5 mg, 0.02 mmol, 0.1 eq.). The vial was sealed and degassed with argon followed by the addition of degassed THF (10 mL), H₂O (1 mL) and a single drop of Aliquat 336. The mixture was heated to 85 °C and stirred vigorously for 48 hours. The reaction was then cooled to room temperature and

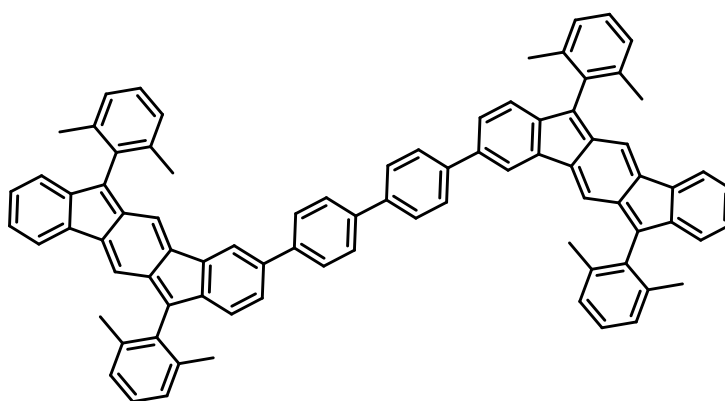
transferred to a separating funnel containing DCM (50 mL) and water (250 mL). The organic layer was separated and dried over anhydrous MgSO_4 , filtered and the solvent was removed under reduced pressure to yield the crude product. The crude was subsequently purified by silica chromatography using mixtures of hexane/ CHCl_3 as an eluent to obtain Di-DX-IDF_[1] as a deep purple metallic solid (348 mg, 75%).

^1H NMR (400 MHz, CDCl_3) δ 7.61 (s, 4H), 7.54 (s, 4H), 7.22 – 7.20 (m, 8H), 7.13 (dd, $J = 8.8, 2.4$ Hz, 2H), 7.00 (d, $J = 6.9$ Hz, 4H), 6.96 (d, $J = 7.2$ Hz, 2H), 6.92 (s, 2H), 6.87 – 6.82 (m, 4H), 6.75 (d, $J = 7.7$ Hz, 2H), 6.69 (d, $J = 7.7$ Hz, 2H), 2.25 (s, 12H), 2.23 (s, 12H).

UV-Vis (CH_2Cl_2) λ_{max} : 542 nm.

Mass (MALDI-ToF): 995.8 $[\text{M}+\text{H}]^+$ (calc. 995.3 $\text{C}_{78}\text{H}_{58}$)

6.2.11 4,4'-bis(6,12-bis(2,6-dimethylphenyl)indeno[1,2-b]fluoren-3-yl)-1,1'-biphenyl (Di-DX-IDF_[2])



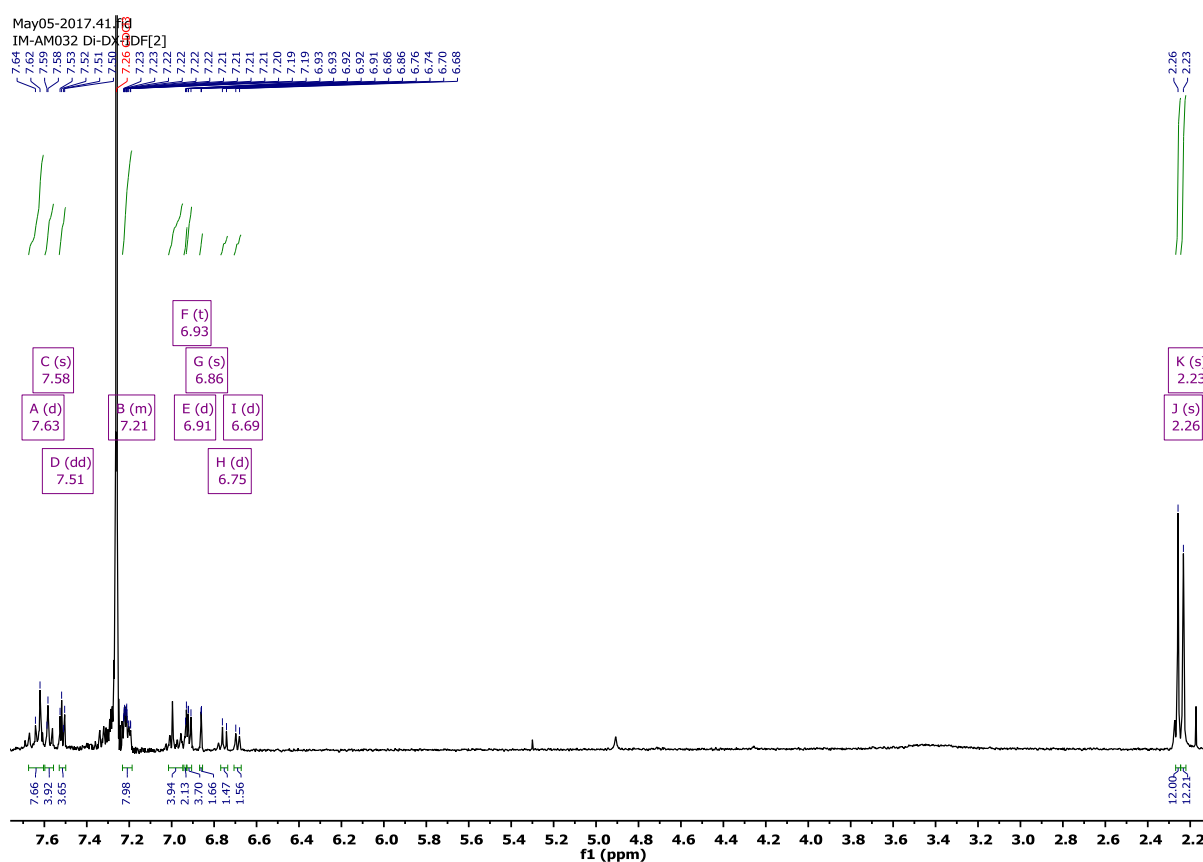
To a 10 mL microwave vial was added mono-Br DX-IDF (**6.2.5**) (100 mg, 0.19 mmol, 2.2 eq.), 4,4'-biphenyldiboronic acid dipinacol ester (34.2 mg, 0.08 mmol, 1.0 eq.), K_2CO_3 (198 mg, 1.43 mmol, 17.0 eq.) and $\text{Pd}(\text{dppf})_2\text{Cl}_2 \cdot \text{DCM}$ (6.91 mg, 0.1 eq.). The vial was sealed and degassed with argon followed by the addition of degassed THF (6 mL), H_2O (0.6 mL) and a single drop of Aliquat 336. The mixture was heated to 85 °C and stirred vigorously for 24

hours. The reaction was then cooled to room temperature and transferred to a separating funnel containing DCM (50 mL) and water (250 mL). The organic layer was separated and dried over anhydrous MgSO_4 , filtered and the solvent was removed under reduced pressure to yield the crude product. The crude was subsequently purified by silica chromatography using mixtures of hexane/DCM as an eluent to obtain Di-DX-IDF_[2] as a deep purple metallic solid (73 mg, 81%).

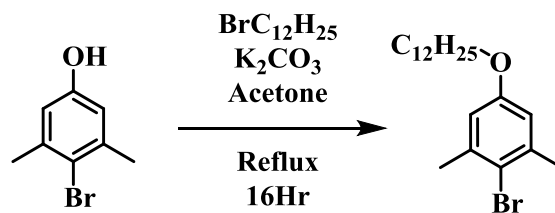
^1H NMR (400 MHz, CDCl_3): δ 7.63 (d, $J = 8.6$ Hz, 8H), 7.58 (s, 4H), 7.51 (dd, $J = 6.2, 2.5$ Hz, 4H), 7.25 – 6.88 (m, 8H), 6.93 (t, $J = 1.7$ Hz, 4H), 6.91 (d, $J = 4.6$ Hz, 4H), 6.86 (s, 2H), 6.75 (d, $J = 7.7$ Hz, 2H), 6.69 (d, $J = 7.2$ Hz, 2H), 2.26 (s, 12H), 2.23 (s, 12H).

UV-Vis (CH_2Cl_2) λ_{max} : 537 nm.

Mass (MALDI-ToF): 1071.4 $[\text{M}+\text{H}]^+$ (calc. 1071.4 $\text{C}_{84}\text{H}_{62}$).



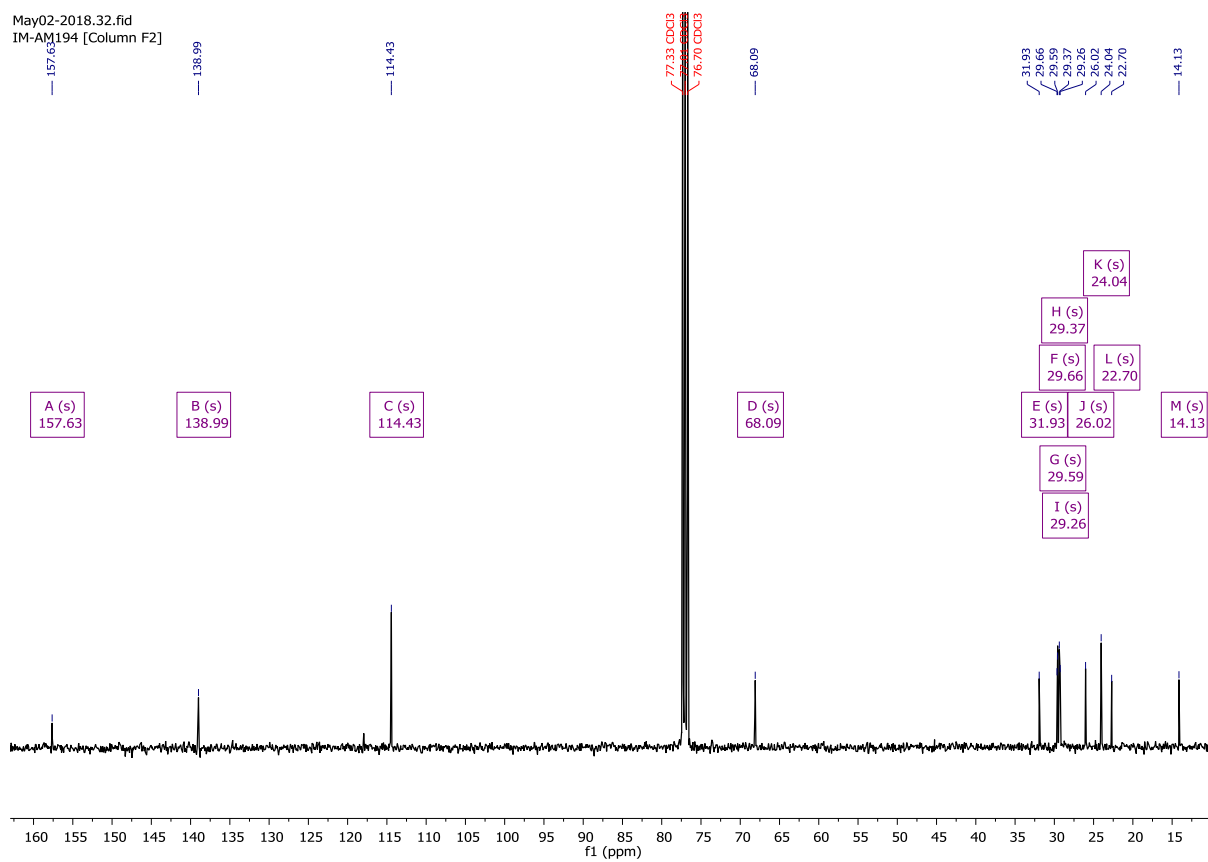
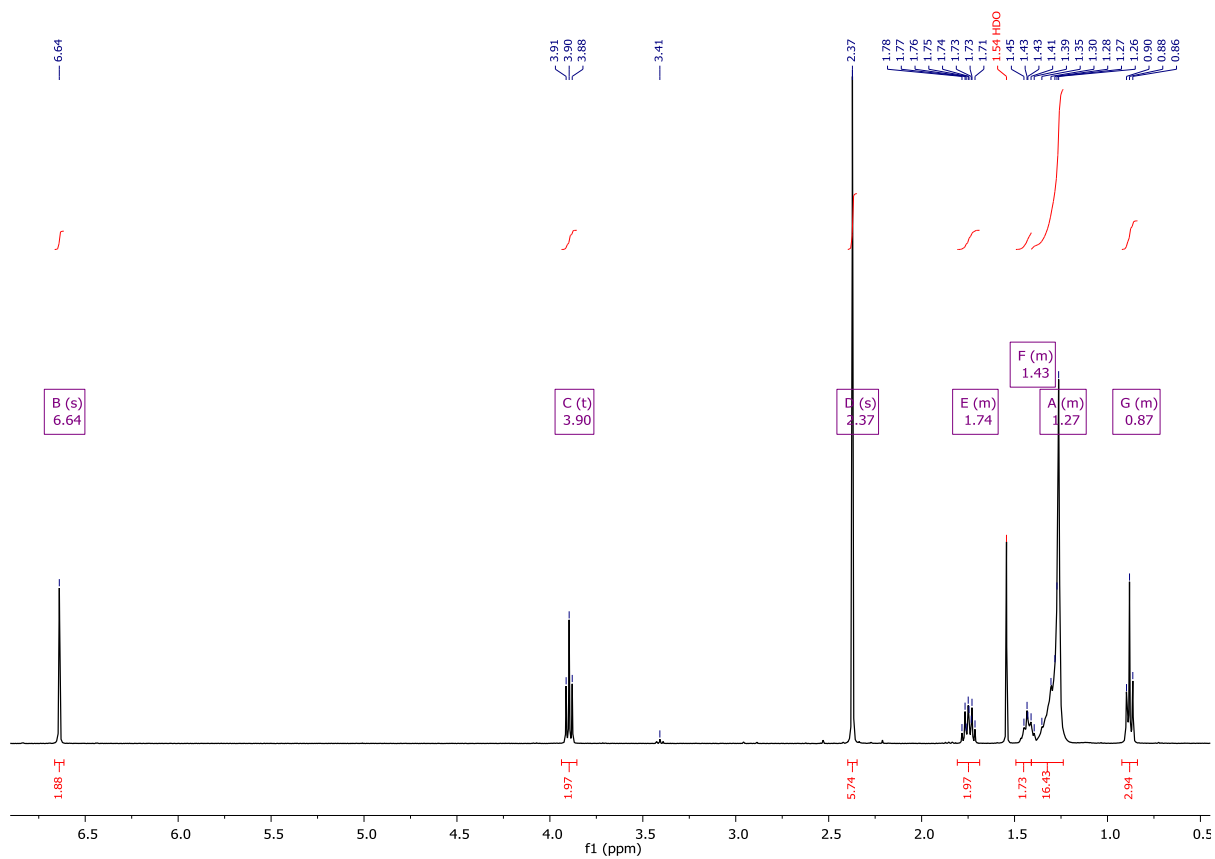
6.2.12 Synthesis of 2-bromo-5-(dodecyloxy)-1,3-dimethylbenzene

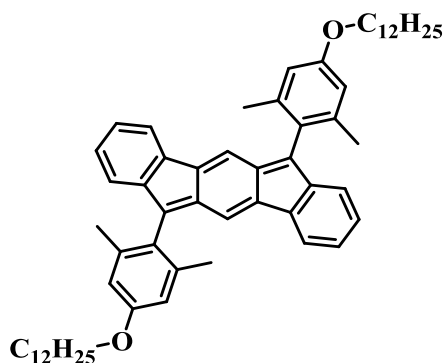


4-bromo-3,5-dimethylphenol (15 g, 74.6 mmol, 1.0 eq.) was dissolved in 200 mL of acetone inside a 2 neck 500 mL RBF. K_2CO_3 (30.9 g, 223.8 mmol, 3.0 eq.) was added to the solution which was then stirred at room temperature for an hour. 1-Bromododecane (21.42 mL, 111.9 mmol, 1.2 eq.) was added via syringe. The mixture was heated to reflux and left stirring overnight. Solvent was removed under reduced pressure before being purified by column chromatography on silica using hexane as the eluent system. The title compound was recrystallised from hot hexane to afford white crystals (5.192 g, 18.8%).

^1H NMR (400 MHz, Chloroform-*d*) δ 6.64 (s, 2H), 3.90 (t, $J = 6.6$ Hz, 2H), 2.37 (s, 6H), 1.81 – 1.69 (m, 2H), 1.49 – 1.39 (m, 2H), 1.42 – 1.24 (m, 16H), 0.92 – 0.84 (m, 3H).

^{13}C NMR (101 MHz, Chloroform-*d*) δ 157.63, 138.99, 114.43, 68.09, 31.93, 29.66, 29.59, 29.37, 29.26, 26.02, 24.04, 22.70, 14.13.



6.2.13 6,12-di(2,6-dimethyl-4-dodecyloxyphenyl)indeno[1,2-*b*]fluorene

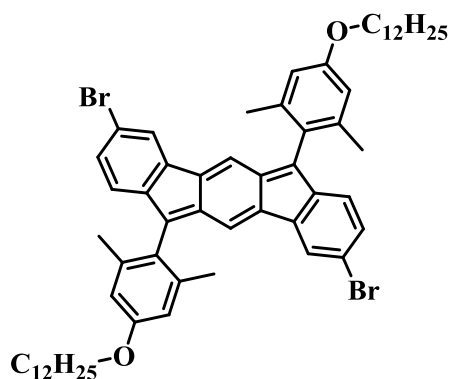
2-bromo-5-(dodecyloxy)-1,3-dimethylbenzene (**6.2.12**) (7.0 g, 19 mmol, 6.0 eq.) was dissolved in THF (150 mL), the solution degassed and cooled to $-78\text{ }^{\circ}\text{C}$. *n*-BuLi solution in hexanes (2.5 M, 6.32 mL, 15.8 mmol, 5.0 eq.) was added dropwise and the mixture stirred for 30 minutes. In a second flask indeno[1,2-*b*]fluorene-6,12-dione (894 mg, 3.16 mmol, 1.0 eq.) was suspended in THF (30 mL) and the mixture cooled to $-78\text{ }^{\circ}\text{C}$. Upon formation of the aryl lithiate, the solution was transferred to the dione suspension by cannula and the combined reaction mixture allowed to warm to room temperature over 2 hours. The reaction was quenched by the addition of HCl solution (10 %, 50 mL), diluted with Et₂O (500 mL) and washed with water (2 x 200 mL) and brine (200 mL). The ethereal phase was dried over MgSO₄ and the solvent removed in vacuo to afford the crude diol product as an orange oil.

This oil was triturated with DCM:hexane to remove xylene-based impurities, affording a solid which was then dissolved in toluene (100 mL). This solution was degassed by purging with argon, SnCl₂ (3.61 g, 19 mmol, 6.0 eq.) was then added and the mixture heated to $65\text{ }^{\circ}\text{C}$ overnight. After cooling, the mixture was diluted with toluene (100 mL) and washed with water (3 x 100 mL) and brine (2 x 100 mL). The solvent was removed in vacuo and the product purified by column chromatography, on silica gel, with hexane as the eluent to afford the title compound as an imperial purple solid with a green metallic sheen (1.94 g, 74%).

^1H NMR (400 MHz, CDCl_3): δ 7.33 (d, $J = 7.2$ Hz, 2H), 7.04 – 6.94 (m, 4H), 6.86 (s, 2H), 6.76 (s, 4H), 6.71 (d, $J = 7.2$ Hz, 2H), 4.04 (t, $J = 6.3$ Hz, 4H), 2.20 (s, 12H), 1.85 (q, $J = 6.3$ Hz, 4H), 1.44 – 1.24 (m, 18H), 0.91 (t, $J = 6.3$ Hz, 3H) ppm.

Mass (MALDI-ToF): 829.3 $[\text{M}+\text{H}]^+$ (calc. 828.6 $\text{C}_{60}\text{H}_{76}\text{O}_2$).

6.2.14 3,9-dibromo-6,12-bis(4-(dodecyloxy)-2,6-dimethylphenyl)indeno[1,2-*b*]fluorene

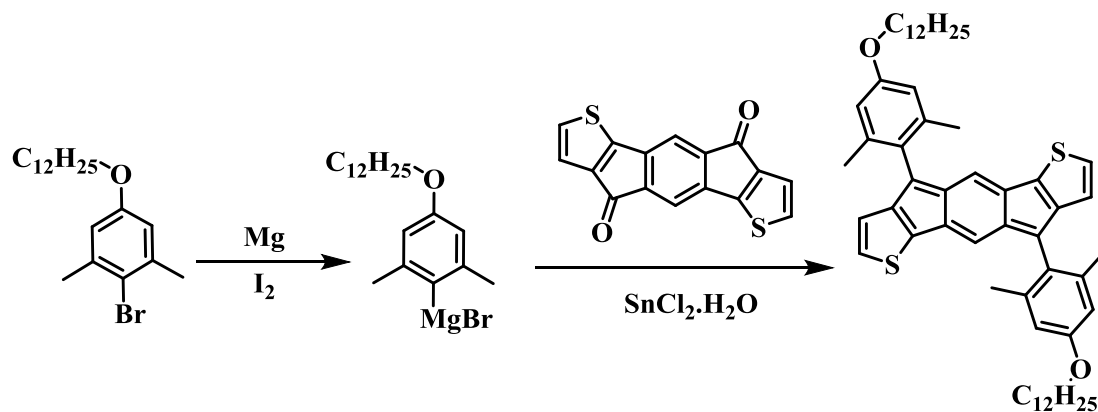


N-bromosuccinimide (1.29 g, 7.24 mmol, 6.0 eq.) was added portionwise to a stirring solution of 6,12-di(2,6-dimethyl-4-dodecyloxyphenyl)indeno[1,2-*b*]fluorene (**6.2.13**) (1.0 g, 1.21 mmol, 1.0 eq.) in chloroform (50 mL) at room temperature. This mixture was stirred in darkness for 16 hours before being quenched by the addition of saturated NaHCO_3 solution (50 mL) and saturated Na_2SO_3 solution (50 mL). The mixture was diluted with chloroform (150 mL) and the organic phase washed with water (3 x 100 mL) and brine (100 mL) before the solvent was removed *in vacuo* to afford the crude product as a black solid. This material was passed through a plug of silica with 1:4 Et_2O :hexane, then repeated trituration of the purple mass with warm hexane afforded the title compound as a violet solid with a vivid lime luster (1.05 g, 88%).

^1H NMR (400 MHz, CDCl_3): δ 7.46 (d, $J = 1.8$, 2H), 7.11 (d, $J = 1.8$ Hz, 2H), 7.09 (d, $J = 1.8$ Hz, 2H), 6.80 (s, 2H), 4.04 (t, $J = 6.3$ Hz, 4H), 2.20 (s, 12H), 1.85 (q, $J = 6.3$ Hz, 4H), 1.44 – 1.24 (m, 18H), 0.91 (t, $J = 6.3$ Hz, 3H) ppm.

Mass (MALDI-ToF): 987.2 $[M+H]^+$ (calc. 986.4 $C_{60}H_{74}Br_2O_2$).

6.2.15 Synthesis of 4,9-bis(4-(dodecyloxy)-2,6-dimethylphenyl)-*s*-indaceno[1,2-*b*:5,6-*b'*]dithiophene (C_{12} -O-DX-IDT)



To a 250 mL 2-neck oven dried RBF was added a large stirrer bar and Mg turnings (505 mg, 20.8 mmol, 12.0 eq.). Subsequently a small spatula head of iodine was added and stirred rapidly for 15 minutes. A noticeable colour change to deep purple was observed almost instantly. Dry THF (10 mL) was then added to yield a dark orange solution. The mixture was stirred for 30 minutes and changed colour to afford a pale-yellow solution. 2 – 4 drops of (6.2.12) 2-bromo-5-(dodecyloxy)-1,3-dimethylbenzene were dripped down the side of the RBF and the mixture was heated to initiate the reaction. The solution was left to stir for an additional 10 minutes upon which the pale-yellow had turned clear. The remaining 2-bromo-5-(dodecyloxy)-1,3-dimethylbenzene (3.6 mL, 10.4 mmol, 6.0 eq.) was added dropwise and left to stir at room temperature for 2 hours. The mixture was cooled to 0 °C prior to the addition of (6.2.2) 6,12-indacenodithiophenediketone (510 mg, 1.73 mmol, 1.0 eq.) then subsequently stirred overnight at room temperature.

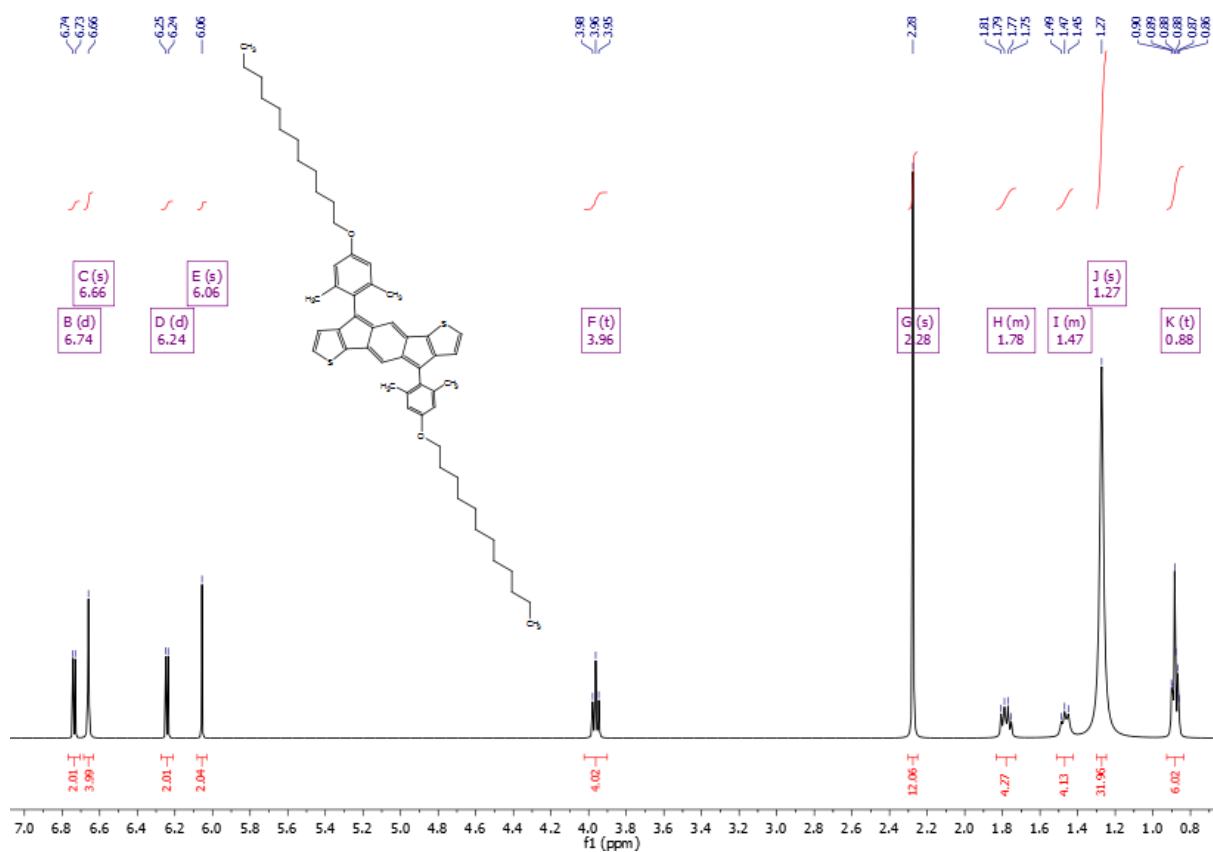
The reaction was poured into a mixture of water and saturated NH_4Cl solution before being extracted into DCM. The organic phase was separated and dried over $MgSO_4$. The solvent was removed under reduced pressure to yield the crude diol as a red oil. The crude diol was

immediately re-dissolved in dry toluene (100 mL) degassed with Argon for 20 minutes prior to the addition of SnCl₂·H₂O (1.65 g, 6.92 mmol, 4.0 eq.). The mixture was heated to 80 °C and stirred overnight. After cooling to room temperature, the reaction was passed through a short silica plug, eluting with DCM. Solvent was then removed under reduced pressure to yield a dark purple solid. The solid was dissolved in the minimum volume of DCM and subsequently precipitated into 150 mL of ethanol. The product was collected via suction filtration to yield a deep purple crystalline solid (620 mg, 43%).

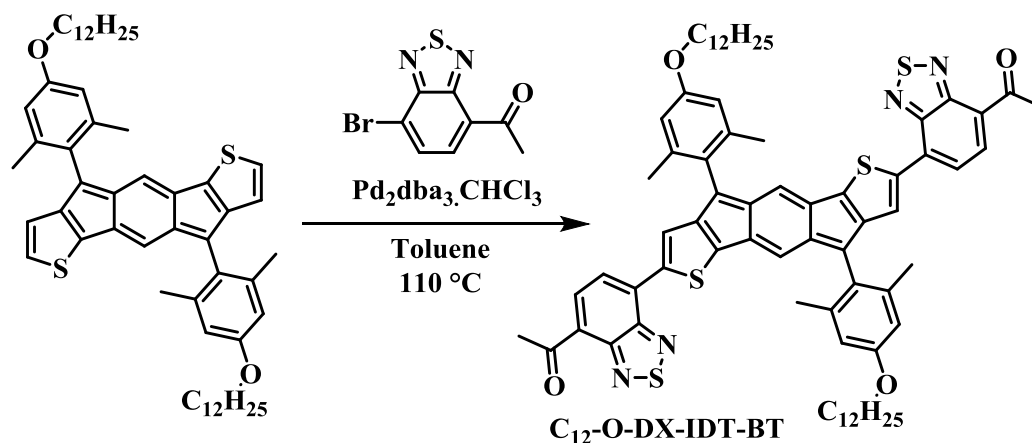
¹H NMR (400 MHz, Chloroform-*d*) δ 6.74 (d, *J* = 4.8 Hz, 2H), 6.66 (s, 4H), 6.24 (d, *J* = 4.8 Hz, 2H), 6.06 (s, 2H), 3.96 (t, *J* = 6.5 Hz, 4H), 2.28 (s, 12H), 1.83 – 1.73 (m, 4H), 1.51 – 1.42 (m, 4H), 1.27 (s, 32H), 0.88 (t, *J* = 7.1 Hz, 6H).

¹³C NMR (101 MHz, Chloroform-*d*) δ 158.29, 144.05, 139.21, 137.01, 127.48, 124.52, 119.53, 113.66, 113.51, 108.51, 96.98, 70.21, 67.86, 31.94, 29.71, 29.65, 29.38, 29.29, 29.25, 26.15, 25.99, 22.71, 14.14.

Mass (MALDI-ToF): 841.3 [M+H]⁺ (calc. 840.5 C₅₆H₇₂O₂S₂).



6.2.16 Synthesis of 7,7'-(4,9-bis(4-(dodecyloxy)-2,6-dimethylphenyl)-s-indaceno[1,2-*b*:5,6-*b'*]dithiophene-2,7-diyl)bis(benzo[*c*][1,2,5]thiadiazole-4-carbaldehyde)
(C₁₂-O-DX-IDT-BT)

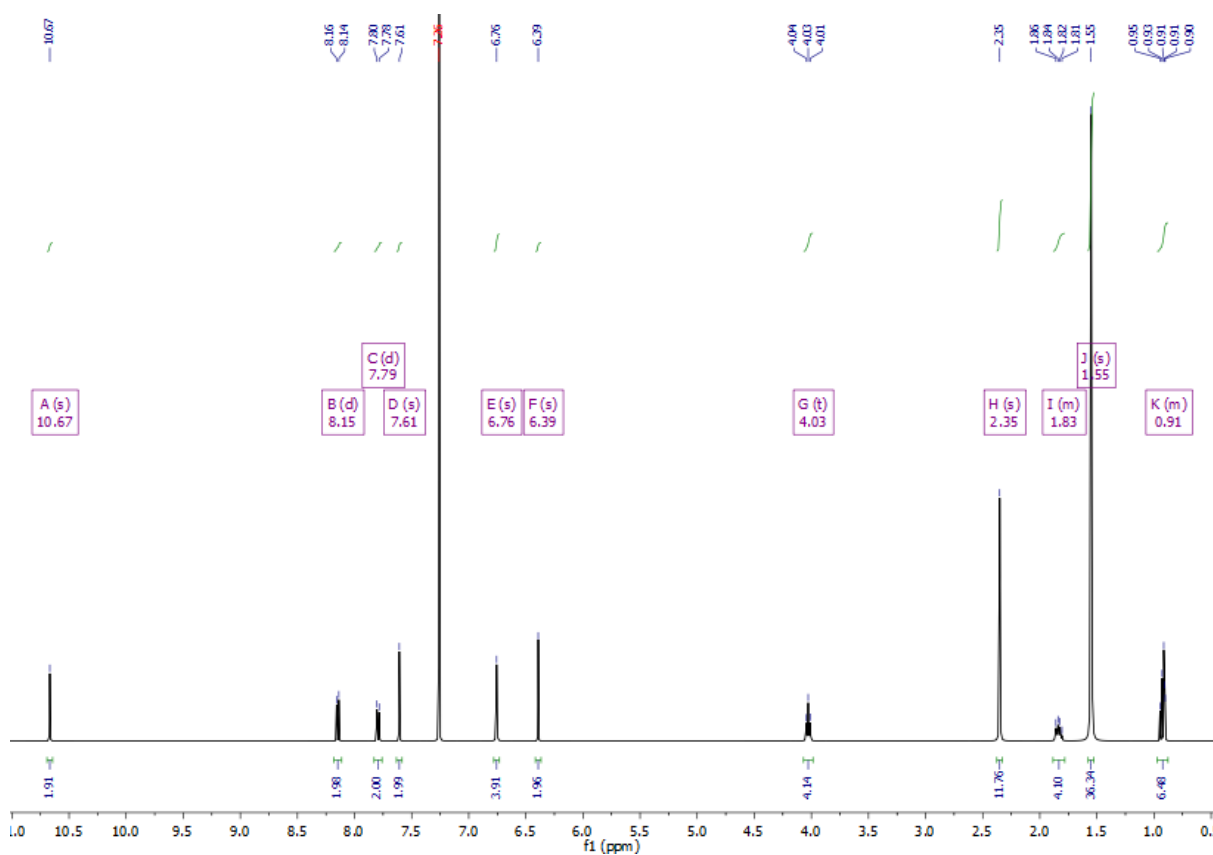


An oven dried 10 mL microwave vial was charged with **C₁₂-O-DX-IDT** (**6.2.15**) 4,9-bis(4-(dodecyloxy)-2,6-dimethylphenyl)-s-indaceno[1,2-*b*:5,6-*b'*]dithiophene (100 mg, 0.119 mmol, 1.0 eq.), 7-bromo-4-formyl-2,1,3-benzothiadiazole (63.6 mg, .261 mmol, 2.2 eq.),

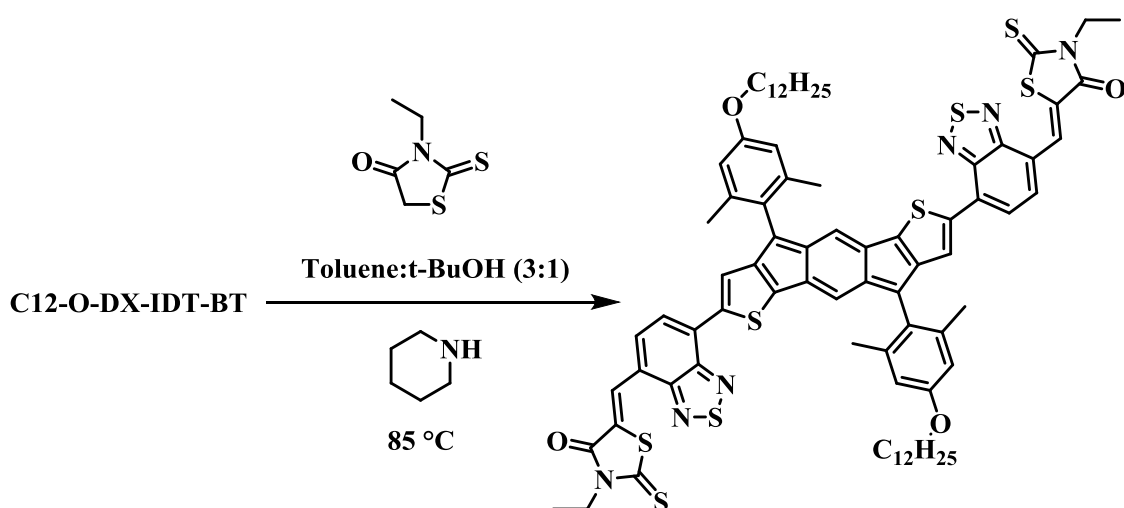
Pd₂dba₃.CHCl₃ (1.23 mg, 0.001 mmol, 0.01 eq.), tris(*o*-anisyl) phosphine [P(*o*-OMePh)₃] (1.68 mg, 0.004 mmol, 0.004 eq.), pivalic acid (12.1 mg, 0.119 mmol, 1.0 eq.) and caesium carbonate (116.2 mg, 0.357 mmol, 3.0 eq.). The cap was sealed, and the vial was degassed with Argon for 10 minutes. Dry toluene (1.2 mL) was added and the solution was degassed for a further 10 minutes. The vial was placed into a pre-heated oil bath at 100 °C and was stirred rapidly overnight. The crude mixture was purified by column chromatography on silica with DCM as the eluent to yield a purple crystalline solid (136 mg, 98%).

¹H NMR (400 MHz, Chloroform-*d*) δ 10.67 (s, 2H), 8.15 (d, *J* = 7.7 Hz, 2H), 7.79 (d, *J* = 7.7 Hz, 2H), 7.61 (s, 2H), 6.76 (s, 4H), 6.39 (s, 2H), 4.03 (t, *J* = 6.5 Hz, 4H), 2.35 (s, 12H), 1.88 – 1.78 (m, 4H), 1.55 (s, 36H), 0.97 – 0.88 (m, 6H).

Mass (MALDI-ToF): 1193.9 [M+H]⁺ (calc. 1192.5 C₇₂H₈₀N₄O₄S₄).



6.2.17 Synthesis of (5Z,5'Z)-5,5'-(((4,9-bis(4-(dodecyloxy)-2,6-dimethylphenyl)-s-indaceno[1,2-b:5,6-b']dithiophene-2,7-diyl)bis(benzo[c][1,2,5]thiadiazole-7,4-diyl))bis(methaneylylidene))bis(3-ethyl-2-thioxothiazolidin-4-one) (C₁₂-O-DX-IDT-BR)



C₁₂-O-DX-IDT-BT (6.2.16) 7,7'-(4,9-bis(4-(dodecyloxy)-2,6-dimethylphenyl)-s-indaceno[1,2-b:5,6-b']dithiophene-2,7-diyl)bis(benzo[c][1,2,5]thiadiazole-4-carbaldehyde)

(136 mg, 0.12 mmol, 1.0 eq.) was added to an oven dried 2-neck RBF. 3-ethylrhodanine (56.4 mg, 0.35 mmol, 3.0 eq.) was then added before the flask was degassed with Nitrogen for 10 minutes. Dry toluene (30 mL) and tert-Butanol (10 mL) was added via syringe, the solution was degassed for a further 30 minutes. Two drops of piperidine was added via syringe, the solution was subsequently heated to 85 °C and stirred overnight. Upon cooling to room temperature, the reaction was poured into water (300 mL) and the organic phase was extracted into DCM. Once separated and dried over MgSO₄ the solvent was removed under reduced pressure. The purple solid was dissolved in the minimum amount of DCM and precipitated into methanol, collected via suction filtration to yield the dark purple crystalline powder (145 mg, 86%).

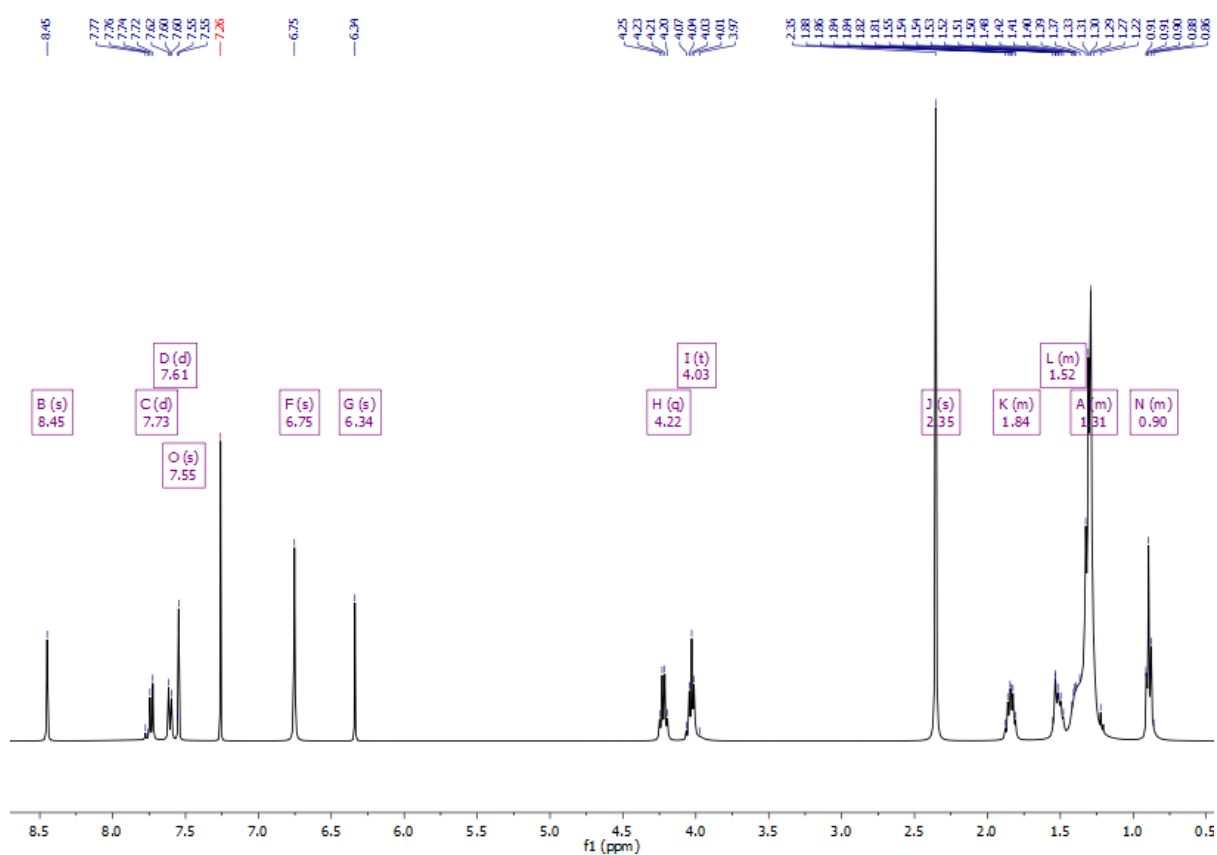
^1H NMR (400 MHz, Chloroform-*d*) δ 8.45 (s, 2H), 7.73 (d, $J = 7.8$ Hz, 2H), 7.61 (d, $J = 7.8$ Hz, 2H), 7.55 (s, 2H), 6.75 (s, 4H), 6.34 (s, 2H), 4.22 (q, $J = 7.1$ Hz, 4H), 4.03 (t, $J = 6.5$ Hz, 4H), 2.35 (s, 12H), 1.89 – 1.78 (m, 4H), 1.52 (p, $J = 7.1, 6.5$ Hz, 4H), 1.45 – 1.22 (m, 38H), 0.94 – 0.83 (m, 6H).

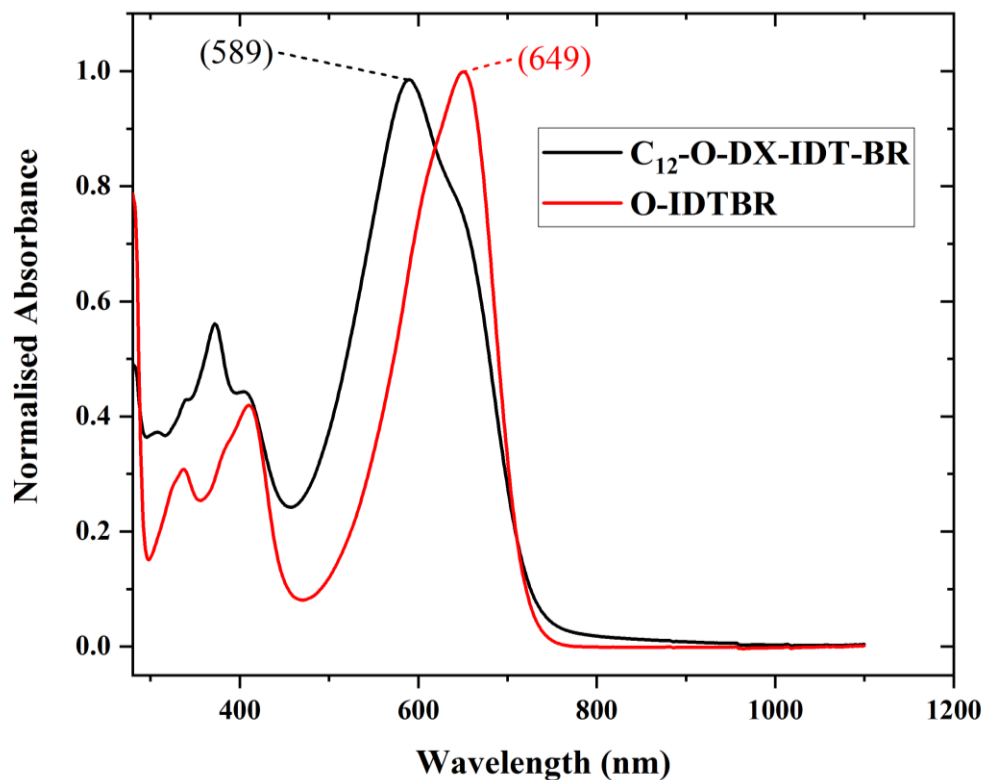
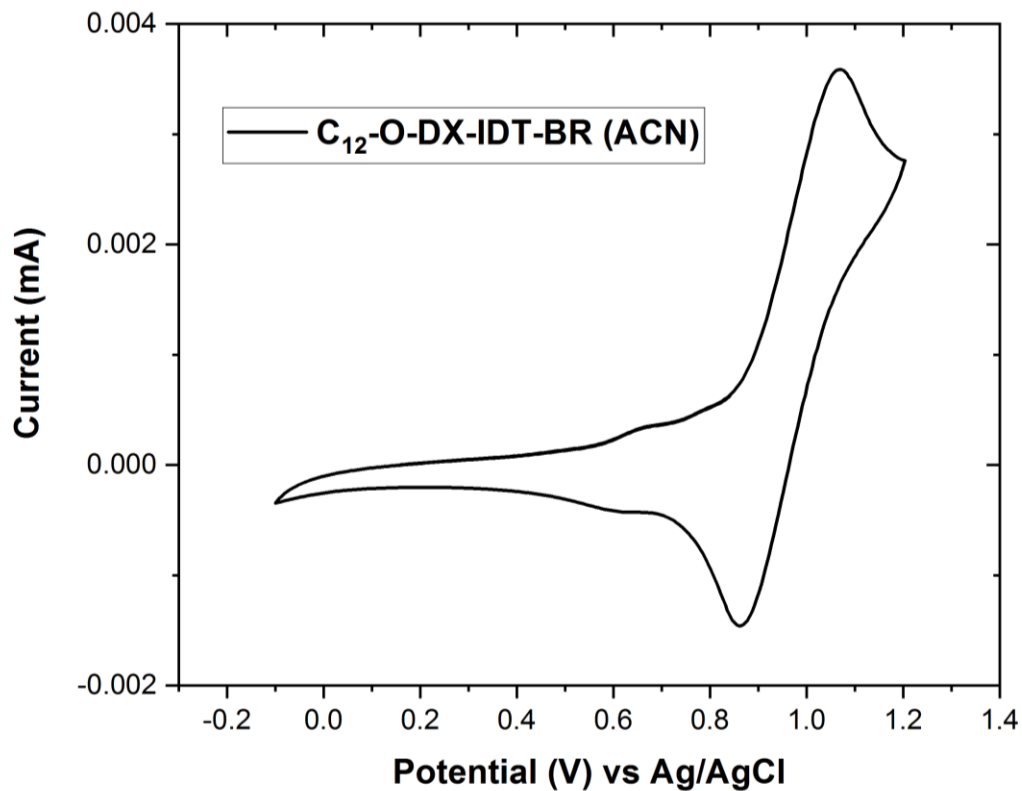
^{13}C NMR (101 MHz, Chloroform-*d*) δ 184.08, 167.66, 159.23, 154.54, 152.23, 151.63, 141.52, 141.22, 138.48, 137.42, 133.89, 133.06, 131.26, 129.96, 127.25, 124.95, 124.62, 124.02, 123.68, 122.83, 113.80, 104.49, 68.08, 40.06, 32.10, 32.00, 29.86, 29.81, 29.62, 29.57, 29.53, 26.32, 22.86, 21.28, 14.29, 12.45.

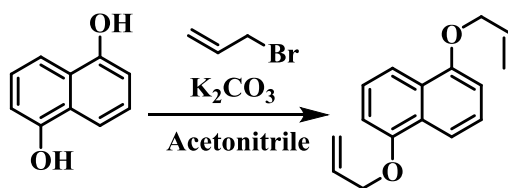
UV-Vis (CH_2Cl_2) λ_{max} : 589 nm.

$E_{\text{gopt}} = 1.69$ eV $EA = 3.64$ eV $IP = 5.33$ eV

Mass (MALDI-ToF): 1452.6 $[\text{M}+\text{H}]^+$ (calc. 1450.5 $\text{C}_{80}\text{H}_{86}\text{N}_6\text{O}_4\text{S}_8$).

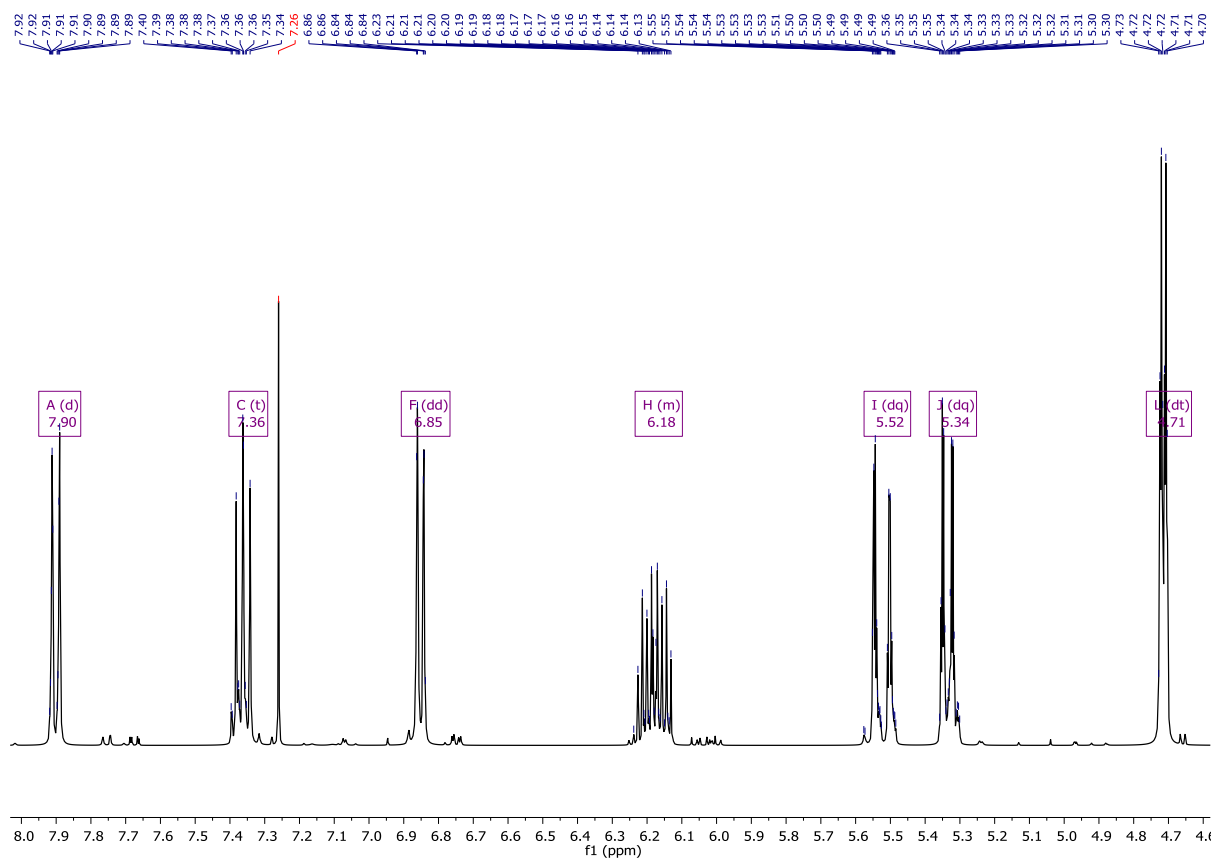




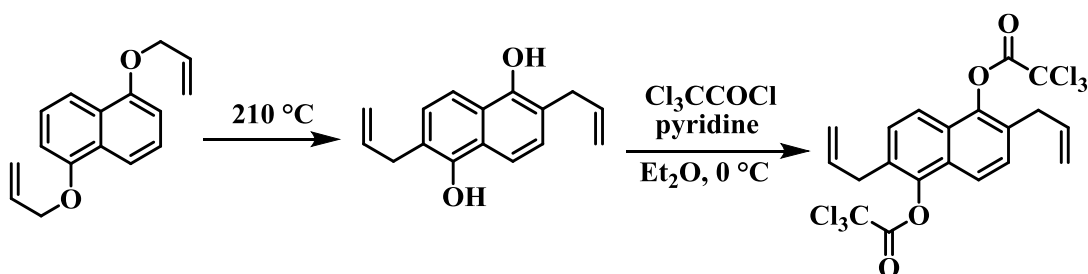
6.2.18 Synthesis of 1,5-bis(allyloxy)naphthalene²⁰⁶

Following a modified literature procedure¹⁴⁴, allyl bromide (29.6 mL, 341 mmol, 2.4 eq.) was added, dropwise, to a suspension of 1,5-dihydroxynaphthalene (22.7 g, 142 mmol, 1.0 eq.) and K₂CO₃ (47 g, 341 mmol, 2.4 eq.) in anhydrous acetonitrile (400 mL). The reaction was stirred overnight at room temperature prior to the removal of inorganic residues by vacuum filtration. The inorganics were washed with diethyl ether (300 mL), the filtrate was poured into water and washed with brine. The organic phase was separated and dried over MgSO₄; solvent removed under reduced pressure. The product was precipitated from 300 mL methanol at -78 °C to afford a light brown solid (19.69 g, 58%).

¹H NMR (400 MHz, Chloroform-*d*) δ 7.90 (d, J = 8.4 Hz, 2H), 7.36 (t, J = 7.4 Hz, 2H), 6.85 (dd, J = 7.6, 0.9 Hz, 2H), 6.26 – 6.10 (m, 2H), 5.52 (dq, J = 17.3, 1.7 Hz, 2H), 5.34 (dq, J = 10.6, 1.5 Hz, 2H), 4.71 (dt, J = 5.1, 1.6 Hz, 4H).



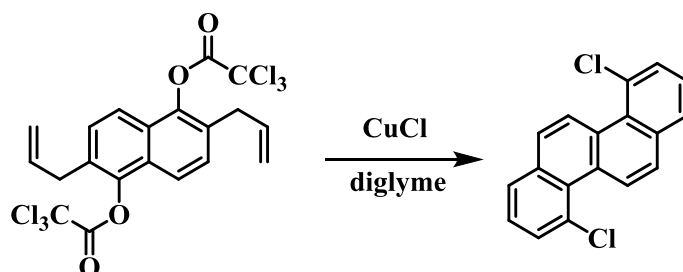
6.2.19 Synthesis of 2,6-diallylnaphthalene-1,5-diyl bis(2,2,2-trichloroacetate)¹⁴⁴



1,5-bis(allyloxy)naphthalene (**6.2.18**) (4 g, 16.6 mmol, 1.0 eq.) was heated for 2 hours at 210 °C under an Argon atmosphere. The orange-brown solid was cooled to room temperature prior to the addition of anhydrous diethyl ether (200 mL) and pyridine (3.24 mL, 40 mmol, 2.4 eq.). The solution was cooled to 0 °C followed by the dropwise addition of trichloroacetyl chloride (4.49 mL, 40 mmol, 2.4 eq.). The mixture was stirred for 2 hours then allowed to warm to room temperature. The brown solution was poured into a slurry of ice-water and NaHCO_3 , washed with water, brine and saturated NH_4Cl solution. The organic phase was separated and dried

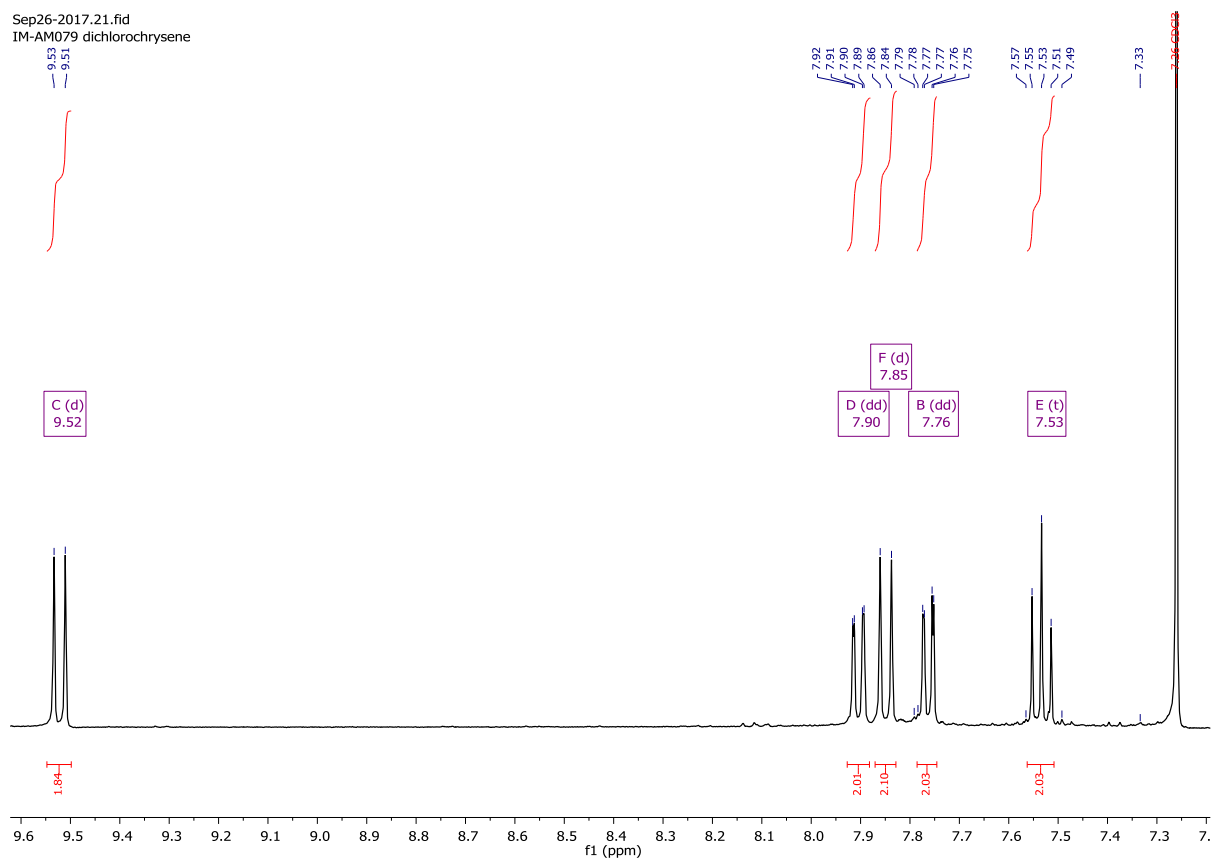
over MgSO_4 , solvent was removed under vacuum to yield the title compound as a yellow solid (6.2 g, 70%) which was used without further purification.

6.2.20 4,10-Dichlorochrysene¹⁴⁴

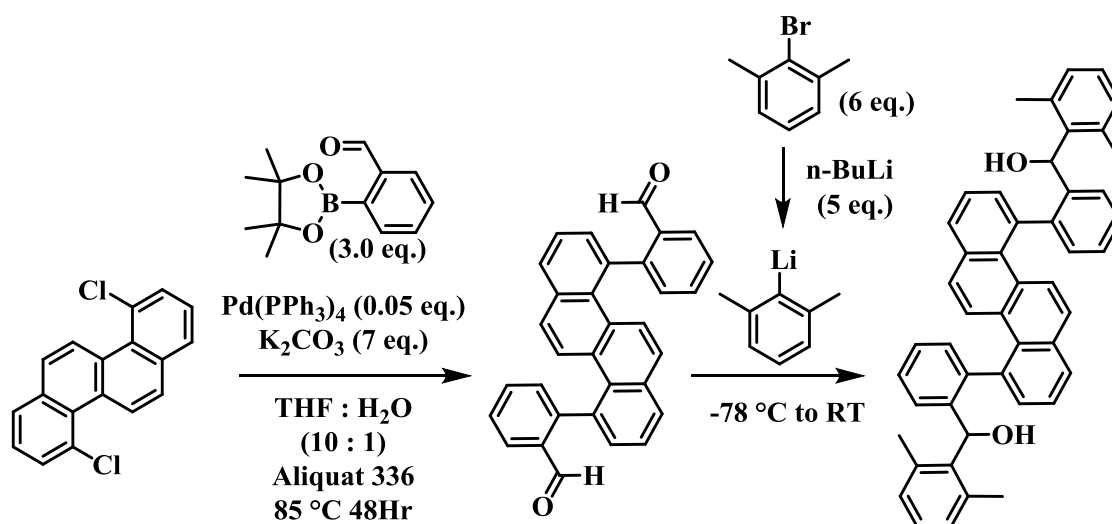


2,6-diallylnaphthalene-1,5-diyl bis(2,2,2-trichloroacetate) (**6.2.19**) (4.0 g, 7.53 mmol, 1.0 eq.) was dissolved in dry diglyme (4 mL) in a 25 mL RBF, the vessel was purged with Argon for 20 minutes. Cuprous chloride (37 mg, 0.38 mmol, 0.05 eq.) was added and the system was purged with Argon for an additional 20 minutes before being stirred at reflux (165 °C) for 2 hours. The reaction was allowed to cool to room temperature and loaded directly onto a flash column chromatography column, using silica gel, eluting with hexane:DCM 9:10 (v/v). Product fractions were combined and left to slowly evaporate to yield 4,10-dichlorochrysene as golden crystals (783 mg, 35%).

^1H NMR (400 MHz, Chloroform-*d*) δ 9.52 (d, $J = 9.1$ Hz, 2H), 7.90 (dd, $J = 7.6, 1.3$ Hz, 2H), 7.85 (d, $J = 9.1$ Hz, 2H), 7.76 (dd, $J = 7.6, 1.3$ Hz, 2H), 7.53 (t, $J = 7.6$ Hz, 2H).



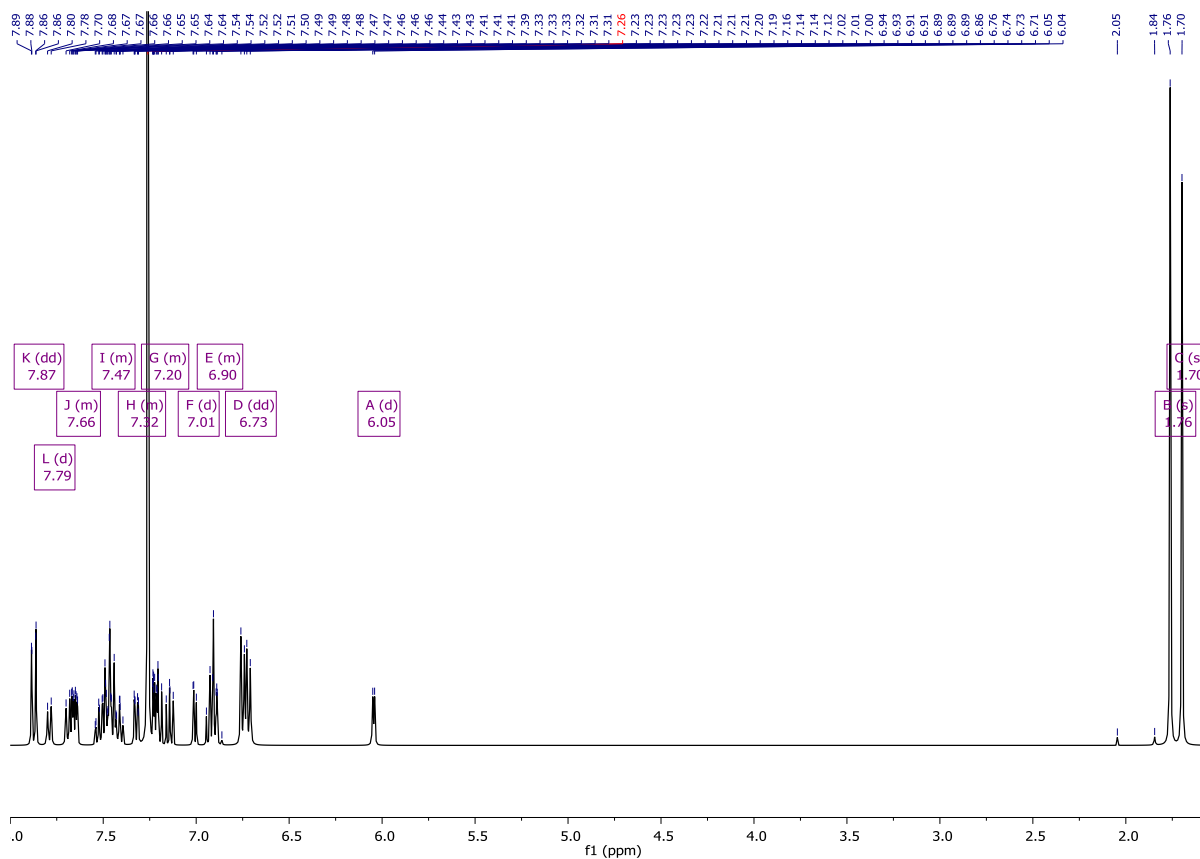
6.2.21 (chrysene-4,10-diylbis(2,1-phenylene))bis((2,6-dimethylphenyl)methanol)



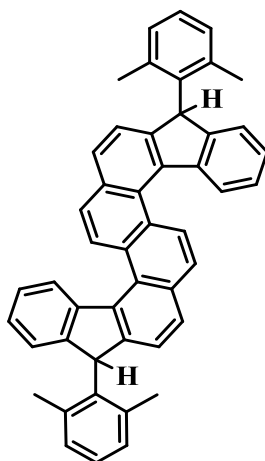
To a 25 mL microwave vial was added 4,10-dichlorochrysene (**6.2.20**) (200 mg, 0.67 mmol, 1.0 eq.), K_2CO_3 (651 mg, 4.71 mmol, 7.0 eq.) and $\text{Pd(PPh}_3)_4$ (38.9 mg, 0.05 eq.). The vial was sealed and degassed with argon followed by the addition of 2-formylphenylboronic acid pinacol ester (0.45 mL, 2.02 mmol, 3.0 eq.) degassed THF (10 mL), H_2O (1 mL) and a single

drop of Aliquat 336. The mixture was heated to 85 °C and stirred vigorously for 48 hours. The reaction was then cooled to room temperature and transferred to a separating funnel containing DCM (100 mL) and water (250 mL). The organic layer was separated and dried over anhydrous MgSO₄, filtered and the solvent was removed under reduced pressure to yield the crude product. The crude was subsequently washed with a small amount of methanol and the filtrate was removed. The obtained residue was redissolved in dry THF (20 mL) degassed with Ar and cooled to -78 °C for 30 minutes. In a second flask 2-bromo-*m*-xylene (0.53 mL, 3.96 mmols, 6.0 eq.) was dissolved in dry THF (30 mL), *n*-BuLi (2.06 mL, 5 eq., 1.6 M in hexane) was added to the cold mixture and stirred for 60 minutes. The cold lithiate solution was transferred by cannula to the dione mixture and subsequently warmed to room temperature for 2 hours. The reaction mixture was quenched with 10% HCl solution (10 mL), extracted in Et₂O (100 mL), water (100 mL) and brine (100 mL). The organic layer was dried over anhydrous magnesium sulphate, filtered and evaporated to dryness. The crude diol was purified by silica chromatography using mixtures of hexane/CHCl₃ as an eluent to obtain (chrysene-4,10-diylbis(2,1-phenylene))bis((2,6-dimethylphenyl)methanol) as a yellow solid (100 mg, 23%).

¹H NMR (400 MHz, Chloroform-*d*) δ 7.87 (dd, *J* = 9.1, 0.8 Hz, 2H), 7.79 (d, *J* = 7.8 Hz, 2H), 7.74 – 7.62 (m, 2H), 7.55 – 7.37 (m, 6H), 7.35 – 7.30 (m, 2H), 7.24 – 7.09 (m, 2H), 7.01 (d, *J* = 1.4 Hz, 2H), 6.95 – 6.88 (m, 4H), 6.73 (dd, *J* = 12.7, 7.5 Hz, 4H), 6.05 (d, *J* = 4.0 Hz, 2H), 1.76 (s, 6H), 1.70 (s, 6H).



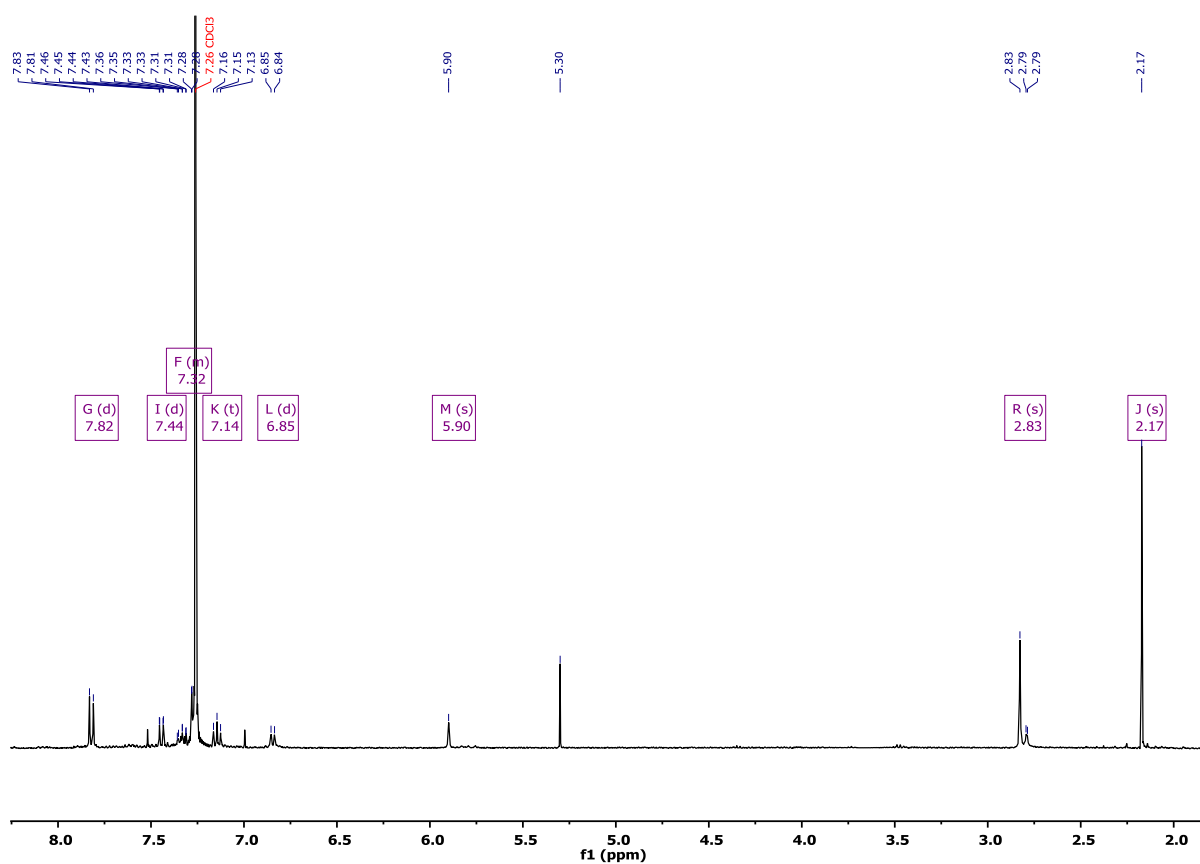
6.2.22 1,10-bis(2,6-dimethylphenyl)-1,10-dihydroindeno[2,1-c:2',1'-l]chrysene



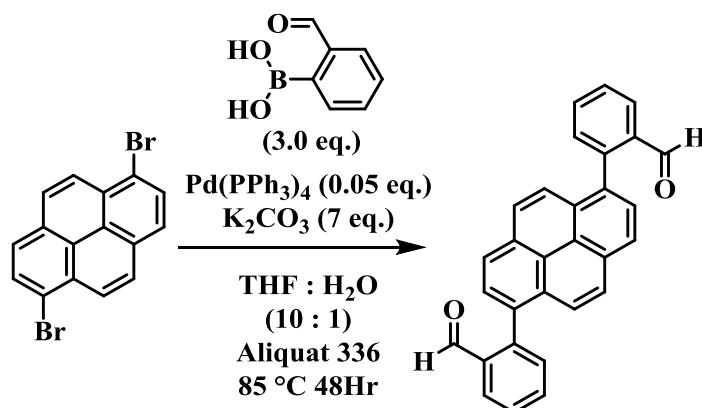
Compound (**6.2.21**) (100 mg, 0.15 mmol, 1.0 eq.) was dissolved in 35 mL dry DCM and stirred under argon atmosphere, 1 mL of $\text{BF}_3 \cdot \text{OEt}_2$ was then added dropwise. The mixture was stirred for 2 hours and then washed with NaHCO_3 solution (3x25 mL) and water (3x50 mL). The organic layer was dried over MgSO_4 and the solvent was removed under reduced pressure. The

crude brown residue was purified by column chromatography, on silica gel, using DCM as the eluent to yield 1,10-bis(2,6-dimethylphenyl)-1,10-dihydrodiindeno[2,1-c:2',1'-l]chrysene as an off-white solid (59 mg, 63%).

^1H NMR (400 MHz, Chloroform-*d*) δ 8.91 (d, $J = 8.4$ Hz, 2H), 8.44 (d, $J = 7.7$ Hz, 2H), 7.82 (d, $J = 8.4$ Hz, 4H), 7.44 (d, $J = 8.4$ Hz, 2H), 7.37 – 7.30 (m, 8H), 7.14 (t, $J = 7.7$ Hz, 2H), 6.85 (d, $J = 7.7$ Hz, 2H), 5.90 (s, 2H), 2.83 (s, 6H), 2.17 (s, 6H).



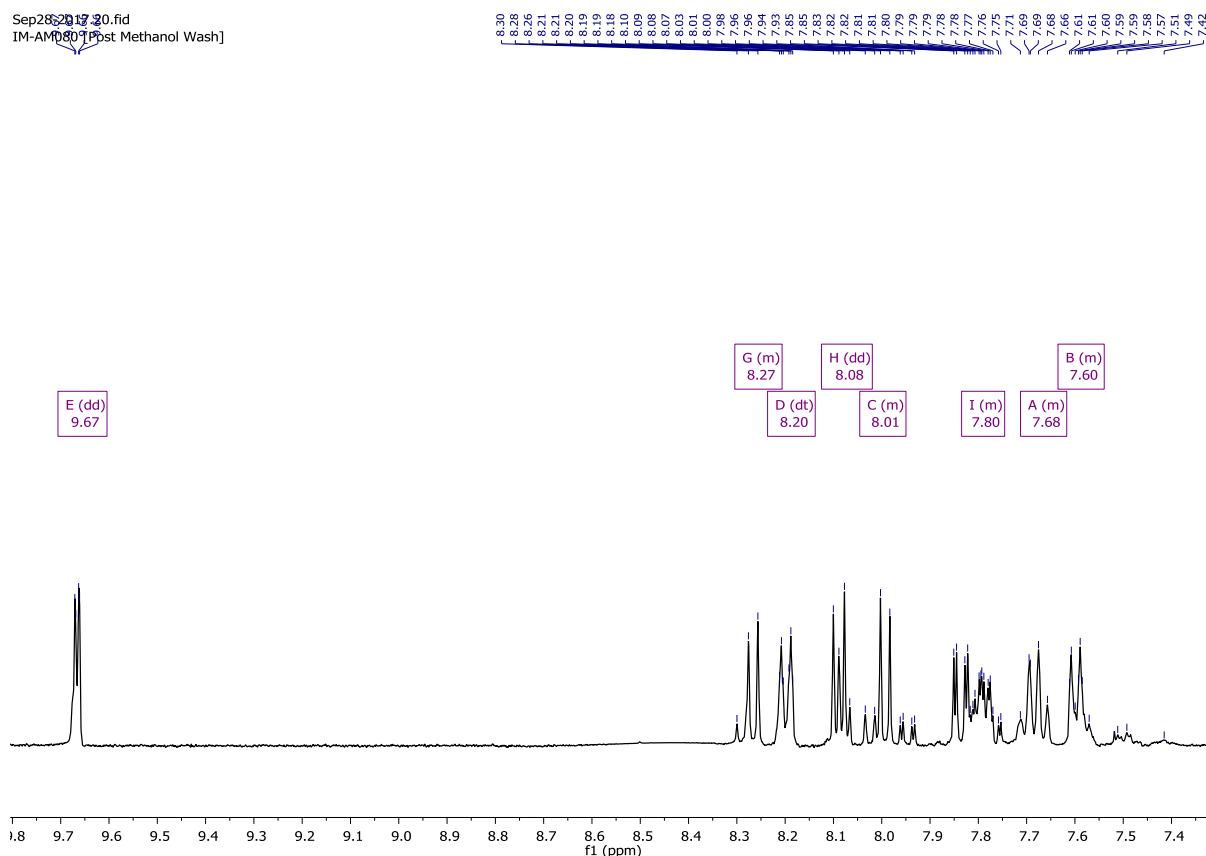
6.2.23 Synthesis of 2,2'-(pyrene-1,6-diyl)dibenzaldehyde (Route 1)



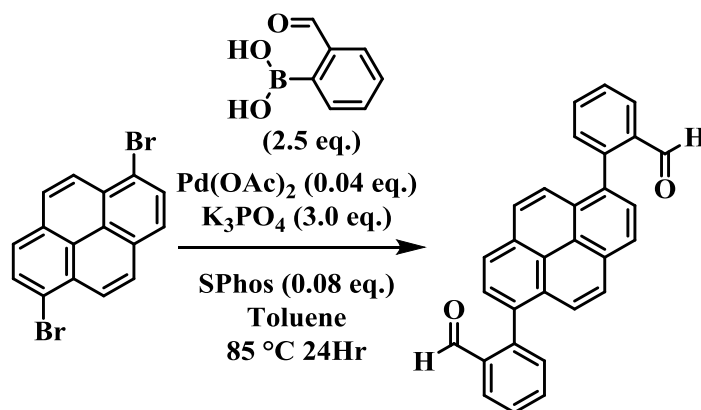
An oven dried 25 mL microwave vial was charged with 1,6-dibromopyrene (200 mg, 0.56 mmol, 1.0 eq.), (2-formylphenyl)boronic acid (250 mg, 1.68 mmol, 3.0 eq.), K₂CO₃ (538 mg, 3.92 mmol, 7.0 eq.) and Pd(PPh₃)₄ (32.1 mg, 0.03 mmol, 0.05 eq.). Cap was sealed and degassed with Argon for 10 minutes prior to the addition of dry THF (10 mL) and H₂O (1 mL). The reaction was stirred rapidly overnight at 100 °C before being allowed to cool to room temperature and loaded directly onto a flash chromatography column, using silica gel. The crude was eluted with DCM and product fractions combined, washed with methanol to remove boronic acid impurities, reduced in vacuo to afford a yellow crystalline solid (209 mg, 91%).

¹H NMR (400 MHz, Chloroform-*d*) δ 9.67 (dd, *J* = 3.2, 0.8 Hz, 2H), 8.32 – 8.23 (m, 2H), 8.20 (dt, *J* = 7.8, 1.6 Hz, 2H), 8.08 (dd, *J* = 9.1, 4.5 Hz, 2H), 8.06 – 7.91 (m, 2H), 7.88 – 7.69 (m, 4H), 7.72 – 7.63 (m, 2H), 7.64 – 7.55 (m, 2H).

Sep28 2017 20.fid
 IM-AM080 [Post Methanol Wash]



6.2.24 Synthesis of 2,2'-(pyrene-1,6-diyl)dibenzaldehyde (Route 2)

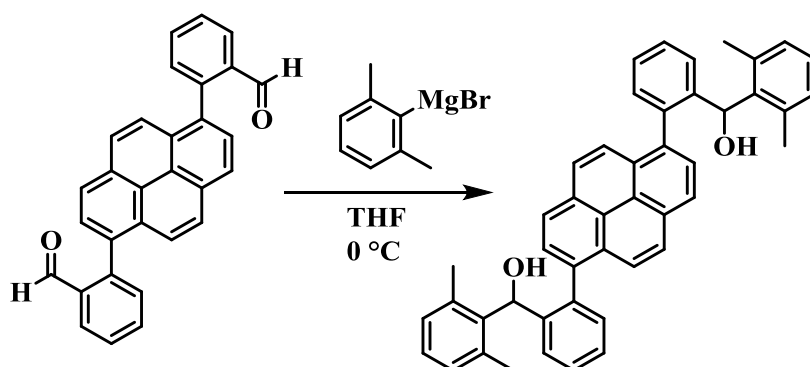


An oven dried 25 mL microwave vial was charged with 1,6-dibromopyrene (500 mg, 1.39 mmol, 1.0 eq.), (2-formylphenyl)boronic acid (520 mg, 3.47 mmol, 2.5 eq.), K_3PO_4 (896 mg, 4.17 mmol, 3.0 eq.), SPhos (45.2 mg, 0.11 mmol, 0.08 eq.) and $\text{Pd}(\text{OAc})_2$ (17.4 mg, 0.06 mmol, 0.04 eq.). Cap was sealed and the vessel was degassed with Argon for 10 minutes. Dry toluene (16 mL) was added and the reaction was stirred rapidly overnight at $85\text{ }^{\circ}\text{C}$. The reaction was

allowed to cool to room temperature then was poured into water, washed with brine and the aqueous phase was extracted three times with DCM. The organic layers were combined, dried over MgSO_4 , solvent removed under reduced pressure. The crude aldehyde was purified by flash column chromatography, on silica gel, with DCM as the eluent system. Product fractions were combined, solvent removed in vacuo to afford the title compound as a yellow solid (560 mg, 98%).

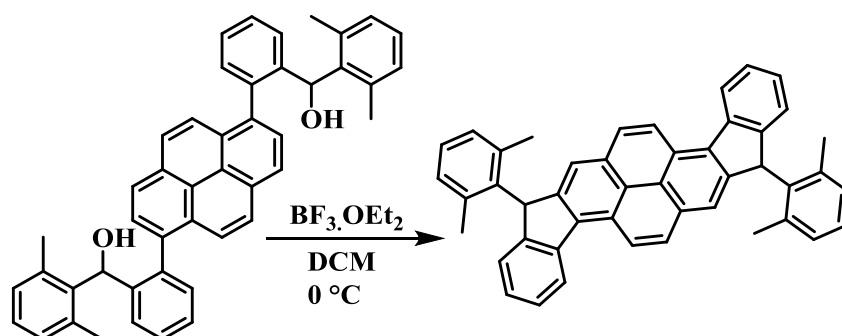
^1H NMR (400 MHz, Chloroform-*d*) δ 9.67 (dd, $J = 3.2, 0.8$ Hz, 2H), 8.32 – 8.23 (m, 2H), 8.20 (dt, $J = 7.8, 1.6$ Hz, 2H), 8.08 (dd, $J = 9.1, 4.5$ Hz, 2H), 8.06 – 7.91 (m, 2H), 7.88 – 7.69 (m, 4H), 7.72 – 7.63 (m, 2H), 7.64 – 7.55 (m, 2H).

6.2.25 (pyrene-1,6-diylbis(2,1-phenylene))bis((2,6-dimethylphenyl)methanol)



2,2'-(pyrene-1,6-diyl)dibenzaldehyde (6.2.24) (560 mg, 1.36 mmol, 1.0 eq.) was dissolved in dry THF and cooled to 0 °C under an Argon atmosphere. (2,6-dimethylphenyl)magnesium bromide (1.0M solution in THF) (5.45 mL, 5.46 mmol, 4.0 eq.) was added dropwise and the reaction was stirred overnight. The reaction was subsequently poured into water, washed with saturated NH_4Cl solution and extracted into DCM three times. The organic phases were combined and dried over MgSO_4 before the solvent was removed in vacuo. The diol was isolated upon precipitation into hexane, filtering to afford an off-white solid (483 mg, 57%). The title compound was used in the next step without further purification.

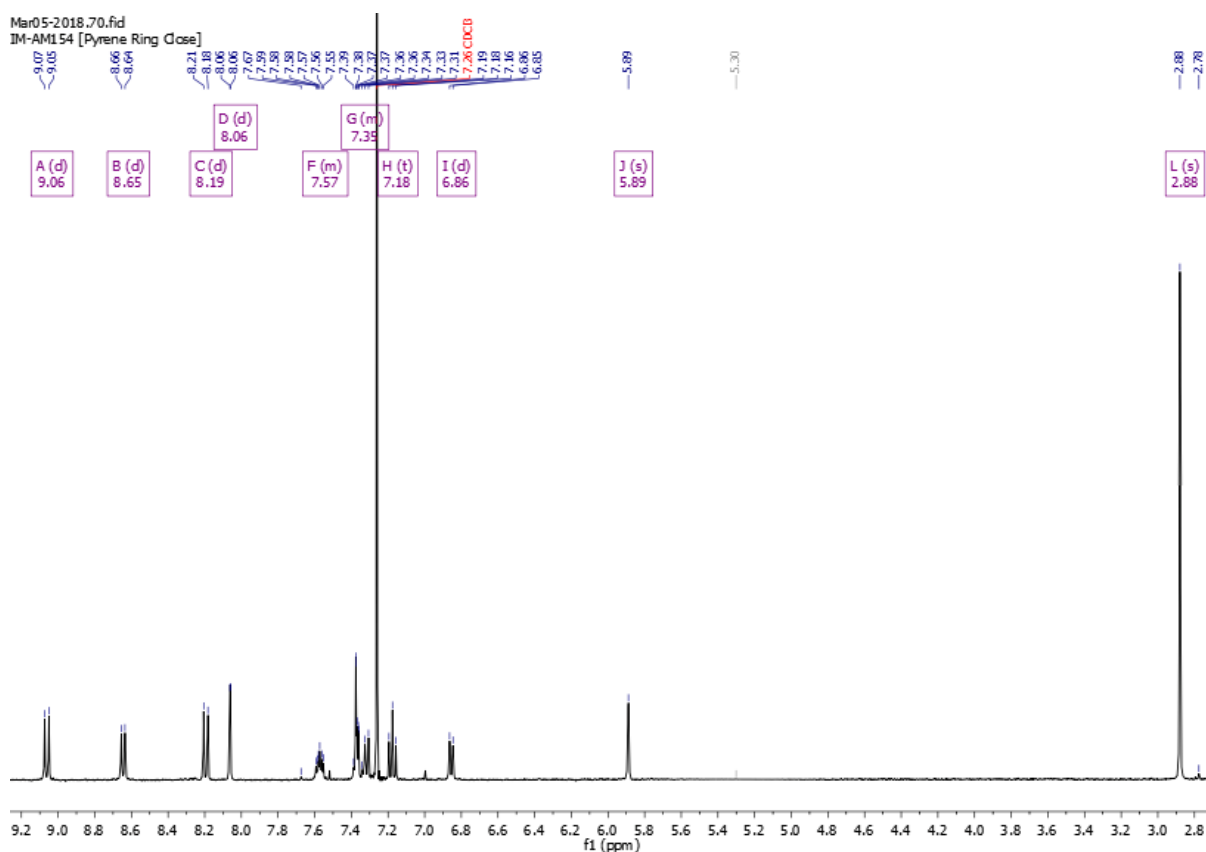
6.2.26 1,9-bis(2,6-dimethylphenyl)-1,9-dihydroindeno[1,2-a:1',2'-h]pyrene



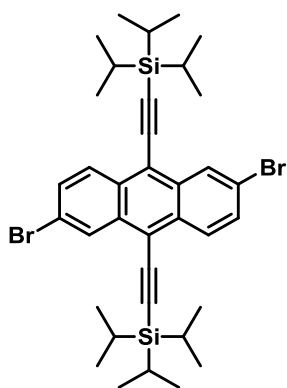
(pyrene-1,6-diylbis(2,1-phenylene))bis((2,6-dimethylphenyl)methanol) (**6.2.25**) (483 mg, 0.78 mmol, 1.0 eq.) was dissolved in dry DCM (20 mL) and cooled to 0 °C. Boron trifluoride diethyl etherate (0.34 mL, 3.11 mmol, 4.0 eq.) was added dropwise, causing an instant colour change from yellow to deep red. The mixture was stirred for 20 minutes before being poured into water, washed with saturated NaHCO₃ solution and extracted three times with DCM. The organic phases were combined, dried over MgSO₄ and solvent removed under reduced pressure. The crude residue was purified via column chromatography, on silica gel, using DCM as the eluent system. Product fractions were combined, and solvent removed in vacuo to yield the title compound as a yellow solid (163 mg, 20%).

¹H NMR (400 MHz, Chloroform-*d*) δ 9.06 (d, *J* = 9.2 Hz, 2H), 8.65 (d, *J* = 8.0 Hz, 2H), 8.19 (d, *J* = 9.2 Hz, 2H), 8.06 (d, *J* = 1.1 Hz, 2H), 7.62 – 7.53 (m, 2H), 7.41 – 7.28 (m, 6H), 7.18 (t, *J* = 7.6 Hz, 2H), 6.86 (d, *J* = 7.6 Hz, 2H), 5.89 (s, 2H), 2.88 (s, 12H).

Mass (MALDI-ToF): 586.9 [M+H]⁺ (calc. 586.3 C₄₆H₃₄).



6.2.27 ((2,6-dibromoanthracene-9,10-diyl)bis(ethyne-2,1-diyl)bis(triisopropylsilane))¹⁵⁵

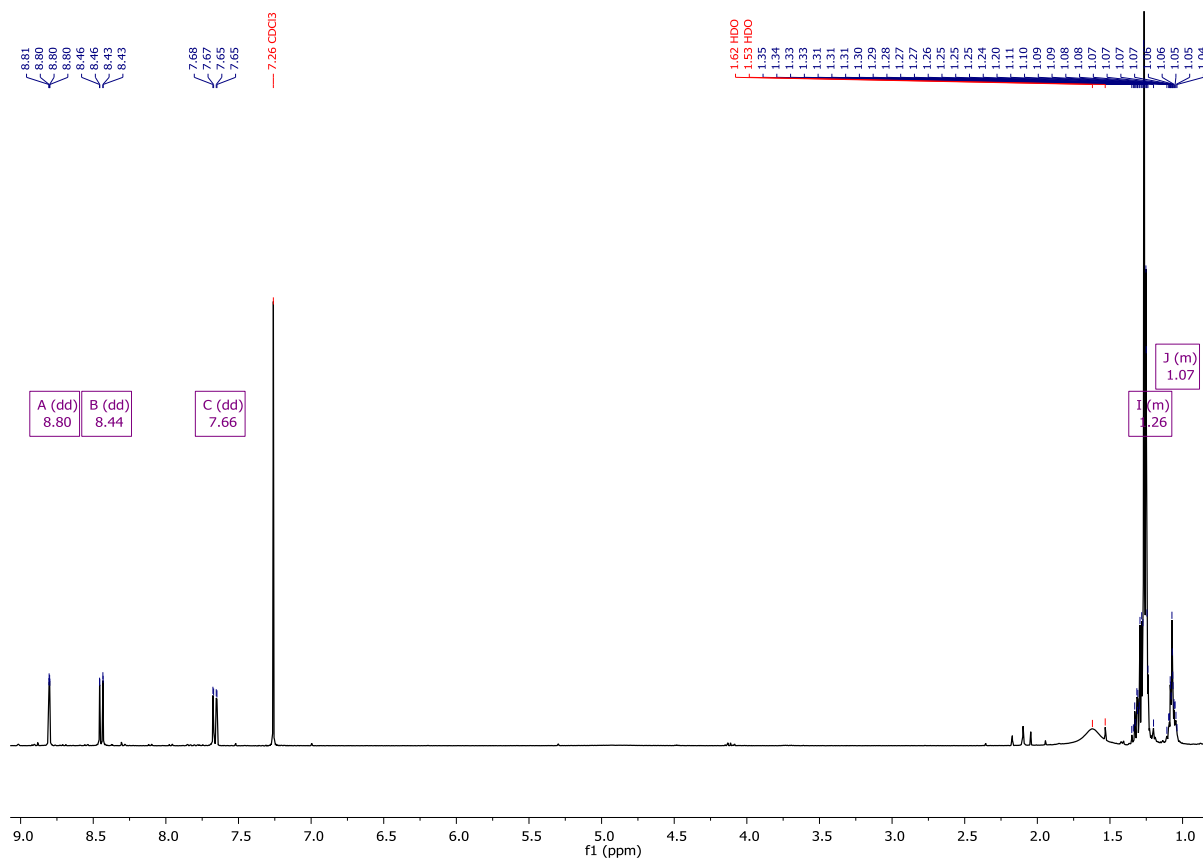


To an oven-dried round-bottom flask, loaded with a stirrer bar and cooled to 0 °C under Ar, was added THF (15 mL) and triisopropylsilyl acetylene (2.45 mL, 10.9 mmol, 4.0 eq.) followed by the dropwise addition of *n*-BuLi (5.1 mL, 8.19 mmol, 1.6 M solution in hexane, 3.0 eq.). This mixture was stirred for 1 hour at room temperature, then transferred to a mixture of 2,6-dibromo-9,10-anthraquinone (1.0 g, 2.73 mmol, 1.0 eq.) dissolved in dry THF (30 mL) cooled to -78 °C. The mixture was stirred at room temperature for 48 hours, and then quenched with

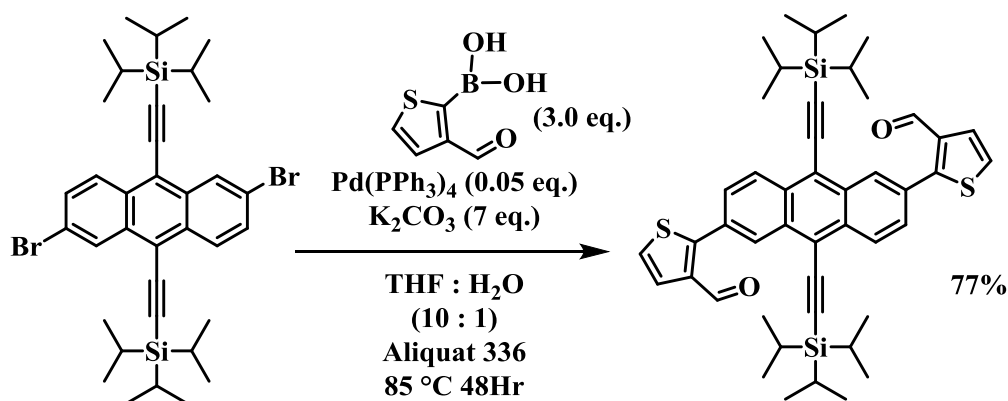
water. The resulting mixture was poured into saturated ammonium chloride solution and extracted with ethyl acetate. The organic layer was washed with brine and dried over anhydrous MgSO_4 . The solvent was removed under vacuum and the resultant yellow residue was dissolved in dry THF (25 mL), $\text{SnCl}_2 \cdot 2\text{H}_2\text{O}$ (3.08 g, 13.7 mmol, 5.0 eq.) was added followed by the dropwise addition of acetic acid (25 mL). The mixture was stirred, under Ar, at room temperature overnight, then poured into water and extracted with ethyl acetate. The organic layer was washed with sodium bicarbonate and brine, then dried over anhydrous MgSO_4 . The solvent was removed under vacuum and the crude product was purified via column chromatography on silica with hexane as the eluent, then crystallised from petroleum ether to yield ((2,6-dibromoanthracene-9,10-diyl)bis(ethyne-2,1-diyl))bis(triisopropylsilane) (1.28 g, 67%) as a bright orange solid.

^1H NMR (400 MHz, Chloroform-*d*) δ 8.80 (dd, $J = 2.0, 0.6$ Hz, 2H), 8.44 (dd, $J = 9.2, 0.6$ Hz, 2H), 7.66 (dd, $J = 9.2, 2.0$ Hz, 2H), 1.37 – 1.16 (m, 36H), 1.13 – 1.00 (m, 6H).

^{13}C NMR (101 MHz, Chloroform-*d*) δ 133.21, 130.96, 130.87, 129.48, 128.95, 121.99, 118.17, 106.31, 102.19, 18.81, 11.44.



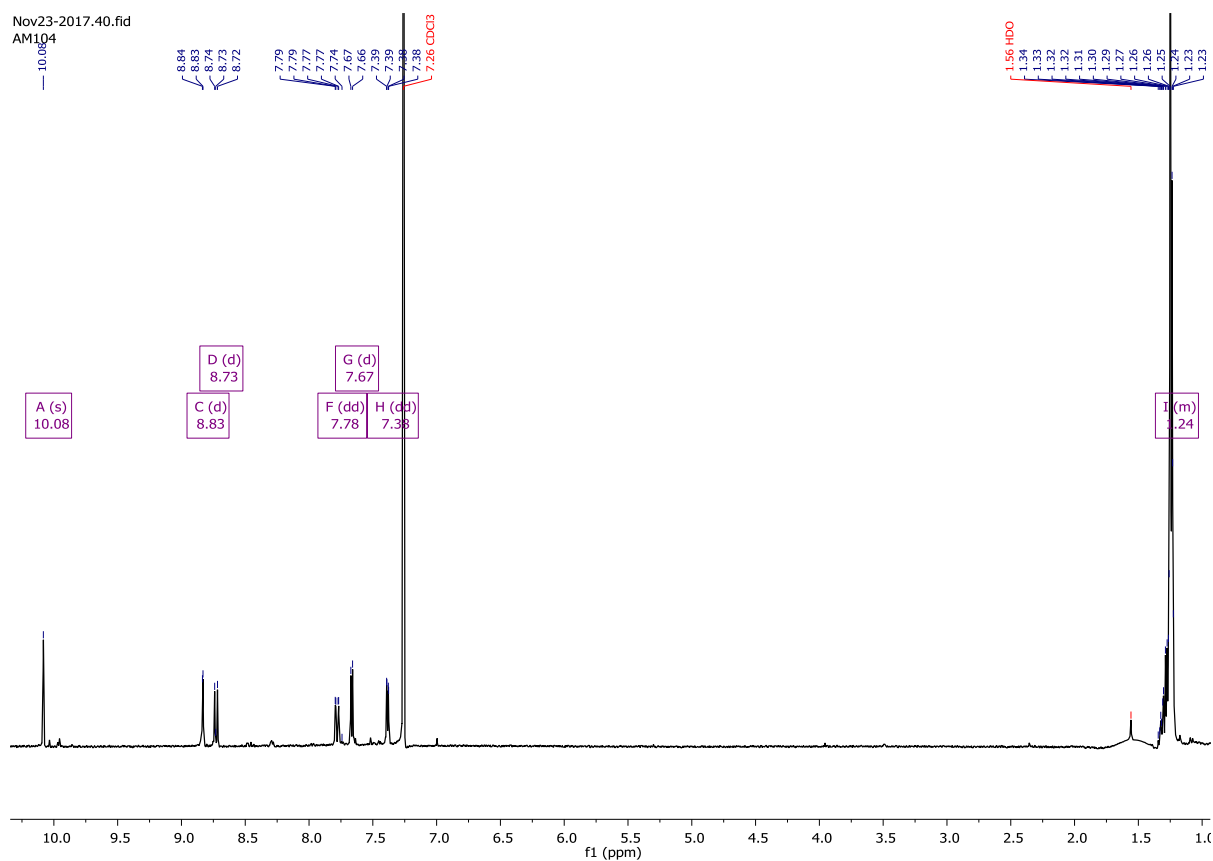
6.2.28 2,2'-(9,10-bis((triisopropylsilyl)ethynyl)anthracene-2,6-diyl)bis(thiophene-3-carbaldehyde) (Route 1)



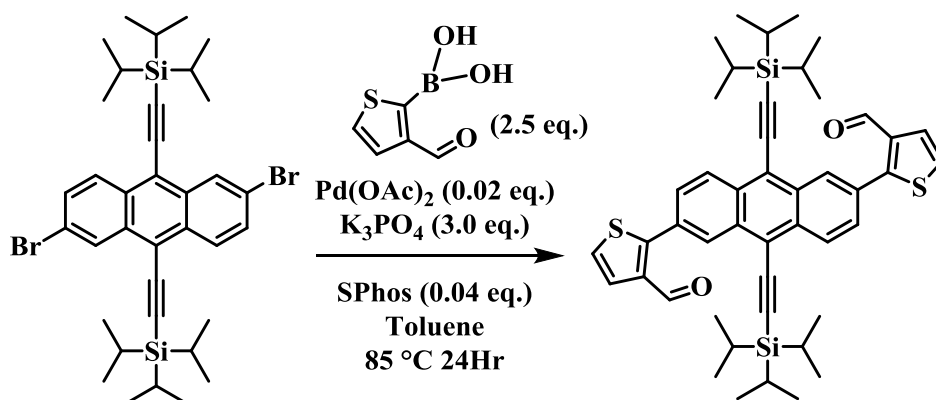
To a 25 mL oven dried microwave vial was added (6.2.27) ((2,6-dibromoanthracene-9,10-diyl)bis(ethyne-2,1-diyl))bis(triisopropylsilane) (200.0 mg, 0.29 mmol, 1.0 eq.), 3-formyl-2-thienyl boronic acid (134.3 mg, 0.86 mmol, 3.0 eq.), Pd(PPh₃)₄ (16.6 mg, 0.01 mmol, 0.05 eq.), K₂CO₃ (277 mg, 2.00 mmol, 7.0 eq.) and a drop of Aliquat 336. The cap was sealed and briefly

degassed with Argon for 10 minutes. Dry THF (10 mL) and H₂O (1 mL) were added via syringe. The vial was then placed into a pre-heated (90 °C) oil bath. The reaction mixture was covered and stirred overnight in the dark. The solution was cooled to room temperature then poured into water and extracted into DCM. The organic layer was washed with brine, then dried over anhydrous MgSO₄. The solvent was removed under vacuum and the crude product was purified via column chromatography on silica with hexane as the eluent, then recrystallised from petroleum ether to yield a dark red solid (167 mg, 77%).

¹H NMR (400 MHz, Chloroform-*d*) δ 10.08 (s, 2H), 8.83 (d, *J* = 1.7 Hz, 2H), 8.73 (d, *J* = 8.9 Hz, 2H), 7.78 (dd, *J* = 8.9, 1.8 Hz, 2H), 7.67 (d, *J* = 5.4 Hz, 2H), 7.38 (dd, *J* = 5.4, 0.9 Hz, 2H), 1.37 – 1.19 (m, 42H).

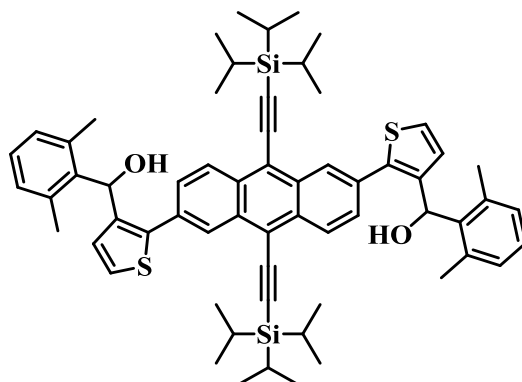


6.2.29 2,2'-(9,10-bis((triisopropylsilyl)ethynyl)anthracene-2,6-diyl)bis(thiophene-3-carbaldehyde) (Route 2)

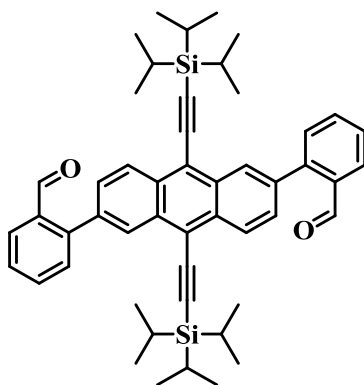


To a 25 mL oven dried microwave vial was charged with **(6.2.27)** ((2,6-dibromoanthracene-9,10-diyl)bis(ethyne-2,1-diyl))bis(triisopropylsilane) (1.0 g, 1.44 mmol, 1.0 eq.), 3-formyl-2-thienyl boronic acid (560 mg, 3.59 mmol, 2.5 eq.), Pd(OAc)₂ (6.44 mg, 0.03 mmol, 0.02 eq.), K₃PO₄ (914 mg, 4.31 mmol, 3.0 eq.) and a SPhos (24.0 mg, .06 mmol, 0.04 eq.). The cap was sealed and briefly degassed with Argon for 10 minutes. Dry Toluene (15 mL) was added via syringe. The vial was then placed into a pre-heated (85 °C) oil bath. The reaction mixture was covered and stirred overnight in the dark. The solution was cooled to room temperature then poured into water and extracted into DCM. The organic layer was washed with brine, then dried over anhydrous MgSO₄. The solvent was removed under vacuum and the crude product was purified via column chromatography on silica with hexane as the eluent, then recrystallised from petroleum ether to yield a dark red solid (1.07 g, 98%).

¹H NMR (400 MHz, Chloroform-*d*) δ 10.08 (s, 2H), 8.83 (d, *J* = 1.7 Hz, 2H), 8.73 (d, *J* = 8.9 Hz, 2H), 7.78 (dd, *J* = 8.9, 1.8 Hz, 2H), 7.67 (d, *J* = 5.4 Hz, 2H), 7.38 (dd, *J* = 5.4, 0.9 Hz, 2H), 1.37 – 1.19 (m, 42H).

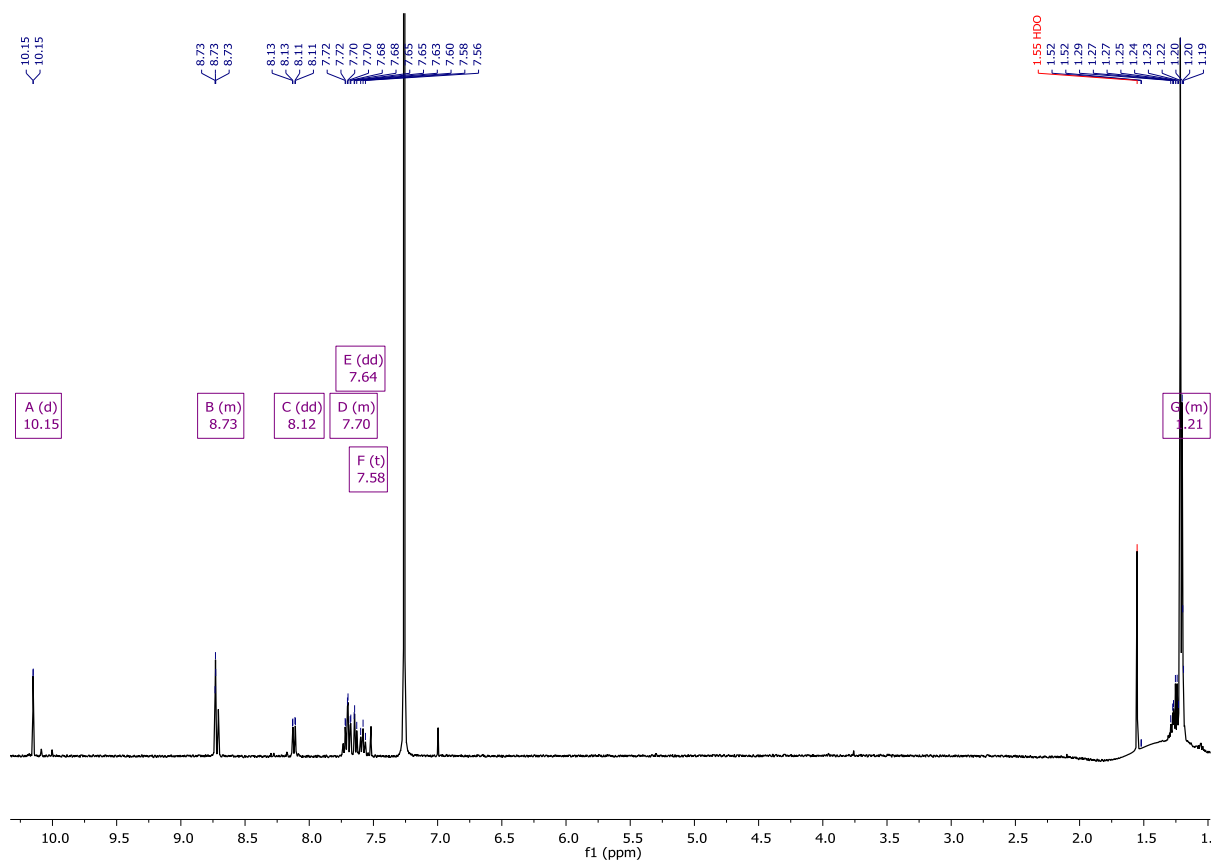
6.2.30 ((9,10-bis((triisopropylsilyl)ethynyl)anthracene-2,6-diyl)bis(thiophene-2,3-diyl))bis((2,6-dimethylphenyl)methanol)

To a 2 neck 250 ml oven dried RBF was added **(6.2.29)** 2,2'-(9,10-bis((triisopropylsilyl)ethynyl)anthracene-2,6-diyl)bis(thiophene-3-carbaldehyde) (167 mg, 0.22 mmols, 1.0 eq.). Dissolved in dry THF (50 mL) and cooled to 0 °C. A solution of 2,6-dimethylphenylmagnesiumbromide (0.88 mL, 0.88 mmols, 4.0 eq.) was added slowly dropwise. The reaction was stirred for 2 hours before being quenched with saturated NH₄Cl (25 mL) and diluted with diethyl ether (50 mL). The organic layer was washed with water and brine before being separated and dried over MgSO₄. Solvent was removed under reduced pressure to yield the crude diol as a deep orange solid which was used immediately in the next step.

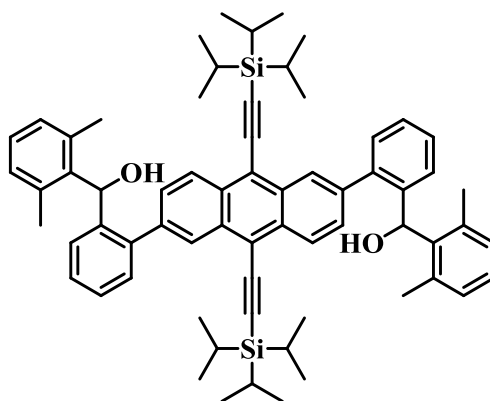
6.2.31 2,2'-(9,10-bis((triisopropylsilyl)ethynyl)anthracene-2,6-diyl)dibenzaldehyde

To a 25 mL oven dried microwave vial was added (**6.2.27**) ((2,6-dibromoanthracene-9,10-diyl)bis(ethyne-2,1-diyl))bis(triisopropylsilane) (1.0 g, 1.44 mmol, 1.0 eq.), 3-formylphenyl boronic acid (538 mg, 3.59 mmol, 2.5 eq.), Pd(OAc)₂ (6.44 mg, 0.03 mmol, 0.02 eq.), K₃PO₄ (914 mg, 4.30 mmol, 3.0 eq.) and SPhos (24 mg, 0.06 mmol, 0.04 eq.). The cap was sealed and briefly degassed with Argon for 10 minutes. Dry toluene (16 mL) was added and the vial was placed into a pre-heated (85 °C) oil bath, stirring rapidly overnight in the dark. The reaction was cooled to room temperature, poured into water, washed with brine and extracted into DCM. The organic phase was collected and dried over MgSO₄ before the solvent was removed under reduced pressure. The crude material was purified by silica column chromatography with hexane as the eluent, followed by recrystallisation from hot hexane to afford a bright orange solid (624 mg, 58%).

¹H NMR (400 MHz, Chloroform-*d*) δ 10.15 (d, *J* = 0.8 Hz, 2H), 8.77 – 8.68 (m, 4H), 8.12 (dd, *J* = 7.8, 1.4 Hz, 2H), 7.75 – 7.67 (m, 4H), 7.64 (dd, *J* = 6.9, 1.4 Hz, 2H), 7.58 (t, *J* = 7.8 Hz, 2H), 1.33 – 1.15 (m, 42H)



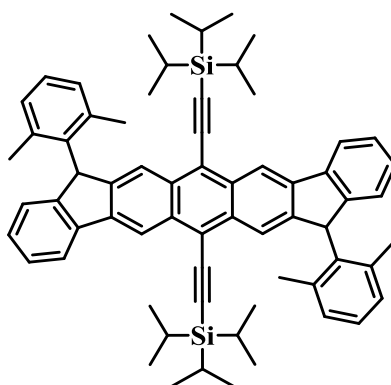
6.2.32 ((9,10-bis((triisopropylsilyl)ethynyl)anthracene-2,6-diyl)bis(2,1-phenylene))bis((2,6-dimethylphenyl)methanol)



Compound **(6.2.31)** 2,2'-(9,10-bis((triisopropylsilyl)ethynyl)anthracene-2,6-diyl)dibenzaldehyde (613 mg, 0.42 mmol, 1.0 eq.) was added to an oven dried 250 mL 2-neck RBF. Dry THF (40 mL) was added and the solution was cooled to 0 °C under an Argon atmosphere. Grignard solution 2,6-dimethylphenylmagnesiumbromide (1.0 M, 3.28 mL, 3.28

mmol, 4.0 eq.) was added slowly via syringe. The reaction mixture was stirred for 2 hours before being quenched by adding saturated NH_4Cl (30 mL) and diluted with diethyl ether (40 mL). The aqueous phase was collected and dried over MgSO_4 . Solvent was removed under reduced pressure, the crude orange solid was dissolved in the minimum volume of DCM, ethanol was slowly added to force precipitation of the desired compound which was collected by filtration and finally washed with water. Yielding an orange solid which was used immediately in the next step (6.2.33).

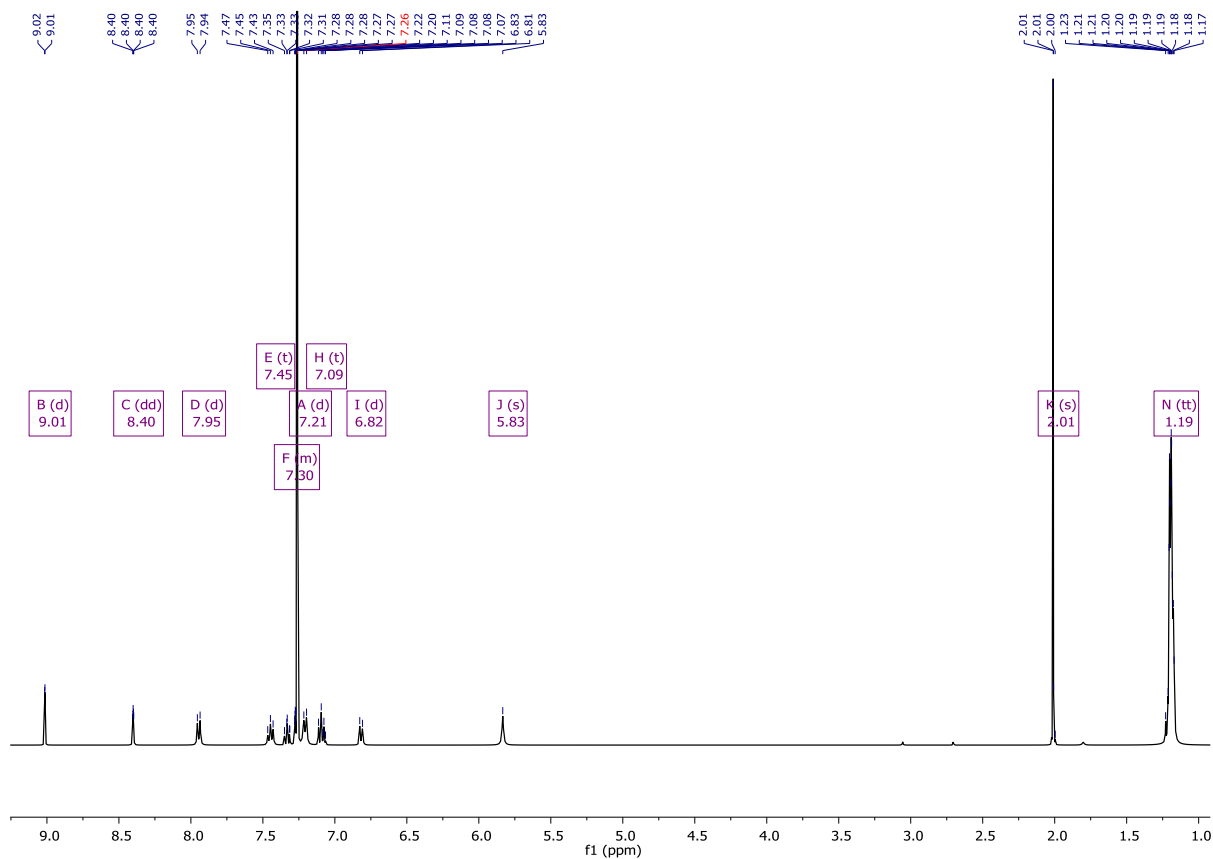
6.2.33 ((8,16-bis(2,6-dimethylphenyl)-8,16-dihydroindeno[1,2-*b*:1',2'-*i*]anthracene-6,14-diyl)bis(ethyne-2,1-diyl))bis(triisopropylsilane)



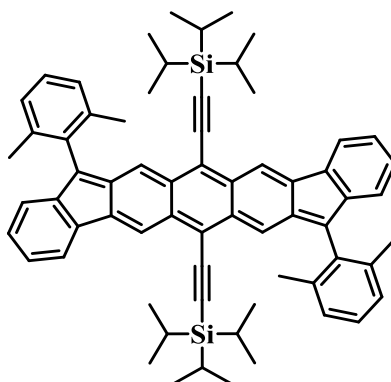
Compound (6.2.32) was dissolved in 35 mL of dry DCM and stirred under an argon atmosphere, 1 mL of $\text{BF}_3 \cdot \text{OEt}_2$ was then added dropwise. The mixture was stirred for 2h and then washed with NaHCO_3 solution (3x25 mL) and water (3x50 mL). The organic layer was collected and dried over MgSO_4 before the solvent was removed under reduced pressure. The crude orange solid was dissolved in the minimum volume of DCM and ethanol was slowly added to force precipitation of the desired compound which was subsequently collected by suction filtration and finally washed with water. Affording the title compound as a bright yellow solid (221 mg, 28% yield over two steps).

^1H NMR (400 MHz, Chloroform-*d*) δ 9.01 (d, $J = 0.8$ Hz, 2H), 8.40 (dd, $J = 1.7, 0.8$ Hz, 2H), 7.95 (d, $J = 7.5$ Hz, 2H), 7.45 (t, $J = 7.5$ Hz, 2H), 7.37 – 7.25 (m, 2H), 7.21 (d, $J = 7.5$ Hz, 4H), 7.09 (t, $J = 7.5$ Hz, 2H), 6.82 (d, $J = 7.5$ Hz, 2H), 5.83 (s, 2H), 2.01 (s, 12H), 1.19 (tt, $J = 6.0, 2.1$ Hz, 42H).

Mass (MALDI-ToF): 923.5 $[\text{M}+\text{H}]^+$ (calc. 922.5 $\text{C}_{66}\text{H}_{74}\text{Si}_2$).



6.2.34 ((8,16-bis(2,6-dimethylphenyl)diindeno[1,2-*b*:1',2'-*i*]anthracene-6,14-diyl)bis(ethyne-2,1-diyl))bis(triisopropylsilane) (DIAnDX)

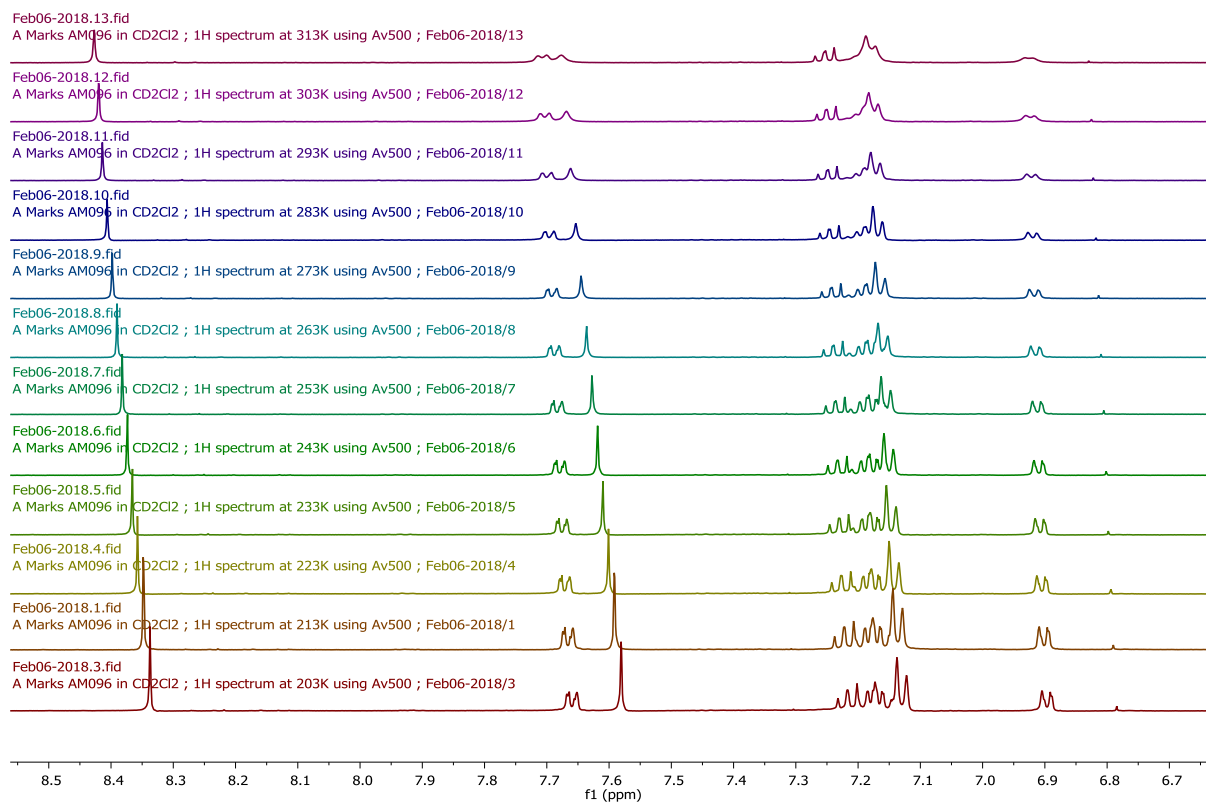
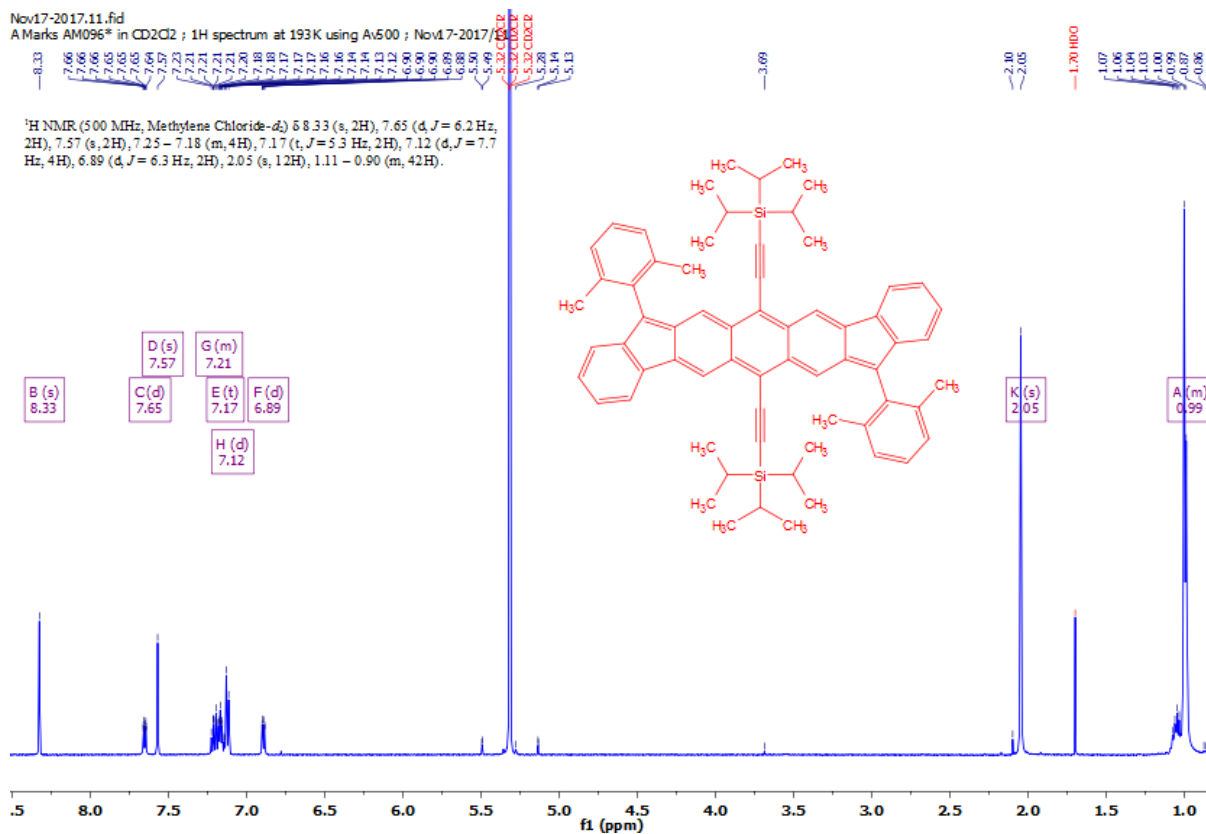


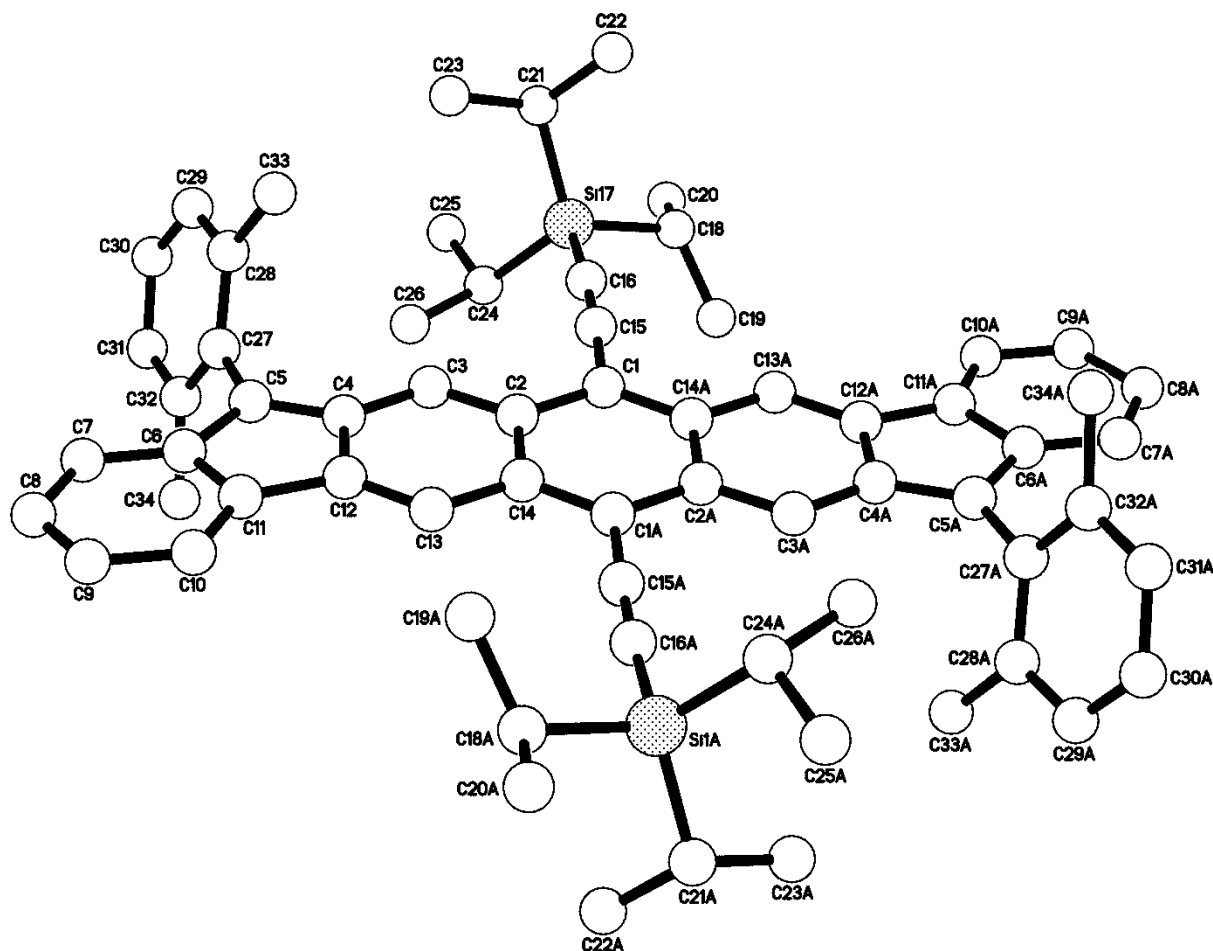
Compound **(6.2.33)** ((8,16-bis(2,6-dimethylphenyl)-8,16-dihydrodiindeno[1,2-*b*:1',2'-*i*]anthracene-6,14-diyl)bis(ethyne-2,1-diyl))bis(triisopropylsilane) (221 mg, 0.24 mmol, 1.0 eq.) was added to a 100 mL 2-neck RBF and dissolved in dry toluene (35 mL). The solution was heated to 85 °C prior to the addition of 2,3-Dichloro-5,6-dicyano-1,4-benzoquinone (DDQ) (82 mg, 0.36 mmol, 1.5 eq.) dissolved in 5 mL dry toluene. The deep blue solution was stirred for 3 hours, then cooled to room temperature and passed through a basic alumina plug (4x8 cm) eluting with hexane:DCM (1:1). Solvent was removed under reduced pressure and the blue solid was re-dissolved in the minimum volume of CHCl₃, acetonitrile was slowly added dropwise before the named compound was collected by suction filtration. The deep blue solid was confirmed by low temperature NMR (96 mg, 44%).

¹H NMR (500 MHz, Methylene Chloride-*d*₂) δ 8.33 (s, 2H), 7.65 (d, *J* = 6.3 Hz, 2H), 7.57 (s, 2H), 7.25 – 7.18 (m, 4H), 7.17 (t, *J* = 5.3 Hz, 2H), 7.12 (d, *J* = 7.7 Hz, 4H), 6.89 (d, *J* = 6.3 Hz, 2H), 2.05 (s, 12H), 1.11 – 0.90 (m, 42H).

Mass (MALDI-ToF): 921.5 [M+H]⁺ (calc. 920.5 C₆₆H₇₂Si₂).

CHAPTER SIX – EXPERIMENTAL





Crystal data and structure refinement for IM1712 (AM096) (**DIAnDX**).

Identification code	IM1712	
Formula	C ₆₆ H ₇₂ Si ₂	
Formula weight	921.41	
Temperature	173(2) K	
Diffractometer, wavelength	Agilent Xcalibur 3 E, 0.71073 Å	
Crystal system, space group	Triclinic, P-1	
Unit cell dimensions	a = 9.5184(4) Å	α = 74.153(5)°
	b = 12.3107(7) Å	β = 73.228(4)°
	c = 12.6827(7) Å	γ = 76.134(4)°
Volume, Z	1347.80(13) Å ³ , 1	
Density (calculated)	1.135 Mg/m ³	
Absorption coefficient	0.106 mm ⁻¹	
F(000)	496	

Crystal colour / morphology	Dark red plates
Crystal size	0.555 x 0.489 x 0.022 mm ³
θ range for data collection	2.499 to 28.192°
Index ranges	-8 ≤ h ≤ 11, -13 ≤ k ≤ 15, -10 ≤ l ≤ 16
Reflns collected / unique	7779 / 5317 [R(int) = 0.0214]
Reflns observed [F > 4σ(F)]	4031
Absorption correction	Analytical
Max. and min. transmission	0.998 and 0.957
Refinement method	Full-matrix least-squares on F ²
Data / restraints / parameters	5317 / 0 / 315
Goodness-of-fit on F ²	1.037
Final R indices [F > 4σ(F)]	R1 = 0.0486, wR2 = 0.1088
R indices (all data)	R1 = 0.0698, wR2 = 0.1195
Largest diff. peak, hole	0.331, -0.270 eÅ ⁻³
Mean and maximum shift/error	0.000 and 0.000

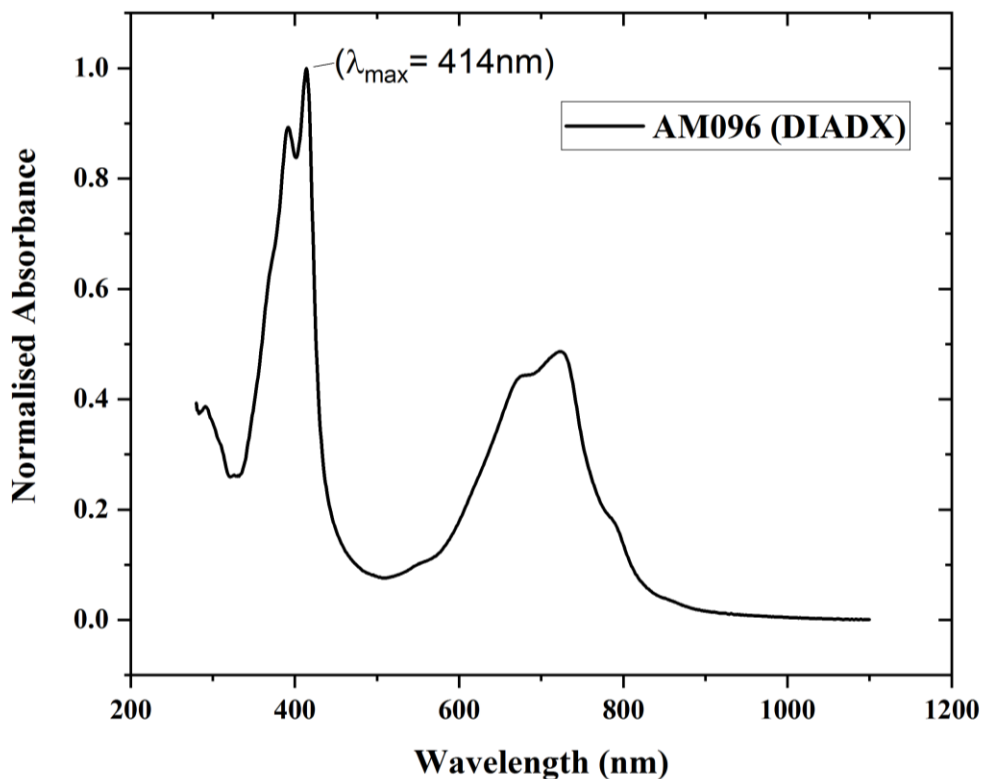
Bond lengths [Å] and angles [°] for	C(5)-C(6)	1.467(3)
IM1712 (DIAnDX).	C(5)-C(27)	1.484(2)
C(1)-C(14)#1	C(6)-C(7)	1.390(2)
1.390(2)	C(6)-C(11)	1.418(2)
C(1)-C(15)	C(7)-C(8)	1.390(3)
1.438(2)	C(8)-C(9)	1.395(3)
C(1)-C(2)	C(9)-C(10)	1.387(3)
1.440(2)	C(10)-C(11)	1.386(3)
C(2)-C(3)	C(11)-C(12)	1.467(3)
1.394(2)	C(12)-C(13)	1.352(2)
C(2)-C(14)		
1.454(2)		
C(3)-C(4)		
1.404(2)		
C(4)-C(5)		
1.391(3)		
C(4)-C(12)		
1.458(2)		

C(13)-C(14)	1.442(2)	C(14)#1-C(1)-C(15)	120.62(16)
C(15)-C(16)	1.207(2)	C(14)#1-C(1)-C(2)	121.43(15)
C(16)-Si(17)	1.8478(18)	C(15)-C(1)-C(2)	117.95(16)
Si(17)-C(21)	1.883(2)	C(3)-C(2)-C(1)	121.45(15)
Si(17)-C(24)	1.889(2)	C(3)-C(2)-C(14)	119.85(16)
Si(17)-C(18)	1.889(2)	C(1)-C(2)-C(14)	118.67(15)
C(18)-C(19)	1.527(3)	C(2)-C(3)-C(4)	120.48(16)
C(18)-C(20)	1.536(3)	C(5)-C(4)-C(3)	131.02(16)
C(21)-C(22)	1.531(3)	C(5)-C(4)-C(12)	109.49(16)
C(21)-C(23)	1.540(3)	C(3)-C(4)-C(12)	119.46(16)
C(24)-C(26)	1.535(3)	C(4)-C(5)-C(6)	107.82(15)
C(24)-C(25)	1.538(3)	C(4)-C(5)-C(27)	127.91(16)
C(27)-C(28)	1.407(3)	C(6)-C(5)-C(27)	124.27(16)
C(27)-C(32)	1.407(3)	C(7)-C(6)-C(11)	120.15(17)
C(28)-C(29)	1.395(3)	C(7)-C(6)-C(5)	131.24(17)
C(28)-C(33)	1.508(3)	C(11)-C(6)-C(5)	108.61(16)
C(29)-C(30)	1.377(3)	C(6)-C(7)-C(8)	118.80(18)
C(30)-C(31)	1.377(3)	C(7)-C(8)-C(9)	120.79(19)
C(31)-C(32)	1.394(3)	C(10)-C(9)-C(8)	120.95(18)
C(32)-C(34)	1.506(3)	C(11)-C(10)-C(9)	118.79(18)

C(10)-C(11)-C(6)	120.51(18)	C(20)-C(18)-Si(17)	112.78(16)
C(10)-C(11)-C(12)	132.02(17)	C(22)-C(21)-C(23)	110.3(2)
C(6)-C(11)-C(12)	107.44(15)	C(22)-C(21)-Si(17)	112.21(16)
C(13)-C(12)-C(4)	120.85(17)	C(23)-C(21)-Si(17)	112.44(15)
C(13)-C(12)-C(11)	132.51(16)	C(26)-C(24)-C(25)	109.98(17)
C(4)-C(12)-C(11)	106.57(15)	C(26)-C(24)-Si(17)	114.73(14)
C(12)-C(13)-C(14)	120.46(16)	C(25)-C(24)-Si(17)	112.41(15)
C(1)#1-C(14)-C(13)	121.32(15)	C(28)-C(27)-C(32)	120.36(17)
C(1)#1-C(14)-C(2)	119.90(16)	C(28)-C(27)-C(5)	120.64(17)
C(13)-C(14)-C(2)	118.78(16)	C(32)-C(27)-C(5)	118.99(17)
C(16)-C(15)-C(1)	177.15(18)	C(29)-C(28)-C(27)	118.72(19)
C(15)-C(16)-Si(17)	173.96(17)	C(29)-C(28)-C(33)	119.63(19)
C(16)-Si(17)-C(21)	107.74(9)	C(27)-C(28)-C(33)	121.64(17)
C(16)-Si(17)-C(24)	107.38(8)	C(30)-C(29)-C(28)	120.7(2)
C(21)-Si(17)-C(24)	113.34(10)	C(31)-C(30)-C(29)	120.7(2)
C(16)-Si(17)-C(18)	106.05(9)	C(30)-C(31)-C(32)	120.6(2)
C(21)-Si(17)-C(18)	110.49(10)	C(31)-C(32)-C(27)	118.8(2)
C(24)-Si(17)-C(18)	111.45(10)	C(31)-C(32)-C(34)	120.1(2)
C(19)-C(18)-C(20)	110.0(2)	C(27)-C(32)-C(34)	121.03(17)
C(19)-C(18)-Si(17)	112.47(14)		

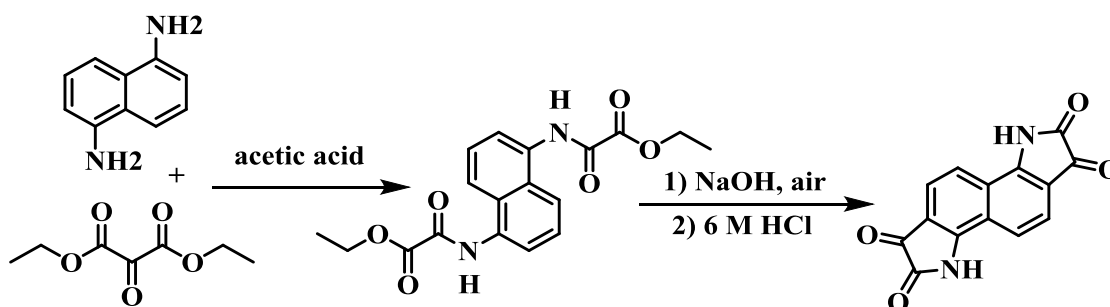
Symmetry transformations used to generate equivalent atoms:

#1 -x+1,-y,-z+1



6.3 CHAPTER FOUR SYNTHESIS & CHARACTERISATION

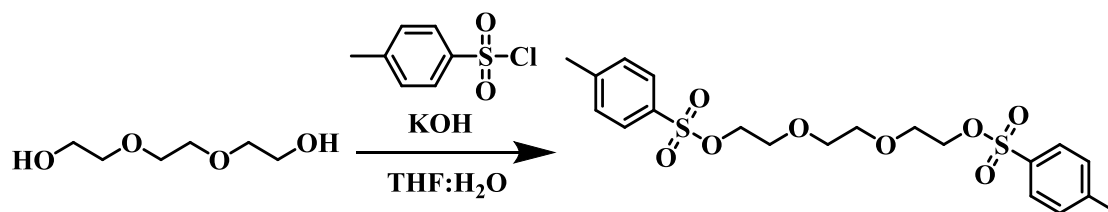
6.3.1 Synthesis of bisisatin¹⁷⁸



1,5-diaminonaphthalene (4.02 g, 25.4 mmol, 1.0 eq.) was dissolved in glacial acetic acid (40 mL) and heated to 120 °C under a Nitrogen atmosphere. Diethylketomalonate (16 mL, 104 mmol, 4.1 eq.) was dissolved in glacial acetic acid (46 mL) and added slowly, via dropping

funnel, over the period of 60 minutes. The solution was heated overnight at 130 °C and consequently cooled to room temperature before removing the acetic acid under reduced pressure. The resultant brown sludge was dissolved in NaOH (1 mol L⁻¹) to a final solution pH between 11 to 12. The dark brown solution was then heated at reflux whilst bubbling air through the mixture for a period of 5 hours. The mixture was poured into ice and acidified, to pH 0) with aq. 2M HCl. The precipitate was collected by vacuum filtration, the resultant solid was washed with ice water (500 mL) followed by methanol (300 mL) to reveal a dark purple solid which was dried under vacuo (5.86 g, 87%). Due to the materials lack of solubility bisisatin was used in subsequent reactions without any further purification, coherent with previous literature procedure.¹⁷⁸

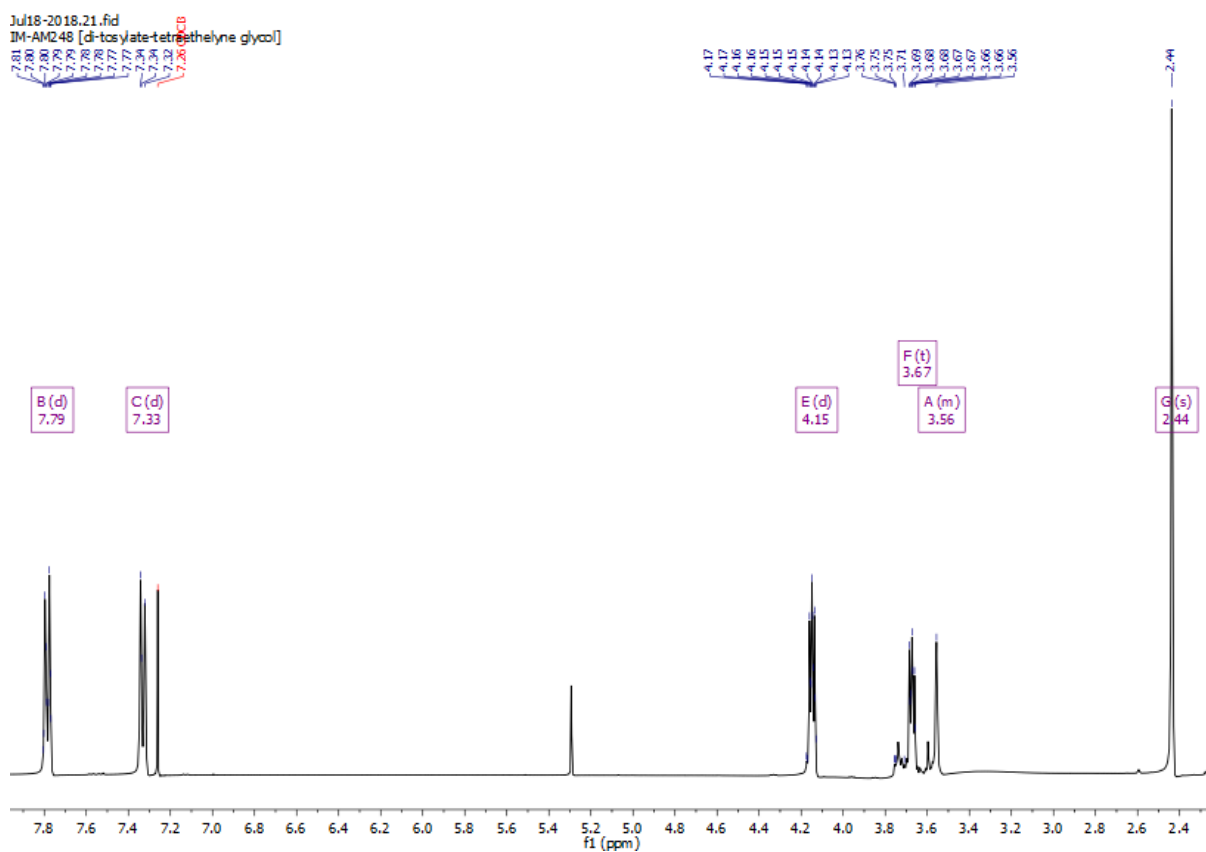
6.3.2 Synthesis of ((oxybis(ethane-2,1-diyl))bis(oxy))bis(ethane-2,1-diyl) bis(4-methylbenzenesulfonate)

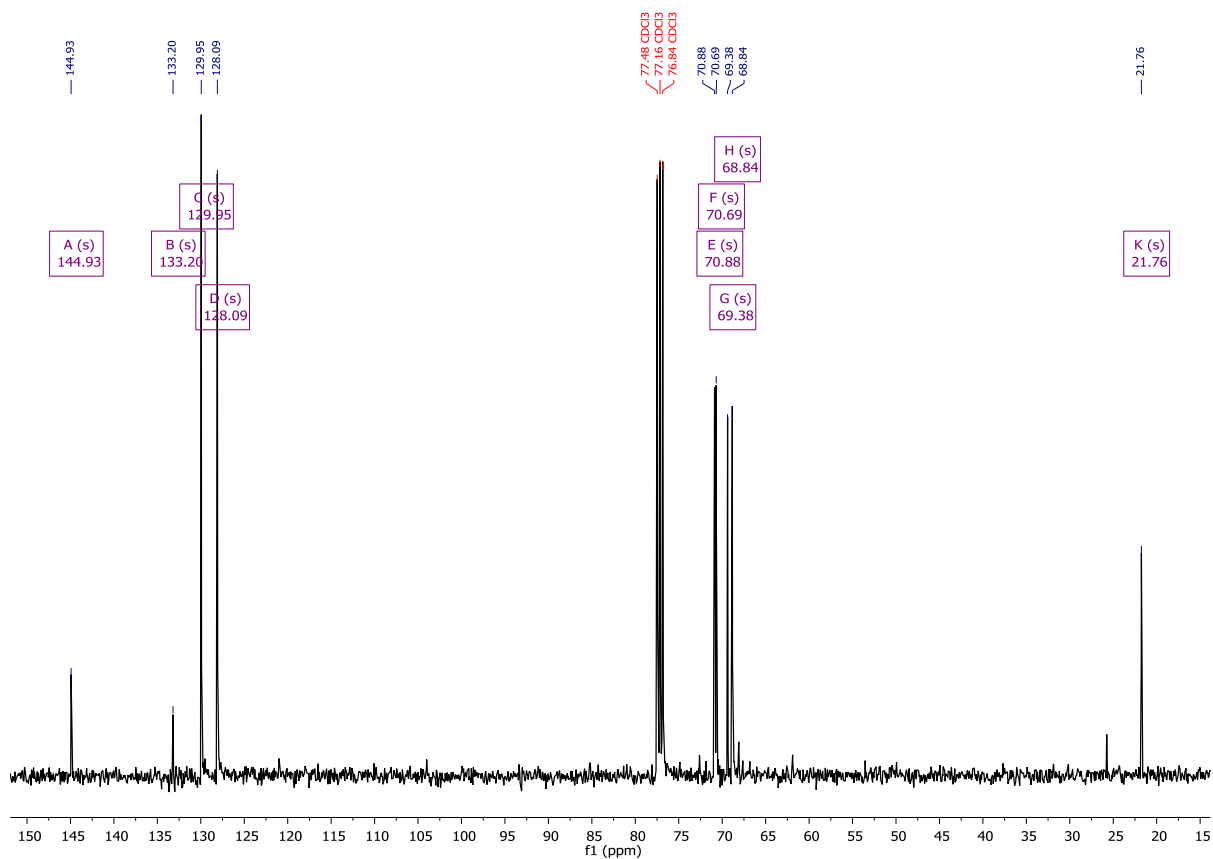


Potassium hydroxide (57.6 g, 1.03 mmol, 4.0 eq.) was added to 500 mL RBF and dissolved in H₂O (65 mL) before being cooled to 0 °C. In a separate vessel triethylene glycol (22.3 mL, 0.257 mmol, 1.0 eq.) was dissolved in THF (125 mL) and added dropwise to the KOH solution. 4-Toluenesulfonyl chloride (104 g, 0.544 mmol, 2.12 eq.) was dissolved in THF (125 mL) then added to the above solution. The reaction was stirred overnight before being poured into ice water (300 mL) and being washed with brine and extracted into DCM. The organic layer was separated and dried over MgSO₄ before the solvent was removed under reduced pressure to afford the title compound as a viscous clear solution (120 g, 93%).

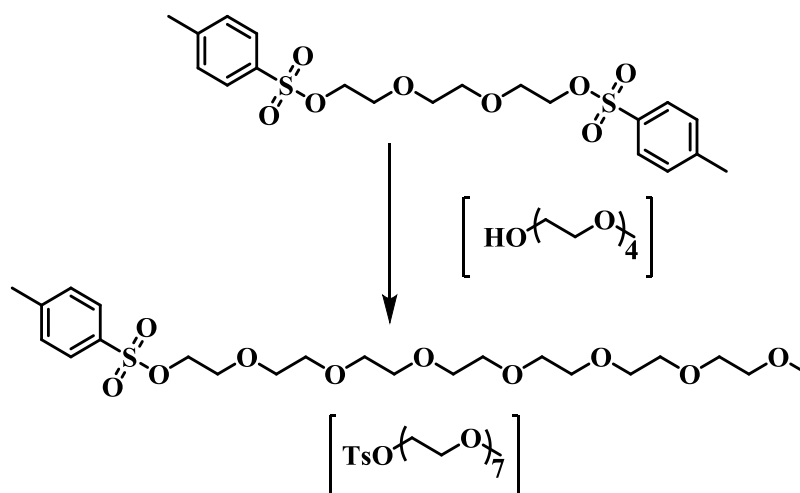
^1H NMR (400 MHz, Chloroform-*d*) δ 7.79 (d, $J = 8.1$ Hz, 4H), 7.33 (d, $J = 8.1$ Hz, 4H), 4.15 (t, $J = 4.4$ Hz, 4H), 3.67 (t, $J = 4.4$ Hz, 4H), 3.68 – 3.51 (m, 4H), 2.44 (s, 6H).

^{13}C NMR (101 MHz, Chloroform-*d*) δ 144.93, 133.20, 129.95, 128.09, 70.88, 70.69, 69.38, 68.84, 21.76.





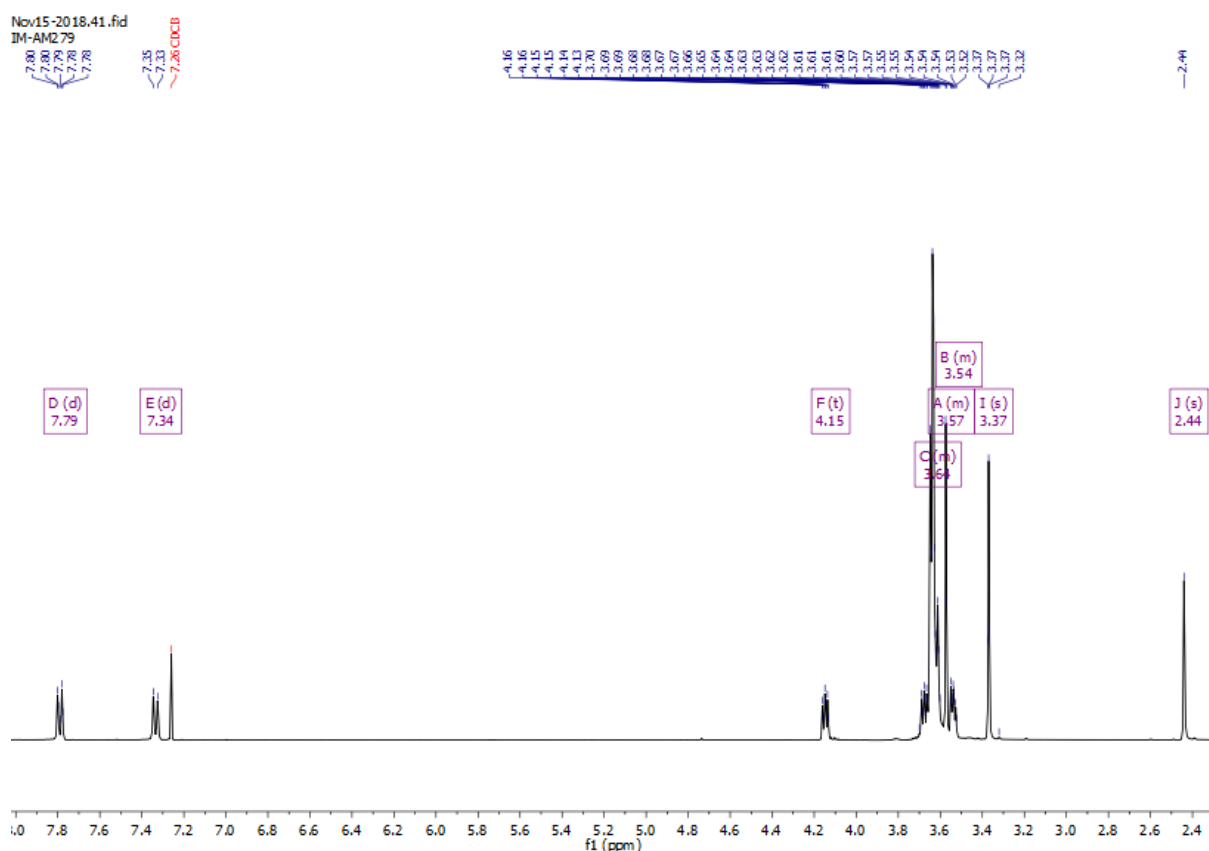
6.3.3 2,5,8,11,14,17,20-hepta(oxadecan-22-yl) 4-methylbenzenesulfonate (7xPEG)



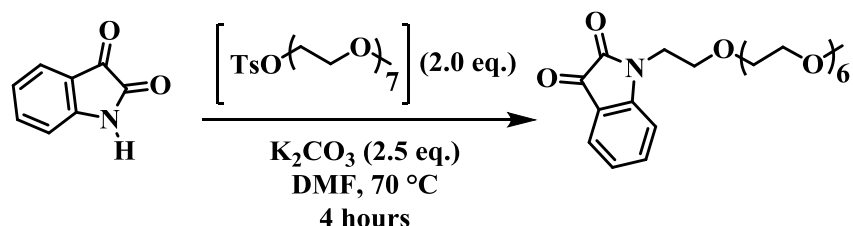
Sodium hydride (60% in mineral oil, 3.58 g, 89.6 mmol, 1.5 eq.) was added to an oven dried 2-neck RBF under a Nitrogen atmosphere and cooled to 0 °C. Dry THF (60 mL) was added via syringe and the mixture was stirred rapidly. Tetraethylene glycol monomethyl ether (9.6 mL, 59.75 mmol, 1.0 eq.) was added slowly dropwise via

syringe. The mixture was warmed to room temperature and stirred for 30 minutes. The reaction was then heated to 65 °C for 60 minutes. Following this the reaction was cooled to 0 °C and compound (6.3.2) (30 g, 59.75 mmol, 1.0 eq.) was added slowly dropwise, before being stirred at room temperature for an hour. The solution was heated to 50 °C and stirred overnight. Upon cooling to room temperature, the mixture was poured into ice water, washed with brine and extracted into DCM. After the organic layer was separated and dried over MgSO₄ the solvent was removed under reduced pressure to yield the crude viscous pale-yellow oil. The crude product was purified via column chromatography on silica gel with ethyl acetate: methanol (98:2) as the eluent system to afford a colourless viscous oil (9.4 g, 32%).

¹H NMR (400 MHz, Chloroform-*d*) δ 7.79 (d, *J* = 8.3 Hz, 2H), 7.34 (d, *J* = 8.3 Hz, 2H), 4.15 (t, *J* = 4.9 Hz, 2H), 3.71 – 3.56 (m, 20H), 3.60 – 3.52 (m, 4H), 3.57 – 3.50 (m, 2H), 3.37 (s, 3H), 2.44 (s, 3H).



6.3.4 Synthesis of 1-(2,5,8,11,14,17,20-heptaoadocosan-22-yl)indoline-2,3-dione

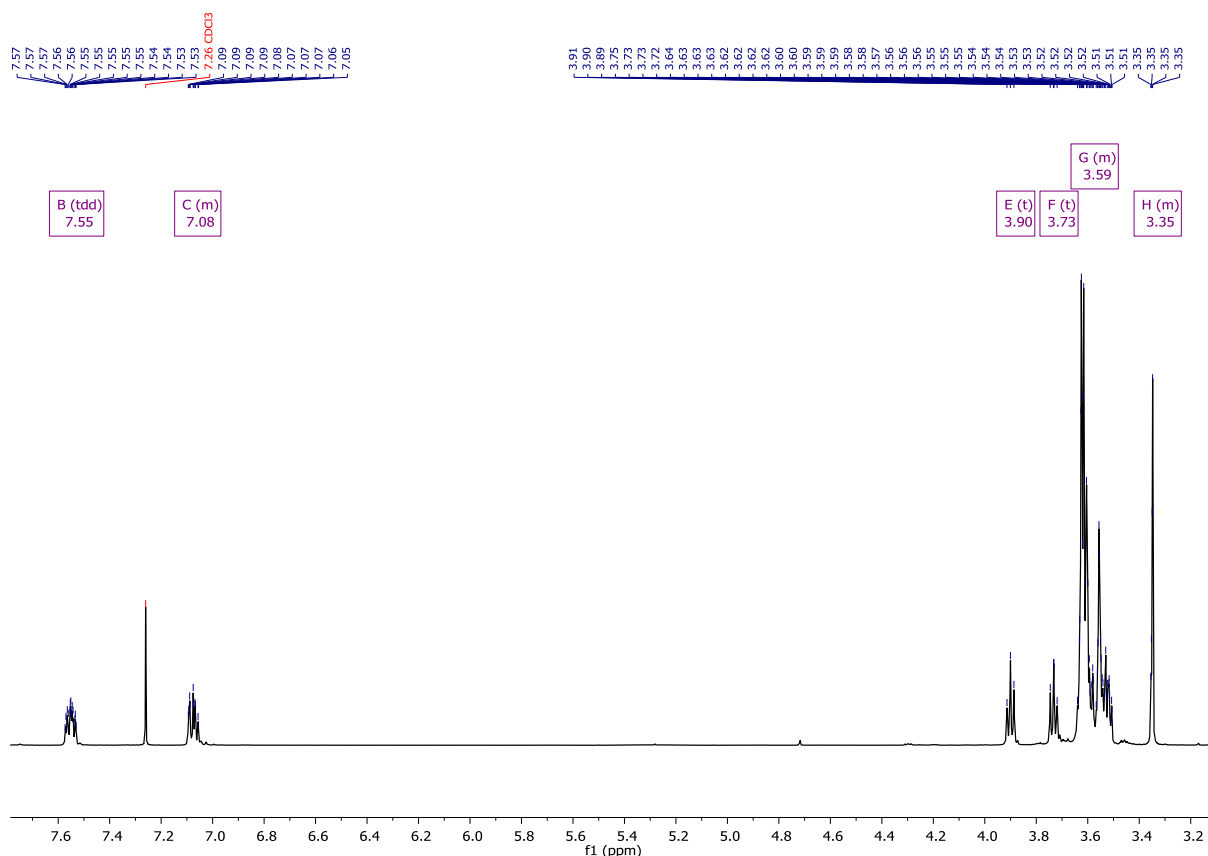


An oven dried 50 mL 2-neck RBF was charged with isatin (397 mg, 2.70 mmol, 1.0 eq.) and K_2CO_3 (931 mg, 6.75 mmol 2.5 eq.), degassed with N_2 for 10 minutes prior to the addition of 10 mL anhydrous DMF. The mixture was heated to 70 °C and stirred for 40 minutes before 2,5,8,11,14,17,20-heptaoadocosan-22-yl 4-methylbenzenesulfonate (2.67 g, 5.39 mmol, 2.0 eq.) was injected as a single portion. After stirring for an additional 4 hours the reaction was cooled to room temperature before ~5 mL of 2M HCl was added. The solution was poured into 400 mL of water, washed three times then extracted into DCM. The organic phases were combined and dried over $MgSO_4$, the solvent was removed under reduced pressure to yield a crude red oil. Column chromatography, on silica gel, using DCM:Acetone (5:1) as the eluent system afforded the product as an orange oil (278 mg, 22%).

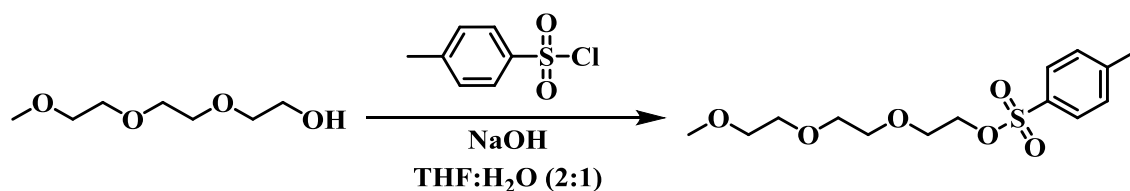
1H NMR (400 MHz, Chloroform-*d*) δ 7.55 (tdd, $J = 6.1, 2.7, 1.7$ Hz, 2H), 7.12 – 7.02 (m, 2H), 3.90 (t, $J = 5.4$ Hz, 2H), 3.73 (t, $J = 5.4$ Hz, 2H), 3.66 – 3.48 (m, 24H), 3.38 – 3.32 (m, 3H).

^{13}C NMR (101 MHz, Chloroform-*d*) δ 183.52, 162.62, 151.64, 138.37, 125.18, 123.70, 117.61, 111.50, 72.01, 70.64, 68.74, 59.11, 40.58, 36.58, 31.52.

Mass (MALDI-ToF): 470.1 $[M+H]^+$ (calc. 469.2 $C_{23}H_{35}NO_9$).



6.3.5 Synthesis of 2-(2-(2-methoxyethoxy)ethoxy)ethyl 4-methylbenzenesulfonate

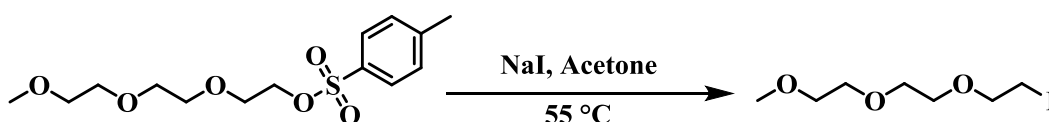


Triethylene glycol monomethyl ether (30 g, 183 mmol, 1.0 eq.) was added to an oven dried 2-neck 500 mL RBF and dissolved in 100 mL THF. The flask was cooled to 0 °C, sodium hydroxide (11 g, 274 mmol, 1.5 eq.) dissolved in 100 mL H₂O was added dropwise and stirred for 20 minutes. 4-Toluenesulfonyl chloride (37.5 g, 192 mmol, 1.05 eq.) dissolved in 100 mL THF was added dropwise, the solution was left to stir overnight. Afterwards the reaction was poured into water, washed with brine and extracted into DCM. The organic layer was separated, dried over MgSO₄ and solvent removed under reduced pressure before being purified by silica

chromatography, ethyl acetate:hexane 1:1 (v/v), to give a colourless liquid (48.8 g, 84%). ^1H NMR is consistent with previously published literature.¹⁶⁶

^1H NMR (400 MHz, Chloroform-*d*), (ppm): 7.76 (d, $J = 8.2$ Hz, 2H), 7.29 (d, $J = 8.2$ Hz, 2H), 4.13 (t, $J = 4.2$ Hz, 2H), 3.65-3.50 (m, 10H), 3.33 (s, 3H), 2.42 (s, 3H).

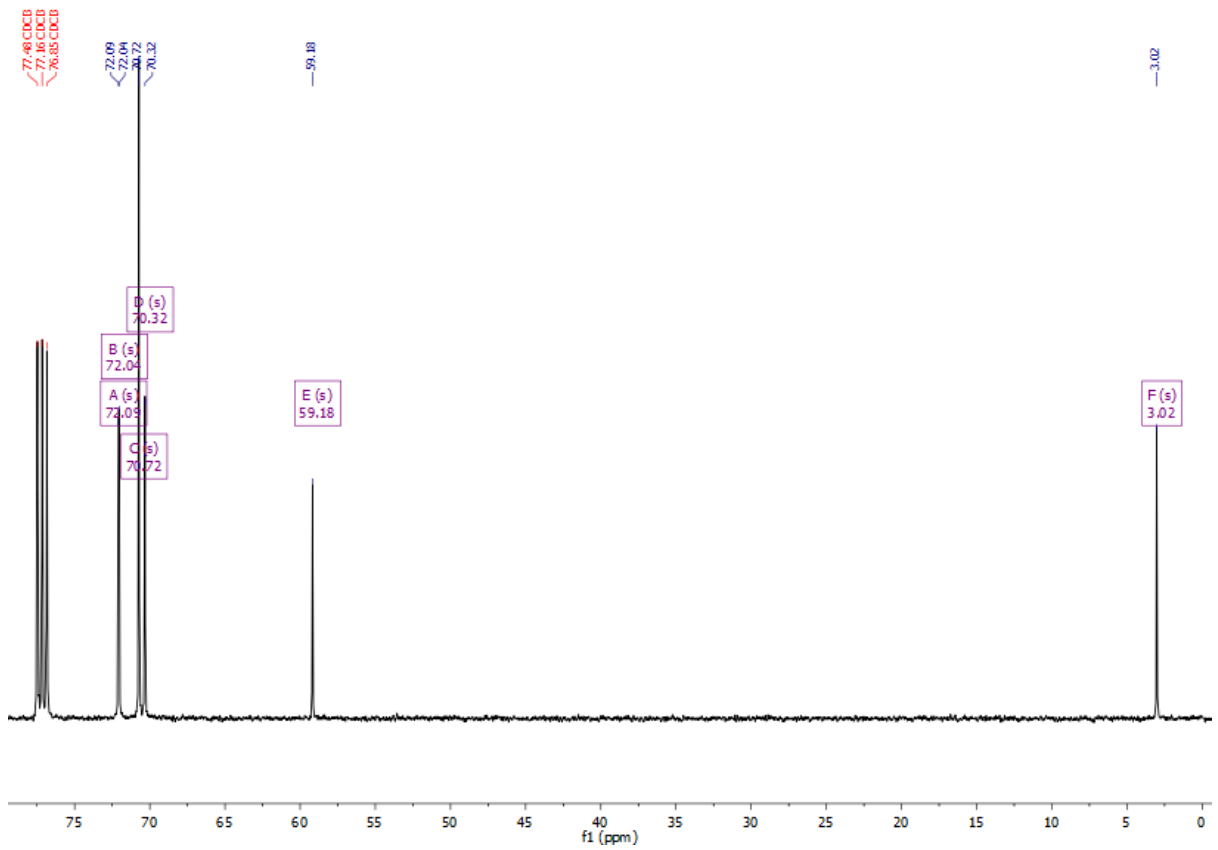
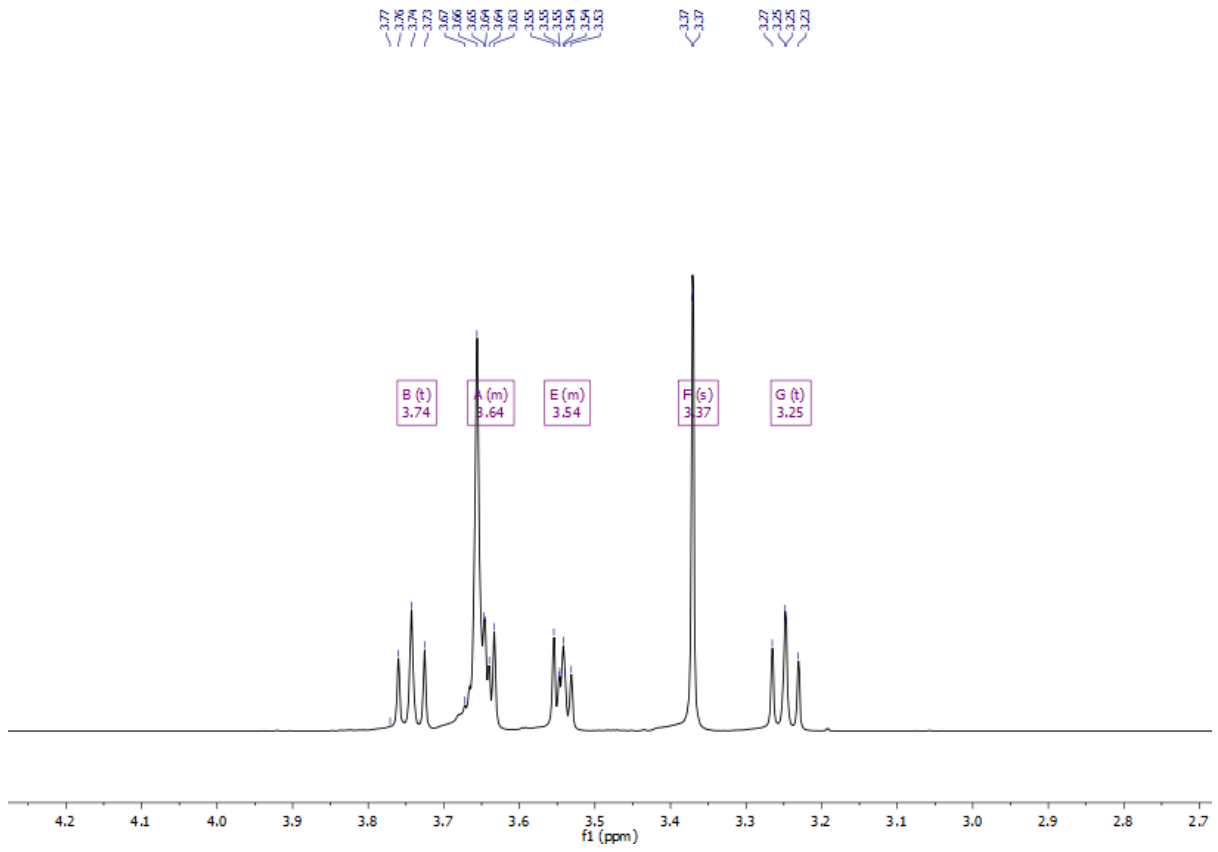
6.3.6 Synthesis of 1-iodo-2-(2-(2-methoxyethoxy)ethoxy)ethane

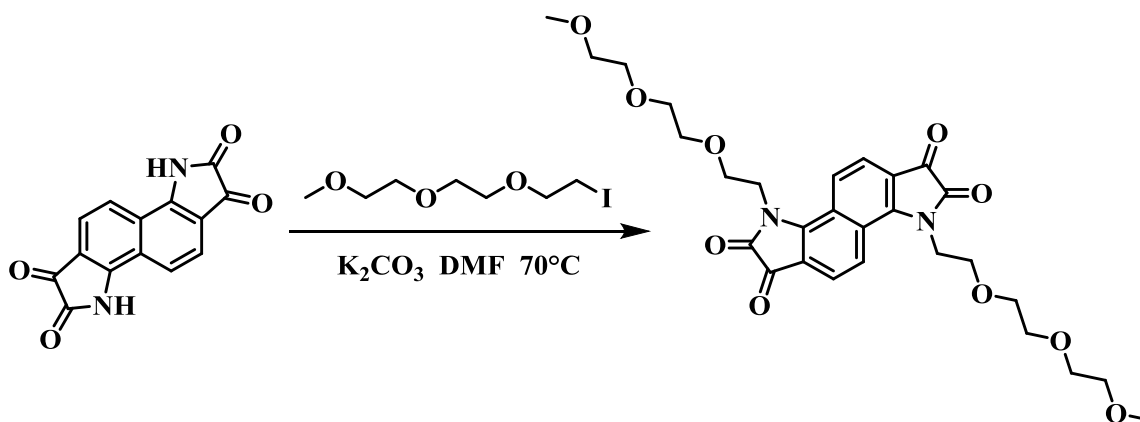


Sodium iodide (47.5 g, 317 mmol, 2.1 eq.) was added to an oven dried 2-neck 500 mL RBF, dissolved in 300 mL of acetone. Compound (6.3.5) 2-(2-(2-methoxyethoxy)ethoxy)ethyl 4-methylbenzenesulfonate (48 g, 151 mmol, 1.0 eq.) dissolved in 50 mL acetone was added dropwise. The solution was heated to 55 °C and stirred overnight. Upon cooling to room temperature, the reaction was poured into water, washed with brine and extracted into DCM. The crude oil was purified by silica column chromatography using ethyl acetate:methanol 9:1 (v/v) as the eluent to yield a colourless liquid (36.8 g, 89%).

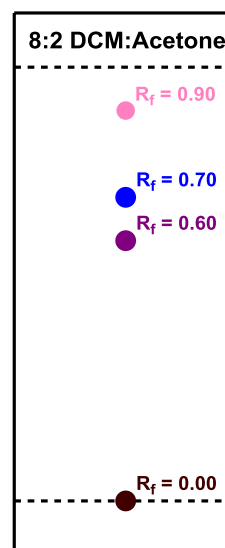
^1H NMR (400 MHz, Chloroform-*d*) δ 3.74 (t, $J = 6.9$ Hz, 2H), 3.68 – 3.62 (m, 6H), 3.58 – 3.51 (m, 2H), 3.37 (s, 3H), 3.25 (t, $J = 7.1$ Hz, 2H).

^{13}C NMR (101 MHz, Chloroform-*d*) δ 72.09, 72.04, 70.72, 70.32, 59.18, 3.02.



6.3.7 Synthesis of 3,8-bis(2-(2-(2-methoxyethoxy)ethoxy)ethyl)-3,8-dihydroindolo[7,6-g]indole-1,2,6,7-tetraone

An oven dried 2-neck 50 mL RBF was charged with bisisatin (**6.3.1**) (2 g, 7.52 mmol, 1.0 eq.) and oven dried potassium carbonate (5.2 g, 37.6 mmol, 5.0 eq.) under a Nitrogen atmosphere. Dry DMF (16 mL) was added, the reaction was heated to $70^\circ C$ and stirred for one hour. 1-iodo-2-(2-(2-methoxyethoxy)ethoxy)ethane (**6.3.6**) (8.24 g, 30.0 mmol, 4.0 eq.) was added in a single portion and the mixture was stirred for a further 4 hours. Upon cooling to room temperature, the mixture was poured into water and acidified to pH 7 using 2M HCl. The organic layer was extracted into

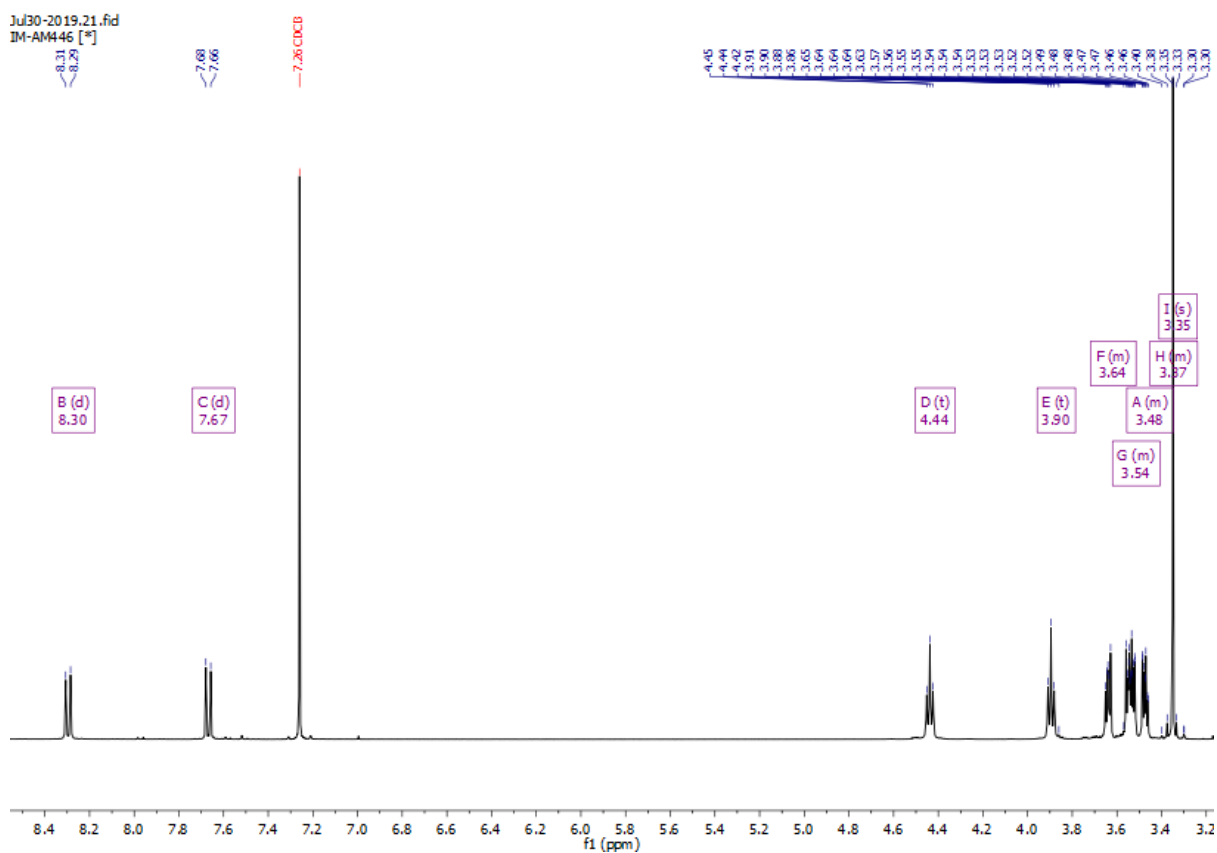


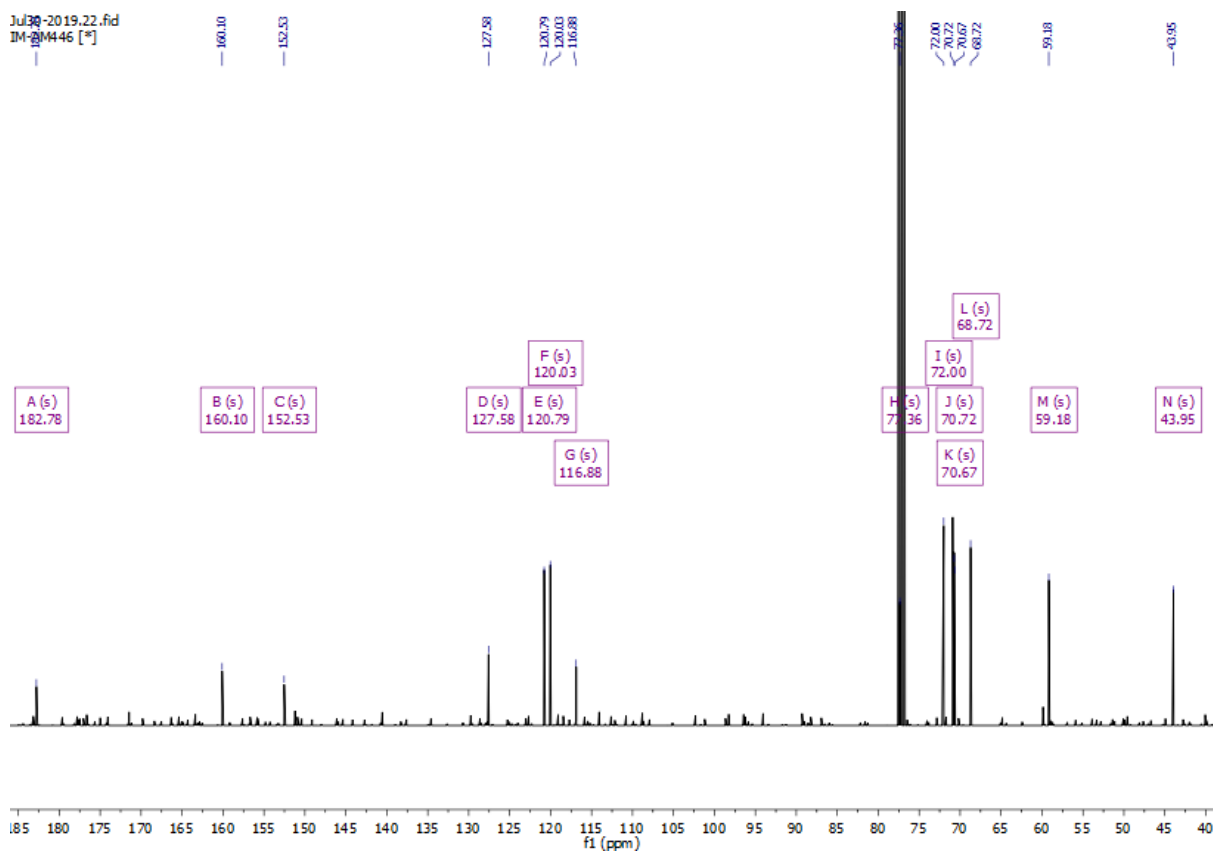
DCM, adding NH_4Cl to assist in separating the resultant emulsion. Once separated the organic layer was dried over $MgSO_4$, solvent removed under reduced pressure to yield a crude purple oil. The crude was purified by silica column chromatography (three times) using DCM:Acetone 8:2 (v/v) as the eluent system. The intensely blue product ($R_f = 0.7$) was dissolved in the minimum amount of DCM and precipitated into ethanol. The blue solid was finally recrystallised from hot ethanol to afford the title compound (390 mg, 9%).

^1H NMR (400 MHz, Chloroform-*d*) δ 8.30 (d, $J = 8.6$ Hz, 2H), 7.67 (d, $J = 8.6$ Hz, 2H), 4.44 (t, $J = 5.6$ Hz, 4H), 3.90 (t, $J = 5.6$ Hz, 4H), 3.69 – 3.60 (m, 4H), 3.60 – 3.49 (m, 8H), 3.51 – 3.43 (m, 4H), 3.35 (s, 6H).

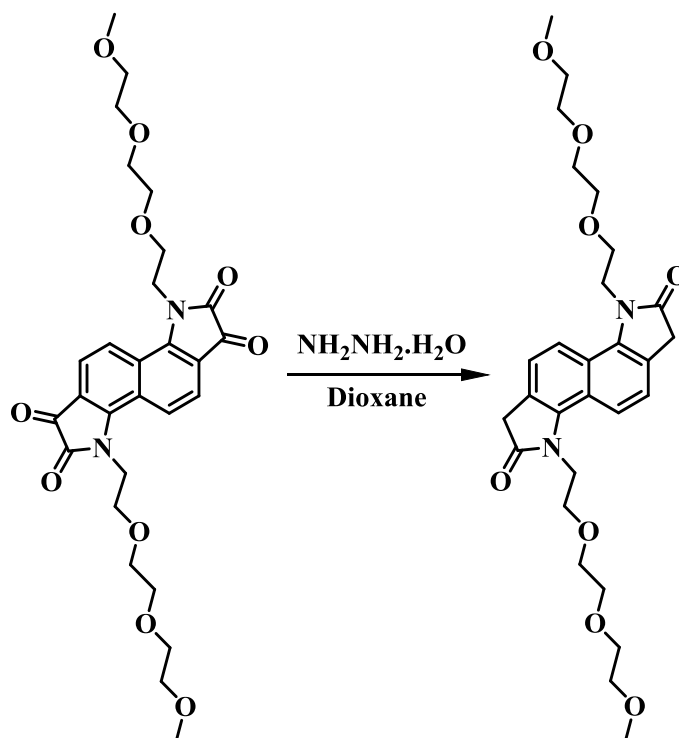
^{13}C NMR (101 MHz, CDCl_3) δ 182.78, 160.10, 152.53, 127.58, 120.79, 120.03, 116.88, 77.36, 72.00, 70.72, 70.67, 68.72, 59.18, 43.95.

TOF MS LD+: $\text{C}_{28}\text{H}_{34}\text{N}_2\text{O}_{10}$, calculated, 558.22, $[\text{M}^+\text{H}]^+$ found 558.6.





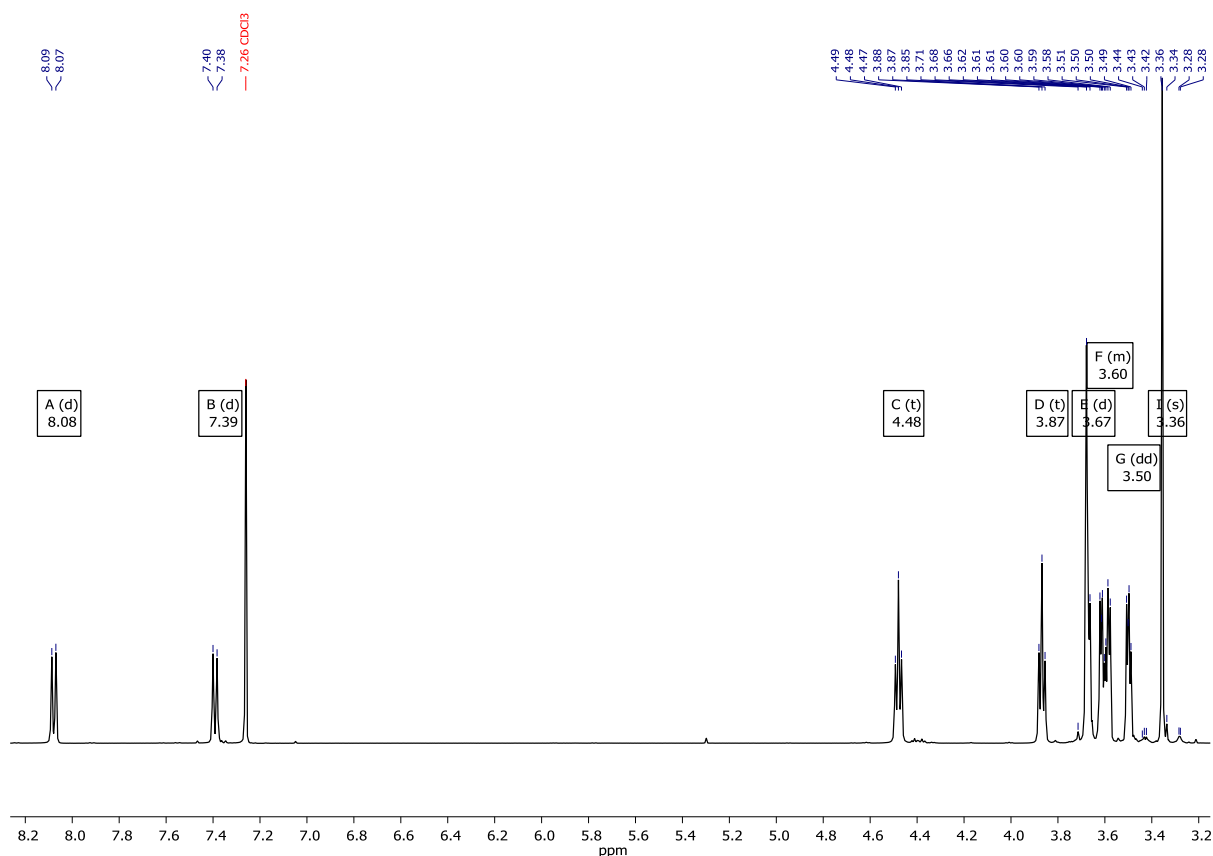
6.3.8 Wolff-Kishner Reduction to yield 3,8-bis(2-(2-(2-methoxyethoxy)ethoxy)ethyl)-1,3,6,8-tetrahydroindolo[7,6-g]indole-2,7-dione



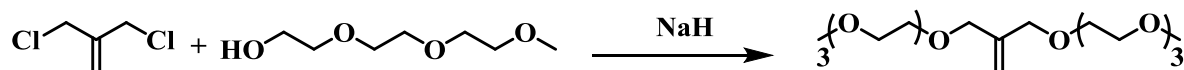
3,8-bis(2-(2-(2-methoxyethoxy)ethoxy)ethyl)-3,8-dihydroindolo[7,6-g]indole-1,2,6,7-tetraone (**6.3.7**) (180mg, 0.34 mmol, 1.0 eq.) was added to an oven dried 10 mL microwave vial, cap sealed and degassed with Nitrogen for 10 minutes. Dry dioxane (2.4 mL) was added, followed by hydrazine monohydrate (0.9 mL). The reaction was stirred overnight at 120 °C, after cooling to room temperature the mixture was poured into water, washed with brine and extracted into DCM. The organic layer was separated and dried over MgSO₄; solvent was removed under reduced pressure. The crude product was purified via column chromatography, on silica gel, using DCM:methanol (98:2) as the eluent system, recrystallisation from ethanol afforded a fluffy white solid (54 mg, 32%).

¹H NMR (500 MHz, Chloroform-*d*) δ 8.08 (d, *J* = 8.6 Hz, 2H), 7.39 (d, *J* = 8.6 Hz, 2H), 4.48 (t, *J* = 6.5 Hz, 4H), 3.87 (t, *J* = 6.5 Hz, 4H), 3.67 (d, *J* = 7.4 Hz, 8H), 3.64 – 3.56 (m, 8H), 3.50 (dd, *J* = 5.7, 3.7 Hz, 4H), 3.36 (s, 6H).

Mass (MALDI-ToF): 531.2 [M+H]⁺ (calc. 530.3 C₂₈H₃₈N₂O₈).

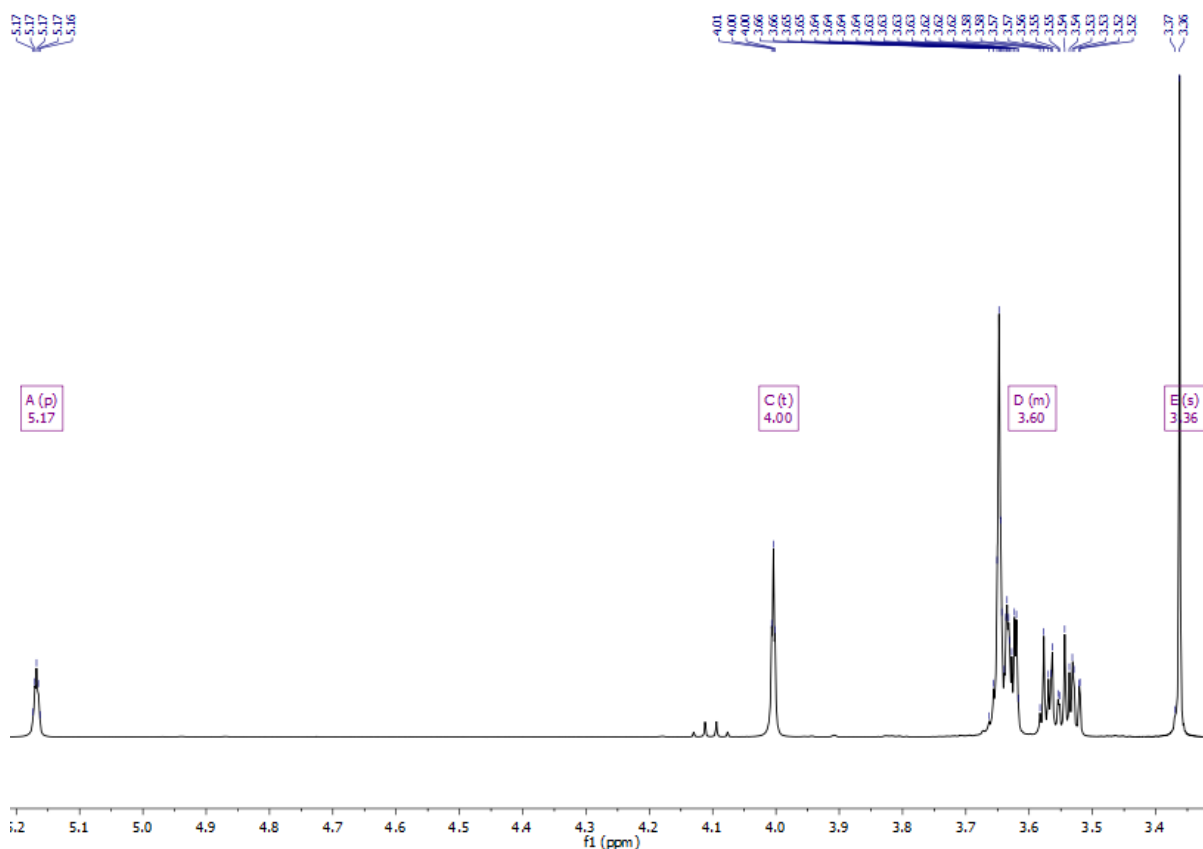


6.3.9 Synthesis of 13-methylene-2,5,8,11,15,18,21,24-octaopentacosane

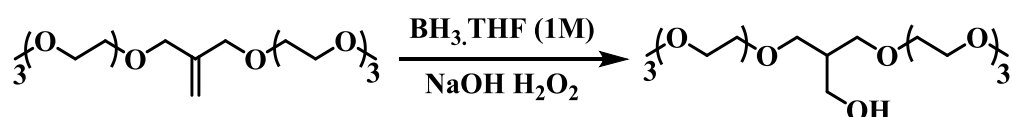


An oven dried 2-neck RBF was charged with NaH (60% in mineral oil, 9.92 g, 248 mmol, 3.1 eq.) cooled to 0 °C and dissolved in dry THF (150 mL) under an Argon atmosphere. Triethylene glycol monomethyl ether (38 mL, 240 mmol, 3.0 eq.) was added dropwise, the solution was then stirred until effervescence ceased. 3-chloro-2-(chloromethyl)prop-1-ene (10 mL, 80 mmol, 1.0 eq.) was added dropwise, the solution was then heated to reflux (70 °C) and stirred overnight. Upon cooling to room temperature, the reaction was poured into water, washed with brine and extracted into DCM. The organic layer was separated and dried over Na₂SO₄ before the solvent was removed under reduced pressure. The crude oil was purified by column chromatography on silica using ethyl acetate as the eluent to afford a colourless oil (26.4 g, 87%).

$^1\text{H NMR}$ (400 MHz, Chloroform-*d*) δ 5.17 (p, $J = 1.1$ Hz, 2H), 4.00 (t, $J = 1.1$ Hz, 4H), 3.70 – 3.49 (m, 24H), 3.36 (s, 6H).



6.3.10 Synthesis of 13-(2,5,8,11-tetraoxadodecyl)-2,5,8,11-tetraoxatetradecan-14-ol

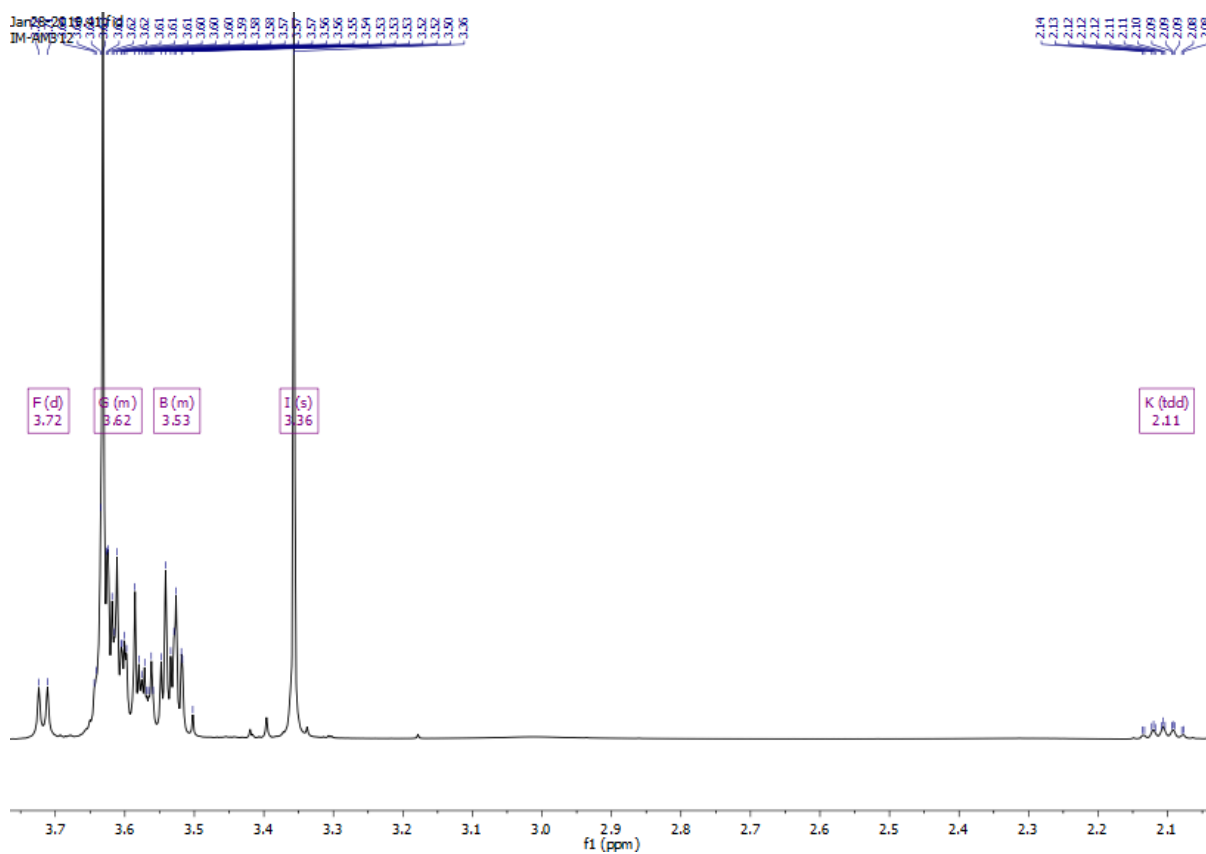


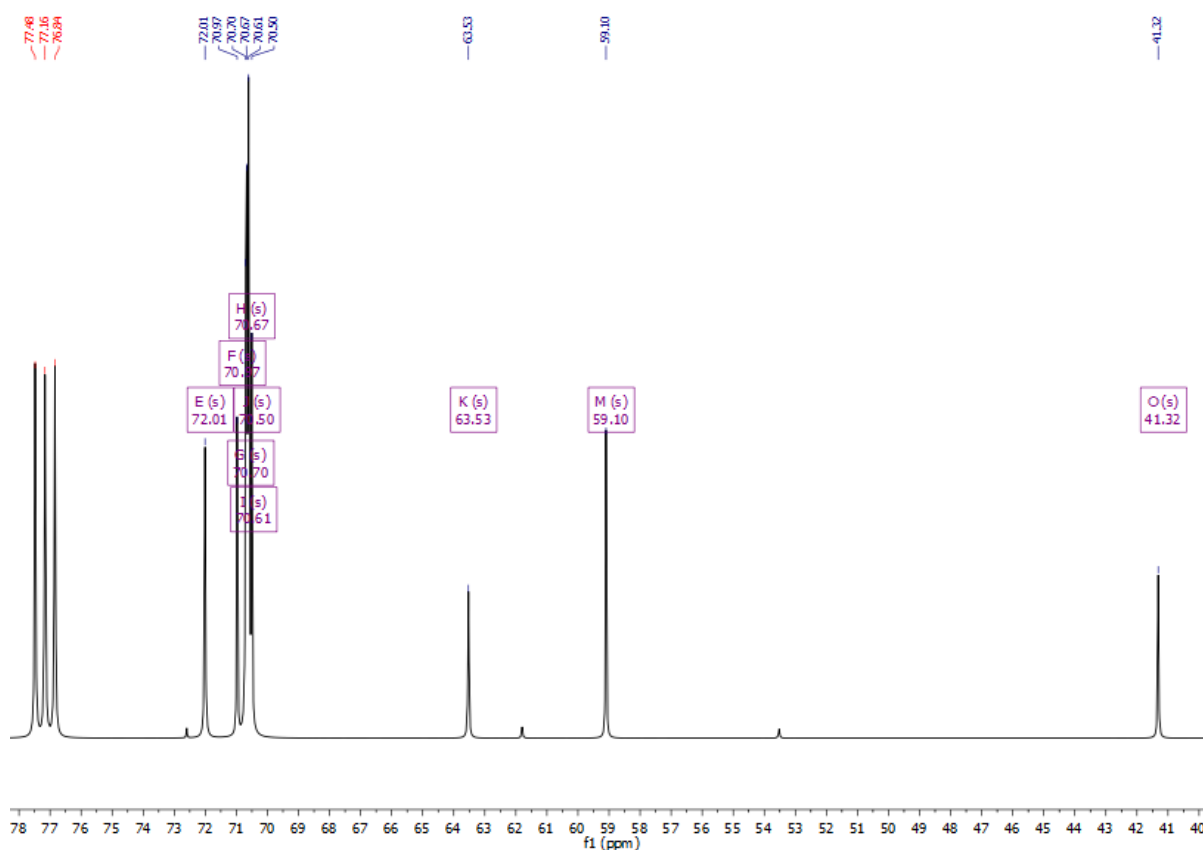
Compound (6.3.9) 13-methylene-2,5,8,11,15,18,21,24-octaoxapentacosane (20 g, 52.6 mmol, 1.0 eq.) was added to a 2-neck oven dried RBF and dissolved in dry THF (60 mL) under an Argon atmosphere. The reaction was cooled to 0 °C, borane tetrahydrofuran complex solution (1M, 55.2 mL, 55.2 mmol, 1.05 eq.) was added dropwise and the solution was stirred rapidly for 2 hours. Sodium hydroxide (2M, 37 mL) was added carefully dropwise and stirred for 15 minutes at 0 °C. Hydrogen peroxide (37 mL) was added dropwise and stirred for a further 30 minutes. Saturated potassium carbonate was added to the solution prior to pouring the reaction

into water and extracting with DCM. The organic layer was separated, dried over Na_2SO_4 and solvent removed under the reduced pressure. The crude oil was passed through a silica plug eluting with ethyl acetate to yield the title compound as a colourless oil (13.6 g, 65%).

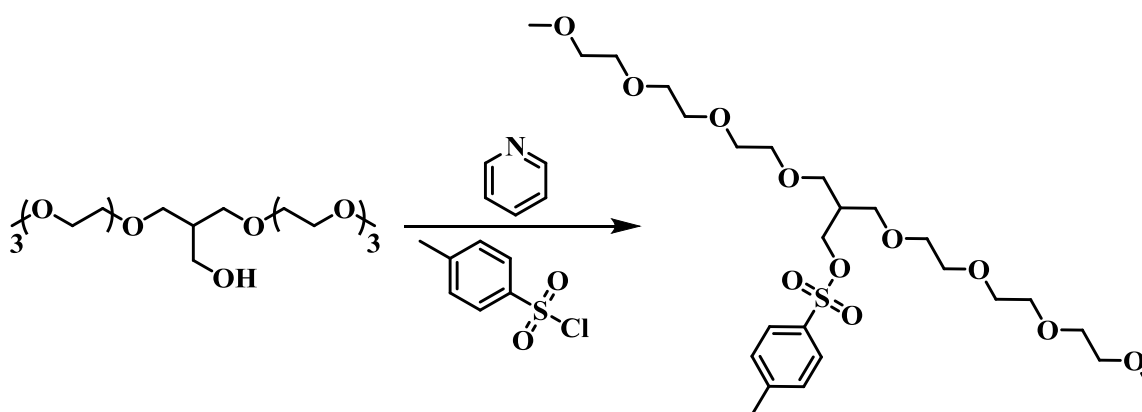
^1H NMR (400 MHz, Chloroform-*d*) δ 3.72 (d, $J = 5.0$ Hz, 2H), 3.68 – 3.53 (m, 20H), 3.57 – 3.48 (m, 8H), 3.36 (s, 6H), 2.11 (tdd, $J = 6.9, 5.8, 3.3$ Hz, 1H).

^{13}C NMR (101 MHz, Chloroform-*d*) δ 75.69, 72.01, 71.15, 70.97, 70.70, 70.67, 70.61, 70.50, 63.53, 62.71, 59.10, 41.32.





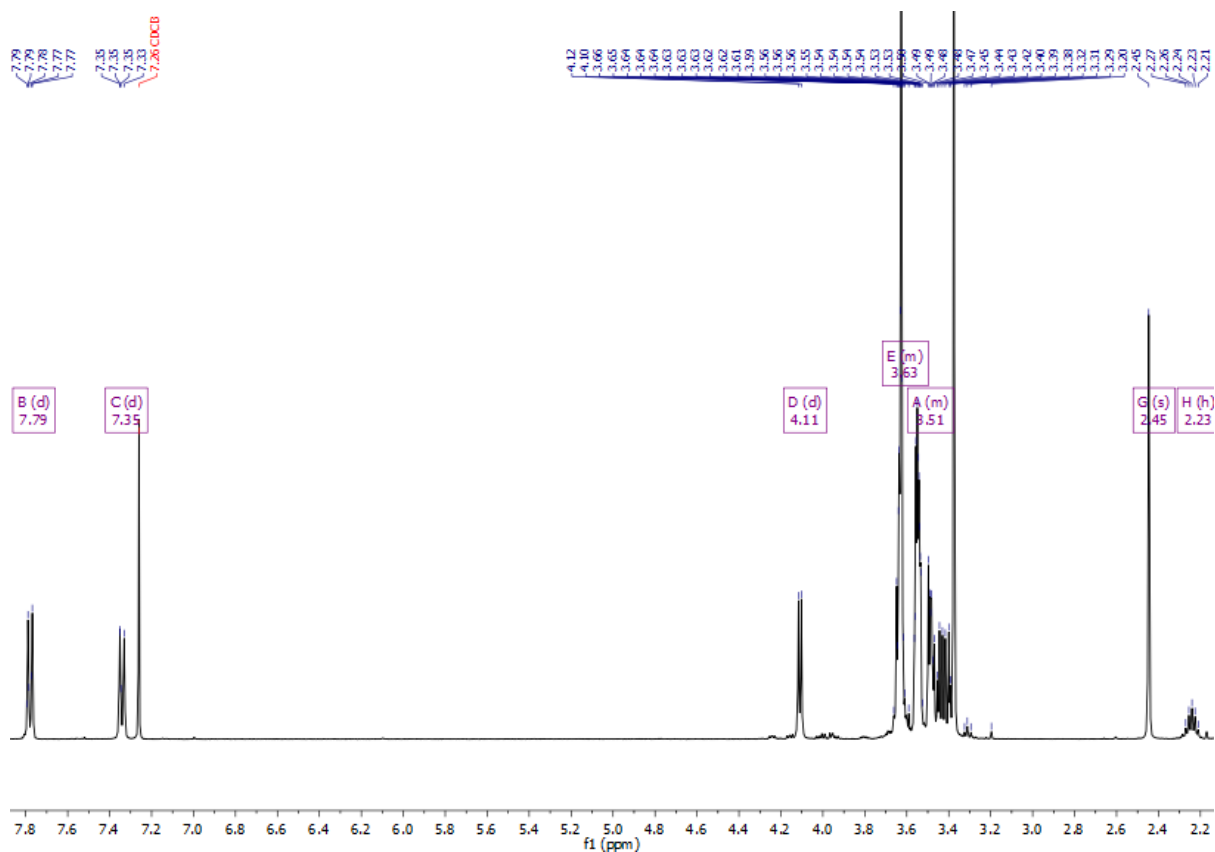
6.3.11 Synthesis of 13-(2,5,8,11-tetraoxadodecyl)-2,5,8,11-tetraoxatetradecan-14-yl 4-methylbenzenesulfonate



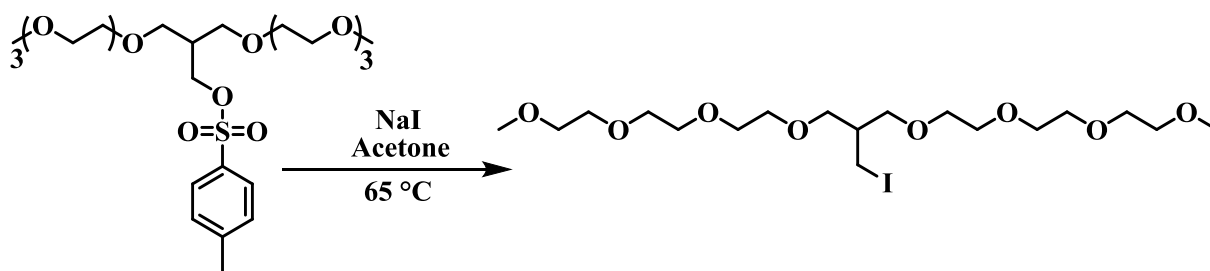
Compound (**6.3.10**) (13.5 g, 33.9 mmol, 1.0 eq.) was dissolved in 30 mL pyridine, cooled to 0 °C and 4-toluenesulfonyl chloride (7.8 g, 40.7 mmol, 1.2 eq.) was added in a single portion upon which the solution turned bright yellow. The mixture was stirred for 20 minutes before being placed into the refrigerator overnight. Cold HCl (2M) was added and the solution was

stirred at 0 °C for 30 minutes before being poured into water and extracted into DCM. The organic phase was separated and dried over MgSO₄, after the solvent had been removed under reduced pressure the resultant solid was purified by column chromatography on silica with ethyl acetate:methanol (9:1) as the eluent. The title compound was isolated as a pale-yellow solid (12.7 g, 68%).

¹H NMR (400 MHz, Chloroform-*d*) δ 7.79 (d, *J* = 8.2 Hz, 2H), 7.35 (d, *J* = 8.2 Hz, 2H), 4.11 (d, *J* = 5.5 Hz, 2H), 3.69 – 3.57 (m, 12H), 3.61 – 3.35 (m, 22H), 2.45 (s, 3H), 2.23 (h, *J* = 6.0 Hz, 1H).



6.3.12 Synthesis of 13-(iodomethyl)-2,5,8,11,15,18,21,24-octaoxapentacosane

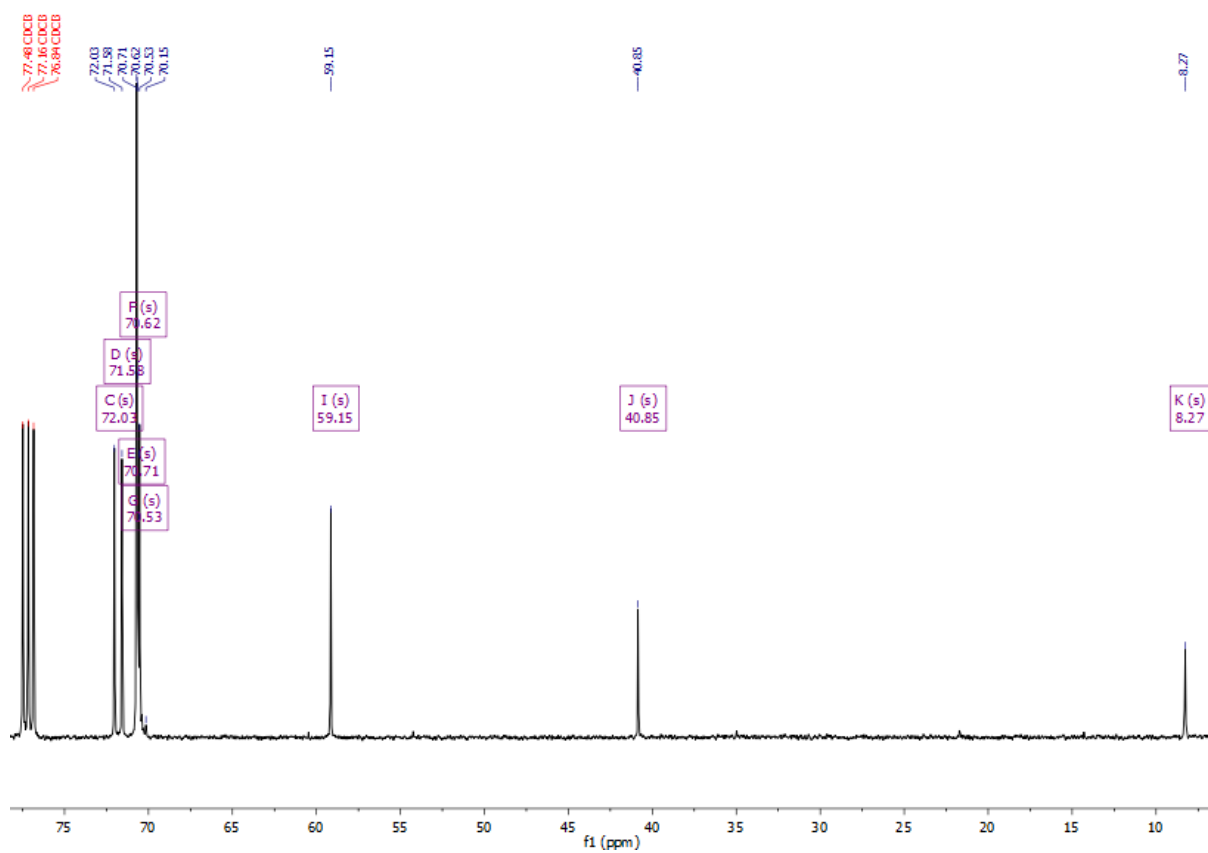
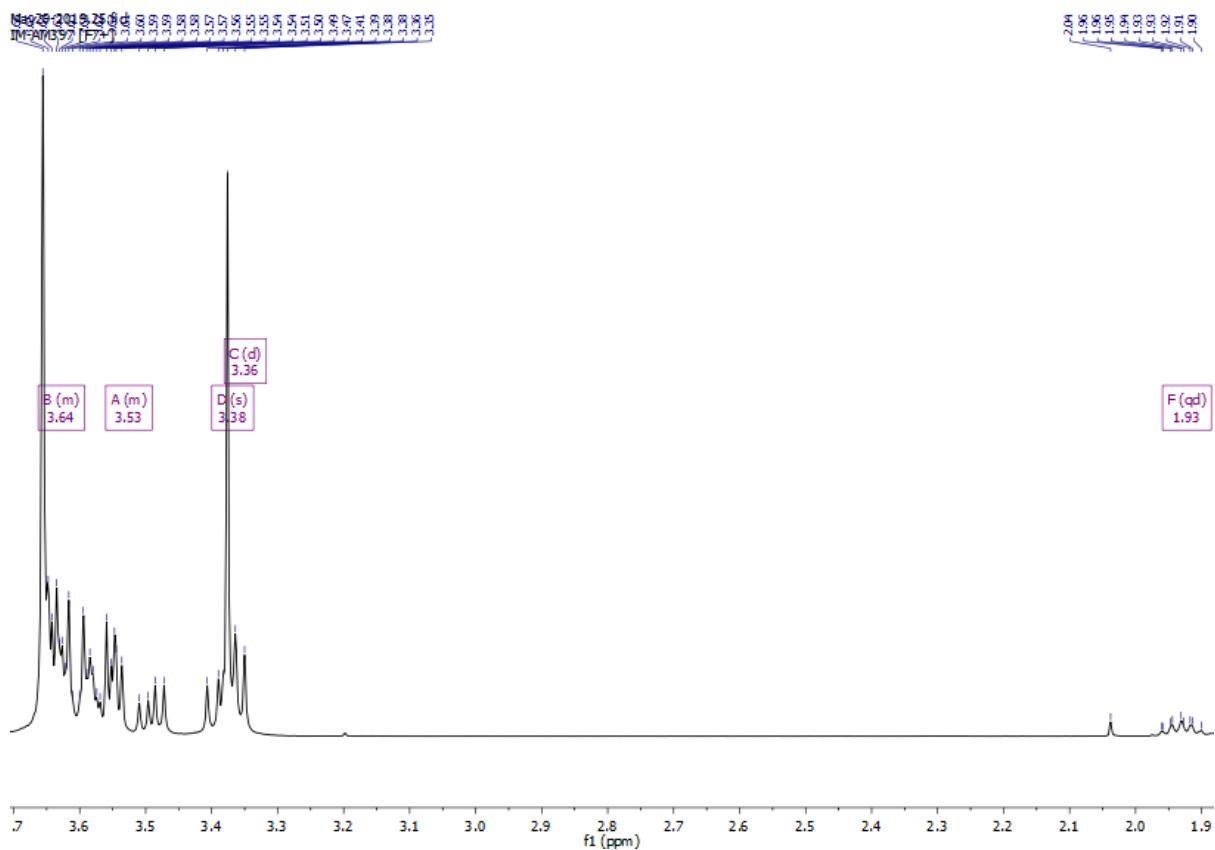


A 2-neck oven dried 250 mL RBF was charged with NaI (4.88 g, 32.6 mmol, 2.0 eq.) and dissolved in acetone (100 mL) under a Nitrogen atmosphere. Compound (6.3.11) 13-(2,5,8,11-tetraoxadodecyl)-2,5,8,11-tetraoxatetradecan-14-yl 4-methylbenzenesulfonate (9 g, 16.3 mmol, 1.0 eq.) was added dropwise via syringe. The reaction was heated to 65 °C and stirred rapidly overnight. Upon cooling to room temperature, the mixture was poured into water, washed with brine and extracted into DCM. The organic layer was separated, dried over MgSO₄ and the solvent removed under reduced pressure to yield a crude pale-yellow oil. The crude was purified by column chromatography on silica using ethyl acetate:methanol (9:1) as the eluent to afford the title compound as colourless viscous oil (7.9 g, 95%).

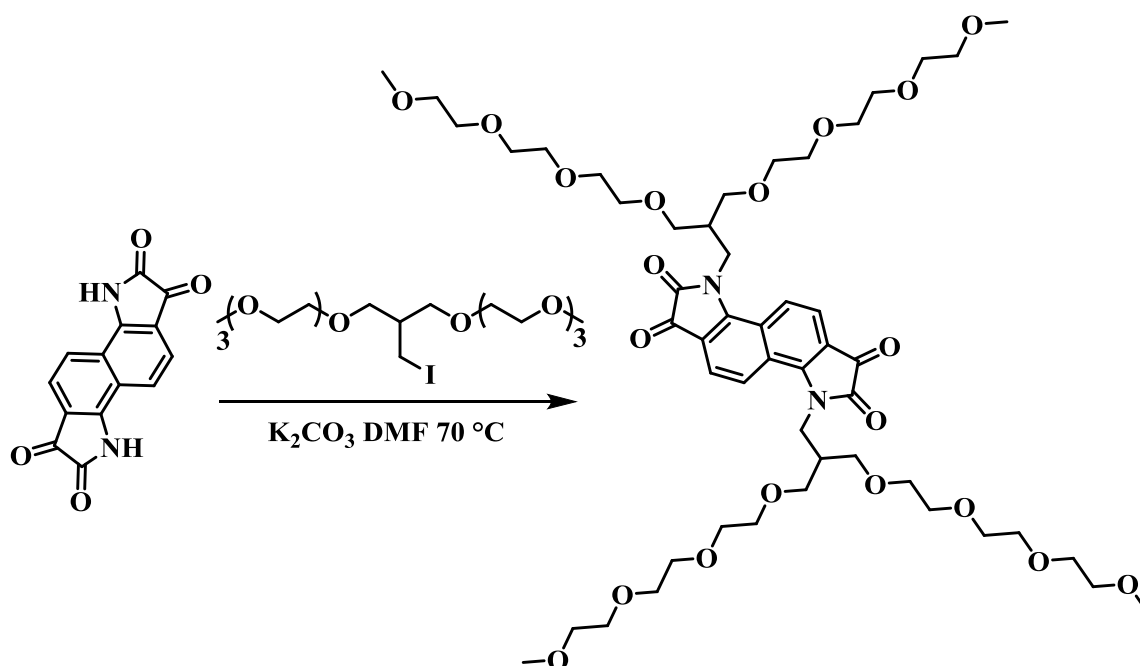
¹H NMR (400 MHz, Chloroform-*d*) δ 3.68 – 3.57 (m, 20H), 3.61 – 3.45 (m, 8H), 3.38 (s, 6H), 3.36 (d, *J* = 5.6 Hz, 2H), 1.93 (qd, *J* = 6.7, 5.3 Hz, 1H).

¹³C NMR (101 MHz, Chloroform-*d*) δ 72.03, 71.58, 70.71, 70.62, 70.53, 59.15, 40.85, 8.27.

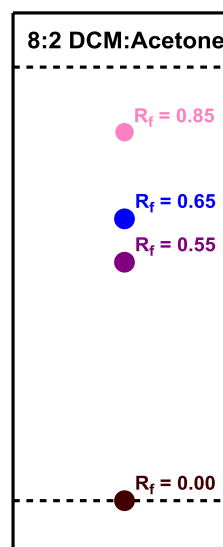
CHAPTER SIX – EXPERIMENTAL



6.3.13 Synthesis of 3,8-bis(13-(2,5,8,11-tetraoxadodecyl)-2,5,8,11-tetraoxatetradecan-14-yl)-3,8-dihydroindolo[7,6-g]indole-1,2,6,7-tetraone



Oven dried potassium carbonate (1.75 g, 12.66 mmol, 5.0 eq.) and bisisatin (**6.3.1**) (674 mg, 2.53 mmol, 1.0 eq.) was dissolved in 10 mL dry DMF inside a 2-neck 50 mL RBF, under a Nitrogen atmosphere. The mixture was heated to 70 °C for one hour. Compound (**6.3.12**) 13-(iodomethyl)-2,5,8,11,15,18,21,24-octaopentacosane (5.6 g, 10.13 mmol, 4.0 eq.) was injected into the reaction in a single portion and the mixture was left to stir for an additional 4 hours. Upon cooling to room temperature, the reaction was poured into water and acidified to pH using

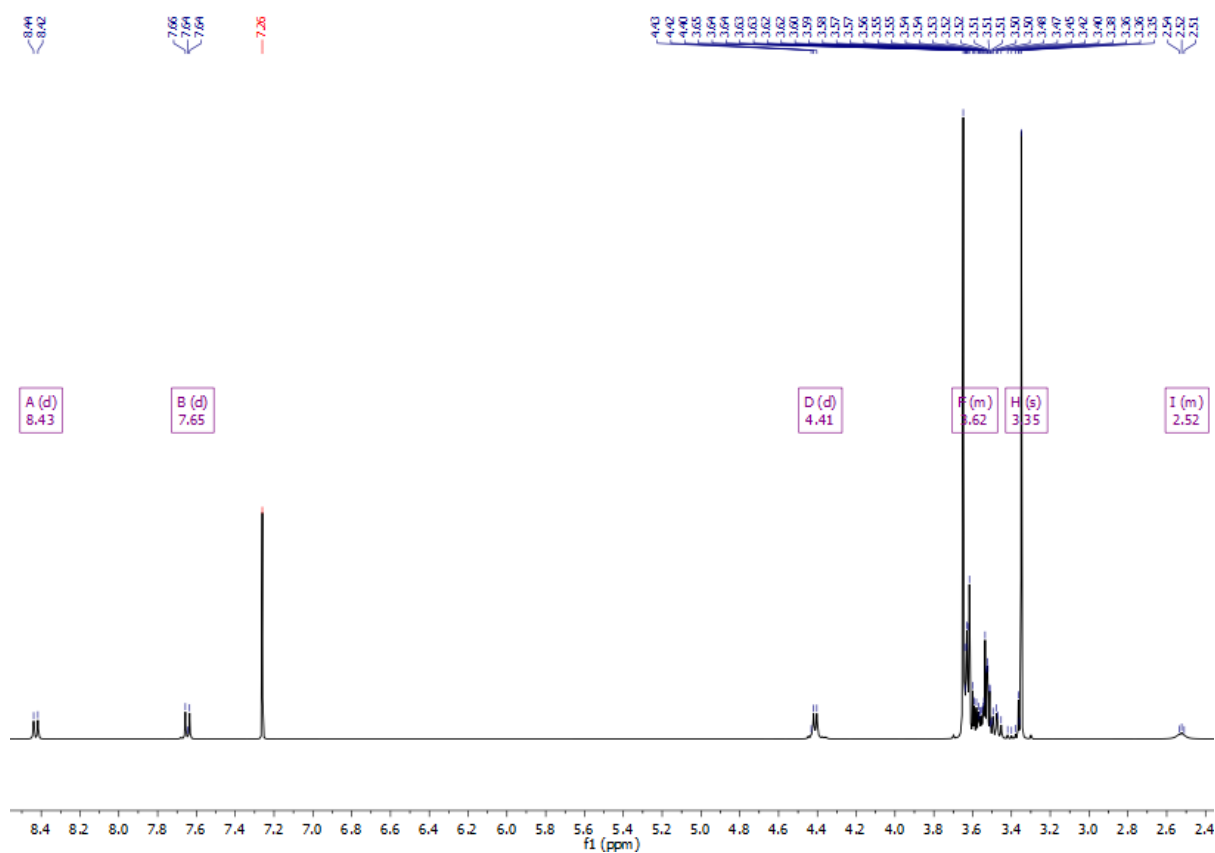


aqueous 2M HCl. Saturated ammonium chloride solution was added to help separate the organic layer upon the addition of DCM. Once separated the organic phase was dried over MgSO_4 and solvent removed to yield a deep purple sticky solid. The crude product was columned on silica twice with a DCM:Acetone (9:1) eluent system and a third time using

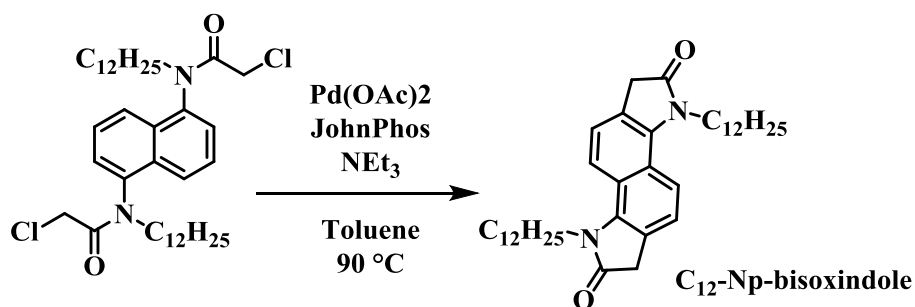
DCM:Acetone (8:2) to isolate the desired blue spot ($R_f=0.65$ TLC inset). The title compound was isolated as a blue solid (347 mg, 13%).

$^1\text{H NMR}$ (400 MHz, Chloroform-*d*) δ 8.43 (d, $J = 8.8$ Hz, 2H), 7.65 (d, $J = 8.8$ Hz, 2H), 4.47 – 4.33 (m, 4H), 3.66 – 3.63 (m, 20H), 3.65 – 3.50 (m, 28H), 3.55 – 3.43 (m, 8H), 3.35 (s, 12H), 2.56 – 2.48 (m, 2H).

Mass (MALDI-ToF): 531.2 $[\text{M}+\text{H}]^+$ (calc. 530.3 $\text{C}_{50}\text{H}_{78}\text{N}_2\text{O}_2$).



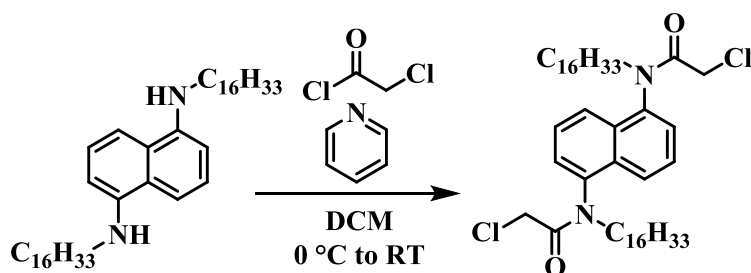
6.3.14 Synthesis of 3,8-didodecyl-1,3,6,8-tetrahydroindolo[7,6-g]indole-2,7-dione



An oven dried 25 mL microwave vial was charged with *N,N'*-(naphthalene-1,5-diyl)bis(2-chloro-*N*-dodecylacetamide) (2 g, 3.09 mmol, 1.0 eq.), Pd(OAc)₂ (83.2 mg, 0.37 mmol, 0.12 eq.) and JohnPhos (221.1 mg, 0.74 mmol, 0.24 eq.). Cap sealed and degassed with Nitrogen for 5 minutes. Dry toluene (12 mL) was added followed by triethylamine (1.27 mL, 9.08 mmol, 2.94 eq.) before being placed into a pre-heated 90 °C oil bath, stirred overnight. Upon cooling to room temperature, the reaction was passed through a short silica plug eluting with DCM before the product was recrystallised from hot hexane to afford an off-white solid (590 mg, 30%).

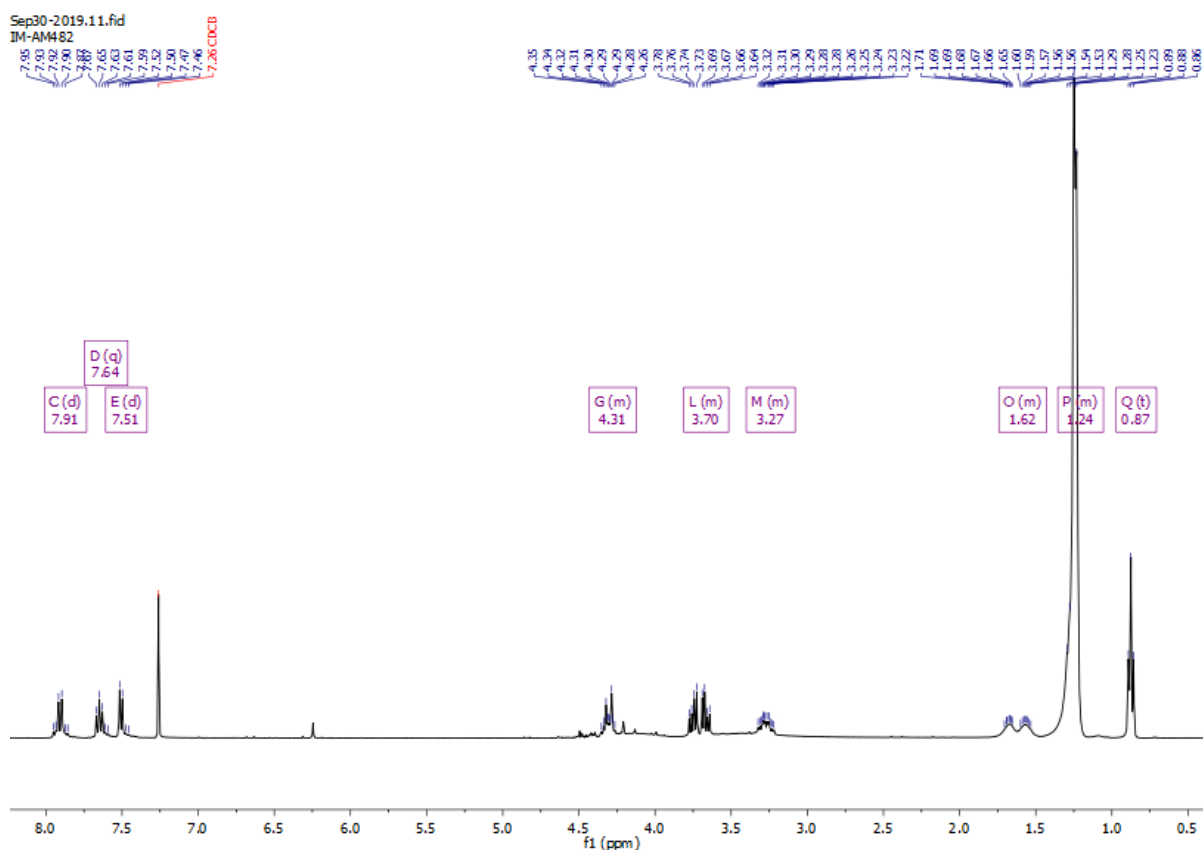
¹H & ¹³C NMR consistent with previously published literature.^{175,180}

6.3.15 Synthesis of *N,N'*-(naphthalene-1,5-diyl)bis(2-chloro-*N*-hexadecylacetamide)

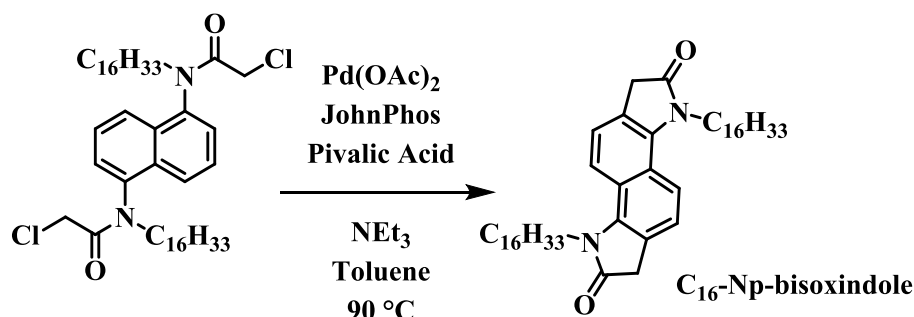


An oven dried 2-neck 50 mL RBF was charged with *N,N'*-dihexadecyl-1,5-naphthalenediamine (416 mg, 0.69 mmol, 1.0 eq.), cooled to 0 °C under a Nitrogen atmosphere. Dry DCM (17 mL) was added followed by pyridine (0.29 mL, 2.06 mmol, 3.0 eq.). 2-chloroacetyl chloride (0.14 mL, 1.71 mmol, 2.5 eq.) was added slowly dropwise, the reaction was warmed to room temperature over 90 minutes. The mixture was poured into water, washed with sodium carbonate solution, brine and extracted into DCM. The organic layer was separated and dried over MgSO₄; solvent removed under reduced pressure to yield a brown residue. The crude was recrystallised from ethanol to afford an off-white solid (406 mg, 78%). ¹H & ¹³C NMR consistent with previously published literature.¹⁷⁵

^1H NMR (400 MHz, Chloroform-*d*) δ 7.91 (d, $J = 8.6$ Hz, 2H), 7.64 (q, $J = 8.0$ Hz, 2H), 7.51 (d, $J = 7.2$ Hz, 2H), 4.38 – 4.18 (m, 2H), 3.80 – 3.62 (m, 4H), 3.37 – 3.19 (m, 2H), 1.71 – 1.51 (m, 4H), 1.32 – 1.21 (m, 52H), 0.87 (t, $J = 6.7$ Hz, 6H).



6.3.16 Synthesis of 3,8-dihexadecyl-1,3,6,8-tetrahydroindolo[7,6-g]indole-2,7-dione

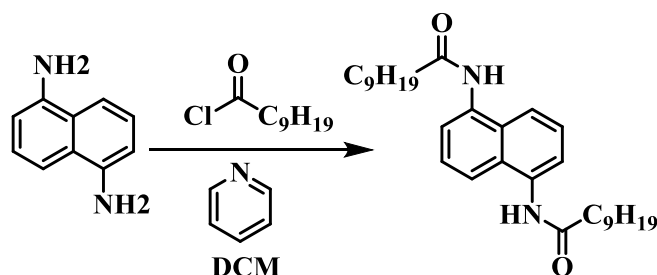


A 10 mL oven dried microwave vial was charged with N,N'-(naphthalene-1,5-diyl)bis(2-chloro-N-hexadecylacetamide) (**6.3.15**) (400 mg, 0.53 mmol, 1.0 eq.), Pd(OAc)₂ (14.2 mg,

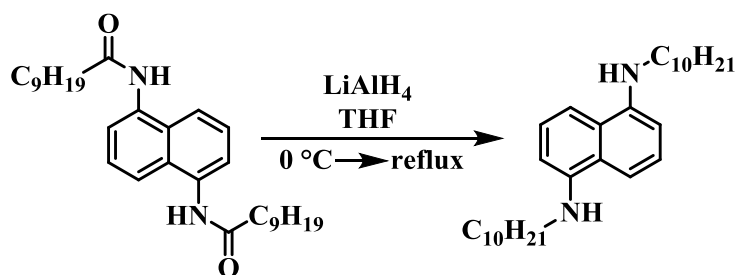
0.06 mmol, 0.12 eq.) JohnPhos (37.7 mg, 0.13 mmol, 0.24 eq.) and pivalic acid (32.3 mg, 0.32 eq.). Cap sealed and degassed with Nitrogen for 5 minutes. Dry toluene (4 mL) was added, followed by triethylamine (0.22 mL, 1.55 eq. 2.94 eq.). Reaction was heated overnight at 90 °C, upon cooling to room temperature the mixture was passed through a short silica plug, eluting with DCM. Solvent was removed under reduced pressure and the crude brown residue was purified by column chromatography, on silica, using ethyl acetate:hexane (1:5) as the eluent system. The title compound was recrystallised from hot hexane to afford a beige solid (300 mg, 83%).

^1H & ^{13}C NMR consistent with previously published literature.¹⁷⁵

6.3.17 Synthesis of N1,N5-didecyl-naphthalene-1,5-diamine



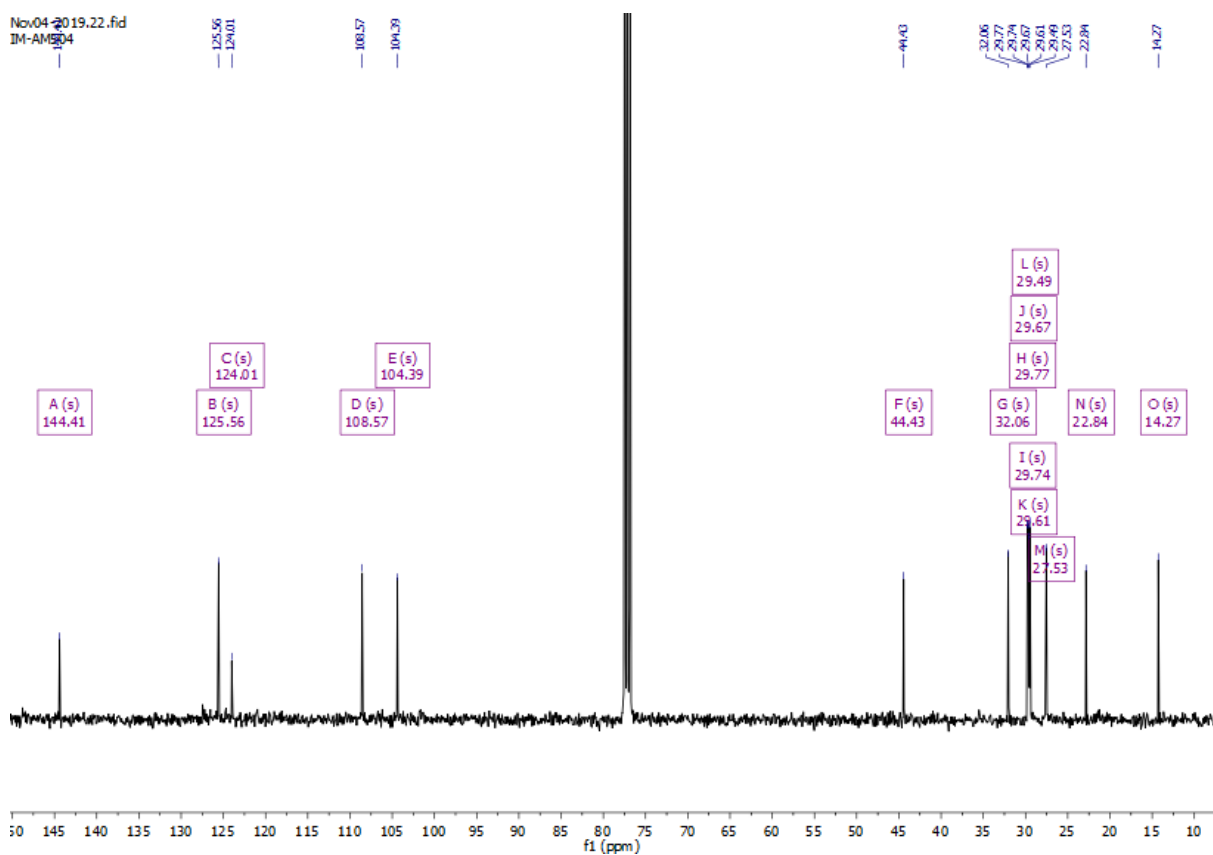
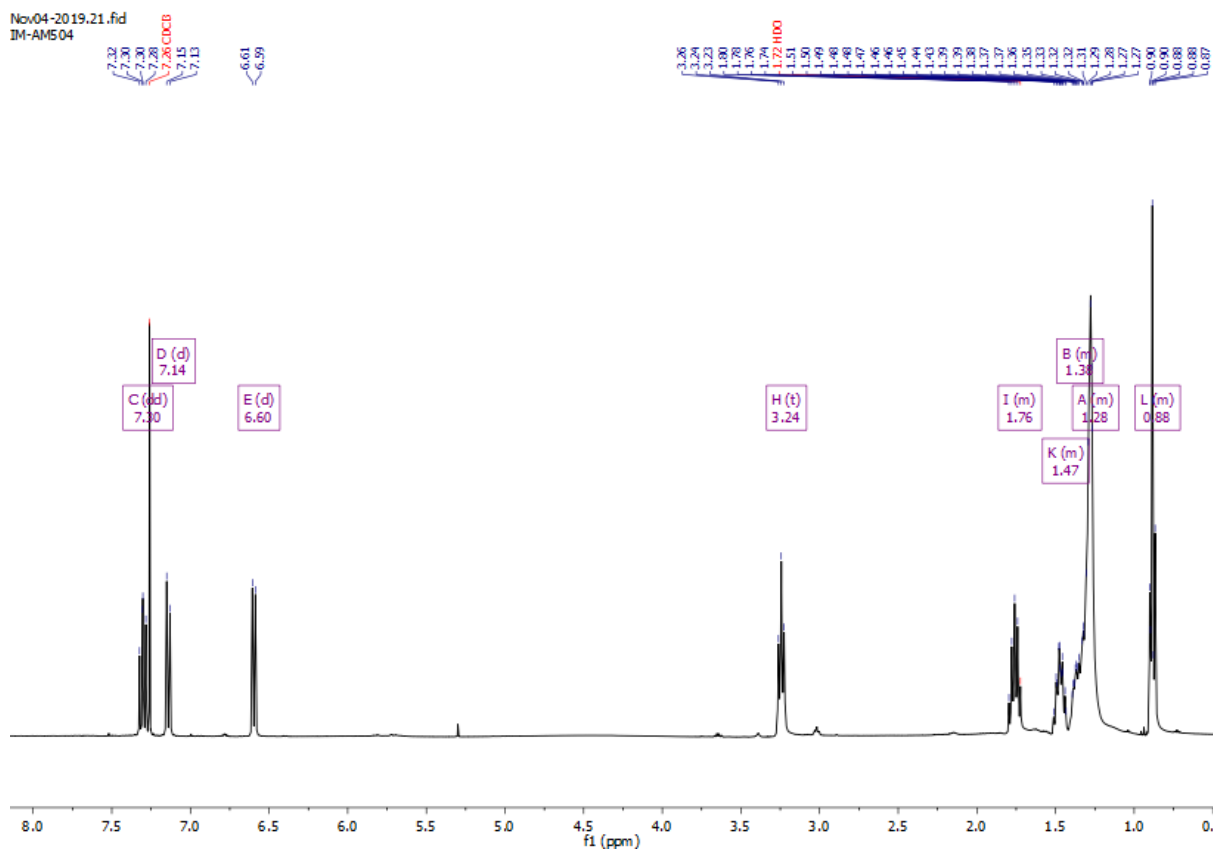
1,5-Diaminonaphthalene (6 g, 37.4 mmol, 1.0 eq.) was dissolved in 100 mL DCM, cooled to 0 °C prior to the addition of pyridine (7.3 mL, 89.9 mmol, 2.4 eq.). Mixture was stirred for 5 minutes before decanoyl chloride (17.1 mL, 82.4 mmol, 2.2 eq.) was added slowly dropwise. Reaction was stirred overnight then filtered through a frit, washed with copious amounts of hexane to afford an off-white solid which was vacuum dried overnight and used in the next step without further purification (12.0 g, 69%).

6.3.18 Synthesis of *N*¹,*N*⁵-didecyl-naphthalene-1,5-diamine

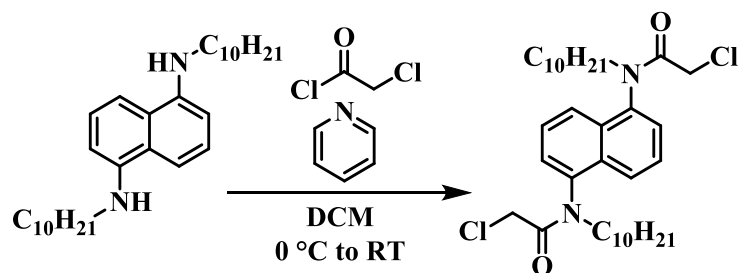
*N*¹,*N*⁵-didecyl-naphthalene-1,5-diamine (**6.3.17**) (12 g, 25.7 mmol, 1.0 eq.) was suspended in dry THF (200 mL) and cooled to 0 °C under a Nitrogen atmosphere. LiAlH₄ (2.4M, 43 mL, 102.8 mmol, 4.0 eq.) was slowly added dropwise, refluxed (66 °C) overnight. Reaction was cooled to 0 °C, 1M NaOH was added dropwise until effervescence ceased, mixture was poured into water, washed with brine and extracted into DCM. Once the organic layer was separated and dried over MgSO₄ the solvent was removed under reduced pressure. The brown residue was purified via silica chromatography using ethyl acetate:hexane (1:5) as the eluent and finally recrystallised from hot hexane to afford a beige solid (2.6 g, 24%).

¹H NMR (400 MHz, Chloroform-*d*) δ 7.30 (dd, *J* = 8.4, 7.5 Hz, 2H), 7.14 (d, *J* = 8.4 Hz, 2H), 6.60 (d, *J* = 7.5 Hz, 2H), 3.24 (t, *J* = 7.1 Hz, 4H), 1.82 – 1.72 (m, 4H), 1.54 – 1.41 (m, 4H), 1.46 – 1.34 (m, 2H), 1.38 – 1.24 (m, 24H), 0.93 – 0.84 (m, 6H).

¹³C NMR (101 MHz, Chloroform-*d*) δ 144.41, 125.56, 124.01, 108.57, 104.39, 44.43, 32.06, 29.77, 29.74, 29.67, 29.61, 29.49, 27.53, 22.84, 14.27.



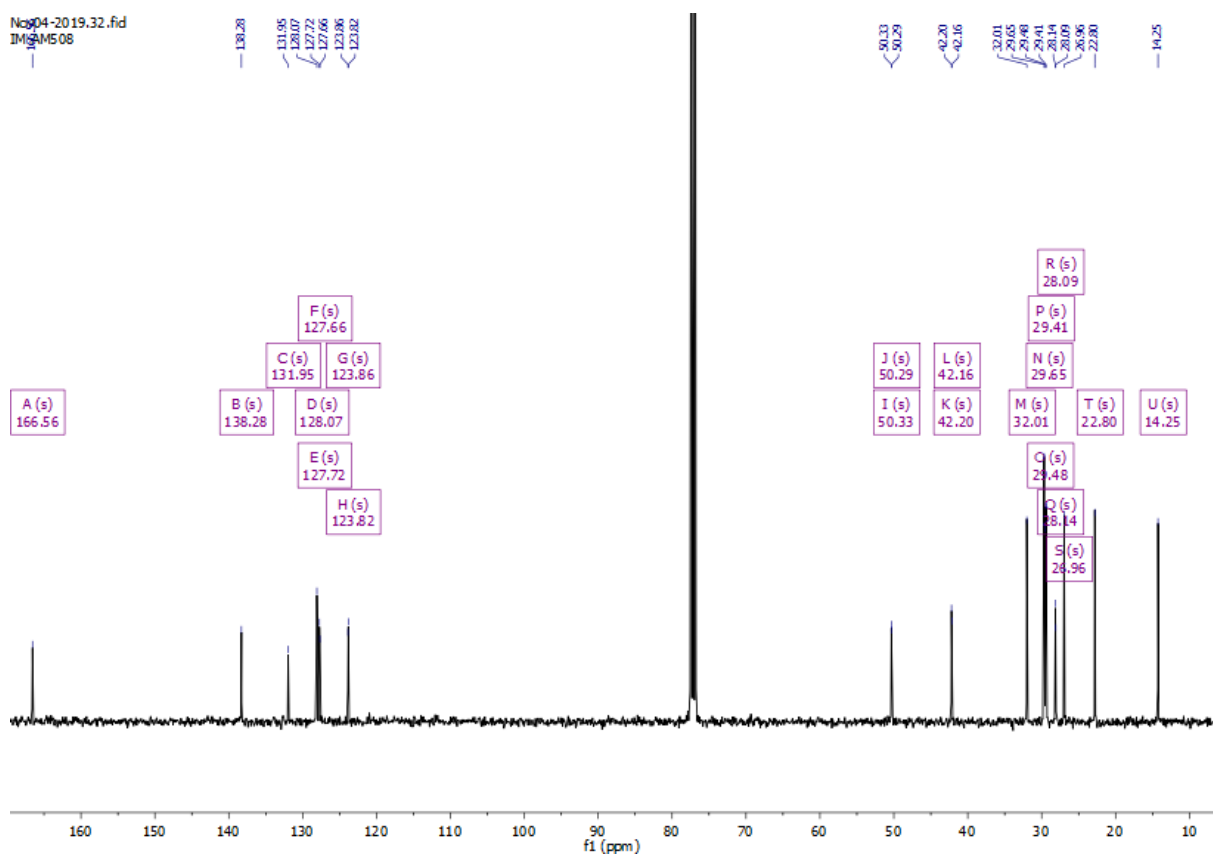
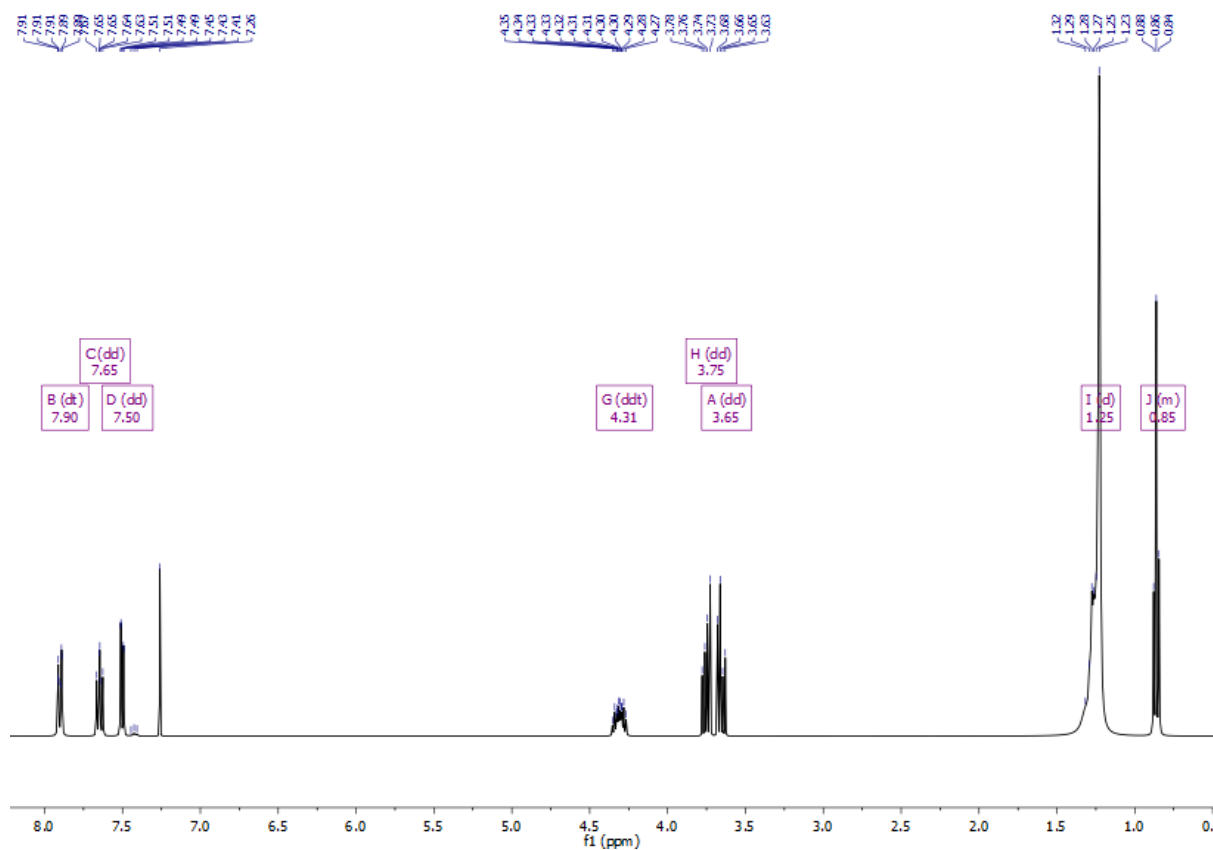
6.3.19 Synthesis of N,N'-(naphthalene-1,5-diyl)bis(2-chloro-N-decylacetamide)



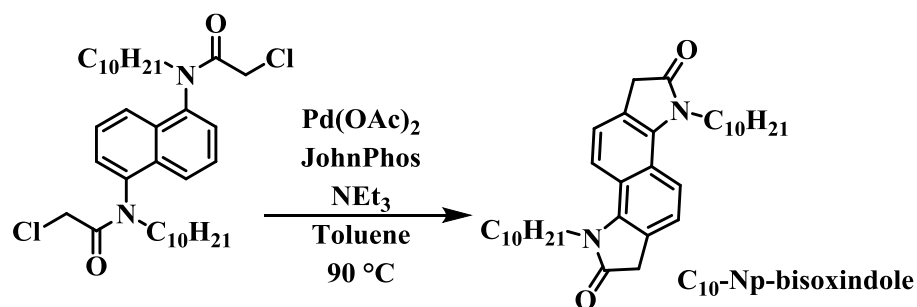
*N*¹,*N*⁵-didecyl-1,5-naphthalenediamine (**6.3.18**) (2.59 g, 5.9 mmol, 1.0 eq.) was suspended in 30 mL dry DCM, cooled to 0 °C under a Nitrogen atmosphere. Pyridine (1.43 mL, 17.71 mmol, 3.0 eq.) and 2-chloroacetyl chloride (1.67 mL, 14.75 mmol, 2.5 eq.) added dropwise, warmed to room temperature over 90 minutes. Mixture poured into water, washed with brine and saturated sodium bicarbonate solution, extracted into DCM. Once separated the organic phase was dried over MgSO₄, solvent removed under reduced pressure. The brown residue was purified using column chromatography, on silica, using ethyl acetate:hexane (1:5) as the eluent system to afford an off-white solid (1.25 g, 36%).

¹H NMR (400 MHz,) δ 7.90 (dt, *J* = 8.0, 1.1 Hz, 2H), 7.65 (dd, *J* = 8.4, 7.4 Hz, 2H), 7.50 (dd, *J* = 7.2, 0.9 Hz, 2H), 4.31 (ddt, *J* = 13.3, 10.2, 5.9 Hz, 2H), 3.75 (dd, *J* = 13.3, 7.0 Hz, 2H), 3.65 (dd, *J* = 13.3, 6.8 Hz, 2H), 1.25 (d, *J* = 19.3 Hz, 34H), 0.90 – 0.82 (m, 6H).

¹³C NMR (101 MHz, Chloroform-*d*) δ 166.56, 138.28, 131.95, 128.07, 127.72, 127.66, 123.86, 123.82, 50.33, 50.29, 42.20, 42.16, 32.01, 29.65, 29.48, 29.41, 28.14, 28.09, 26.96, 22.80, 14.25.



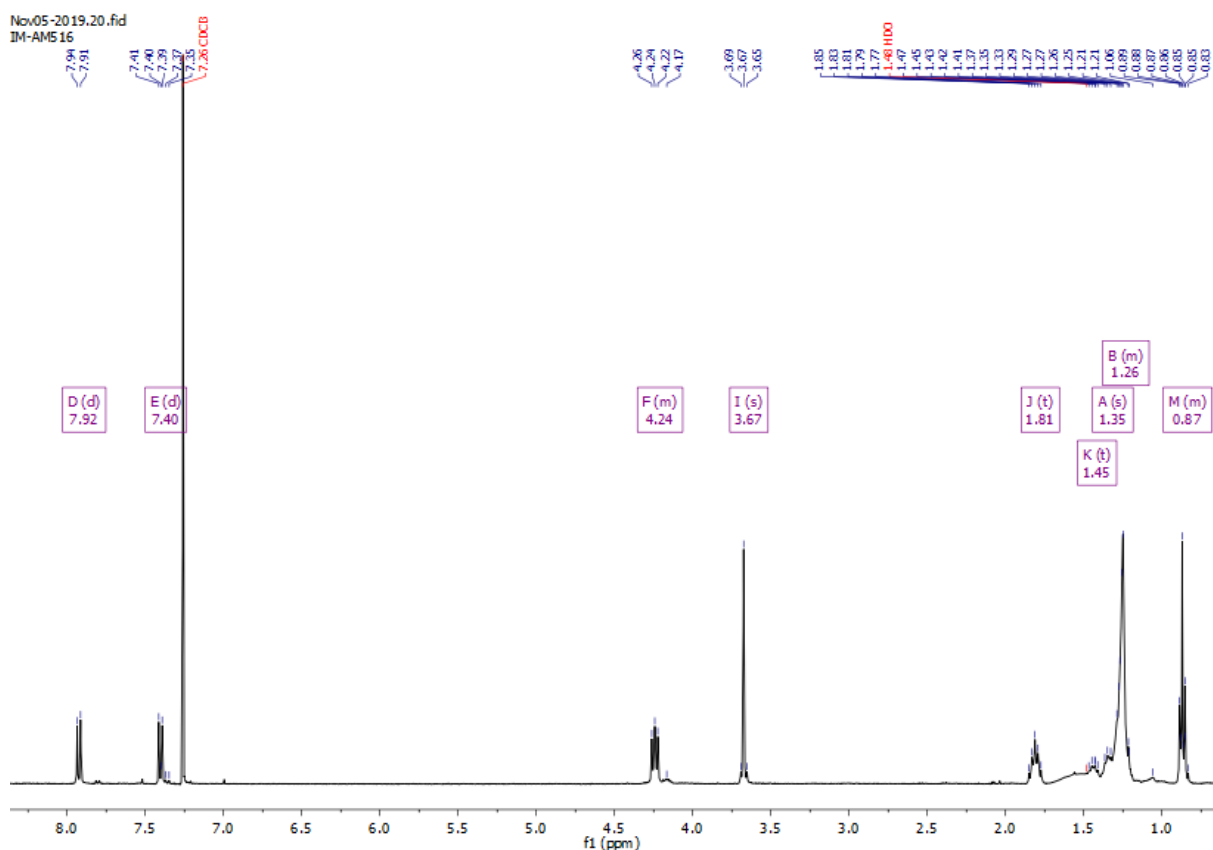
6.3.20 Synthesis of 3,8-didecyl-1,3,6,8-tetrahydroindolo[7,6-g]indole-2,7-dione



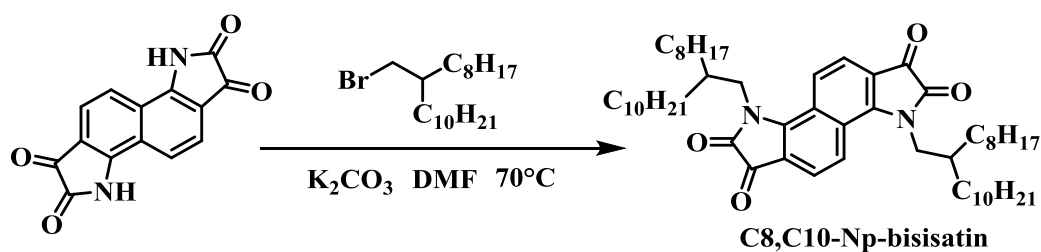
An oven dried 10 mL microwave vial was charged with N,N'-(naphthalene-1,5-diyl)bis(2-chloro-N-decylacetamide) (**6.3.19**) (0.7 g, 1.18 mmol, 1.0 eq.), Pd(OAc)₂ (43.18 mg, 0.14 mmol, 0.12 eq.), JohnPhos (111 mg, 0.28 mmol, 0.24 eq.) and pivalic acid (94.4.92 mg, 0.61 mmol, 0.61 eq.). Cap was sealed and degassed with Nitrogen for 10 minutes, prior to the addition of 6 mL dry toluene. Triethylamine (0.64 mL, 2.98 mmol, 2.94 eq.) was slowly added, reaction placed into a pre-heated oil bath (90 °C) and stirred rapidly overnight. The mixture was cooled to room temperature passed through a short pad of silica, eluting with DCM, solvent removed under reduced pressure. The crude brown residue was purified via column chromatography on silica using ethyl acetate:hexane (1:5) as the eluent, recrystallisation from hot hexane afforded a beige solid (95mg, 16%).

¹H NMR (400 MHz, Chloroform-*d*) δ 7.92 (d, *J* = 8.6 Hz, 1H), 7.40 (d, *J* = 8.6 Hz, 1H), 4.29 – 4.20 (m, 2H), 3.67 (s, 2H), 1.81 (t, *J* = 7.5 Hz, 2H), 1.45 (t, *J* = 7.5 Hz, 2H), 1.35 (s, 2H), 1.33 – 1.17 (m, 12H), 0.91 – 0.81 (m, 3H).

Mass (MALDI-ToF): 519.2 [M+H]⁺ (calc. 518.4 C₃₄H₅₀N₂O₂).



6.3.21 3,8-bis(2-octyldodecyl)-3,8-dihydroindolo[7,6-g]indole-1,2,6,7-tetraone

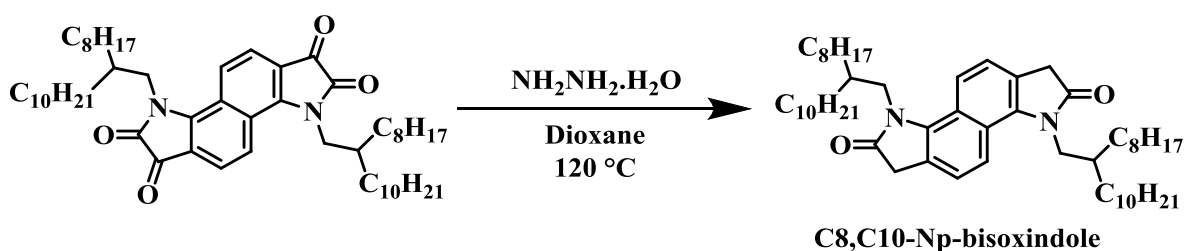


An oven dried 2-neck 50 mL RBF was charged with bisatin (**6.3.1**) (300 mg, 1.13 mmol, 1.0 eq.) and oven dried potassium carbonate (779 mg, 5.65 mmol, 5.0 eq.) under a Nitrogen atmosphere. Dry DMF (8 mL) was added via syringe and the mixture was stirred for 45 minutes at 70 °C. 9-(Bromomethyl)nonadecane (1.63 g, 4.52 mmol, 4.0 eq.) was added as a single portion and the mixture was stirred for a further 4 hours. Following this the reaction was poured into water and acidified to pH 7 with 2M HCl solution. The aqueous phase was extracted with DCM dried over MgSO₄ and the solvent removed under reduced pressure to yield a brown

residue. The crude was purified by column chromatography on silica with DCM:Hexane (2:3) as the eluent system, followed by recrystallisation from hot hexane to afford a blue solid (198 mg, 21%).

^1H & ^{13}C NMR consistent with previously published literature.¹⁷⁵

6.3.22 Wolff-Kishner Reduction to form 3,8-bis(2-octyldodecyl)-1,3,6,8-tetrahydroindolo[7,6-g]indole-2,7-dione

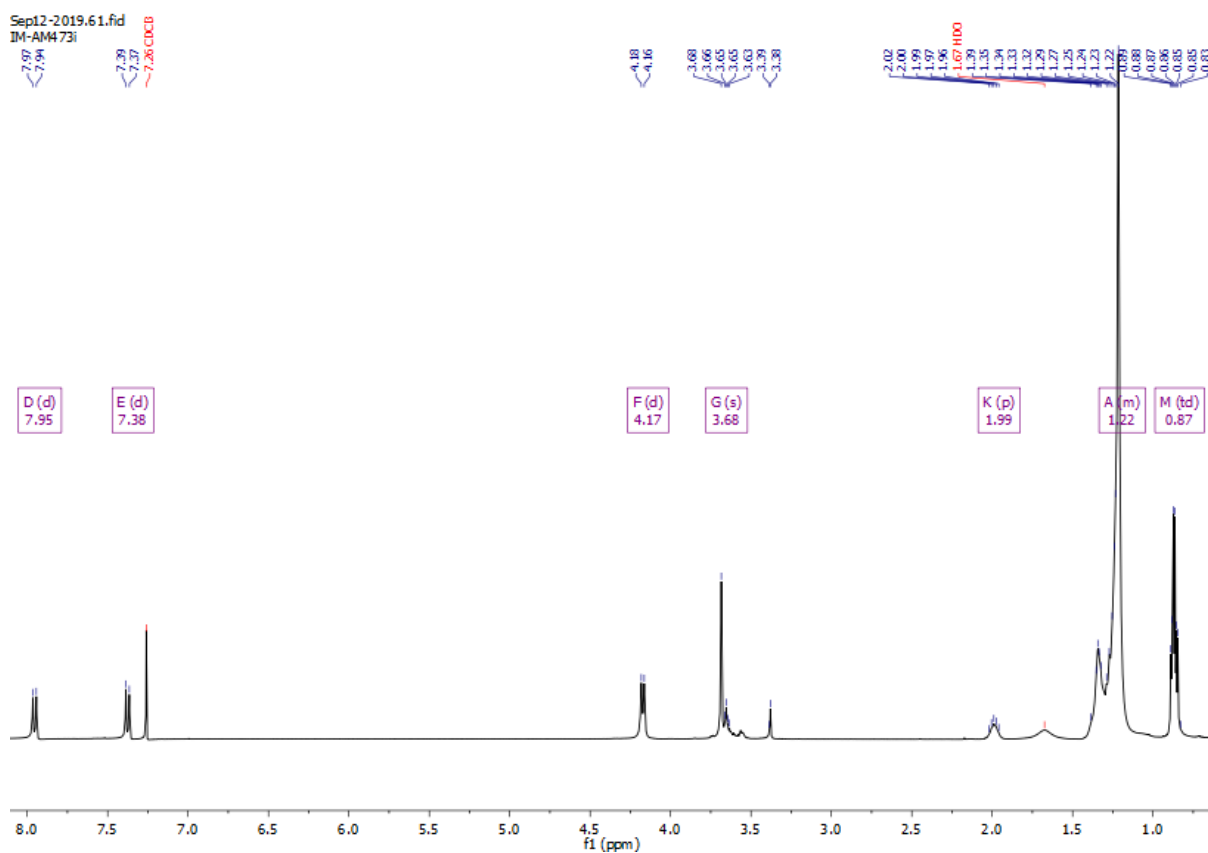


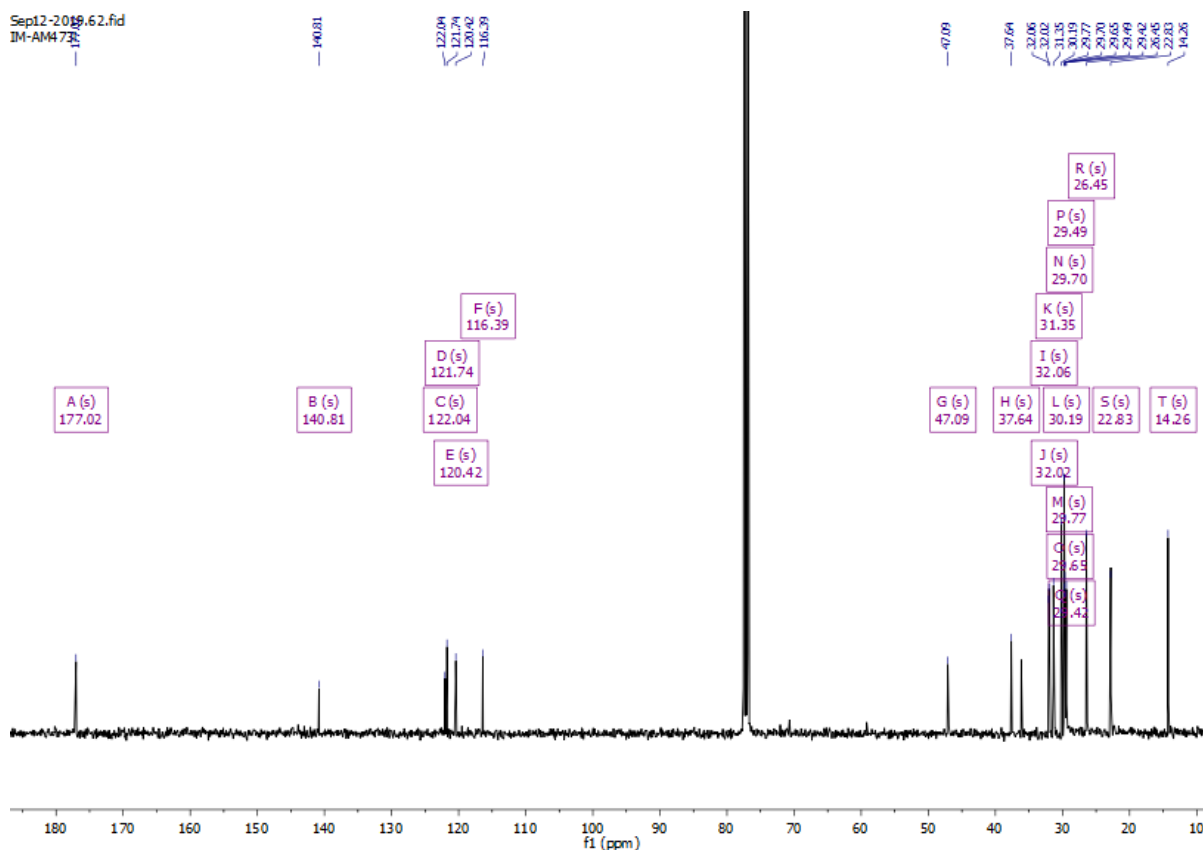
An oven dried 5 mL microwave vial was charged with 3,8-bis(2-octyldodecyl)-3,8-dihydroindolo[7,6-g]indole-1,2,6,7-tetraone (**6.3.21**) (198 mg, 0.24 mmol, 1.0 eq.) cap sealed and degassed with Nitrogen for 5 minutes. Dry dioxane (1 mL) was added followed by hydrazine monohydrate (0.5 mL), causing the mixture to turn a deep orange instantaneously. The reaction was stirred overnight at 120 °C, the reaction was cooled to 0 °C, turning yellow in the process. 2M HCL solution (3 mL) was added before pouring the mixture into water and extracting into DCM. The organic layer was separated and dried over MgSO₄, the solvent was removed under reduced pressure and the crude oil was recrystallised from ethyl acetate to afford a pale-yellow solid. Both TLC and ^1H NMR showed that the reaction was incomplete with both product and mono-reduced species present. The reaction was re-run, using the same conditions as above, but altering the amount of dioxane to 1.5 mL and increasing hydrazine monohydrate to 0.8 mL. The same work-up procedure as above was employed to yield an off-white solid (78 mg, 41%).

^1H NMR (400 MHz, Chloroform-*d*) δ 7.95 (d, $J = 8.6$ Hz, 2H), 7.38 (d, $J = 8.6$ Hz, 2H), 4.17 (d, $J = 7.3$ Hz, 4H), 3.68 (s, 4H), 1.99 (p, $J = 6.0$ Hz, 2H), 1.48 – 1.13 (m, 64H), 0.87 (td, $J = 6.9, 3.5$ Hz, 12H).

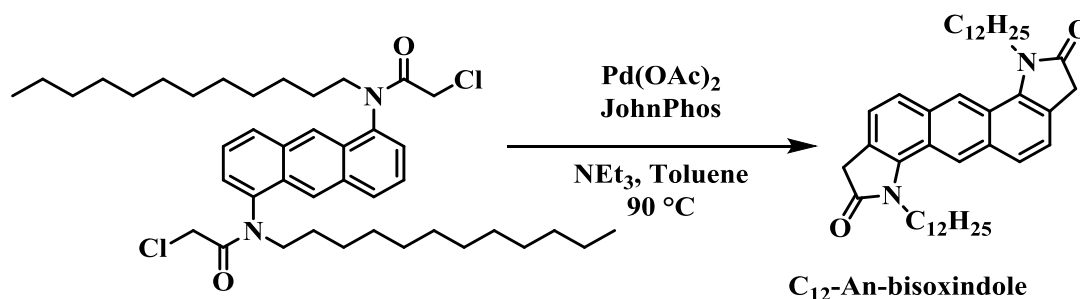
^{13}C NMR (101 MHz, Chloroform-*d*) δ 177.02, 140.81, 122.04, 121.74, 120.42, 116.39, 47.09, 37.64, 32.06, 32.02, 31.35, 30.19, 29.77, 29.70, 29.65, 29.49, 29.42, 26.45, 22.83, 14.26.

TOF MS LD+: calculated, $\text{C}_{54}\text{H}_{90}\text{N}_2\text{O}_2$, 798.70, $[\text{M}^+\text{H}]^+$ found 800.8.





6.3.23 Synthesis of 1,7-didodecyl-1,3,7,9-tetrahydrobenzo[1,2-g:4,5-g']diindole-2,8-dione



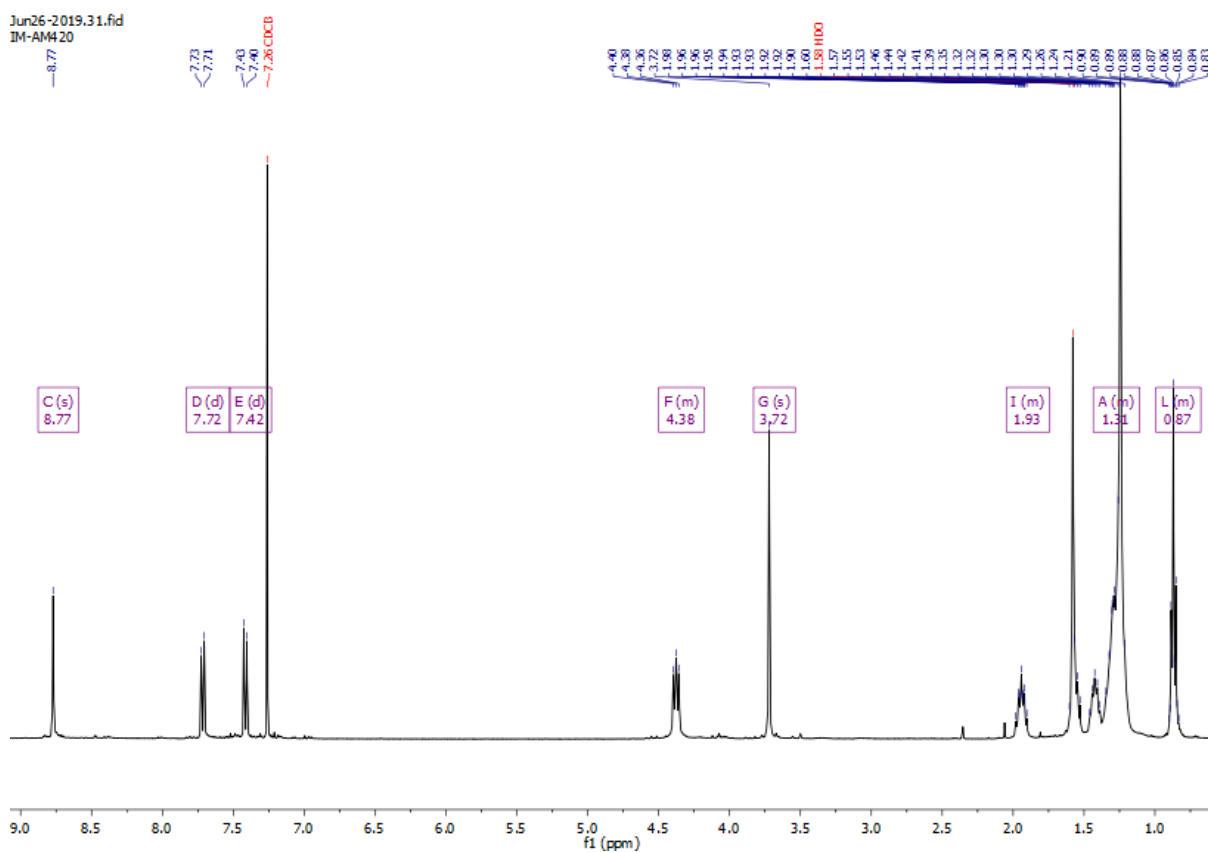
A 10 mL oven dried microwave vial was charged with N,N'-(anthracene-1,5-diyl)bis(2-chloro-N-dodecylacetamide) (400 mg, 0.57 mmol, 1.0 eq.) Pd(OAc)₂ (15.4 mg, 0.07 mmol, 0.12 eq.) and JohnPhos (41.0 mg, 0.14 mmol, 0.24 eq.). The cap was sealed and degassed with Nitrogen for 10 minutes. Toluene (4 mL) was added followed lastly by the addition of triethylamine (0.23 mL, 1.69 mmol, 2.94 eq.) before placing the vial into a preheated oil bath at 90 °C before stirring overnight in the dark. The reaction was cooled to room temperature then passed through

a silica plug, eluting with DCM. The title compound was obtained from a hot hexane recrystallisation to afford a green solid (160 mg, 45%).

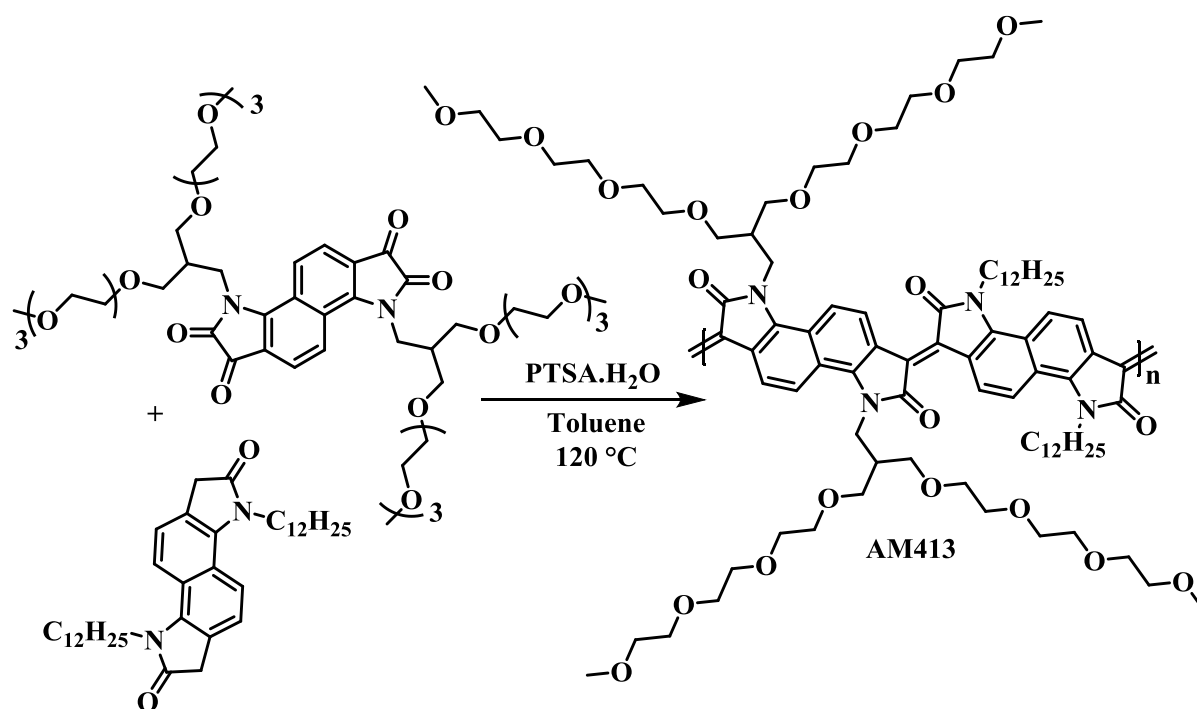
^1H NMR (400 MHz, Chloroform-*d*) δ 8.77 (s, 2H), 7.72 (d, $J = 8.4$ Hz, 2H), 7.42 (d, $J = 8.4$ Hz, 2H), 4.42 – 4.33 (m, 4H), 3.72 (s, 4H), 2.01 – 1.88 (m, 4H), 1.56 – 1.17 (m, 36H), 0.92 – 0.81 (m, 6H).

^{13}C NMR (101 MHz, Chloroform-*d*) δ 176.69, 138.94, 132.44, 123.75, 122.32, 121.82, 119.83, 119.71, 42.68, 36.88, 32.06, 29.78, 29.73, 29.54, 29.49, 27.12, 22.83, 14.26.

Mass (MALDI-ToF): 625.3 $[\text{M}+\text{H}]^+$ (calc. 624.5 $\text{C}_{42}\text{H}_{60}\text{N}_2\text{O}_2$).



6.3.24 Synthesis of Polymer AM413



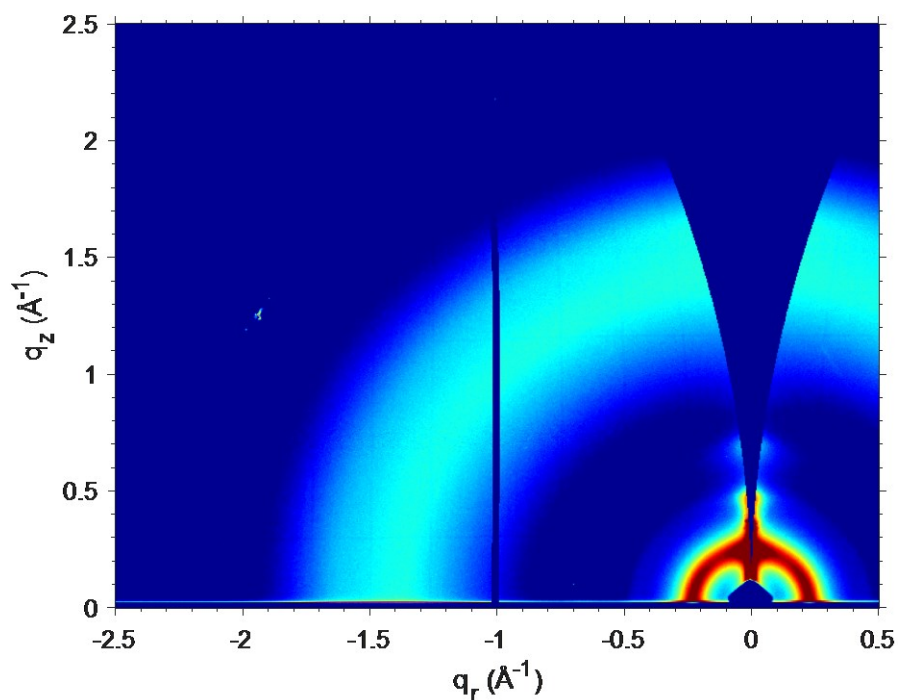
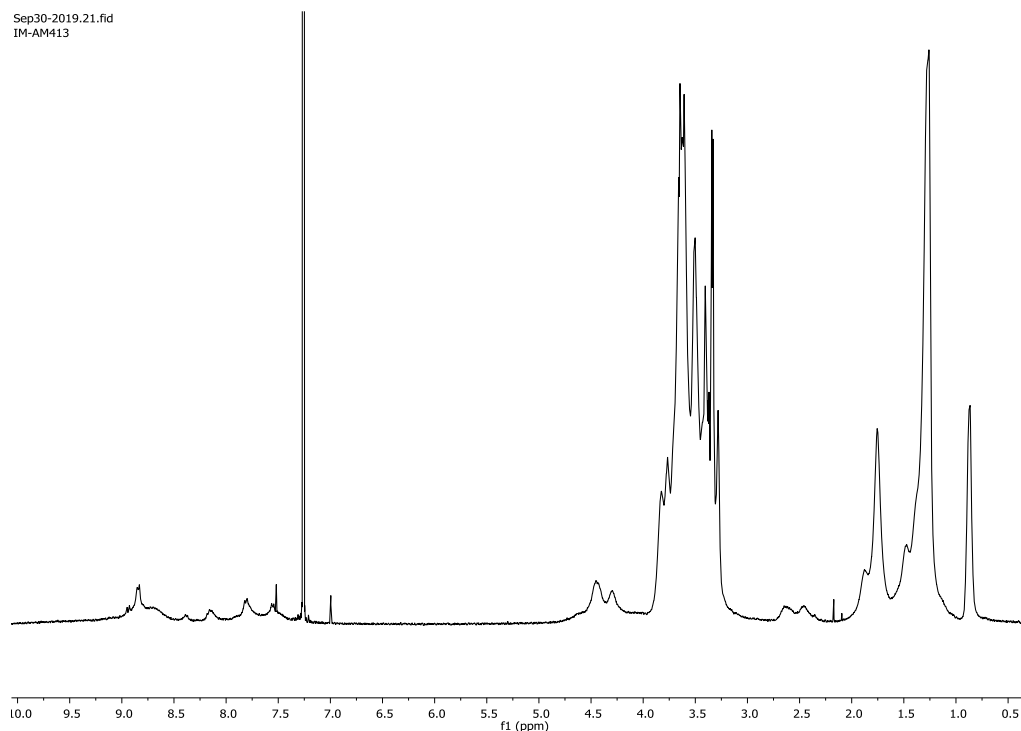
An oven dried 10 mL microwave vial was charged with (6.3.13) 3,8-bis(13-(2,5,8,11-tetraoxadodecyl)-2,5,8,11-tetraoxatetradecan-14-yl)-3,8-dihydroindolo[7,6-g]indole-1,2,6,7-tetraone (105 mg, 0.10 mmol, 1.0 eq.), 3,8-didodecyl-1,3,6,8-tetrahydroindolo[7,6-g]indole-2,7-dione (6.3.14) (58.8 mg, 0.10 mmol, 1.0 eq.) and p-toluenesulfonic acid monohydrate (5.9 mg, 0.03 mmol, 0.3 eq.). Cap sealed, purged with Nitrogen for 10 minutes. Degassed toluene (3.5 mL) added, vial placed into pre-heated oil bath (120 °C) stirred overnight. Upon cooling to room temperature, the dark purple solution was precipitated into 100 mL of hexane, filtered into a thimble and purified by Soxhlet extraction with hexane, heptane, toluene, methanol and chloroform (in that order). The chloroform fraction was collected and reduced under vacuum, the polymer was re-precipitated into hexane, filtered and dried to obtain a dark purple film (155 mg, 95%).

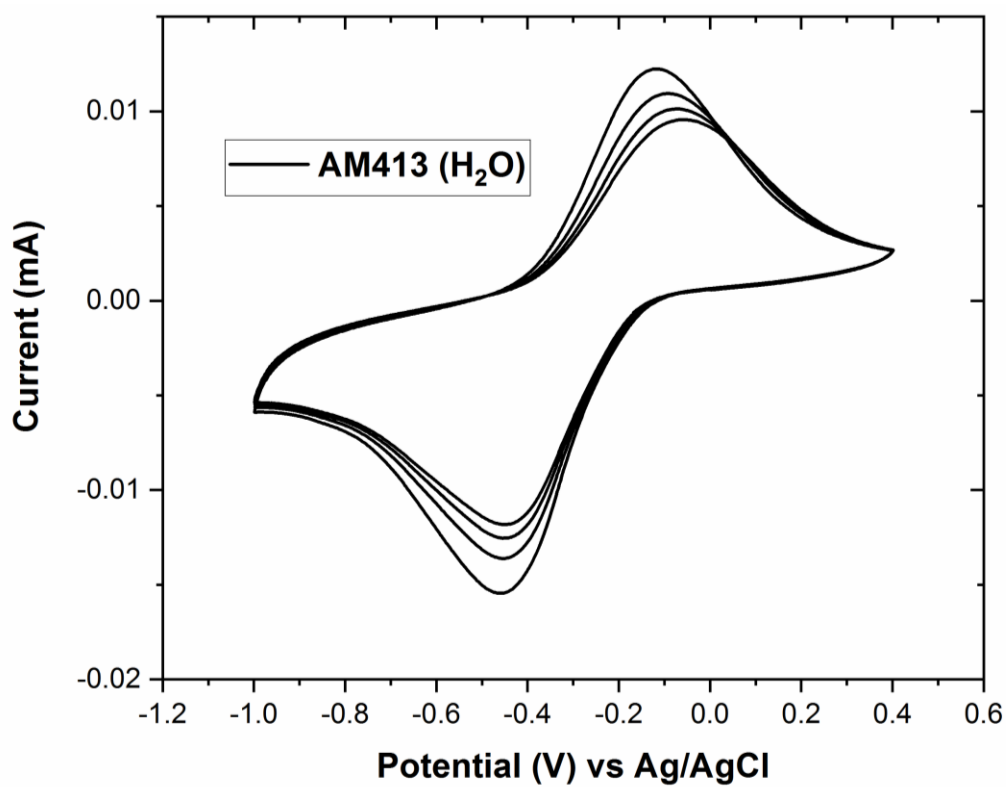
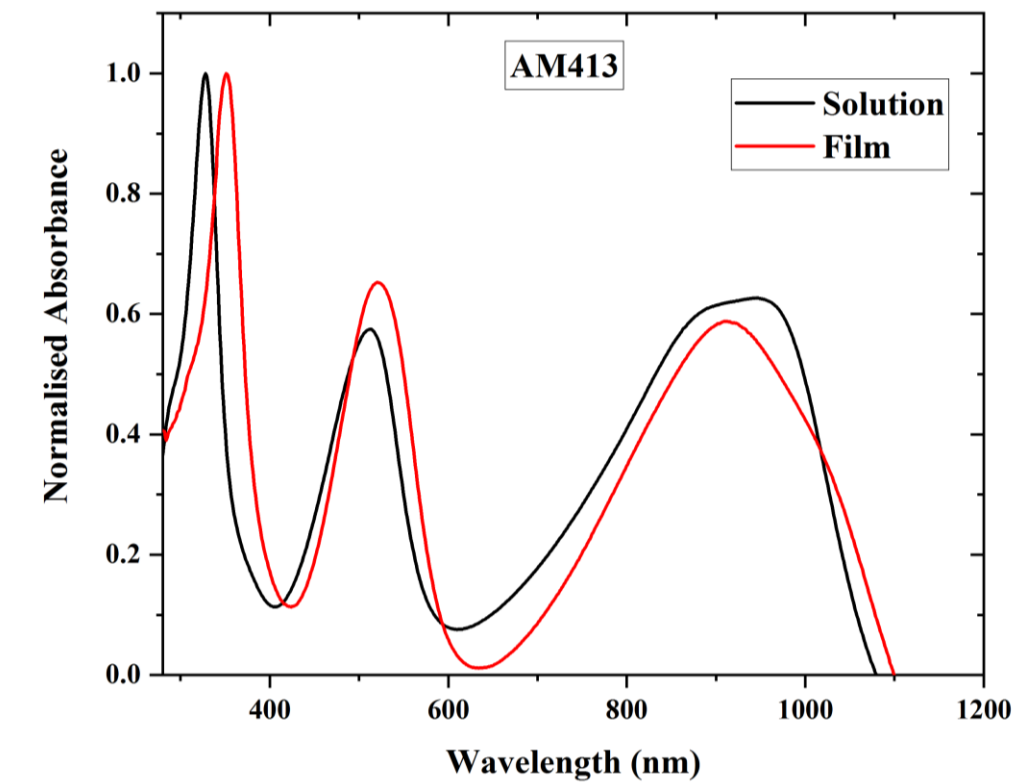
$\lambda_{\text{MAX}}^{\text{a}}$ (nm)	λ_{ONSET} (nm)	$E_{\text{opt}}^{\text{b}}$ (eV)	EA^{c} (UV)	IP (PESA)	EA (CV)	E_{GAP} (eV)	M_{n}	M_{w}	PDI
902	1102	1.13	4.09	5.22	3.70	1.52	10200	15100	1.48

^a λ is the peak of the first low energy absorption band of the polymers

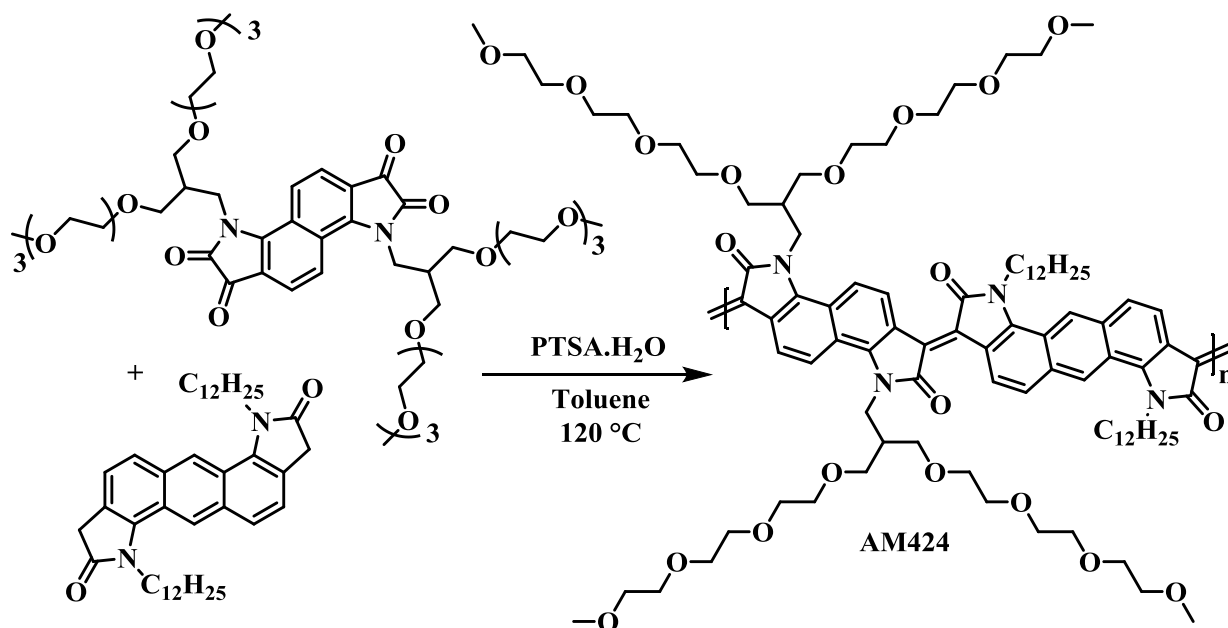
^b E_{opt} estimated optical gap using onset of the thin-film absorption spectra $E_{\text{GAP}} = 1240 / \lambda_{\text{ONSET}}$

^cEA crudely estimated by subtraction of the UV-Vis absorption onset from IP ($EA = IP - E_{\text{opt}}$), a procedure that neglects the exciton binding energy





6.3.25 Synthesis of Polymer AM424



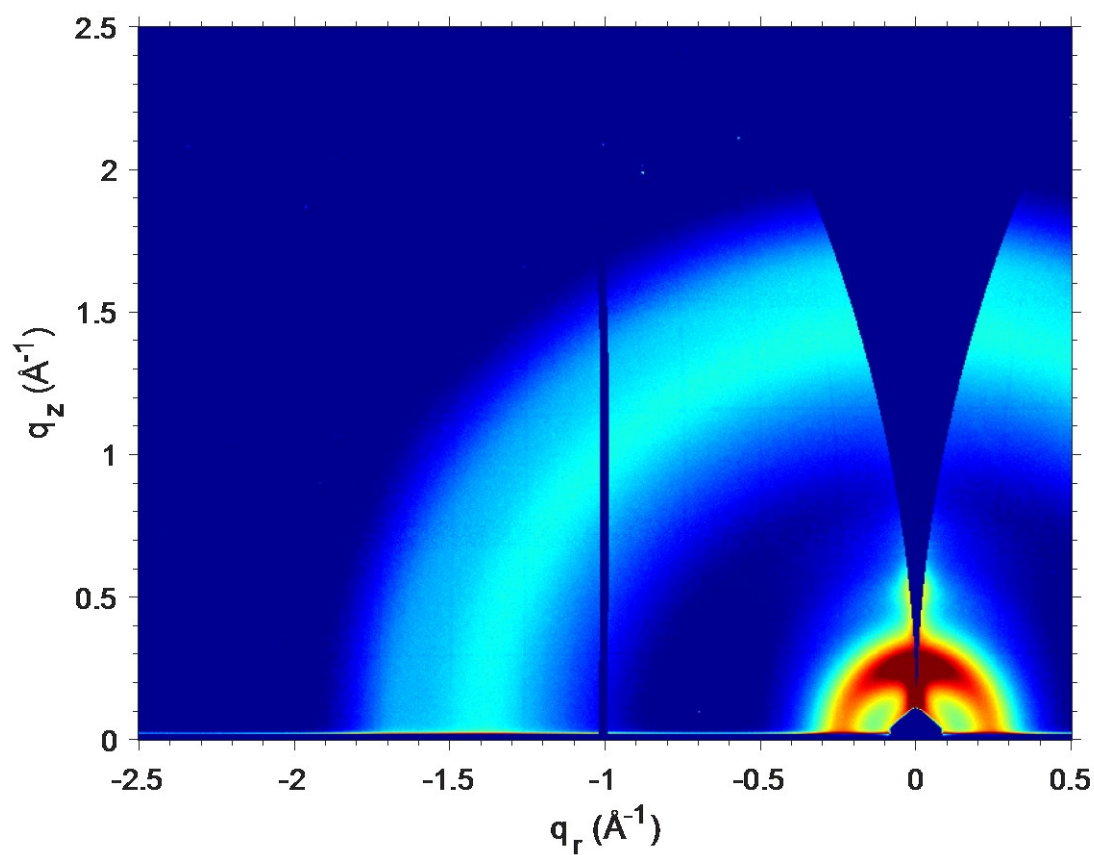
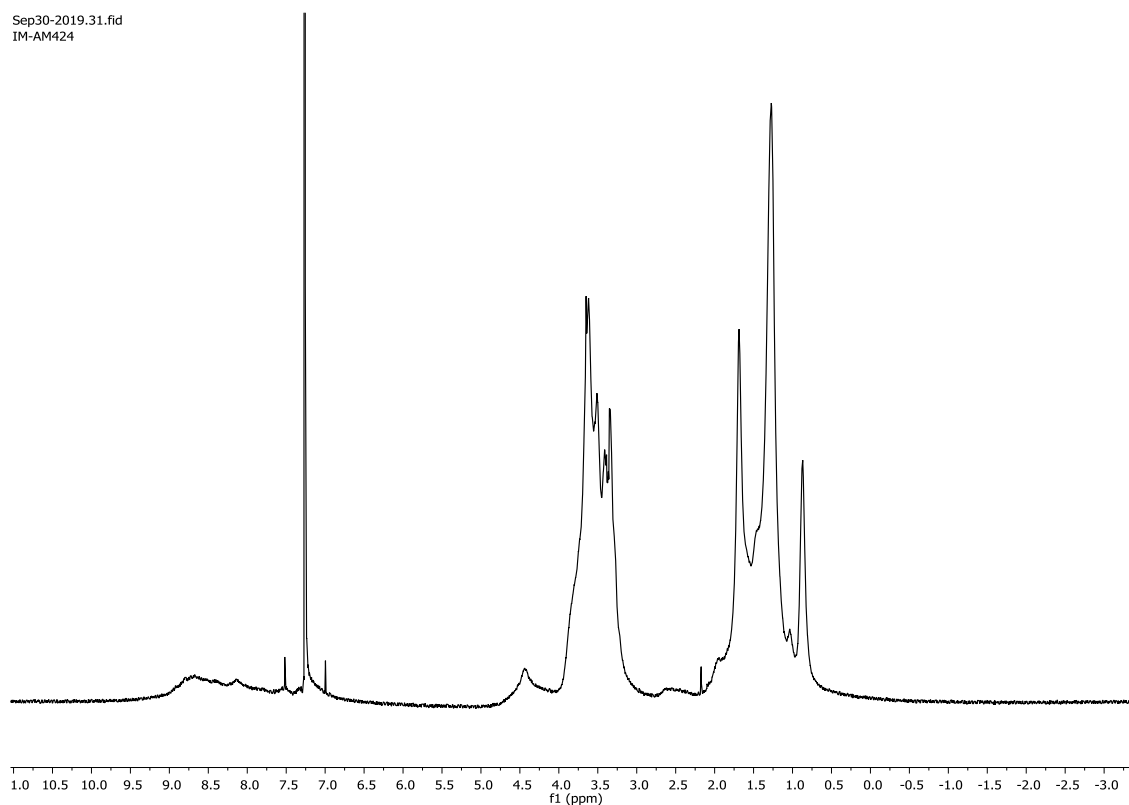
An oven dried 5 mL microwave vial was charged with 3,8-bis(13-(2,5,8,11-tetraoxadodecyl)-2,5,8,11-tetraoxatetradecan-14-yl)-3,8-dihydroindolo[7,6-g]indole-1,2,6,7-tetraone (6.3.13) (117 mg, 0.11 mmol, 1.0 eq.), 1,7-didodecyl-1,3,7,9-tetrahydrobenzo[1,2-g:4,5-g']diindole-2,8-dione (6.3.23) (71.2 mg, 0.11 mmol, 1.0 eq.) and *p*-toluenesulfonic acid monohydrate (6.5 mg, 0.03 mmol, 0.3 eq.). Cap was sealed and the vessel was purged with Nitrogen for 5 minutes. Dry DMF (1 mL) was added and the vial was placed into a pre-heated oil bath (120 °C) left stirring overnight. Upon cooling to room temperature, the gelled purple solution was precipitated into 100 mL of methanol, filtered into a thimble. Crude polymer was purified by Soxhlet extraction into hexane, heptane, methanol, toluene and chloroform (in that order). The chloroform fraction was collected, solvent removed under reduced pressure precipitated into hexane, filtered to afford a purple film (99 mg, 53%).

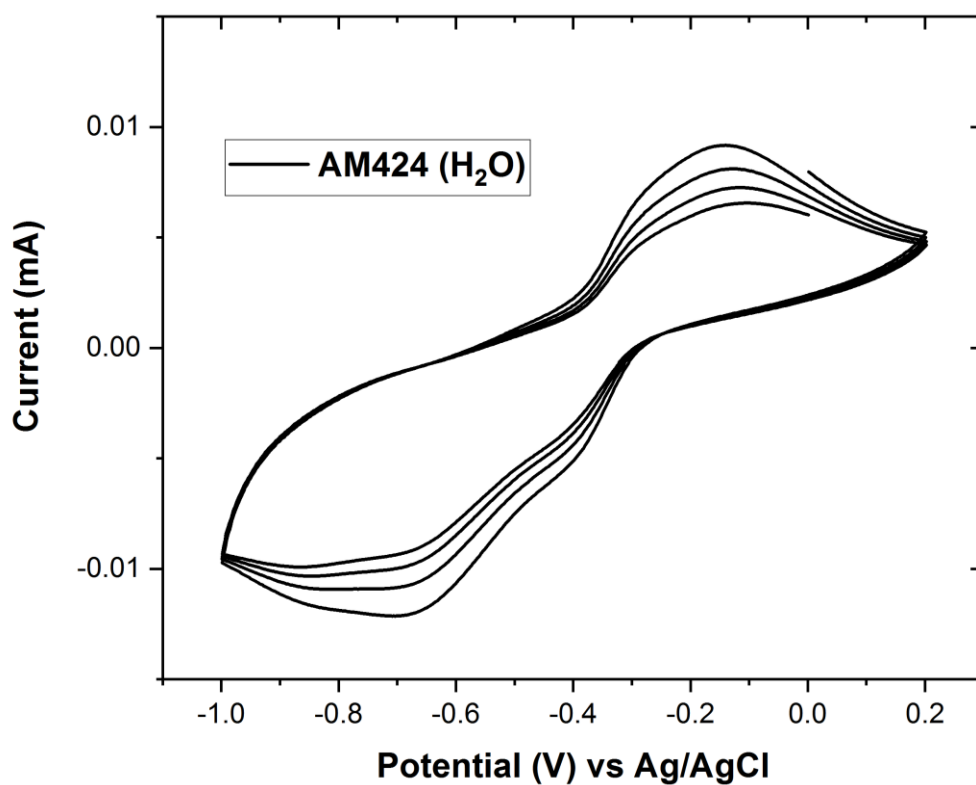
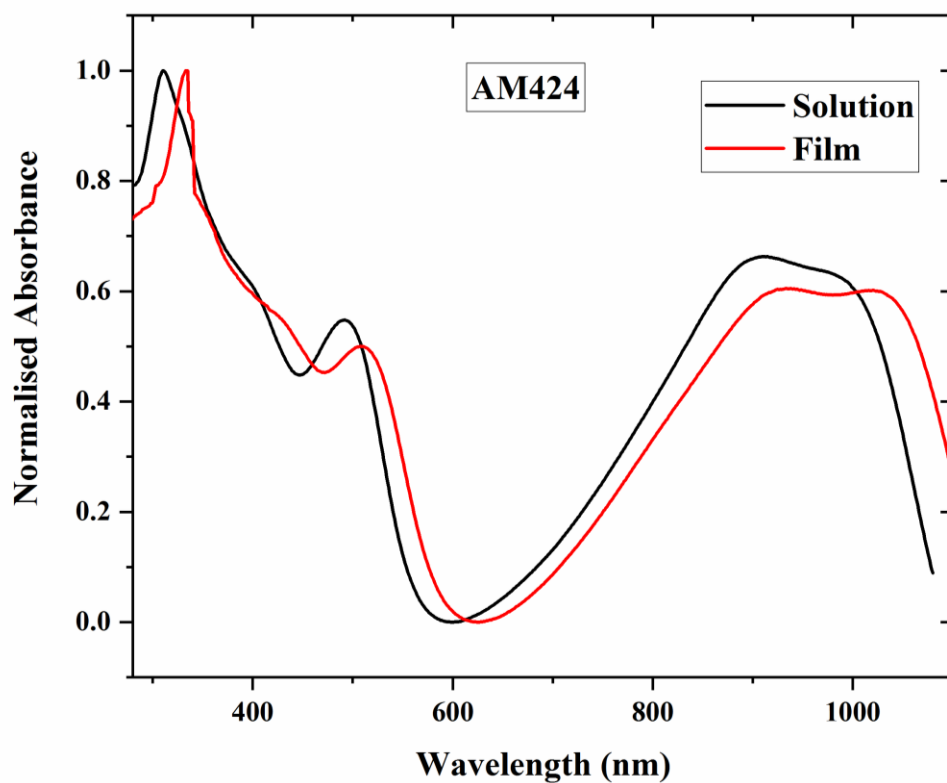
$\lambda_{\text{MAX}}^{\text{a}}$ (nm)	λ_{ONSET} (nm)	$E_{\text{opt}}^{\text{b}}$ (eV)	E_{A}^{c} (UV)	IP (PESA)	EA (CV)	E_{GAP} (eV)	M_{n}	M_{w}	PDI
930	1162	1.07	4.00	5.07	3.66	1.41	9200	17700	1.92

^a λ is the peak of the first low energy absorption band of the polymers

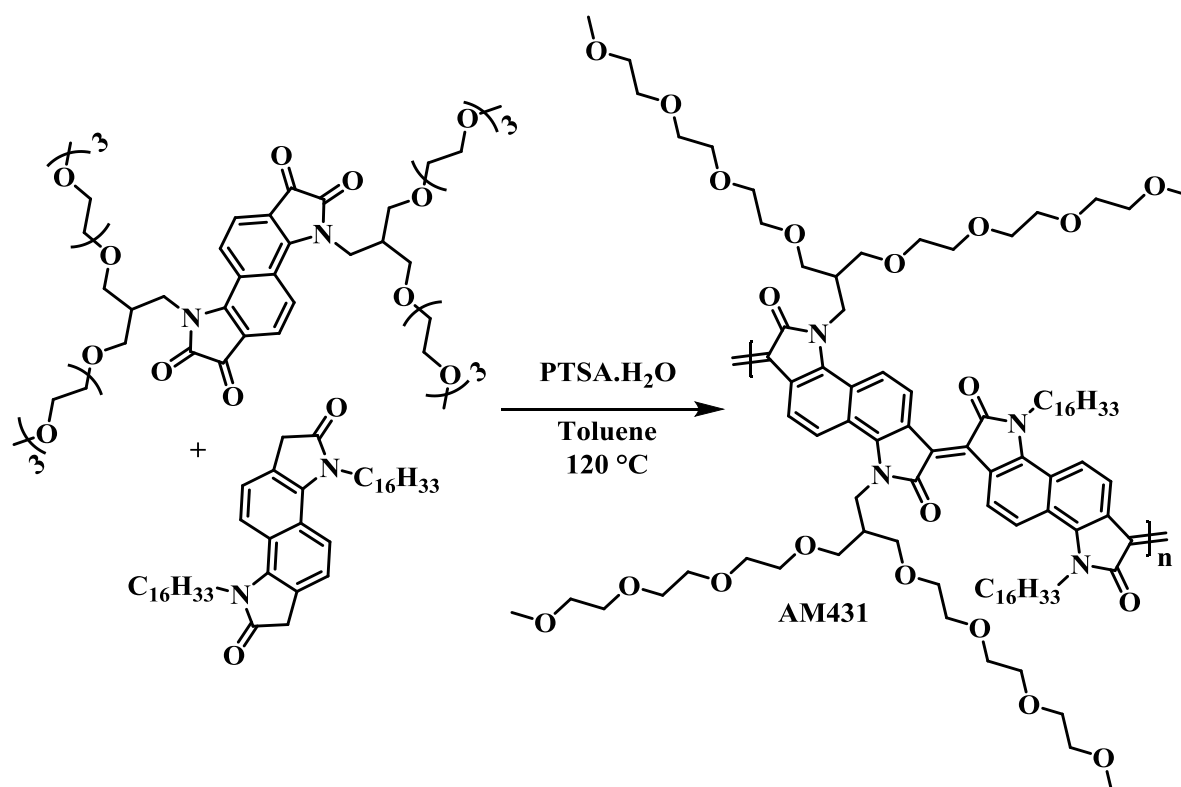
^b E_{opt} estimated optical gap using onset of the thin-film absorption spectra $E_{\text{GAP}} = 1240/\lambda_{\text{ONSET}}$
^c EA crudely estimated by subtraction of the UV-Vis absorption onset from IP ($EA = IP - E_{\text{opt}}$),
a procedure that neglects the exciton binding energy

Sep30-2019.31.fid
IM-AM424





6.3.26 Synthesis of Polymer AM431



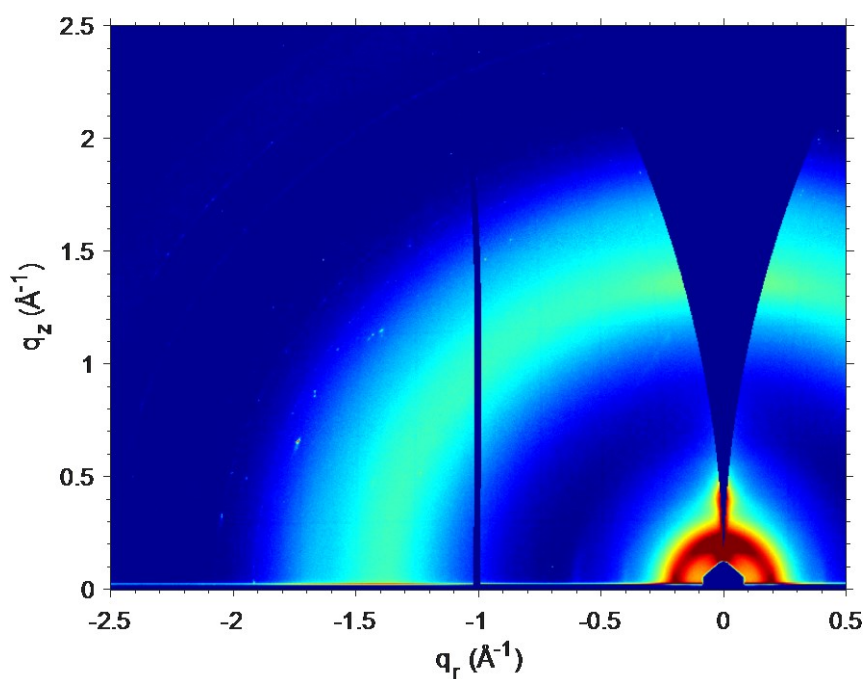
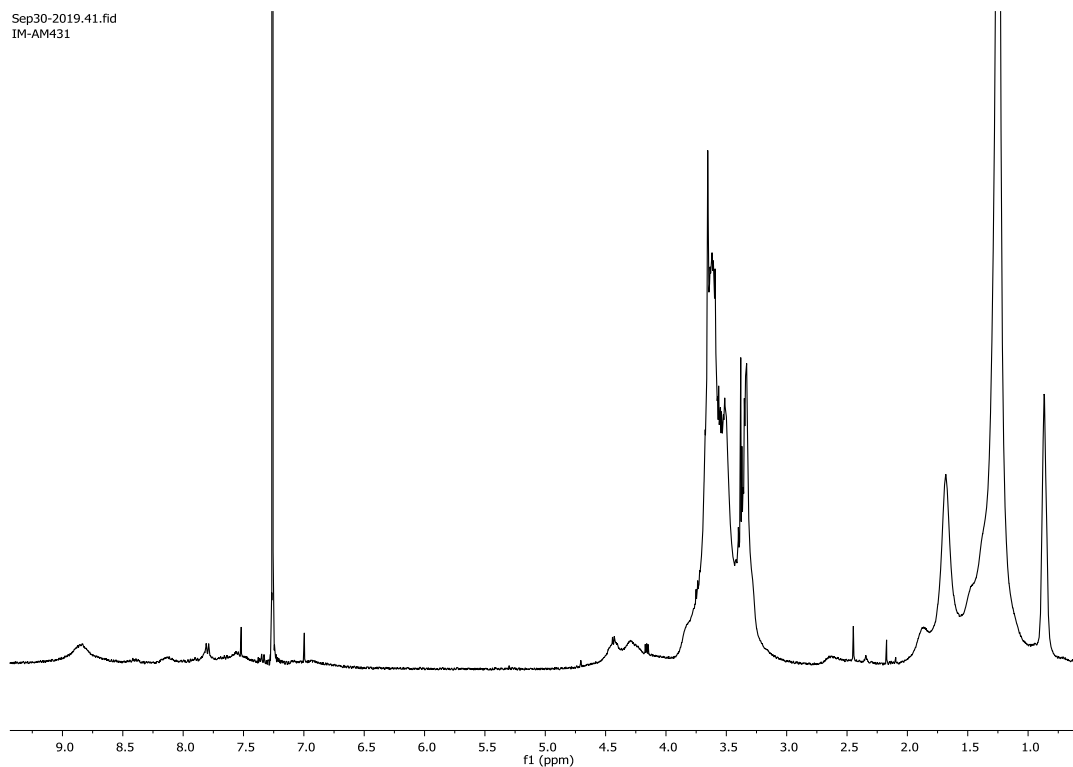
An oven dried 5 mL microwave vial was charged with 3,8-bis(13-(2,5,8,11-tetraoxadodecyl)-2,5,8,11-tetraoxatetradecan-14-yl)-3,8-dihydroindolo[7,6-g]indole-1,2,6,7-tetraone (6.3.13) (92 mg, 0.09 mmol, 1.0 eq.), 3,8-dihexadecyl-1,3,6,8-tetrahydroindolo[7,6-g]indole-2,7-dione (6.3.16) (61.5 mg, 0.09 mmol, 1.0 eq.) and *p*-toluenesulfonic acid monohydrate (5.11 mg, 0.03 mmol, 0.3 eq.). Cap was sealed and the vial was degassed with Nitrogen for 10 minutes prior to the addition of 1 mL anhydrous DMF. Reaction was stirred overnight at 120 °C, upon cooling to room temperature the mixture gelled and had turned a deep purple. The crude polymer was precipitated into 100 mL of methanol and subsequently filtered into a thimble. Purification via Soxhlet extraction into hexane, methanol, toluene, acetone and chloroform (in that order) afforded a majority fraction in chloroform which was reduced then precipitated into methanol. The product was filtered to yield a purple film (99 mg, 65%).

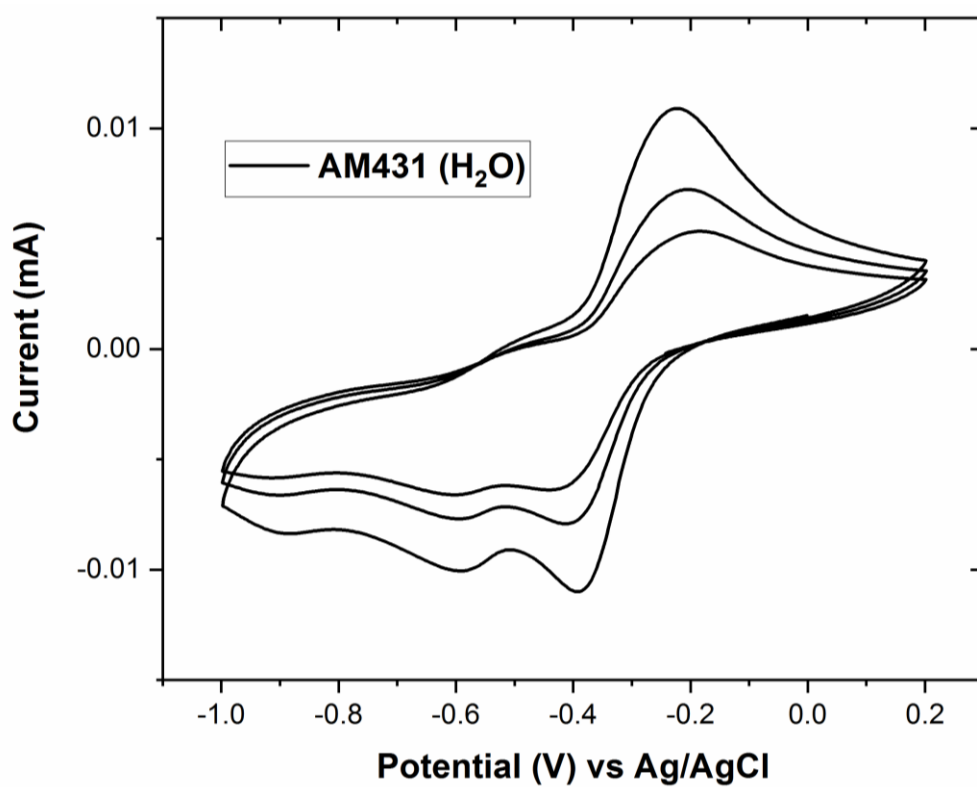
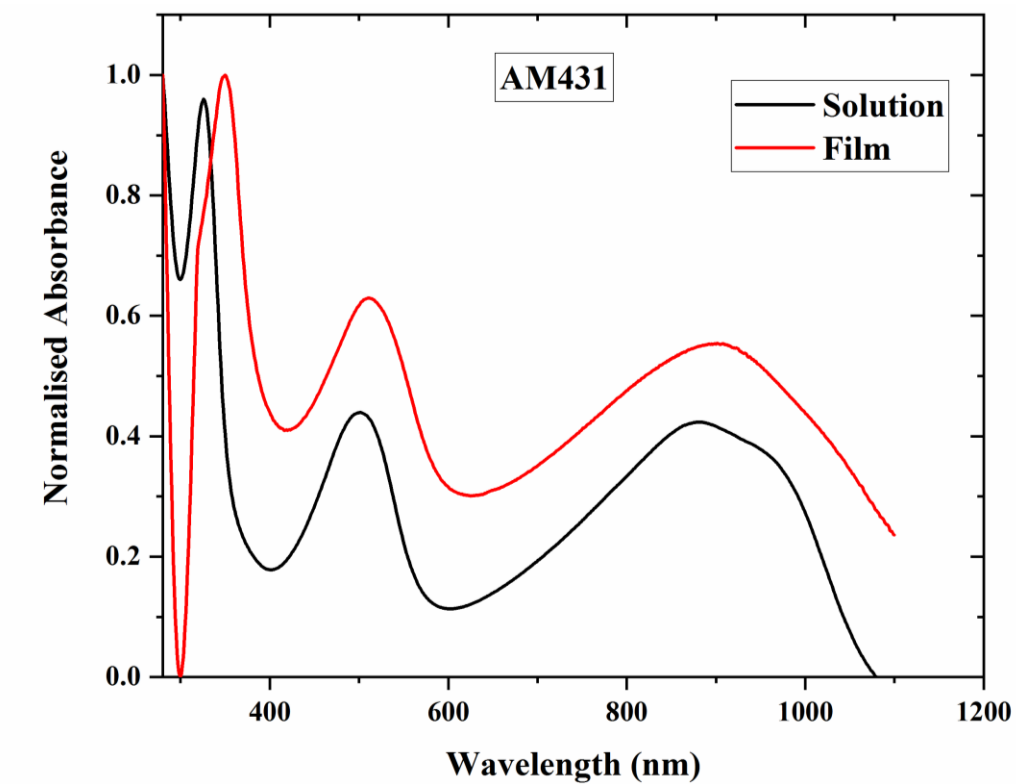
$\lambda_{\text{MAX}}^{\text{a}}$ (nm)	λ_{ONSET} (nm)	$E_{\text{opt}}^{\text{b}}$ (eV)	EA^{c} (UV)	IP (PESA)	EA (CV)	E_{GAP} (eV)	M_{n}	M_{w}	PDI
901	1149	1.08	4.11	5.19	3.69	1.50	13500	20800	1.54

^a λ is the peak of the first low energy absorption band of the polymers

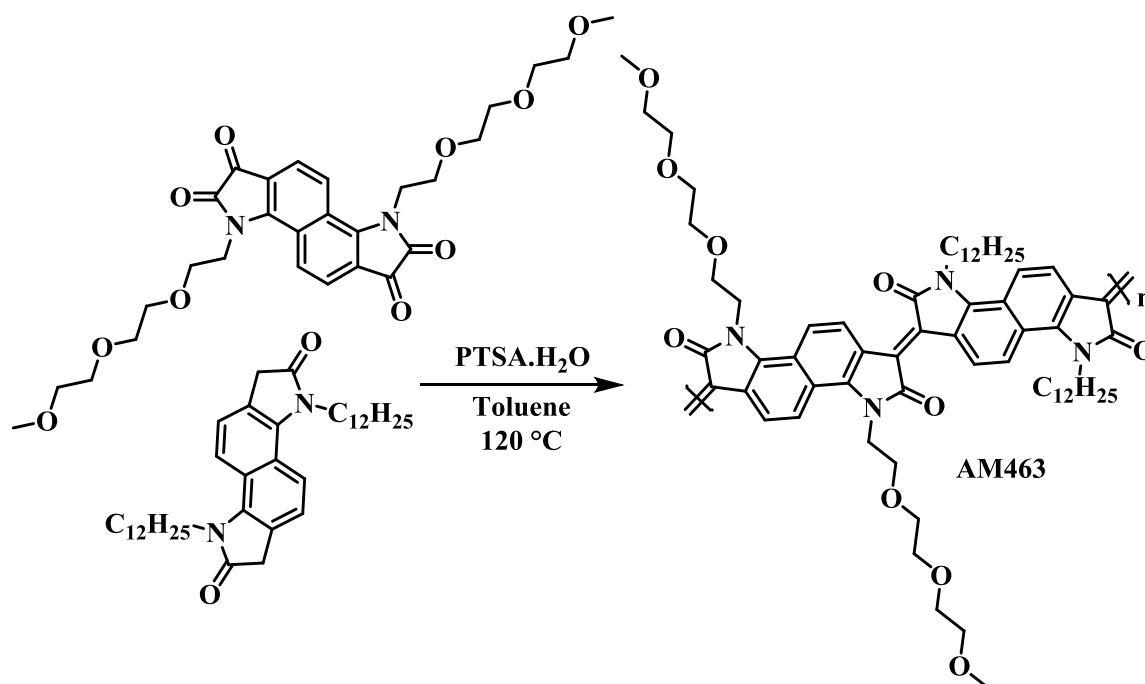
^b E_{opt} estimated optical gap using onset of the thin-film absorption spectra $E_{\text{GAP}} = 1240 / \lambda_{\text{ONSET}}$

^cEA crudely estimated by subtraction of the UV-Vis absorption onset from IP ($EA = IP - E_{\text{opt}}$), a procedure that neglects the exciton binding energy





6.3.27 Synthesis of Polymer AM463



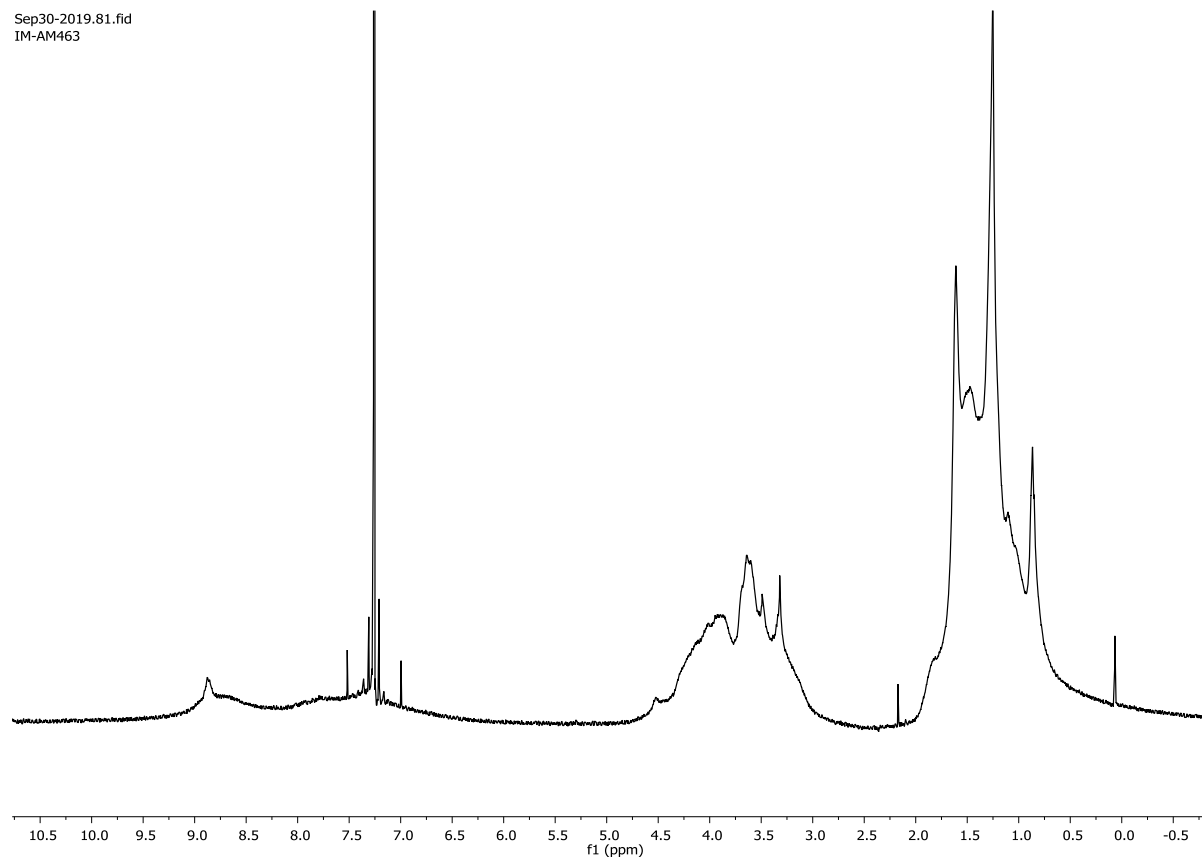
To an oven dried 5 mL microwave vial was added 3,8-bis(2-(2-(2-methoxyethoxy)ethoxy)ethyl)-1,3,6,8-tetrahydroindolo[7,6-g]indole-2,7-dione (**6.3.8**) (54 mg, 0.097 mmol, 1.0 eq.), 3,8-didodecyl-1,3,6,8-tetrahydroindolo[7,6-g]indole-2,7-dione (**6.3.14**) (55.6 mg, 0.097 mmol, 1.0 eq.) and *p*-toluenesulfonic acid monohydrate (5.5 mg, 0.029 mmol, 0.3 eq.). Cap sealed; vessel purged with Nitrogen for 10 minutes prior to the addition of anhydrous DMF (1 mL). Reaction was stirred for 2 nights at 120 °C upon which the solution turned a deep purple. After cooling to room temperature, the crude polymer was precipitated into 100 mL of methanol, filtered into a thimble. Purification was conducted via Soxhlet extraction into hexane, toluene, methanol, acetone and chloroform (in that order) the final fraction was collected, solvent removed under reduced pressure. The polymer was precipitated into methanol and filtered to afford a purple film (36 mg, 33%).

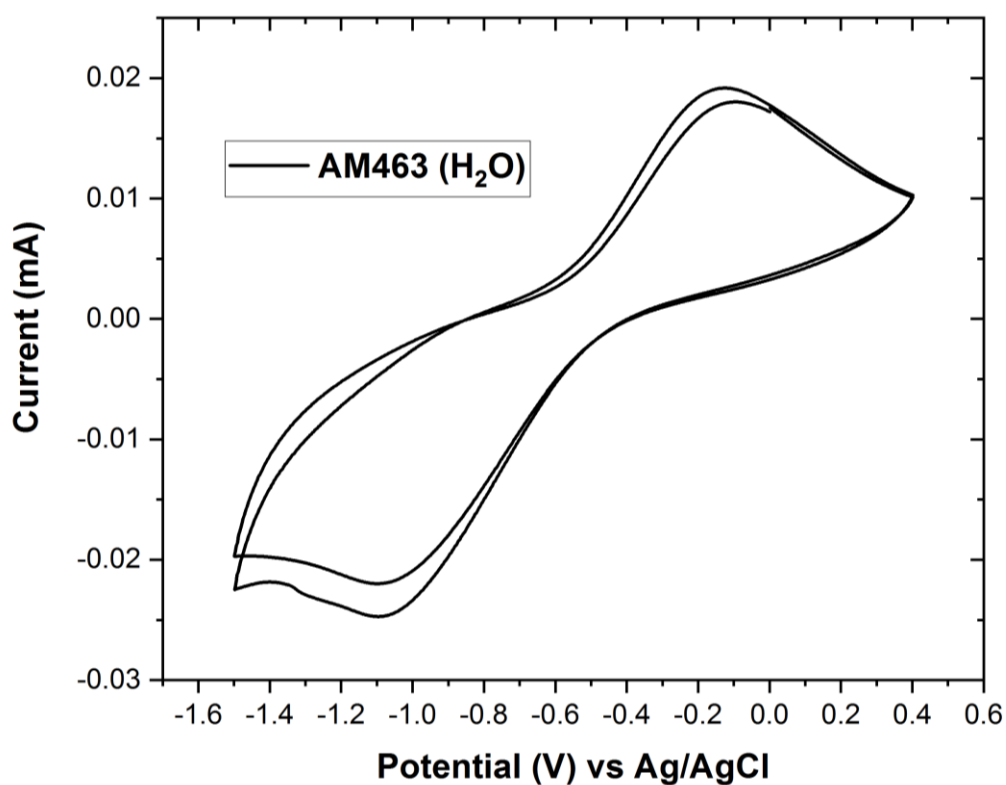
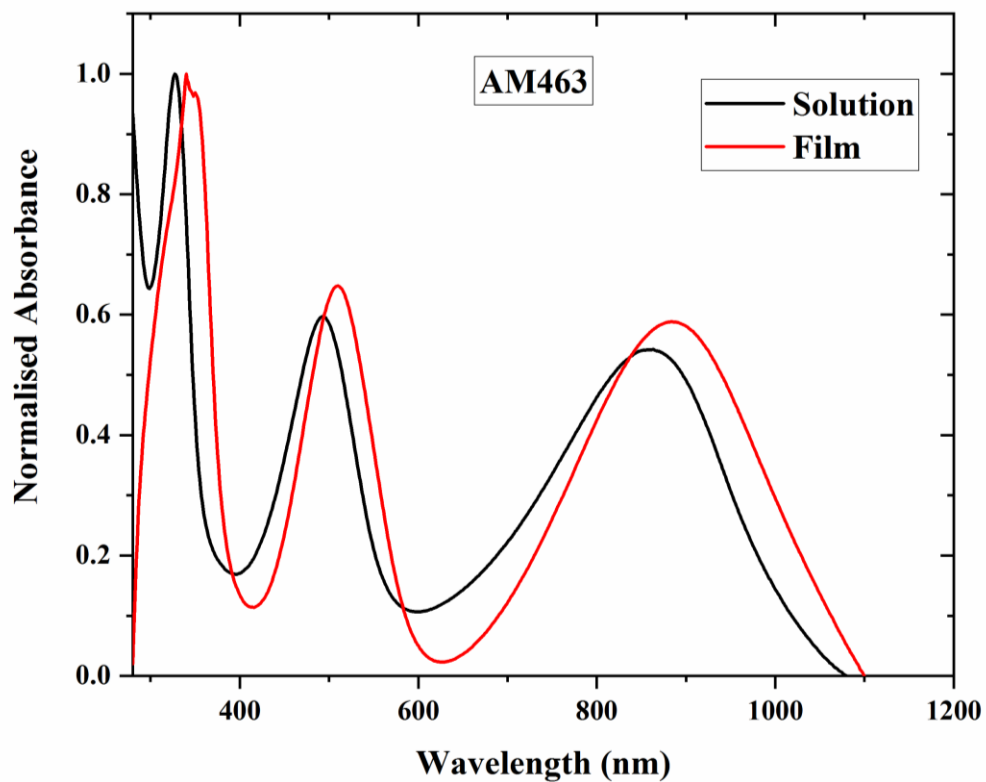
$\lambda_{\text{MAX}}^{\text{a}}$ (nm)	λ_{ONSET} (nm)	$E_{\text{opt}}^{\text{b}}$ (eV)	EA (UV)	IP (PESA)	EA (CV)	E_{GAP} (eV)	M_{n}	M_{w}	PDI
887	1102	1.13	4.03	5.16	3.72	1.44	24100	67500	2.80

^a λ is the peak of the first low energy absorption band of the polymers

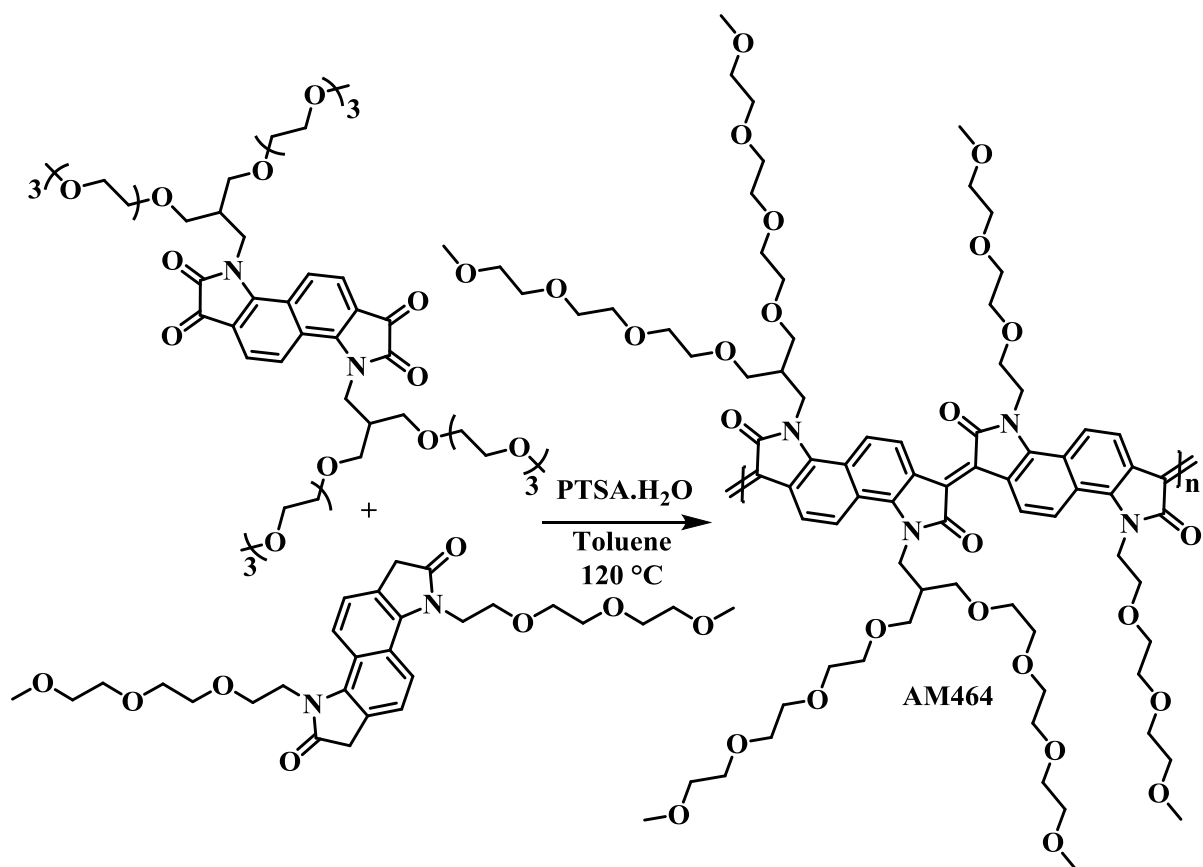
^b E_{opt} estimated optical gap using onset of the thin-film absorption spectra $E_{\text{GAP}} = 1240 / \lambda_{\text{ONSET}}$

^c EA crudely estimated by subtraction of the UV-Vis absorption onset from IP ($EA = IP - E_{\text{opt}}$), a procedure that neglects the exciton binding energy





6.3.28 Synthesis of Polymer AM464



An oven dried 5 mL microwave vial was charged with 8-bis(13-(2,5,8,11-tetraoxadodecyl)-2,5,8,11-tetraoxatetradecan-14-yl)-3,8-dihydroindolo[7,6-g]indole-1,2,6,7-tetraone (6.3.13) (84 mg, 0.08 mmol, 1.0 eq.), 3,8-bis(2-(2-(2-methoxyethoxy)ethoxy)ethyl)-1,3,6,8-tetrahydroindolo[7,6-g]indole-2,7-dione (6.3.8) (43.4 mg, 0.08 mmol, 1.0 eq.) and *p*-toluenesulfonic acid monohydrate (4.7 mg, 0.025 mmol, 0.3 eq.). The cap was sealed, the vial was then degassed with Nitrogen for 10 minutes prior to the addition of 1 mL anhydrous toluene. Mixture was stirred for 48 hours at 120 °C, turning purple and gelling upon cooling to room temperature. The crude polymer was precipitated into methanol and filtered into a thimble prior to purification via Soxhlet extraction. The crude polymer was washed with hexane, methanol, toluene, acetone, ethyl acetate and chloroform (in that order) the final

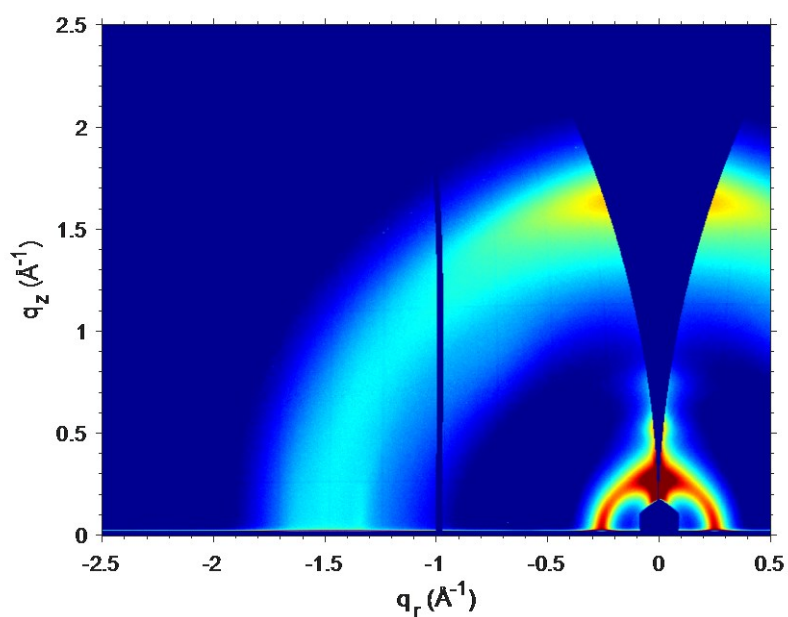
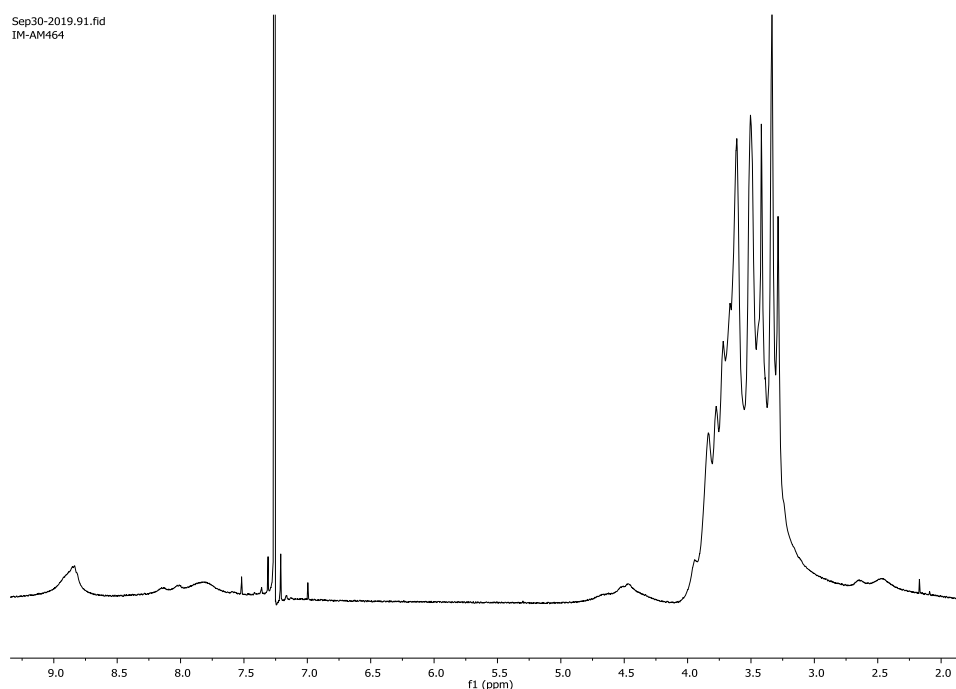
fraction was collected and solvent removed under reduced pressure. The polymer was then re-precipitated into methanol and filtered to afford a deep purple film (84 mg, 66%).

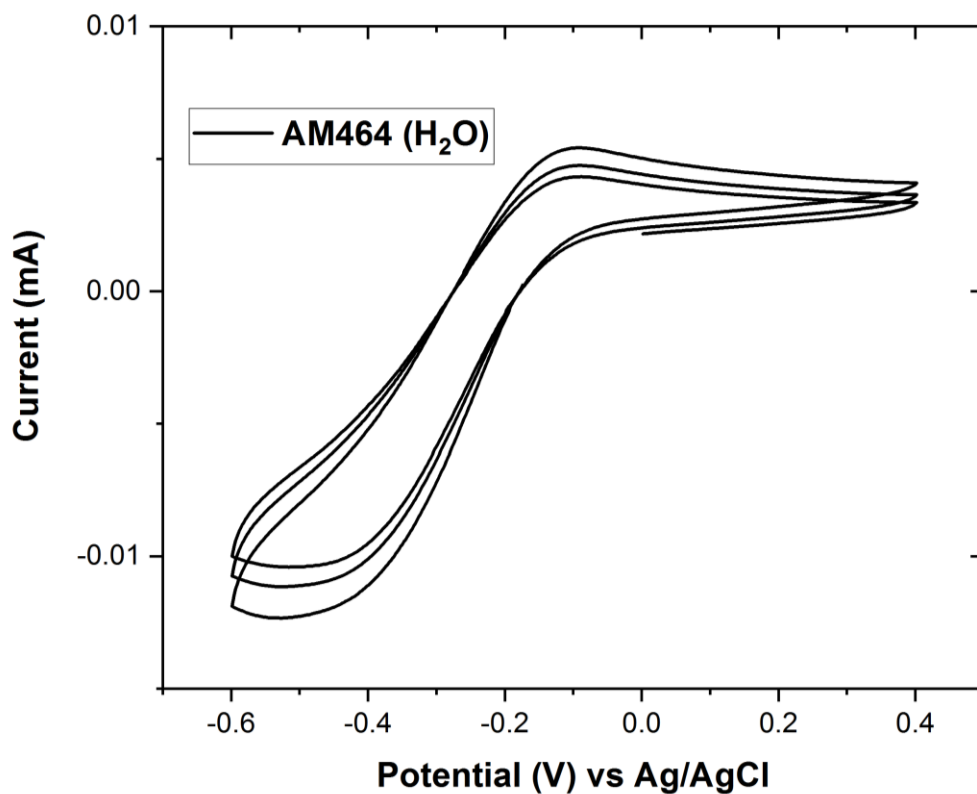
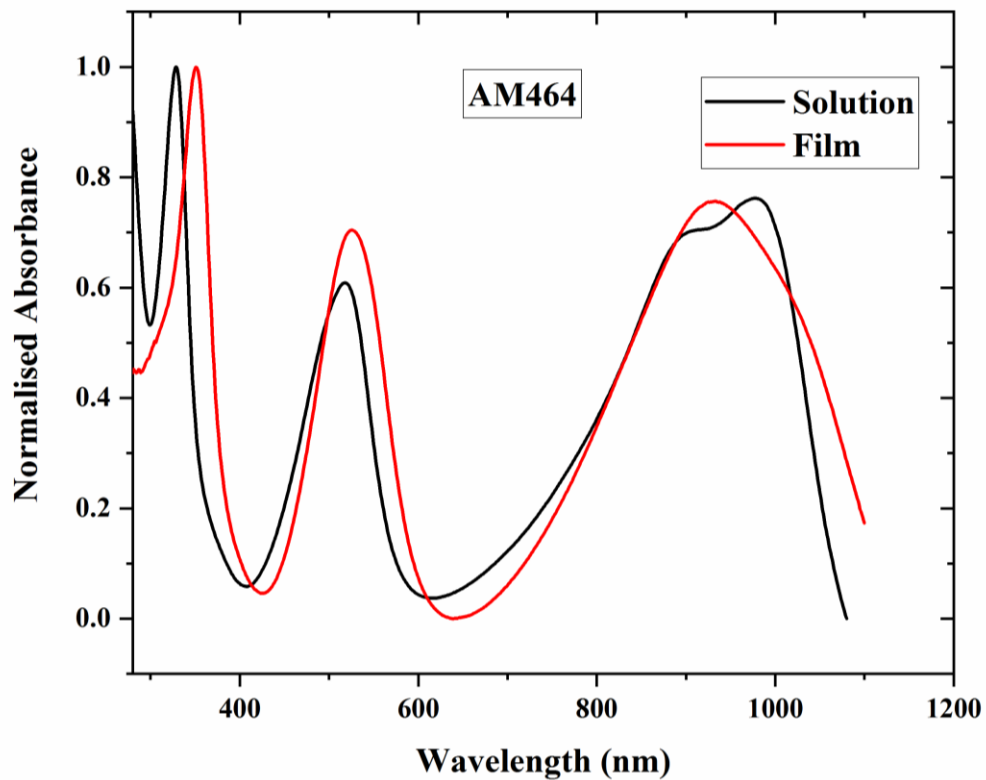
$\lambda_{\text{MAX}}^{\text{a}}$ (nm)	λ_{ONSET} (nm)	$E_{\text{opt}}^{\text{b}}$ (eV)	EA^{c} (UV)	IP (PESA)	EA (CV)	E_{GAP} (eV)	M_{n}	M_{w}	PDI
929	1100	1.13	4.02	5.15	3.66	1.49	17200	64500	3.70

^a λ is the peak of the first low energy absorption band of the polymers

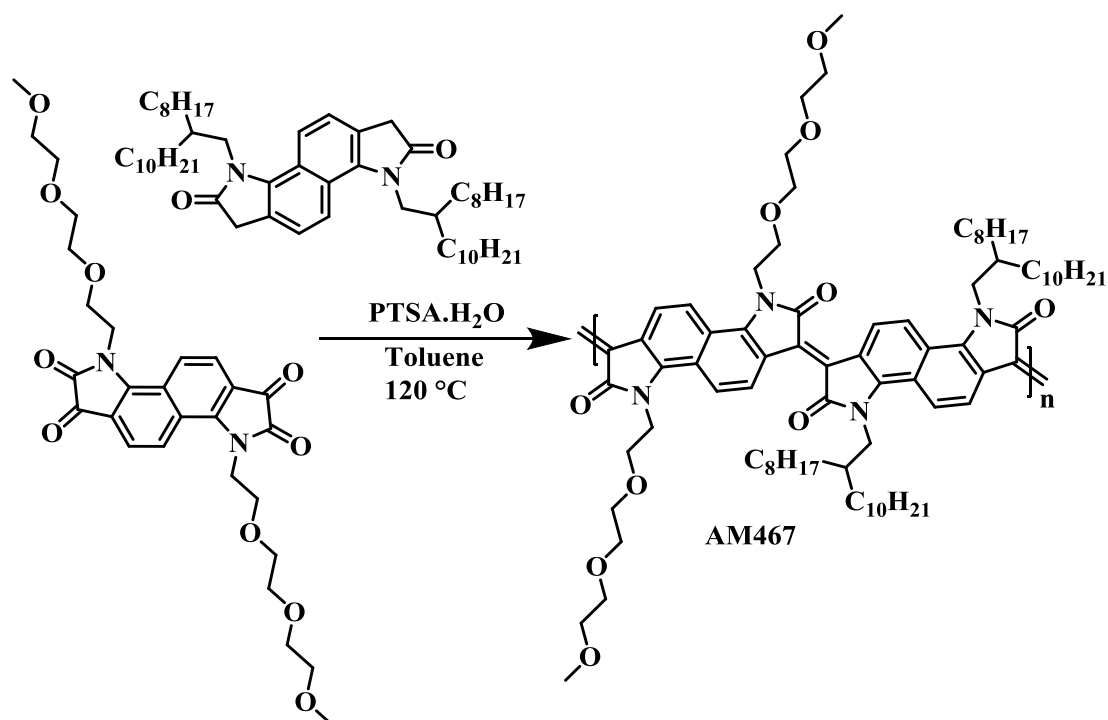
^b E_{opt} estimated optical gap using onset of the thin-film absorption spectra $E_{\text{GAP}} = 1240 / \lambda_{\text{ONSET}}$

^c EA crudely estimated by subtraction of the UV-Vis absorption onset from IP ($EA = IP - E_{\text{opt}}$), a procedure that neglects the exciton binding energy





6.3.29 Synthesis of Polymer AM467



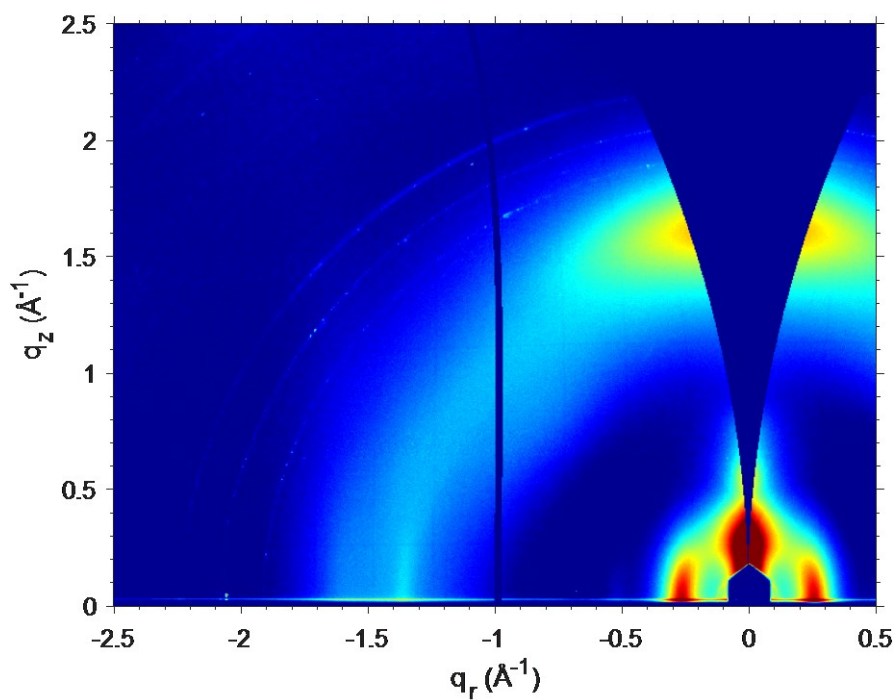
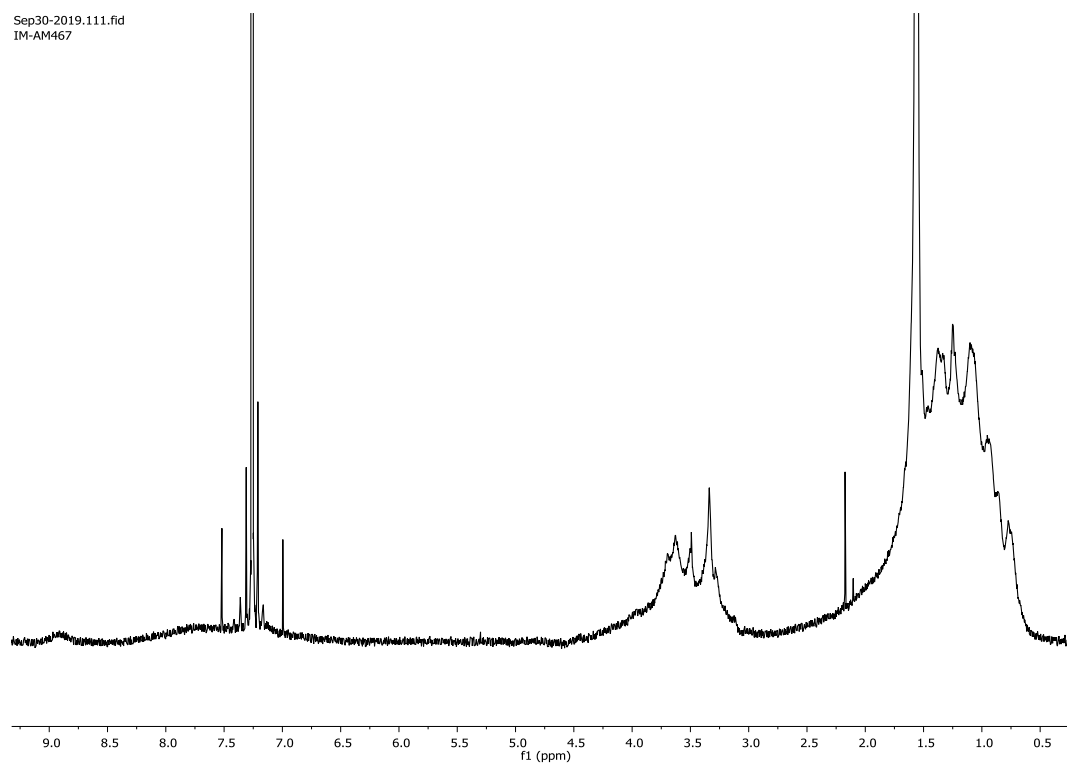
To an oven dried 5 mL microwave vial was added 3,8-bis(2-(2-(2-methoxyethoxy)ethoxy)ethyl)-3,8-dihydroindolo[7,6-g]indole-1,2,6,7-tetraone (**6.3.7**) (39.5 mg, 0.074 mmol, 1.0 eq.), 3,8-bis(2-octyldodecyl)-1,3,6,8-tetrahydroindolo[7,6-g]indole-2,7-dione (**6.3.22**) (61.6 mg, 0.074 mmol, 1.0 eq.) and *p*-toluenesulfonic acid monohydrate (4.25 mg, 0.022 mmol, 0.3 eq.). The vial was sealed then purged with Nitrogen for 10 minutes prior to the addition of 1 mL dry toluene. The reaction was stirred for 48 hours at 120 °C, upon cooling to room temperature the purple solution was precipitated into methanol. The crude polymer was filtered into a thimble and purified via Soxhlet extraction with hexane, methanol, toluene, acetone, ethyl acetate and chloroform (in that order). The chloroform fraction was collected, and solvent removed under reduced pressure before re-precipitation into methanol. Filtration yielded the polymer as a metallic purple film (69 mg, 69%).

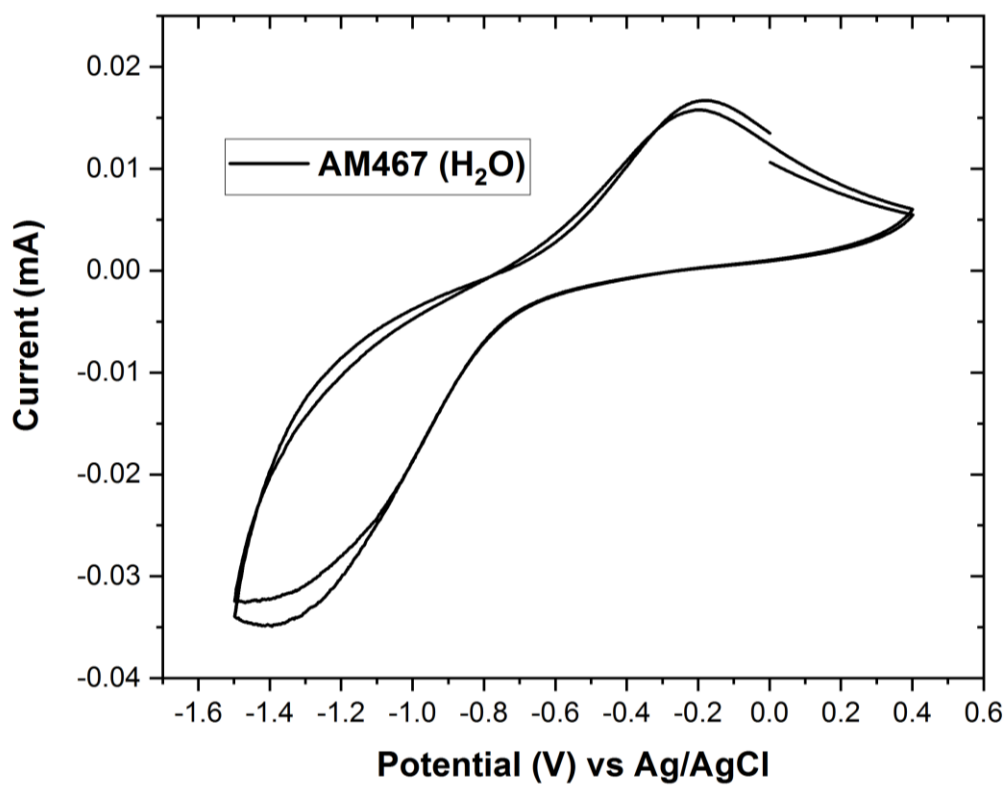
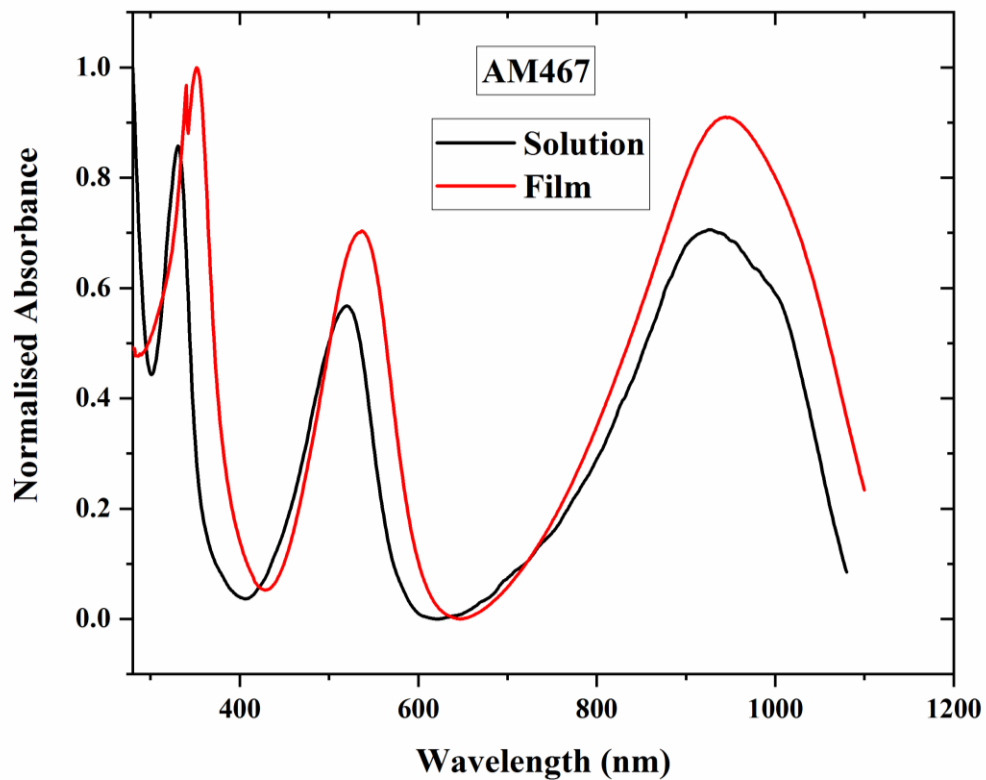
$\lambda_{\text{MAX}}^{\text{a}}$ (nm)	λ_{ONSET} (nm)	$E_{\text{opt}}^{\text{b}}$ (eV)	EA^{c} (UV)	IP (PESA)	EA (CV)	E_{GAP} (eV)	M_{n}	M_{w}	PDI
944	1117	1.11	4.10	5.21	4.01	1.20	89300	864600	9.70

^a λ is the peak of the first low energy absorption band of the polymers

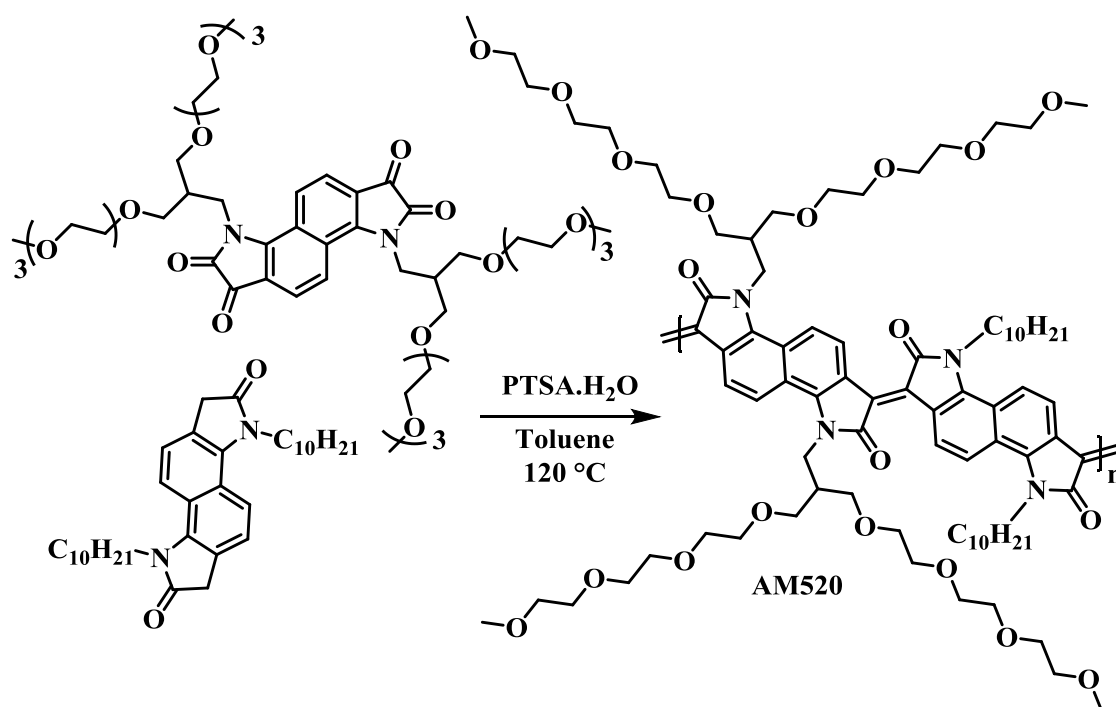
^b E_{opt} estimated optical gap using onset of the thin-film absorption spectra $E_{\text{GAP}} = 1240 / \lambda_{\text{ONSET}}$

^cEA crudely estimated by subtraction of the UV-Vis absorption onset from IP ($EA = IP - E_{\text{opt}}$), a procedure that neglects the exciton binding energy





6.3.30 Synthesis of Polymer AM520



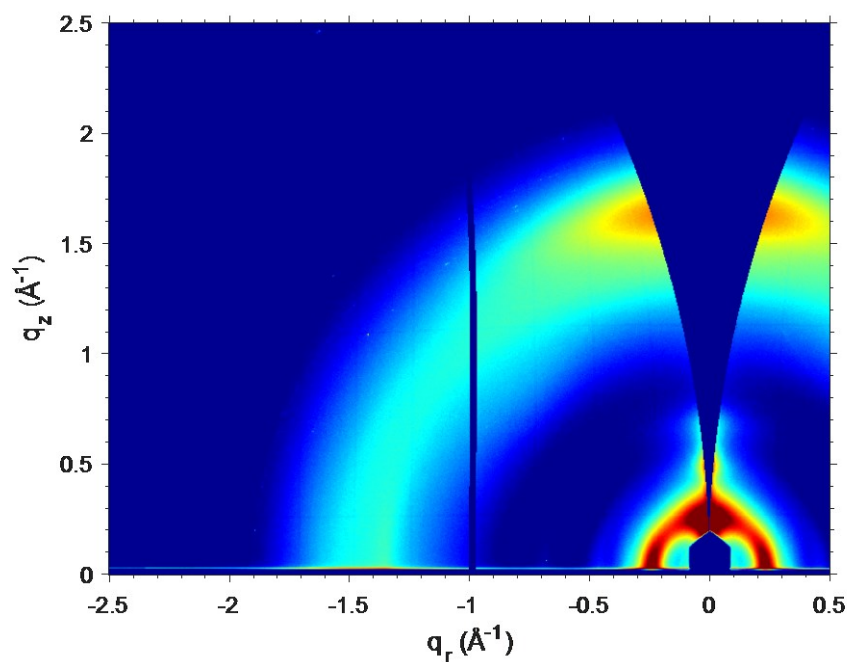
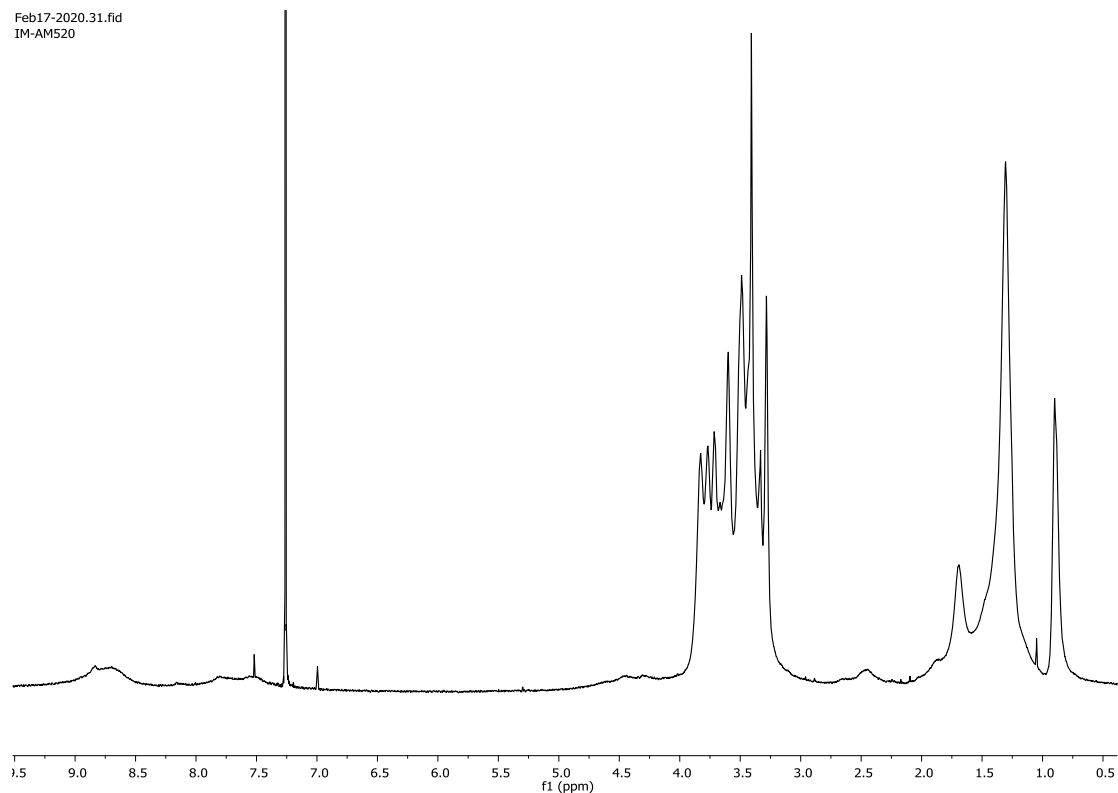
An oven dried 5 mL microwave vial was charged with 3,8-bis(13-(2,5,8,11-tetraoxadodecyl)-2,5,8,11-tetraoxatetradecan-14-yl)-3,8-dihydroindolo[7,6-g]indole-1,2,6,7-tetraone (6.3.13) (89 mg, 0.087 mmol, 1.0 eq.), 3,8-didecyl-1,3,6,8-tetrahydroindolo[7,6-g]indole-2,7-dione (6.3.20) (45 mg, 0.087 mmol, 1.0 eq.) and *p*-toluenesulfonic acid monohydrate (4.94 mg, 0.026 mmol, 0.3 eq.). The cap was sealed, and the vessel was purged with Nitrogen for 10 minutes prior to the addition of anhydrous toluene (0.7 mL). The reaction was stirred at 120 °C overnight, upon cooling to room temperature the purple solution gelled. The crude polymer was precipitated into 100 mL followed by filtration into a thimble. Purification was conducted via Soxhlet extraction with hexane, methanol, toluene, acetone, ethyl acetate and chloroform (in that order). The chloroform fraction was isolated, solvent was removed under reduced pressure and re-precipitation was performed into methanol. Filtration afforded the metallic purple film (125 mg, 93%).

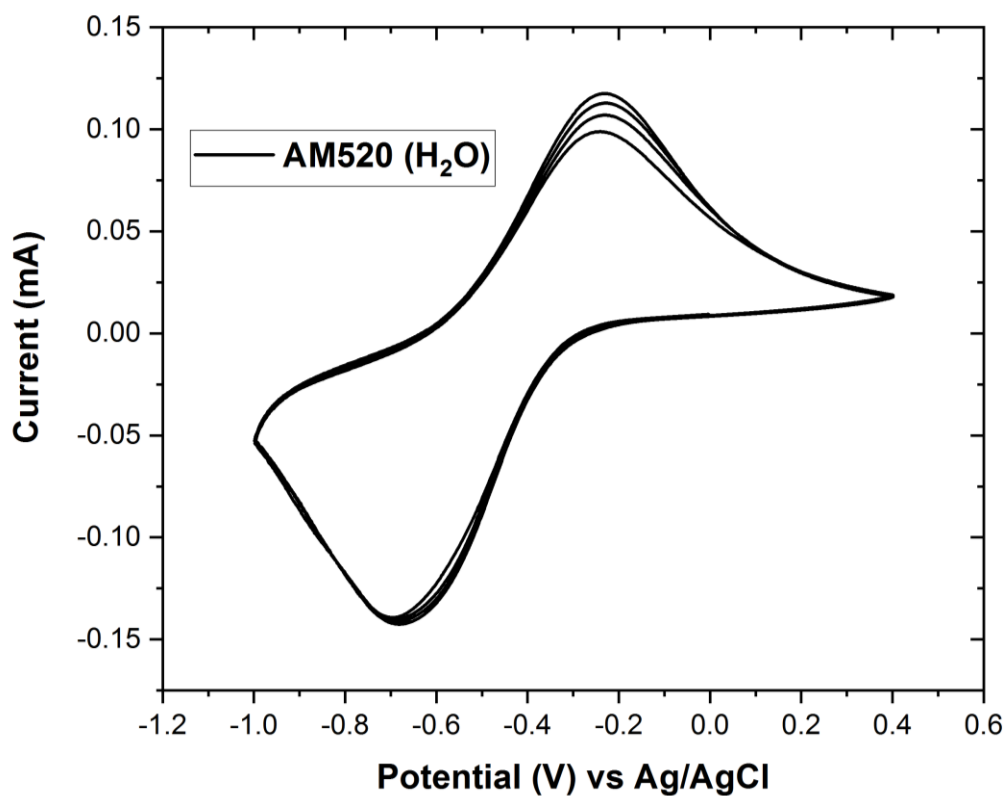
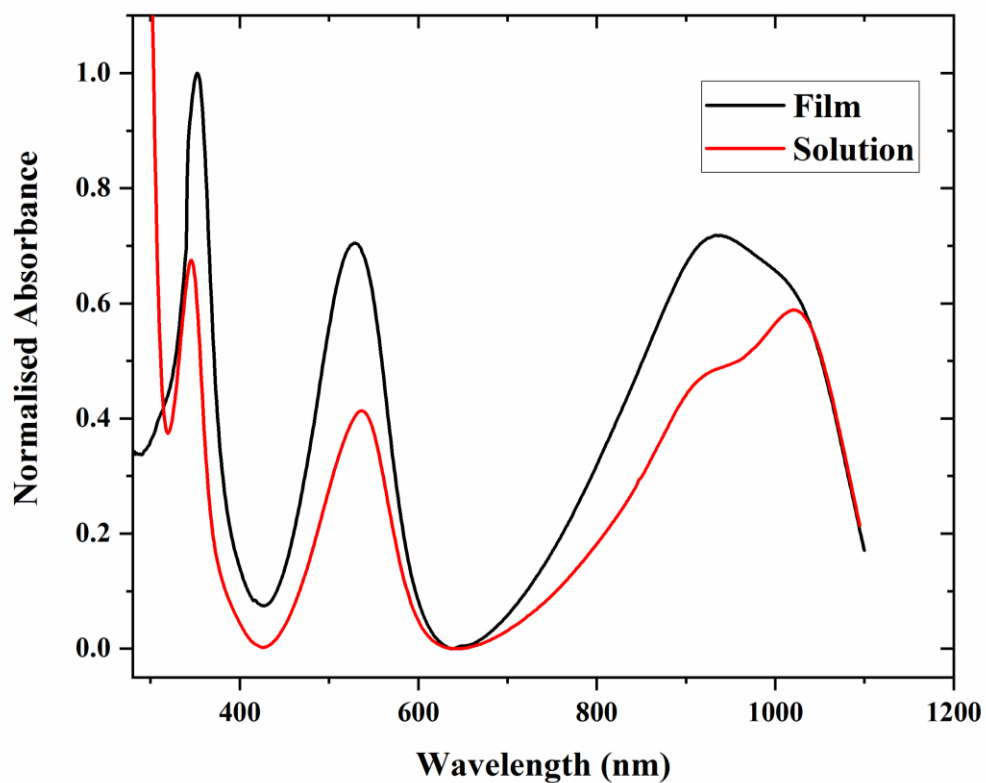
$\lambda_{\text{MAX}}^{\text{a}}$ (nm)	λ_{ONSET} (nm)	$E_{\text{opt}}^{\text{b}}$ (eV)	EA^{c} (eV)	IP (PESA)	EA (CV)	E_{GAP} (eV)	M_n	M_w	PDI
933	1132	1.10	4.15	5.25	3.63	1.62	27358	75476	2.76

^a λ is the peak of the first low energy absorption band of the polymers

^b E_{opt} estimated optical gap using onset of the thin-film absorption spectra $E_{\text{GAP}} = 1240 / \lambda_{\text{ONSET}}$

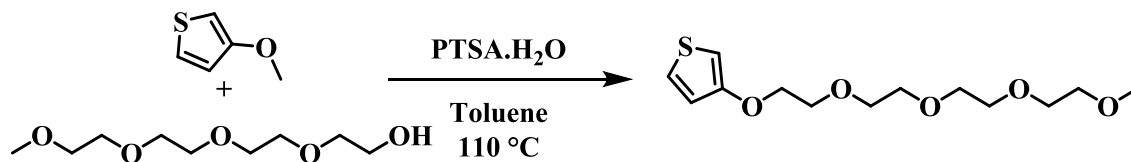
^c EA crudely estimated by subtraction of the UV-Vis absorption onset from IP ($EA = IP - E_{\text{opt}}$), a procedure that neglects the exciton binding energy





6.4 CHAPTER FIVE SYNTHESIS & CHARACTERISATION

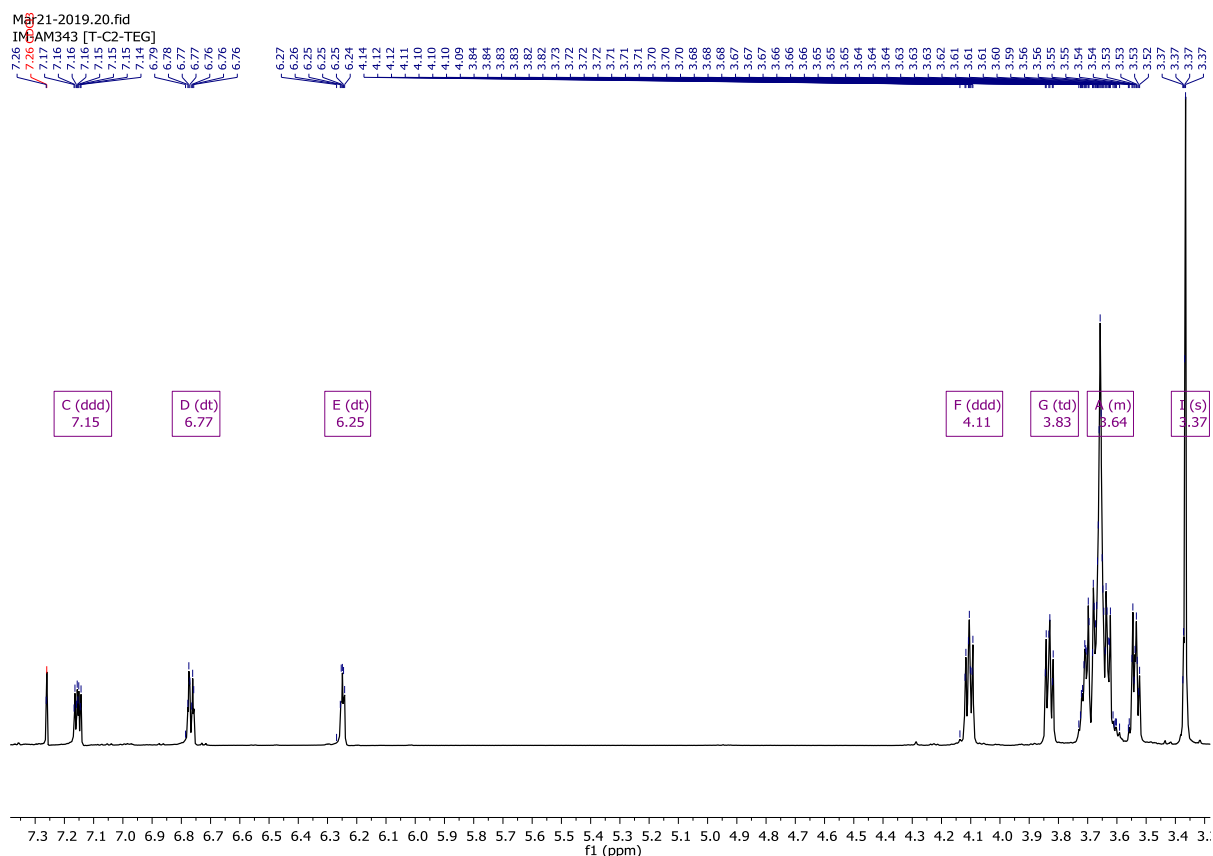
6.4.1 Synthesis of 13-(thiophen-3-yloxy)-2,5,8,11-tetraoxatridecane



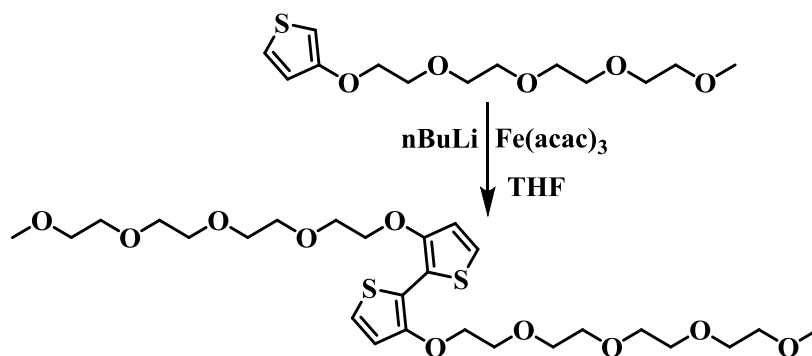
3-Methoxythiophene (6.1 mL, 61.4 mmol, 1.0 eq.) was dissolved in 70 mL toluene, inside a 2-neck 250 mL RBF. 2,5,8,11-tetraoxatridecan-13-ol (18.4 mL, 92.1 mmol, 1.5 eq.) was added dropwise, followed by the addition of *p*-toluenesulfonic acid monohydrate (1.16 g, 6.14 mmol, 0.1 eq.) in a single portion. The reaction was refluxed overnight at 110 °C before being cooled to room temperature poured into water, washed with brine and extracted into DCM. The organic layer was separated, dried over MgSO₄ and the solvent removed under reduced pressure. The crude was purified via column chromatography on silica gel using DCM as the eluent to afford a yellow oil (9.99 g, 56%).

¹H NMR (400 MHz, Chloroform-*d*) δ 7.15 (ddd, *J* = 5.2, 3.1, 1.2 Hz, 1H), 6.77 (dt, *J* = 5.2, 1.4 Hz, 1H), 6.25 (dt, *J* = 3.1, 1.4 Hz, 1H), 4.11 (ddd, *J* = 4.9, 4.1, 1.2 Hz, 2H), 3.83 (td, *J* = 4.7, 1.2 Hz, 2H), 3.75 – 3.48 (m, 12H), 3.37 (s, 3H).

¹³C NMR (101 MHz, Chloroform-*d*) δ 157.71, 124.74, 119.71, 97.63, 72.05, 70.90, 70.74, 70.63, 69.80, 69.70, 59.14.



6.4.2 Synthesis of 3,3'-bis((2,5,8,11-tetraoxatridecan-13-yl)oxy)-2,2'-bithiophene

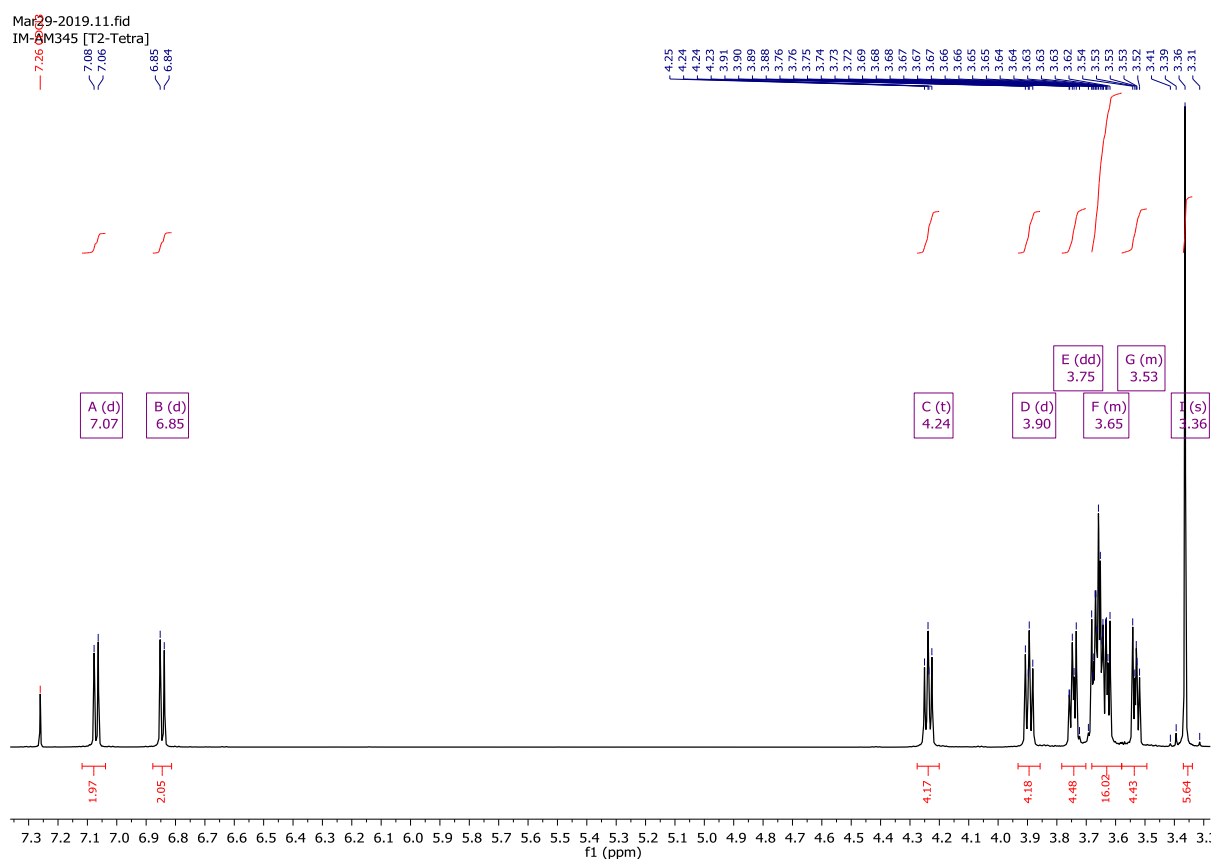


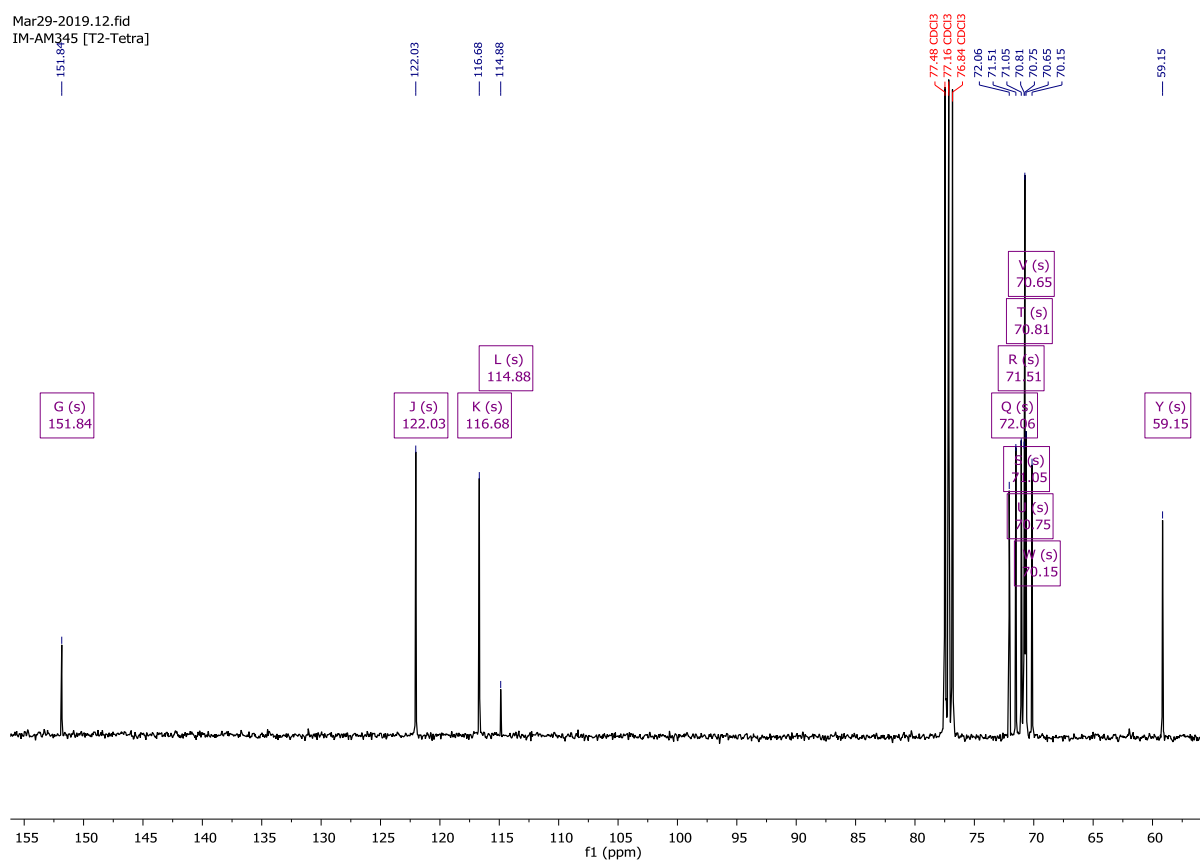
13-(thiophen-3-yloxy)-2,5,8,11-tetraoxatridecane (**6.4.1**) (9.99 g, 34.4 mmol, 1.0 eq.) was dissolved in dry THF (100 mL) cooled to $-10\text{ }^\circ\text{C}$, under a Nitrogen atmosphere. $n\text{-BuLi}$ (1.6M, 16.5 mL, 41.3 mmol, 1.2 eq.) was added slowly dropwise and the reaction was stirred for 2 hours at $0\text{ }^\circ\text{C}$. In a separate flask $\text{Fe}(\text{acac})_3$ (12.15 g, 34.4 mmol, 1.0 eq.) was dissolved in 100 mL anhydrous THF, under a Nitrogen atmosphere, cooled to $0\text{ }^\circ\text{C}$. The lithiate solution was transferred via cannula to the $\text{Fe}(\text{acac})_3$ solution over a period of 15 minutes. The reaction was

heated at reflux for 2 hours before cooling to room temperature and passing through a short silica plug, eluting with ethyl acetate. The crude material was purified by column chromatography on silica gel using ethyl acetate as the eluent system. Solvent was removed under reduced pressure to yield a yellow oil (4.41 g, 44%).

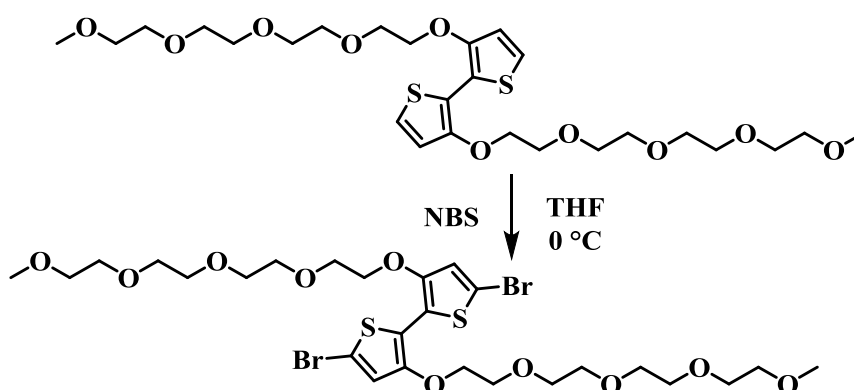
^1H NMR (400 MHz, Chloroform-*d*) δ 7.07 (d, $J = 5.6$ Hz, 2H), 6.85 (d, $J = 5.6$ Hz, 2H), 4.24 (t, $J = 4.9$ Hz, 4H), 3.90 (d, $J = 4.9$ Hz, 4H), 3.75 (dd, $J = 6.1, 3.7$ Hz, 4H), 3.72 – 3.58 (m, 16H), 3.59 – 3.49 (m, 4H), 3.36 (s, 6H).

^{13}C NMR (101 MHz, Chloroform-*d*) δ 151.84, 122.03, 116.68, 114.88, 72.06, 71.51, 71.05, 70.81, 70.75, 70.65, 70.15, 59.15.





6.4.3 13,13'-((5,5'-dibromo-[2,2'-bithiophene]-3,3'-diyl)bis(oxy))bis(2,5,8,11-tetraoxatridecane)



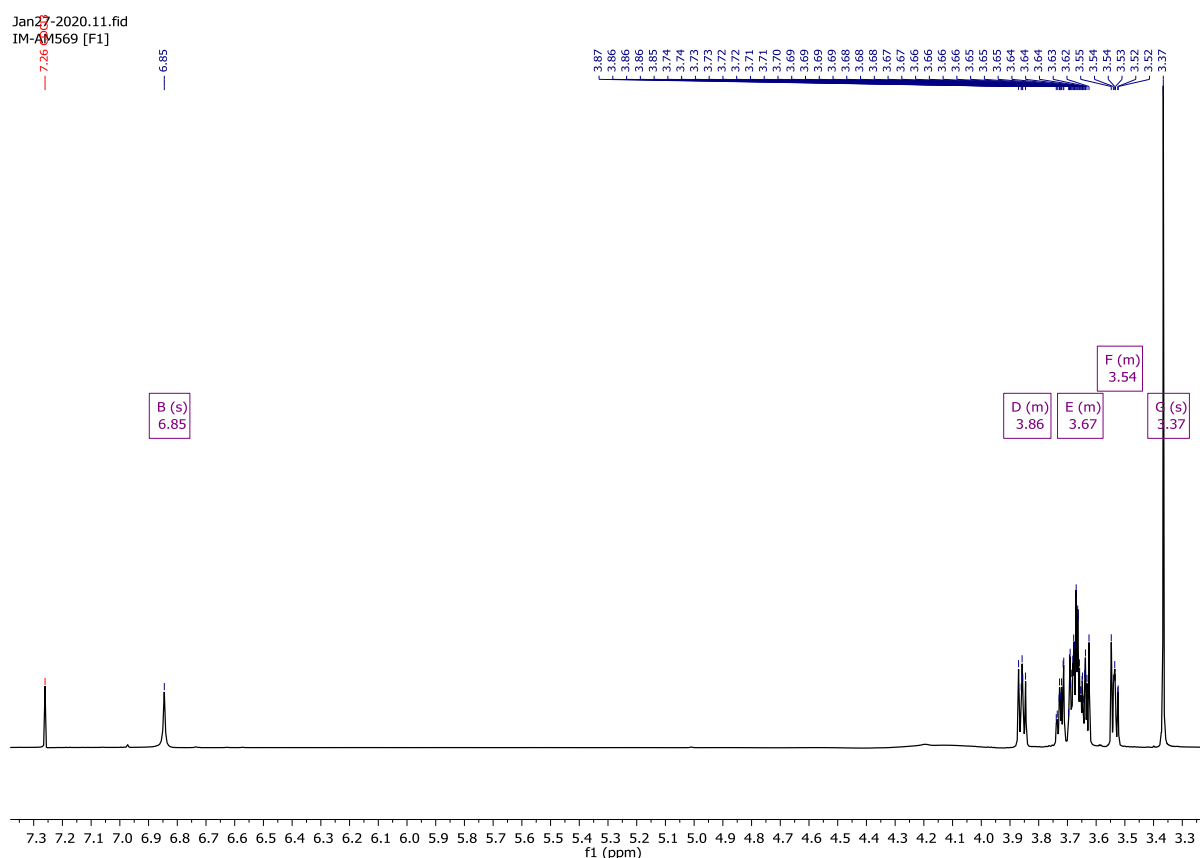
3,3'-bis((2,5,8,11-tetraoxatridecyl)oxy)-2,2'-bithiophene (**6.4.2**) (2g, was added to an oven dried 2-neck 100 mL RBF, dissolved in dry THF (40 mL) under a Nitrogen atmosphere. Cooled to 0 °C and covered from light prior to the portion wise addition of N-

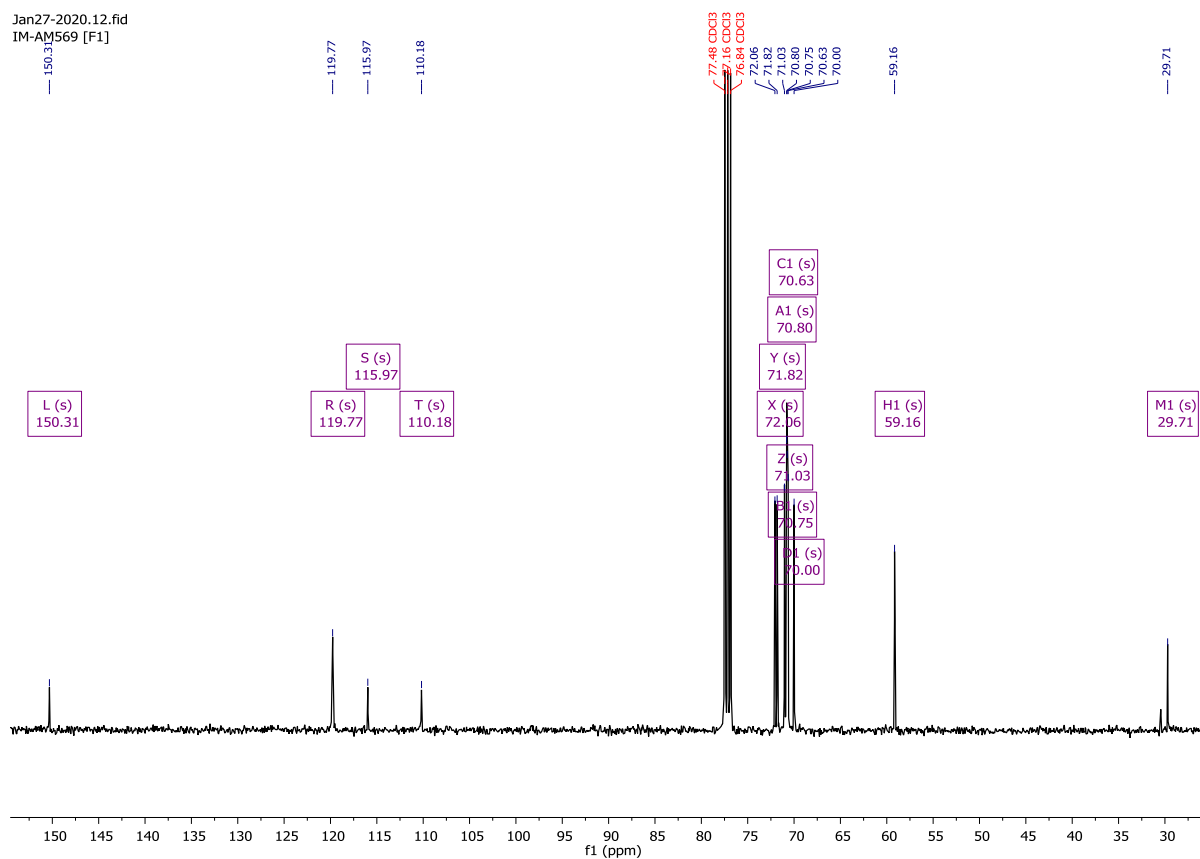
bromosuccinimide (4x325 mg, 7.27 mmol, 2.1 eq.) leaving approximately 5 minutes between the addition of each portion. The reaction was stirred for 45 minutes before being poured into water, washed with saturated sodium carbonate and quenched with sodium metabisulphite. The organic layer was extracted into DCM and dried over Na₂SO₄; solvent removed under reduced pressure. The crude was purified by column chromatography, on silica gel, using ethyl acetate as the eluent to afford a yellow oil which solidified at low temperature (2.46 g, 97%).

¹H NMR (400 MHz, Chloroform-*d*) δ 6.85 (s, 2H), 3.90 – 3.82 (m, 4H), 3.78 – 3.60 (m, 16H), 3.57 – 3.50 (m, 4H), 3.37 (s, 6H).

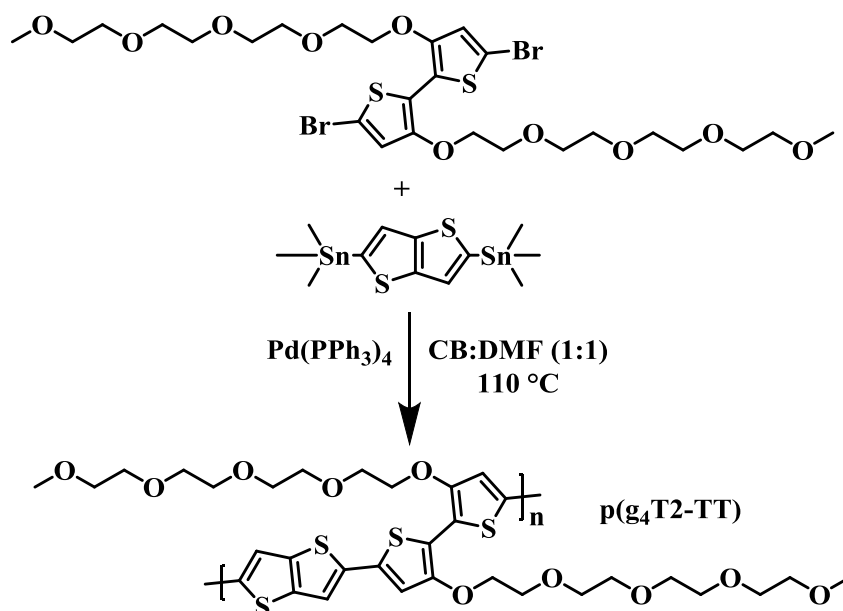
¹³C NMR (101 MHz, Chloroform-*d*) δ 150.31, 119.77, 115.97, 110.18, 72.06, 71.82, 71.03, 70.80, 70.75, 70.63, 70.00, 59.16, 29.71.

Mass (MALDI-ToF): 736.9 [M+H]⁺ (calc. 736.0 C₂₆H₄₀Br₂O₁₀S₂).





6.4.4 Synthesis of Polymer AM573 p(g₄T2-TT)



An oven dried 5 mL microwave vial was charged with 13,13'-((5,5'-dibromo-[2,2'-bithiophene]-3,3'-diyl)bis(oxy))bis(2,5,8,11-tetraoxatridecane) (**6.4.3**) (200 mg, 0.31 mmol,

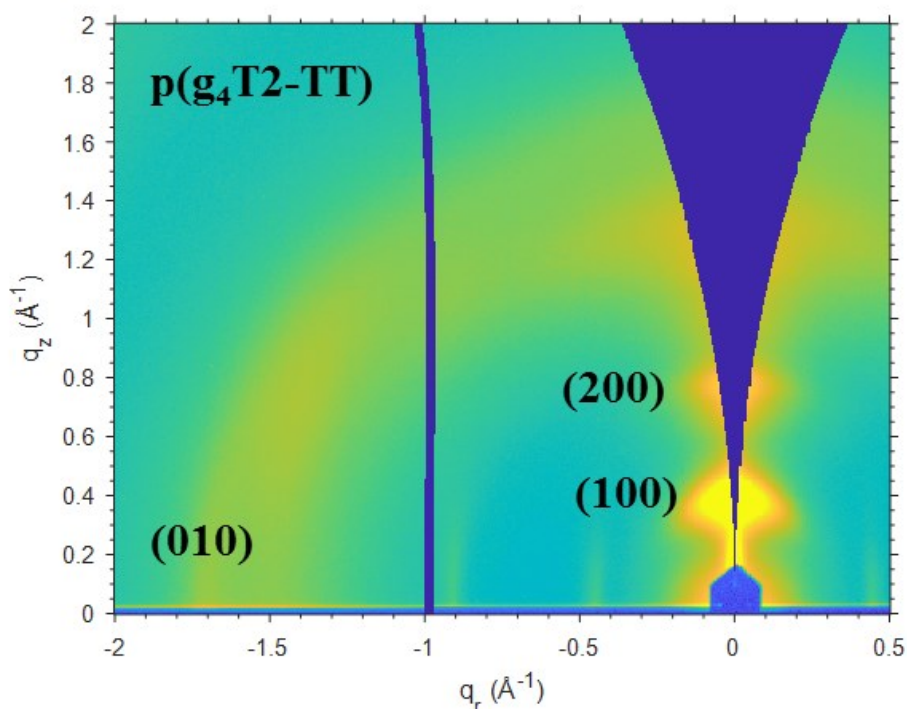
1.0 eq.), 2,5-bis(trimethylstannyl)thieno[3,2-*b*]thiophene (144 mg, 0.31 mmol, 1.0 eq.) and Pd(PPh₃)₄ (7.1 mg, 0.006 mmol, 0.02 eq.). Cap was sealed and the vial was purged with Nitrogen for 5 minutes prior to the addition of anhydrous DMF (2.06 mL) and anhydrous chlorobenzene (2.06 mL). The reaction was stirred overnight at 110 °C then cooled to room temperature, upon which the solution formed a purple gel. Crude polymer was precipitated into 100 mL methanol and subsequently filtered into a thimble. Purification was conducted via Soxhlet extraction, washing with hexane, methanol, acetone, ethyl acetate and chloroform (in that order). The chloroform fraction was collected, solvent removed under reduced pressure and re-precipitated into 100 mL methanol, filtered to yield a blue metallic film (140 mg, 61%).

$\lambda_{\text{MAX}}^{\text{a}}$ (nm)	λ_{ONSET} (nm)	$E_{\text{opt}}^{\text{b}}$ (eV)	IP [CV] (eV)	EA ^c (eV)	E_{onset} [ACN](V)	E_{onset} [H ₂ O](V)	M_{n} (kDa)	M_{w} (kDa)	PDI
573	674	1.84	4.30	2.46	-0.09	-0.15	7.1	13.5	1.91

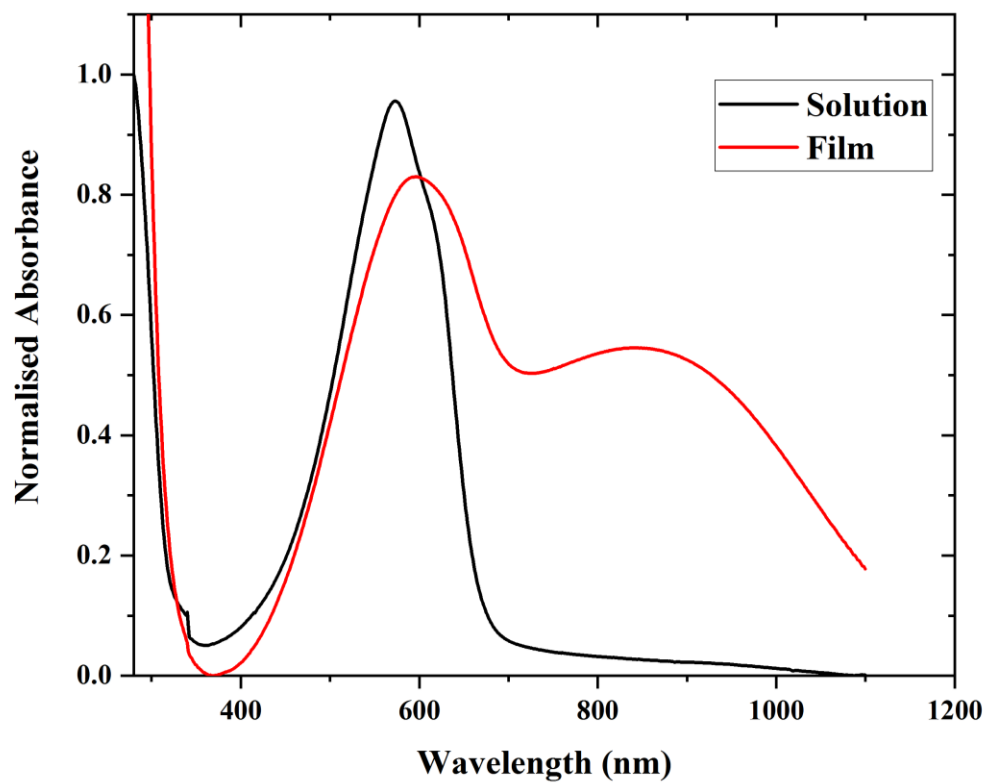
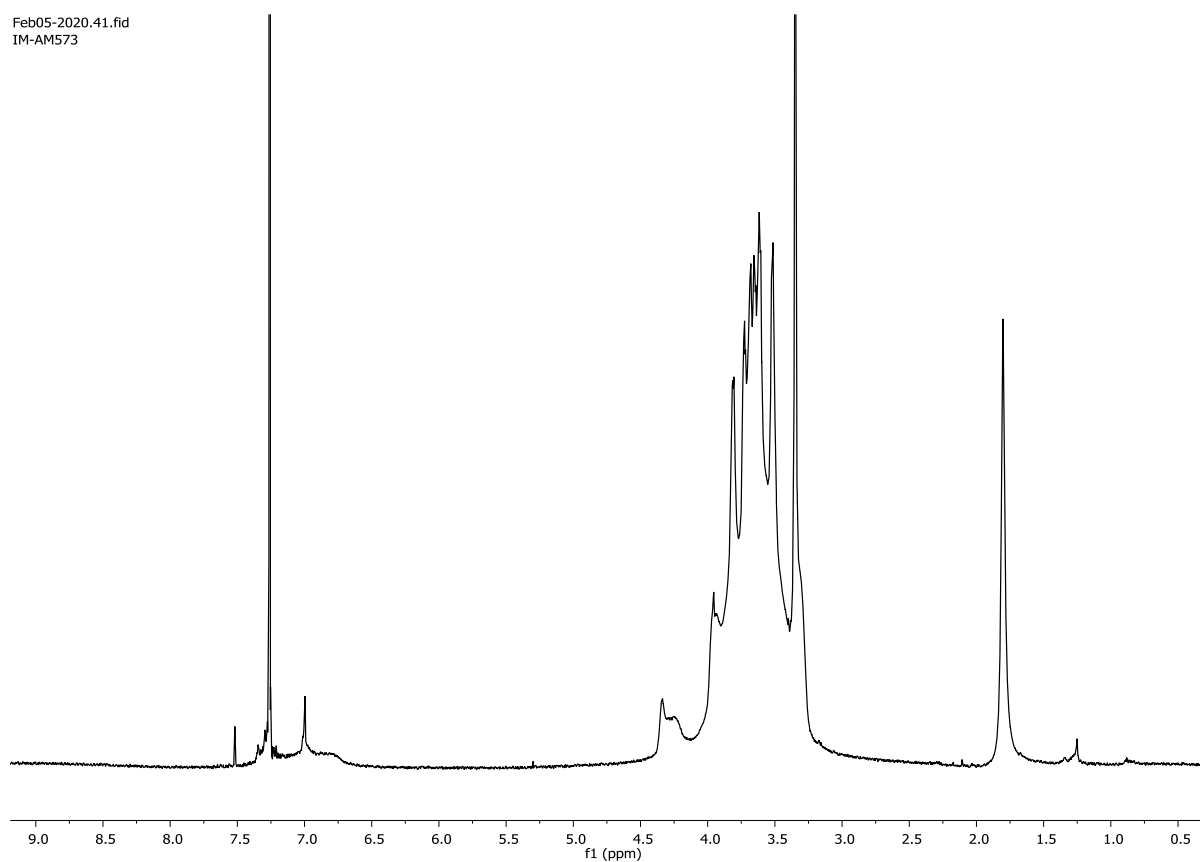
^a λ is the peak of the first low energy absorption band of the polymers

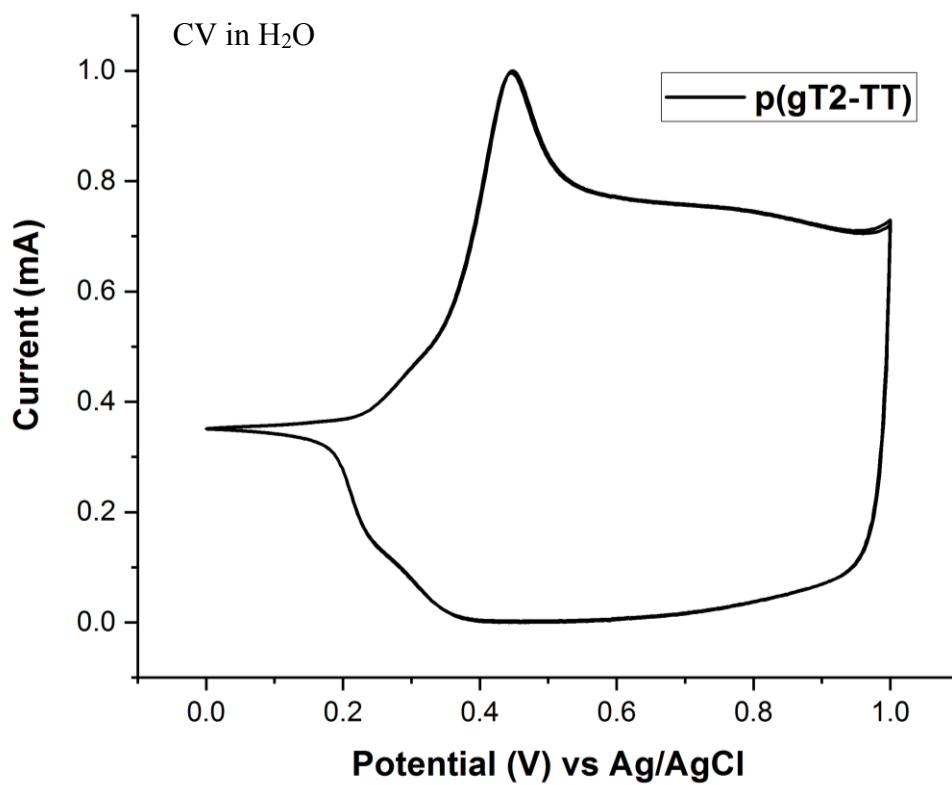
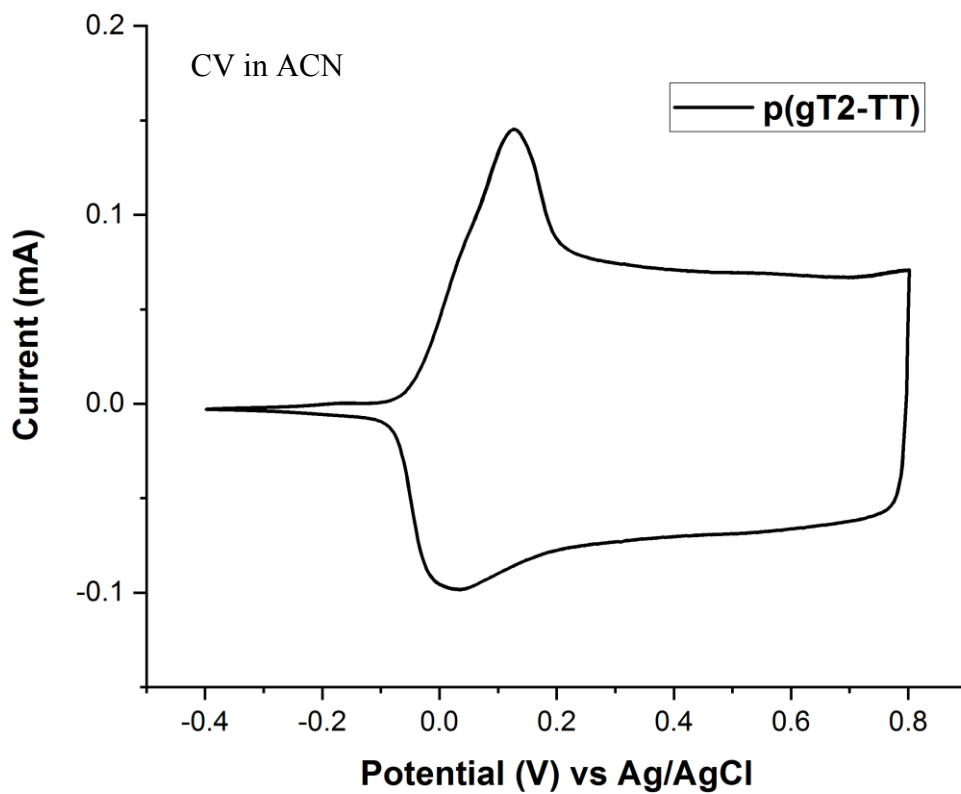
^b E_{opt} estimated optical gap using onset of the thin-film absorption spectra $E_{\text{GAP}} = 1240 / \lambda_{\text{ONSET}}$

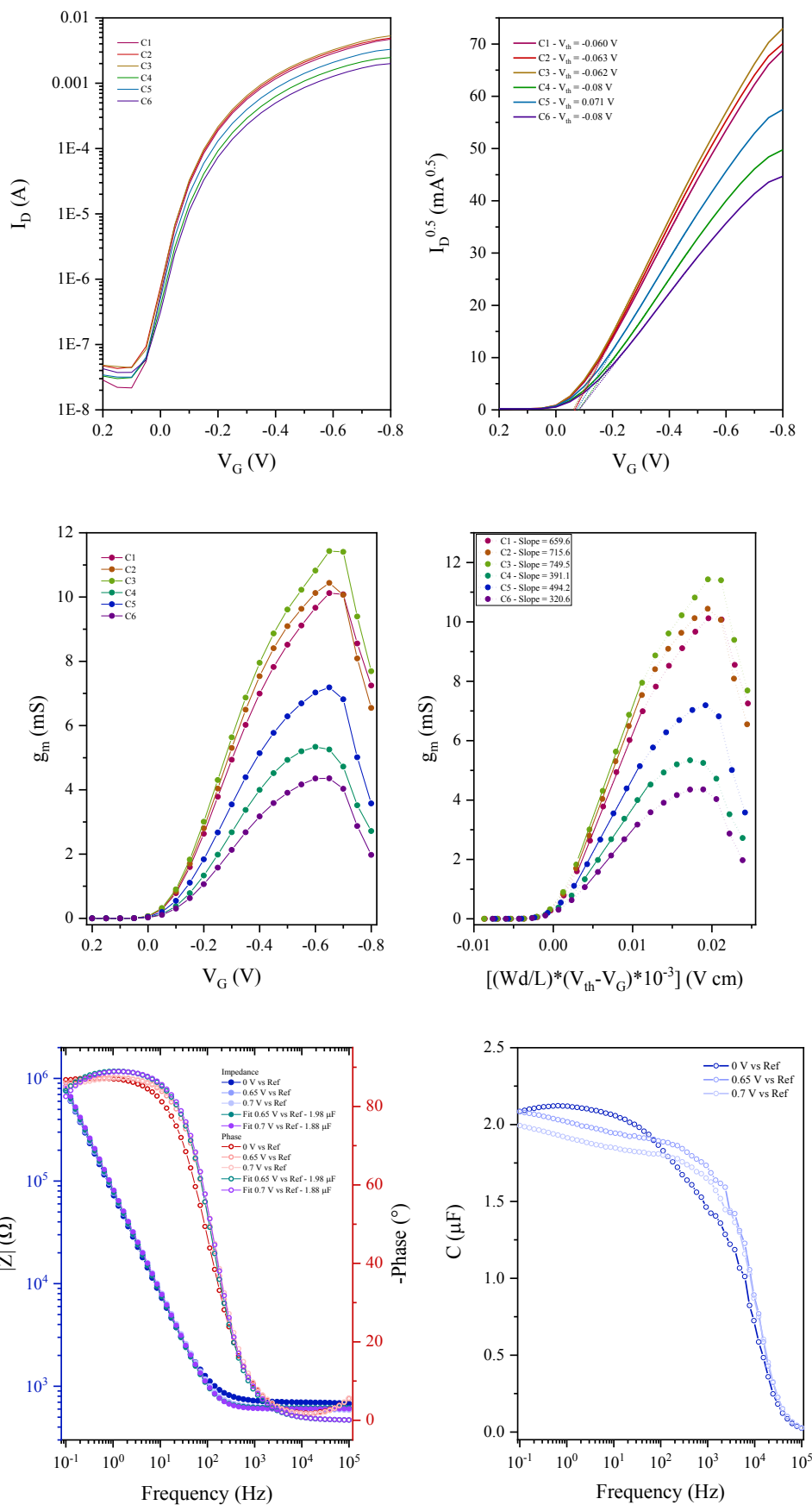
^cEA crudely estimated by subtraction of the UV-Vis absorption onset from IP ($EA = IP - E_{\text{opt}}$), a procedure that neglects the exciton binding energy

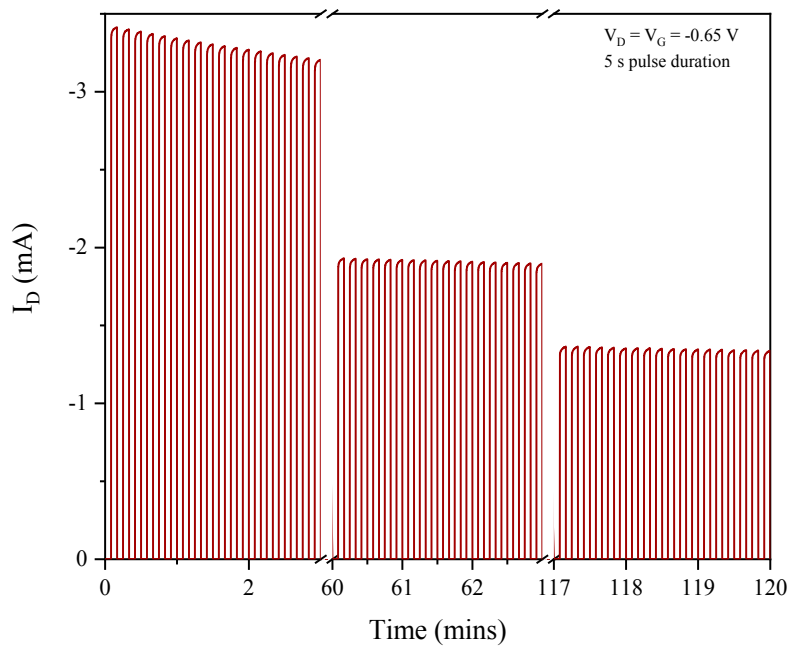
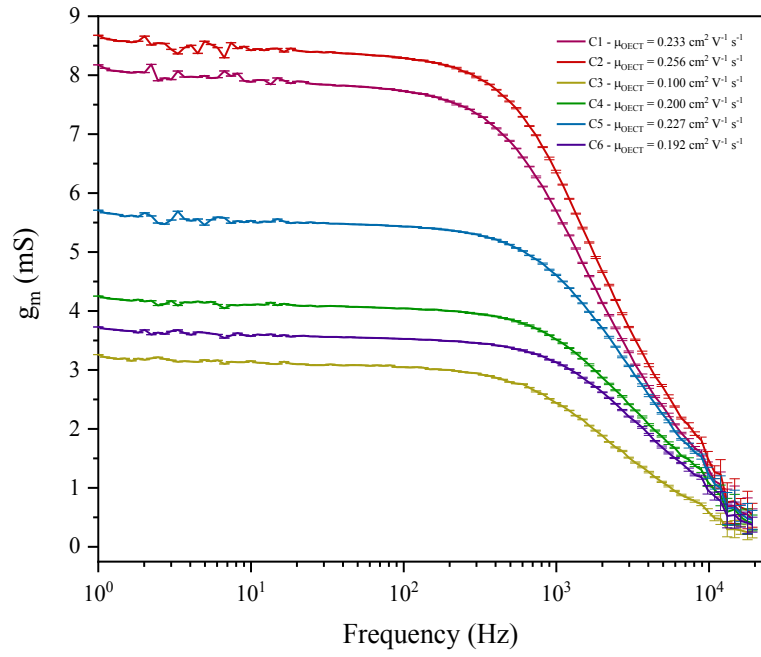


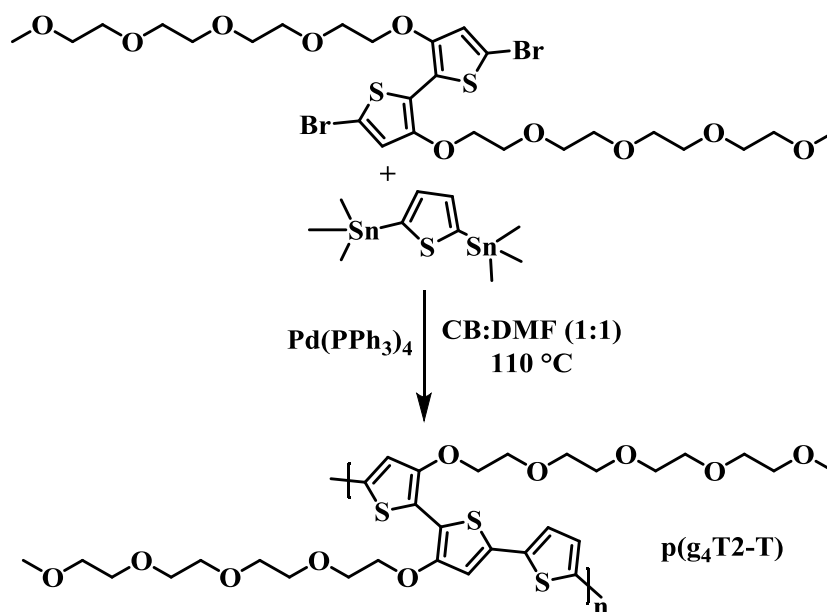
Feb05-2020.41.fid
IM-AM573









6.4.5 Synthesis of Polymer AM575 p(g₄T2-T)

An oven dried 5 mL microwave vial was charged with 13,13'-((5,5'-dibromo-[2,2'-bithiophene]-3,3'-diyl)bis(oxy))bis(2,5,8,11-tetraoxatridecane) (**6.4.3**) (200 mg, 0.31 mmol, 1.0 eq.), 2,5-bis(trimethylstannyl)thiophene (126.4 mg, 0.31 mmol, 1.0 eq.) and Pd(PPh₃)₄ (7.1 mg, 0.006 mmol, 0.02 eq.). Cap was sealed and the vial was purged with Nitrogen for 5 minutes prior to the addition of anhydrous DMF (2.06 mL) and anhydrous chlorobenzene (2.06 mL). The reaction was stirred overnight at 110 °C then cooled to room temperature, upon which the solution formed a purple gel. Crude polymer was precipitated into 100 mL methanol and subsequently filtered into a thimble. Purification was conducted via Soxhlet extraction, washing with hexane, methanol, acetone, ethyl acetate and chloroform (in that order). The chloroform fraction was collected, solvent removed under reduced pressure and re-precipitated into 100 mL methanol, filtered to yield a blue metallic film (167 mg, 79%).

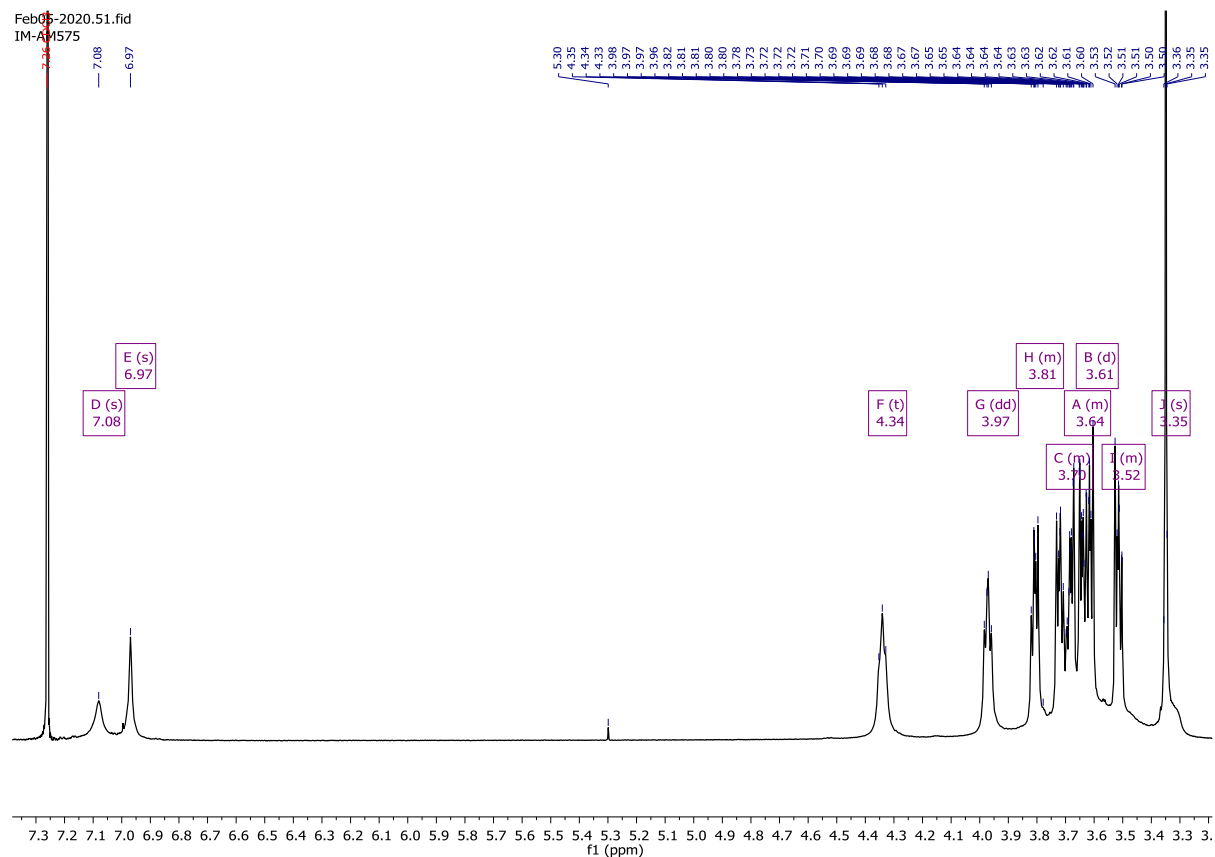
¹H NMR (400 MHz, Chloroform-*d*) δ 7.08 (s, 2H), 6.97 (s, 2H), 4.34 (t, *J* = 4.8 Hz, 4H), 3.97 (dd, *J* = 5.9, 4.0 Hz, 4H), 3.84 – 3.77 (m, 4H), 3.80 – 3.65 (m, 6H), 3.70 – 3.59 (m, 8H), 3.61 (d, *J* = 3.0 Hz, 2H), 3.55 – 3.48 (m, 4H), 3.35 (s, 6H).

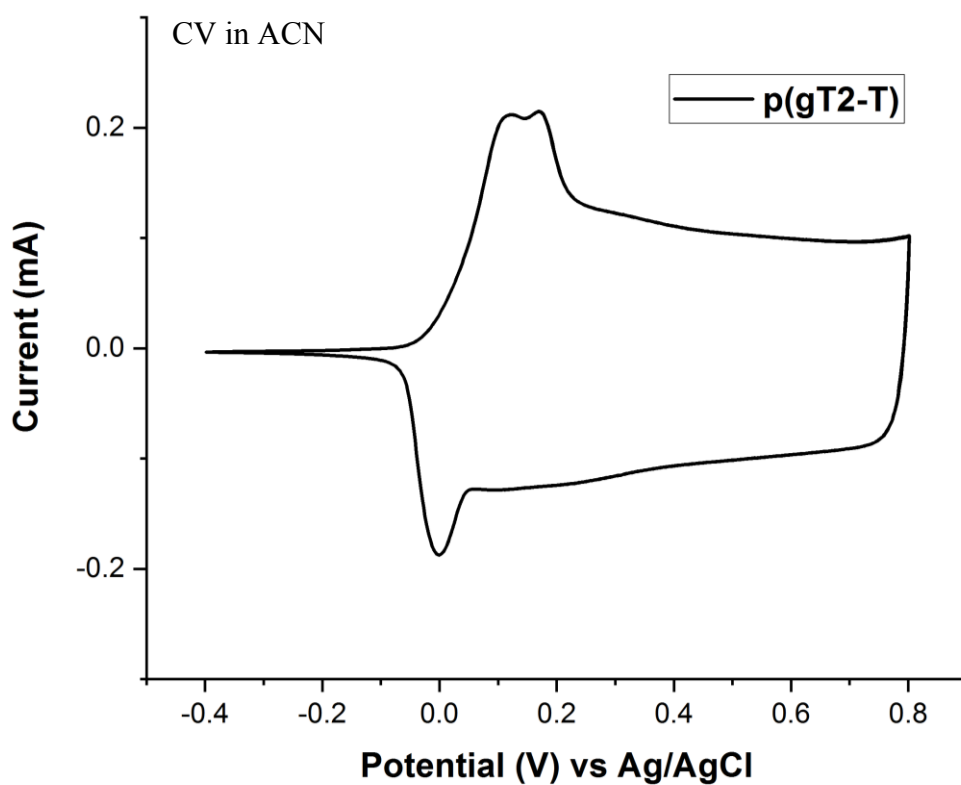
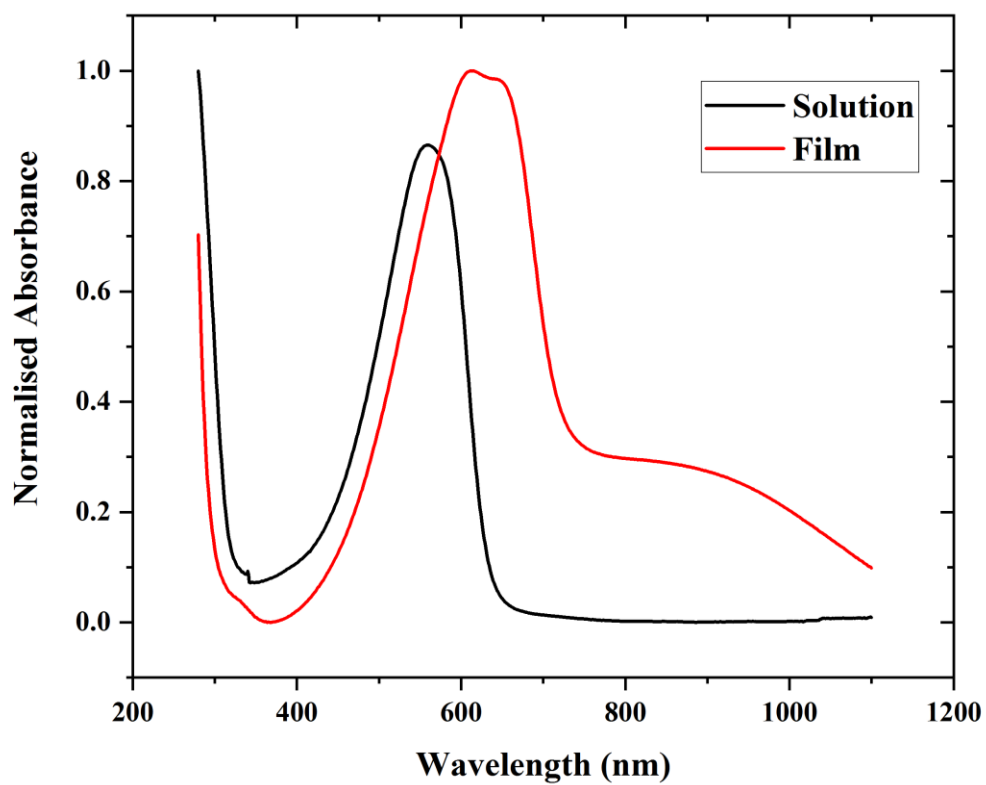
λ_{MAX}^a (nm)	λ_{ONSET} (nm)	E_{opt}^b (eV)	IP [CV] (eV)	EA ^c (eV)	E_{onset} [ACN](V)	E_{onset} [H ₂ O](V)	M_n (kDa)	M_w (kDa)	PDI
561	638	1.94	4.30	2.36	-0.09	-0.14	51.1	109.6	2.15

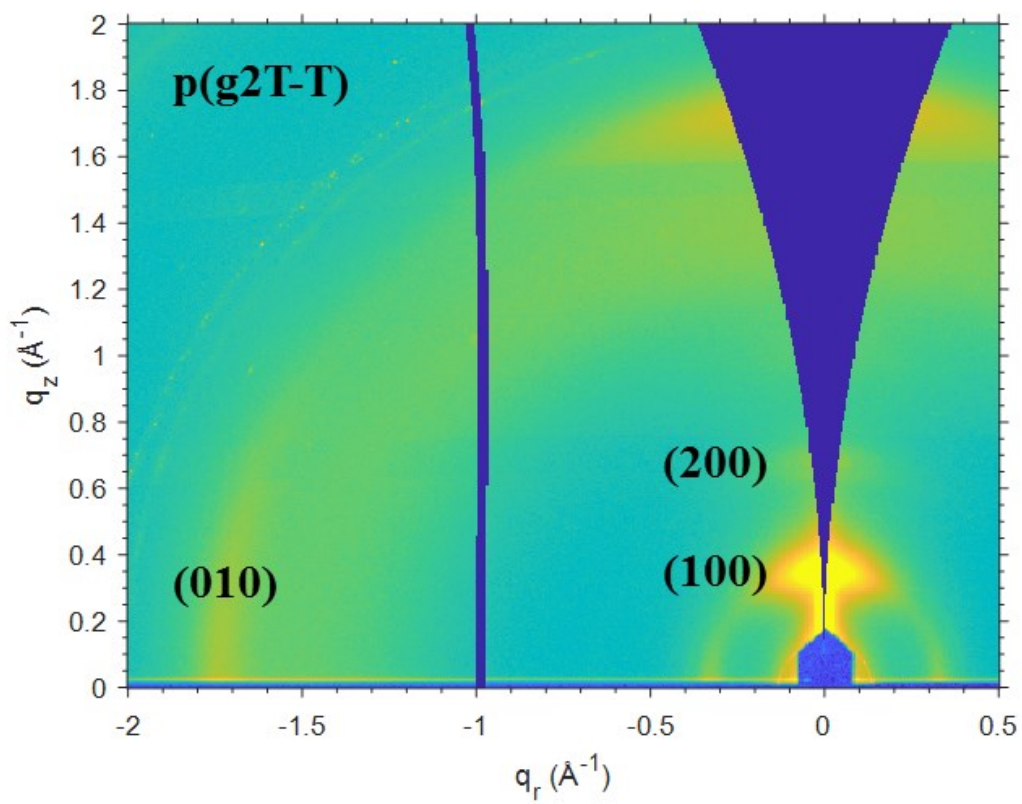
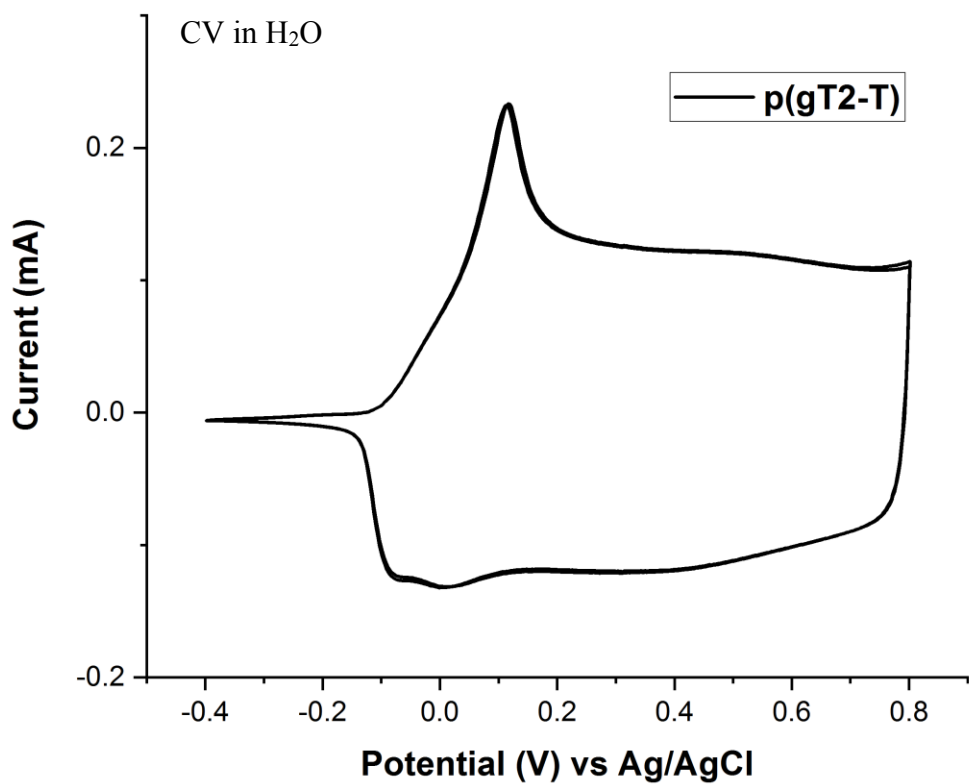
^a λ is the peak of the first low energy absorption band of the polymers

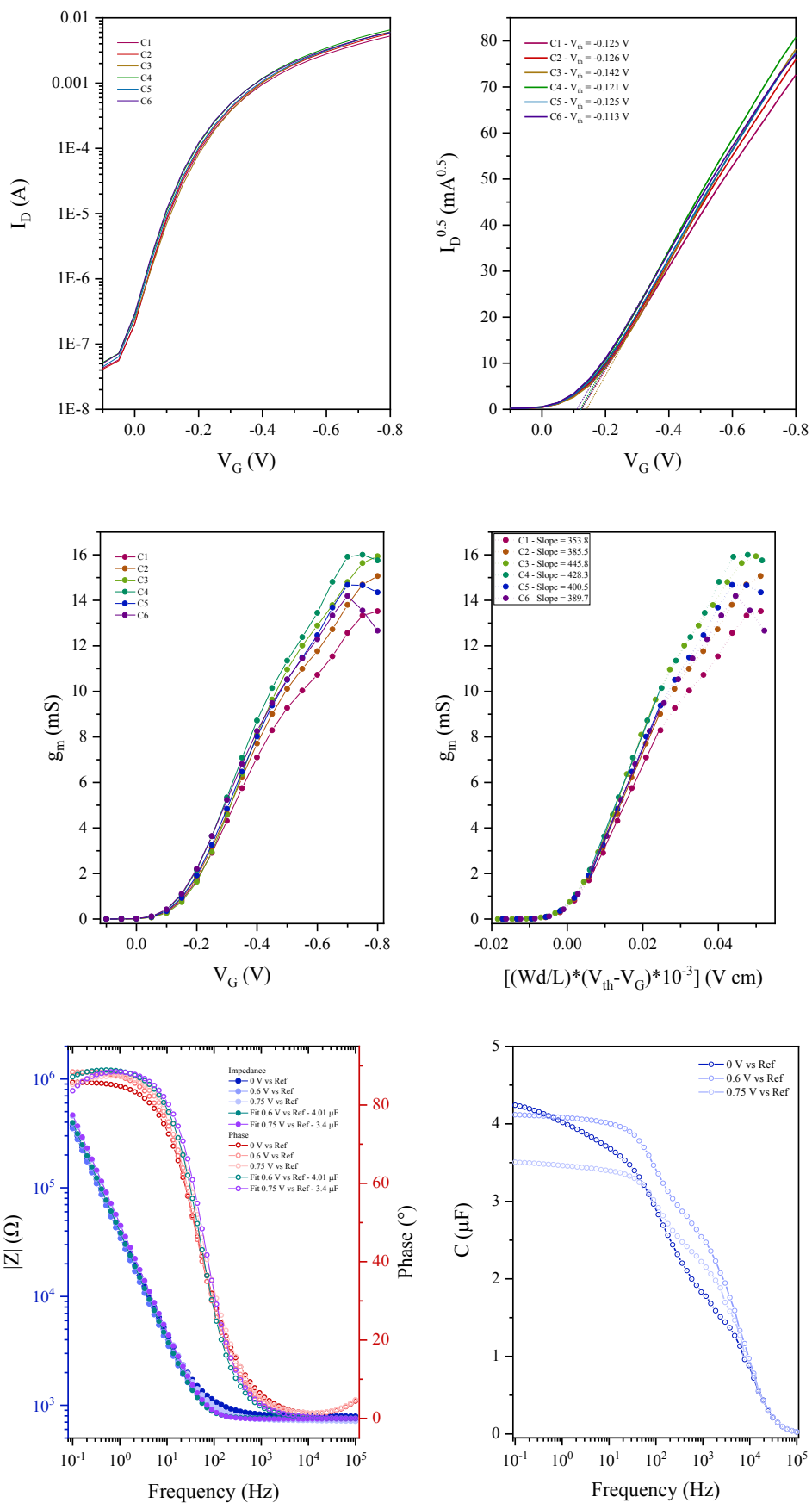
^b E_{opt} estimated optical gap using onset of the thin-film absorption spectra $E_{GAP} = 1240 / \lambda_{ONSET}$

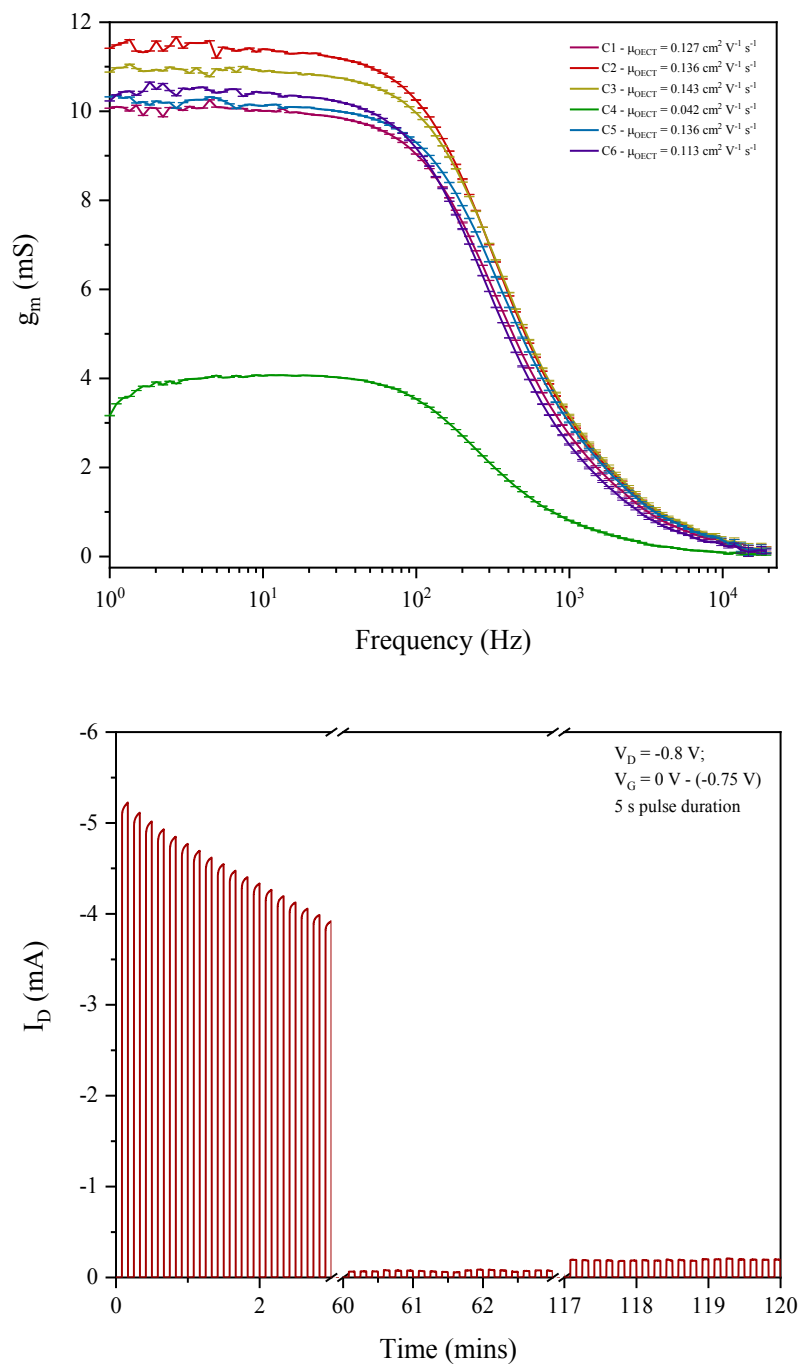
^cEA crudely estimated by subtraction of the UV-Vis absorption onset from IP ($EA = IP - E_{opt}$), a procedure that neglects the exciton binding energy



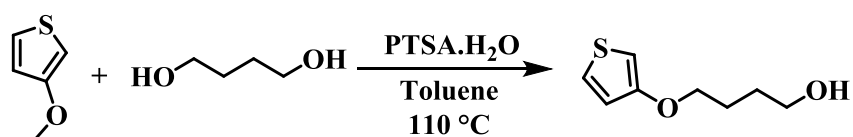








6.4.6 Synthesis of 4-(thiophen-3-yloxy)butan-1-ol

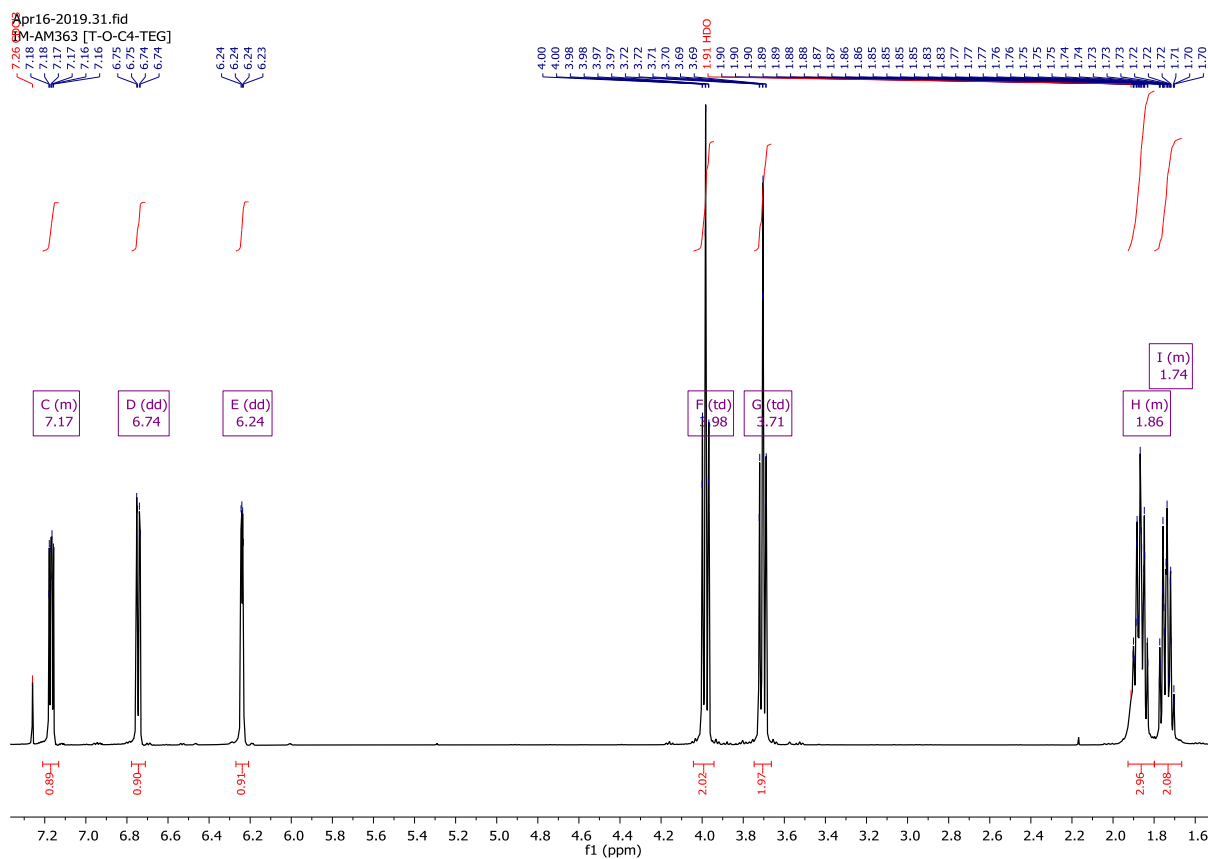


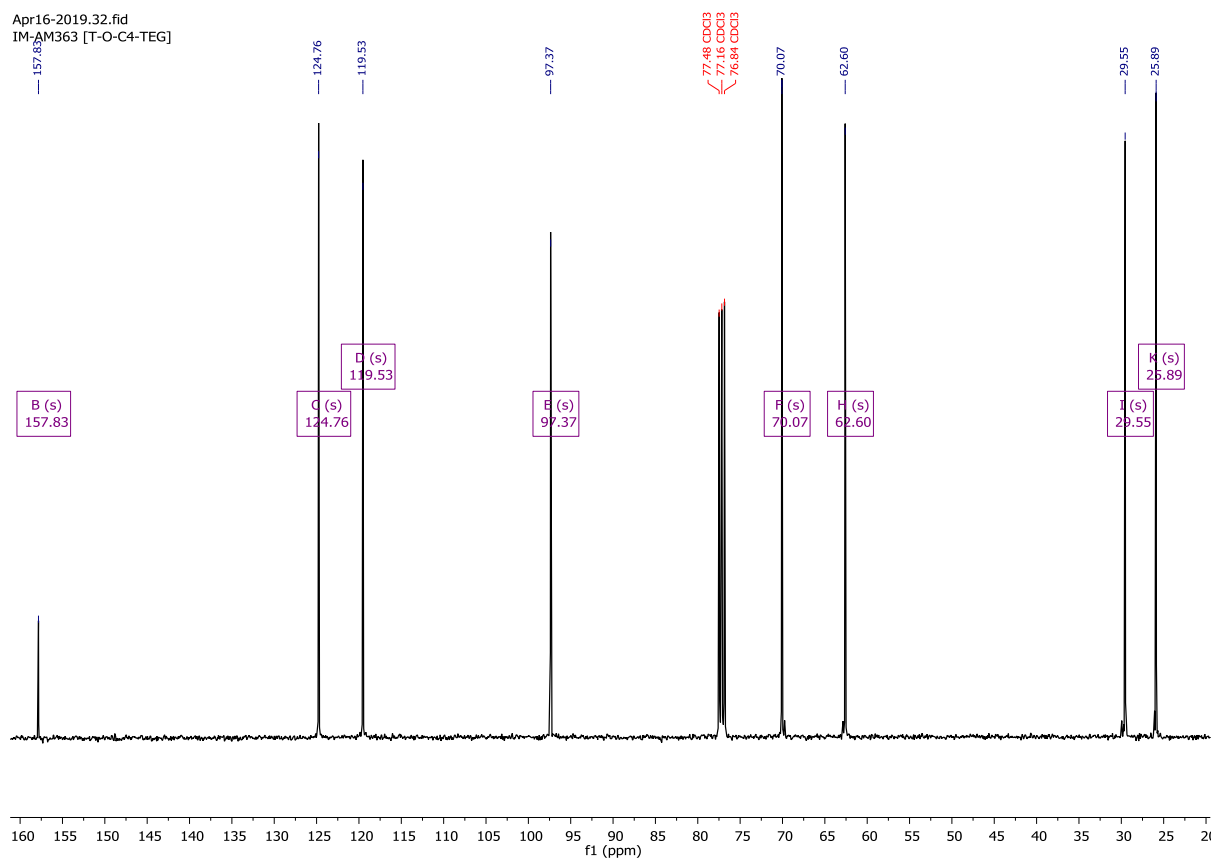
3-Methoxythiophene (17.5 mL, 175.4 mmol, 1.0 eq.) was dissolved in 250 mL of toluene, inside a 2-neck 500 mL RBF. 1,4-Butanediol (23.3 mL, 263.2 mmol, 1.5 eq.) was added

dropwise prior to the addition of *p*-toluenesulfonic acid monohydrate (3.3 g, 17.5 mmol, 0.1 eq.) in a single portion. The reaction was heated to reflux (110 °C) and stirred for 90 minutes. Upon cooling to room temperature, the mixture was poured into water, the organic layer was extracted into DCM, separated and dried over MgSO₄. After the solvent was removed, under reduced pressure, the crude material was purified by column chromatography, on silica gel, using DCM as the eluent. Product fractions were consolidated to afford the title compound (11.55 g, 38%).

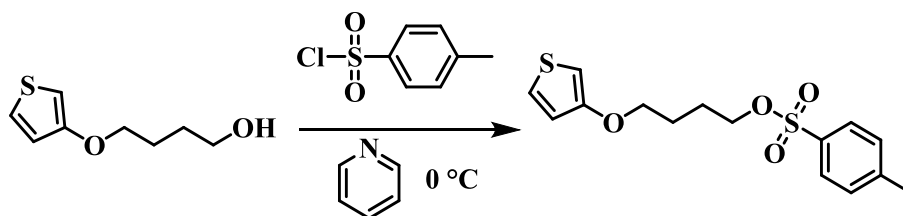
¹H NMR (400 MHz, Chloroform-*d*) δ 7.21 – 7.13 (m, 1H), 6.74 (dd, *J* = 5.2, 1.5 Hz, 1H), 6.24 (dd, *J* = 3.1, 1.5 Hz, 1H), 3.98 (td, *J* = 6.2, 0.7 Hz, 2H), 3.71 (td, *J* = 6.3, 1.0 Hz, 2H), 1.93 – 1.78 (m, 3H), 1.82 – 1.67 (m, 2H).

¹³C NMR (101 MHz, Chloroform-*d*) δ 157.83, 124.76, 119.53, 97.37, 70.07, 62.60, 29.55, 25.89.





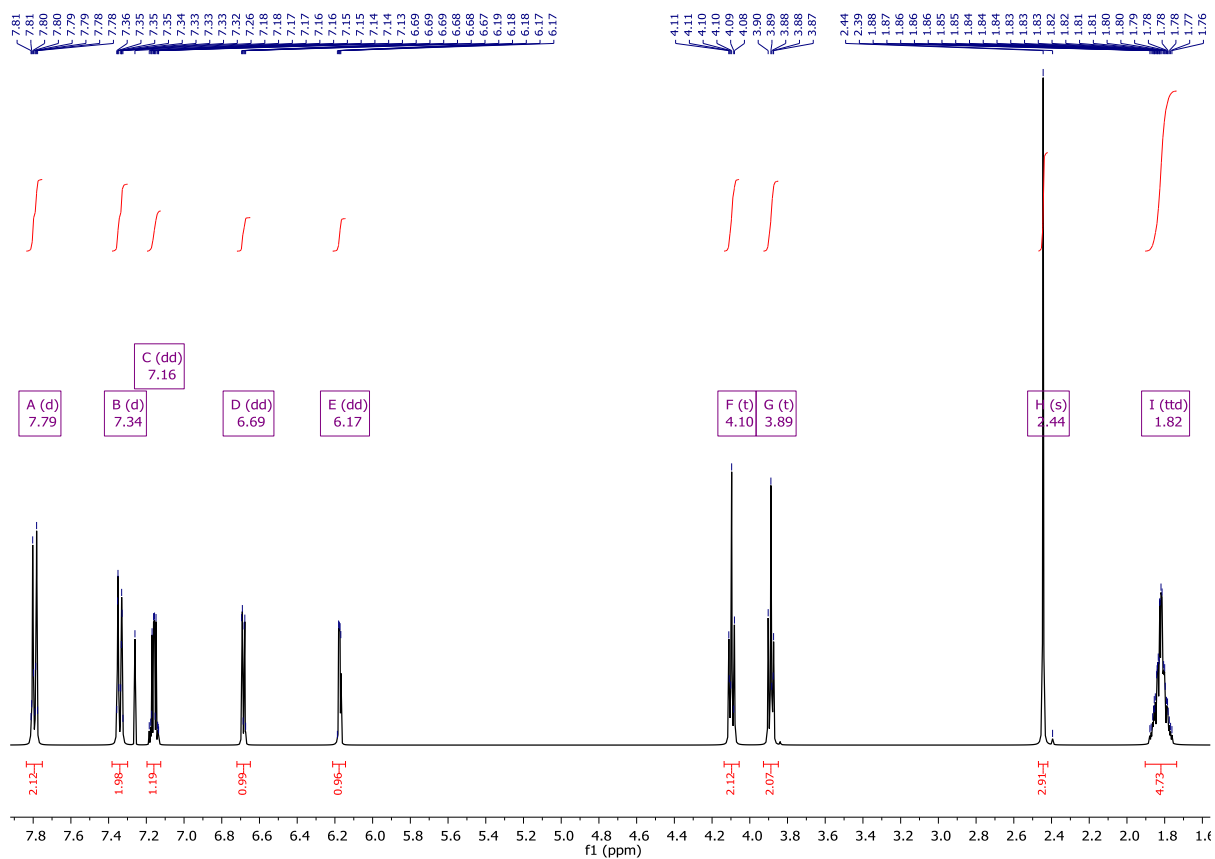
6.4.7 Synthesis of 4-(thiophen-3-yloxy)butyl 4-methylbenzenesulfonate

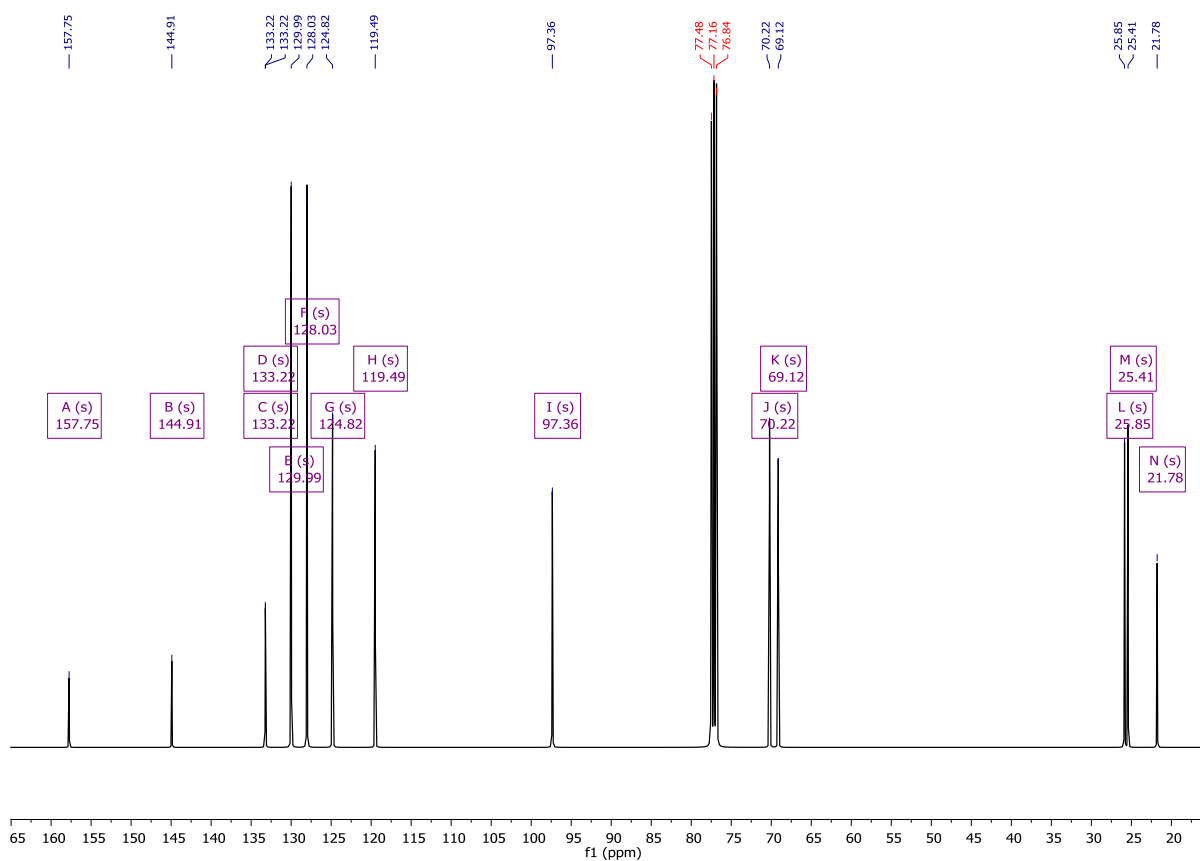


4-(thiophen-3-yloxy)butan-1-ol (**6.4.6**) (11.55 g, 67.1 mmol, 1.0 eq.) was dissolved in 30 mL pyridine and cooled to 0 °C. 4-Toluenesulfonyl chloride (15.4 g, 80.6 mmol, 1.2 eq.) was added, in a single portion, and the reaction was stirred vigorously for 20 minutes, during which the solution turned an intense yellow colour. The reaction was stored in the refrigerator overnight, afterwards 30 mL 2M HCl was added and the solution stirred rapidly for 30 minutes. The mixture was poured into water, extracted with DCM and the organic layer was dried over Na₂SO₄ prior to removing the solvent under reduced pressure. The product was dried under vacuum and used in the next step without further purification. (18.41 g, 84%).

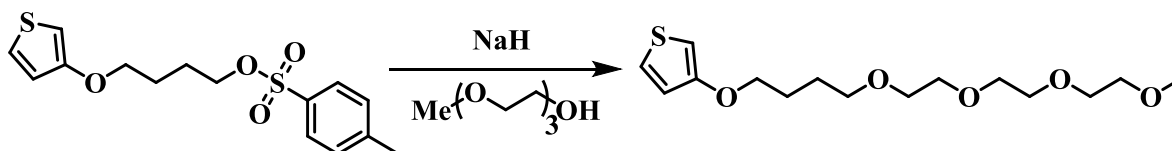
^1H NMR (400 MHz, Chloroform-*d*) δ 7.79 (d, $J = 8.3$ Hz, 2H), 7.34 (d, $J = 8.2$ Hz, 2H), 7.16 (dd, $J = 5.2, 3.2$ Hz, 1H), 6.69 (dd, $J = 5.2, 1.5$ Hz, 1H), 6.17 (dd, $J = 3.1, 1.6$ Hz, 1H), 4.10 (t, $J = 6.0$ Hz, 2H), 3.89 (t, $J = 5.8$ Hz, 2H), 2.44 (s, 3H), 1.82 (ttt, $J = 11.7, 6.1, 5.6, 2.3$ Hz, 4H).

^{13}C NMR (101 MHz, Chloroform-*d*) δ 157.75, 144.91, 133.22, 133.22, 129.99, 128.03, 124.82, 119.49, 97.36, 70.22, 69.12, 25.85, 25.41, 21.78.





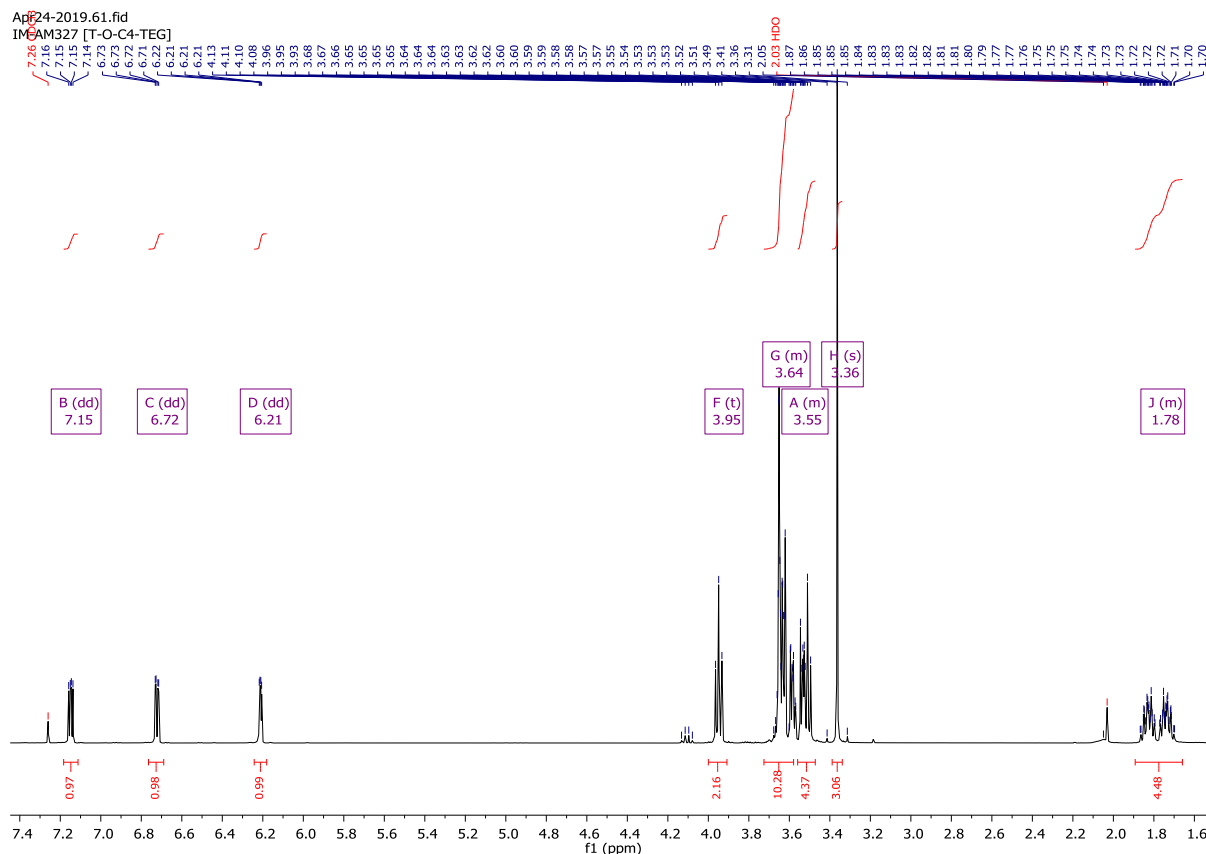
6.4.8 Synthesis of 15-(thiophen-3-yloxy)-2,5,8,11-tetraoxapentadecane

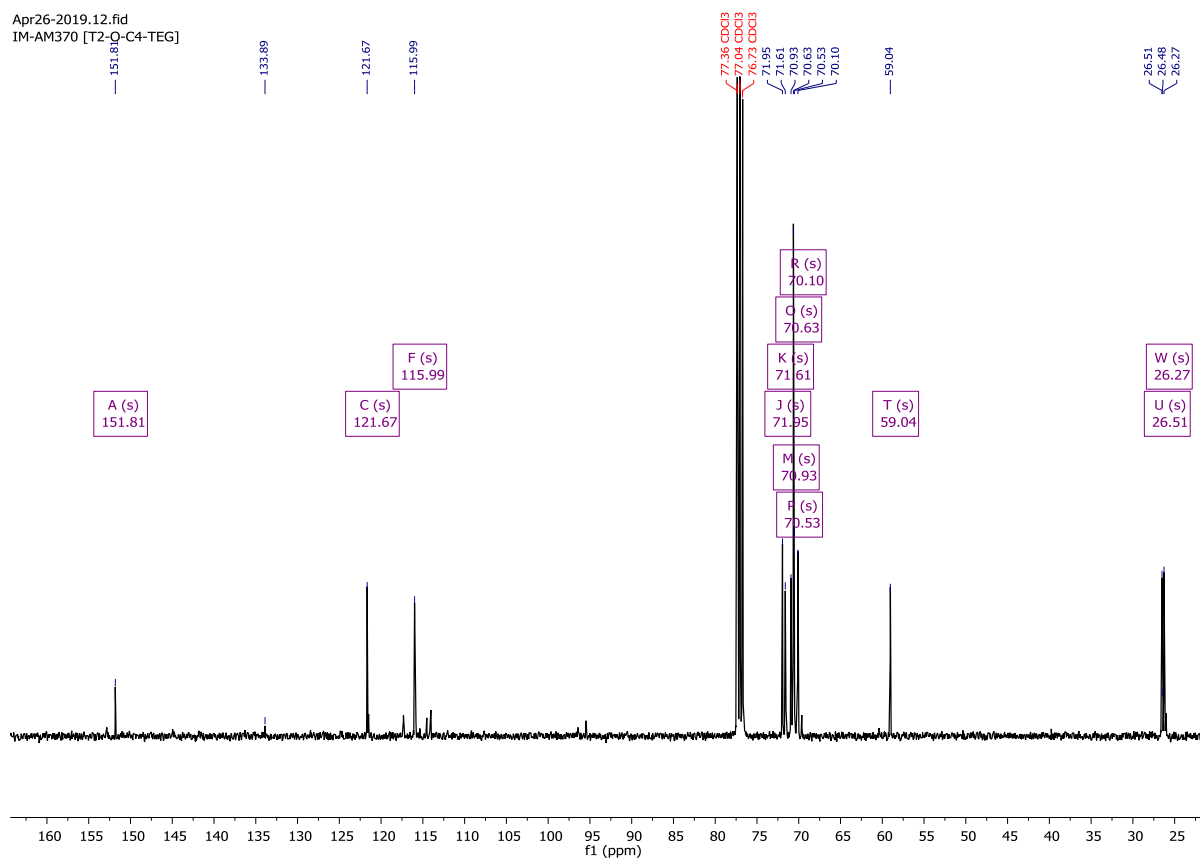


To an oven dried 2-neck 250 mL RBF was added sodium hydride (60% in mineral oil) (6.62 g, 165.4 mmol, 3.0 eq.), dissolved in dry THF (50 mL) at 0 °C, under a Nitrogen atmosphere. Triethylene glycol monomethyl ether (26.5 mL, 165.4 mmol, 3.0 eq.) was added dropwise and the mixture was stirred for 30 minutes until effervescence ceased. 4-(thiophen-3-yloxy)butyl 4-methylbenzenesulfonate (**6.4.7**) (18 g, 55.14 mmol, 1.0 eq.) dissolved in 30 mL THF was added dropwise, the reaction was stirred overnight. The mixture was then poured into water, washed multiple times before being extracted into DCM and dried over MgSO₄. The crude residue was purified via column chromatography, on silica gel, using hexane:ethyl acetate (1:1) as the eluent system, product fractions were consolidated to afford a yellow oil (4.73 g, 27%).

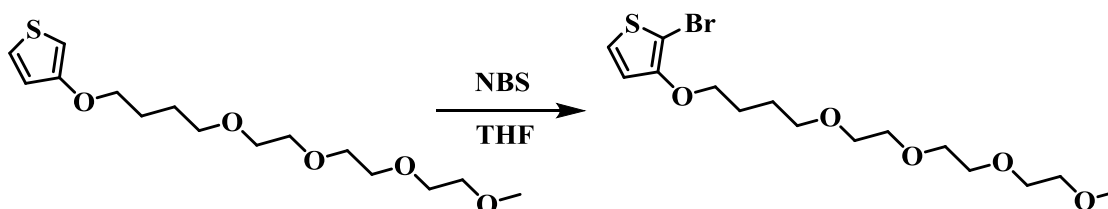
^1H NMR (400 MHz, Chloroform-*d*) δ 7.15 (dd, $J = 5.2, 3.1$ Hz, 1H), 6.72 (dd, $J = 5.2, 1.6$ Hz, 1H), 6.21 (dd, $J = 3.1, 1.5$ Hz, 1H), 3.95 (t, $J = 6.3$ Hz, 2H), 3.73 – 3.60 (m, 10H), 3.63 – 3.45 (m, 4H), 3.36 (s, 3H), 1.89 – 1.66 (m, 4H).

^{13}C NMR (101 MHz, Chloroform-*d*) δ 151.81, 121.67, 115.99, 71.95, 71.61, 70.93, 70.63, 70.53, 70.10, 59.04, 26.51, 26.27.





6.4.9 Synthesis of 15-((2-bromothiophen-3-yl)oxy)-2,5,8,11-tetraoxapentadecane

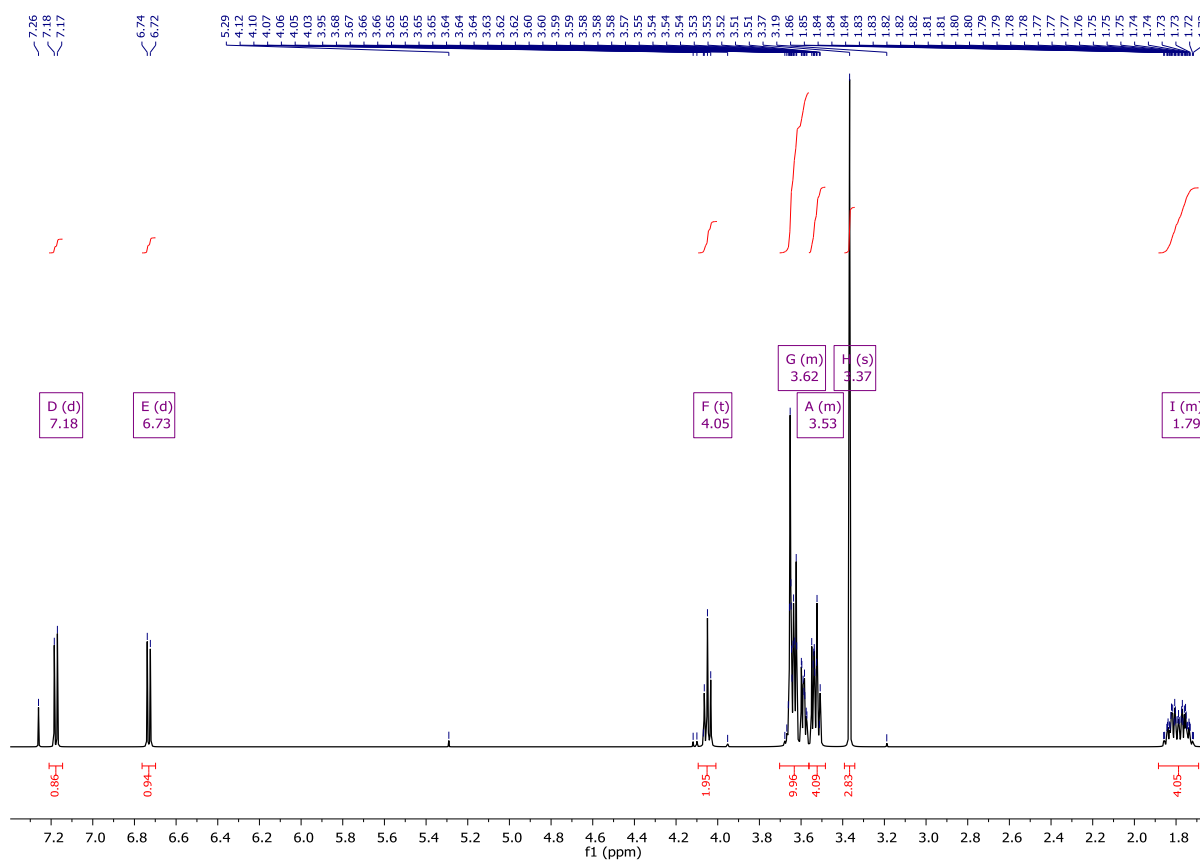


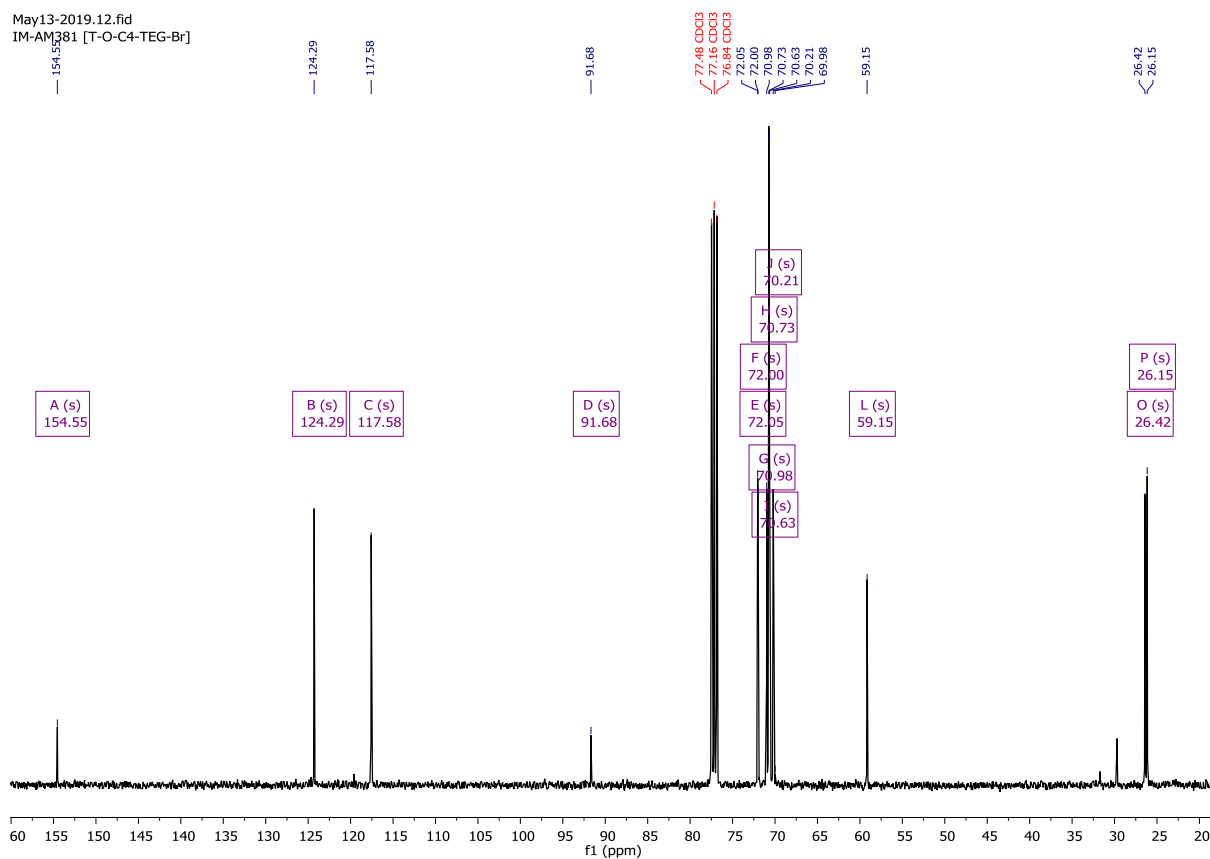
15-(thiophen-3-yloxy)-2,5,8,11-tetraoxapentadecane (**6.4.8**) (4.7 g, 14.8 mmol, 1.0 eq.) was added to an oven dried 250 mL 2-neck RBF, dissolved in 100 mL dry THF. Cooled to 0 °C, in the dark prior to the portion wise addition of N-bromosuccinimide (4x700 mg, 15.01 mmol, 1.02 eq.) leaving approximately 4 minutes between each addition. After stirring for 90 minutes the reaction was poured into water, washed with saturated sodium bicarbonate solution and quenched with sodium metabisulphite. The aqueous phase was extracted three times with DCM, the organic layers were combined, dried over Na₂SO₄ and solvent removed under reduced pressure. The crude was purified via column chromatography, on silica gel, using

hexane:ethyl acetate (1:1) (v/v) as the eluent system. Product fractions were consolidated to yield a pale-yellow oil (5.79 g, 97%).

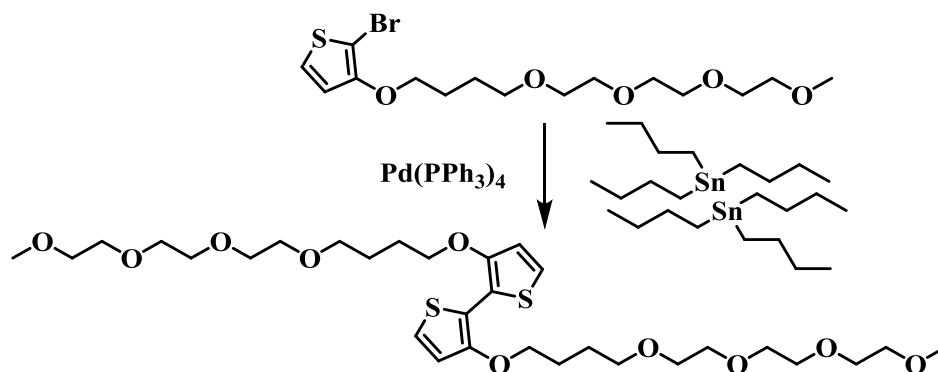
^1H NMR (400 MHz, Chloroform-*d*) δ 7.18 (d, $J = 6.0$ Hz, 1H), 6.73 (d, $J = 5.9$ Hz, 1H), 4.05 (t, $J = 6.2$ Hz, 2H), 3.70 – 3.54 (m, 10H), 3.57 – 3.47 (m, 4H), 3.37 (s, 3H), 1.88 – 1.69 (m, 4H).

^{13}C NMR (101 MHz, Chloroform-*d*) δ 154.55, 124.29, 117.58, 91.68, 72.05, 72.00, 70.98, 70.73, 70.63, 70.21, 59.15, 26.42, 26.15.





6.4.10 Synthesis of 3,3'-bis((2,5,8,11-tetraoxapentadecan-15-yl)oxy)-2,2'-bithiophene

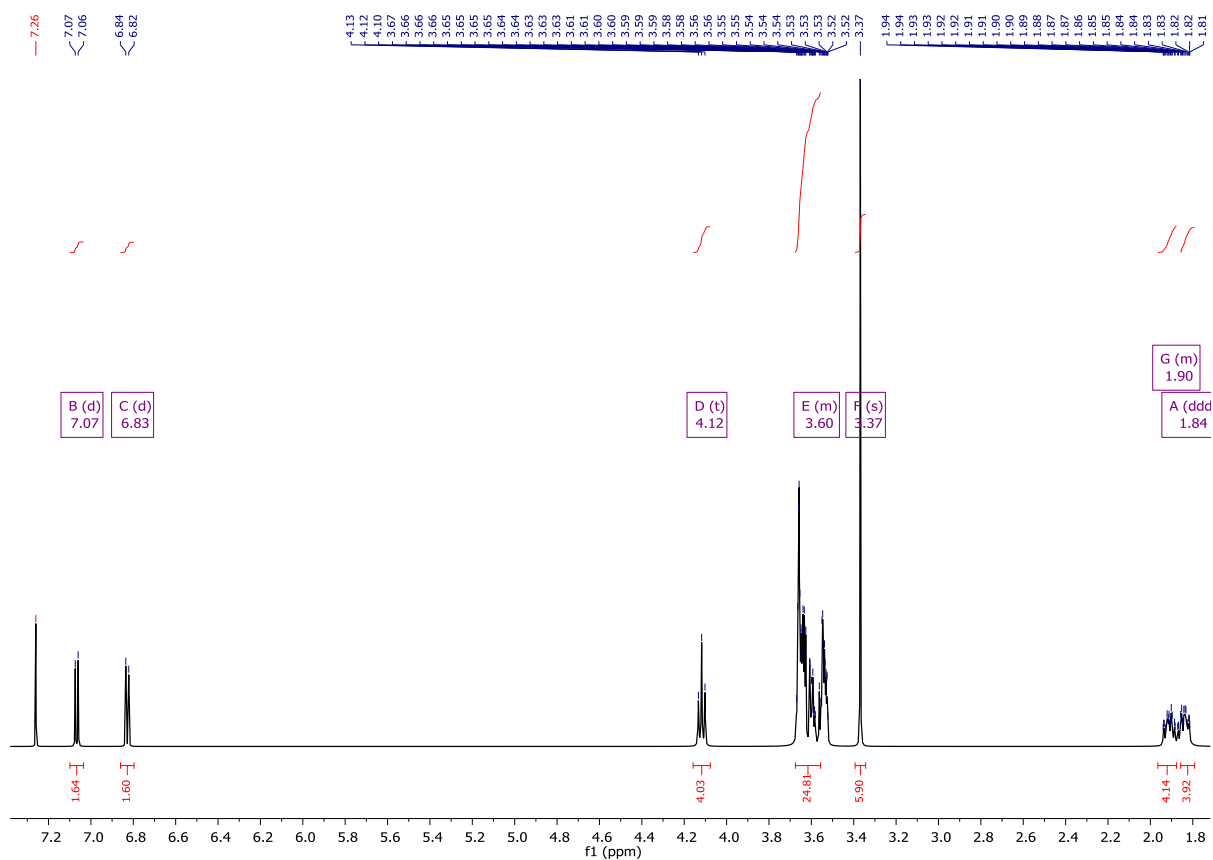


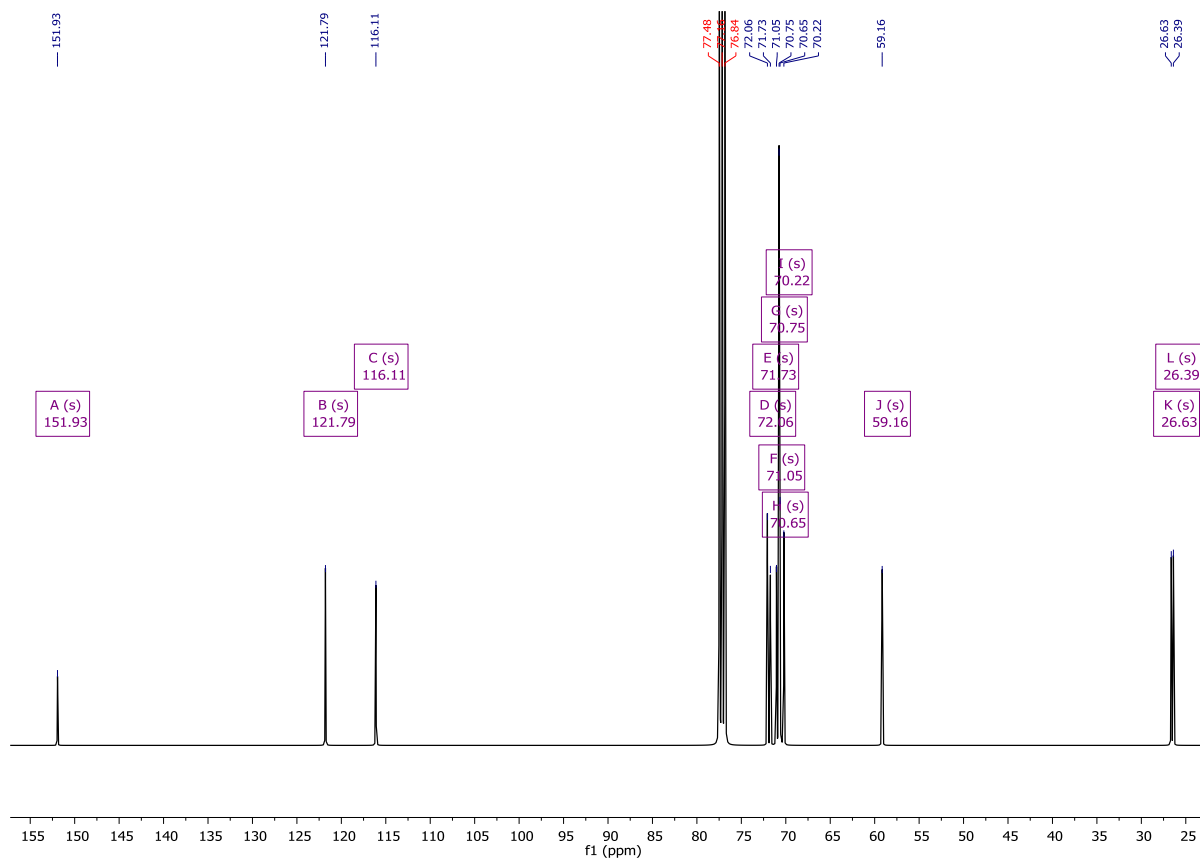
15-(thiophen-3-yloxy)-2,5,8,11-tetraoxapentadecane (**6.4.9**) (4.7 g, 11.8 mmol, 1.0 eq.) was added to an oven dried 2-neck 250 mL RBF and dissolved in a 1:1 mixture of anhydrous chlorobenzene (37 mL) and dry DMF (37 mL), under a nitrogen atmosphere. Bis(tributyltin) (3.73 mL, 5.91 mmol, 0.5 eq.) was added dropwise, followed by the addition of $\text{Pd}(\text{PPh}_3)_4$ (1.71 g, 1.18 mmol, 0.01 eq.). The reaction was stirred for 48 hours at 100 °C, upon cooling to room temperature the mixture was passed through a short silica plug, eluting with ethyl acetate. The

solvent was removed under reduced pressure and the crude was purified by column chromatography, on silica gel, using ethyl acetate as the eluent system. Product fractions were consolidated to yield a yellow oil which solidified at reduced temperature (3.37 g, 58%).

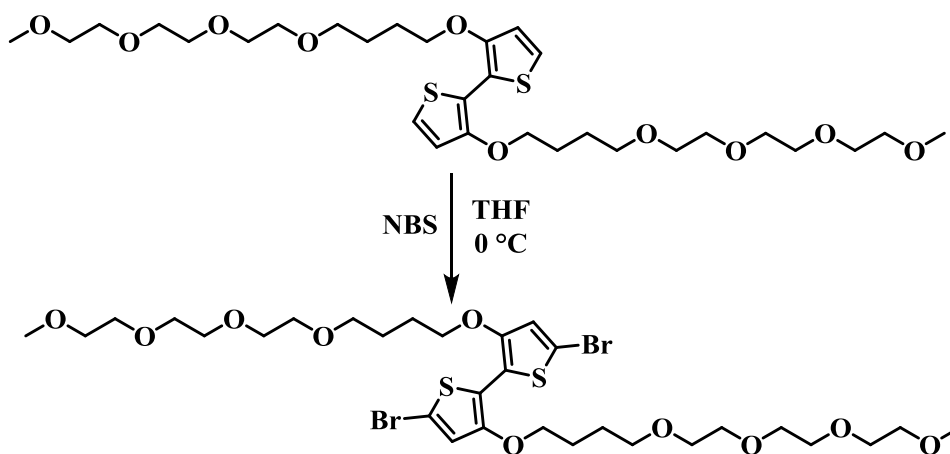
^1H NMR (400 MHz, Chloroform-*d*) δ 7.07 (d, $J = 5.5$ Hz, 2H), 6.83 (d, $J = 5.6$ Hz, 2H), 4.12 (t, $J = 6.2$ Hz, 4H), 3.69 – 3.50 (m, 28H), 3.37 (s, 6H), 1.96 – 1.84 (m, 4H), 1.84 (ddd, $J = 8.1$, 4.9, 1.6 Hz, 4H).

^{13}C NMR (101 MHz, Chloroform-*d*) δ 151.93, 121.79, 116.11, 72.06, 71.73, 71.05, 70.75, 70.65, 70.22, 59.16, 26.63, 26.39.





6.4.11 15,15'-((5,5'-dibromo-[2,2'-bithiophene]-3,3'-diyl)bis(oxy))bis(2,5,8,11-tetraoxapentadecane)



3,3'-bis((2,5,8,11-tetraoxapentadecan-15-yl)oxy)-2,2'-bithiophene (**6.4.10**) (2 g, 3.15 mmol, 1.0 eq.) was dissolved in 50 mL anhydrous THF and cooled to 0 °C, under a Nitrogen atmosphere. The reaction was covered and kept in the dark, N-bromosuccinimide (1.15 g, 6.46

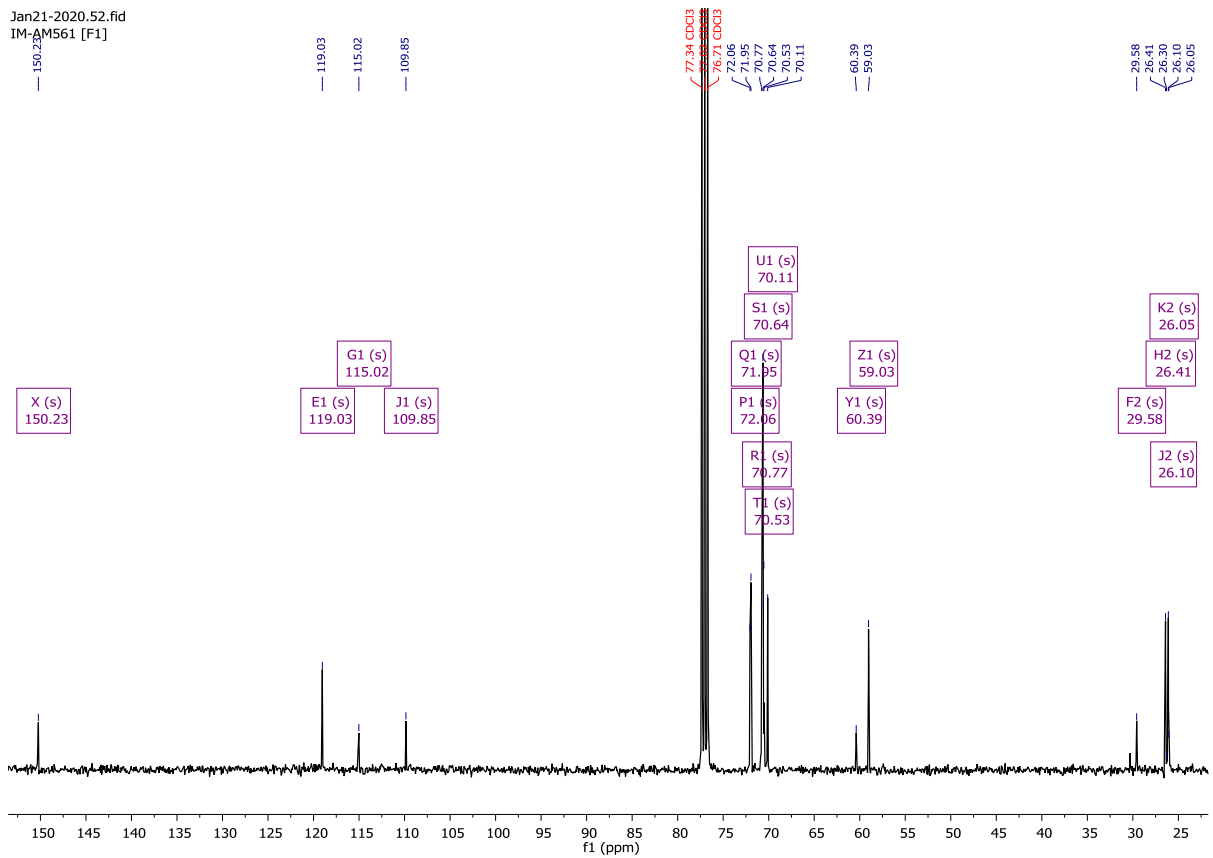
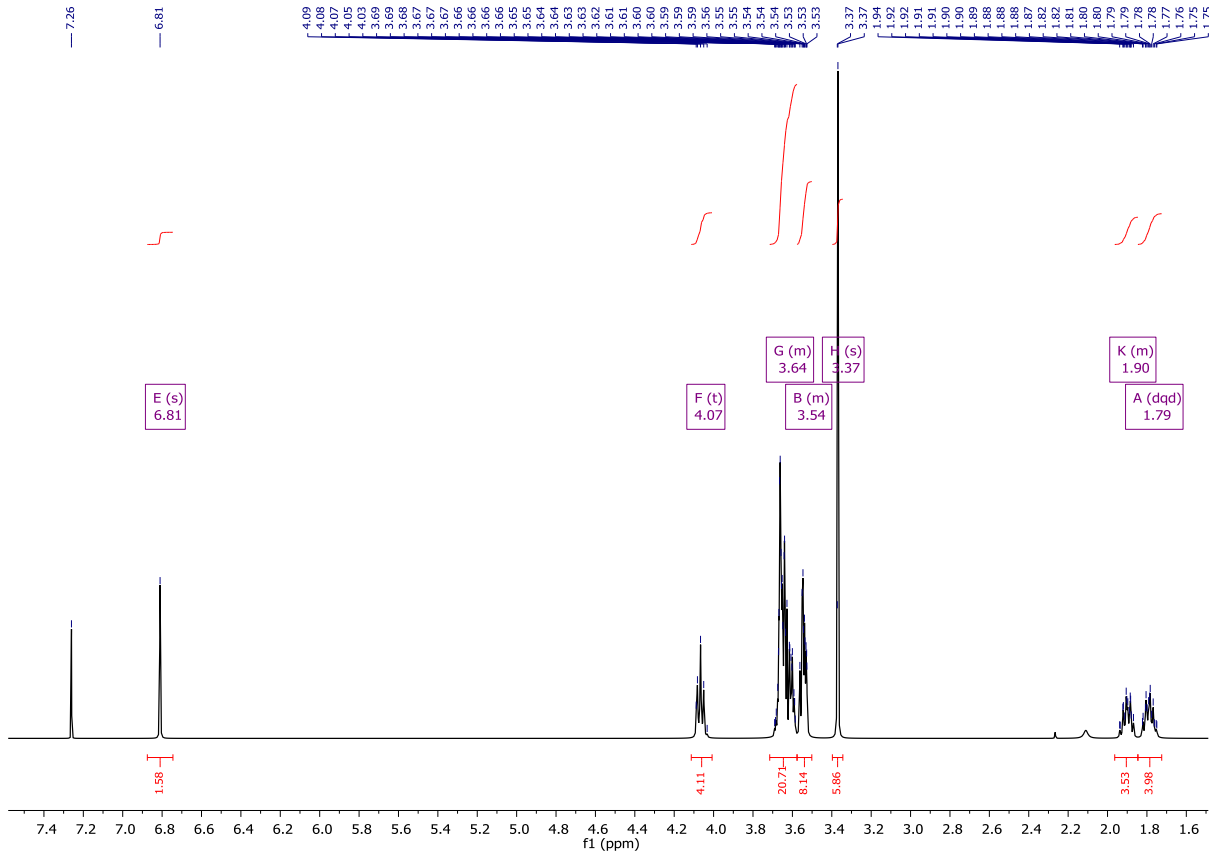
mmol, 2.05 eq.) was added in four equal portions, leaving 4 minutes between each addition. After stirring for 30 minutes the reaction was poured into water, washed with saturated sodium bicarbonate solution and quenched with sodium metabisulphite. The aqueous phase was extracted into DCM three times, the organic layers were combined and dried over Na₂SO₄, solvent removed under reduced pressure. The crude product was purified by column chromatography, on silica gel, using ethyl acetate as the eluent system to afford a yellow oil, which solidified at low temperatures (2.4 g, 96%).

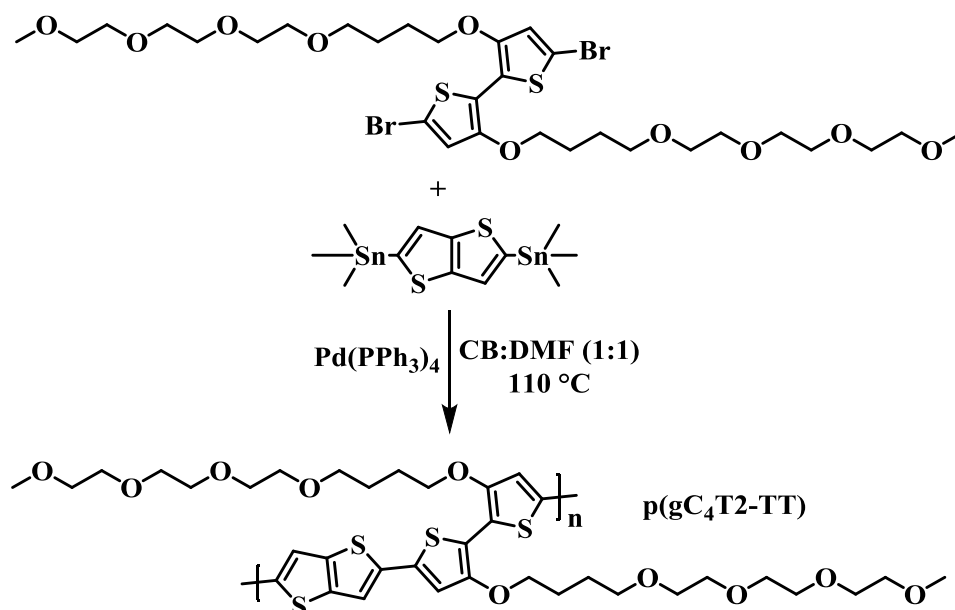
¹H NMR (400 MHz, Chloroform-*d*) δ 6.81 (s, 2H), 4.07 (t, *J* = 6.4 Hz, 4H), 3.72 – 3.56 (m, 20H), 3.59 – 3.50 (m, 8H), 3.37 (s, 6H), 1.96 – 1.84 (m, 4H), 1.79 (dq, *J* = 12.1, 6.0, 2.4 Hz, 4H).

¹³C NMR (101 MHz, Chloroform-*d*) δ 239.55, 223.91, 176.83, 171.13, 150.23, 119.03, 115.02, 109.85, 72.06, 71.95, 70.77, 70.64, 70.53, 70.11, 60.39, 59.03, 29.58, 26.41, 26.10, 26.05, -15.85.

Mass (MALDI-ToF): 792.7 [M+H]⁺ (calc. 792.1 C₃₀H₄₈Br₂O₁₀S₂).

CHAPTER FIVE SYNTHESIS & CHARACTERISATION



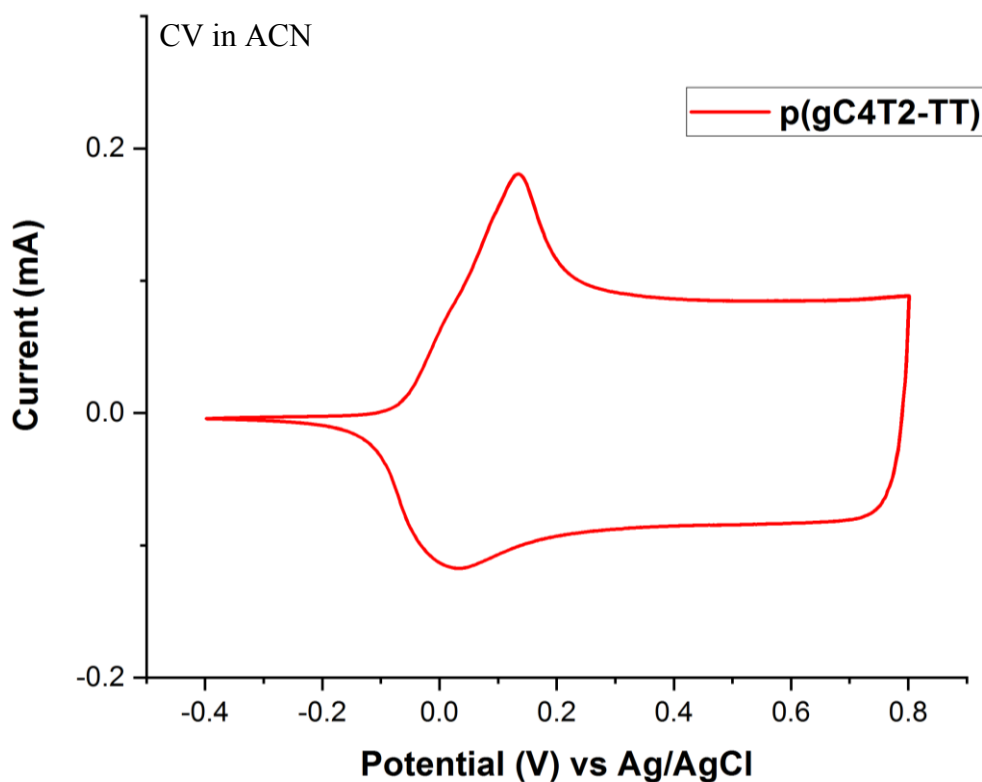
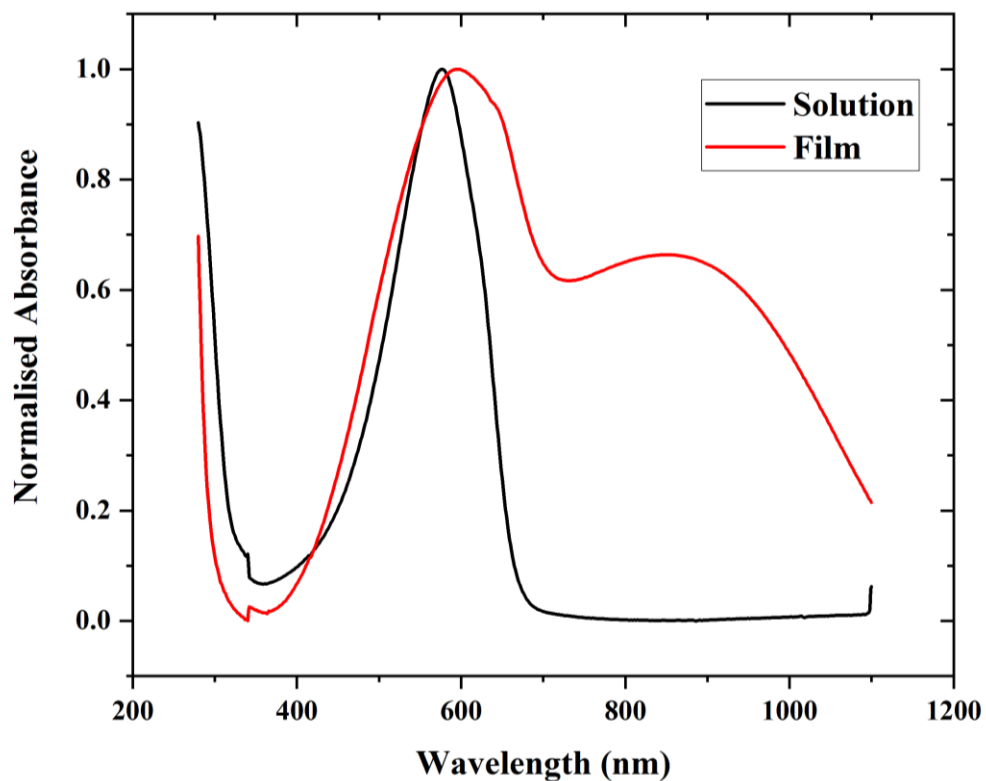
6.4.12 Synthesis of Polymer AM578 p(gC₄T2-TT)

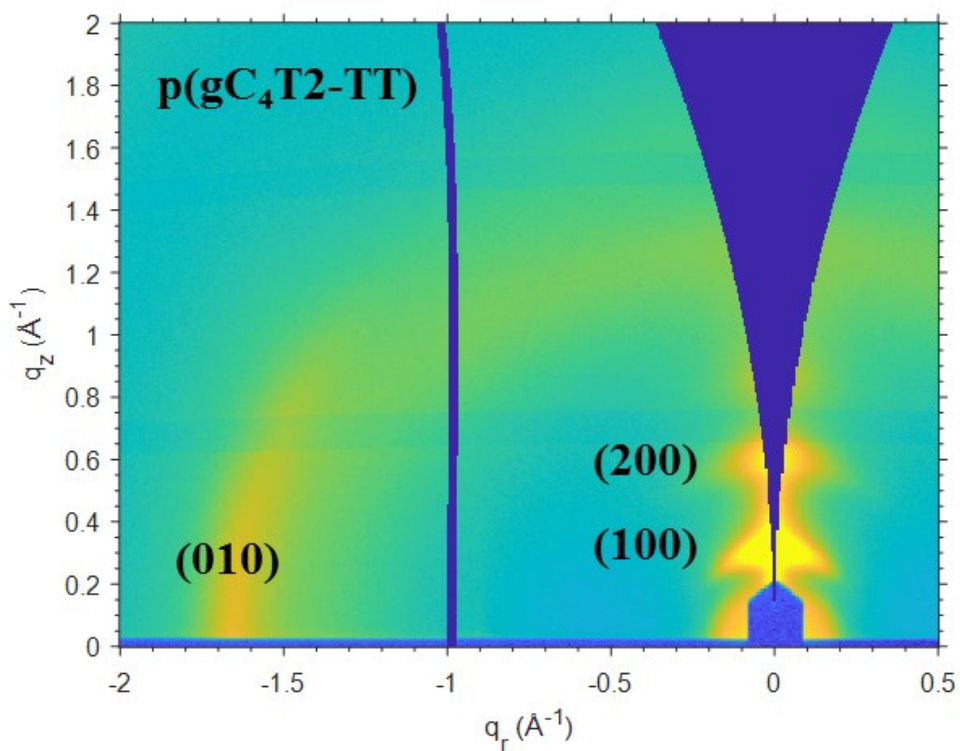
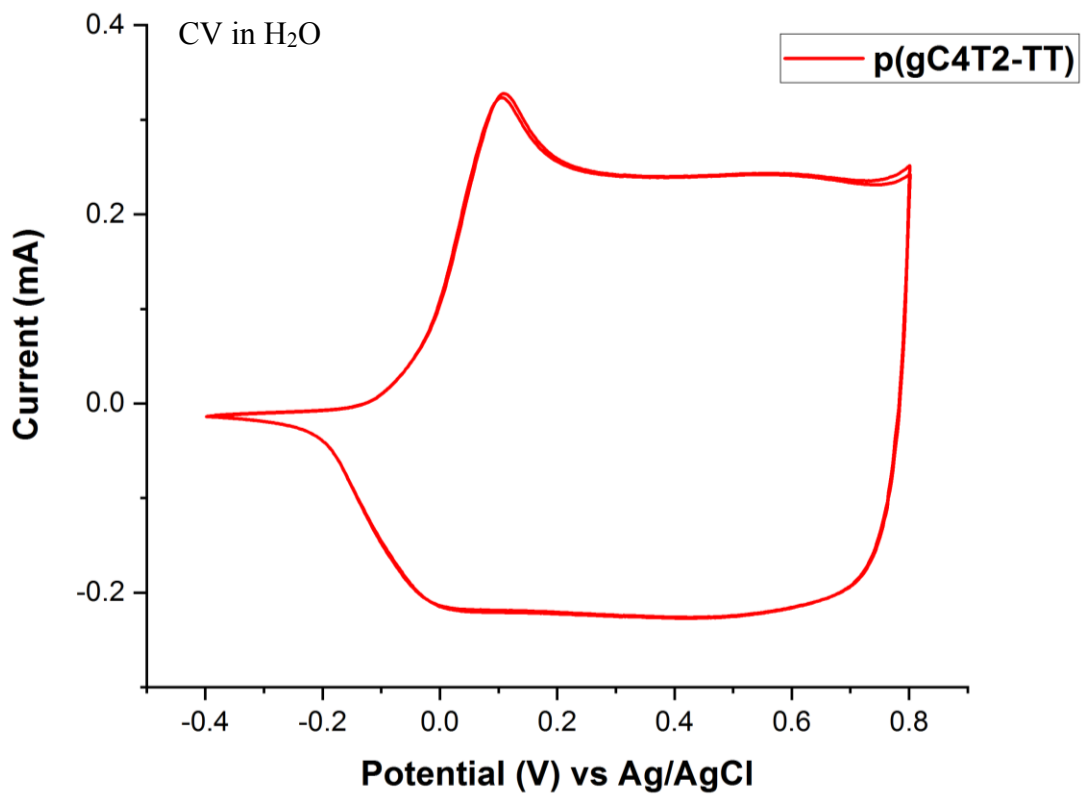
An oven dried 5 mL microwave vial was charged with 15,15'-((5,5'-dibromo-[2,2'-bithiophene]-3,3'-diyl)bis(oxy))bis(2,5,8,11-tetraoxapentadecane) (**6.4.11**) (200 mg, 0.25 mmol, 1.0 eq.), 2,5-bis(trimethylstannyl)thieno[3,2-*b*]thiophene (117.6 mg, 0.25 mmol, 1.0 eq.) and Pd(PPh₃)₄ (5.80 mg, 0.005 mmol, 0.02 eq.). Cap was sealed and the vial was purged with Nitrogen for 5 minutes prior to the addition of anhydrous DMF (1.70 mL) and anhydrous chlorobenzene (1.70 mL). The reaction was stirred overnight at 110 °C then cooled to room temperature, upon which the solution formed a purple gel. Crude polymer was precipitated into 100 mL methanol and subsequently filtered into a thimble. Purification was conducted via Soxhlet extraction, washing with hexane, methanol, acetone, ethyl acetate and chloroform (in that order). The chloroform fraction was collected, solvent removed under reduced pressure and re-precipitated into 100 mL methanol, filtered to yield a blue metallic film (126 mg, 63%).

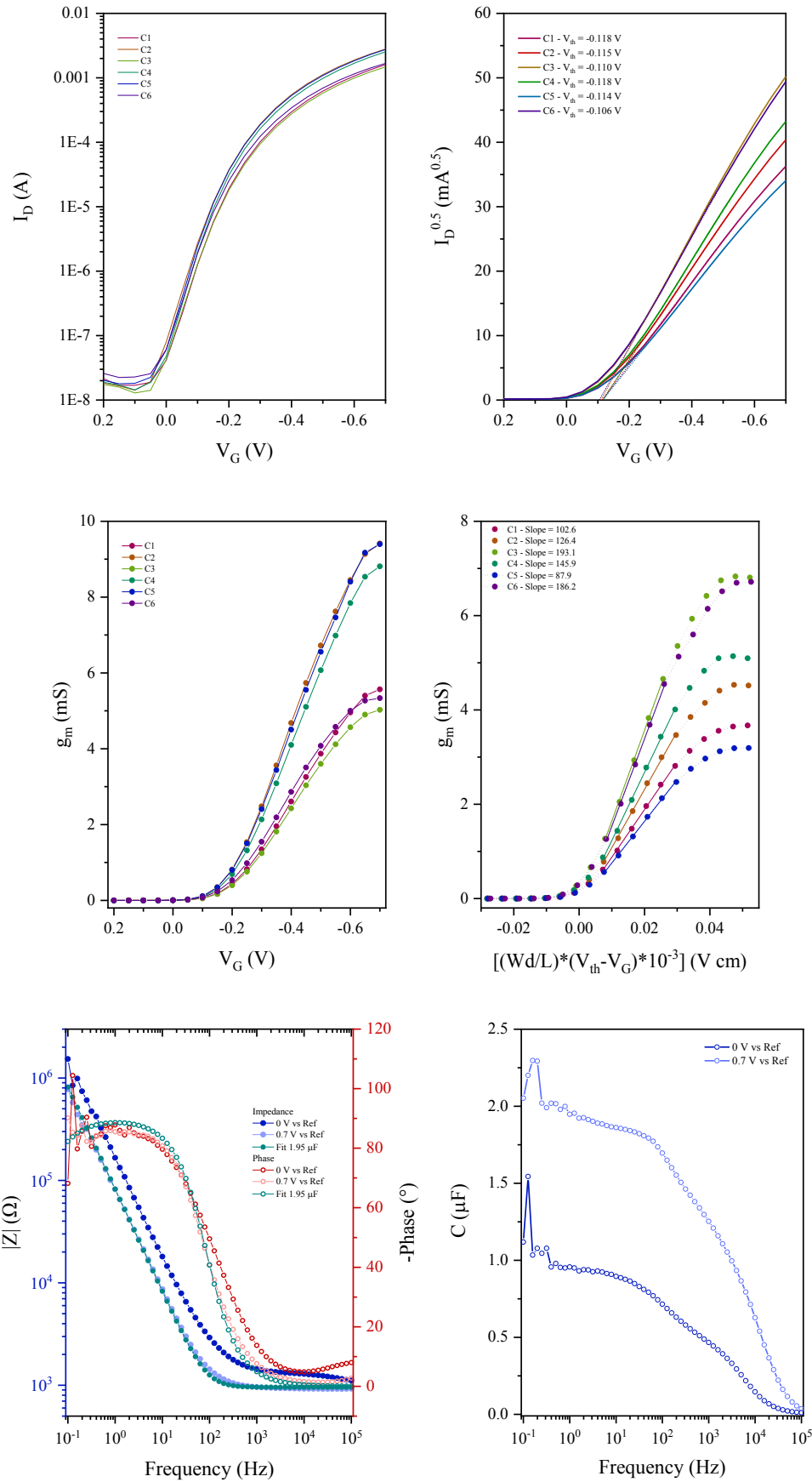
$\lambda_{\text{MAX}}^{\text{a}}$ (nm)	λ_{ONSET} (nm)	$E_{\text{opt}}^{\text{b}}$ (eV)	IP [CV] (eV)	EA ^c (eV)	E_{onset} [ACN](V)	E_{onset} [H ₂ O](V)	M_{n} (kDa)	M_{w} (kDa)	PDI
577	671	1.85	4.29	2.44	-0.10	-0.16	10.0	21.4	2.14

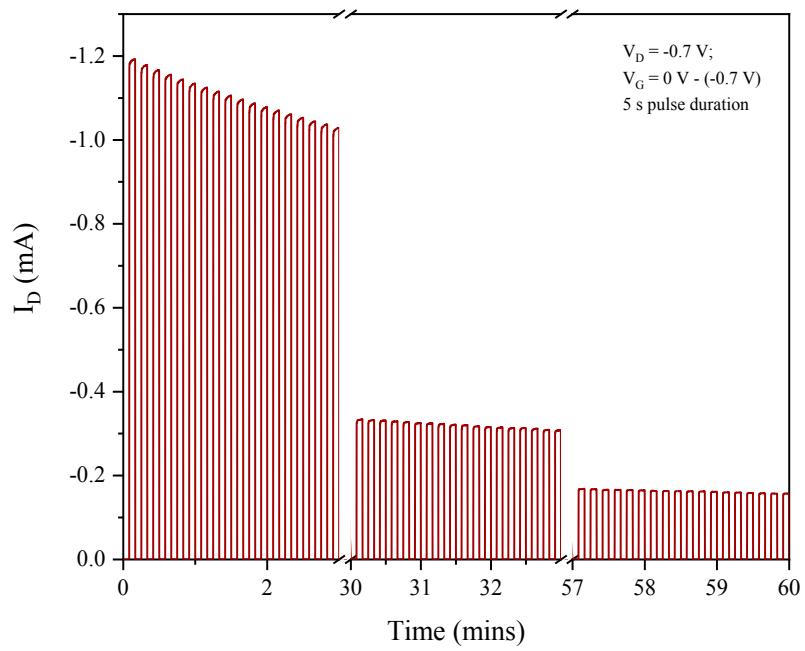
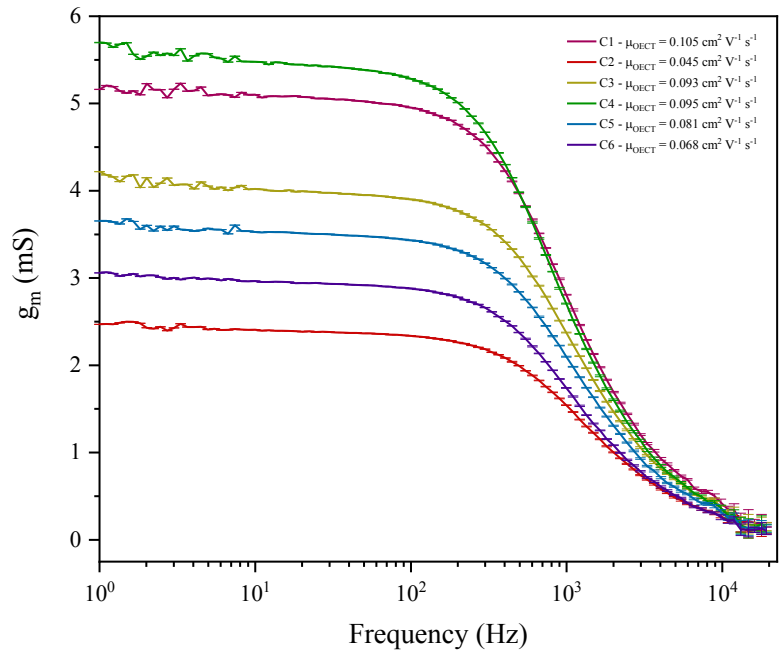
^a λ is the peak of the first low energy absorption band of the polymers

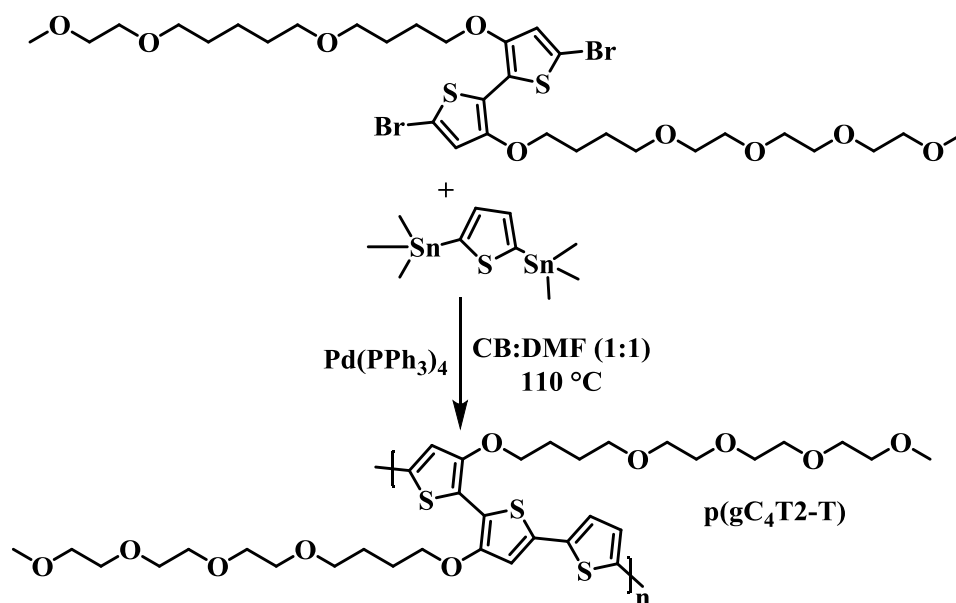
^b E_{opt} estimated optical gap using onset of the thin-film absorption spectra $E_{\text{GAP}} = 1240/\lambda_{\text{ONSET}}$
^cEA crudely estimated by subtraction of the UV-Vis absorption onset from IP ($EA = IP - E_{\text{opt}}$),
a procedure that neglects the exciton binding energy









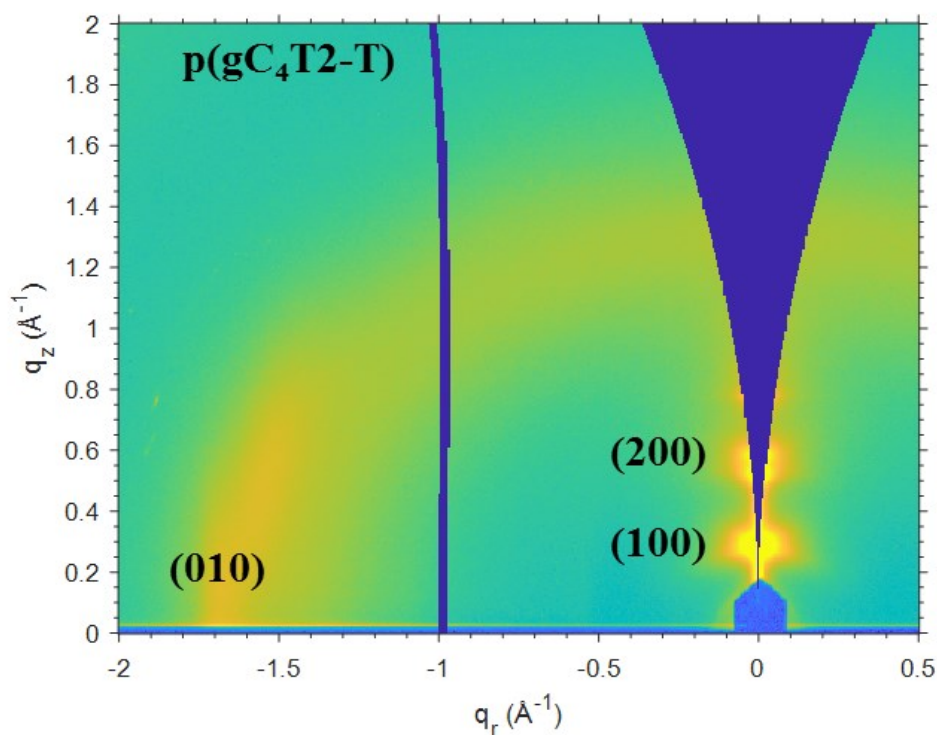
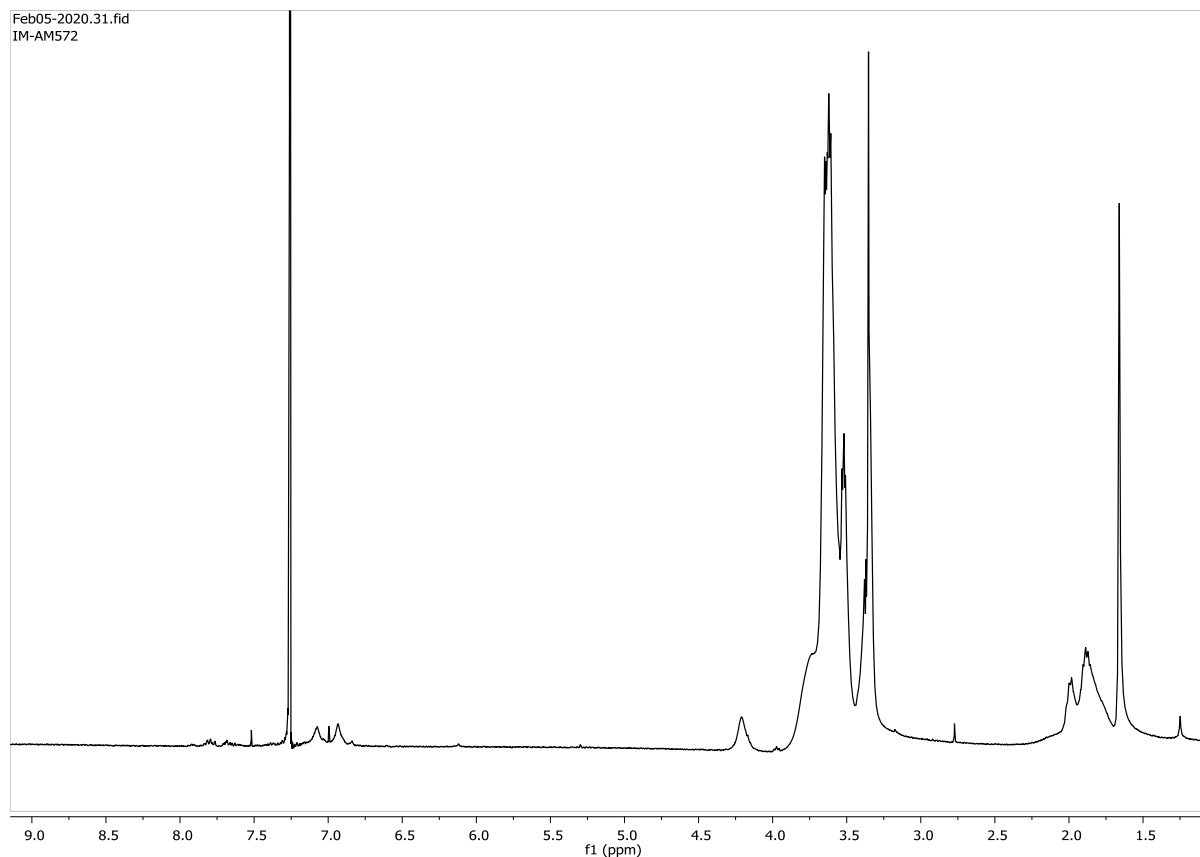
6.4.13 Synthesis of Polymer AM572 p(gC₄T2-T)

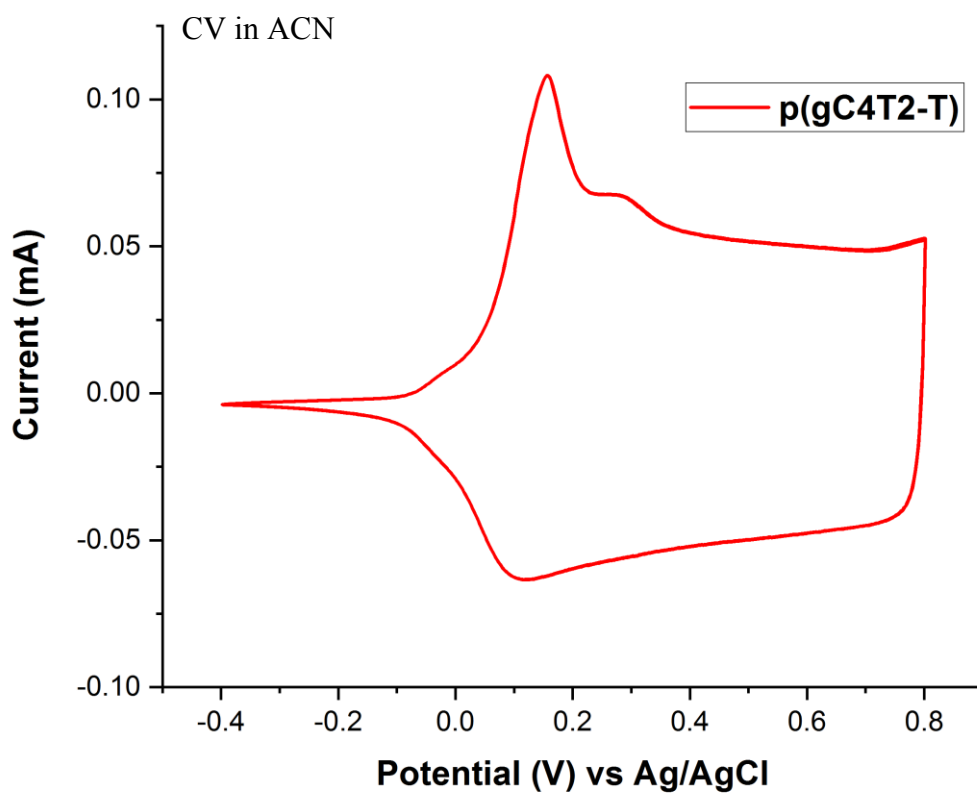
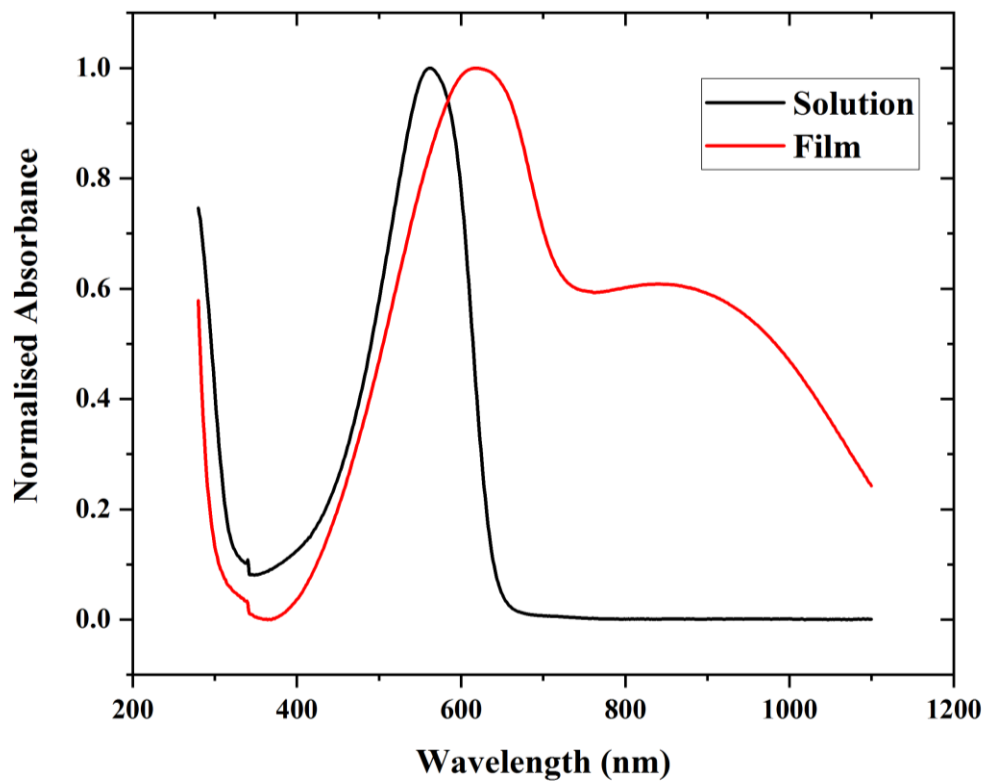
An oven dried 5 mL microwave vial was charged with 15,15'-((5,5'-dibromo-[2,2'-bithiophene]-3,3'-diyl)bis(oxy))bis(2,5,8,11-tetraoxapentadecane) (**6.4.11**) (200 mg, 0.25 mmol, 1.0 eq.), 2,5-bis(trimethylstannyl)thiophene (103.4 mg, 0.25 mmol, 1.0 eq.) and Pd(PPh₃)₄ (5.80 mg, 0.005 mmol, 0.02 eq.). Cap was sealed and the vial was purged with Nitrogen for 5 minutes prior to the addition of anhydrous DMF (1.70 mL) and anhydrous chlorobenzene (1.70 mL). The reaction was stirred overnight at 110 °C then cooled to room temperature, upon which the solution formed a purple gel. Crude polymer was precipitated into 100 mL methanol and subsequently filtered into a thimble. Purification was conducted via Soxhlet extraction, washing with hexane, methanol, acetone, ethyl acetate and chloroform (in that order). The chloroform fraction was collected, solvent removed under reduced pressure and re-precipitated into 100 mL methanol, filtered to yield a blue metallic film (101 mg, 51%).

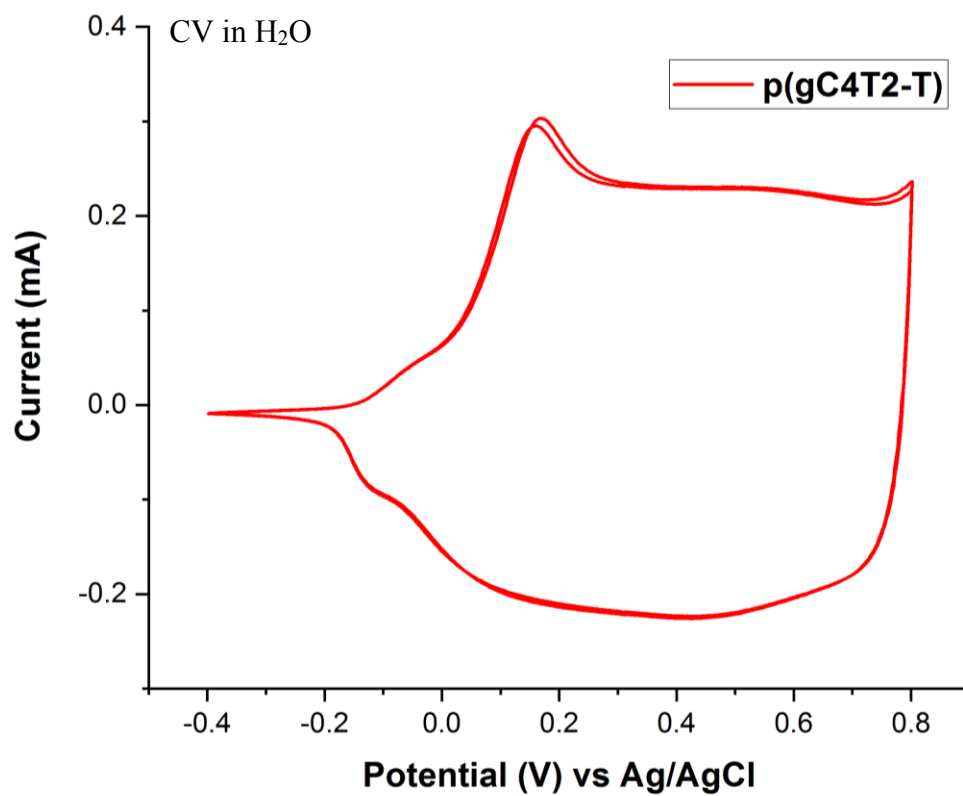
λ_{MAX}^a (nm)	λ_{ONSET} (nm)	E_{opt}^b (eV)	IP [CV] (eV)	EA ^c (eV)	E_{onset} [ACN](V)	E_{onset} [H ₂ O](V)	M_n (kDa)	M_w (kDa)	PDI
562	645	1.92	4.28	2.36	-0.10	-0.15	19.9	43.7	2.20

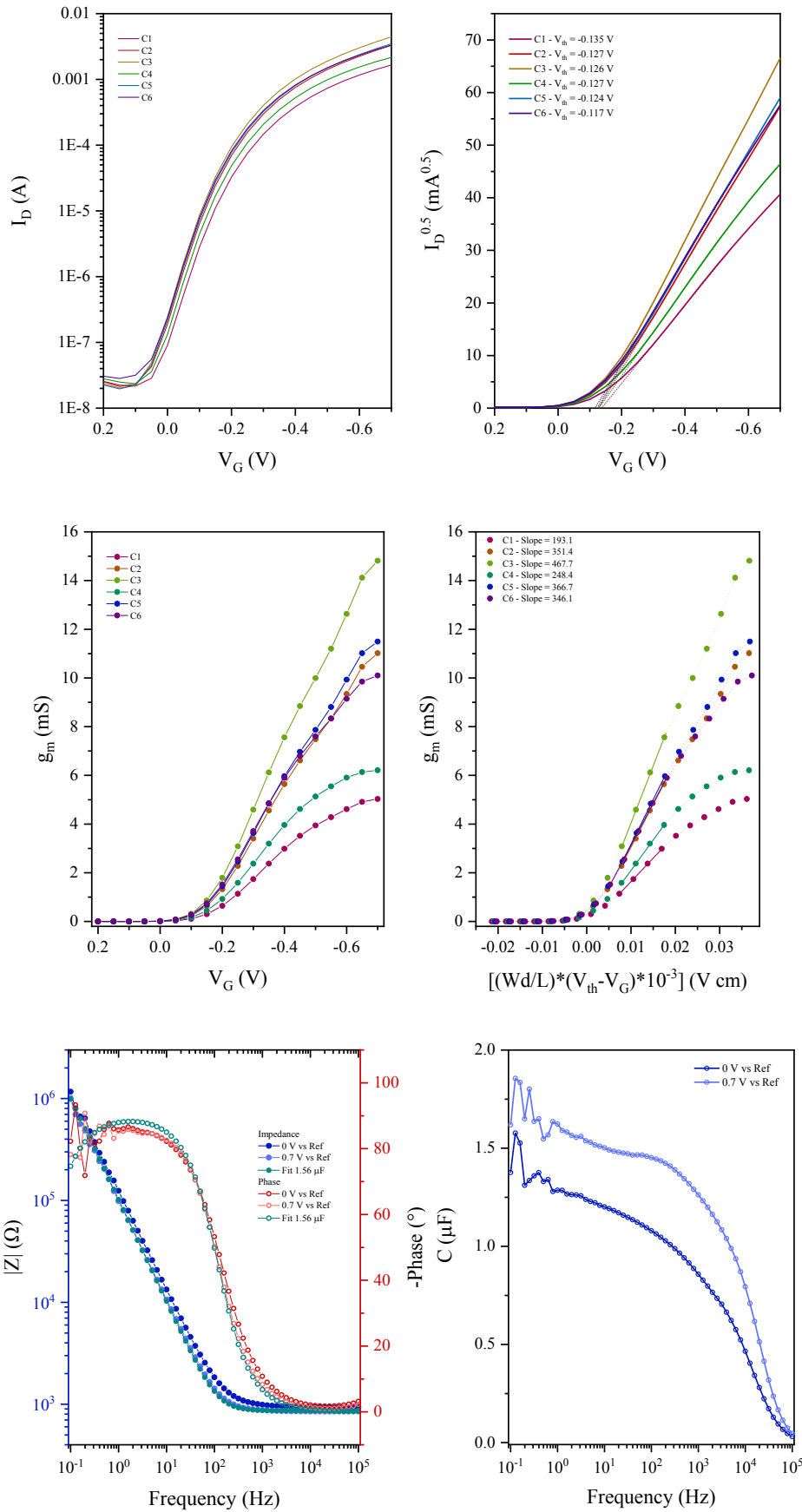
^a λ is the peak of the first low energy absorption band of the polymers

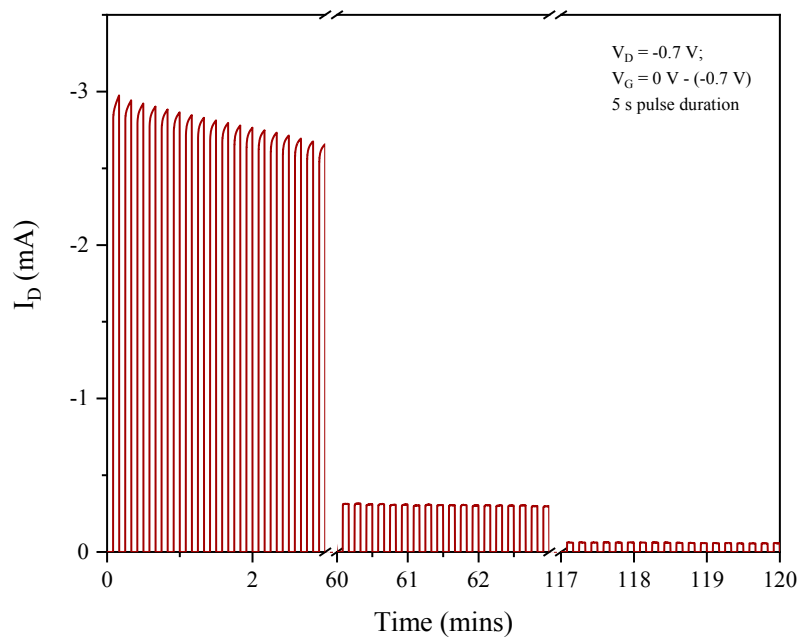
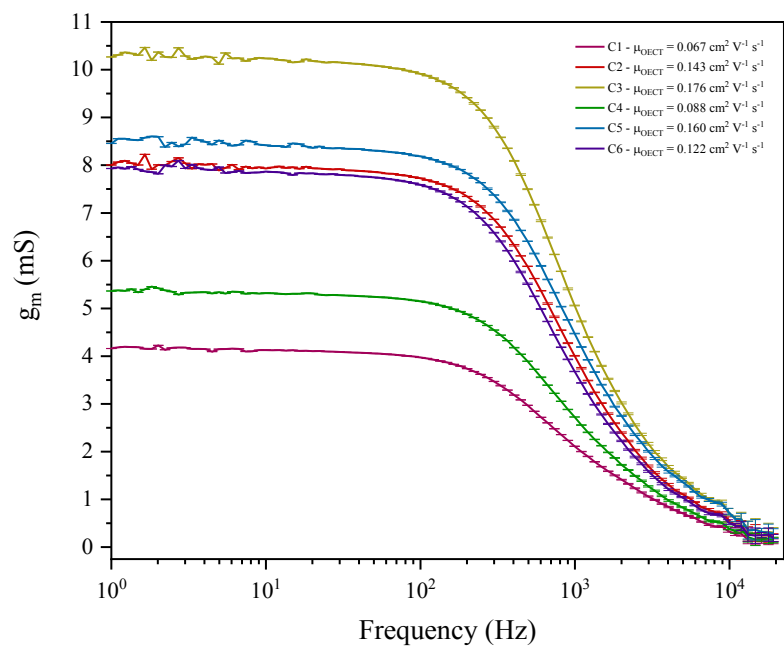
^b E_{opt} estimated optical gap using onset of the thin-film absorption spectra $E_{\text{GAP}} = 1240/\lambda_{\text{ONSET}}$
^c EA crudely estimated by subtraction of the UV-Vis absorption onset from IP ($EA = IP - E_{\text{opt}}$),
a procedure that neglects the exciton binding energy



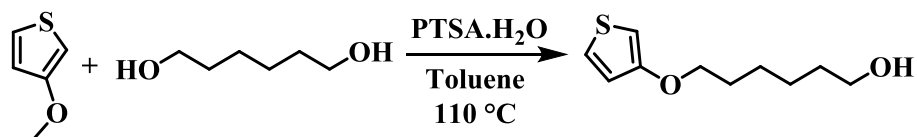








6.4.14 Synthesis of 6-(thiophen-3-yloxy)hexan-1-ol

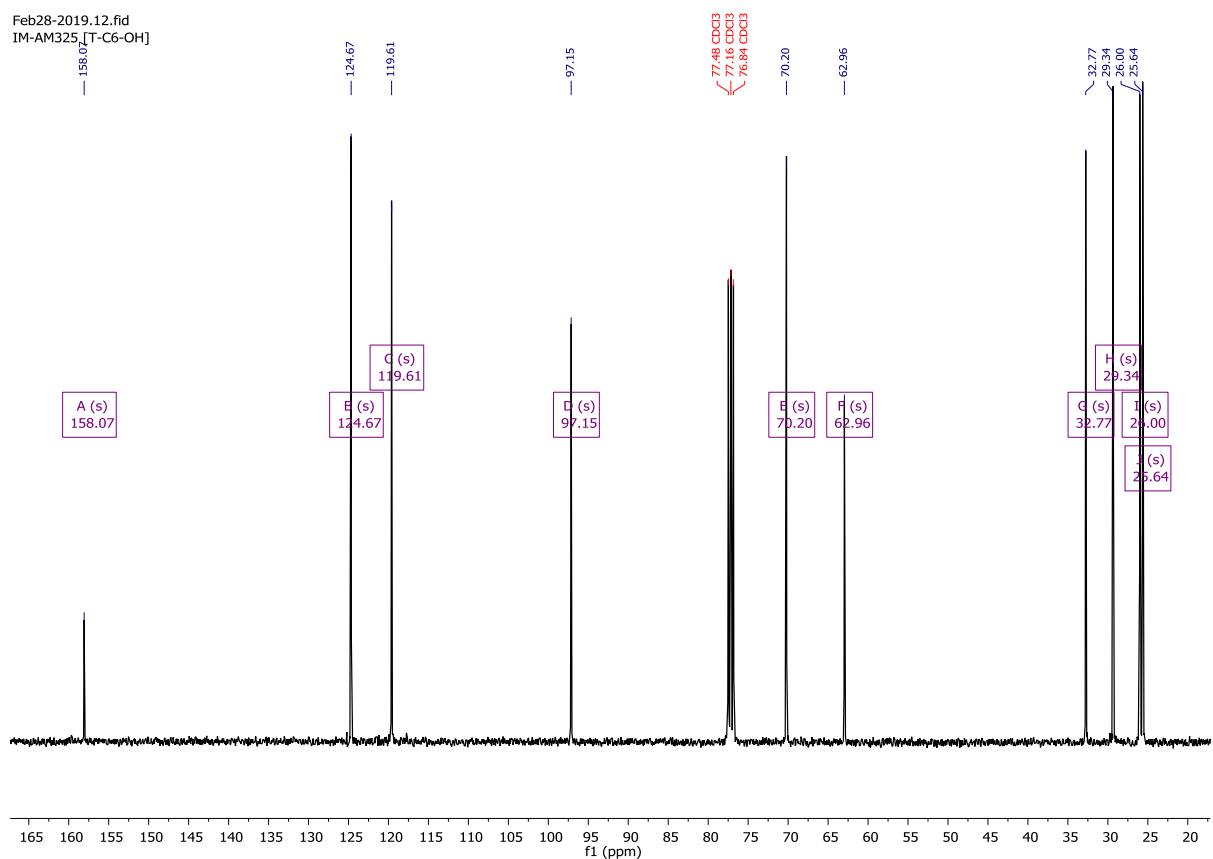
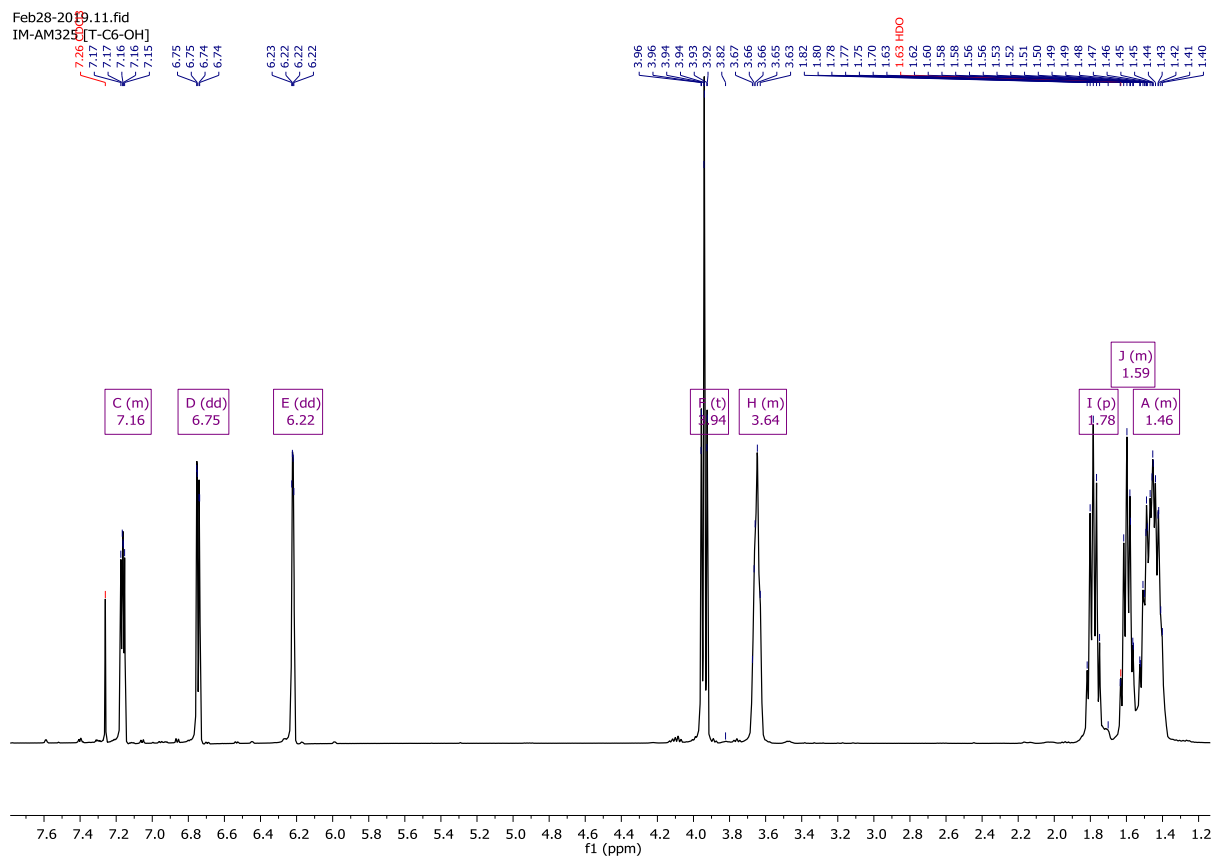


1,6-Hexanediol (33.6 g, 284.3 mmol, 1.5 eq.) was dissolved in 200 mL of toluene, *p*-toluenesulfonic acid monohydrate (4.15g, 18.9 mmol, 0.1 eq.) was added in a single portion. The mixture was heated to reflux (120 °C) prior to the addition of 3-methoxythiophene (25 g, 189.6 mmol, 1.0 eq.) and left to stir for 90 minutes. Upon cooling to room temperature, the reaction was poured into water and the aqueous layer was extracted three times with DCM. The organic layers were combined and dried over MgSO₄; solvent was removed under reduced pressure. The crude material was purified by column chromatography, on silica gel, using DCM as the eluent system. Product fractions were combined to afford the title compound (19.3 g, 44%).

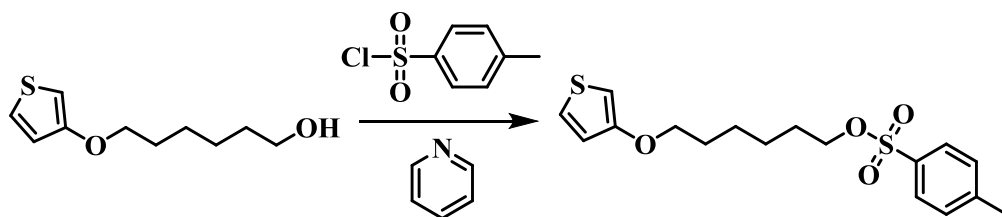
¹H NMR (400 MHz, Chloroform-*d*) δ 7.20 – 7.13 (m, 1H), 6.75 (dd, *J* = 5.2, 1.4 Hz, 1H), 6.22 (dd, *J* = 3.2, 1.5 Hz, 1H), 3.94 (t, *J* = 6.5 Hz, 2H), 3.70 – 3.60 (m, 2H), 1.78 (p, *J* = 6.7 Hz, 2H), 1.66 – 1.54 (m, 2H), 1.57 – 1.36 (m, 4H).

¹³C NMR (101 MHz, Chloroform-*d*) δ 158.07, 124.67, 119.61, 97.15, 70.20, 62.96, 32.77, 29.34, 26.00, 25.64.

CHAPTER SIX – EXPERIMENTAL

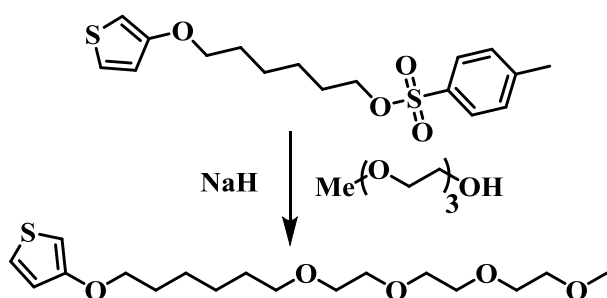


6.4.15 Synthesis of 6-(thiophen-3-yloxy)hexyl 4-methylbenzenesulfonate



6-(thiophen-3-yloxy)hexan-1-ol (**6.4.15**) (19.26 g, 96.2 mmol, 1.0 eq.) was dissolved in 30 mL pyridine and cooled to 0 °C. 4-Toluenesulfonyl chloride (22.0 g, 115.4 mmol, 1.2 eq.) was added, in a single portion, the reaction was stirred vigorously for 20 minutes, during which the solution turned an intense yellow colour. The reaction was then stored in the refrigerator overnight, afterwards 30 mL 2M HCl was added and the solution stirred rapidly for 30 minutes. The mixture was poured into water, the aqueous phase was extracted with DCM three times, the organic layers were combined and dried over Na₂SO₄ prior to removing the solvent under reduced pressure. The product was dried under vacuum and used in the next step without further purification. (34 g, 99%).

6.4.16 Synthesis of 17-(thiophen-3-yloxy)-2,5,8,11-tetraoxaheptadecane

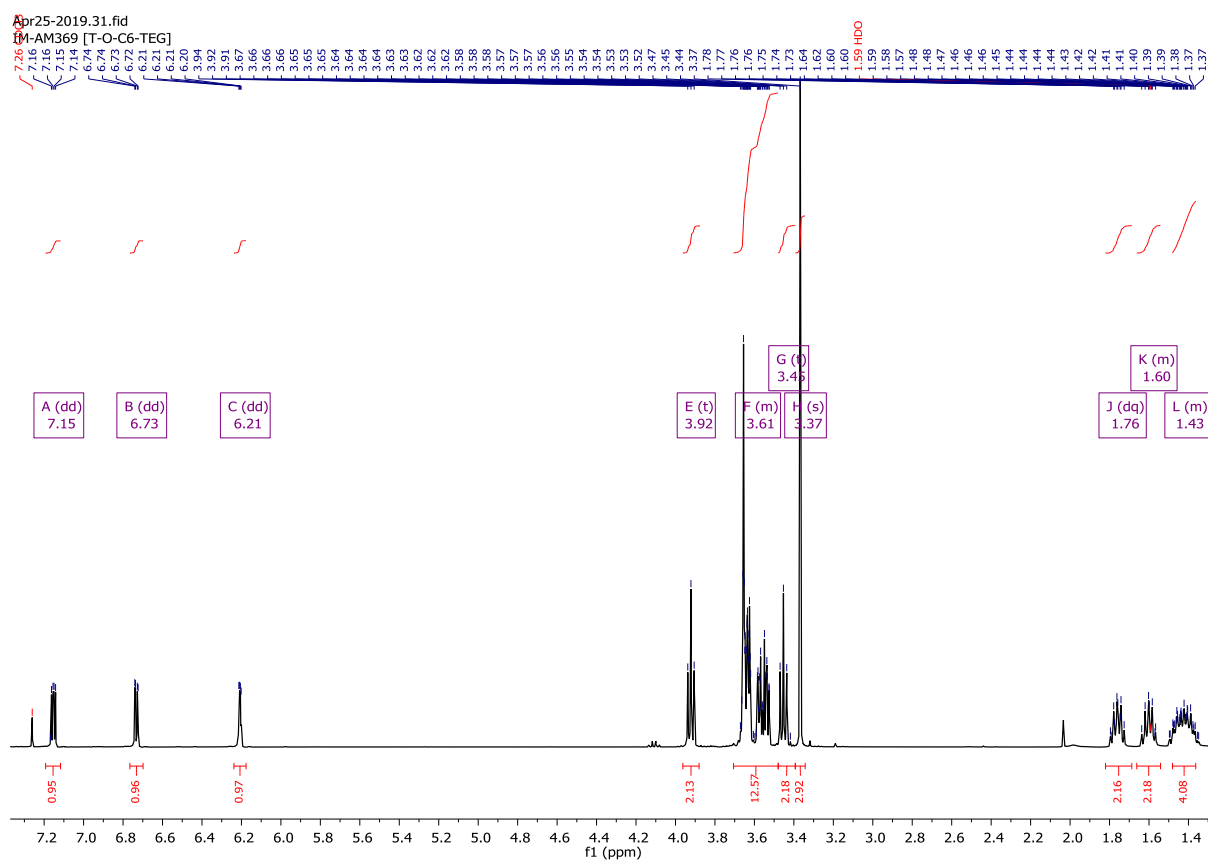


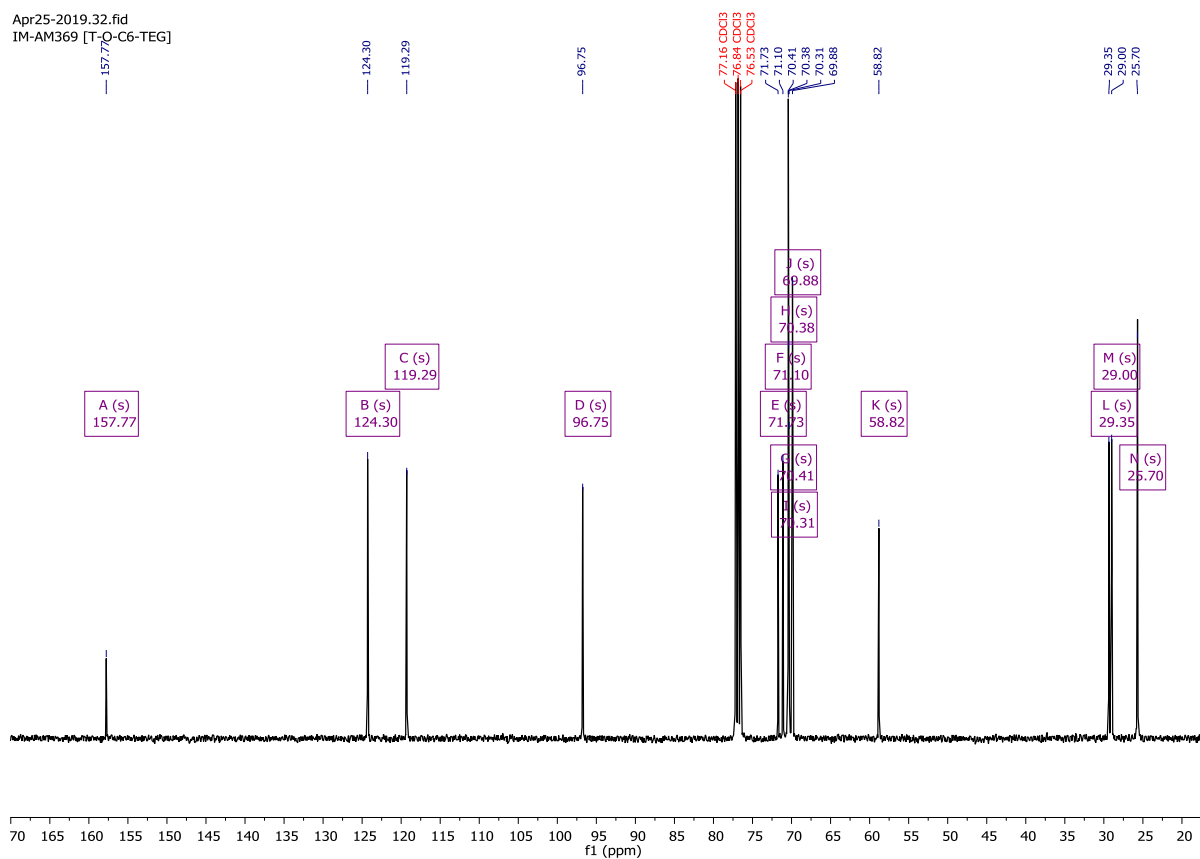
An oven dried 2-neck 250 mL RBF was charged with sodium hydride (60% in mineral oil) (11.51 g, 287.7 mmol, 3.0 eq.), dissolved in anhydrous THF (50 mL) cooled to 0 °C, under a Nitrogen atmosphere. Triethylene glycol monomethyl ether (46.1 mL, 287.7 mmol, 3.0 eq.) was added dropwise and the mixture was stirred for 30 minutes until effervescence ceased. 6-

(thiophen-3-yloxy)hexyl 4-methylbenzenesulfonate (**6.4.15**) (34 g, 95.9 mmol, 1.0 eq.) dissolved in 50 mL THF was added dropwise, the reaction was stirred overnight. The mixture was then poured into water, the aqueous layer was extracted three times with DCM, the organic layers were combined and dried over MgSO₄. The crude residue was purified via column chromatography, on silica gel, using hexane:ethyl acetate (1:1) (v/v) (R_f=0.2) as the eluent system, product fractions were consolidated to afford a yellow oil (18.45 g, 55%).

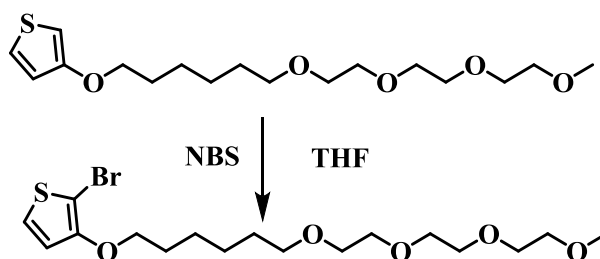
¹H NMR (400 MHz, Chloroform-*d*) δ 7.15 (dd, *J* = 5.2, 3.1 Hz, 1H), 6.73 (dd, *J* = 5.2, 1.5 Hz, 1H), 6.21 (dd, *J* = 3.1, 1.5 Hz, 1H), 3.92 (t, *J* = 6.5 Hz, 2H), 3.71 – 3.48 (m, 12H), 3.45 (t, *J* = 6.7 Hz, 2H), 3.37 (s, 3H), 1.76 (dq, *J* = 8.1, 6.5 Hz, 2H), 1.66 – 1.54 (m, 2H), 1.52 – 1.32 (m, 4H).

¹³C NMR (101 MHz, Chloroform-*d*) δ 157.77, 124.30, 119.29, 96.75, 71.73, 71.10, 70.41, 70.38, 70.31, 69.88, 58.82, 29.35, 29.00, 25.70.





6.4.17 Synthesis of 17-((2-bromothiophen-3-yl)oxy)-2,5,8,11-tetraoxaheptadecane

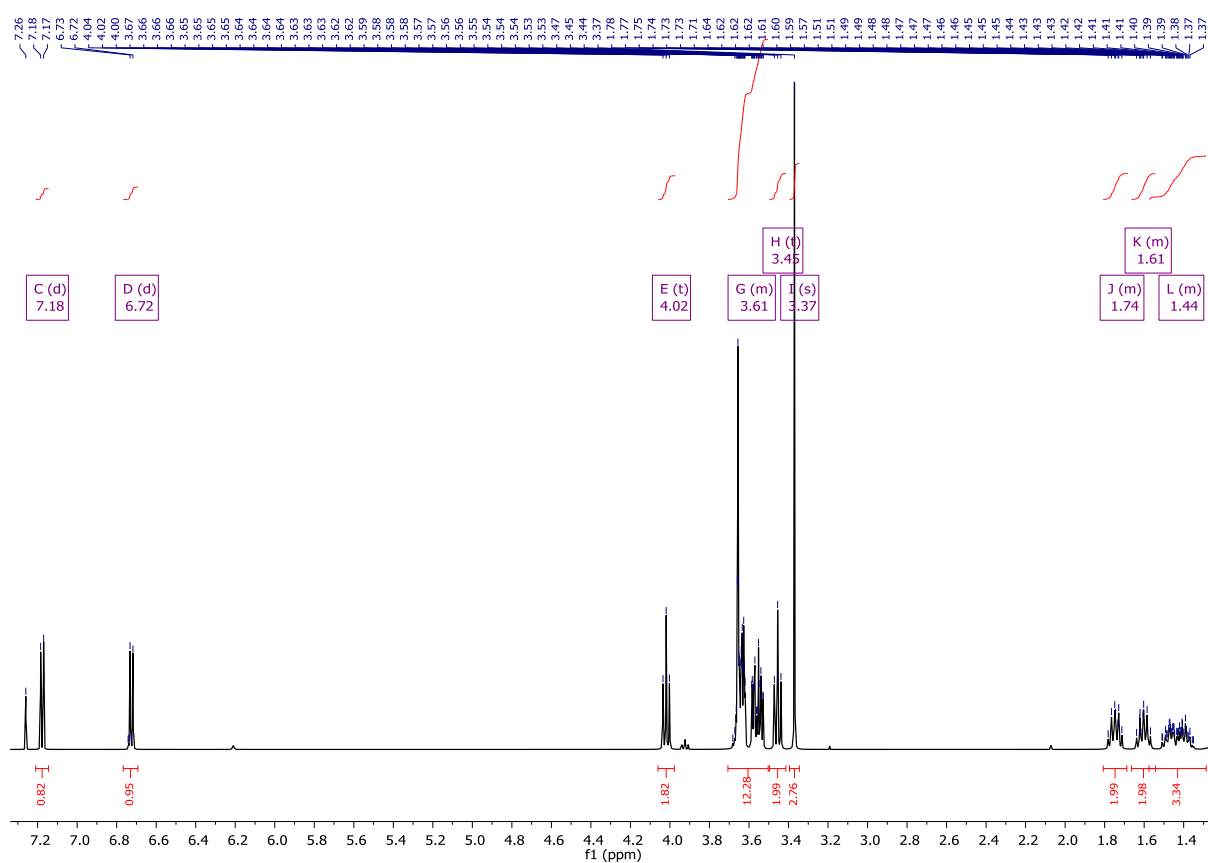


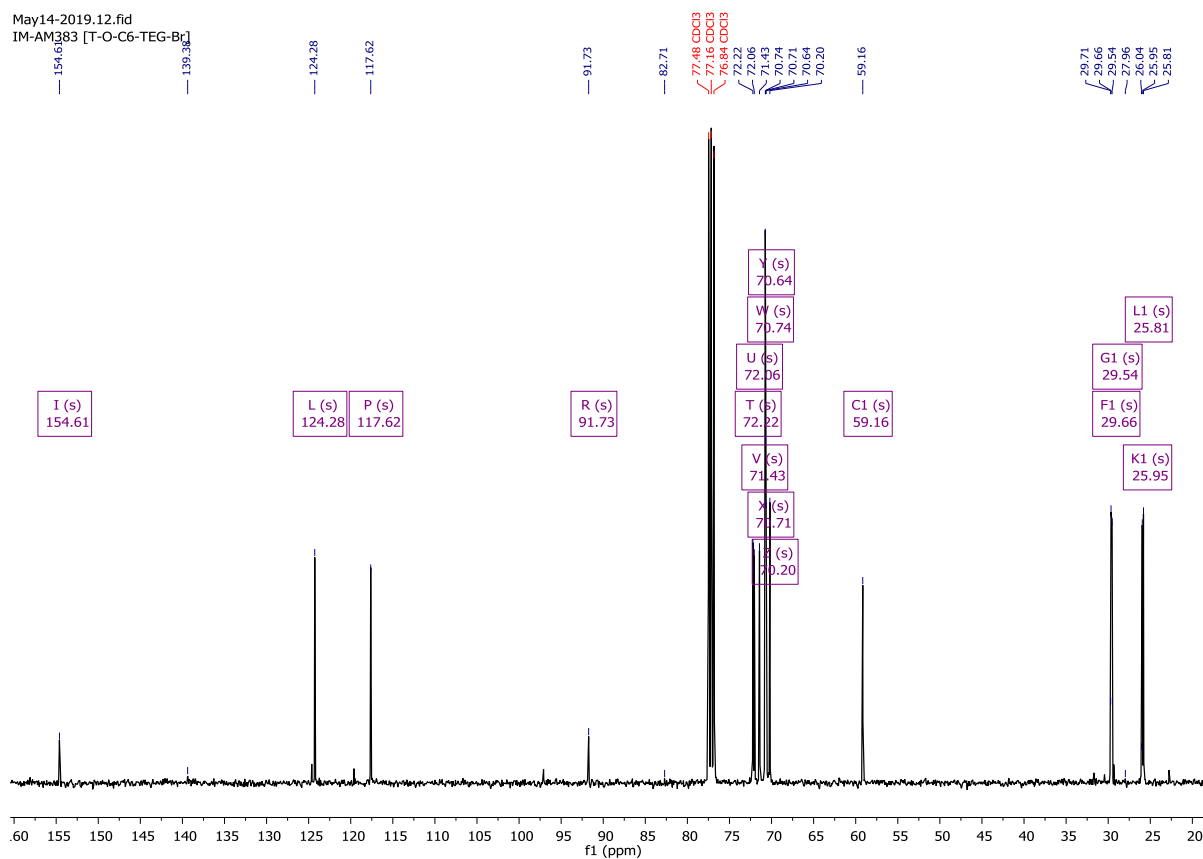
17-(thiophen-3-yloxy)-2,5,8,11-tetraoxaheptadecane (**6.4.16**) (3.0 g, 8.66 mmol, 1.0 eq.) was added to an oven dried 250 mL 2-neck RBF, dissolved in 15 mL dry THF. Cooled to 0 °C, in the dark, prior to the portion wise addition of N-bromosuccinimide (4x394 mg, 8.83 mmol, 1.02 eq.) leaving approximately 4 minutes between each addition. After stirring for 60 minutes the reaction was poured into water, washed with saturated sodium bicarbonate solution and quenched with sodium metabisulphite. The aqueous phase was extracted three times with DCM, the organic layers were combined, dried over Na₂SO₄ and solvent removed under

reduced pressure. The crude was purified via column chromatography, on silica gel, using hexane:ethyl acetate (1:1) (v/v) as the eluent system. Product fractions were consolidated to yield an orange oil (3.37 g, 91%).

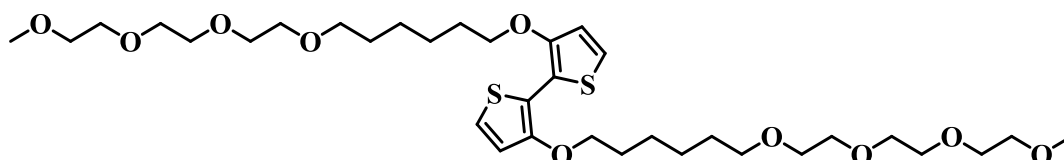
^1H NMR (400 MHz, Chloroform-*d*) δ 7.18 (d, J = 6.0 Hz, 1H), 7.18 – 7.12 (m, 1H), 6.72 (d, J = 6.0 Hz, 1H), 4.02 (t, J = 6.5 Hz, 2H), 3.71 – 3.50 (m, 12H), 3.45 (t, J = 6.7 Hz, 2H), 3.37 (s, 3H), 1.82 – 1.69 (m, 2H), 1.66 – 1.54 (m, 2H), 1.53 – 1.33 (m, 4H).

^{13}C NMR (101 MHz, Chloroform-*d*) δ 154.61, 124.28, 117.62, 91.73, 72.22, 72.06, 71.43, 70.74, 70.71, 70.64, 70.20, 59.16, 29.66, 29.54, 25.95, 25.81.





6.4.18 Synthesis of 3,3'-bis((2,5,8,11-tetraoxaheptadecan-17-yl)oxy)-2,2'-bithiophene

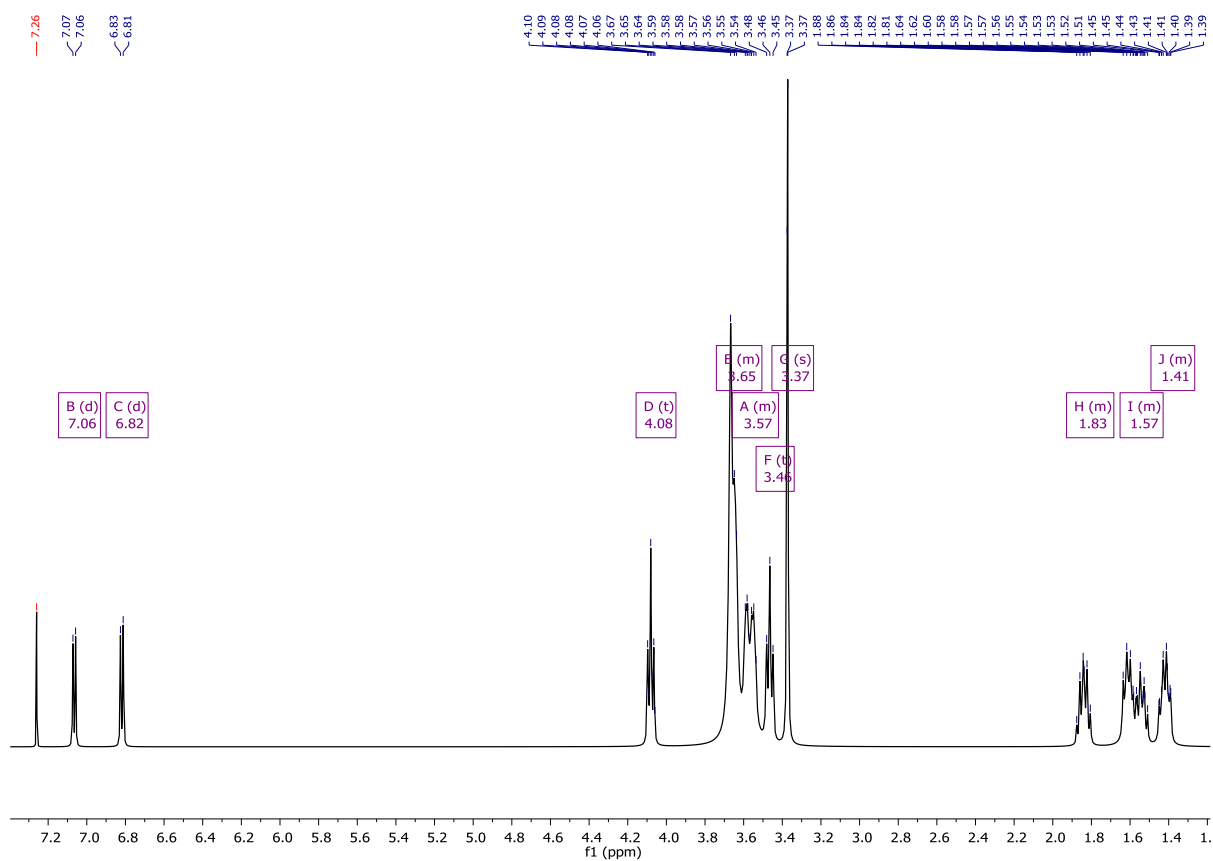


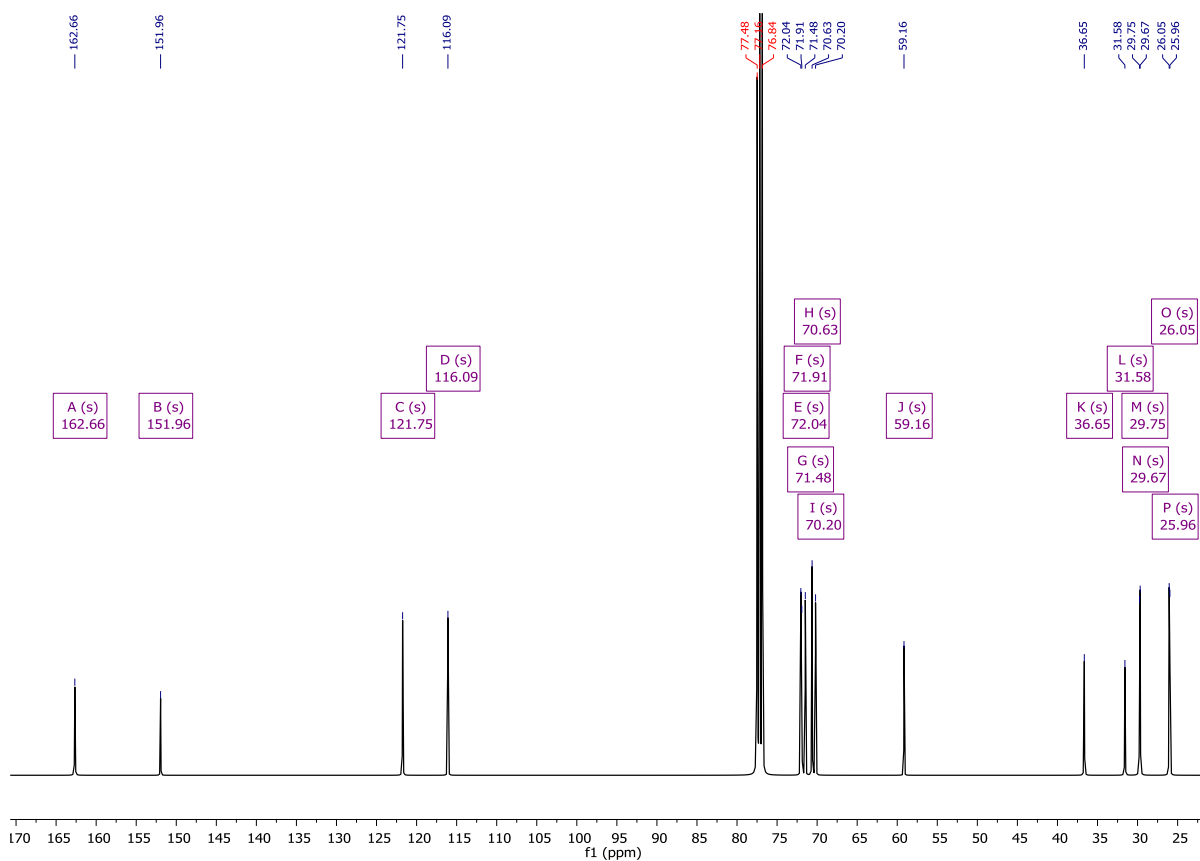
17-((2-bromothiophen-3-yl)oxy)-2,5,8,11-tetraoxaheptadecane (**6.4.17**) (2.2 g, 5.17 mmol, 1.0 eq.) was added to an oven dried 2-neck 100 mL RBF and dissolved in a 1:1 mixture of anhydrous chlorobenzene (12 mL) and dry DMF (12 mL), under a Nitrogen atmosphere. Bis(tributyltin) (1.30 mL, 1.29 mmol, 0.5 eq.) was added dropwise, followed by the addition of Pd(PPh₃)₄ (299 mg, 0.129 mmol, 0.05 eq.). The reaction was stirred for 48 hours at 100 °C, upon cooling to room temperature the mixture was passed through a short silica plug, eluting with ethyl acetate. The solvent was removed under reduced pressure and the crude was purified by column chromatography, on silica gel, using ethyl acetate as the eluent system. Product

fractions were consolidated to yield a yellow oil which solidified at reduced temperature (820 mg, 46%).

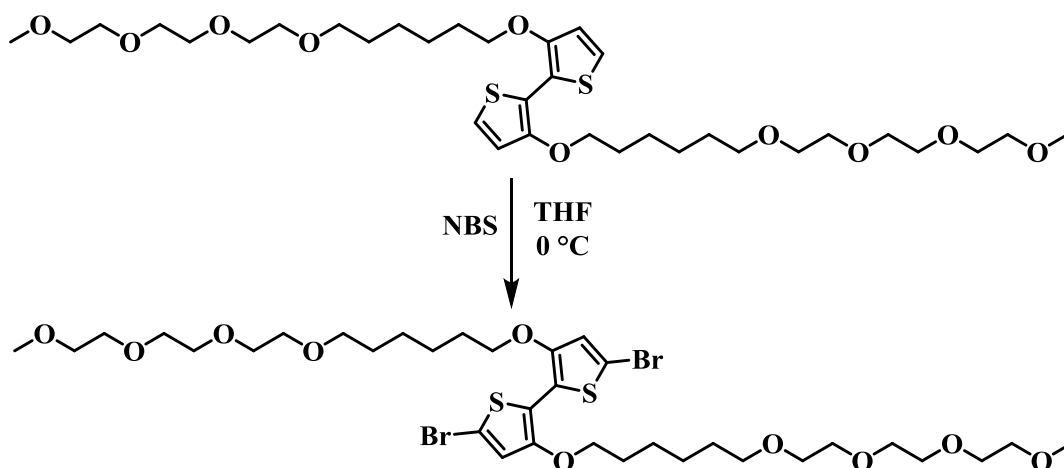
^1H NMR (400 MHz, Chloroform-*d*) δ 7.06 (d, $J = 5.5$ Hz, 2H), 6.82 (d, $J = 5.7$ Hz, 2H), 4.08 (t, $J = 6.4$ Hz, 4H), 3.69 – 3.57 (m, 16H), 3.61 – 3.51 (m, 8H), 3.46 (t, $J = 6.6$ Hz, 4H), 3.37 (s, 6H), 1.90 – 1.78 (m, 4H), 1.66 – 1.48 (m, 8H), 1.48 – 1.36 (m, 4H).

^{13}C NMR (101 MHz, Chloroform-*d*) δ 162.66, 151.96, 121.75, 116.09, 72.04, 71.91, 71.48, 70.63, 70.20, 59.16, 36.65, 31.58, 29.75, 29.67, 26.05, 25.96.





6.4.19 17,17'-((5,5'-dibromo-[2,2'-bithiophene]-3,3'-diyl)bis(oxy))bis(2,5,8,11-tetraoxaheptadecane)



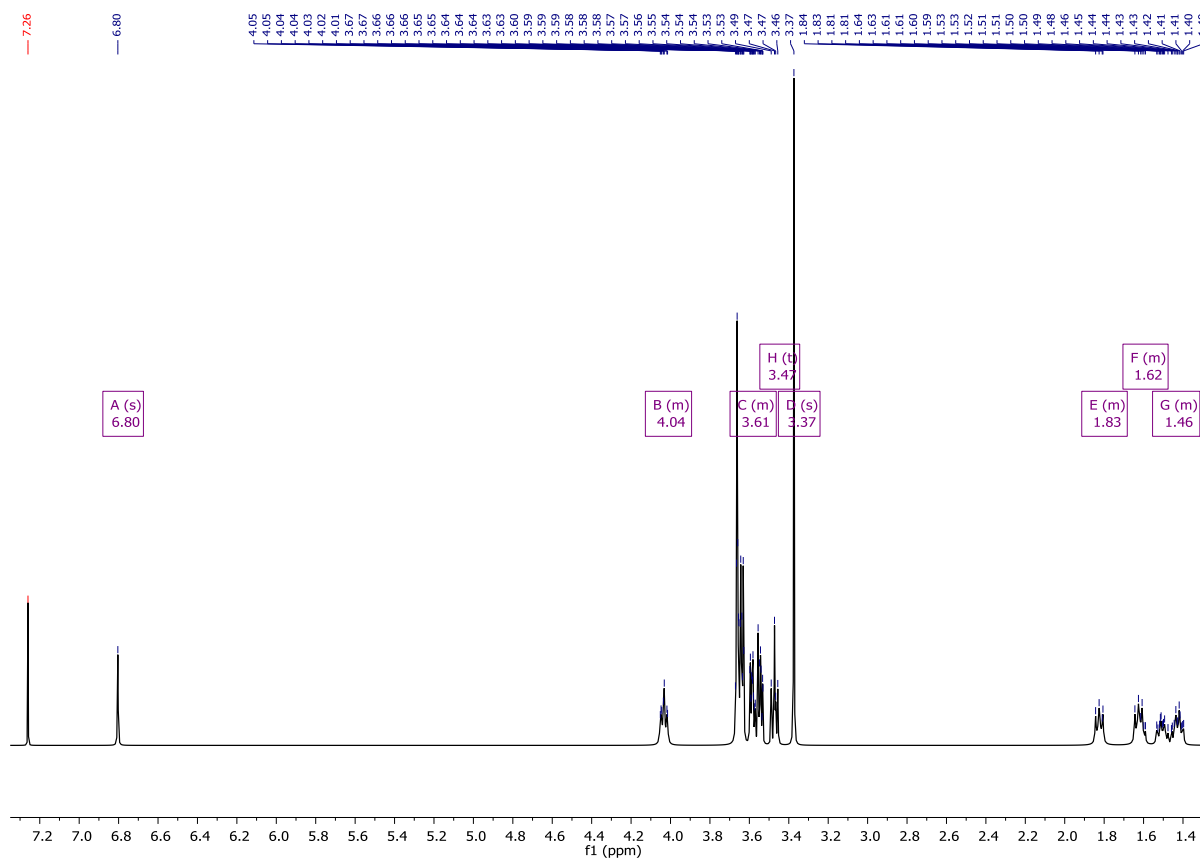
3,3'-bis((2,5,8,11-tetraoxaheptadecan-17-yl)oxy)-2,2'-bithiophene (**6.4.18**) (600 mg, 0.87 mmol, 1.0 eq.) was dissolved in 40 mL anhydrous THF, cooled to 0 °C under a Nitrogen atmosphere. The reaction was covered and kept in the dark, N-bromosuccinimide (316.8 mg,

1.78 mmol, 2.05 eq.) was subsequently added in four equal portions, leaving 4 minutes between each addition. After stirring for 30 minutes the reaction was poured into water, washed with saturated sodium bicarbonate solution and quenched with sodium metabisulphite. The aqueous layer was extracted three times with DCM, the organic phases were consolidated and dried over Na₂SO₄. The crude material was purified by column chromatography, on silica gel, using ethyl acetate as the eluent to afford a yellow oil, which solidified at low temperatures (700 mg, 95%).

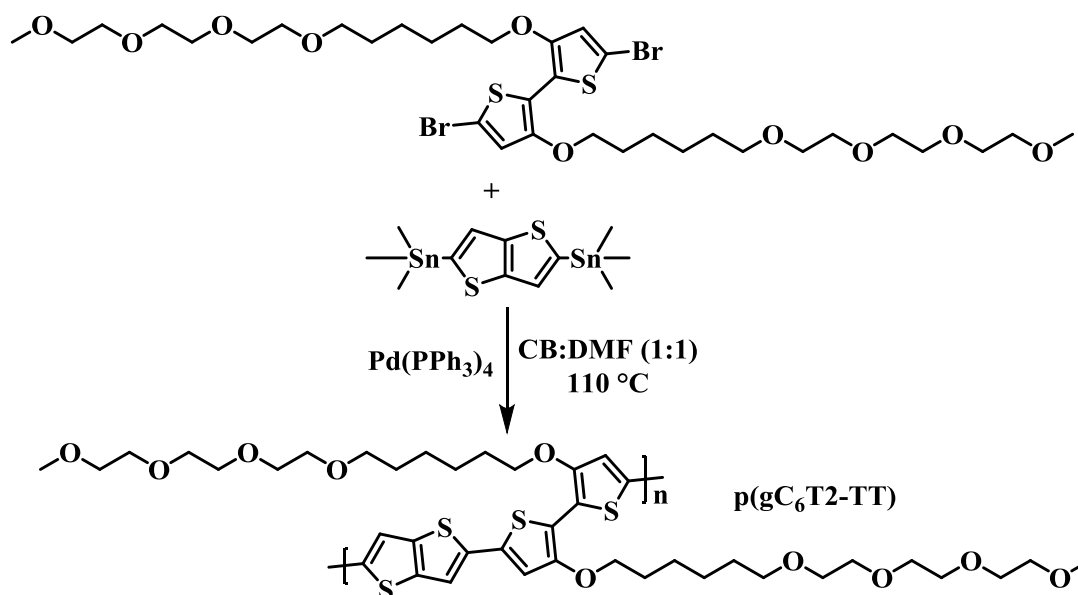
¹H NMR (400 MHz, Chloroform-*d*) δ 6.80 (s, 2H), 4.08 – 3.99 (m, 4H), 3.70 – 3.43 (m, 24H), 3.47 (t, *J* = 6.7 Hz, 4H), 3.37 (s, 6H), 1.87 – 1.78 (m, 4H), 1.67 – 1.57 (m, 4H), 1.56 – 1.37 (m, 8H).

¹³C NMR (101 MHz, Chloroform-*d*) δ 149.38, 132.26, 128.76, 119.03, 72.23, 71.95, 71.31, 70.64, 70.60, 70.53, 70.12, 59.05, 29.58, 29.54, 29.47, 25.80.

Mass (MALDI-ToF): 848.9 [M+H]⁺ (calc. 848.1 C₃₄H₅₆Br₂O₁₀S₂).



6.4.20 Synthesis of Polymer AM558 p(gC₆T₂-TT)



An oven dried 5 mL microwave vial was charged with 17,17'-((5,5'-dibromo-[2,2'-bithiophene]-3,3'-diyl)bis(oxy))bis(2,5,8,11-tetraoxaheptadecane) (**6.4.19**) (200 mg, 0.24

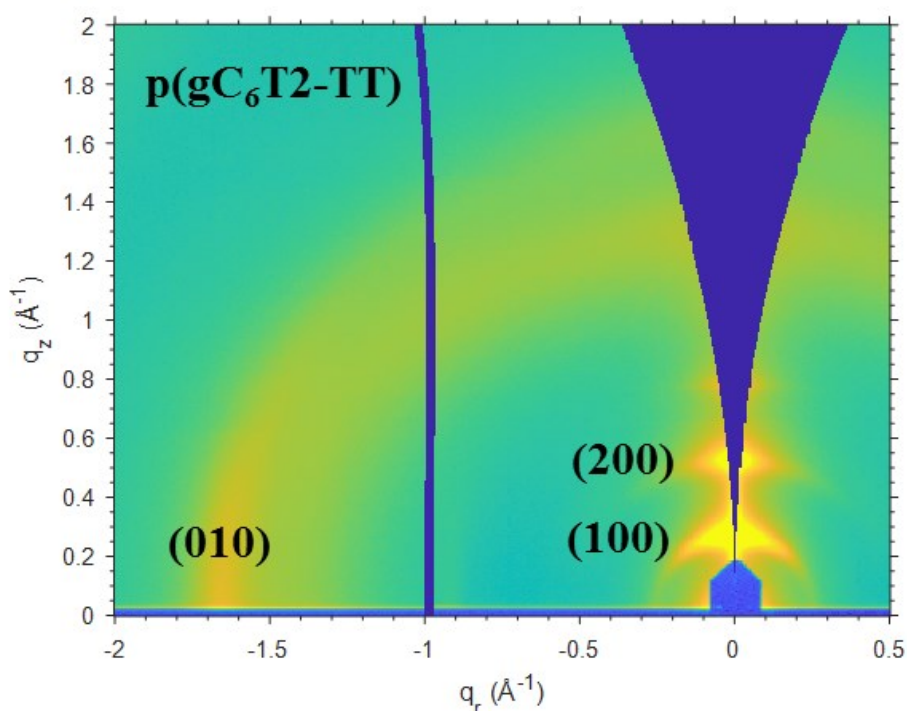
mmol, 1.0 eq.), 2,5-bis(trimethylstannyl)thieno[3,2-*b*]thiophene (109.8 mg, 0.24 mmol, 1.0 eq.) and Pd(PPh₃)₄ (5.44 mg, 0.005 mmol, 0.02 eq.). Cap was sealed and the vial was purged with Nitrogen for 5 minutes prior to the addition of anhydrous DMF (1.57 mL) and anhydrous chlorobenzene (1.57 mL). The reaction was stirred overnight at 110 °C then cooled to room temperature, upon which the solution formed a purple gel. Crude polymer was precipitated into 100 mL methanol and subsequently filtered into a thimble. Purification was conducted via Soxhlet extraction, washing with hexane, methanol, acetone, ethyl acetate and chloroform (in that order). The chloroform fraction was collected, solvent removed under reduced pressure and re-precipitated into 100 mL methanol, filtered to yield a blue metallic film (163 mg, 81%).

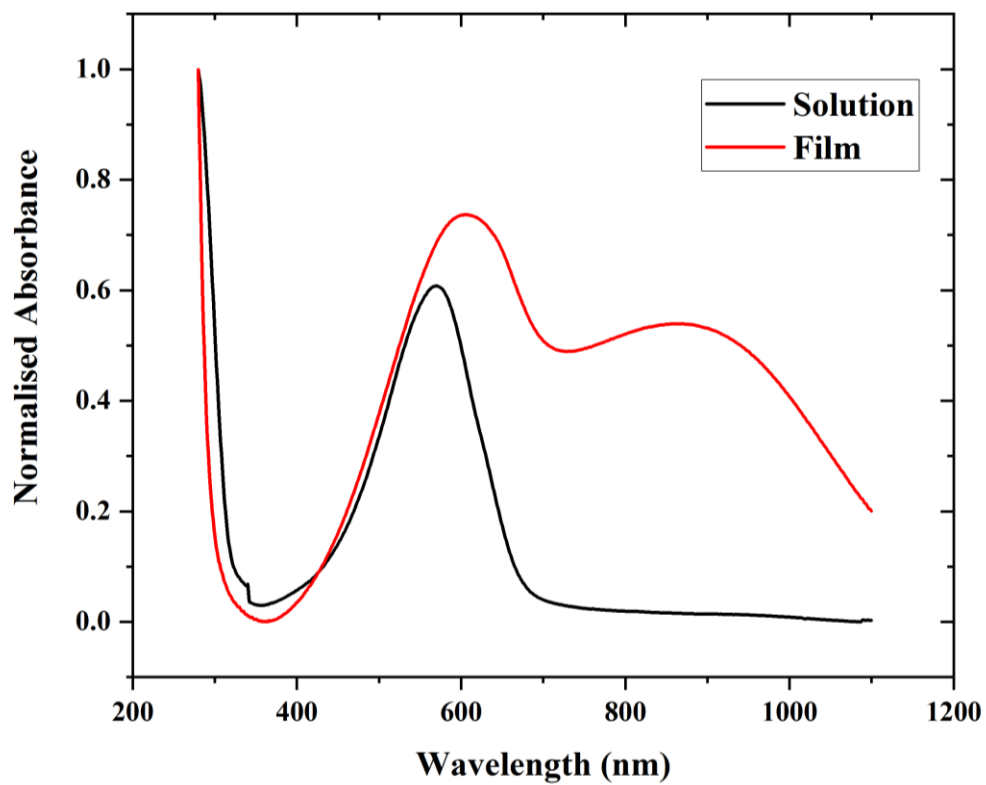
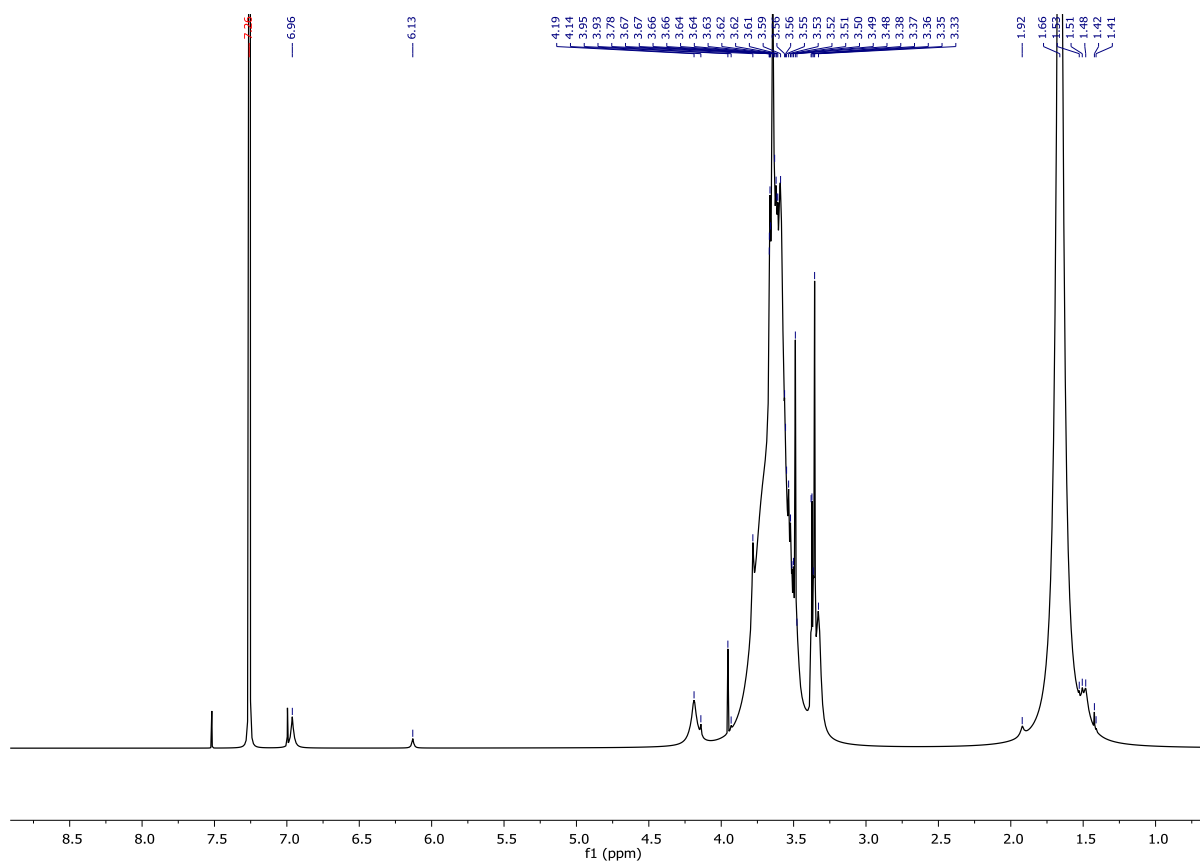
$\lambda_{\text{MAX}}^{\text{a}}$ (nm)	λ_{ONSET} (nm)	$E_{\text{opt}}^{\text{b}}$ (eV)	IP [CV] (eV)	EA ^c (eV)	E_{onset} [ACN](V)	E_{onset} [H ₂ O](V)	M_{n} (kDa)	M_{w} (kDa)	PDI
570	696	1.78	4.26	2.48	-0.13	-0.16	11.6	29.9	2.59

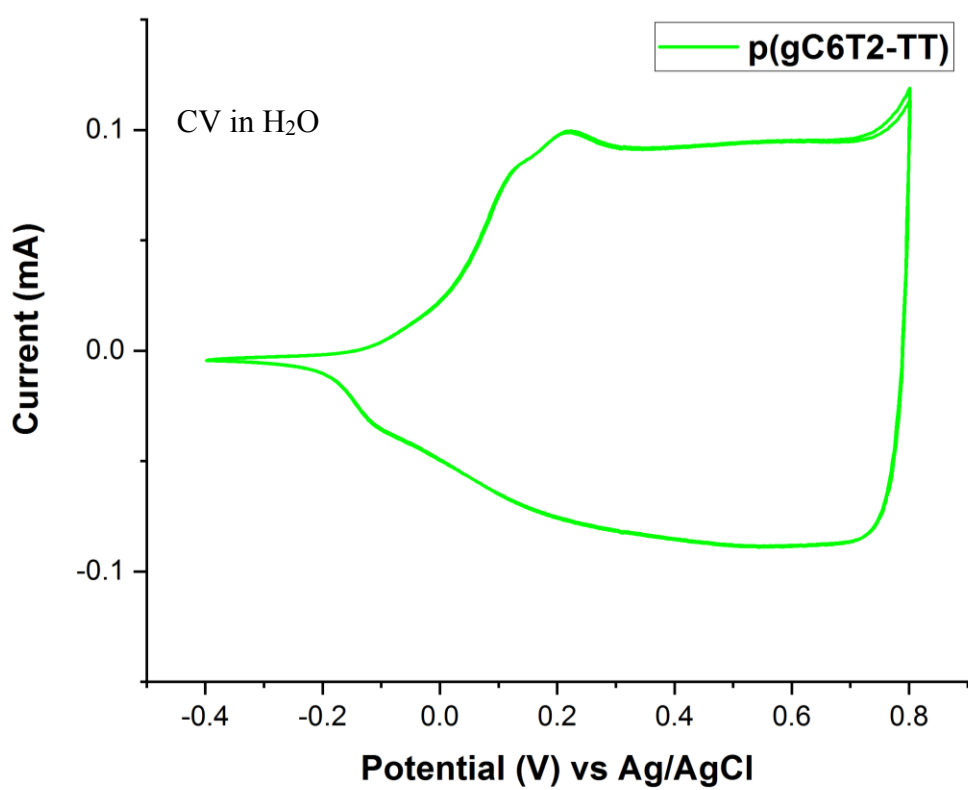
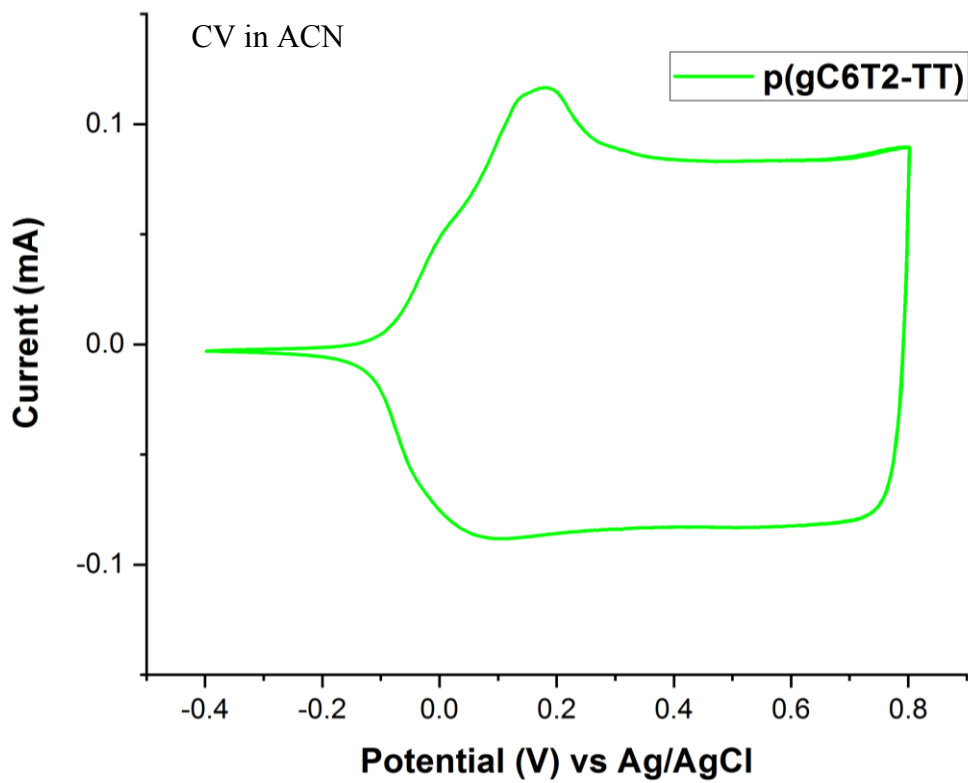
^a λ is the peak of the first low energy absorption band of the polymers

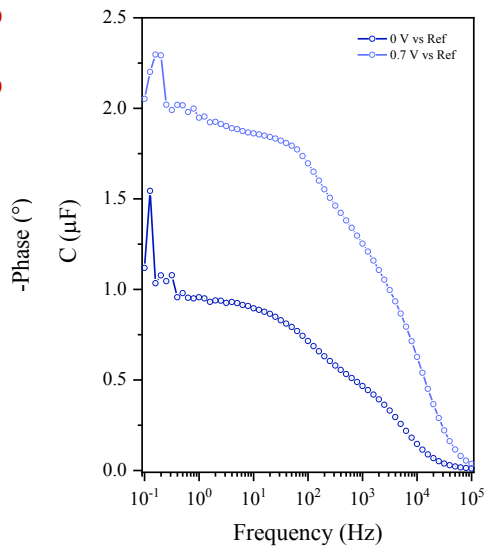
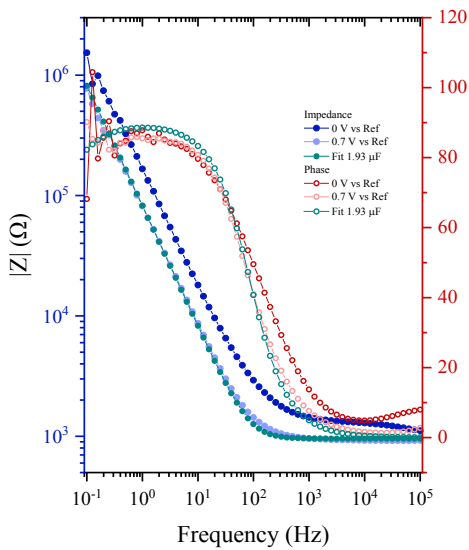
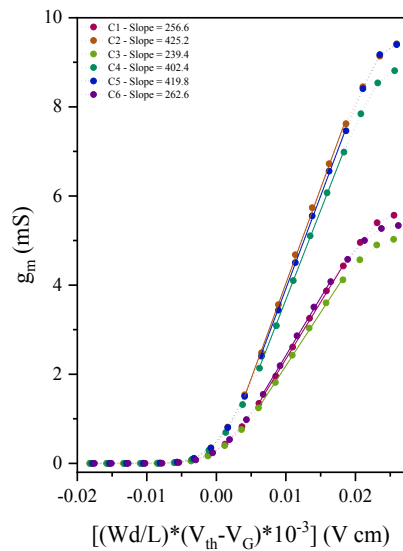
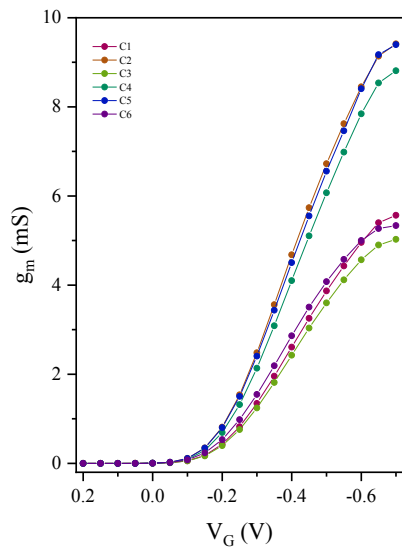
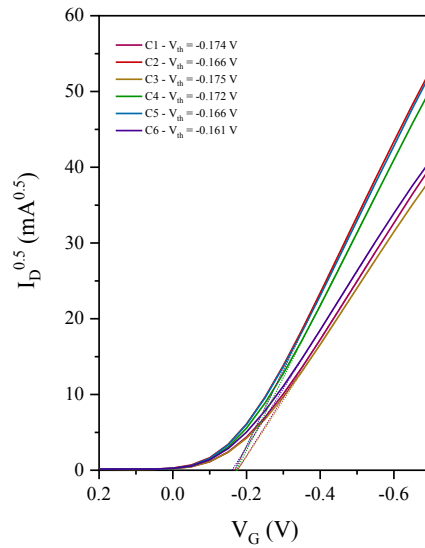
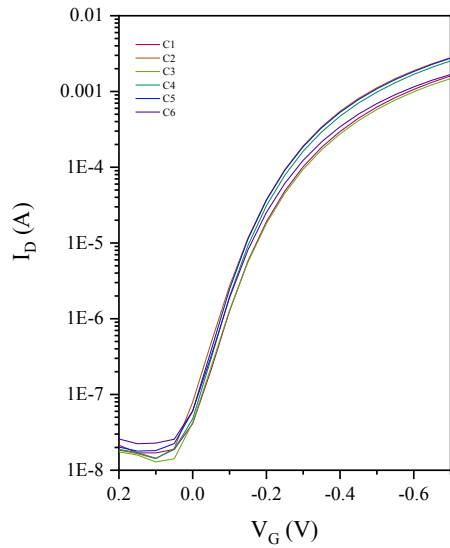
^b E_{opt} estimated optical gap using onset of the thin-film absorption spectra $E_{\text{GAP}} = 1240 / \lambda_{\text{ONSET}}$

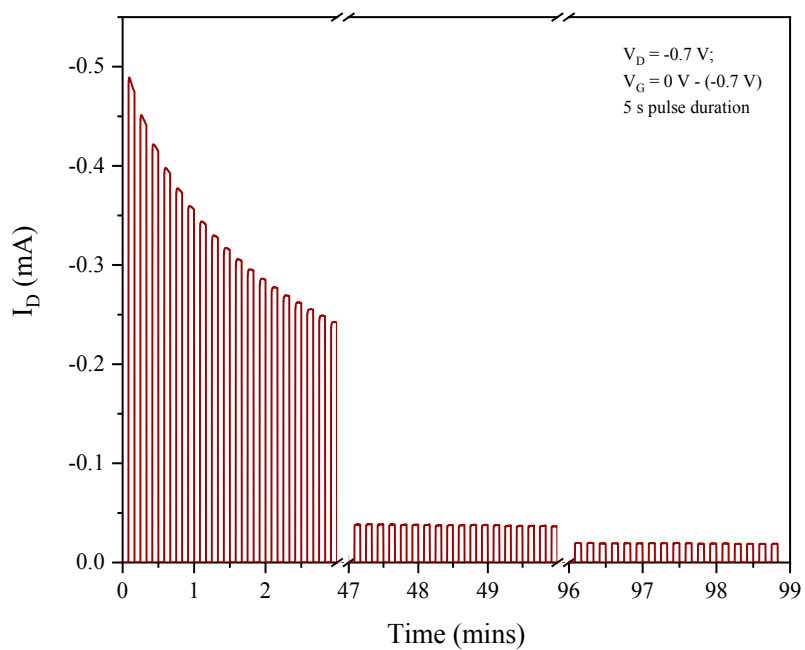
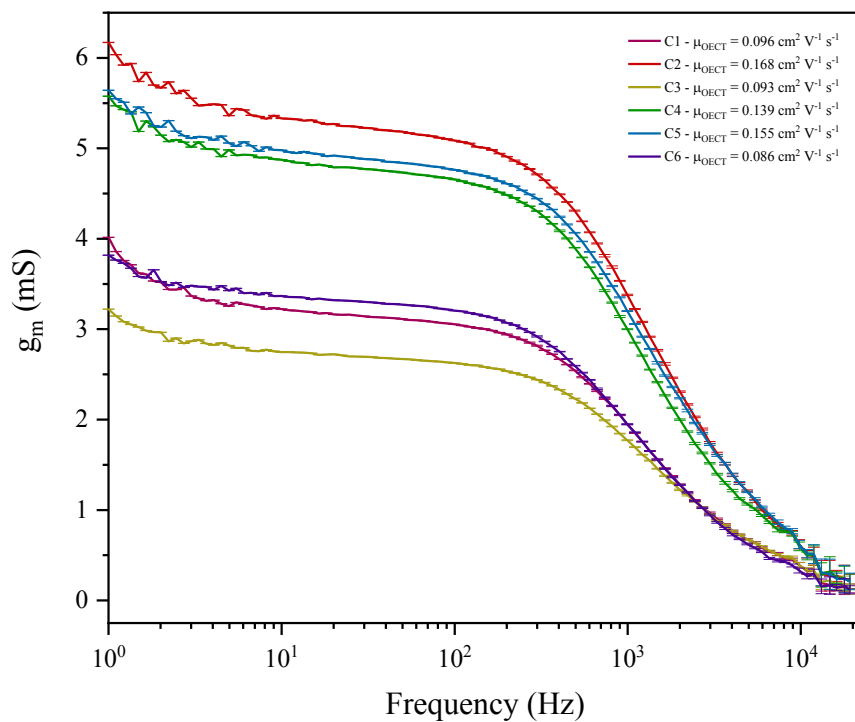
^cEA crudely estimated by subtraction of the UV-Vis absorption onset from IP ($EA = IP - E_{\text{opt}}$), a procedure that neglects the exciton binding energy

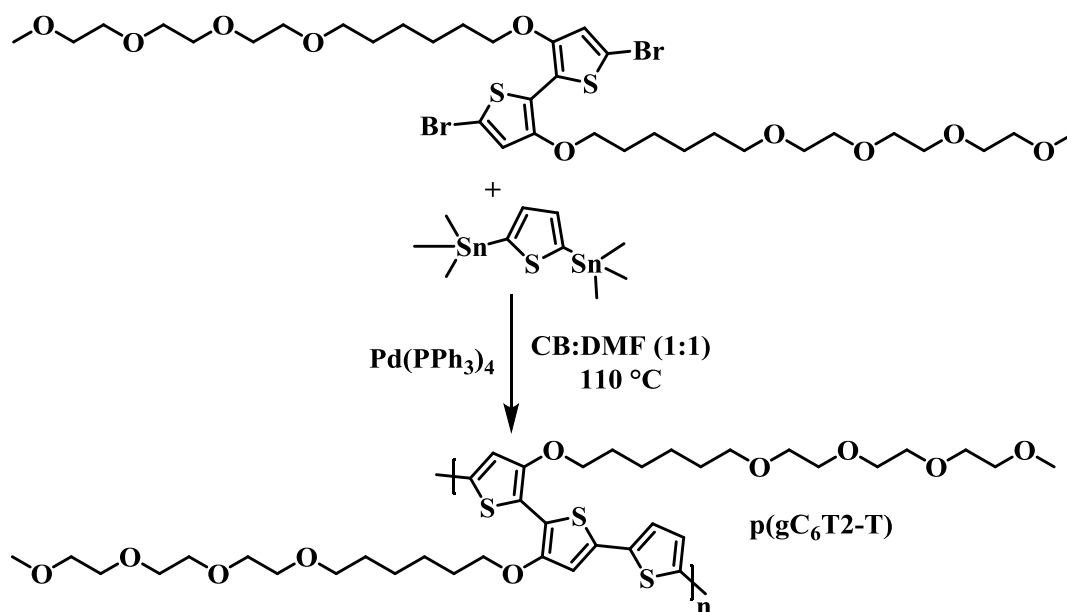










6.4.21 Synthesis of Polymer AM568 p(gC₆T2-T)

An oven dried 5 mL microwave vial was charged with 17,17'-((5,5'-dibromo-[2,2'-bithiophene]-3,3'-diyl)bis(oxy))bis(2,5,8,11-tetraoxaheptadecane) (**6.4.19**) (200 mg, 0.24 mmol, 1.0 eq.), 2,5-bis(trimethylstannyl)thiophene (96.6 mg, 0.24 mmol, 1.0 eq.) and Pd(PPh₃)₄ (5.44 mg, 0.005 mmol, 0.02 eq.). Cap was sealed and the vial was purged with Nitrogen for 5 minutes prior to the addition of anhydrous DMF (1.57 mL) and anhydrous chlorobenzene (1.57 mL). The reaction was stirred overnight at 110 °C then cooled to room temperature, upon which the solution formed a purple gel. Crude polymer was precipitated into 100 mL methanol and subsequently filtered into a thimble. Purification was conducted via Soxhlet extraction, washing with hexane, methanol, acetone, ethyl acetate and chloroform (in that order). The chloroform fraction was collected, solvent removed under reduced pressure and re-precipitated into 100 mL methanol, filtered to yield a blue metallic film (127 mg, 66%).

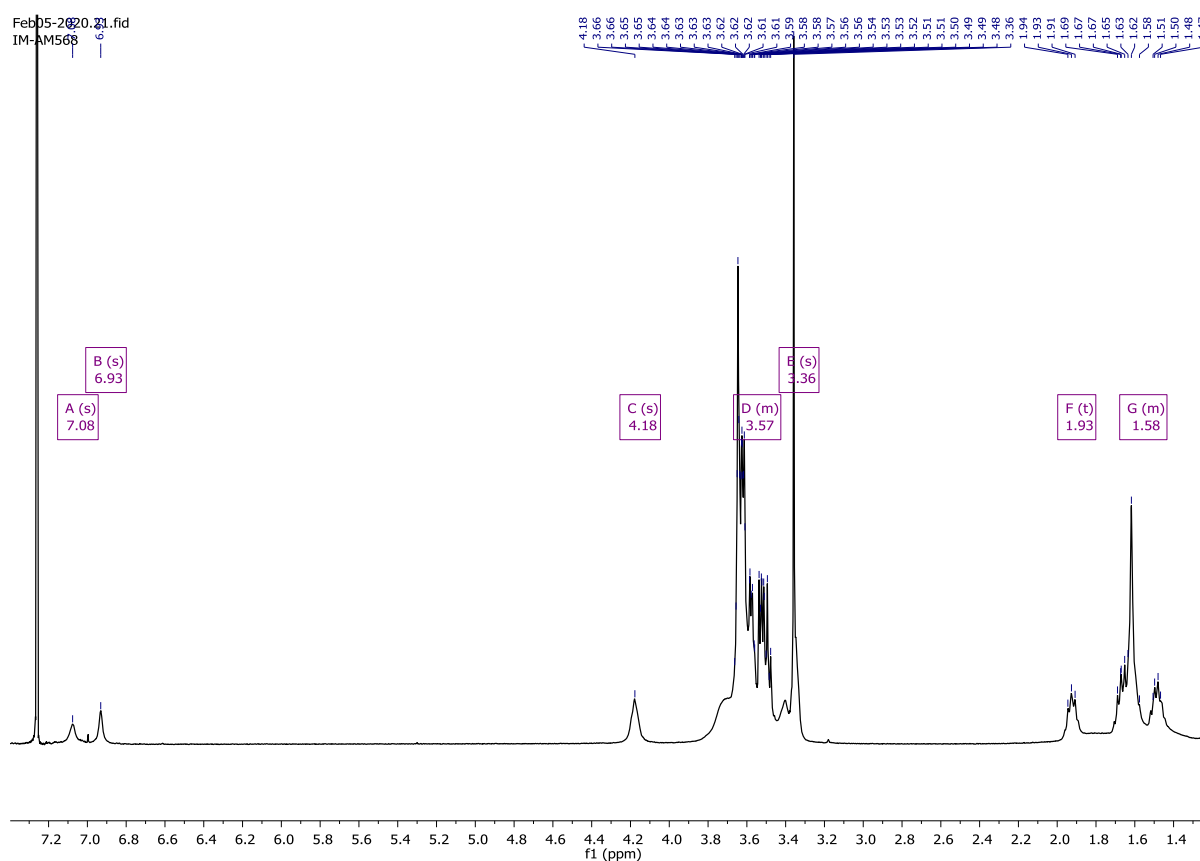
¹H NMR (400 MHz, Chloroform-*d*) δ 7.08 (s, 2H), 6.93 (s, 2H), 4.18 (s, 2H), 3.82 – 3.44 (m, 36H), 3.36 (s, 6H), 1.93 (t, *J* = 7.4 Hz, 4H), 1.76 – 1.37 (m, 12H).

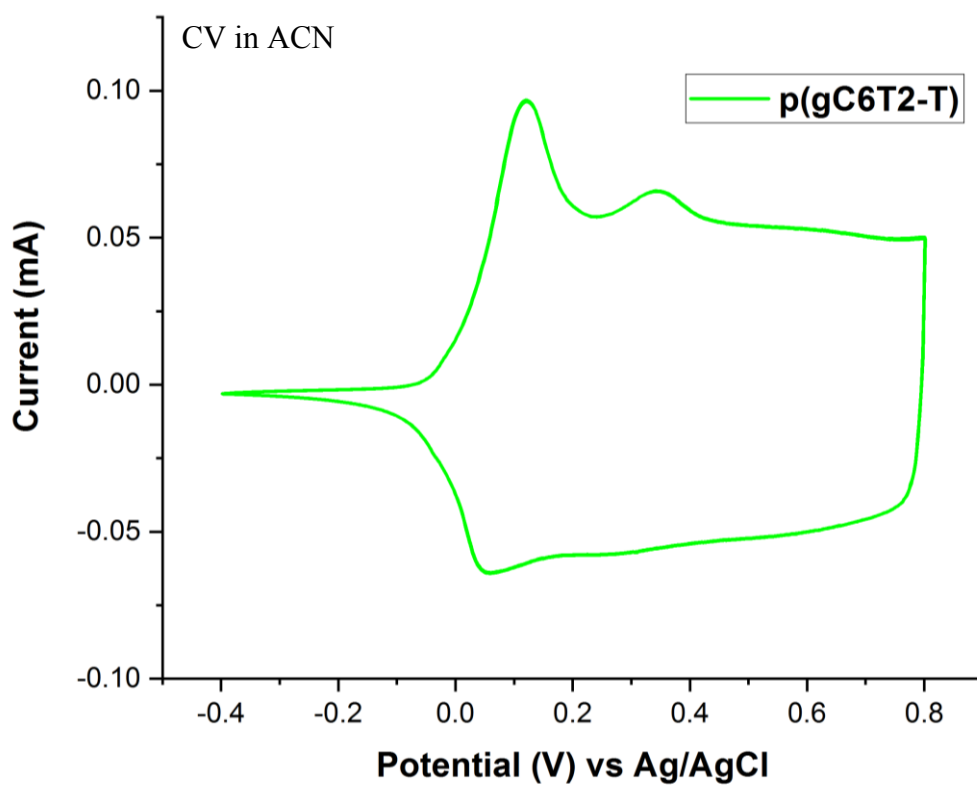
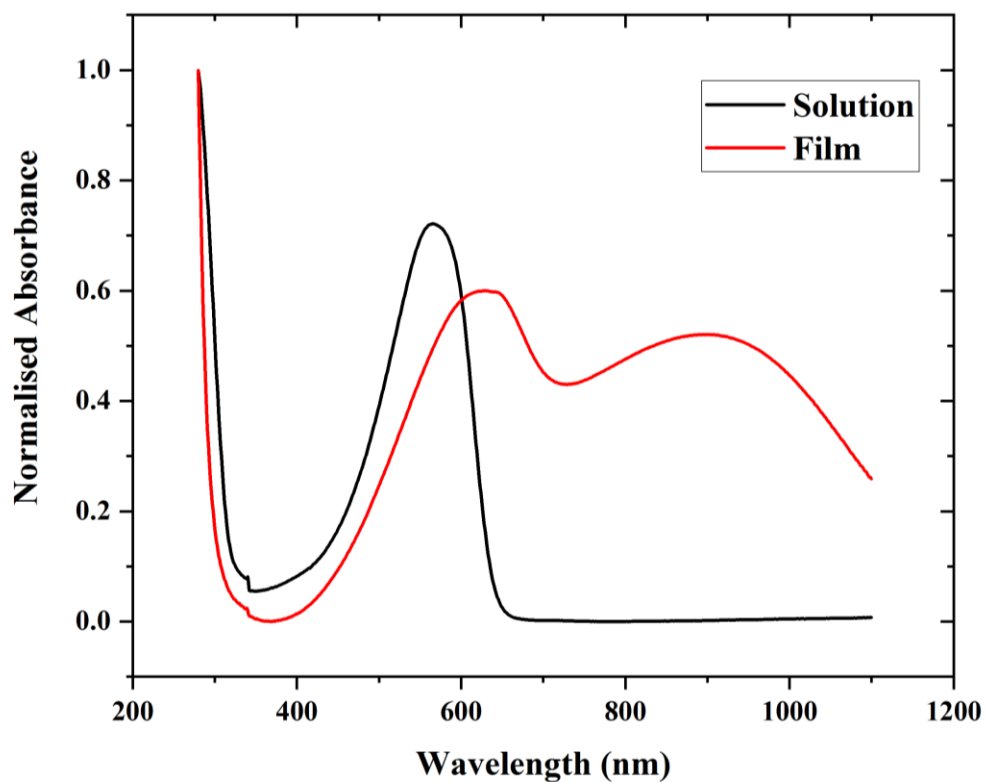
$\lambda_{\text{MAX}}^{\text{a}}$ (nm)	λ_{ONSET} (nm)	$E_{\text{opt}}^{\text{b}}$ (eV)	IP [CV] (eV)	EA ^c (eV)	E_{onset} [ACN](V)	E_{onset} [H ₂ O](V)	M_{n} (kDa)	M_{w} (kDa)	PDI
566	644	1.93	4.31	2.38	-0.08	-0.16	28.0	59.2	2.11

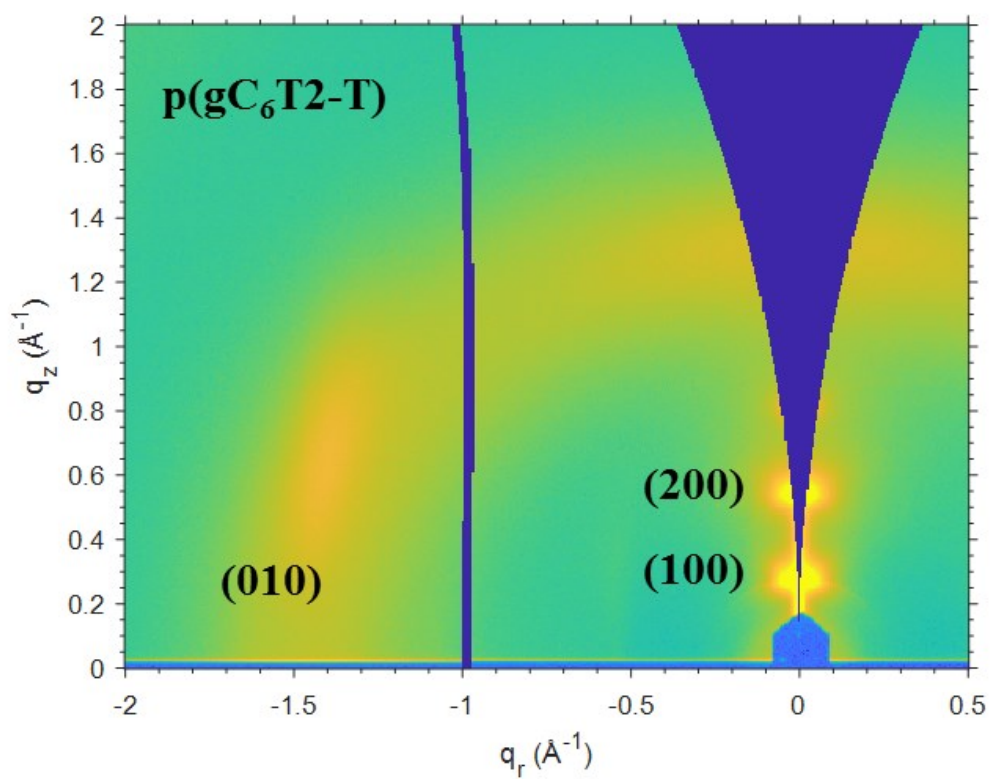
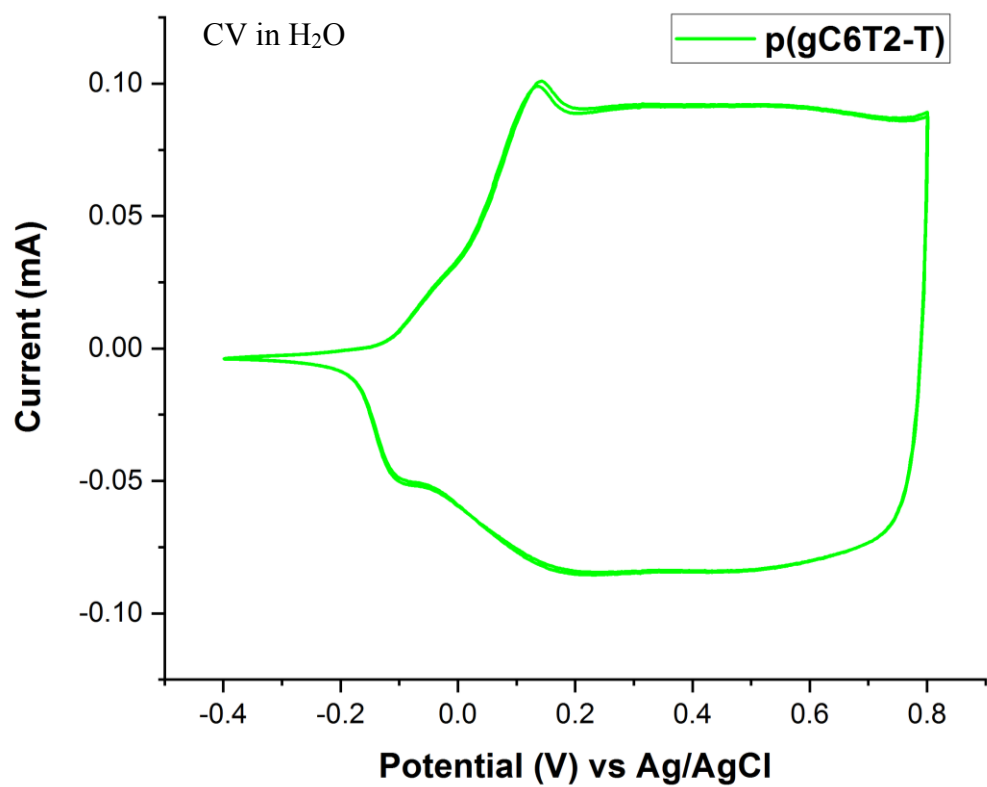
^a λ is the peak of the first low energy absorption band of the polymers

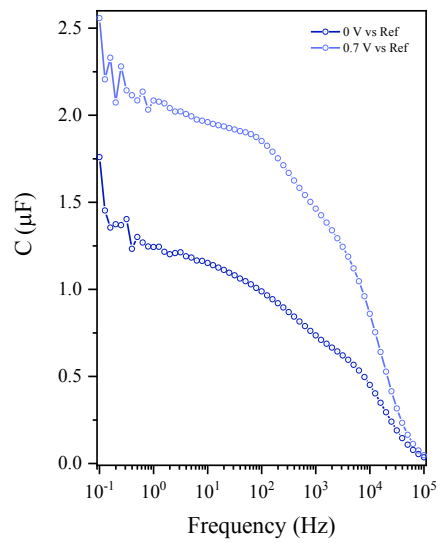
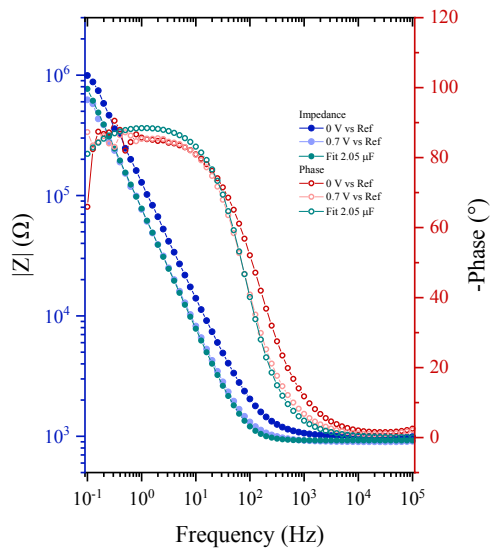
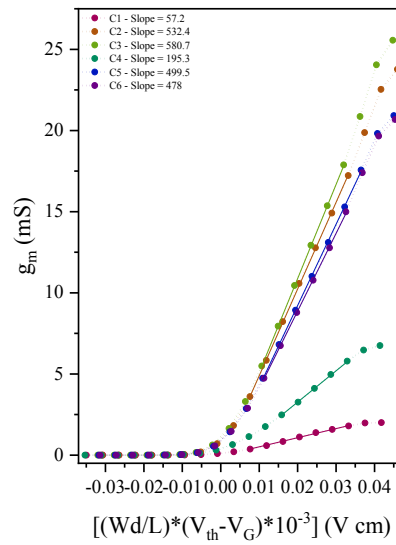
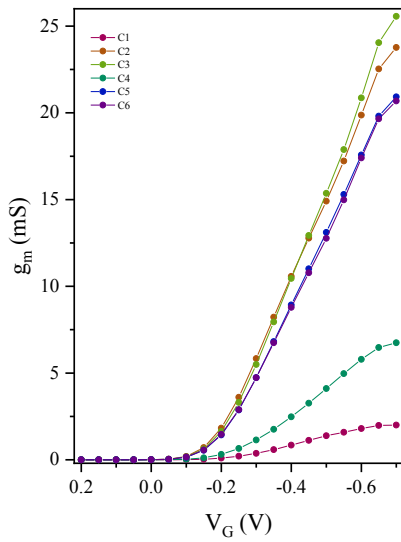
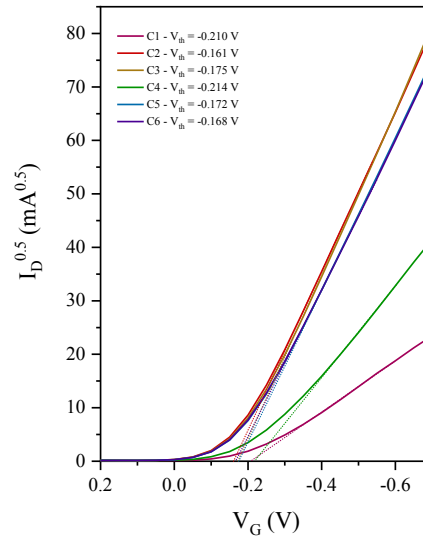
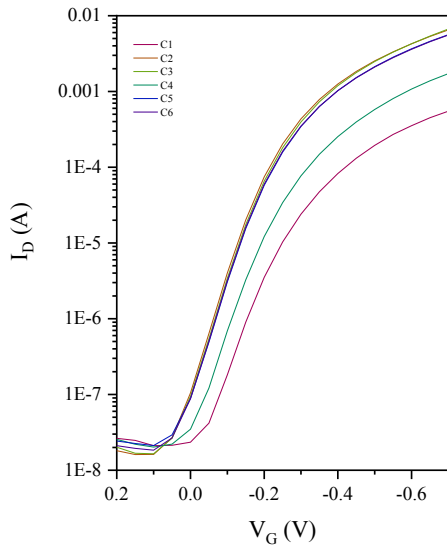
^b E_{opt} estimated optical gap using onset of the thin-film absorption spectra $E_{\text{GAP}} = 1240 / \lambda_{\text{ONSET}}$

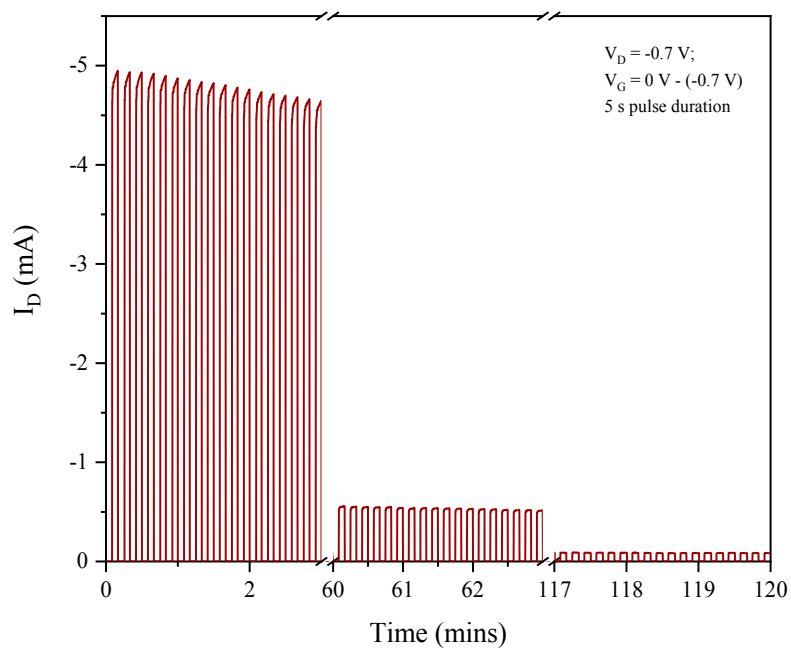
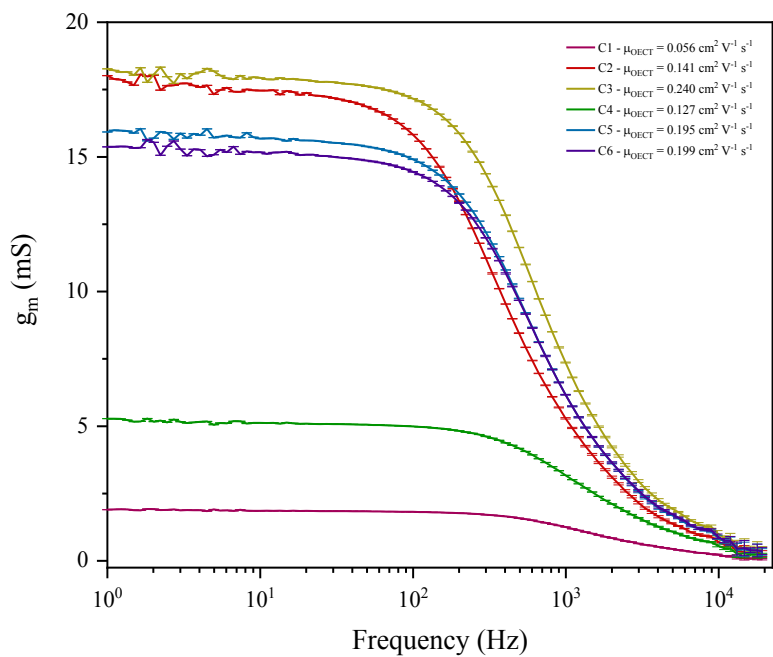
^cEA crudely estimated by subtraction of the UV-Vis absorption onset from IP ($EA = IP - E_{\text{opt}}$), a procedure that neglects the exciton binding energy



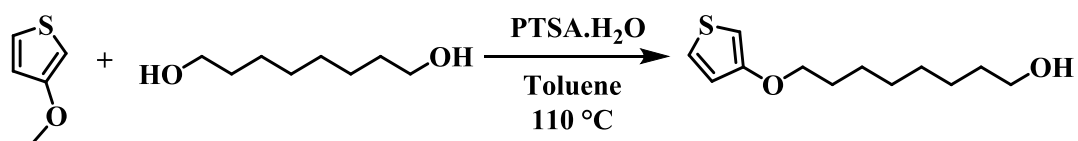








6.4.22 Synthesis of 8-(thiophen-3-yloxy)octan-1-ol



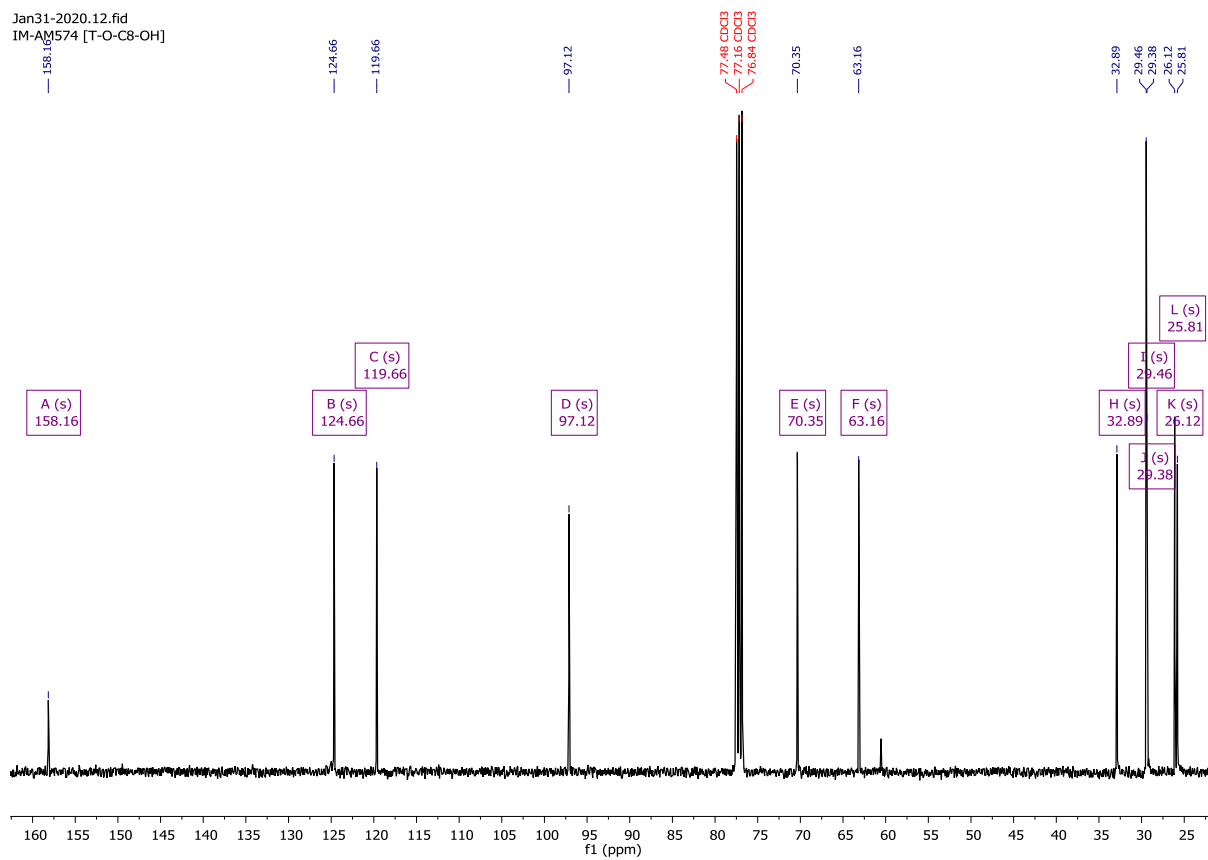
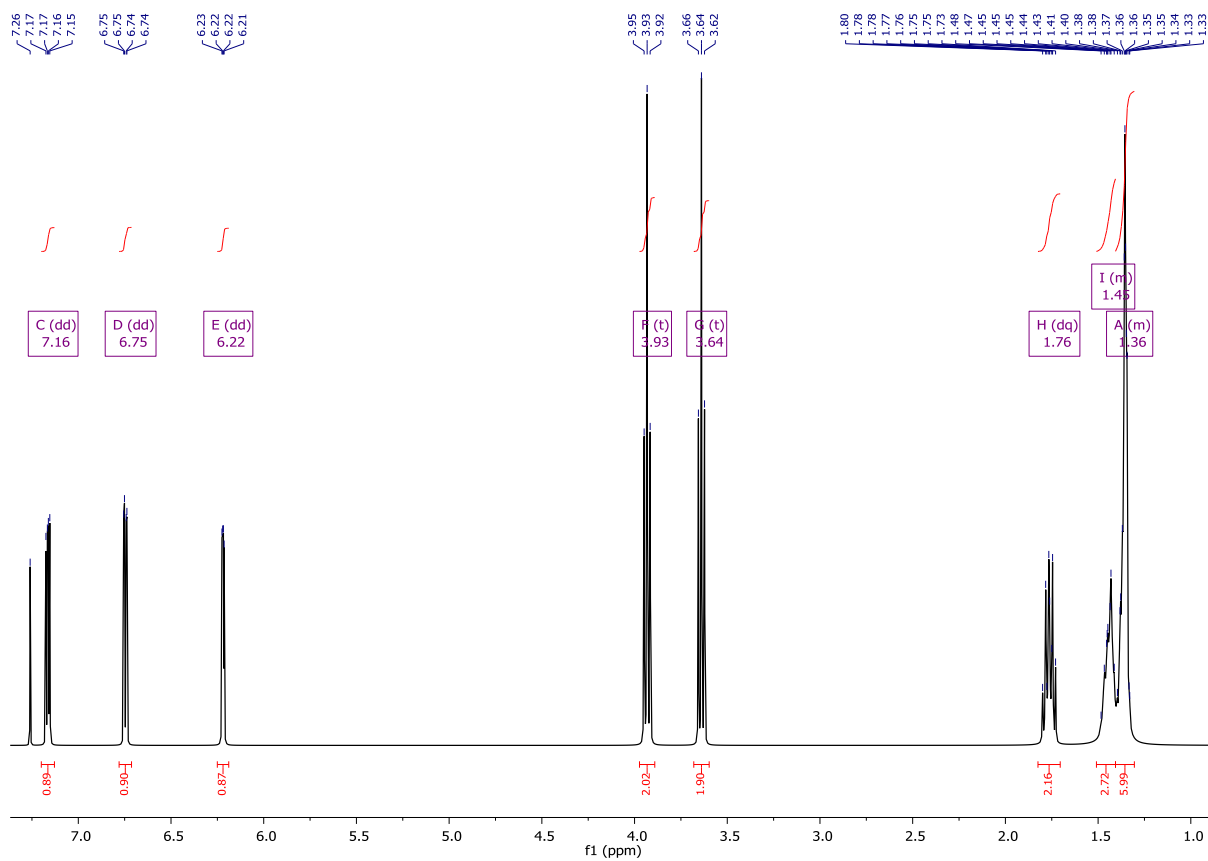
1,8-Octanediol (28.47 g, 194.7 mmol, 1.3 eq.) was dissolved in 200 mL toluene (required heating to reflux), followed by the addition of *p*-toluenesulfonic acid monohydrate (2.85 g,

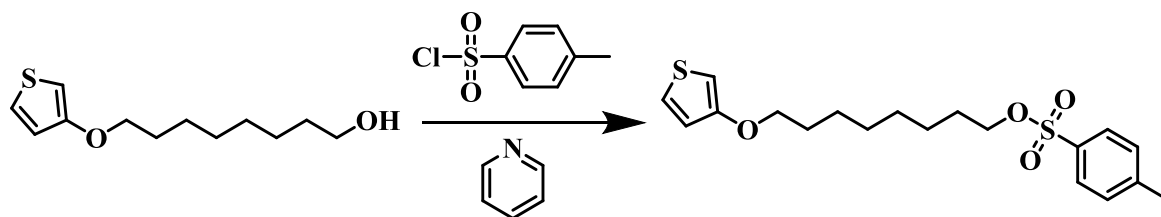
15.0 mmol, 0.1 eq.). 3-Methoxythiophene (17.1 g, 149.8 mmol, 1.0 eq.) was added and the reaction was stirred at reflux (110 °C) for 90 minutes. Once cooled to room temperature the reaction was poured into water, the aqueous layer was extracted three times with DCM. The organic phases were combined, dried over Na₂SO₄ and solvent removed under reduced pressure. The crude alcohol was purified via column chromatography, on silica gel, using DCM as the eluent (R_f = 0.2). Product fractions were consolidated to afford a white fluffy solid (14 g, 41%).

¹H NMR (400 MHz, Chloroform-*d*) δ 7.16 (dd, *J* = 5.2, 3.1 Hz, 1H), 6.75 (dd, *J* = 5.2, 1.6 Hz, 1H), 6.22 (dd, *J* = 3.1, 1.5 Hz, 1H), 3.93 (t, *J* = 6.5 Hz, 2H), 3.64 (t, *J* = 6.6 Hz, 2H), 1.76 (dq, *J* = 8.2, 6.6 Hz, 2H), 1.51 – 1.41 (m, 4H), 1.44 – 1.30 (m, 6H).

¹³C NMR (101 MHz, Chloroform-*d*) δ 158.16, 124.66, 119.66, 97.12, 70.35, 63.16, 32.89, 29.46, 29.38, 26.12, 25.81.

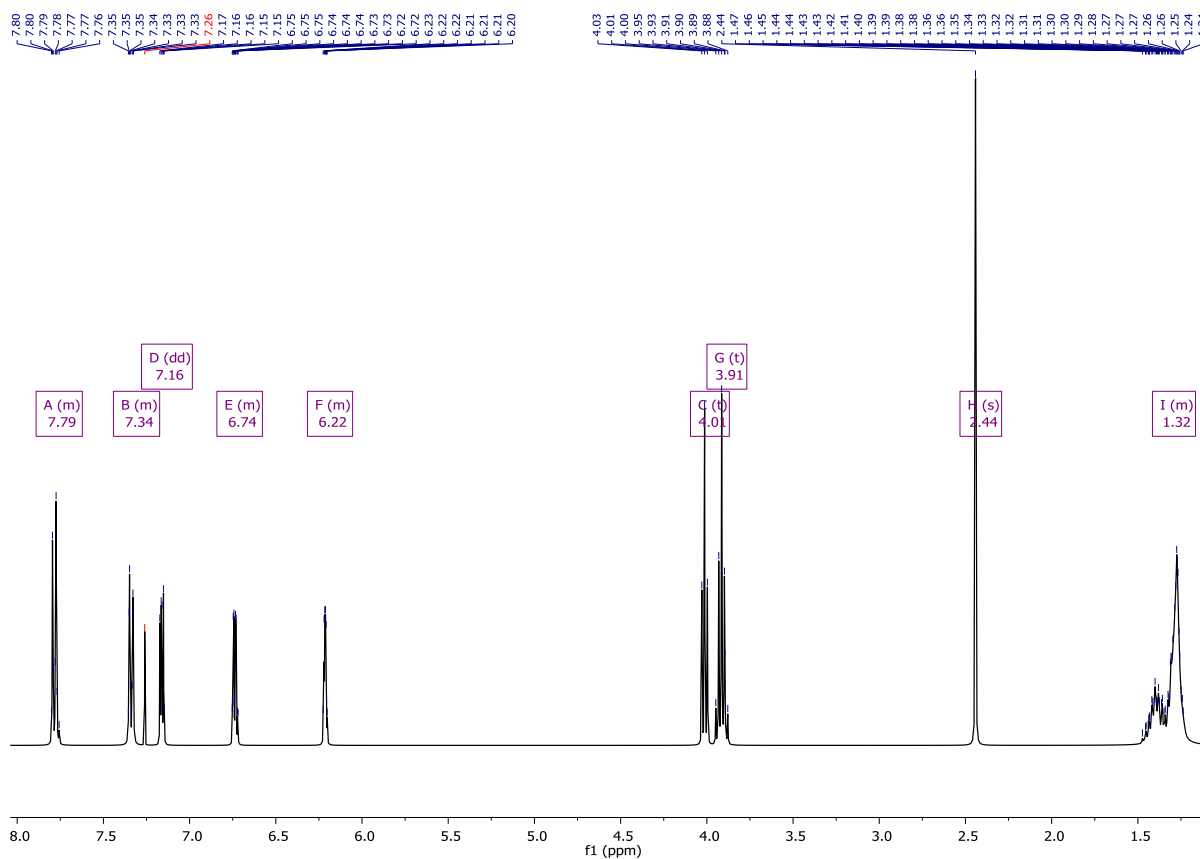
CHAPTER SIX – EXPERIMENTAL



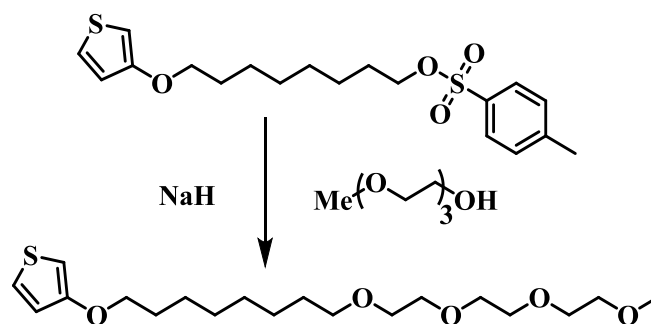
6.4.23 Synthesis of 8-(thiophen-3-yloxy)octyl 4-methylbenzenesulfonate

8-(thiophen-3-yloxy)octan-1-ol (**6.4.22**) (14.0 g, 61.3 mmol, 1.0 eq.) was dissolved in 30 mL of pyridine, cooled to 0 °C. 4-Toluenesulfonyl chloride (14.0 g, 73.6 mmol, 1.2 eq.) was added as a single portion and the reaction was stirred vigorously for 20 minutes before being left in the refrigerator overnight. Afterwards, 2M HCl (30 mL) was added, the reaction was stirred for 30 minutes before being poured into water, the aqueous phase was extracted three times with DCM. The organic layers were combined, dried over Na₂SO₄ and solvent removed under reduced pressure. The isolated product was used in the next step without further purification (19.5 g, 83%).

¹H NMR (400 MHz, Chloroform-*d*) δ 7.83 – 7.73 (m, 2H), 7.38 – 7.30 (m, 2H), 7.16 (dd, *J* = 5.3, 3.1 Hz, 1H), 6.78 – 6.69 (m, 1H), 6.25 – 6.18 (m, 1H), 4.01 (t, *J* = 6.5 Hz, 2H), 3.91 (t, *J* = 6.6 Hz, 2H), 2.44 (s, 3H), 1.50 – 1.21 (m, 12H).



6.4.24 Synthesis of 19-(thiophen-3-yloxy)-2,5,8,11-tetraoxanonadecane

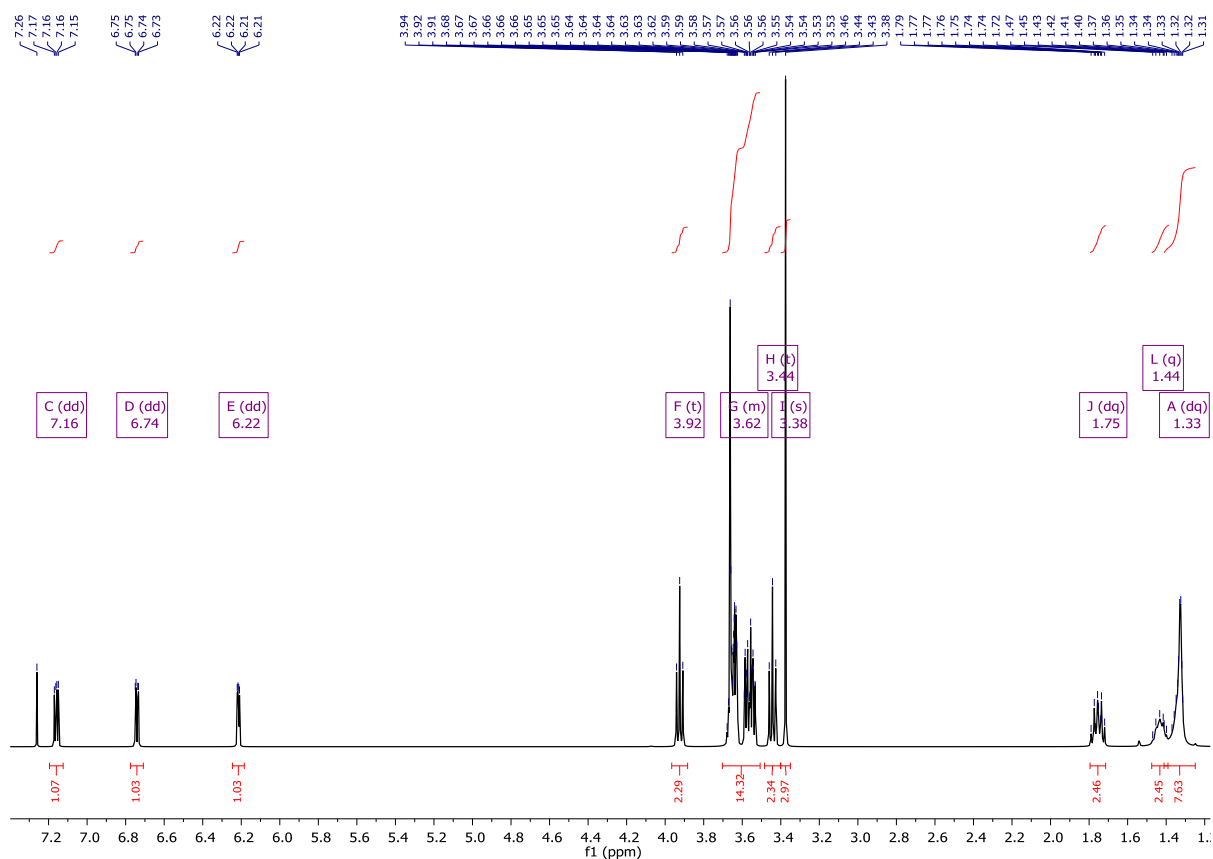


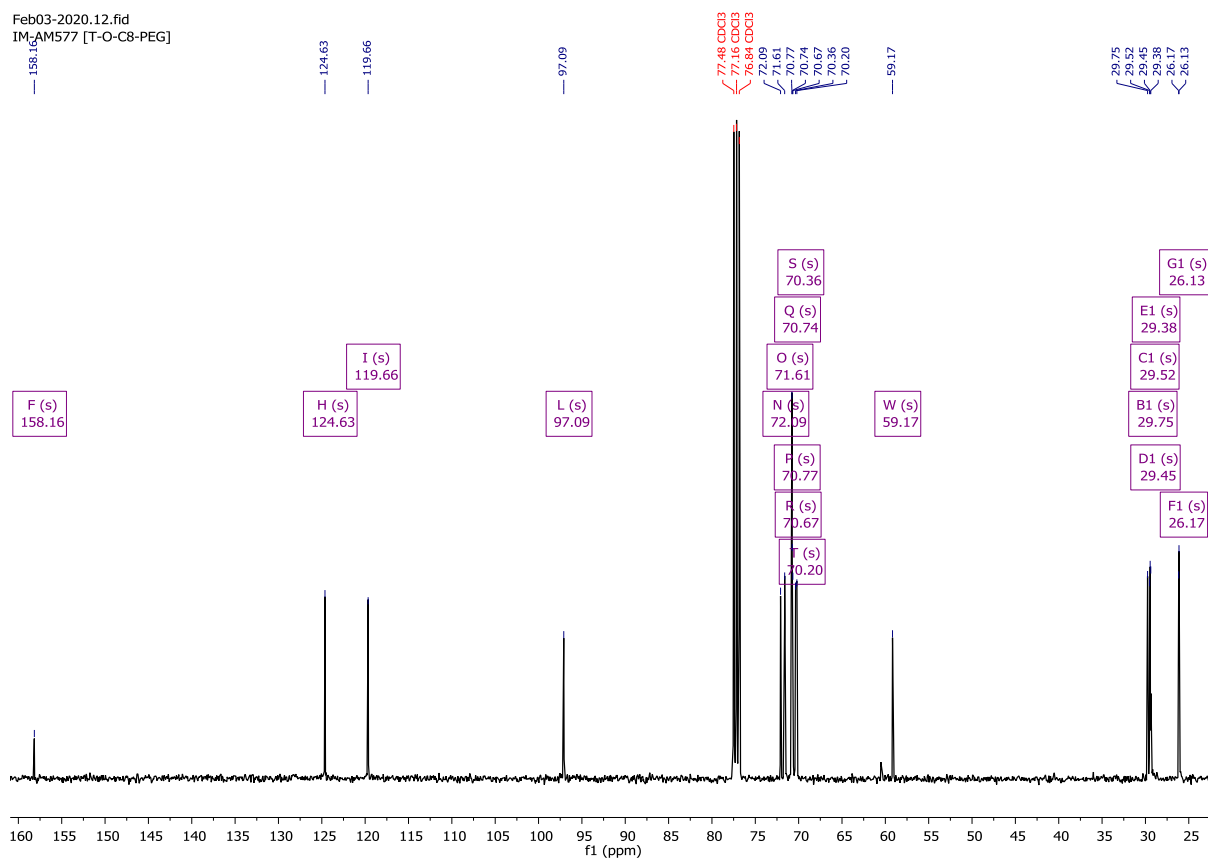
A 2-neck oven dried 250 mL RBF was charged with sodium hydride (60% in mineral oil) (5.93 g, 149 mmol, 3.0 eq.) and dissolved in anhydrous THF (60 mL) under a Nitrogen atmosphere. The suspension was cooled to 0 °C and triethylene glycol monomethyl ether (23.7 mL, 149 mmol, 3.0 eq.) was added slowly dropwise. The reaction was stirred for 30 minutes, until effervescence ceased, then 8-(thiophen-3-yloxy)octyl 4-methylbenzenesulfonate (**6.4.23**) (19 g, 49.7 mmol, 1.0 eq.) was added. The reaction was stirred overnight before pouring into water,

the aqueous phase was extracted three times with DCM. The organic layers were combined, dried over Na₂SO₄ and solvent removed under reduced pressure. The crude product was purified by column chromatography, on silica gel, using hexane:ethyl acetate (1:1) (v/v) as the eluent system to afford a yellow oil (11.5 g, 62%).

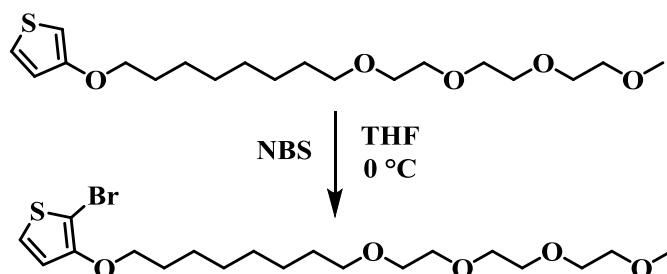
¹H NMR (400 MHz, Chloroform-*d*) δ 7.16 (dd, *J* = 5.2, 3.1 Hz, 1H), 6.74 (dd, *J* = 5.2, 1.6 Hz, 1H), 6.22 (dd, *J* = 3.1, 1.5 Hz, 1H), 3.92 (t, *J* = 6.5 Hz, 2H), 3.70 – 3.51 (m, 14H), 3.44 (t, *J* = 6.8 Hz, 2H), 3.38 (s, 3H), 1.75 (dq, *J* = 8.4, 6.6 Hz, 2H), 1.44 (q, *J* = 6.9 Hz, 2H), 1.33 (dq, *J* = 4.4, 2.7, 2.2 Hz, 8H).

¹³C NMR (101 MHz, Chloroform-*d*) δ 158.16, 124.63, 119.66, 97.09, 72.09, 71.61, 70.77, 70.74, 70.67, 70.36, 70.20, 59.17, 29.75, 29.52, 29.45, 29.38, 26.17, 26.13.





6.4.25 Synthesis of 19-((2-bromothiophen-3-yl)oxy)-2,5,8,11-tetraoxanonadecane

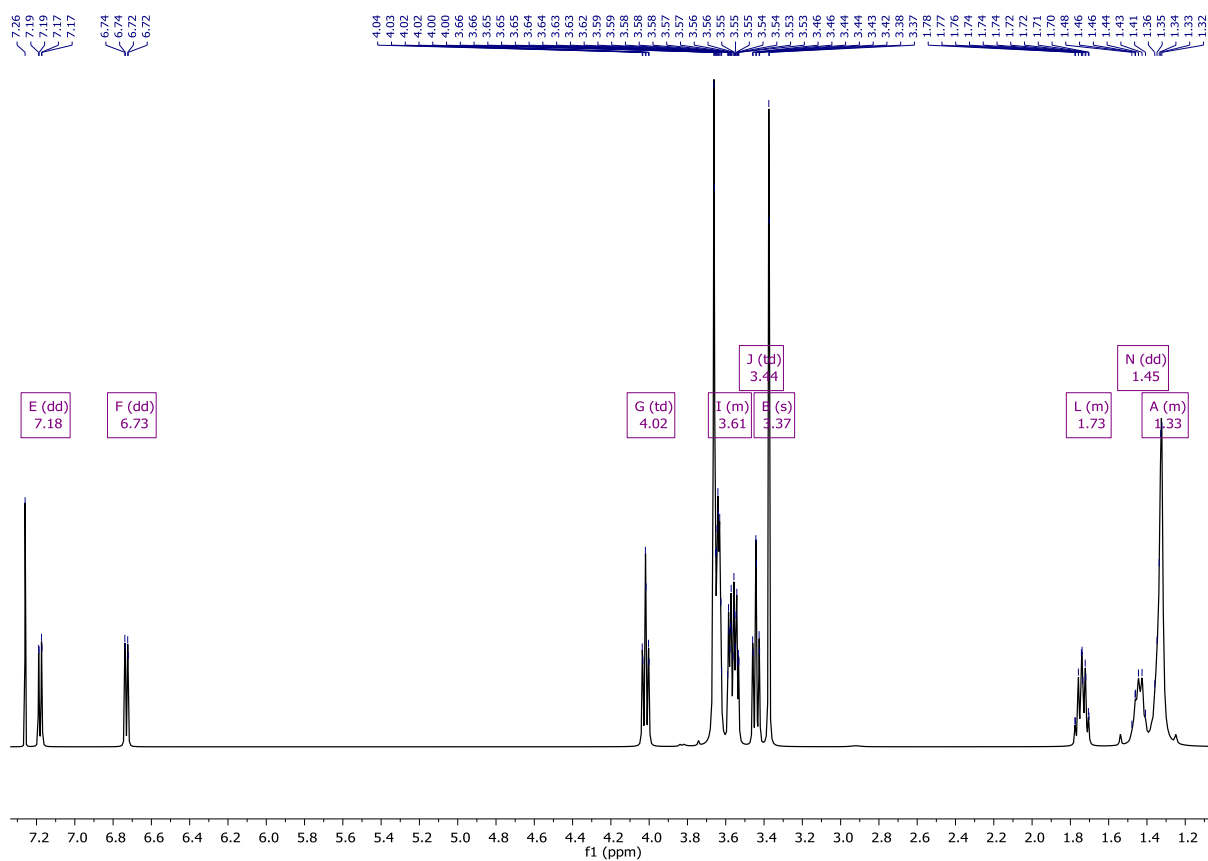


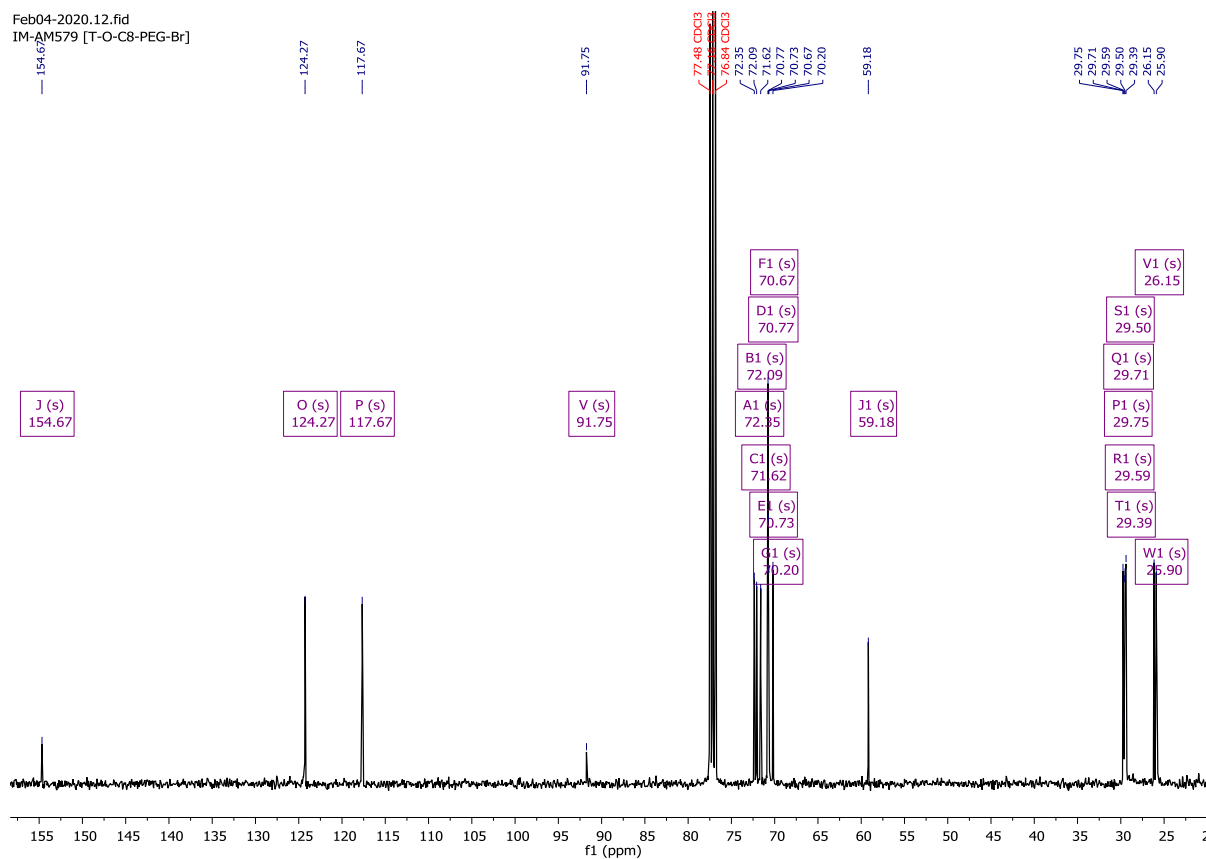
19-(thiophen-3-yloxy)-2,5,8,11-tetraoxanonadecane (**6.4.24**) (4.5 g, 12.0 mmol, 1.0 eq.) was added to an oven-dried 2-neck 100 mL RBF, under a Nitrogen atmosphere. Dry THF (20 mL) was added, vessel cooled to 0 °C in the dark. N-bromosuccinimide (4x545 mg, 12.3 mmol, 1.02 eq.) was added portion wise, leaving approximately 4 minutes between each addition. The reaction was stirred for 30 minutes before being poured into water, washed with saturated sodium bicarbonate solution and quenched with sodium metabisulphite. The aqueous phase was extracted three times with DCM, the organic phases were combined and dried over

Na_2SO_4 . The crude product was purified via column chromatography, on silica gel, using 1:1 hexane:ethyl acetate (v/v) as the eluent system to afford a yellow oil (5.23 g, 96%).

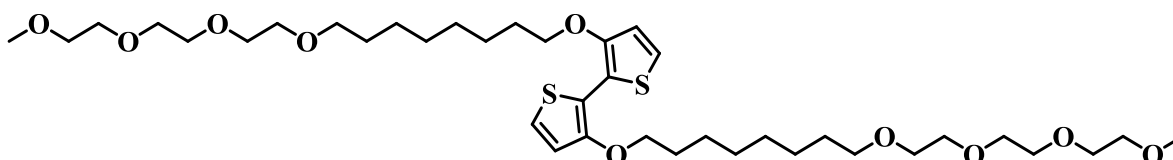
^1H NMR (400 MHz, Chloroform-*d*) δ 7.18 (dd, $J = 6.0, 1.1$ Hz, 1H), 6.73 (dd, $J = 6.0, 1.1$ Hz, 1H), 4.02 (td, $J = 6.6, 1.2$ Hz, 2H), 3.69 – 3.51 (m, 12H), 3.44 (td, $J = 6.8, 1.0$ Hz, 2H), 3.37 (s, 3H), 1.80 – 1.68 (m, 2H), 1.45 (dd, $J = 10.4, 4.1$ Hz, 2H), 1.45 – 1.30 (m, 8H).

^{13}C NMR (101 MHz, Chloroform-*d*) δ 154.67, 124.27, 117.67, 91.75, 72.35, 72.09, 71.62, 70.77, 70.73, 70.67, 70.20, 59.18, 29.75, 29.71, 29.59, 29.50, 29.39, 26.15, 25.90.



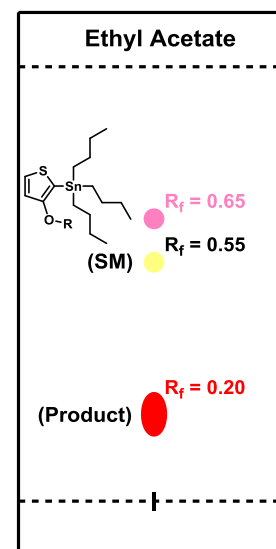


6.4.26 Synthesis of 3,3'-bis((2,5,8,11-tetraoxanonadecan-19-yl)oxy)-2,2'-bithiophene



19-((2-bromothiophen-3-yl)oxy)-2,5,8,11-tetraoxanonadecane

(6.4.25) (4g, 8.82 mmol, 1.0 eq.) was added to an oven dried 2-neck 250 mL RBF, under a Nitrogen atmosphere. Anhydrous chlorobenzene (22 mL) was added, followed by anhydrous DMF (22 mL). Bis(tributyltin) (2.45 mL, 4.85 mmol, 0.55 eq.) was slowly added dropwise, the reaction was heated to 100 °C and Pd(PPh₃)₄ (713 mg, 0.62 mmol, 0.07 eq.) was added in a single portion. The mixture was stirred overnight and subsequently cooled to room temperature then

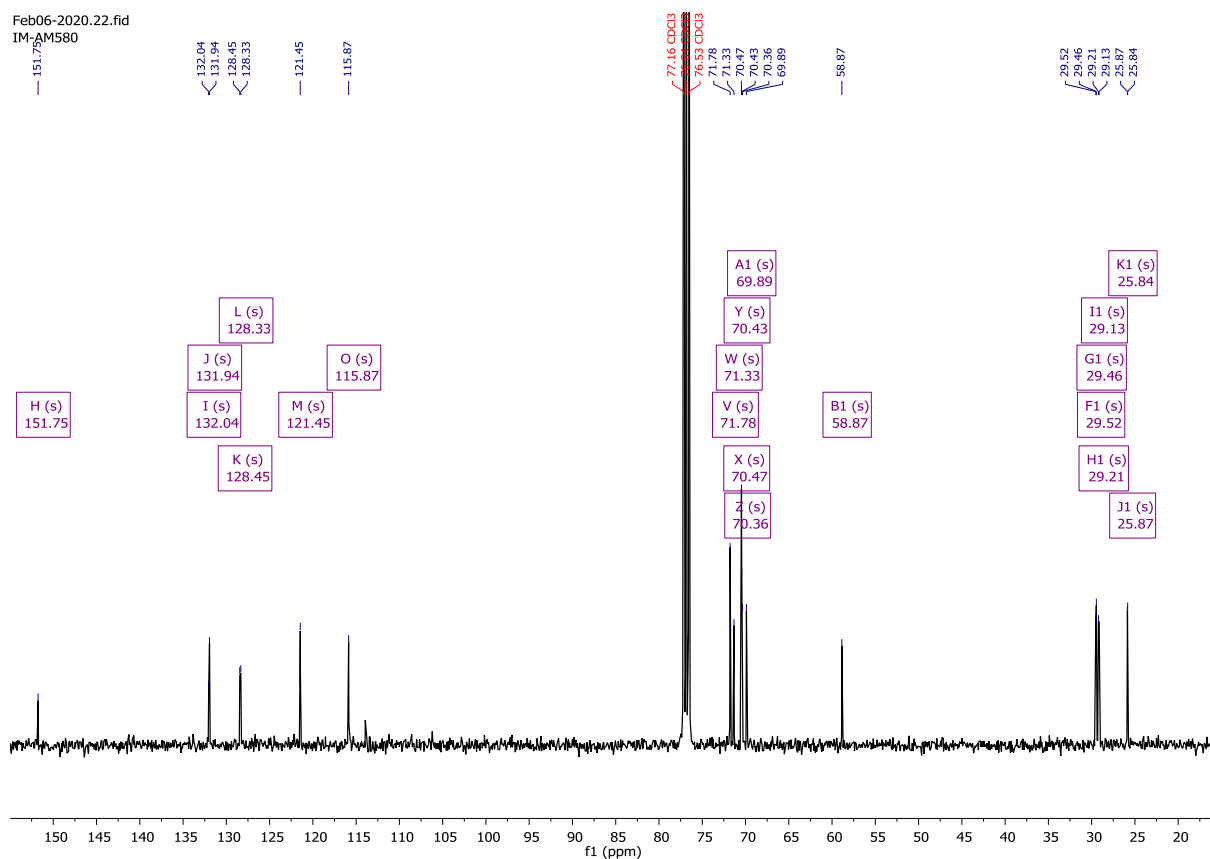
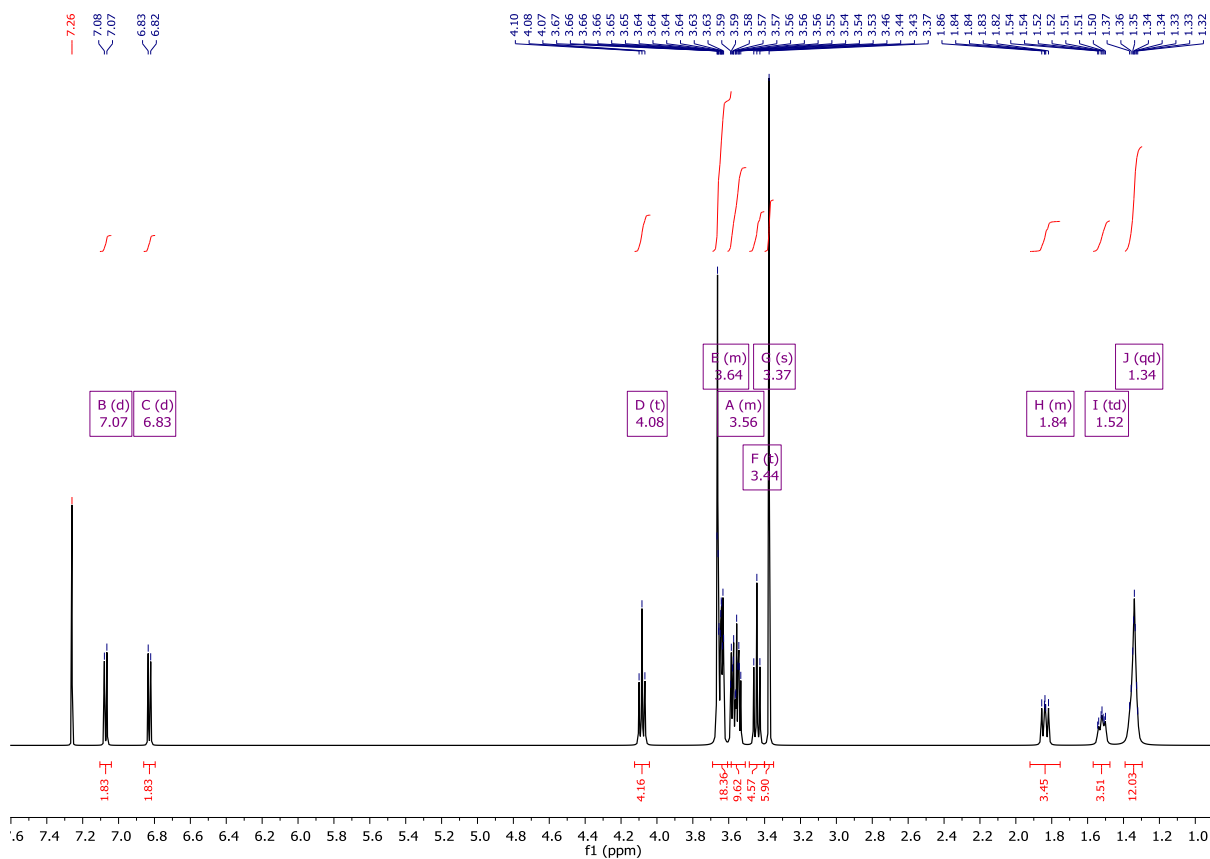


passed through a short silica plug, eluting with ethyl acetate. Most tin by-products remained on the baseline and were carefully disposed of as solid tin waste. Solvent was removed under reduced pressure and thin-layer chromatography, using ethyl acetate as the eluent, showed three distinct spots. Co-spotting with (6.4.25) shows the 2nd spot ($R_f=0.55$) correlates to the starting material, the top spot ($R_f=0.65$) corresponds to unreacted tin intermediate and the desired product spot resided at $R_f=0.20$. The crude residue was hence purified by column chromatography, on silica gel, using ethyl acetate as the eluent. Product fractions were combined to yield a yellow oil, which solidified under reduced temperatures (1.05 g, 32%).

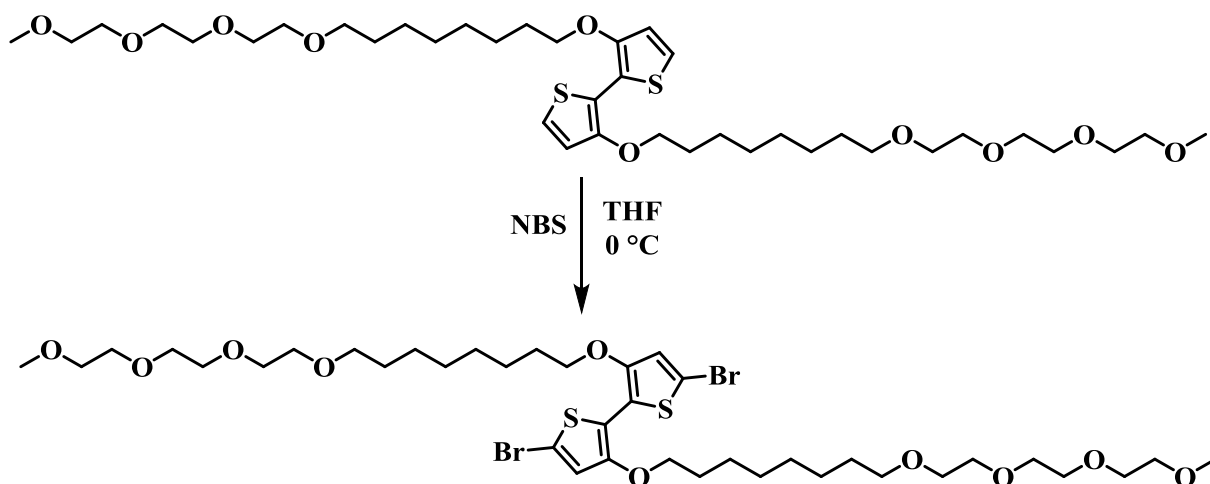
¹H NMR (400 MHz, Chloroform-*d*) δ 7.07 (d, $J = 5.6$ Hz, 2H), 6.83 (d, $J = 5.5$ Hz, 2H), 4.08 (t, $J = 6.5$ Hz, 4H), 3.69 – 3.60 (m, 18H), 3.61 – 3.51 (m, 10H), 3.44 (t, $J = 6.8$ Hz, 4H), 3.37 (s, 6H), 1.88 – 1.79 (m, 4H), 1.52 (td, $J = 7.7, 2.6$ Hz, 4H), 1.34 (qd, $J = 6.3, 5.6, 3.1$ Hz, 12H).

¹³C NMR (101 MHz, Chloroform-*d*) δ 151.75, 132.04, 131.94, 128.45, 128.33, 121.45, 115.87, 71.78, 71.33, 70.47, 70.43, 70.36, 69.89, 58.87, 29.52, 29.46, 29.21, 29.13, 25.87, 25.84.

CHAPTER SIX – EXPERIMENTAL



6.4.27 19,19'-((5,5'-dibromo-[2,2'-bithiophene]-3,3'-diyl)bis(oxy))bis(2,5,8,11-tetraoxanonadecane)

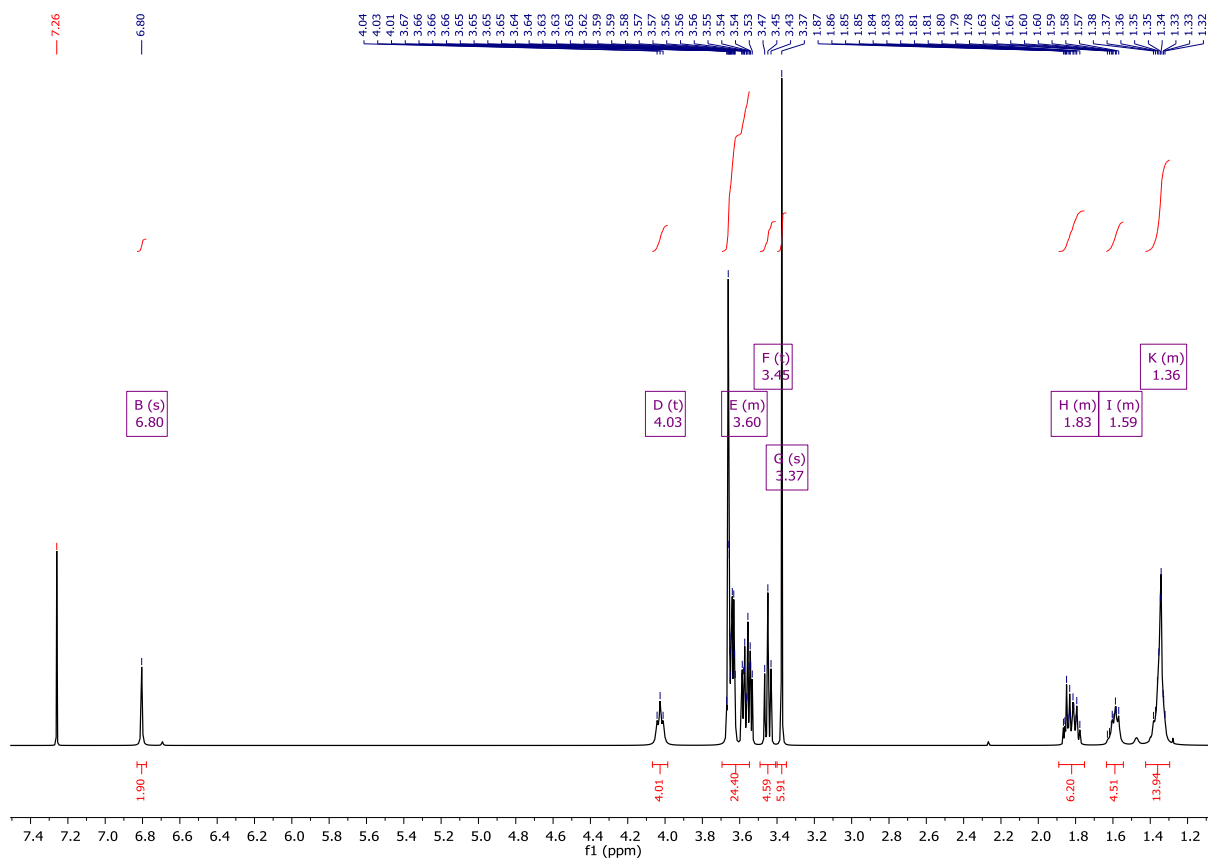


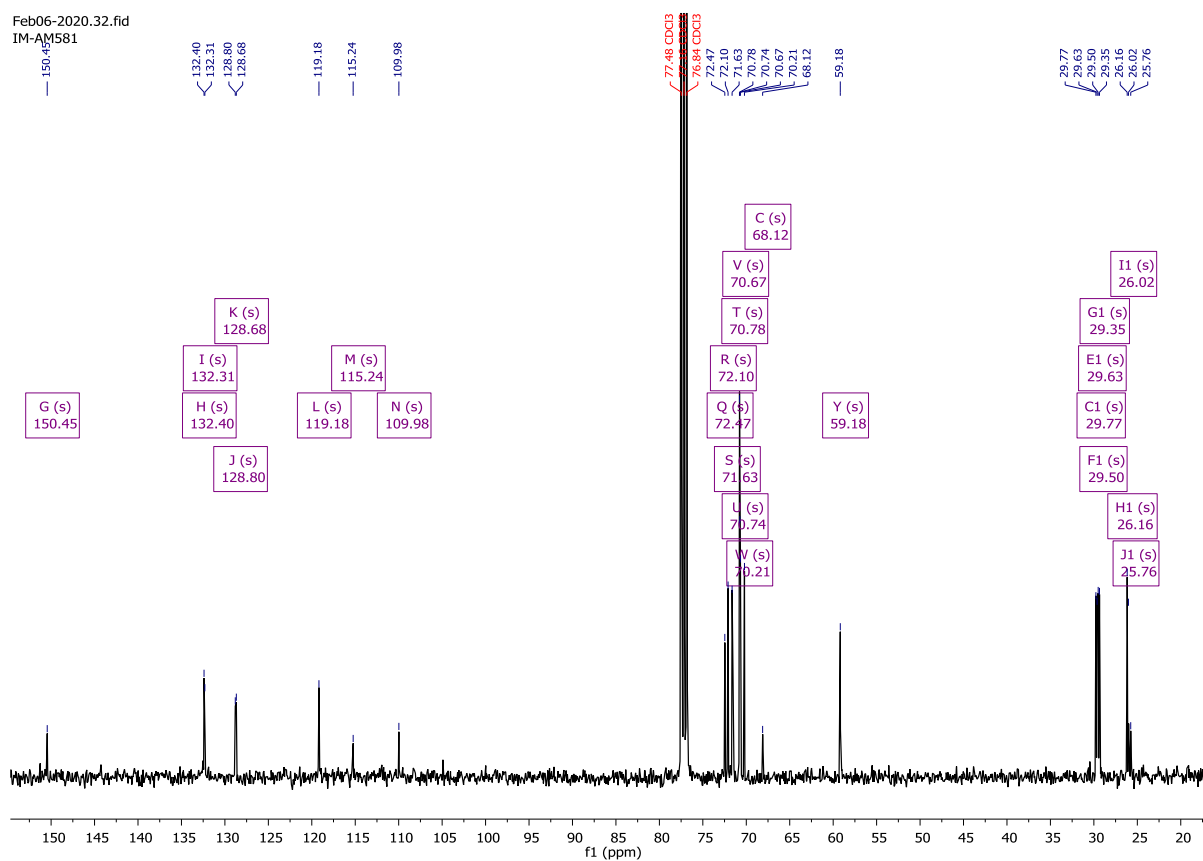
3,3'-bis((2,5,8,11-tetraoxanonadecan-19-yl)oxy)-2,2'-bithiophene (**6.4.26**) (800 mg, 1.07 mmol, 1.0 eq.) was dissolved in 40 mL of anhydrous THF and cooled to 0 °C. The solution was covered and kept in the dark, N-bromosuccinimide (400.2 mg, 2.25 mmol, 2.1 eq.) was subsequently added in 4 even portions, with approximately 4 minutes between each addition. The reaction was stirred for 30 minutes before being poured into water, washed with saturated sodium bicarbonate solution and quenched with sodium metabisulphite. The aqueous phase was extracted three times with DCM, the organic phases were combined and dried over Na₂SO₄ before the solvent was removed under reduced pressure. The crude oil was purified via column chromatography, on silica gel, using 1:1 hexane:ethyl acetate (v/v) as the eluent system. Product fractions were combined, and solvent removed to afford a yellow oil, which solidified at reduced temperature (948 mg, 98%).

¹H NMR (400 MHz, Chloroform-*d*) δ 6.80 (s, 2H), 4.03 (t, *J* = 6.5 Hz, 4H), 3.69 – 3.51 (m, 24H), 3.45 (t, *J* = 6.8 Hz, 4H), 3.37 (s, 6H), 1.89 – 1.75 (m, 6H), 1.65 – 1.54 (m, 4H), 1.42 – 1.30 (m, 14H).

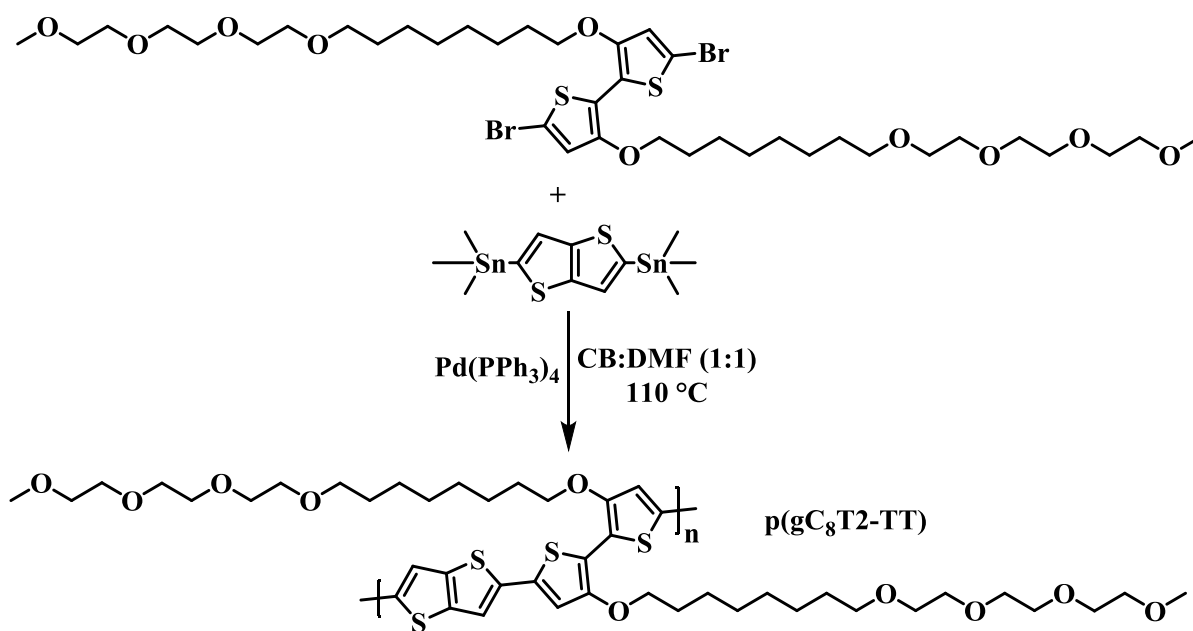
^{13}C NMR (101 MHz, Chloroform-*d*) δ 227.02, 199.51, 150.45, 132.40, 132.31, 128.80, 128.68, 119.18, 115.24, 109.98, 72.47, 72.10, 71.63, 70.78, 70.74, 70.67, 70.21, 68.12, 59.18, 29.77, 29.63, 29.50, 29.35, 26.16, 26.02, 25.76.

Mass (MALDI-ToF): 904.9 $[\text{M}+\text{H}]^+$ (calc. 904.2 $\text{C}_{38}\text{H}_{64}\text{Br}_2\text{O}_{10}\text{S}_2$).





6.4.28 Synthesis of Polymer AM585 p(gC₈T2-TT)



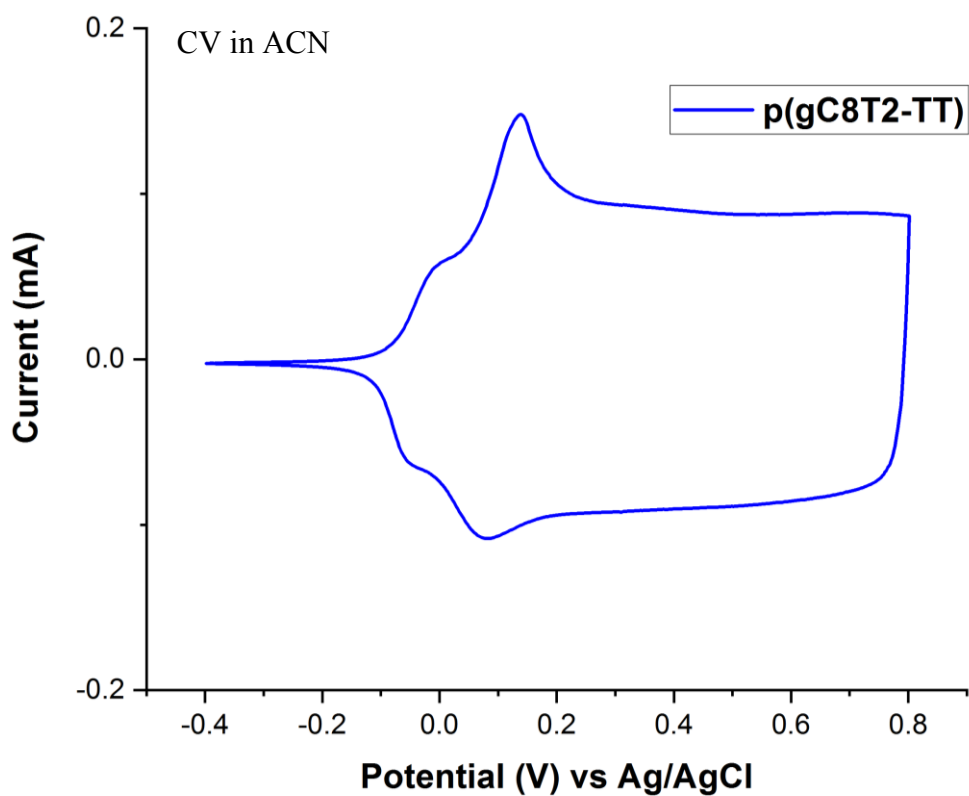
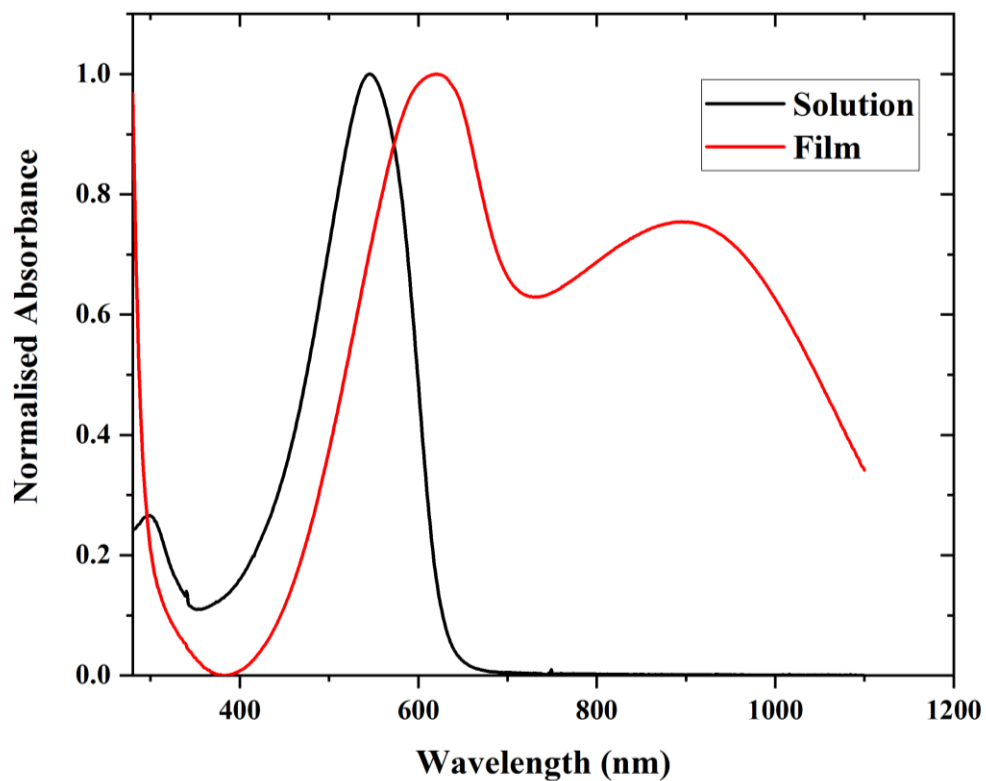
An oven dried 5 mL microwave vial was charged with 19,19'-((5,5'-dibromo-[2,2'-bithiophene]-3,3'-diyl)bis(oxy))bis(2,5,8,11-tetraoxanonadecane) (**6.4.27**) (200 mg, 0.22 mmol, 1.0 eq.), 2,5-bis(trimethylstannyl)thieno[3,2-*b*]thiophene (103 mg, 0.22 mmol, 1.0 eq.) and Pd(PPh₃)₄ (5.11 mg, 0.004 mmol, 0.02 eq.). Cap was sealed and the vial was purged with Nitrogen for 5 minutes prior to the addition of anhydrous DMF (1.47 mL) and anhydrous chlorobenzene (1.47 mL). The reaction was stirred overnight at 110 °C then cooled to room temperature, upon which the solution formed a purple gel. Crude polymer was precipitated into 100 mL methanol and subsequently filtered into a thimble. Purification was conducted via Soxhlet extraction, washing with hexane, methanol, acetone, ethyl acetate and chloroform (in that order). The chloroform fraction was collected, solvent removed under reduced pressure and re-precipitated into 100 mL methanol, filtered to yield a blue metallic film (148 mg, 73%).

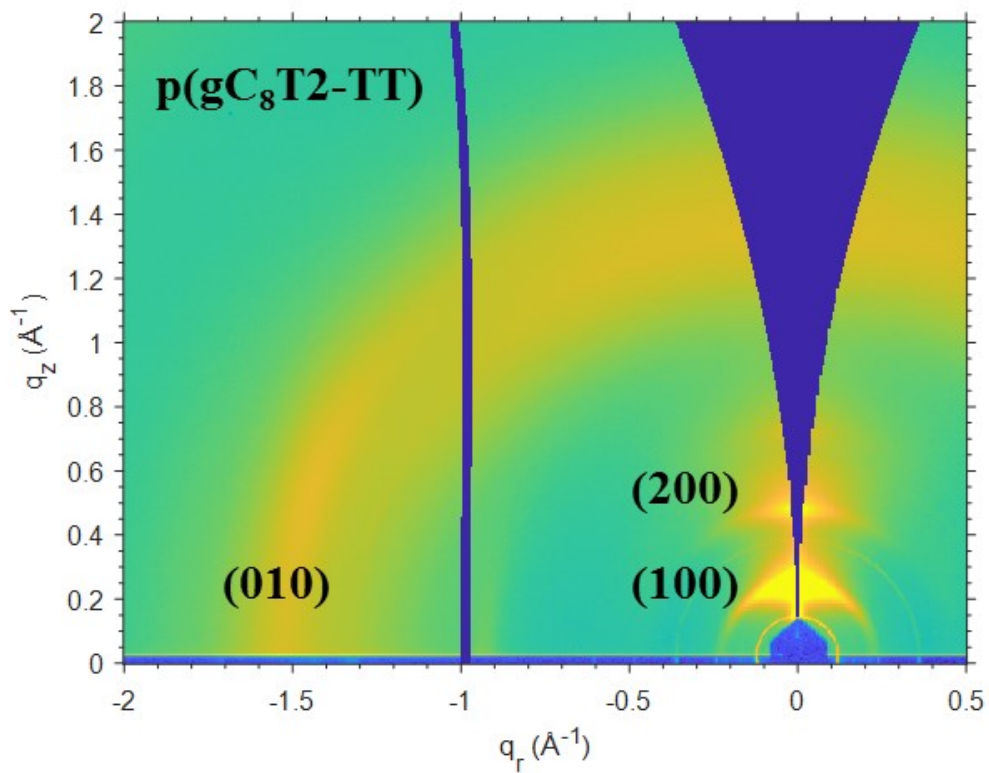
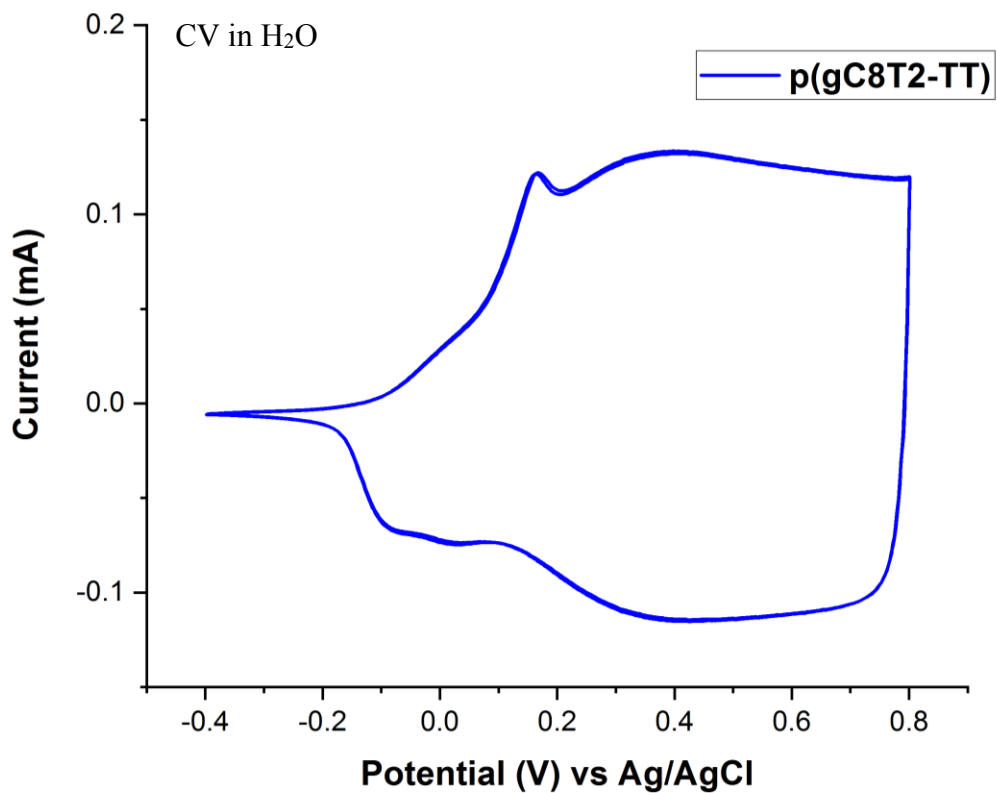
$\lambda_{\text{MAX}}^{\text{a}}$ (nm)	λ_{ONSET} (nm)	$E_{\text{opt}}^{\text{b}}$ (eV)	IP [CV] (eV)	EA ^c (eV)	E_{onset} [ACN](V)	E_{onset} [H ₂ O](V)	M_{n} (kDa)	M_{w} (kDa)	PDI
545	631	1.97	4.26	2.29	-0.12	-0.18	5.9	11.4	1.92

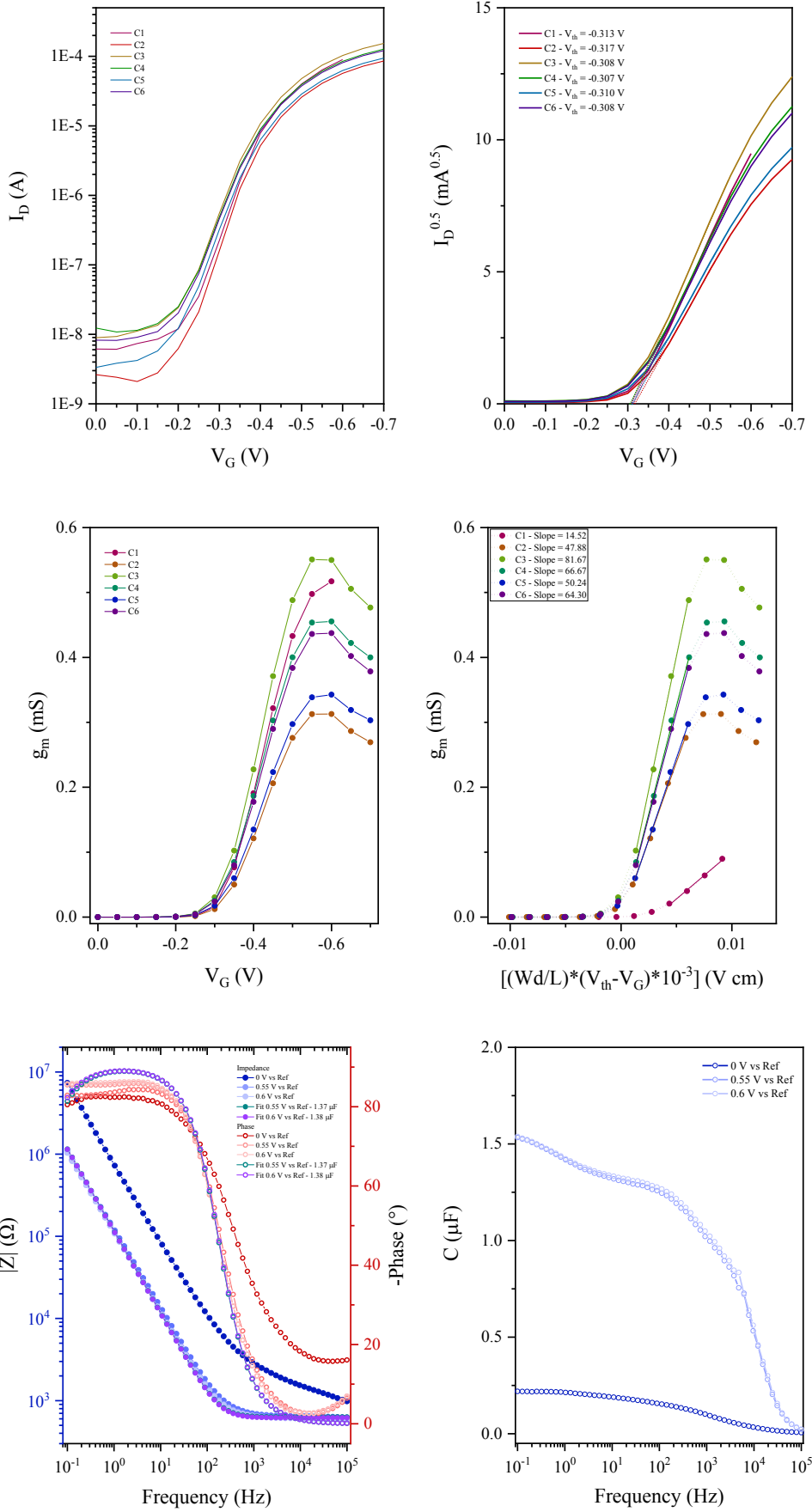
^a λ is the peak of the first low energy absorption band of the polymers

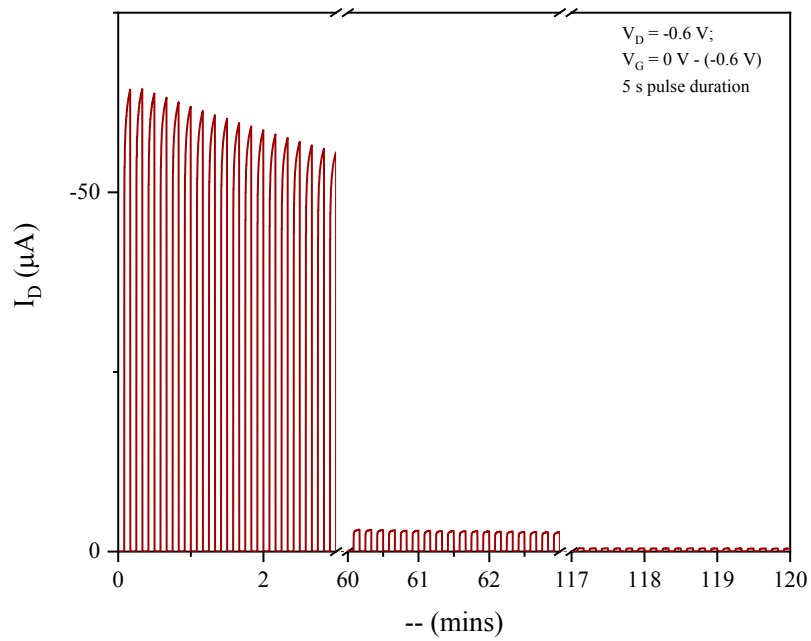
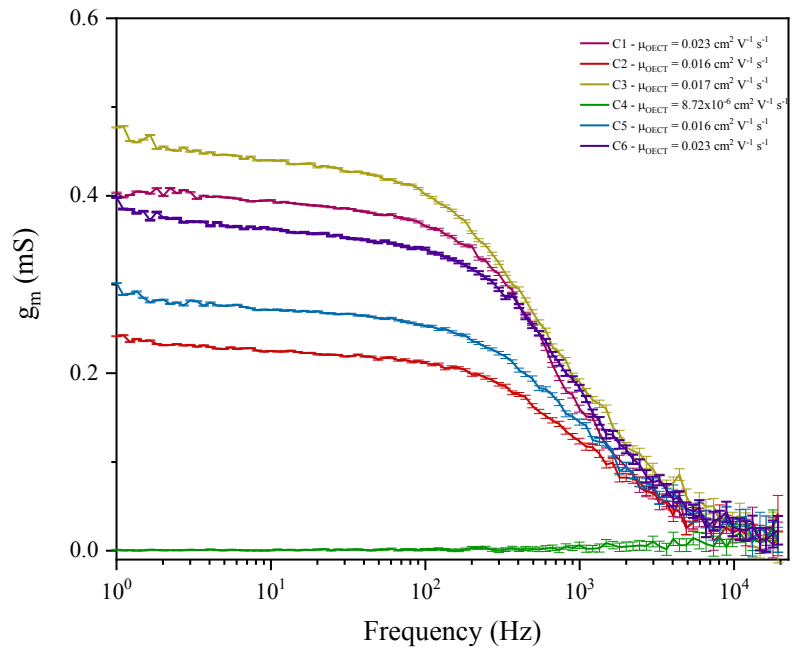
^b E_{opt} estimated optical gap using onset of the thin-film absorption spectra $E_{\text{GAP}} = 1240 / \lambda_{\text{ONSET}}$

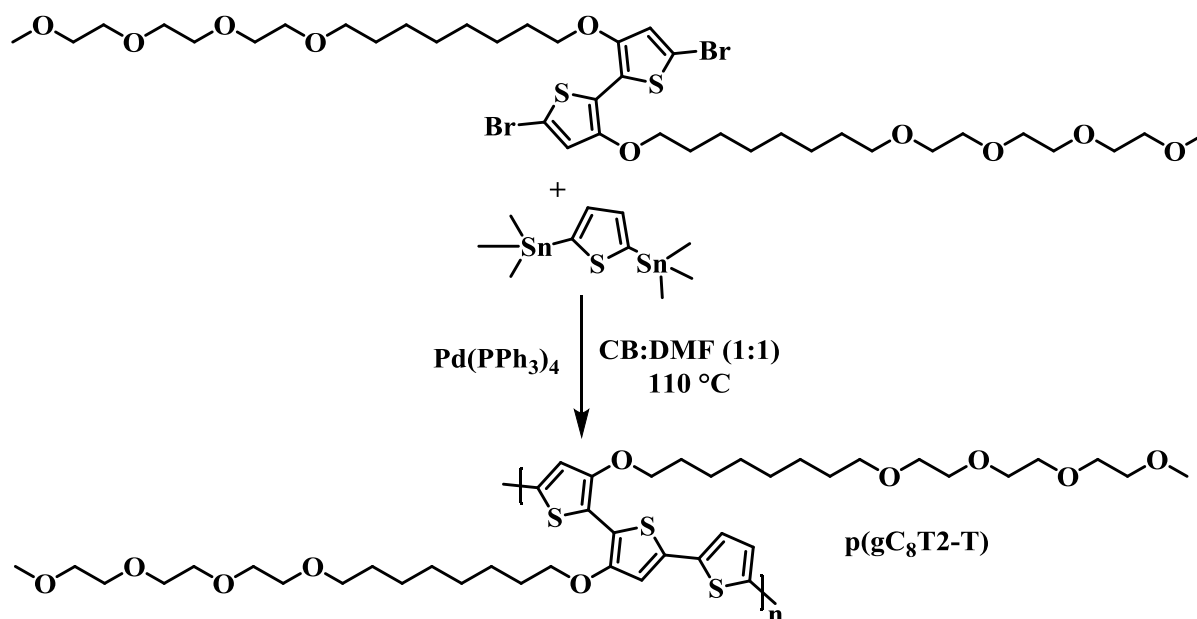
^cEA crudely estimated by subtraction of the UV-Vis absorption onset from IP ($EA = IP - E_{\text{opt}}$), a procedure that neglects the exciton binding energy









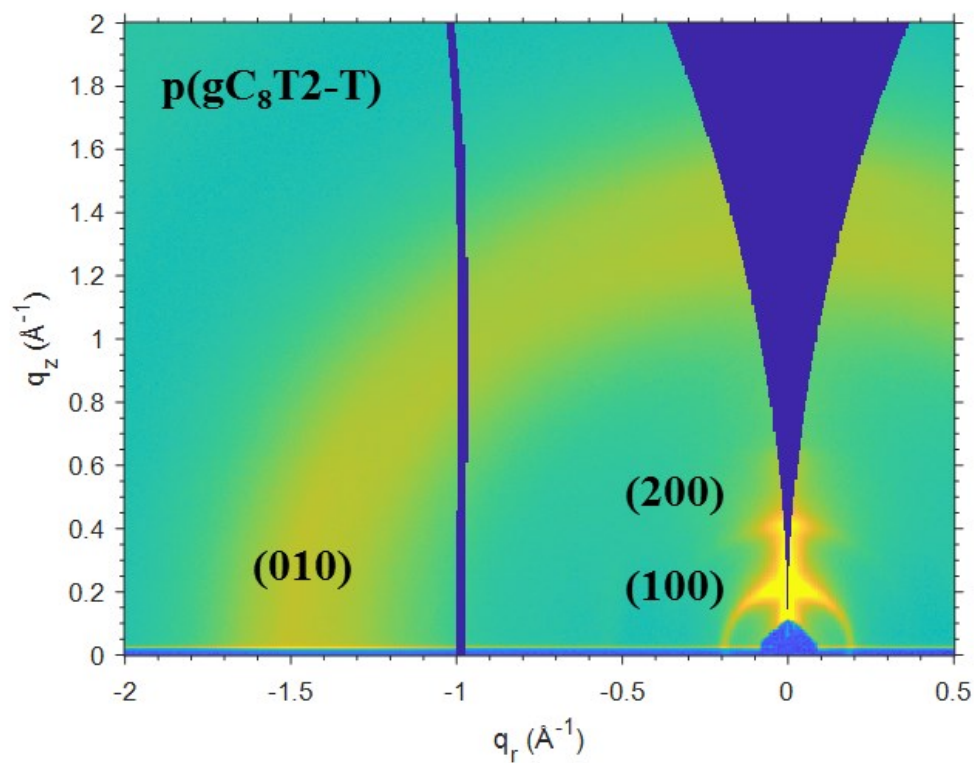
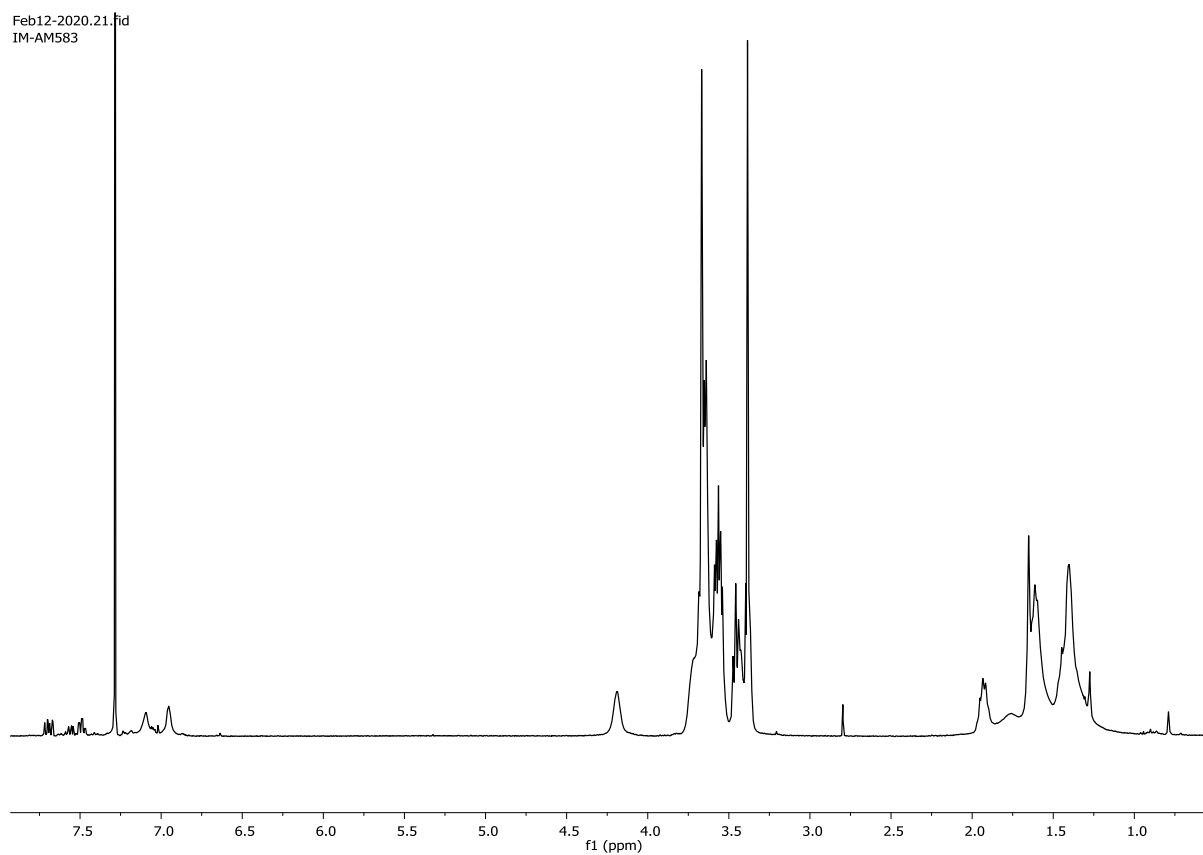
6.4.29 Synthesis of Polymer AM583 p(gC₈T2-T)

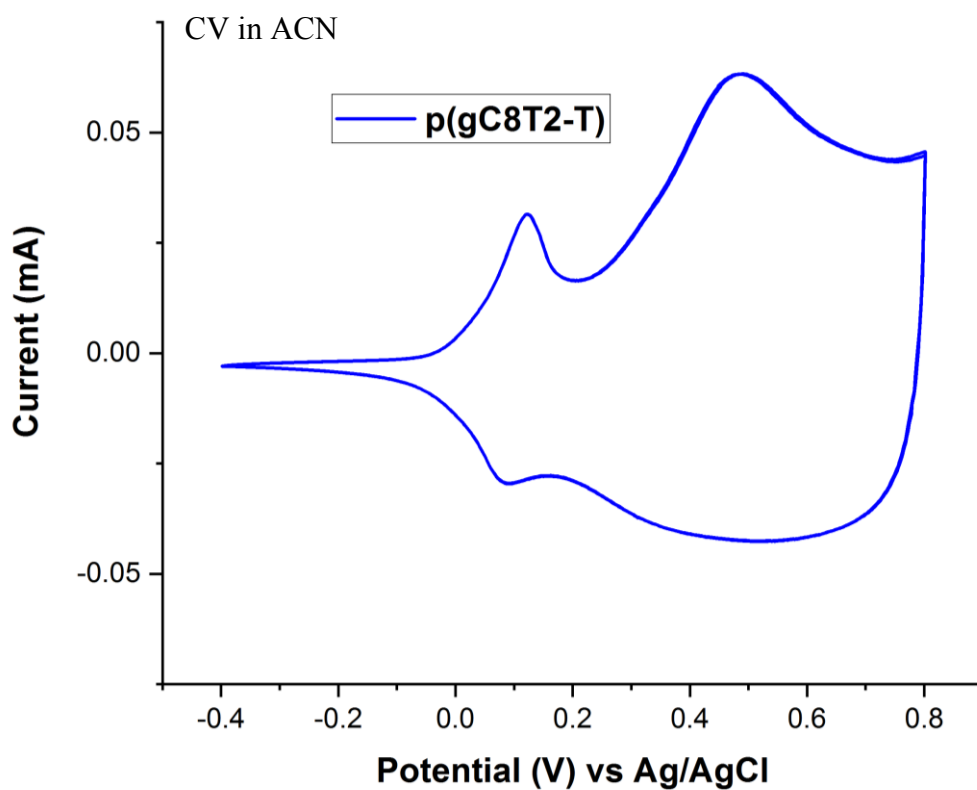
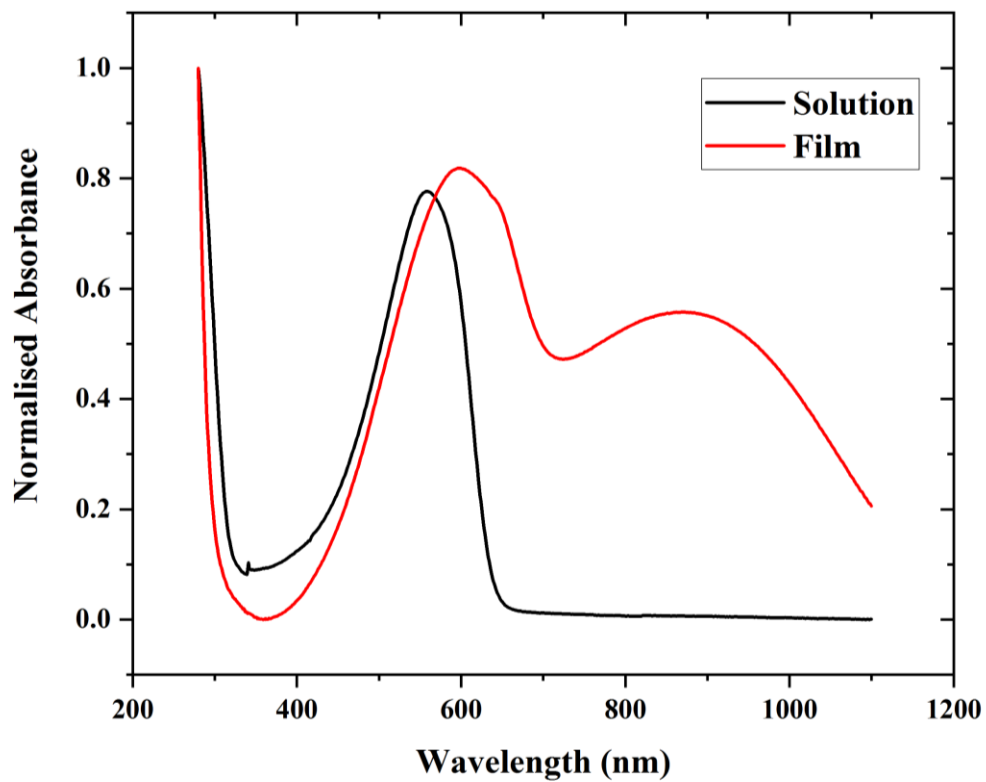
An oven dried 5 mL microwave vial was charged with 19,19'-((5,5'-dibromo-[2,2'-bithiophene]-3,3'-diyl)bis(oxy))bis(2,5,8,11-tetraoxanonadecane) (**6.4.27**) (200 mg, 0.22 mmol, 1.0 eq.), 2,5-bis(trimethylstannyl)thiophene (90.57 mg, 0.22 mmol, 1.0 eq.) and Pd(PPh₃)₄ (5.11 mg, 0.004 mmol, 0.02 eq.). Cap was sealed and the vial was purged with Nitrogen for 5 minutes prior to the addition of anhydrous DMF (1.47 mL) and anhydrous chlorobenzene (1.47 mL). The reaction was stirred overnight at 110 °C then cooled to room temperature, upon which the solution formed a purple gel. Crude polymer was precipitated into 100 mL methanol and subsequently filtered into a thimble. Purification was conducted via Soxhlet extraction, washing with hexane, methanol, acetone, ethyl acetate and chloroform (in that order). The chloroform fraction was collected, solvent removed under reduced pressure and re-precipitated into 100 mL methanol, filtered to yield a blue metallic film (74 mg, 39%).

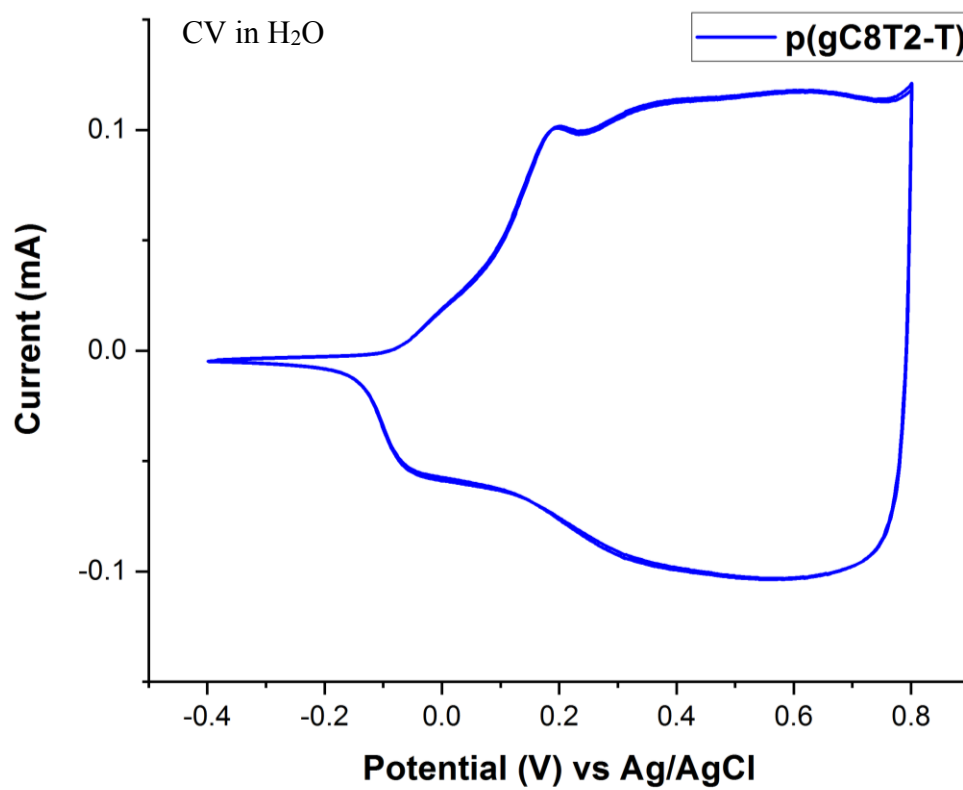
$\lambda_{\text{MAX}}^{\text{a}}$ (nm)	λ_{ONSET} (nm)	$E_{\text{opt}}^{\text{b}}$ (eV)	IP [CV] (eV)	EA ^c (eV)	E_{onset} [ACN](V)	E_{onset} [H ₂ O](V)	M_{n} (kDa)	M_{w} (kDa)	PDI
559	645	1.92	4.34	2.42	-0.04	-0.10	13.3	30.0	2.26

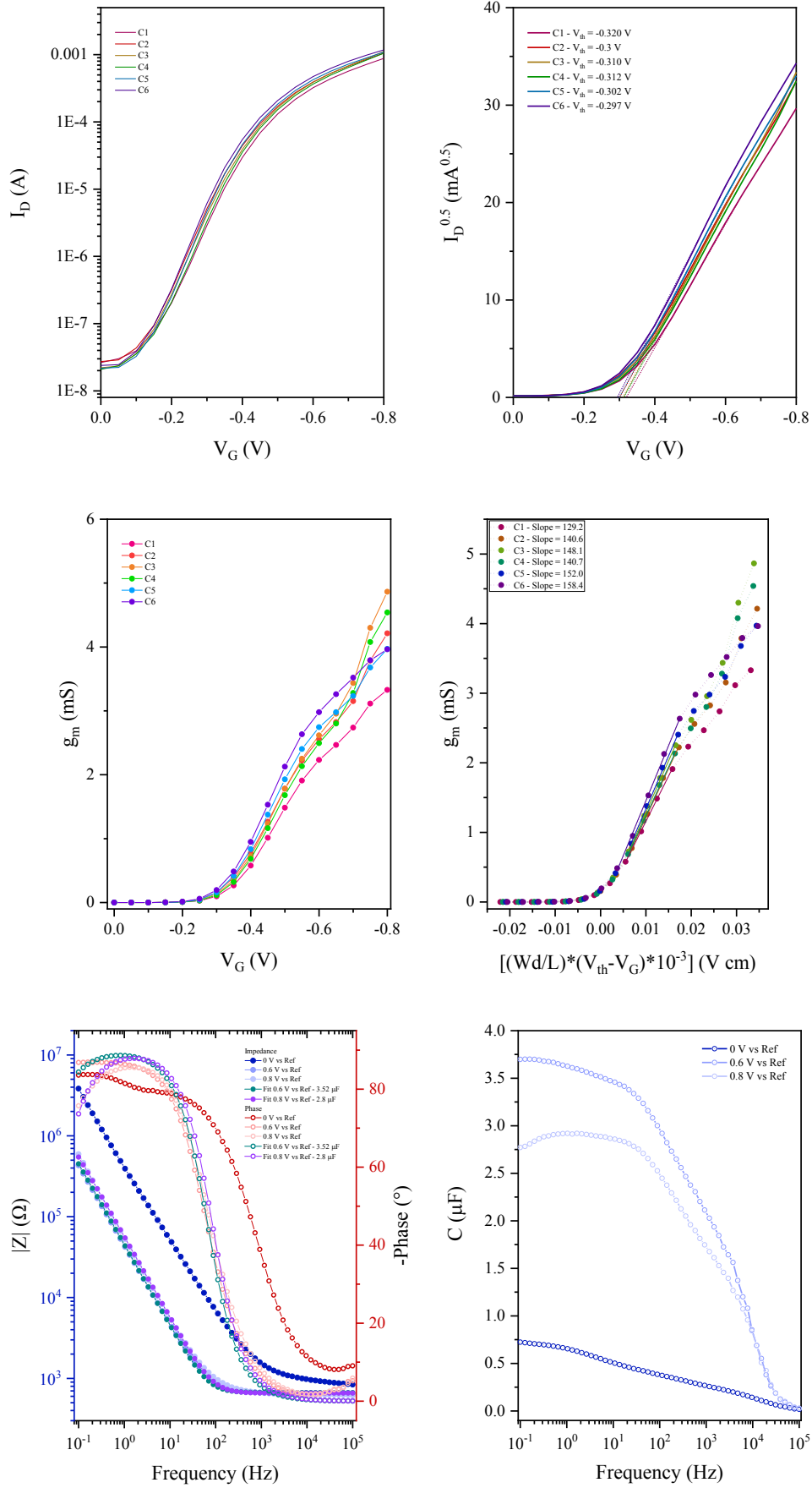
^a λ is the peak of the first low energy absorption band of the polymers

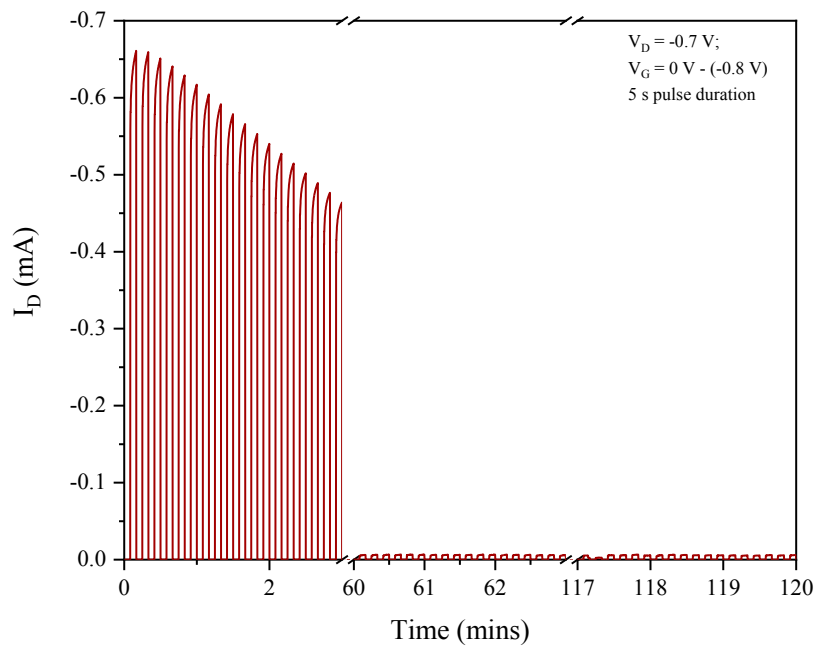
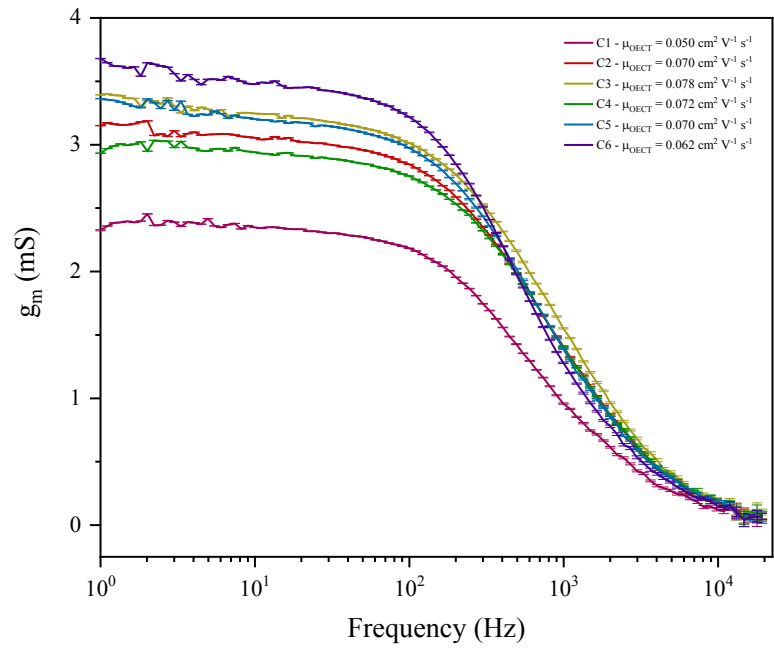
^b E_{opt} estimated optical gap using onset of the thin-film absorption spectra $E_{\text{GAP}} = 1240/\lambda_{\text{ONSET}}$
^c EA crudely estimated by subtraction of the UV-Vis absorption onset from IP ($EA = IP - E_{\text{opt}}$),
a procedure that neglects the exciton binding energy











BIBLIOGRAPHY

- 1 S. M. Sze and K. K. Ng, *Physics of Semiconductor Devices*, Wiley, 2006.
- 2 C. G. Zhan, J. A. Nichols and D. A. Dixon, *J. Phys. Chem. A*, 2003, **107**, 4184–4195.
- 3 J. L. Bredas, *Mater. Horizons*, 2014, **1**, 17–19.
- 4 P. Chandrasekhar, *Conducting Polymers, Fundamentals and Applications*, Springer US, 1999.
- 5 O. Bubnova and X. Crispin, *Energy Environ. Sci.*, 2012, **5**, 9345–9362.
- 6 V. Coropceanu, J. Cornil, D. A. da Silva Filho, Y. Olivier, R. Silbey and J.-L. Brédas, *Chem. Rev.*, 2007, **107**, 926–952.
- 7 T. K. Das and S. Prusty, *Polym. Plast. Technol. Eng.*, 2012, **51**, 1487–1500.
- 8 H. F. Haneef, A. M. Zeidell and O. D. Jurchescu, *J. Mater. Chem. C*, 2020, **8**, 759–787.
- 9 D. Abbaszadeh, A. Kunz, N. B. Kotadiya, A. Mondal, D. Andrienko, J. J. Michels, G. J. A. H. Wetzelaer and P. W. M. Blom, *Chem. Mater.*, 2019, **31**, 6380–6386.
- 10 Y. Yamashita, *Sci. Technol. Adv. Mater.*, 2009, **10**, 24313.
- 11 J. Zaumseil and H. Sirringhaus, *Chem. Rev.*, 2007, **107**, 1296–1323.
- 12 M. Balkanski, R. F. Wallis and R. F. Wallis, *Semiconductor Physics and Applications*, OUP Oxford, 2000.
- 13 J. T. E. Quinn, J. Zhu, X. Li, J. Wang and Y. Li, *J. Mater. Chem. C*, 2017, **5**, 8654–8681.
- 14 A. W. Hains, Z. Liang, M. A. Woodhouse and B. A. Gregg, *Chem. Rev.*, 2010, **110**, 6689–6735.
- 15 N. S. Sariciftci, L. Smilowitz, A. J. Heeger and F. Wudl, *Science*, 1992, **258**, 1474–1476.
- 16 A. Facchetti, *Mater. Today*, 2007, **10**, 28–37.

-
- 17 A. Wadsworth, M. Moser, A. Marks, M. S. Little, N. Gasparini, C. J. Brabec, D. Baran and I. McCulloch, *Chem. Soc. Rev.*, 2019, **48**, 1596.
- 18 S. H. Kim, K. Hong, W. Xie, K. H. Lee, S. Zhang, T. P. Lodge and C. D. Frisbie, *Adv. Mater.*, 2013, **25**, 1822–1846.
- 19 H. S. White, G. P. Kittlesen and M. S. Wrighton, *J. Am. Chem. Soc.*, 1984, **106**, 5375–5377.
- 20 H. Sun, J. Gerasimov, M. Berggren and S. Fabiano, *J. Mater. Chem. C*, 2018, **6**, 11778–11784.
- 21 M. Moser, J. F. Ponder, A. Wadsworth, A. Giovannitti and I. McCulloch, *Adv. Funct. Mater.*, 2019, **29**, 1807033.
- 22 A. Giovannitti, C. B. Nielsen, D.-T. Sbircea, S. Inal, M. Donahue, M. R. Niazi, D. A. Hanifi, A. Amassian, G. G. Malliaras, J. Rivnay and I. McCulloch, *Nat. Commun.*, 2016, **7**, 13066.
- 23 D. Khodagholy, J. Rivnay, M. Sessolo, M. Gurfinkel, P. Leleux, L. H. Jimison, E. Stavrinidou, T. Herve, S. Sanaur, R. M. Owens and G. G. Malliaras, *Nat. Commun.*, 2013, **4**, 2133.
- 24 J. Rivnay, P. Leleux, M. Ferro, M. Sessolo, A. Williamson, D. A. Koutsouras, D. Khodagholy, M. Ramuz, X. Strakosas, R. M. Owens, C. Benar, J. M. Badier, C. Bernard and G. G. Malliaras, *Sci. Adv.*, 2015, **1**, e1400251.
- 25 S. Inal, G. G. Malliaras and J. Rivnay, *Nat. Commun.*, 2017, **8**, 1767.
- 26 H. Shirakawa, *Angew. Chemie Int. Ed.*, 2001, **40**, 2574–2580.
- 27 Y.-J. Cheng, S.-H. Yang and C.-S. Hsu, *Chem. Rev.*, 2009, **109**, 5868–5923.
-

- 28 W. R. Salaneck, R. H. Friend and J. L. Brédas, *Phys. Rep.*, 1999, **319**, 231–251.
- 29 H. Sirringhaus, P. J. Brown, R. H. Friend, M. M. Nielsen, K. Bechgaard, B. M. W. Langeveld-Voss, A. J. H. Spiering, R. A. J. Janssen, E. W. Meijer, P. Herwig and D. M. De Leeuw, *Nature*, 1999, **401**, 685–688.
- 30 I. McCulloch, M. Heeney, C. Bailey, K. Genevicius, I. MacDonald, M. Shkunov, D. Sparrowe, S. Tierney, R. Wagner, W. Zhang, M. L. Chabynyc, R. J. Kline, M. D. McGehee and M. F. Toney, *Nat. Mater.*, 2006, **5**, 328–333.
- 31 C. Wang, H. Dong, W. Hu, Y. Liu and D. Zhu, *Chem. Rev.*, 2012, **112**, 2208–2267.
- 32 M. Sommer, *J. Mater. Chem. C*, 2014, **2**, 3088–3098.
- 33 C. B. Nielsen, M. Turbiez and I. McCulloch, *Adv. Mater.*, 2013, **25**, 1859–1880.
- 34 R. Stalder, J. Mei, K. R. Graham, L. A. Estrada and J. R. Reynolds, *Chem. Mater.*, 2014, **26**, 664–678.
- 35 A. Facchetti, *Chem. Mater.*, 2011, **23**, 733–758.
- 36 X. Zhan, A. Facchetti, S. Barlow, T. J. Marks, M. A. Ratner, M. R. Wasielewski and S. R. Marder, *Adv. Mater.*, 2011, **23**, 268–284.
- 37 S. Holliday, J. E. Donaghey and I. McCulloch, *Chem. Mater.*, 2014, **26**, 647–663.
- 38 Z. Chen, Y. Zheng, H. Yan and A. Facchetti, *J. Am. Chem. Soc.*, 2009, **131**, 8–9.
- 39 C. B. Nielsen, A. Giovannitti, D.-T. T. Sbircea, E. Bandiello, M. R. Niazi, D. A. Hanifi, M. Sessolo, A. Amassian, G. G. Malliaras, J. Rivnay and I. McCulloch, *J. Am. Chem. Soc.*, 2016, **138**, 10252–10259.
- 40 J. K. Stille, *Angew. Chemie Int. Ed. English*, 1986, **25**, 508–524.
- 41 N. Miyaura and A. Suzuki, *Chem. Rev.*, 1995, **95**, 2457–2483.

-
- 42 N. Miyaura, K. Yamada and A. Suzuki, *Tetrahedron Lett.*, 1979, **20**, 3437–3440.
- 43 J. Roncali, *Chem. Rev.*, 1997, **97**, 173–205.
- 44 J. Roncali, *Macromol. Rapid Commun.*, 2007, **28**, 1761–1775.
- 45 N. Kleinhenz, L. Yang, H. Zhou, S. C. Price and W. You, *Macromolecules*, 2011, **44**, 872–877.
- 46 D. Chandran and K.-S. Lee, *Macromol. Res.*, 2013, **21**, 272–283.
- 47 J. Mei and Z. Bao, *Chem. Mater.*, 2014, **26**, 604–615.
- 48 T. Lei, J.-Y. Wang and J. Pei, *Chem. Mater.*, 2014, **26**, 594–603.
- 49 D. Moia, A. Giovannitti, A. A. Szumska, I. P. Maria, E. Rezasoltani, M. Sachs, M. Schnurr, P. R. F. Barnes, I. McCulloch and J. Nelson, *Energy Environ. Sci.*, 2019, **12**, 1349–1357.
- 50 R. Szweda, C. Chendo, L. Charles, P. N. W. Baxter and J. F. Lutz, *Chem. Commun.*, 2017, **53**, 8312–8315.
- 51 A. Giovannitti, D. T. Sbircea, S. Inal, C. B. Nielsen, E. Bandiello, D. A. Hanifi, M. Sessolo, G. G. Malliaras, I. McCulloch and J. Rivnay, *Proc. Natl. Acad. Sci. U. S. A.*, 2016, **113**, 12017–12022.
- 52 B. Meng, H. Song, X. Chen, Z. Xie, J. Liu and L. Wang, *Macromolecules*, 2015, **48**, 4357–4363.
- 53 A. Giovannitti, I. P. Maria, D. Hanifi, M. J. Donahue, D. Bryant, K. J. Barth, B. E. Makdah, A. Savva, D. Moia, M. M. M. Zetek, P. R. F. F. Barnes, O. G. Reid, S. Inal, G. Rumbles, G. G. Malliaras, J. Nelson, J. Rivnay and I. McCulloch, *Chem. Mater.*, 2018, **30**, 2945–2953.
-

- 54 A. Giovannitti, C. B. Nielsen, J. Rivnay, M. Kirkus, D. J. Harkin, A. J. P. White, H. Sirringhaus, G. G. Malliaras and I. McCulloch, *Adv. Funct. Mater.*, 2016, **26**, 514–523.
- 55 X. Chen, Z. Zhang, Z. Ding, J. Liu and L. Wang, *Angew. Chemie Int. Ed.*, 2016, **55**, 10376–10380.
- 56 A. M. Pappa, D. Ohayon, A. Giovannitti, I. P. Maria, A. Savva, I. Uguz, J. Rivnay, I. McCulloch, R. M. Owens and S. Inal, *Sci. Adv.*, 2018, **4**, eaat0911.
- 57 M. Berggren and A. Richter-Dahlfors, *Adv. Mater.*, 2007, **19**, 3201–3213.
- 58 J. Rivnay, R. M. Owens and G. G. Malliaras, *Chem. Mater.*, 2014, **26**, 679–685.
- 59 A.-M. Pappa, O. Parlak, G. Scheiblin, P. Mailley, A. Salleo and R. M. Owens, *Trends Biotechnol.*, 2018, **36**, 45–59.
- 60 A.-M. Pappa, V. F. Curto, M. Braendlein, X. Strakosas, M. J. Donahue, M. Fiocchi, G. G. Malliaras and R. M. Owens, *Adv. Healthc. Mater.*, 2016, **5**, 2295–2302.
- 61 A. P. F. Turner, *Chem. Soc. Rev.*, 2013, **42**, 3184–3196.
- 62 G. J. Snyder and E. S. Toberer, *Nat. Mater.*, 2008, **7**, 105–114.
- 63 K. Kang, S. Watanabe, K. Broch, A. Sepe, A. Brown, I. Nasrallah, M. Nikolka, Z. Fei, M. Heeney, D. Matsumoto, K. Marumoto, H. Tanaka, S. I. Kuroda and H. Sirringhaus, *Nat. Mater.*, 2016, **15**, 896–902.
- 64 R. Kroon, D. Kiefer, D. Stegerer, L. Yu, M. Sommer and C. Müller, *Adv. Mater.*, 2017, **29**, 1700930.
- 65 J. Yamamoto and Y. Furukawa, *J. Phys. Chem. B*, 2015, **119**, 4788–4794.
- 66 A. Giovannitti, Imperial College London, 2018.
- 67 D. Beljonne, J. Cornil, H. Sirringhaus, P. J. Brown, M. Shkunov, R. H. Friend and J. -

- L. Brédas, *Adv. Funct. Mater.*, 2001, **11**, 229–234.
- 68 P. Pingel and D. Neher, *Phys. Rev. B - Condens. Matter Mater. Phys.*, 2013, **87**, 115209.
- 69 A. M. Glaudell, J. E. Cochran, S. N. Patel and M. L. Chabinyk, *Adv. Energy Mater.*, 2015, **5**, 1401072.
- 70 Y. Liu, B. Nell, K. Ortstein, Z. Wu, Y. Karpov, T. Beryozkina, S. Lenk, A. Kiriy, K. Leo and S. Reineke, *ACS Appl. Mater. Interfaces*, 2019, **11**, 11660–11666.
- 71 B. Russ, A. Glaudell, J. J. Urban, M. L. Chabinyk and R. A. Segalman, *Nat. Rev. Mater.*, 2016, **1**, 16050.
- 72 Y. Xia, K. Sun and J. Ouyang, *Adv. Mater.*, 2012, **24**, 2436–2440.
- 73 H. Shimotani, G. Diguët and Y. Iwasa, *Appl. Phys. Lett.*, 2005, **86**, 022104.
- 74 M. Zebarjadi, K. Esfarjani, M. S. Dresselhaus, Z. F. Ren and G. Chen, *Energy Environ. Sci.*, 2012, **5**, 5147–5162.
- 75 O. Ostroverkhova, *Chem. Rev.*, 2016, **116**, 13279–13412.
- 76 A. Armin, D. M. Stoltzfus, J. E. Donaghey, A. J. Clulow, R. C. R. Nagiri, P. L. Burn, I. R. Gentle and P. Meredith, *J. Mater. Chem. C*, 2017, **5**, 3736–3747.
- 77 O. V. Mikhnenko, P. W. M. Blom and T.-Q. Nguyen, *Energy Environ. Sci.*, 2015, **8**, 1867–1888.
- 78 J. L. Brédas, D. Beljonne, V. Coropceanu and J. Cornil, *Chem. Rev.*, 2004, **104**, 4971–5003.
- 79 A. Köhler and H. Bässler, *Mater. Sci. Eng. R Reports*, 2009, **66**, 71–109.
- 80 D. Lubert-Perquel, E. Salvadori, M. Dyson, P. N. Stavrinou, R. Montis, H. Nagashima, Y. Kobori, S. Heutz and C. W. M. Kay, *Nat. Commun.*, 2018, **9**, 4222.

- 81 M. B. Smith and J. Michl, *Chem. Rev.*, 2010, **110**, 6891–6936.
- 82 S. Singh, W. J. Jones, W. Siebrand, B. P. Stoicheff and W. G. Schneider, *J. Chem. Phys.*, 1965, **42**, 330–342.
- 83 M. B. Smith and J. Michl, *Annu. Rev. Phys. Chem.*, 2013, **64**, 361–386.
- 84 K. Miyata, F. S. Conrad-Burton, F. L. Geyer and X.-Y. Zhu, *Chem. Rev.*, 2019, **119**, 4261–4292.
- 85 W. Shockley and H. J. Queisser, *J. Appl. Phys.*, 1961, **32**, 510–519.
- 86 M. C. Hanna and A. J. Nozik, *J. Appl. Phys.*, 2006, **100**, 074510.
- 87 R. E. Merrifield, P. Avakian and R. P. Groff, *Chem. Phys. Lett.*, 1969, **3**, 155–157.
- 88 W. L. Chan, M. Ligges, A. Jailaubekov, L. Kaake, L. Miaja-Avila and X. Y. Zhu, *Science (80-.)*, 2011, **334**, 1541–1545.
- 89 W. L. Chan, M. Ligges and X. Y. Zhu, *Nat. Chem.*, 2012, **4**, 840–845.
- 90 M. Kasha, *Discuss. Faraday Soc.*, 1950, **9**, 14.
- 91 J. Ren, Q. Peng, X. Zhang, Y. Yi and Z. Shuai, *J. Phys. Chem. Lett.*, 2017, **8**, 2175–2181.
- 92 X. Feng and A. I. Krylov, *Phys. Chem. Chem. Phys.*, 2016, **18**, 7751–7761.
- 93 P. M. Zimmerman, Z. Zhang and C. B. Musgrave, *Nat. Chem.*, 2010, **2**, 648–652.
- 94 G. B. Piland, J. J. Burdett, R. J. Dillon and C. J. Bardeen, *J. Phys. Chem. Lett.*, 2014, **5**, 2312–2319.
- 95 R. Tempelaar and D. R. Reichman, *J. Chem. Phys.*, 2017, **146**, 174704.
- 96 I. Paci, J. C. Johnson, X. Chen, G. Rana, D. Popović, D. E. David, A. J. Nozik, M. A.

- Ratner and J. Michl, *J. Am. Chem. Soc.*, 2006, **128**, 16546–16553.
- 97 T. Minami and M. Nakano, *J. Phys. Chem. Lett.*, 2012, **3**, 145–150.
- 98 P. M. Zimmerman, F. Bell, D. Casanova and M. Head-Gordon, 2011, **133**, 19944–19952.
- 99 C. K. Frederickson, B. D. Rose and M. M. Haley, *Acc. Chem. Res.*, 2017, **50**, 977–987.
- 100 B. S. Basel, I. Papadopoulos, D. Thiel, R. Casillas, J. Zirzmeier, T. Clark, D. M. Guldi and R. R. Tykwinski, *Trends Chem.*, 2019, **1**, 11–21.
- 101 M. Solà, *Front. Chem.*, 2013, **1**, 22.
- 102 K. Fukuda, T. Nagami, J. Fujiyoshi and M. Nakano, *J. Phys. Chem. A*, 2015, **119**, 10620–10627.
- 103 D. T. Chase, A. G. Fix, S. J. Kang, B. D. Rose, C. D. Weber, Y. Zhong, L. N. Zakharov, M. C. Lonergan, C. Nuckolls and M. M. Haley, *J. Am. Chem. Soc.*, 2012, **134**, 10349–10352.
- 104 B. S. Young, D. T. Chase, J. L. Marshall and M. M. Haley, 2014, **5**, 1008–1014.
- 105 M. J. Y. Tayebjee, S. N. Sanders, E. Kumarasamy, L. M. Campos, M. Y. Sfeir and D. R. McCamey, *Nat. Phys.*, 2016, **13**, 182–188.
- 106 R. Berera, R. van Grondelle and J. T. M. M. Kennis, *Photosynth. Res.*, 2009, **101**, 105–118.
- 107 J. J. Dressler, M. Teraoka, G. L. Espejo, R. Kishi, S. Takamuku, C. J. Gómez-García, L. N. Zakharov, M. Nakano, J. Casado and M. M. Haley, *Nat. Chem.*, 2018, **10**, 1134–1140.
- 108 S. N. Sanders, E. Kumarasamy, A. B. Pun, M. T. Trinh, B. Choi, J. Xia, E. J. Taffet, J.

- Z. Low, J. R. Miller, X. Roy, X.-Y. Zhu, M. L. Steigerwald, M. Y. Sfeir and L. M. Campos, *J. Am. Chem. Soc.*, 2015, **137**, 8965–8972.
- 109 B. S. Basel, J. Zirzmeier, C. Hetzer, B. T. Phelan, M. D. Krzyaniak, S. R. Reddy, P. B. Coto, N. E. Horwitz, R. M. Young, F. J. White, F. Hampel, T. Clark, M. Thoss, R. R. Tykwinski, M. R. Wasielewski and D. M. Guldi, *Nat. Commun.*, 2017, **8**, 15171.
- 110 E. G. Fuemmeler, S. N. Sanders, A. B. Pun, E. Kumarasamy, T. Zeng, K. Miyata, M. L. Steigerwald, X.-Y. Zhu, M. Y. Sfeir, L. M. Campos and N. Ananth, *ACS Cent. Sci.*, 2016, **2**, 316–324.
- 111 T.-P. Liu, C.-H. Xing and Q.-S. Hu, *Angew. Chemie Int. Ed.*, 2010, **49**, 2909–2912.
- 112 J. Mei, Y. Diao, A. L. Appleton, L. Fang and Z. Bao, *J. Am. Chem. Soc.*, 2013, **135**, 6724–6746.
- 113 D. T. Chase, B. D. Rose, S. P. McClintock, L. N. Zakharov and M. M. Haley, *Angew. Chemie - Int. Ed.*, 2011, **50**, 1127–1130.
- 114 J. L. Marshall, D. Lehnerr, B. D. Lindner and R. R. Tykwinski, *Chempluschem*, 2017, **82**, 967–1001.
- 115 J. Nishida, S. Tsukaguchi and Y. Yamashita, *Chem. - A Eur. J.*, 2012, **18**, 8964–8970.
- 116 B. D. Rose, L. E. Shoer, M. R. Wasielewski and M. M. Haley, *Chem. Phys. Lett.*, 2014, **616**, 137–141.
- 117 H. J. Reich, *Chem. Rev.*, 2013, **113**, 7130–7178.
- 118 T. Ishiyama, M. Murata and N. Miyaura, *J. Org. Chem.*, 1995, **60**, 7508–7510.
- 119 A. J. J. Lennox, G. C. Lloyd-Jones, C.-M. Chou, M. Suginome, M. Suginome, D. R. Cefalo, B. M. Sutton, G. L. Watts, A. J. Whitehead and T. B. Marder, *Chem. Soc. Rev.*,

- 2014, **43**, 412–443.
- 120 C. Hetzer, D. M. Guldi and R. R. Tykwinski, *Chem. - A Eur. J.*, 2018, **24**, 8245–8257.
- 121 C. Wang, Y. Wei, K. Chang, P. Chou and Y. Wu, *Angew. Chemie Int. Ed.*, 2019, **58**, 10158–10162.
- 122 I. Žutić, J. Fabian and S. Das Sarma, *Rev. Mod. Phys.*, 2004, **76**, 323–410.
- 123 V. Baltz, A. Manchon, M. Tsoi, T. Moriyama, T. Ono and Y. Tserkovnyak, *Rev. Mod. Phys.*, 2018, **90**, 015005.
- 124 Y. P. Feng, L. Shen, M. Yang, A. Wang, M. Zeng, Q. Wu, S. Chintalapati and C.-R. Chang, *Wiley Interdiscip. Rev. Comput. Mol. Sci.*, 2017, **7**, e1313.
- 125 M. V. Costache, M. Sladkov, S. M. Watts, C. H. van der Wal and B. J. van Wees, *Phys. Rev. Lett.*, 2006, **97**, 216603.
- 126 Y. Tserkovnyak, A. Brataas and G. E. W. Bauer, *Phys. Rev. Lett.*, 2002, **88**, 4.
- 127 A. Wittmann, G. Schweicher, K. Broch, J. Novak, V. Lami, D. Cornil, E. R. McNellis, O. Zadvorna, D. Venkateshvaran, K. Takimiya, Y. H. Geerts, J. Cornil, Y. Vaynzof, J. Sinova, S. Watanabe and H. Siringhaus, *Phys. Rev. Lett.*, 2020, **124**, 027204.
- 128 L. D. Landau and E. Lifshitz, *Phys. Z. Sowjet.*, 1935, **8**, 153.
- 129 T. L. Gilbert, *IEEE Trans. Magn.*, 2004, **40**, 3443–3449.
- 130 O. Mosendz, J. E. Pearson, F. Y. Fradin, G. E. W. Bauer, S. D. Bader and A. Hoffmann, *Phys. Rev. Lett.*, 2010, **104**, 046601.
- 131 G. Schmidt, *J. Phys. D. Appl. Phys.*, 2005, **38**, R107–R122.
- 132 A. Slachter, F. L. Bakker, J. P. Adam and B. J. Van Wees, *Nat. Phys.*, 2010, **6**, 879–882.

- 133 D. Sun, E. Ehrenfreund and Z. V. Vardeny, *Analyst*, 2014, **50**, 1781–1793.
- 134 R. Geng, T. T. Daugherty, K. Do, H. M. Luong and T. D. Nguyen, *J. Sci. Adv. Mater. Devices*, 2016, **1**, 128–140.
- 135 S. Watanabe, K. Ando, K. Kang, S. Mooser, Y. Vaynzof, H. Kurebayashi, E. Saitoh and H. Sirringhaus, *Nat. Phys.*, 2014, **10**, 308–313.
- 136 H. Nagai, M. Nakano, K. Yoneda, R. Kishi, H. Takahashi, A. Shimizu, T. Kubo, K. Kamada, K. Ohta, E. Botek and B. Champagne, *Chem. Phys. Lett.*, 2010, **489**, 212–218.
- 137 E. Clar, *The aromatic sextet*, New York, Wiley, 1972.
- 138 Z. Sun and J. Wu, *J. Mater. Chem.*, 2012, **22**, 4151–4160.
- 139 J. E. Anthony, *Chem. Rev.*, 2006, **106**, 5028–5048.
- 140 A. Shimizu, R. Kishi, M. Nakano, D. Shiomi, K. Sato, T. Takui, I. Hisaki, M. Miyata and Y. Tobe, *Angew. Chemie - Int. Ed.*, 2013, **52**, 6076–6079.
- 141 S. Schott, E. R. McNellis, C. B. Nielsen, H.-Y. Chen, S. Watanabe, H. Tanaka, I. McCulloch, K. Takimiya, J. Sinova and H. Sirringhaus, *Nat. Commun.*, 2017, **8**, 15200.
- 142 I. McCulloch, R. S. Ashraf, L. Biniek, H. Bronstein, C. Combe, J. E. Donaghey, D. I. James, C. B. Nielsen, B. C. Schroeder and W. Zhang, *Acc. Chem. Res.*, 2012, **45**, 714–722.
- 143 J. L. Marshall, K. Uchida, C. K. Frederickson, C. Schütt, A. M. Zeidell, K. P. Goetz, T. W. Finn, K. Jarolimek, L. N. Zakharov, C. Risko, R. Herges, O. D. Jurchescu and M. M. Haley, *Chem. Sci.*, 2016, **7**, 5547–5558.
- 144 M. S. Little, The University of Manchester, 2014.
- 145 J. A. Bull, M. G. Hutchings and P. Quayle, *Angew. Chemie - Int. Ed.*, 2007, **46**, 1869–

- 1872.
- 146 X. Yang, X. Dou and K. Müllen, *Chem. – An Asian J.*, 2008, **3**, 759–766.
- 147 D. Lorbach, A. Keerthi, T. M. Figueira-Duarte, M. Baumgarten, M. Wagner and K. Müllen, *Angew. Chemie Int. Ed.*, 2016, **55**, 418–421.
- 148 G. H. Posner, E. M. Shulman-Roskes, C. H. Oh, J. C. Carry, J. V. Green, A. B. Clark, H. Dai and T. E. N. Anjeh, *Tetrahedron Lett.*, 1991, **32**, 6489–6492.
- 149 P. P. Fu and R. G. Harvey, *Chem. Rev.*, 1978, **78**, 317–361.
- 150 C. K. Frederickson, J. E. Barker, J. J. Dressler, Z. Zhou, E. R. Hanks, J. P. Bard, L. N. Zakharov, M. A. Petrukhina and M. M. Haley, *Synlett*, 2018, **29**, 2562–2566.
- 151 S. D. Walker, T. E. Barder, J. R. Martinelli and S. L. Buchwald, *Angew. Chemie - Int. Ed.*, 2004, **43**, 1871–1876.
- 152 G. E. Rudebusch, J. L. Zafra, K. Jorner, K. Fukuda, J. L. Marshall, I. Arrechea-Marcos, G. L. Espejo, R. Ponce Ortiz, C. J. Gómez-García, L. N. Zakharov, M. Nakano, H. Ottosson, J. Casado and M. M. Haley, *Nat. Chem.*, 2016, **8**, 753–759.
- 153 J. E. Anthony, J. S. Brooks, D. L. Eaton and S. R. Parkin, *J. Am. Chem. Soc.*, 2001, **123**, 9482–9483.
- 154 W. Fudickar and T. Linker, *J. Am. Chem. Soc.*, 2012, **134**, 15071–15082.
- 155 J.-H. J.-W. Park, D. Sung Chung, J.-H. J.-W. Park, T. Ahn, H. Kong, Y. Kwan Jung, J. Lee, M. Hye Yi, C. Eon Park, S.-K. Kwon and H.-K. Shim, *Org. Lett.*, 2007, **9**, 2573–2576.
- 156 F. F. Karam, F. H. Hussein, S. J. Baqir, A. F. Halbus, R. Dillert and D. Bahnemann, *Int. J. Photoenergy*, 2014, **2014**, 1–6.

- 157 T. Nishinaga, M. M. Haley and J. L. Marshall, *Organic redox systems : synthesis, properties, and applications*, Wiley, 2016.
- 158 T. Kubo, A. Shimizu, M. Sakamoto, M. Uruichi, K. Yakushi, M. Nakano, D. Shiomi, K. Sato, T. Takui, Y. Morita and K. Nakasuji, *Angew. Chemie Int. Ed.*, 2005, **44**, 6564–6568.
- 159 | Presto-Jst ; Berson, J. A. Matsuda, K. Iwamura, H. McMasters, D. R. Wirz, J. Abe, M. Kawakami, T. Ohata, S. Nozaki and K. Nojima, *J. Am. Chem. Soc.*, 1997, **30**, 5.
- 160 A. Wittmann, University of Cambridge, 2019.
- 161 S. M. Ryno, C. Risko and J.-L. Bre, *J. Am. Chem. Soc.*, 2014, **136**.
- 162 T. Liu and A. Troisi, *Adv. Mater.*, 2013, **25**, 1038–1041.
- 163 S. Holliday, R. S. Ashraf, A. Wadsworth, D. Baran, S. A. Yousaf, C. B. Nielsen, C.-H. Tan, S. D. Dimitrov, Z. Shang, N. Gasparini, M. Alamoudi, F. Laquai, C. J. Brabec, A. Salleo, J. R. Durrant and I. McCulloch, *Nat. Commun.*, 2016, **7**, 11585.
- 164 W. Liu, W. Li, J. Yao and C. Zhan, *Chinese Chem. Lett.*, 2018, **29**, 381–384.
- 165 J.-R. Pouliot, F. Grenier, J. T. Blaskovits, S. Beaupré and M. Leclerc, *Chem. Rev.*, 2016, **116**, 14225–14274.
- 166 X. Wang and M. Wang, *Polym. Chem.*, 2014, **5**, 5784–5792.
- 167 C. Li, M. Cai, X. Bao, Y. Liu, R. Yang and X. Wan, *RSC Adv.*, 2019, **9**, 12310–12318.
- 168 H. Fu, Z. Wang, Y. Sun, Y. Zheng, J. Huang, G. Wang, J. Kong, D. Huang, M. Mohadjer Beromi, N. Hazari, A. D. Taylor, J. Yu, L. Vinet, A. Zhedanov, S. Li, L. Ye, W. Zhao, S. Zhang, S. Mukherjee, H. Ade, J. Hou, Z. Fei, F. D. Eisner, X. Jiao, M. Azzouzi, J. A. Röhr, Y. Han, M. Shahid, A. S. R. Chesman, C. D. Easton, C. R. McNeill, T. D.

- Anthopoulos, J. Nelson, M. Heeney, F. Huang, Y. Cao, Z. Fei, F. D. Eisner, X. Jiao, M. Azzouzi, J. A. Röhr, Y. Han, M. Shahid, A. S. R. Chesman, C. D. Easton, C. R. McNeill, T. D. Anthopoulos, J. Nelson, M. Heeney, S. Holliday, R. S. Ashraf, A. Wadsworth, D. Baran, S. A. Yousaf, C. B. Nielsen, C. H. Tan, S. D. Dimitrov, Z. Shang, N. Gasparini, M. Alamoudi, F. Laquai, C. J. Brabec, A. Salleo, J. R. Durrant and I. McCulloch, *Adv. Mater.*, 2016, **28**, 9423–9429.
- 169 Y. Sun, Y. Guo and Y. Liu, *Mater. Sci. Eng. R Reports*, 2019, **136**, 13–26.
- 170 B. Carsten, F. He, H. J. Son, T. Xu and L. Yu, *Chem. Rev.*, 2011, **111**, 1493–1528.
- 171 A. Marrocchi, D. Lanari, A. Facchetti and L. Vaccaro, *Energy Environ. Sci.*, 2012, **5**, 8457.
- 172 D. Venkateshvaran, M. Nikolka, A. Sadhanala, V. Lemaur, M. Zelazny, M. Kepa, M. Hurhangee, A. J. Kronemeijer, V. Pecunia, I. Nasrallah, I. Romanov, K. Broch, I. McCulloch, D. Emin, Y. Olivier, J. Cornil, D. Beljonne and H. Sirringhaus, *Nature*, 2014, **515**, 384–388.
- 173 J.-K. Lee, M. C. Gwinner, R. Berger, C. Newby, R. Zentel, R. H. Friend, H. Sirringhaus and C. K. Ober, *J. Am. Chem. Soc.*, 2011, **133**, 9949–9951.
- 174 T. Lei, X. Xia, J. Y. Wang, C. J. Liu and J. Pei, *J. Am. Chem. Soc.*, 2014, **136**, 2135–2141.
- 175 A. Onwubiko, W. Yue, C. Jellett, M. Xiao, H.-Y. Chen, M. K. Ravva, D. A. Hanifi, A.-C. Knall, B. Purushothaman, M. Nikolka, J.-C. Flores, A. Salleo, J.-L. Bredas, H. Sirringhaus, P. Hayoz and I. McCulloch, *Nat. Commun.*, 2018, **9**, 416.
- 176 D. Feng, G. Barton and C. N. Scott, *Org. Lett.*, 2019, **21**, 1973–1978.
- 177 A. Guyot and J. Marineit, *Comptes Rendus Hebd. des seances l Acad. des Sci.*, 1913,

- 156, 1625–1628.
- 178 N. M. Randell, P. C. Boutin and T. L. Kelly, *J. Mater. Chem. A*, 2016, **4**, 6940–6945.
- 179 J. F. M. da Silva, S. J. Garden and A. C. Pinto, *J. Braz. Chem. Soc.*, 2001, **12**, 273–324.
- 180 C. Jellett, Imperial College London, 2019.
- 181 Y. Jiang, Y. Gao, H. Tian, J. Ding, D. Yan, Y. Geng and F. Wang, *Macromolecules*, 2016, **49**, 2135–2144.
- 182 E. J. Hennessy and S. L. Buchwald, *J. Am. Chem. Soc.*, 2003, **125**, 12084–12085.
- 183 B. Meng, J. Liu and L. Wang, *Polym. Chem.*, 2020, **11**, 1261–1270.
- 184 Z. Xu, S.-J. Zhao, J.-L. Deng, Q. Wang and Z.-S. Lv, *J. Heterocycl. Chem.*, 2019, **56**, 325–330.
- 185 J. L. Romera, J. M. Cid and A. A. Trabanco, *Tetrahedron Lett.*, 2004, **45**, 8797–8800.
- 186 X. Chen, Z. Zhang, J. Liu and L. Wang, *Polym. Chem.*, 2017, **8**, 5496–5503.
- 187 J. T. Friedlein, R. R. McLeod and J. Rivnay, *Org. Electron.*, 2018, **63**, 398–414.
- 188 R. J. Kline, M. D. McGehee, E. N. Kadnikova, J. Liu and J. M. J. Fréchet, *Adv. Mater.*, 2003, **15**, 1519–1522.
- 189 H. Sun, M. Vagin, S. Wang, X. Crispin, R. Forchheimer, M. Berggren and S. Fabiano, *Adv. Mater.*, 2018, **30**, 1704916.
- 190 C. M. Proctor, J. Rivnay and G. G. Malliaras, *J. Polym. Sci. Part B Polym. Phys.*, 2016, **54**, 1433–1436.
- 191 X. Yan, M. Xiong, J. T. Li, S. Zhang, Z. Ahmad, Y. Lu, Z. Y. Wang, Z. F. Yao, J. Y. Wang, X. Gu and T. Lei, *J. Am. Chem. Soc.*, 2019, **141**, 20215–20221.

-
- 192 S. Wang, H. Sun, U. Ail, M. Vagin, P. O. Å. Persson, J. W. Andreasen, W. Thiel, M. Berggren, X. Crispin, D. Fazzi and S. Fabiano, *Adv. Mater.*, 2016, **28**, 10764–10771.
- 193 C. Kanimozhi, N. Yaacobi-Gross, E. K. Burnett, A. L. Briseno, T. D. Anthopoulos, U. Salzner and S. Patil, *Phys. Chem. Chem. Phys.*, 2014, **16**, 17253–17265.
- 194 Y. Wang, E. Zeglio, H. Liao, J. Xu, F. Liu, Z. Li, I. P. Maria, D. Mawad, A. Herland, I. McCulloch and W. Yue, *Chem. Mater.*, 2019, **31**, 9797–9806.
- 195 W. Du, King Abdullah University of Science and Technology, 2018.
- 196 T. C. Parker and S. R. Marder, *Synthetic Methods in Organic Electronic and Photonic Materials: A Practical Guide*, Royal Society of Chemistry, 2019.
- 197 D. W. Slocum, P. L. Gierer, S. Gronowitz, B. Cederland, A. B. Hornfeldt, Y. L. Litvinov, V. P. Sukiasyan, A. N. Gronowitz and S. Arkiv, *The Directing Ability of the Methylthio Substituent in Lithiation Reactions of Thiophenes*, 1985, vol. 50.
- 198 A. Savva, R. Hallani, C. Cendra, J. Surgailis, T. C. Hidalgo, S. Wustoni, R. Sheelamanthula, X. Chen, M. Kirkus, A. Giovannitti, A. Salleo, I. McCulloch and S. Inal, *Adv. Funct. Mater.*, 2020, **30**, 1907657.
- 199 D. A. Bernards and G. G. Malliaras, *Adv. Funct. Mater.*, 2007, **17**, 3538–3544.
- 200 A. G. Dixon, R. Visvanathan, N. A. Clark, N. Stingelin, N. Kopidakis and S. E. Shaheen, *J. Polym. Sci. Part B Polym. Phys.*, 2018, **56**, 31–35.
- 201 A. Giovannitti, K. J. Thorley, C. B. Nielsen, J. Li, M. J. Donahue, G. G. Malliaras, J. Rivnay and I. McCulloch, *Adv. Funct. Mater.*, 2018, **28**, 1706325.
- 202 H. P. H. M. J. Frisch, G. W. Trucks, H. B. Schlegel, G. E. Scuseria, M. A. Robb, J. R. Cheeseman, G. Scalmani, V. Barone, B. Mennucci, G. A. Petersson, H. Nakatsuji, M.

- Caricato, X. Li and and D. J. F. A. F. Izmaylov, J. Bloino, G. Zheng, J. L. Sonnenberg, M. Hada, M. Ehara, K. Toyota, R. Fukuda, J. Hasegawa, M. Ishida, T. Nakajima, Y. Honda, O. Kitao, H. Nakai, T. Vreven, J. A. Montgomery, Jr., J. E. Peralta, F. Ogliaro, M. Bearpark, J. J. Heyd, E. Bro, 2010.
- 203 A. Das, T. Müller, F. Plasser and H. Lischka, *J. Phys. Chem. A*, 2016, **120**, 1625–1636.
- 204 S. Wang, D. Fazzi, Y. Puttisong, M. J. Jafari, Z. Chen, T. Ederth, J. W. Andreasen, W. M. Chen, A. Facchetti and S. Fabiano, *Chem. Mater.*, 2019, **31**, 3395–3406.
- 205 J. Rivnay, M. Ramuz, P. Leleux, A. Hama, M. Huerta and R. M. Owens, *Appl. Phys. Lett.*, 2015, **106**, 043301.
- 206 K. Majumdar, B. Chattopadhyay and S. Chakravorty, *Synthesis (Stuttg.)*, 2009, **2009**, 674–680.